



HAL
open science

Diversity of organic richness in solar-type protostars : did the proto-solar-system experience a hot corino phase ?

Mathilde Bouvier

► To cite this version:

Mathilde Bouvier. Diversity of organic richness in solar-type protostars : did the proto-solar-system experience a hot corino phase?. Solar and Stellar Astrophysics [astro-ph.SR]. Université Grenoble Alpes [2020-..], 2022. English. NNT : 2022GRALY001 . tel-03736446

HAL Id: tel-03736446

<https://theses.hal.science/tel-03736446>

Submitted on 22 Jul 2022

HAL is a multi-disciplinary open access archive for the deposit and dissemination of scientific research documents, whether they are published or not. The documents may come from teaching and research institutions in France or abroad, or from public or private research centers.

L'archive ouverte pluridisciplinaire **HAL**, est destinée au dépôt et à la diffusion de documents scientifiques de niveau recherche, publiés ou non, émanant des établissements d'enseignement et de recherche français ou étrangers, des laboratoires publics ou privés.

THÈSE

Pour obtenir le grade de

DOCTEUR DE L'UNIVERSITÉ GRENOBLE ALPES

Spécialité : Astrophysique et Milieux Dilués

Arrêté ministériel : 25 mai 2016

Présentée par

Mathilde BOUVIER

Thèse dirigée par **Cecilia CECCARELLI**, Astronome, Université Grenoble Alpes
et co-encadrée par **Ana LÓPEZ-SEPULCRE**, Astronome-adjoint, Université Grenoble Alpes et Institut de Radio Astronomie Millimétrique

préparée au sein du **Laboratoire Institut de Planétologie et d'Astrophysique de Grenoble**
dans l'**École Doctorale Physique**

Diversité chimique organique dans les proto-étoiles de type solaire: le proto-système solaire a-t-il connu une phase 'hot corino' ?

Diversity of organic richness in solar-type protostars: did the proto-Solar-System experience a hot corino phase?

Thèse soutenue publiquement le **21 janvier 2022**,
devant le jury composé de :

Madame MARYVONNE GERIN

Directrice de recherche, LERMA, CNRS, Rapporteure

Madame SERENA VITI

Professeure, Universiteit Leiden, Rapporteure

Madame CHARLOTTE VASTEL

Astronome, IRAP, Examinatrice

Monsieur PETER SCHILKE

Professeur, Universität zu Köln, Examineur

Monsieur ERIC QUIRICO

Professeur des Universités, Université Grenoble Alpes, Président

Monsieur SATOSHI YAMAMOTO

Professeur, University of Tokyo, invité



“Fais de ta vie un rêve, et d’un rêve, une réalité.”

Antoine de Saint-Exupéry

Acknowledgements

Thesis. Such a small word to describe such a great adventure. The thesis is the beginning of a life of research and the end of a student's life. The thesis is about conferences, meetings, deadlines, articles. It is successes, failures, difficulties to overcome. It is also laughter, tears, stress, wonder, questioning. In short, the thesis is a lot of things and nobody will describe it the same way. One cannot leave it on its doorstep when you come home at night. It follows us like a shadow. It is part of our days, our nights and our weekends. We can both adore it and hate it. Fortunately, I can say today that I spent more time adoring it than hating it. Finally, my thesis is also about being surrounded by a team, friends and a family. I have not spent the last three years alone, far from it, and I would like to thank the following people.

First of all, I would like to thank my two thesis supervisors, Cecilia and Ana, without whom I would not be writing these lines today. I cannot thank you enough for trusting me for almost four years. Thank you for training me as an astrochemist and for guiding me and continuing to do so. Thanks also to the local members of ACO/DOC, for creating a more than a pleasant environment in which to evolve. Thanks to Joan, Arezu, Eleonora, Fanny, Pedro, Cécile, Layal, Lorenzo, Marie, André, Simon, Juan, Bertrand, Claudine, and all the other ACO students. Most of all, a big thank you to my wonderful co-bureau, Marta, for being a great friend, for putting up with me and for our memorable adventures (especially in the USA!). A big thank you to all the other PhD students/post-docs in the lab with whom I shared wonderful moments and years at IPAG. Thank you so much Jolantha, Aina, Junko, Ricardo, Robin, Jian, Léo, Van Phan, Alois, Guillaume, Simon, Kim, Jonatan, Noemi, Benjamin. To end with the working environment, a big thank you also to the members of the Interstellar team and more generally to all the IPAG staff for your welcome.

Now, I would also like to thank my family enormously for all the emotional support they have given me: Anouk and Thaïs, you are wonderful sisters and I wish you to blossom in the path you have chosen, as I have done. Thank you for all the amazing moments of sisterhood that we share on a daily basis. Thank you to you, my grandparents, for your curiosity about my research and for your support. I also thank my cats, Brindille and Saturn, for their company and for making my life more beautiful with their purrs and cuddles. Then, of course, a huge thank you to you, my amazing parents. You have given me tremendous support since the beginning of this adventure, which, after all, started more than 10 years ago when I told you that I wanted to do research in astrophysics. Thank you for your emotional AND financial support, because studies are not free, especially abroad. Thank you, I owe you a lot. Thibault, "thank you" is too weak to express my gratitude. In fact, I will even start by asking for your forgiveness. I am sorry for having abandoned you many times to go to the four corners of the world for conferences and for having taken care of the cat alone. I am sorry for having my thesis on my mind all the time and for having had trouble thinking about anything else. Sorry for (often) taking out my stress on you. For the last four years, you have had no choice but to put up with both me and my thesis. So thank you for putting up with both of us, for being there all these years and for following me through the next ones. I love you.

Remerciements

Thèse. Un si petit mot pour décrire une si grande aventure. La thèse, c'est le début d'une vie de recherche et c'est la fin d'une vie étudiante. La thèse, c'est des conférences, des rencontres, des échéances, des articles. C'est des réussites, des échecs, des difficultés à surpasser. C'est aussi des rires, des larmes, du stress, de l'émerveillement, de la remise en question. Bref, la thèse c'est beaucoup de choses et personne ne la décrira pareil. La thèse, on ne peut pas la laisser sur le pas de notre porte quand on rentre le soir. Elle nous suit comme une ombre. Elle fait partie de nos jours, de nos nuits et de nos week-end. On peut à la fois l'adorer et la détester. Heureusement, je peux dire aujourd'hui que j'ai passé plus de temps à l'adorer qu'à la détester. Enfin, ma thèse, c'est aussi d'avoir été entourée. Entourée d'une équipe, d'amis, de ma famille. Je n'ai pas passé ces trois dernières années seule, loin de là, et je tiens à remercier les personnes suivantes.

Tout d'abord, je remercie énormément mes deux directrices de thèse, Cecilia et Ana, sans qui je ne serais pas en train d'écrire ces lignes aujourd'hui. Je ne pourrais jamais assez vous remercier de m'avoir accordé votre confiance depuis presque quatre ans. Merci de m'avoir formée en tant qu'astrochimiste et de m'avoir guidée et de continuer à le faire. Merci aussi aux membres locaux de ACO/DOC, pour avoir créé un environnement plus qu'agréable dans lequel évoluer. Merci à Joan, Arezu, Eleonora, Fanny, Pedro, Cécile, Layal, Lorenzo, Marie, André, Simon, Juan, Bertrand, Claudine, et aussi tous les autres étudiants ACO. Surtout, un grand merci à ma formidable co-bureau, Marta, pour être une grande amie, pour m'avoir supportée et pour avoir beaucoup échangé, discuté et pour nos aventures mémorables (surtout aux USA !). Un grand merci à tous les autres doctorants/post-doctorants du labo avec qui j'ai partagé de merveilleux moments et de magnifiques années à l'IPAG. Merci donc à Jolantha, Aina, Junko, Ricardo, Robin, Jian, Léo, Van Phan, Alois, Guillaume, Simon, Kim, Jonatan, Noemi, Benjamin. Pour finir avec l'environnement de travail, un grand merci aussi aux membres de l'équipe Interstellaire et plus généralement à tout le personnel de l'IPAG pour votre accueil.

Maintenant, je voudrais aussi énormément remercier ma famille pour tout le support émotionnel qu'elle m'a apporté: Anouk et Thaïs, vous êtes des soeurs formidables et je vous souhaite de vous épanouir dans la voie que vous avez choisit, comme je l'ai fait moi-même. Merci pour tous les merveilleux moments de sororité qu'on partage au quotidien. Merci à vous, mes grand-parents, pour votre curiosité concernant mes recherches et pour votre soutien. Je remercie aussi mes chats, Brindille et Saturne, pour leur compagnie et pour me rendre la vie plus belle grâce à leurs ronronnements et câlins. Ensuite, évidemment, un énorme merci à vous, mes formidables parents. Vous m'avez apporté un soutien hors norme depuis le début de cette aventure, qui, au final, a commencé il y a plus de 10 ans quand je vous ai annoncé que je voulais faire de l'astrophysique. Merci pour votre soutien émotionnel ET financier, car les études ne sont pas gratuites, surtout à l'étranger. Merci, je vous dois énormément. Enfin, "merci" est trop faible pour t'exprimer ma gratitude, Thibault. En fait, je vais même plutôt commencer par te demander pardon. Pardon de t'avoir abandonné moult et moult fois pour aller en conférence aux quatre coins du monde et de t'avoir occupé du chat seul. Pardon d'avoir eu continuellement ma thèse en tête et d'avoir eu du mal à penser à autre chose. Pardon d'avoir (souvent) expulsé mon stress sur toi. Pendant ces quatre dernières années, tu n'as pas eu le choix que nous supporter toutes les deux, moi et ma thèse. Donc merci de nous avoir supporté toutes les deux, d'avoir été là toutes ces années et de me suivre pour celles qui viennent. Je t'aime.

Résumé

Le système solaire est né il y a 4,5 milliards d'années dans un nuage moléculaire de la Voie lactée. L'astrochimie est un outil puissant pour élucider (1) ce qui est arrivé aux premières phases de la formation du système solaire et (2) comment elles ont pu influencer le début du développement de la chimie organique et peut-être de l'apparition de la vie sur Terre. Les observations effectuées jusqu'à présent montrent une grande diversité dans la composition chimique des proto-étoiles de masse solaire. En particulier, les "hot corinos" et les objets WCCC ("Warm Carbon-Chain Chemistry", soit la chimie chaude des chaînes carbonées) sont chimiquement distincts : les "hot corinos" sont riches en molécules organiques complexes interstellaires, ou iCOMs (qui pourraient être les briques des grandes biomolécules terrestres), tandis que les objets WCCC sont riches en hydrocarbures. Cette diversité chimique protostellaire pourrait refléter une différence dans la composition chimique du manteau de glace des grains mis en place pendant la phase pré-stellaire. La question de savoir si l'environnement affecte cette diversité et comment, reste ouverte.

Peu de "hot corinos" et objets WCCC ont été identifiés à ce jour. La plupart des études ciblant les "hot corinos" vise des régions de formation d'étoiles de faible masse, alors que notre Soleil est censé être né près d'étoiles massives ($> 8 M_{\odot}$). Les études de proto-étoiles dans ces régions sont essentielles pour comprendre le passé chimique du Soleil. Le premier but de ma thèse est d'étudier la nature chimique des proto-étoiles situées dans une région similaire à celle où notre Soleil est né, et de déterminer si le Soleil a subi une phase "hot corino" pendant sa formation. Le second but est de comprendre si l'environnement joue un rôle dans la diversité chimique des proto-étoiles. Pour cela, j'ai étudié neuf proto-étoiles du filament OMC-2/3, la plus proche région similaire à l'environnement de naissance du Soleil. J'ai exploité des jeux de données "single-dish" et interférométriques, et ciblé seulement les traceurs moléculaires des "hot corinos" et des objets WCCC.

Les observations "single-dish" se sont révélées inefficaces dans la recherche de "hot corinos" et d'objets WCCC dans OMC-2/3, à cause de la contamination des traceurs moléculaires utilisés par la région de photodissociation entourant le filament. Ensuite, j'ai réalisé une analyse de la poussière et des raies moléculaires avec les observations ALMA. L'étude de la poussière montre que ses propriétés ne sont pas affectées par l'illumination UV, et que la formation d'étoiles est simultanée dans tout le filament. Enfin, à partir de l'analyse des raies moléculaires, j'ai détecté cinq nouveaux "hot corino" dans OMC-2/3. Ce résultat diffère de ce qui a été trouvé dans les autres régions de formation d'étoiles, où les "hot corinos" sont abondants. Ceux-ci semblent donc être rares dans un environnement fortement illuminé, ce qui suggère que l'environnement affecte probablement la diversité chimique des proto-étoiles. Enfin, l'ancienne nature "hot corino" du Soleil doit faire l'objet d'une étude plus approfondie.

Abstract

The Solar System was born 4.5 billion years ago from a cold clump of a molecular cloud of the Milky Way. Astrochemistry is a powerful tool to elucidate (1) what happened to the first phases of the Solar System formation and (2) how they might have influenced the early development of organic chemistry and perhaps the appearance of life on Earth. The observations so far show a large diversity in the chemical composition of solar-mass protostars. In particular, hot corinos and WCCC (Warm Carbon-Chain Chemistry) objects are chemically distinct: while hot corinos are rich in interstellar complex organic molecules, or iCOMs (which might be bricks of large terrestrial biomolecules), WCCC objects are rich in hydrocarbons. This protostellar chemical diversity could reflect a difference in the chemical composition of the grains ice mantle set during the pre-stellar core phase. Whether the environment affects this diversity and how is still an open question.

Only a few solar-mass hot corinos and WCCC objects have been identified to date, thus making it difficult to assess which one of these is dominant in our Galaxy, if any. Most studies targeting hot corinos are performed towards low-mass star-forming regions whereas our Sun is believed to be born in a large cluster with high-mass ($>8 M_{\odot}$) stars. Studies of solar-mass protostars in low- to high-mass star-forming regions are mandatory to shed light on the Sun's chemical past. The first objective of my thesis is to investigate the chemical nature of solar-mass protostars located in a region similar to the one where our Sun was born and to address the question of whether or not the Sun underwent a hot corino phase during its formation. The second objective is to understand whether the environment plays a role in the chemical diversity of solar-mass protostars. To do so, I explored the chemical contents of nine bona fide solar-mass protostars located in the OMC-2/3 filament, the best and closest analogue to our Sun's birth environment. I exploited single-dish and interferometric datasets and targeted exclusively the molecular tracers of hot corinos and WCCC objects.

Unexpectedly, single-dish observations proved to be ineffective in searching for hot corinos and WCCC objects in OMC-2/3. The molecular tracers used are very likely contaminated by the photodissociation region surrounding the filament. Then, I performed both a dust continuum and a molecular line analysis with the ALMA observations. The dust continuum study shows that the dust properties of the OMC-2/3 protostars are not affected by the high-UV illumination, and that star formation is simultaneous throughout the filament. Finally, from the molecular line analysis, I detected five new bona fide hot corinos in OMC-2/3. This result is different from what was found in low-mass star-forming regions where hot corinos are abundant. Hot corinos seem therefore to be scarcer in a high UV-illuminated environment, which suggests that the latter is very likely playing a role in the chemical content of solar-mass protostars. Finally, hot corinos do not seem to prevail in a region similar to the Sun's birth environment. The question of whether our Sun experienced a hot corino phase needs further research to be answered.

Contents

Acknowledgements	ii
Résumé	v
Abstract	vi
Introduction	1
1 Solar-type star formation and molecular complexity	1
1.1 The pre-stellar core phase: A frozen era	3
1.2 The proto-stellar core phase: The molecular complexity in its full glory	4
1.3 The protoplanetary disk phase: Playing hide-and-seek	5
1.4 The planetary system: Life's playground?	6
1.5 Chemical heritage: A possible Ariadne's thread?	6
2 Interstellar dust: a starlight player	8
2.1 Interstellar dust grains and related properties	8
2.2 Dust emission	10
3 The protostellar stage: A rich chemistry	13
3.1 Envelope structure of Class 0/I protostars	13
3.2 Hot corinos	15
3.3 Warm Carbon Chain Chemistry protostars	20
3.4 Hot corino and WCCC objects: an exclusive nature ?	24
3.5 On the origin of the chemical differentiation	27
4 The Sun's birth environment: A lively nursery	30
4.1 On the trail of our Sun's past	31
4.2 The OMC-2/3 filament: The closest analogue to our Sun's birth environment	33
5 Context and Objectives	37
5.1 The DOC (Dawn of Organic Chemistry) project	37
5.2 Shedding light on the Sun's chemical past: Objectives of the the- sis	38
1 Observing Tools and Methodology	41
1 Observing Tools: Radio Telescopes	41
1.1 The radio window	41
1.2 Black-body radiation and Brightness temperature	42
1.3 Single-dish telescopes	43
1.4 Radio interferometers	51

2	Molecular line analysis	58
2.1	The radiative transfer equation	58
2.2	Level populations and Local Thermodynamic Equilibrium	60
2.3	Line formation and broadening mechanisms	63
2.4	Deriving the physical properties of a gas emitting molecular species	64
2	Hunting hot corinos and WCCC objets in OMC-2/3	69
3	ORion Alma New GEneration Survey (ORANGES)	97
3.1	ORANGES I. Dust continuum	98
3.2	ORANGES II. Molecular lines	130
3.3	Identification of WCCC objects	149
3.3.1	The spatial distribution of carbon chains in WCCC objects	149
3.3.2	ORANGES looking at hydrocarbons: CCH and c-C ₃ H ₂ moment 0 maps	149
3.3.3	Conclusions	150
4	The OMC-2 FIR6c-a outflow	153
4.1	OMC-2 FIR6c-a: The discovery of a chemically active outflow	153
4.2	Motivation for new observations	156
4.3	Observations	158
4.4	Preliminary results	159
4.4.1	A new iCOMs-rich outflow	159
4.4.2	Spatial distribution of acetaldehyde and formamide	160
4.4.3	A shock-induced star formation?	161
5	Conclusions & Prospects	165
5.1	Conclusions	165
5.1.1	The large-scale study or how to face a PDR wall	165
5.1.2	The small-scale study or how to see protostars in ORANGES	166
5.1.3	The OMC-2 FIR6c outflow or how to be an unexpected guest joining the party	167
5.1.4	Conclusive remarks	168
5.2	Prospects	169
5.2.1	Short-term prospects	169
5.2.2	Long-term prospects	171
	Bibliography	173
	List of Figures	197
	List of Tables	200
	Résumé Français	203

Introduction

Since the dawn of time, a question remains: Where did life originate? As philosophical as this question can be, many scientific theories exist. Indeed, this question concerns numerous fields: exobiology, biochemistry, astronomy, palaeontology, among many others. Moreover, one does not always agree on where and when the story could have begun: is it on Earth 3.5 billion years ago with the cyanobacteria? Or is it long before in space? The debate remains open. Here I present a piece of the story from the point of view of an Astrochemist.

The story of our Solar System began 4.5 billion years ago in a clump of a molecular cloud, in the Orion spur finger of the Milky Way. Like every other solar-mass star, our Sun experienced several different phases before reaching the final planetary system that we know today. Central questions in Astronomy are 1) what happened to the first phases of the Solar System formation and 2) how they might have influenced the early development of organic chemistry and perhaps the appearance of life on Earth. A jump in the past is required to answer these questions. To do so, we can search for other nascent solar-like planetary systems and seek to understand what is happening there. Chemistry is a powerful tool to do that, and this is a fundamental tool used in this thesis to provide some parts of the answers.

1 Solar-type star formation and molecular complexity: unraveling the physics from the chemistry

Solar-type stars can form in different kinds of star-forming regions though the overall process of their formation is roughly the same, independently of their birth environment. Their birthplace is located in interstellar clouds, composed of gas and dust grains, and hence where chemistry can happen in both the gas phase and on the dust grain icy surfaces. During the formation of solar-type stars, molecules that are formed become more and more complex (Caselli & Ceccarelli 2012; Yamamoto 2017). Molecules with C-bearing molecules with at least six atoms are called interstellar Complex Organic Molecules (iCOMs; Herbst & van Dishoeck 2009; Ceccarelli et al. 2017) and might be essential to form pre-biotic molecules, themselves important to shape the bricks of life. The literature evokes the possibility that iCOMs played an important role in the apparition of life on Earth by being preserved and re-processed during the different stages of the formation of our Solar System before finally being released on Earth through impacts from comets and asteroids. I present below the various steps occurring when forming solar-like planetary

systems from both a physical and a chemical point of view. A summary of solar-mass protostars formations processes is presented in Figure. 1.

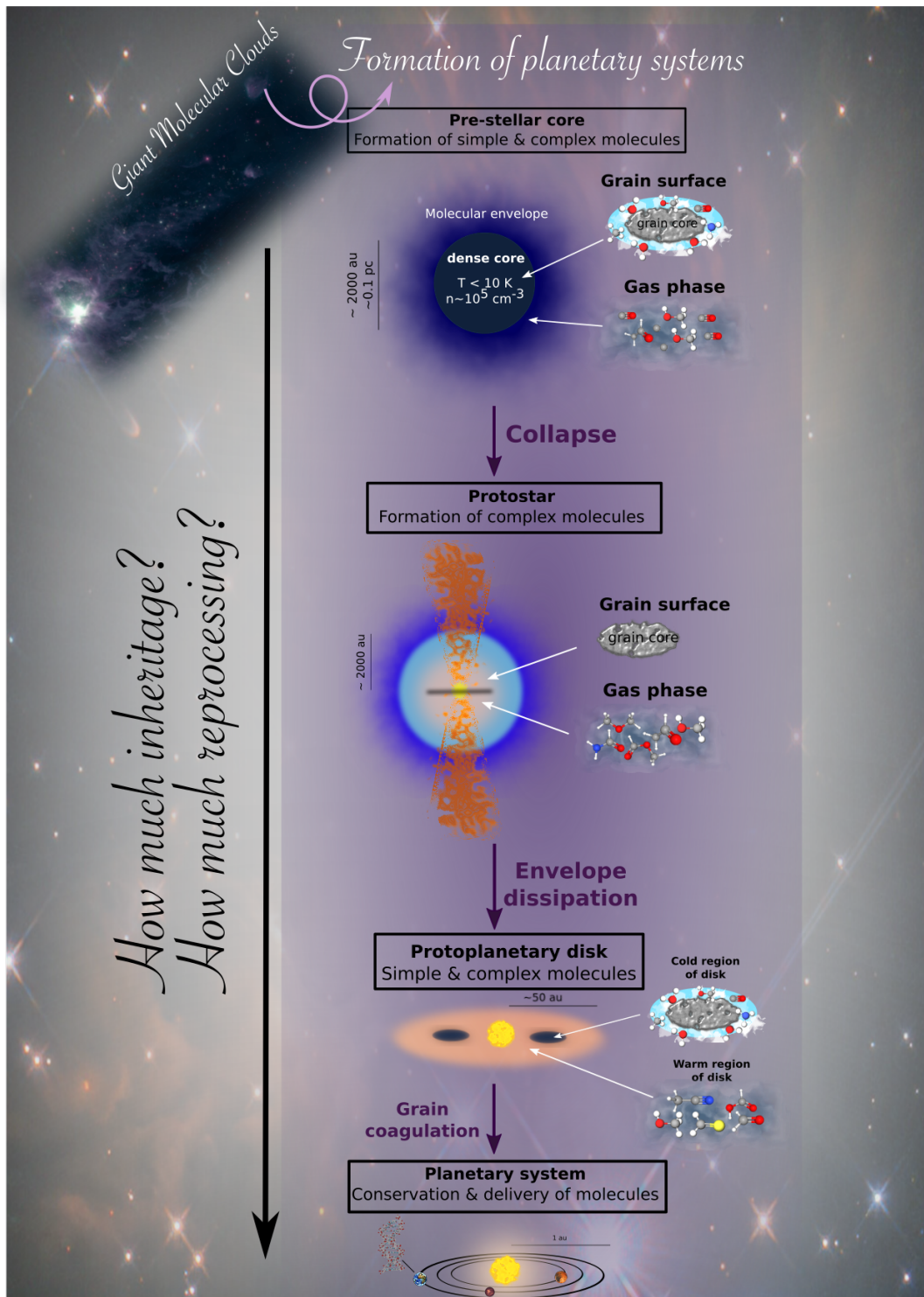


Figure 1: Scheme representing the different steps of the formation of a Solar-like planetary system, from a physical and a chemical point of view. Adapted from Caselli & Ceccarelli (2012).

1.1 The pre-stellar core phase: A frozen era

The pre-stellar core phase is the onset of star formation and starts within molecular clouds (Benson & Myers 1989; Bergin et al. 2007). During this stage, dense ($n > 10^4 \text{ cm}^{-3}$; André et al. 1996; Ward-Thompson et al. 1999) and cold ($T \approx 10 \text{ K}$) cloud fragments with 0.1 pc typical sizes ($\approx 2000 \text{ au}$; Myers & Benson 1983; Benson & Myers 1989) slowly contract due to the interplay between gravitational force, magnetic field, thermal pressure and turbulence (Shu 1977; Shu et al. 1987; Hennebelle & Fromang 2008). These fragments are called pre-stellar cores (PSCs). The duration of this phase is $\approx 10^6$ years (Beichman et al. 1986).

The temperatures being low, atoms (e.g. C, O, N) and molecules (e.g. CO, CS, N_2 , H_2O , HCN, HCO) are freezing-out onto the dust grain surfaces, forming icy grain mantles (e.g. Tielens & Hagen 1982; Hasegawa et al. 1992; Caselli et al. 1999; Bacmann et al. 2002; Bergin et al. 2002; Tafalla et al. 2002, 2006). Those molecules undergo hydrogenation processes which lead to the production of H_2O ices mainly, as well as small amounts of methanol (CH_3OH), formaldehyde (H_2CO), ammonia (NH_3), methane (CH_4) and carbon dioxide (CO_2) ices (Tielens & Hagen 1982, Boogert et al. 2015 and references therein). Under non-thermal desorption processes and UV irradiation (photodesorption), small molecules can desorb into the gas phase of molecular clouds (e.g. Leger et al. 1985; Shen et al. 2004; Öberg et al. 2009a,b; Ivlev et al. 2015; Wakelam et al. 2021) where they are detected (e.g. CO, CS, C_2H , H_2O , HNC, HNCO; e.g. Pratap et al. 1997; Marcelino et al. 2010; Caselli et al. 2012). Unexpectedly, not only small molecules are detected in the gas phase of such environments, but more complex ones like iCOMs (e.g. CH_3OH , HCOOCH_3 , CH_3OCH_3 ; (e.g. Öberg et al. 2010; Bacmann et al. 2012; Cernicharo et al. 2012; Vastel et al. 2014; Jiménez-Serra et al. 2016; Punanova et al. 2018; Soma et al. 2018; Harju et al. 2020; Scibelli & Shirley 2020; Scibelli et al. 2021; Agúndez et al. 2021), which are supposed to form at higher temperature ($>20 \text{ K}$) where other grain surface reactions than hydrogenation can occur. The presence of such molecules, their formation and their destruction routes are still a source of debate (e.g. Vasyunin & Herbst 2013; Balucani et al. 2015; Jin & Garrod 2020).

Finally, deuterium fractionation is an important process that takes place in the cold environment of pre-stellar cores. High level of deuterium fractionation have been measured towards dense cores (e.g. Gerin et al. 1987, 1992a; Bacmann et al. 2002, 2003; Caselli et al. 2003; Roueff et al. 2005; Caselli et al. 2008). In the gas phase, the H_3^+ ions react with the HD species leading to the production of H_2D^+ and H_2 (Watson 1976). The abundance ratio $\text{H}_2\text{D}^+/\text{H}_3^+$ is then larger than the D elemental abundance with respect to H of 1.5×10^{-5} (Linsky et al. 1995). When the freeze-out of species is important enough, and in particular that of CO and O the two major species destructing H_2D^+ , the deuterium fractionation is enhanced (Dalgarno & Lepp 1984; Caselli et al. 1998). A large D/H ratio in the gas phase leads to efficient deuteration of the surface species (e.g. Tielens 1983; Charnley et al. 1997; Caselli et al. 2002; Taquet et al. 2012). Several singly, doubly and triply deuterated molecules have indeed been observed in pre-stellar cores (e.g. Ceccarelli et al. 2002; Bacmann et al. 2003; Vastel et al. 2004, 2006, 2018; Roueff et al. 2005). Figure 2 summarises the reactions occurring in the cold gas leading to deuterium fractionation.

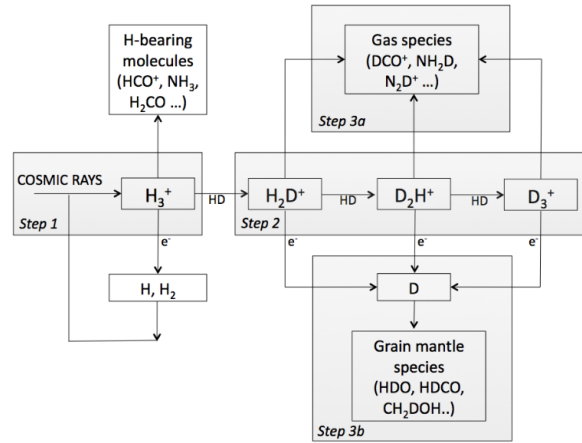


Figure 2: Scheme of the three main steps for molecular deuteration. First, H_3^+ is formed through cosmic ray ionization of H_2 and H . Then, the deuterated form of H_3^+ is formed and finally, the D-atoms are transferred to other species. From [Ceccarelli et al. \(2014a\)](#)

1.2 The proto-stellar core phase: The molecular complexity in its full glory

When the gravitational force takes over, the gravitational collapse of the core starts and gravitational energy under the form of radiation heats the central part of the object up to 3000 K. Before the appearance of a protostar, there is a brief stable phase ($\sim 10^3 - 10^4$ yr; e.g. [Shu 1977](#); [Masunaga et al. 1998](#); [Saigo & Tomisaka 2006](#); [Matsumoto & Hanawa 2011](#); [Commerçon et al. 2012](#); [Bate et al. 2014](#)) the called the First Hydrostatic Core (FHSC; [Larson 1969](#)). During this stage, the core continues to accrete material from the surrounding and once the temperature reaches 2000 K, the core becomes unstable again and the proto-stellar phase begins ([Larson 1969](#); [Shu et al. 1987](#)). This phase is called the embedded phase, during which most of the envelope is accreted, and lasts $\sim 0.5\text{Myr}$ ([Wilking et al. 1989](#); [Evans et al. 2009](#); [Dunham et al. 2015](#); [Kristensen & Dunham 2018](#)). Two different classes of embedded protostars are defined: Class 0 protostars and Class I protostars based on the $L_{\text{smm}}/L_{\text{bol}}$ ratio ([André et al. 1993](#)). I will develop more this criteria in Sec. 2.2.2.

Class 0 protostars Class 0 protostars are the youngest protostars and represent the (early) main accretion phase. Class 0 protostars are still very embedded in the molecular cloud, and their continuum emission is dominated by the envelope dust grains that re-emit radiation in the millimetre and (sub)-millimetre range ([André et al. 1993](#); [André & Montmerle 1994](#)). During this accretion stage, powerful and highly collimated bipolar outflows and jets are present and eject material into the interstellar medium (e.g. [Bontemps et al. 1996](#); [Bachiller 1996](#)). The presence of a circumstellar disk has already been established in several Class 0 sources (e.g. [Jørgensen et al. 2009](#); [Tobin et al. 2012](#); [Murillo et al. 2013](#); [Ohashi et al. 2014](#); [Codella et al. 2014](#); [Tobin et al. 2016a](#); [Yen et al. 2017](#); [Oya et al. 2016, 2017](#); [Gerin et al. 2017](#); [Sakai et al. 2017](#); [Segura-Cox et al. 2018](#); [Hsieh et al. 2019](#); [Tobin et al. 2020](#)).

Class I protostars Class I protostars are evolved Class 0 protostars. The protostellar object mass becomes larger than the envelope mass as the latter accretes onto the central object (Dunham et al. 2014): this is the late accretion phase. The Class I protostars are still associated with dense molecular gas (Myers et al. 1987; Wilking et al. 1989). They present a disk, commonly found around these objects (Williams & Cieza 2011; Harsono et al. 2014), and a circumstellar envelope. Class I protostars show less powerful and less collimated CO outflows than Class 0 protostars (Bontemps et al. 1996; Saraceno et al. 1996).

During the protostellar phase warming up, after reaching a temperature of 10 to 20-30 K in the envelope, mixed ice mantles sublimate with some carbon monoxide (CO), CH₄ and nitrogen (N₂). Heavier radicals such as formyl radical (HCO) and methyl radical (CH₃), among others, acquire mobility on the surface of the grains, leading to the formation of more complex molecules (e.g. acetaldehyde: CH₃CHO) even though recent studies challenge this theory (e.g. Enrique-Romero et al. 2019, 2020). Then, when the temperature is high enough for the mantle to sublimate ($T \geq 100\text{K}$), complex molecules previously trapped in the ices are released onto the gas phase where the formation of even more complex molecules through reactions with the gas in the envelope of the protostars occur (see Section 3.2.3; e.g. Skouteris et al. 2018, 2019; López-Sepulcre et al. 2019; Vazart et al. 2020). Also, outflows and jets are ejecting matter in the interstellar medium (ISM). Shocks between the outflows/jets and the surrounding quiescent molecular cloud produce the sputtering (e.g. Schilke et al. 1997b; Caselli et al. 1997; Pineau des Forêts et al. 1993; May et al. 2000) of grains, and molecules trapped in ices are released allowing gas phase reactions to occur and that can lead to the formation of iCOMs. A handful of complex molecules is found in outflows (e.g. Codella et al. 2010, 2017; Lefloch et al. 2017; Holdship et al. 2019b). The protostellar stage is thus known to be particularly chemically enriched.

1.3 The protoplanetary disk phase: Playing hide-and-peek

Once the envelope around the protostar is almost entirely accreted or dissipated due to the outflows that are present during the protostellar stage, solely a circumstellar disk (or protoplanetary disk) remains around the protostars. The lifetime of the protoplanetary phase is $\approx (2 - 3) \cdot 10^6$ yr (e.g. Evans et al. 2009; Williams & Cieza 2011). The protoplanetary disk stage begins and the protostars are Class II and Class III protostars, also called Pre-Main Sequence (PMS) stars (Classical T Tauri and Weak T Tauri stars respectively). From the Class II phase to the Class III phase, the gas-rich circumstellar disk accreting materials becomes a gas-poor evolved disk. Class III disks are called debris disks (e.g. Williams & Cieza 2011; Dunham et al. 2014; Wyatt et al. 2015). Planets formation is thought to take place inside protoplanetary disks, through dust grains accretion processes (e.g. Lissauer 1993; Montmerle et al. 2006; Ormel & Klahr 2010; Lambrechts & Johansen 2012; Johansen et al. 2014; Johansen & Lambrechts 2017; Coleman 2021), forming larger structures called planetesimals.

During this stage, new complex molecules can be formed in the hot regions of the disk, close to the central object whereas in the cold regions of the disk, molecules formed during the previous phase freeze-out onto the grain mantles again. About 25 species have been detected towards disks (McGuire 2018, 2021), among which only some O-bearing

molecules, defined as starting-point towards the molecular complexity, have been detected in the gas phase of protoplanetary disks (CH₃OH, H₂CO and HCOOH; e.g. [Dutrey et al. 1997](#); [Walsh et al. 2016](#); [Öberg et al. 2017](#); [Bergner et al. 2018](#); [Favre et al. 2018](#); [Loomis et al. 2018](#); [Lee et al. 2019](#); [Booth et al. 2021](#)). This lack of iCOMs detection is because they are much more difficult to observe as they are expected to be frozen onto dust grains in the disk. Indeed, molecules have to be in the gas phase to be observable and identified by (sub)-mm telescopes for example. Moreover, considering the small angular sizes of the disks (\leq few arcsecs) and the relatively weak emission of iCOMs, both high resolution and high sensitivity are required to detect them (e.g. [Walsh et al. 2014](#)). A substantial amount of the carbon is believed to be stored in organic species and in particular in complex ones ([Favre et al. 2013](#); [Schwarz et al. 2016](#)). During the planetesimal formation process, the grain mantles representing part of our chemical heritage are "presumably preserved" until the next phase ([Caselli & Ceccarelli 2012](#)).

1.4 The planetary system: Life's playground?

Once the planetesimals have cleaned their orbit, planets are formed and the formation of the planetary system is complete. The planet formation process has left some residuals, small bodies called comets and asteroids. Those remnants are usually covered by ices in which complex molecules, inherited from the previous phases, are likely trapped. Were these complex molecules delivered to Earth? How? Meteorite impact events "showing down" on Earth, could have possibly delivered the preserved chemical heritage from the previous phases, and thus contributing to the apparition of Life on Earth a few hundreds of million years later (e.g. [Alwegg et al. 2019](#); [Osinski et al. 2020](#), and references therein). No clear consensus exists today.

1.5 Chemical heritage: A possible Ariadne's thread?

The question of our chemical heritage is still open and unanswered. We need to prove that a chemical link, called metaphorically Ariadne's thread ([Ceccarelli et al. 2014a](#)), exists between the earliest and latest phases of our Solar System formation. One way to do that is to compare chemical abundances, deuteration levels of water and other species for example between the pre- and proto- stellar phases with what is found in comets (e.g. [Busquet et al. 2010](#); [Caselli & Ceccarelli 2012](#); [Ceccarelli et al. 2014a](#); [Cleeves et al. 2016](#); [Drozdovskaya et al. 2019](#); [Bianchi et al. 2019](#); [Rivilla et al. 2020](#)). Isotope¹ and deuterium fractionation show whether the molecular material of the Solar System inherited from the pre-stellar core phase or is likely reprocessed at later stages (e.g. water; [Visser et al. 2009](#); [Hily-Blant et al. 2013](#); [Cleeves et al. 2014](#); [De Simone et al. 2018](#); [Kahane et al. 2018](#); [Fontani et al. 2020](#); [Jensen et al. 2021](#)). In particular, complex organic molecules are targeted since species such as formamide have been shown to be the basis of pre-biotic molecules synthesis (e.g. amino acids) in versions of Urey-Miller experiments ([Saladino et al. 2012, 2016](#)).

Several studies aimed to compare the chemical content of the different phases of the formation of a planetary system (e.g. [Öberg et al. 2015](#); [Drozdovskaya et al. 2018, 2019](#); [Bianchi et al. 2019](#); [Rivilla et al. 2020](#)). In particular, [Drozdovskaya et al. \(2019\)](#) compare

¹Isotopes of a given chemical element have the same number of protons but different number of neutrons. In other words, two isotopes have different atomic masses.

the observed relative abundances of several species (e.g. CHO-, N-, S- bearing molecules) between the protostellar disk of the protostar IRAS16293-2422 B, assumed to be the closest Solar-like embedded system, and the comet 67P/Churyumov-Gerasimenko (hereafter 67P), considered as representative of the bulk cometary ices. They saw a correlation between abundances of CHO-, N- and S- bearing molecules with some scatter, implying partial preservation of pre-stellar and proto-stellar chemistry in cometary ices. In another study, Bianchi et al. (2019) compared relative iCOMs abundances between the Class I protostars SVS13-A and four comets (Hale-Bopp, Lemmon, Lovejoy and 67P) and found different results depending on the iCOMs. Indeed, while methyl formate (HCOOCH₃) and ethanol (CH₃CH₂OH) are consistent with what is found in comets within a factor of 10, acetaldehyde (CH₃CHO) and formamide (NH₂CHO) show up to a factor of 20 of difference as an example. Besides those specific studies, a great number of molecules observed in comets are also detected in star-forming regions and with similar abundances (e.g. Drozdovskaya et al. 2018; Bianchi et al. 2019; Rivilla et al. 2020). In particular, formamide (NH₂CHO), one of the amide-bond molecules, has been detected in comets and meteorites (Pizzarello et al. 1991; Elsila et al. 2009) but also towards solar-type protostars (Kahane et al. 2013; López-Sepulcre et al. 2015). This implies a possible link between the organic chemistry in the ISM and the Solar System (Ceccarelli et al. 2007, 2014b).

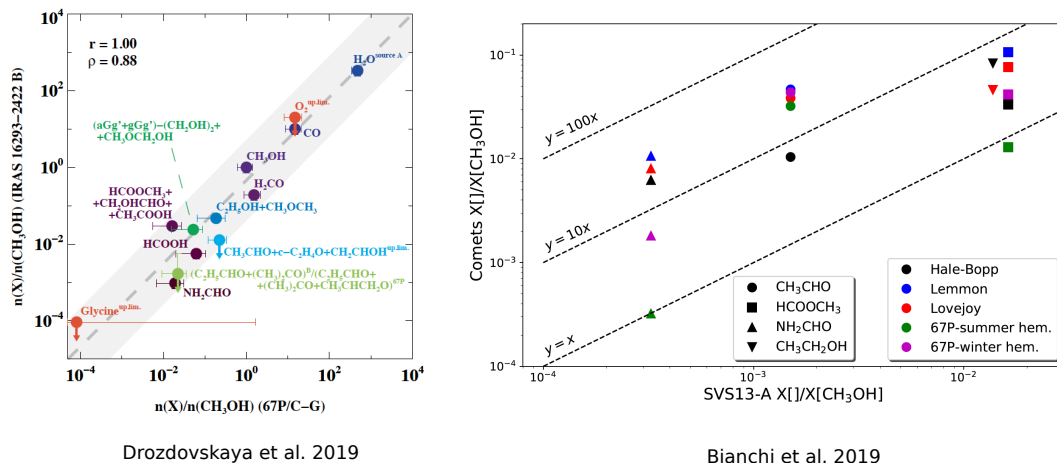


Figure 3: Abundance of iCOMs with respect to methanol in a hot corino compared to that of comets. *Left:* The hot corino prototype IRAS 16293-2422 B is compared to the 67P/C-G comet. Extracted from Drozdovskaya et al. (2019). *Right:* The hot corino SVS13-A is compared to several comets. Extracted from Bianchi et al. (2019).

Can molecules survive the journey and play a role in the apparition of life on Earth? We need more studies before getting a somewhat definitive answer. The statistics are quite poor and one needs to increase the systematic studies of measured molecular abundances between protostellar/planetary disk phases and comets before drawing definitive conclusions. Moreover, one needs to find accurate analogues to our Sun's progenitor to do the comparison. Indeed, in Section 3, we will see that not all protostars share the same chemical content and today, we do not know what is the chemical past of our Sun. In Section 4, we will see that not all solar-type stars are born in the same type of environment and that our Sun is believed to have formed in one specific kind of environment. But before focussing on the protostars chemistry, I would like to introduce a bit more the interstellar

dust and the continuum emission of Young Stellar Objects in the next Section.

2 Interstellar dust: a starlight player

The night is already well underway. The public lights of the nearest village are faint, it is quite dark. A blanket, a red torch, and utter silence. The stars are bright and a band of light and dark lanes lie above my head: our home galaxy, the Milky Way. Figure 4 shows an all-sky view of the Milky Way. The dark regions across the Galactic plane indicate the presence of foreground clouds of interstellar dust and gas, which absorb the light of the stars located behind. These clouds are those mentioned in the previous section, they are the cradle of stars.

Historically, inferring the presence of interstellar dust has not been straightforward. In 1785, Herschel ([Herschel 1785](#)) catalogued several "dark" nebulae and described them as "holes in the heavens". At the beginning of the 20th century, it was recognized that the "starless holes" were structures in front of the stars able to absorb starlight ([Clerke 1903](#); [Barnard 1919](#)). Finally, in 1930, the existence of diffuse interstellar dust was inferred by R. J. Trumpler ([Trumpler 1930](#)) from obscuration or "extinction" of the starlight. We know now that the ISM is composed of dust and gas and that the dust represents $\sim 1/100$ of the gas in mass. Despite its small fraction of the ISM, interstellar dust is important and plays substantial roles: it is the dominant source of opacity in the ISM, it dominates the ISM Spectral Energy Distribution (SED) at all wavelengths longwards 912 \AA and is where the most abundant molecule in the universe, H_2 , forms.

2.1 Interstellar dust grains and related properties

The interstellar dust is composed of small grains of solid material, namely silicates and carbonaceous grains. A substantial fraction of heavy elements is locked onto these grains. This is important for the formation of planets and perhaps life because what is locked onto the dust grains governs what element is available for biotic chemistry. Also as I will describe in the next sections, several chemical reactions can occur on the dust grain surfaces, and in particular that of H_2 (e.g. [Gould & Salpeter 1963](#); [Hollenbach & Salpeter 1970, 1971](#); [Vidali 2013](#); [Wakelam et al. 2017](#); [Pantaleone et al. 2021](#)), the main component of the ISM.

The properties of the interstellar grains are derived from observations, on how they absorb, emit and scatter photons. From those observations, we know that dust grains have irregular puffy shapes and are rather small with sizes ranging from $0.005 \mu\text{m}$ to $0.25 \mu\text{m}$ ([Mathis et al. 1977](#)). In the Milky Way, their average size in diameter is $0.1 \mu\text{m}$. In cold environments such as molecular clouds, interstellar dust grains can be surrounded by iced mantles. Absorbing, emitting and scattering photons are the properties of interstellar dust. The combination of absorption and scattering causes the extinction of starlight by interstellar dust. This process is also called *reddening* because blue light is more easily scattered than red light, the stars appear to be reddened. A view of the dust interstellar reddening is shown in Figure 5. For a more complete review of the observed properties of the interstellar dust grains, see [Draine \(2003\)](#).

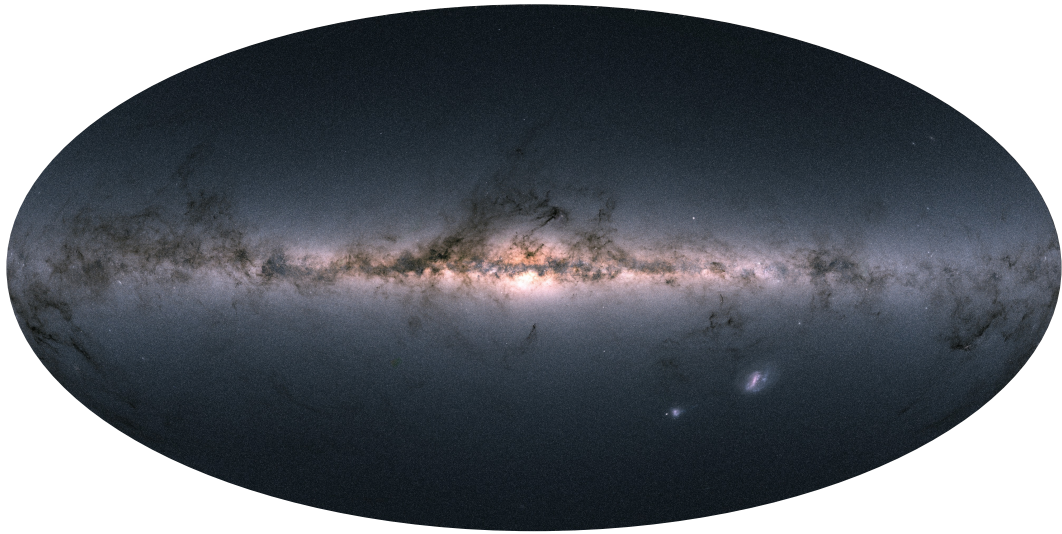


Figure 4: An all-sky view of the Milky Way by the Gaia satellite. The brighter regions indicate the concentration of bright stars while darker regions indicate the presence of interstellar dust between us and the stars. Most of the stars form in the Galactic plane, the horizontal structure that dominates the image. The brightest feature represents the Galactic centre. The two bright spots in the lower right are the Large and Small Magellanic Clouds, two dwarf galaxies orbiting our Galaxy. Image Credits and Copyright: ESA/Gaia/DPAC.

Interstellar dust reddening

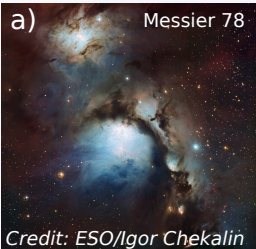

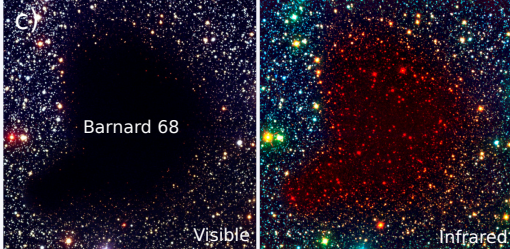
<p>Scattering of dust: Reflection Nebulae</p>	<p>Absorption of dust: Dark nebulae</p>	<p>Scattering + absorption: Reddening</p>
<p>a) Messier 78</p>  <p><small>Credit: ESO/Igor Chekalin</small></p>	<p>b) Horsehead Nebula</p>  <p><small>Credit: ESO</small></p>	<p>c) Barnard 68</p>  <p><small>Visible Infrared</small></p> <p><small>Credit: ESO</small></p>

Figure 5: Dust interstellar reddening process. This mechanism is due to the combination of dust scattering and absorption. *a)* Messier 78 is an example of a reflection nebula that is due to dust scattering. As for most reflection nebulae, Messier 78 presents a blue shading. *b)* The Horsehead Nebula is an example of a dark nebula resulting from dust absorption. In this case, the light of the background stars is blocked by dust. *c)* Example of a reddening effect on the Bok Globule Barnard 68. Contrarily to the visible light (left), the infrared light (right) is not blocked by the dust but the stars appear redder.

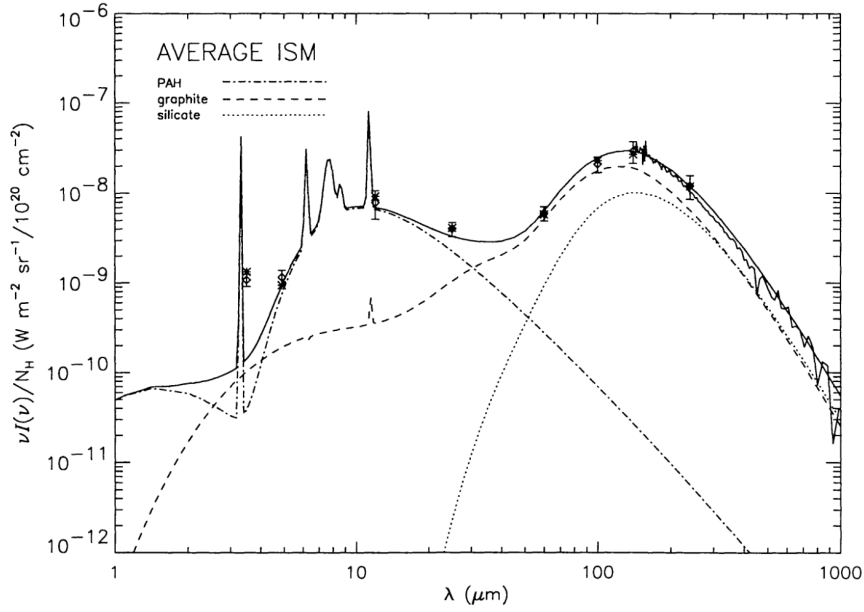


Figure 6: Average Spectral Energy Distribution of the ISM in the Milky Way. Image taken from [Dwek \(1997\)](#).

2.2 Dust emission

2.2.1 Generalities

The dust emission is a thermal emission and resembles that of a black-body:

$$I_\nu \sim B_\nu(T_d)[1 - e^{-\tau(\nu)}] \quad (1)$$

The average dust temperature varies between 10 and 1500 K. Above 1500 K, grains are vaporized. The dust absorbs the interstellar visible to UV photons, is heated up and re-emits in the Near-IR to mm wavelengths where we can observe it. Figure 6 shows the (averaged) Spectral Energy Distribution (SED) of the ISM in the Milky Way. The SED can be characterized by two components, a cold one (15-20K) emitting longwards in the FIR ($\lambda = 25 - 1000 \mu\text{m}$) and a hot one (500 K) component emitting in the near to mid-IR ($\lambda = 0.8 - 25 \mu\text{m}$). The cold component is due to large ($\sim 0.1 \mu\text{m}$) grains whilst the hot component is due to small and very small grains (VSG) and large carbon cycles molecules called Poly-Aromatic Hydrocarbons (PAHs) containing more than 50 carbon atoms.

2.2.2 Spectral Energy Distribution of Young Stellar Objects

Historically, Young Stellar Objects (YSOs) have been classified in an evolutionary sequence, from protostars (Class I) to pre-main-sequence stars using the infrared (IR) SED (Class III) ([Lada & Wilking 1984](#); [Lada 1987](#)). The infrared sources were first divided into three categories, based on the shape of the observed energy distribution and the IR spectral index. The infrared spectral index is defined for the wavelength range $\lambda = 2 - 25 \mu\text{m}$:

$$\alpha = \frac{d(\log \lambda F_\lambda)}{d(\log \lambda)} \quad (2)$$

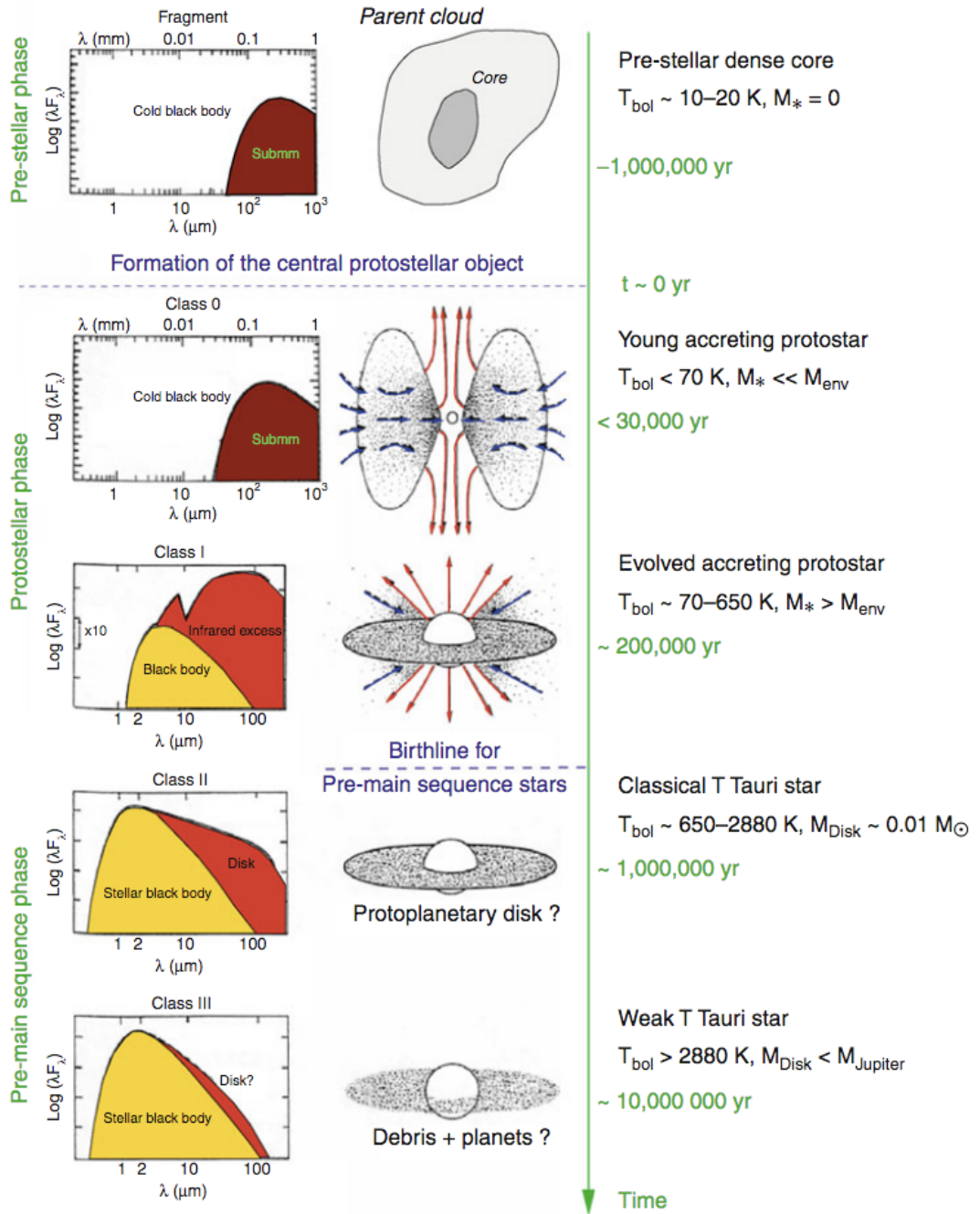


Figure 7: Spectral Classification of embedded young stellar objects based on the shape of the spectral energy distribution (left), and on the bolometric temperature and (envelope + disk) mass (right). From André (2011).

where F_{λ} is the spectral flux density per wavelength interval.

At first, Class I sources were classified as the youngest protostars, with their luminosity deriving mainly from accretion. Their IR spectral index is $\alpha \geq 0$ and their SED peaks in the infrared. Class II and III are less embedded sources. Class II have $-2 \leq \alpha \leq 0$, their SED peaks in the near-IR but they show a mid-IR excess. Class III have $\alpha \leq -2$ and their SED resembles reddened black-bodies. This evolutionary sequence was supported

by theoretical modelling of the SED (Adams et al. 1987).

Later, Class 0 sources were added to the evolutionary sequence. Those sources were defined as even more embedded and young than Class I sources (André et al. 1993). Their SED peaks longwards $100 \mu\text{m}$ and they have faint NIR emission. The frontier between Class 0 and I objects has been defined using the submillimetre ($\lambda > 350 \mu\text{m}$) to bolometric luminosity ratio, $L_{\text{smm}}/L_{\text{bol}}$: A Class 0 protostar has $L_{\text{smm}}/L_{\text{bol}} \geq 0.05$. An alternative approach to classify the YSOs is based on the bolometric temperature (Myers & Ladd 1993; Chen et al. 1995, 1997) and on the (envelope + disk) mass (e.g. Terebey et al. 1993; André et al. 1993; André & Montmerle 1994). The evolutionary sequence of the YSOs and their SED shape, their bolometric luminosity and (envelope+disk) mass is shown in Fig. 7.

From the millimetre wavelength range and beyond (at larger frequencies), thermal dust emission dominates the overall spectrum of YSOs and more generally, of star-forming regions. However, below ~ 100 GHz, i.e. in the radio domain, other emission mechanisms can also contribute to the SED such as thermal Bremsstrahlung (also called *free-free*) emission, non-thermal gyrosynchrotron emission, and Anomalous Microwave Emission (AME). Between ~ 1 and 100 GHz, the AME emission does not dominate so I will not discuss it further in this Thesis. However, I will introduce the other types of emission that can contribute to the radio emission of YSOs as it is relevant in the context of this thesis.

2.2.3 Radio emission of YSOs

Most YSOs show compact radio emission (e.g. Bontemps et al. 1995; Anglada 1995; Rodriguez 1997; Tychoniec et al. 2018). As I just explained above, this emission is not necessarily a contribution from the dust emission. Depending on the evolutionary stage of the YSO, the radio emission can be attributed to different mechanisms. Usually, radio emission from the Class III objects is due to gyro-synchrotron radiation (e.g. Feigelson & Montmerle 1985; André 1996; Anglada et al. 1998; Dzib et al. 2013; Pech et al. 2016) due to mildly relativistic electrons gyrating in the YSO's magnetosphere. This type of emission can also be detected in some Class I and II sources (e.g. Dzib et al. 2010; Dellar et al. 2013). On the other hand, radio emission from younger YSOs (mainly Class 0 and I and some Class II) is usually attributed to free-free emission associated with outflow activity (e.g. Anglada 1996; Anglada et al. 1998; Rodriguez 1997; Tychoniec et al. 2018) or associated with Class II disk photo-evaporation (e.g. Pascucci & Gorti 2012; Owen et al. 2013; Macías et al. 2016). There can be some exceptions where non-thermal emission can be detected towards jets associated with young (Class 0 and I) protostars or because the sources have their emission dominated by gyrosynchrotron emission (e.g. Rodriguez et al. 1989; Curiel et al. 1993; Feigelson et al. 1998; Dzib et al. 2013; Dellar et al. 2013; Tychoniec et al. 2018; Anglada et al. 2018).

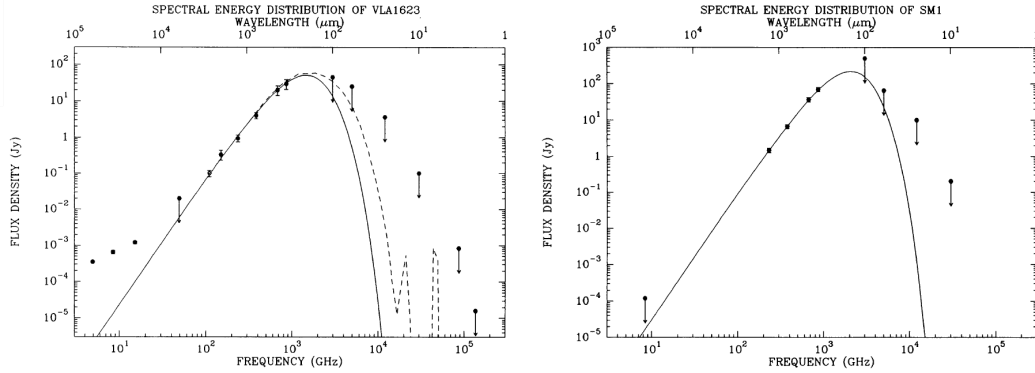


Figure 8: Spectral Energy Distribution of VLA 1623 (left) and SM1 (right). In both panels, the solid curve is a fit of the SED of the form $B_\nu(T)(1 - e^{-\tau})$. Figure extracted from [André et al. \(1993\)](#).

The spectral index α at centimetre wavelengths, defined as $F_\nu \propto \nu^\alpha$, can be used to determine whether the emission is thermal or non thermal. For thermal emission, the spectral index is flat or positive, i.e. $-0.1 \leq \alpha \leq 2$ whilst for non thermal emission, the spectral index is negative, i.e. $\alpha \leq -0.1$ (e.g. [Panagia & Felli 1975](#); [Rodriguez et al. 1993](#); [Anglada et al. 1998](#)). Thermal dust emission has also a positive spectral index ($\alpha = 2 + \beta$; β is the dust emissivity spectral index) but its contribution dominates at IR and (sub)-mm wavelengths while it is small at cm wavelengths.

Most embedded protostars, i.e. Class 0 and I protostars, drive powerful outflows and jets (e.g. [Bontemps et al. 1996](#); [Bachiller 1996](#); [Arce & Sargent 2006](#); [Frank et al. 2014](#); [Podio et al. 2021](#)). It has been shown that the thermal radio emission associated with these sources, is due to the radiation of charged particles which are de-accelerated in thermal jets, i.e. collimated outflows (partially) ionized by shocks (e.g. [Rodriguez 1994](#); [Anglada 1995](#); [Rodriguez 1997](#); [Anglada et al. 2018](#)). On the SED, free-free emission translates into a centimetre excess. Figure 8 is taken from [André et al. \(1993\)](#) and shows the SED of a Class 0 protostar, VLA1623, and of a starless core, SM1. Free-free emission is only present towards VLA1623, as we see the flux density measurements deviating from the fitted black-body curve.

3 The protostellar stage: A rich chemistry

Our Sun has been through the protostellar stage during its childhood. If life appearance on Earth has been supported by any kind of chemical heritage from the interstellar medium (ISM), studying the protostellar stage known to be chemically rich seems to be a good starting point. However, determining what was the molecular content of the proto-Sun is proving to be a more complicated task than expected.

3.1 Envelope structure of Class 0/I protostars

During the protostellar stage, a plethora of molecules is formed as the temperature increases from 10 K to more than 100 K (see Section 1). The temperature increases gradually, different chemical zones form in protostar envelopes. According to [Caselli & Cec-](#)

carelli (2012), the structure of Class 0/I protostars can be represented by four main zones that are described hereinbelow and schematised in Figure 9.

1. The outer zone is chemically similar to the placental molecular cloud that is always present around the young Class 0/I protostars. Temperature is around 10 K and densities $n_{\text{H}_2} \leq 10^5 \text{ cm}^{-3}$.
2. The cold envelope zone, or CO-depleted region, is found in several Class 0/I protostars (Jørgensen et al. 2005). The temperature is cold enough ($T \leq 22 \text{ K}$) for the species (especially CO) to freeze out onto grain surfaces. Deuterium fractionation can occur. This chemistry is also found in pre-stellar cores.
3. The Warm Carbon Chain Chemistry (WCCC) zone is a CH_4 sublimation region. This zone requires a temperature of at least 25 K to release the CH_4 into the gas phase (Collings et al. 2004; Ferrero et al. 2020) where it will initiate the formation of carbon chains molecules (Hassel et al. 2008, 2011; Aikawa et al. 2008). However, to trigger significant WCCC chemistry, the CH_4 abundance has to be larger than 10^{-7} . This zone can extend to about a few thousand au around the protostar.
4. The hot corino zone is the innermost, where water-rich ice mantles sublimate and hot gas chemistry occurs. The temperature is $\geq 100 \text{ K}$, leading to water ice sublimation. All the molecules that were trapped into the ice mantles are thus released into the gas phase. Rich chemistry is then triggered between the released species and the surrounding gas, leading to the formation of iCOMs. This zone has a radius of about a hundred au or less.

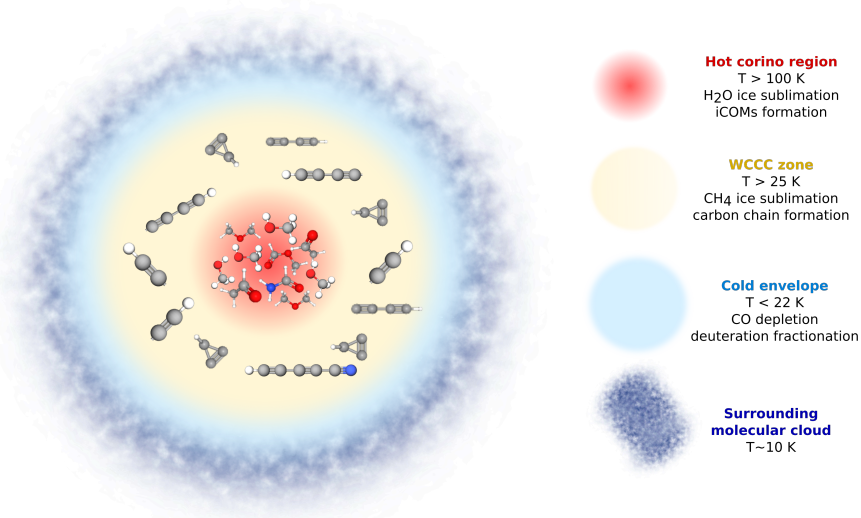


Figure 9: Scheme representing the typical structure of Class 0/I protostars envelope. For simplicity and because I aim to focus on the chemical structure of a Class 0/I protostar, the outflow and disk are not represented. The different region sizes can vary from one protostar to another and are not scaled.

Following this scheme, we would then naively expect that all Class 0/I protostar share the same envelope structure and composition. Yet, this is not the case and that is why understanding the chemical past of our Sun is challenging and important. Some objects of

the same age show extreme chemical differences. Those two types of objects are respectively called hot corinos and WCCC objects and are considered as key pieces of evidence that a particularly rich chemical diversity can occur at the protostellar stage.

3.2 Hot corinos

Hot corinos are the first objects found among the solar-type protostars population showing a specific type of chemistry (Ceccarelli et al. 2000b; Cazaux et al. 2003). Even though they present some peculiar characteristics, their identification is not always straightforward due to sometimes lack of spatial resolution and sensitivity, or due to high dust opacity (De Simone et al. 2020a). Hence, only about a dozen hot corinos have been confirmed up to now. The list of identified hot corinos is given in Table 1. An overview of the hot corino characteristics, the hot corino prototype and the hot corino chemistry are detailed in this section.

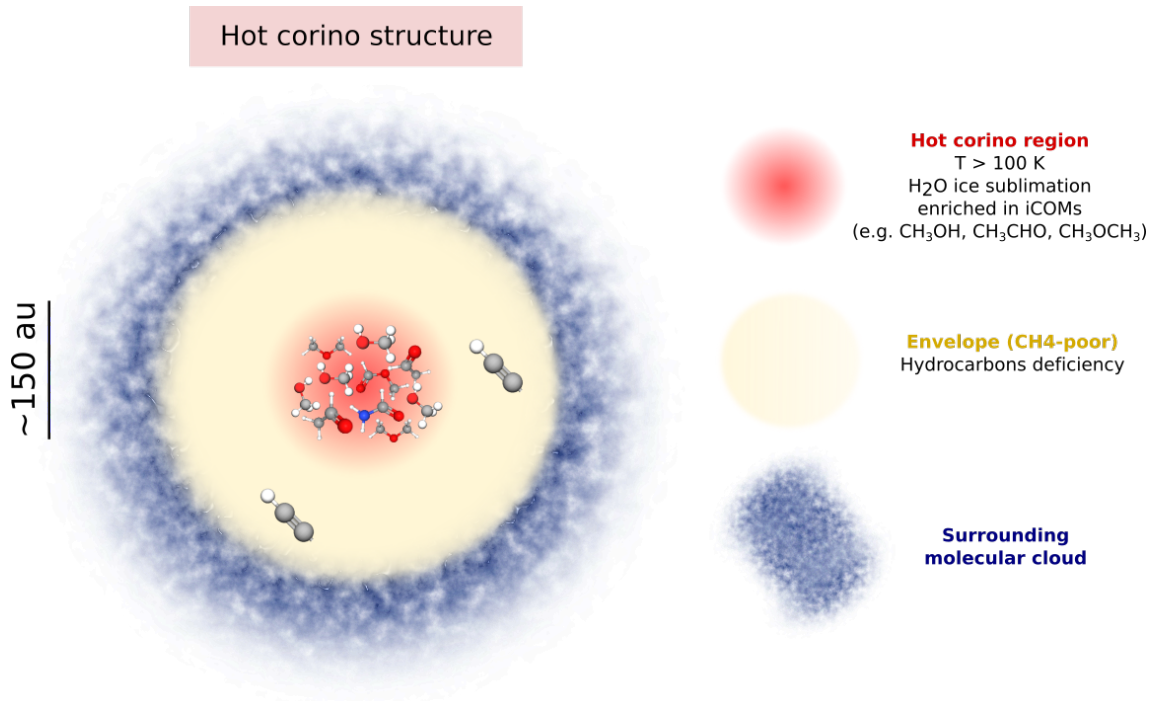


Figure 10: Scheme of the structure of a hot corino. The hot corino has a hot central component (red) enriched in iCOMs. This central region is surrounded by a methane-poor WCCC region (i.e. deficient in carbon chain molecules; light yellow). The cold envelope is not represented here. For simplicity and because I aim to focus on the chemical structure of a Class 0/I protostar, the outflow and disk are not represented. The scheme is not at scale.

3.2.1 Characteristics

Hot corinos are compact (≤ 100 au), hot ($T \geq 100$ K) and dense ($n \geq 10^7$ cm⁻³) regions around the central object (Ceccarelli 2004; Ceccarelli et al. 2007). The name comes from the fact that there are many similarities with hot cores, high-mass protostars showing a rich organic chemistry (e.g. Snyder et al. 1974; Fourikis et al. 1974; Brown et al. 1975;

Table 1: List of detected or potentially detected hot corinos, their classification and location. Hybrid sources (see Sec. 3.4.1) are shown in *italic*.

Hot corinos detected before the PhD thesis	Class	Region	Reference
IRAS 16293-2422	0	ρ Ophiuchus	Cazaux et al. 2003
NGC1333-IRAS 4A2	0	Perseus	Bottinelli et al. 2004
NGC1333-IRAS 4B1	0	Perseus	Bottinelli et al. 2007
NGC1333-IRAS 2A1	0/I	Perseus	Jørgensen et al. 2005; Bottinelli et al. 2007
HH212-MM1	0	Orion	Codella et al. 2016
<i>IRAS 19347+0727 (hereafter B335)</i>	0	<i>Aquila</i>	<i>Imai et al. 2016</i>
<i>L483</i>	0	<i>Aquila Rift</i>	<i>Oya et al. 2017</i>
NGC1333-SVS13 A	I	Perseus	De Simone et al. 2017; Bianchi et al. 2019
Hot corinos detected during the PhD thesis			
Barnard1b-S	very early Class 0	Perseus	Lefloch et al. 2018; Marcelino et al. 2018
CephE-mm (IRAS 23011+6126)	Intermediate mass	Cepheus E	Ospina-Zamudio et al. 2018
Ser-emb 1	0	Serpens	Martín-Doménech et al. 2019; Bergner et al. 2019
Ser-emb 8	0	Serpens	Bergner et al. 2019
Ser-emb 17	I	Serpens	Bergner et al. 2019
<i>BHR71-IRS1</i>	0	<i>Musca (BHR 71 cloud)</i>	<i>Yang et al. 2020</i>
NGC1333-IRAS 4A1	0	Perseus	De Simone et al. 2020a
L1551 IRS5	I	Taurus	Bianchi et al. 2020
G211.47-19.27S	0	Orion A	Hsu et al. 2020
G208.68-19.20N1 (OMC-3 MMS6)	intermediate mass	Orion A	Hsu et al. 2020
G210.49-19.79W	0	Orion A	Hsu et al. 2020
G192.12-11.10	?	λ Orionis	Hsu et al. 2020
HOPS-108	0	Orion A (OMC-2 FIR4)	Tobin et al. 2019, Chahine et al. 2021
HOPS-370	intermediate mass	Orion A (OMC-2 FIR3)	Tobin et al. 2019
<i>L1448 C (Per-emb 26)</i>	0	<i>Perseus</i>	<i>Belloche et al. 2020; Yang et al. 2021</i>
L1448-2A (Per-emb 22 A)	0	Perseus	Belloche et al. 2020; Yang et al. 2021
L1448-2Ab (Per-emb 22 B)	0	Perseus	Belloche et al. 2020 ; Yang et al. 2021
B1-c (Per-emb 29)	0	Perseus	van Gelder et al. 2020; Yang et al. 2021
NGC-1333 IRAS7 SM2 (Per-emb 21)	0	Perseus	Yang et al. 2021
NGC-1333 IRAS7 SM1 (Per-emb 18)	0	Perseus	Yang et al. 2021
L1448 IRS 3A	I	Perseus	Yang et al. 2021
Per-emb 33 A	0	Perseus	Yang et al. 2021
Per-emb 42	I	Perseus	Yang et al. 2021
L1455 IRS 1 (Per-emb 17)	0	Perseus	Yang et al. 2021
<i>L1455 IRS 4 (Per-emb 20)</i>	0/I	<i>Perseus</i>	<i>Yang et al. 2021</i>
<i>Per-emb 35 A (NGC1333 IRAS 1)</i>	I	<i>Perseus</i>	<i>Yang et al. 2021</i>
Per-emb 35 B (NGC1333 IRAS 1)	I	Perseus	Yang et al. 2021
Per-emb 5	0	Perseus	Yang et al. 2021
Per-emb 2	0	Perseus	Yang et al. 2021
B1-d (Per-emb 10)	0	Perseus	Yang et al. 2021
HH211 MMS (Per-emb 1)	0	Perseus	Yang et al. 2021
Per-emb 11 A (IC 348 MMS)	0	Perseus	Yang et al. 2021
Per-emb 11 C (IC 348 MMS)	0	Perseus	Yang et al. 2021
<i>B5 IRS 1 (Per-emb 53)</i>	I	<i>Perseus</i>	<i>Yang et al. 2021</i>
Hot corino candidates ^a			
L1157-mm	0	Cepheus	Belloche et al. 2020
SerpS MM18a	0	Serpens	Belloche et al. 2020
SerpM S68N	0	Serpens	Belloche et al. 2020; van Gelder et al. 2020

^a A hot corino candidate is a source in which methanol and/or other iCOMs are detected but the emission region of these species is not constrained enough to confirm a hot corino origin.

van Dishoeck & Blake 1998; Kurtz et al. 2000; Schilke et al. 1997a, 2001, 2006; Comito et al. 2005; Belloche et al. 2008a,b, 2009, 2013; Calcutt et al. 2014; Mininni et al. 2020; Johnston et al. 2020). A lot of iCOMs found towards hot cores were detected in the hot corino prototype IRAS16296-2422 with abundances of at least ten times higher than what was found in hot cores (Ceccarelli et al. 2000b; Cazaux et al. 2003), suggesting that hot corinos are not just smaller in size but that they are also chemically different from their massive counterpart. A recent study from Higuchi et al. (2018) in the Perseus molecular cloud showed that hot corinos would tend to be located deep inside molecular clouds.

The major specificity of hot corinos compared to other low-mass protostars is their particular enrichment in iCOMs (e.g. CH₃OH, CH₃OCH₃, HCOOCH₃) in the inner region of the protostellar envelope (<150 au), i.e. in the hot corino zone (Ceccarelli et al. 2007). A scheme of hot corinos is presented in Figure 10. A handful of studies have been dedicated to the detection of iCOMs in hot corinos (e.g. Bottinelli et al. 2004; Jør-

gensen et al. 2005, 2016; Kahane et al. 2013; Öberg et al. 2014; De Simone et al. 2017; López-Sepulcre et al. 2017; Bianchi et al. 2019; Belloche et al. 2020; Yang et al. 2021). However, objects showing only an enhancement in iCOMs are not always categorised as hot corinos. A second condition sine qua non is a deficiency in carbon chains in the 2000 au region around the central object, i.e. in the WCCC zone, compared to pure WCCC objects. However, some small carbon chains are still detected towards hot corinos, but with low abundances compared to other objects (Sakai et al. 2009a).

Another characteristic of hot corinos is an high deuteration level. Deuterated molecules have been detected towards hot corinos (e.g. Ceccarelli et al. 1998; van der Tak et al. 2002; Parise et al. 2002; Vastel et al. 2003, 2010; Parise et al. 2004; Coudert et al. 2019; Agúndez et al. 2021), and heavy deuterium fractionation levels have been calculated, in particular for CH₃OH and H₂CO (e.g. Ceccarelli et al. 1998; Loinard et al. 2000; Ceccarelli et al. 2001, 2007; Parise et al. 2006; Taquet et al. 2019; Martín-Doménech et al. 2021). Heavy deuterium fractionation is a shared characteristic with the coldest starless cores (see Section 1.1). The hot corino prototype IRAS 16293-2422 is a perfect example to characterise the common chemical features of hot corinos.

3.2.2 The hot corino prototype IRAS 16293-2422: A quick overview

The first identified hot corino is the protostellar binary IRAS 16293-2422 (IRAS 16293 hereafter; Cazaux et al. 2003; Bottinelli et al. 2004). IRAS 16293 is located in the ρ Ophiuchus complex at ~ 141 pc of distance (Dzib et al. 2018). The two binary components are separated by about 5.2'' (~ 700 au) and share a circumbinary envelope extending up to 6000 au (e.g. Wootten 1989; Mundy et al. 1992; Looney et al. 2000; Ceccarelli et al. 2000a,b, 2001; Schöier et al. 2004; Chandler et al. 2005; Jaber Al-Edhari et al. 2014). The component A of the binary system is itself a triple system (A1, A2 and Ab, e.g. Wootten 1989; Chandler et al. 2005; Loinard et al. 2007; Pech et al. 2010; Maureira et al. 2020) and recently, it has been suggested that the component A1 is a tight binary system (Hernández-Gómez et al. 2019). The source continuum emission at millimetre wavelengths is presented in Figure 11.

Chemically, some chemical similarities with hot cores (in particular with Orion-KL) have first been pointed-out. In the 90s-2000s, studies showed that IRAS 16293 presents rich spectra with several deuterated molecules (van Dishoeck et al. 1995; Ceccarelli et al. 1998, 2001; Loinard et al. 2000) which showed similarity with hot cores. The presence of a hot core-like region at the heart of the protostars has however been indicated using H₂CO line emission modelling (Ceccarelli et al. 2000b). A few years later, the detection of several iCOMs towards the system by Cazaux et al. (2003) definitively labelled IRAS 16293 as a hot corino. With the improvements in angular resolution, studies showed that iCOMs emission is detected towards both components of IRAS16293, therefore indicating the presence of two hot corinos with some chemical differentiation between them (e.g. Bottinelli et al. 2004; Kuan et al. 2004; Huang et al. 2005; Remijan & Hollis 2006; Bisschop et al. 2008; Caux et al. 2011; Jørgensen et al. 2011; Manigand et al. 2020). Additionally, pre-biotic molecules such as glycolaldehyde (HCOCH₂OH; Jørgensen et al. 2012, formamide (NH₂CHO; Kahane et al. 2013), cyanamide (NH₂CN; Coutens et al. 2018), hydroxyacetone (CH₃CCOCH₂OH; Zhou et al. 2020) and very recently, propenal (C₂H₃CHO; Manigand et al. 2021) have been detected towards the source.

Besides iCOMs, many other molecules were detected towards IRAS 16293-2422, such as S-bearing species (Blake et al. 1994; Wakelam et al. 2004; Ceccarelli et al. 2010;

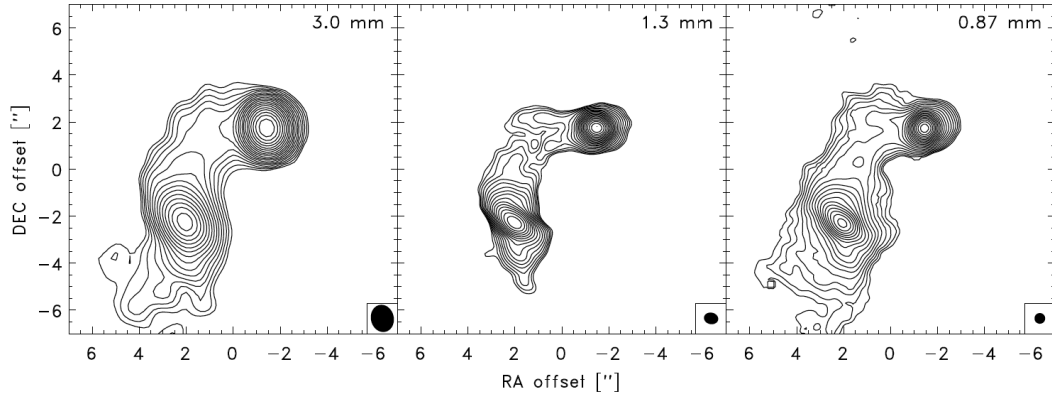


Figure 11: Continuum image of IRAS 16293 at 3mm, 1.3mm and 0.98mm from ALMA observations (Jørgensen et al. 2016). The phase center is $\alpha_{J2000} = 16^{\text{h}}32^{\text{m}}22^{\text{s}}.72$ and $\delta_{J2000} = -24^{\circ}28'34''.3$.

Caux et al. 2011; Jørgensen et al. 2011; Drozdovskaya et al. 2018), N-bearing species (e.g. Bisschop et al. 2008; Ceccarelli et al. 2010; Hily-Blant et al. 2010; Caux et al. 2011; Jørgensen et al. 2011; Jaber Al-Edhari et al. 2017; Calcutt et al. 2018a,b), deuterated species (e.g. Ceccarelli et al. 2001; Parise et al. 2002; Stark et al. 2004; Parise et al. 2004, 2005; Ceccarelli et al. 2010; Bacmann et al. 2010; Caux et al. 2011; Coutens et al. 2012, 2016; Persson et al. 2018; Manigand et al. 2019; Melosso et al. 2020). Small carbon chains such as C_2H , C_4H , $\text{c-C}_3\text{H}_2$ and CH_3CCH have been detected towards the hot corino source envelope (e.g. Sakai et al. 2009a; Caux et al. 2011) but with abundances lower by a factor 2 (CCH) to 10 (C_4H) of that of WCCC sources (Sakai et al. 2009a). Only cyanopolyynes (HC_{2n}N), another type of carbon chain molecules, have been detected both towards the cold envelope and the inner region of $T \geq 80$ K with abundances in the former lower compared to WCCC sources and in the latter similar to that of WCCC sources (HC_3N , HC_5N ; Jaber Al-Edhari et al. 2017).

3.2.3 Hot corino chemistry

To understand hot corino chemistry, we need to understand the formation of iCOMs. For decades, iCOMs have been observed in the ISM in various environments, e.g. star-forming regions (e.g. Rubin et al. 1971; Cazaux et al. 2003; Kahane et al. 2013; López-Sepulcre et al. 2015; Coutens et al. 2015; Potapov et al. 2016; Ligterink et al. 2018; McGuire 2018; Scibelli & Shirley 2020), in shocked regions and outflows (e.g. Arce et al. 2008; Öberg et al. 2011; Mendoza et al. 2014; Codella et al. 2015, 2020; Gerin et al. 2015; Lefloch et al. 2017, 2018; Holdship et al. 2019b; De Simone et al. 2020b; Tychoniec et al. 2021), and external galaxies (e.g. Henkel et al. 1987; Martín et al. 2006, 2021; Muller et al. 2011, 2013; Aladro et al. 2015; Sewiło et al. 2018; Qiu et al. 2018). Yet, no reliable theory of their formation exists in order to explain their observed molecular abundances.

First, until the early 2000s, iCOMs were thought to form through gas-phase reactions, this is the gas-phase paradigm (Fig. 12). As explained in Section 1, during the cold phase of cold cores, atoms and molecules accrete onto the surface of the grains leading to the formation of icy mantles composed of, among other small molecules, CH_3OH and H_2CO . In hot cores, at temperatures around 200-300K, grain mantles sublimate and those hydrogenated species are liberated into the gas phase. Further reactions will lead to the

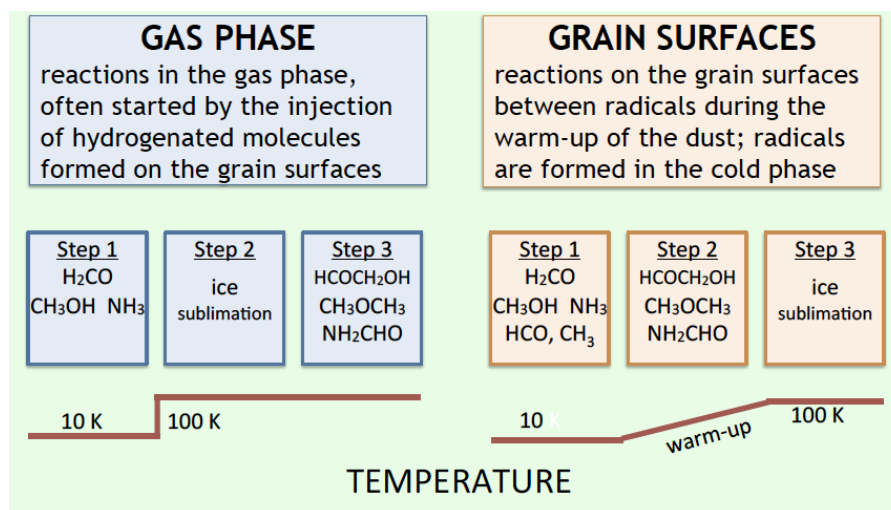


Figure 12: The two paradigms of the iCOMS formations explained: gas-phase (left) and grain surface (right). From the DOC proposal (P.I. C. Ceccarelli)

formation of iCOMs (e.g. Charnley et al. 1992; Caselli et al. 1993; Brown et al. 1988; Millar et al. 1991; Charnley et al. 1997). This gas-phase paradigm became obsolete with the discovery of iCOMs in hot corinos and the galactic centre molecular clouds (e.g. Cazaux et al. 2003; Requena-Torres et al. 2006), where the temperature does not reach 200 K.

The next and most accredited paradigm is that of the dust grain (Fig. 12) where all iCOMs are formed (Garrod & Herbst 2006; Garrod et al. 2008; Öberg et al. 2009c). This theory is based on several laboratory experiments showing that hydrogenated molecules irradiated by UV photons or particles could lead to the formation of iCOMs, amino acids and even more complex molecules (Allamandola et al. 1999; Bernstein et al. 1999; Muñoz Caro et al. 2002; Strazzulla & Palumbo 2001; Fedoseev et al. 2015, 2017). First, as for the previous theory, hydrogenated molecules and radicals (e.g. CH₃OH, H₂CO, NH₃) are formed on the grain surface during the pre-stellar core phase (e.g. Boogert et al. 2015). Then, there is the warm-up phase (Viti & Williams 1999; Viti et al. 2004) during which the temperature increases from 10 to more than 100 K. When a temperature of 30 K is reached, radicals on the grain surface acquire mobility leading to the formation of iCOMs. At a temperature larger than 100 K, the dust grain ice mantle sublimate and the iCOMs are released onto the gas phase, where they are observed (e.g. Viti et al. 2004; Garrod & Herbst 2006; Garrod et al. 2008; Aikawa et al. 2008; Awad et al. 2010; Garrod & Widicus Weaver 2013; Choudhury et al. 2015). Unfortunately, models struggle to reproduce observations of iCOMs in hot corinos and in shocks (e.g. Occhiogrosso et al. 2011; Taquet et al. 2015; Codella et al. 2015; Jørgensen et al. 2016; Coutens et al. 2018; Quénard et al. 2018) and radical combination reactions, essential to form iCOMs in this theory, have also been challenged by quantum chemistry works (e.g. the case of CH₃CHO and NH₂CHO; Enrique-Romero et al. 2016; Rimola et al. 2018; Enrique-Romero et al. 2019, 2020, 2021). The theory is also challenged by the detection of iCOMs in PSCs and cold regions (Öberg et al. 2010; Bacmann et al. 2012; Cernicharo et al. 2012; Vastel et al. 2014; Jaber Al-Edhari et al. 2014; Potapov et al. 2016; Jiménez-Serra et al. 2016).

Following the detection of iCOMs in cold gas, several theoretical and experimental studies have been published to understand the formation of iCOMs at low temperatures

(e.g. Rawlings et al. 2013; Vasyunin & Herbst 2013; Vasyunin et al. 2017; Balucani et al. 2015; Ruaud et al. 2015; Chuang et al. 2016; Minissale et al. 2016; Quénard et al. 2018; Shingledecker et al. 2018; Holdship et al. 2019a; Harju et al. 2020; Jin & Garrod 2020; Wakelam et al. 2021). The abundance of several iCOMs could be reproduced by a combination of grain surface and gas-phase reaction (e.g. Vasyunin & Herbst 2013; Balucani et al. 2015; Skouteris et al. 2018; Quénard et al. 2018; Vazart et al. 2020). Laboratory experiments and quantum chemistry works showed that quantum effect could help reactions to occur when one first thought they could not (e.g. Shannon et al. 2014; Barone et al. 2015). In summary, both gas-phase reactions and dust grain surfaces processes are important in the formation of iCOMs.

3.3 Warm Carbon Chain Chemistry protostars

After the discovery of hot corinos, it was first thought that every low-mass protostar was then hiding a hot corino in its heart, including the proto-Sun (Bottinelli et al. 2007). Several studies aiming to detect iCOMs in solar-type protostars and hence to detect new hot corinos flourished afterwards. Surprisingly, it is by searching for iCOMs in IRAS 04368+2557 (hereafter L1527) that Sakai et al. (2008a) discovered a chemically different object, the first WCCC protostar. Unlike hot corinos, not many other WCCC protostellar sources have been confirmed since. Overall, four objects have been classified as WCCC protostars but there are currently 17 WCCC candidates. The list of detected WCCC objects and candidates is presented in Table 2.

Table 2: List of detected WCCC objects, their classification and location. Hybrids (see Sec. 3.4.1) are shown in *italic*.

WCCC objects	Class	Region	Reference
L1527	0/I	Taurus	Sakai et al. 2008a
IRAS15398-3359 (B228)	0/I	Lupus	Sakai et al. 2009b
IRAS 04365+2535 (TMC-1A)	I	Taurus	Sakai et al. 2016
<i>B335</i>	0	<i>Aquila (Bok globule B335)</i>	<i>Imai et al. 2016</i>
<i>L483</i>	0	<i>Aquila Rift</i>	<i>Sakai et al. 2009a; Oya et al. 2017</i>
WCCC candidates ^a			
IRAS 03301+3057 (B1)	0	Perseus	Sakai et al. 2009a
L1448N	0	Perseus	Sakai et al. 2009a
<i>L1448C</i>	0	<i>Perseus</i>	<i>Sakai et al. 2009a</i>
L1521F	0	Taurus	Sakai et al. 2009a
SMM4	0	Serpens	Sakai et al. 2009a
<i>BHR71 IRS1</i>	0	<i>Musca (BHR71 cloud)</i>	<i>Sakai et al. 2009a</i>
L1251A-IRS3	0	Cepheus	Cordiner et al. 2011
Cha-MMS1	VeLLO ^b or FHSC	Chameleon	Cordiner et al. 2012
L1157-mm	0	Cepheus	Lefloch et al. 2018
<i>Per-emb 35 A (NGC1333 IRAS 1)</i>	<i>I</i>	<i>Perseus</i>	<i>Higuchi et al. 2018</i>
SVS 3	II?	Perseus	Higuchi et al. 2018
<i>B5 IRS 1 (Per-emb 53)</i>	<i>I</i>	<i>Perseus</i>	<i>Higuchi et al. 2018</i>
<i>L1455 IRS 4 (Per-emb 20)</i>	<i>0/I</i>	<i>Perseus</i>	<i>Higuchi et al. 2018</i>
IRAS 03235+3004 (Per-emb 25)	I	Perseus	Higuchi et al. 2018; Taniguchi et al. 2021b
IRAS 03245+3002 (Per-emb 17; L1455 IRS1)	0/I	Perseus	Taniguchi et al. 2021b
L1524	I	Taurus	Zhang et al. 2021
IRAS 04181+2655	I	Taurus	Zhang et al. 2021

^a A WCCC candidate is a source for which carbon chains have been detected with single-dish observations only, thus for which the WCCC nature needs to be confirmed by interferometric observations. ^b Very low-luminosity Class 0 protostar

3.3.1 Characteristics

Warm Carbon Chain Chemistry objects are enriched in carbon chain molecules i.e. molecules of the form HC_{2n+1}N , C_nH , C_nH_2 , among others. Unlike hot corinos where iCOMs are

mainly located at the center inner region of the protostellar envelopes, carbon chain molecules are located up to ~ 2000 au around the central object, where the envelope temperature exceeds 25 K. A scheme of WCCC sources is presented in Figure 13. Results from large surveys showed that WCCC sources would tend to be located at the edge of molecular clouds or in isolation (Lefloch et al. 2018; Higuchi et al. 2018). There exist two main conditions to fulfil to classify an object as a WCCC object (Sakai & Yamamoto 2013):

1. Abundant various carbon chain molecules present in the protostellar core.
2. Carbon chain emissions concentrated around the protostar, in the warm dense part.

However, the presence of solely small carbon chains is not enough to classify an object as WCCC source. The presence of long carbon chains is also required (see Section 3.4). Several long carbon chains have been detected towards WCCC sources (e.g. C_6H , C_7H , C_6H_2 , HC_7N , HC_9N ; Sakai et al. 2008a; Cordiner et al. 2012; Araki et al. 2017; Yoshida et al. 2019). Finally, carbon chain molecules detected towards WCCC sources originate from a warm (≈ 30 K) and dense part of the protostar envelope, as lines with high excited conditions are detected.

Another characteristic of WCCC sources is that on top of being enriched in carbon chains, they show a deficiency in iCOMs in the inner zone of the protostellar envelope. This does not mean that no iCOMs are detected, but they are present in smaller amounts compared to other protostars (see the example of L1527 in Section 3.3.2). Compared to starless cores, S- and N-bearing molecules are rather deficient in WCCC sources (Sakai et al. 2008b; Yoshida et al. 2019) whilst carbon chains molecules and the complex molecules CH_3OH and CH_3CHO have similar column densities in both types of objects (Yoshida et al. 2019). Compared to hot corinos, S-bearing molecules seem also deficient towards WCCC sources (Yoshida et al. 2019). Another characteristic of WCCC sources is the detection of molecular anions (C_6H^- , C_4H^- ; e.g. Sakai et al. 2007, 2008b; Agúndez et al. 2008; Cordiner et al. 2011). Finally, WCCC sources present moderate deuterium fractionation ranging between 2% and 7% (Sakai et al. 2009b; Yoshida et al. 2019), which is less than in hot corinos (see Section 3.2.1) and similar or lower than in "evolved" starless cores (e.g. L1544, L63, L1689B; Sakai et al. 2009b). The WCCC prototype L1527 is presented in the next section.

3.3.2 The WCCC prototype L1527: A quick overview

L1527 is a protostar in transition between the Class 0 and Class I stages (Tobin et al. 2013), located in the Taurus molecular cloud at 137 pc of distance (Torres et al. 2007). This source is a close binary system with a separation of 25 au (Loinard et al. 2002).

The name *Warm Carbon Chain Chemistry (WCCC)* has been proposed by Sakai et al. (2008a) and is because the carbon chains detected towards L1527 are coming from a lukewarm (~ 30 K) environment where they are efficiently produced (see Section 3.3.3). The source stands out from the other solar-type protostars as a handful of carbon chains (and in particular long ones such as C_7H or HC_9N) have been detected (e.g. Sakai et al. 2008b, 2010; Araki et al. 2017; Yoshida et al. 2019). The detected lines are tracing relatively high-excitation conditions, implying their emission from the lukewarm envelope and hence showing the existence of a strong WCCC zone in L1527. The origin of the

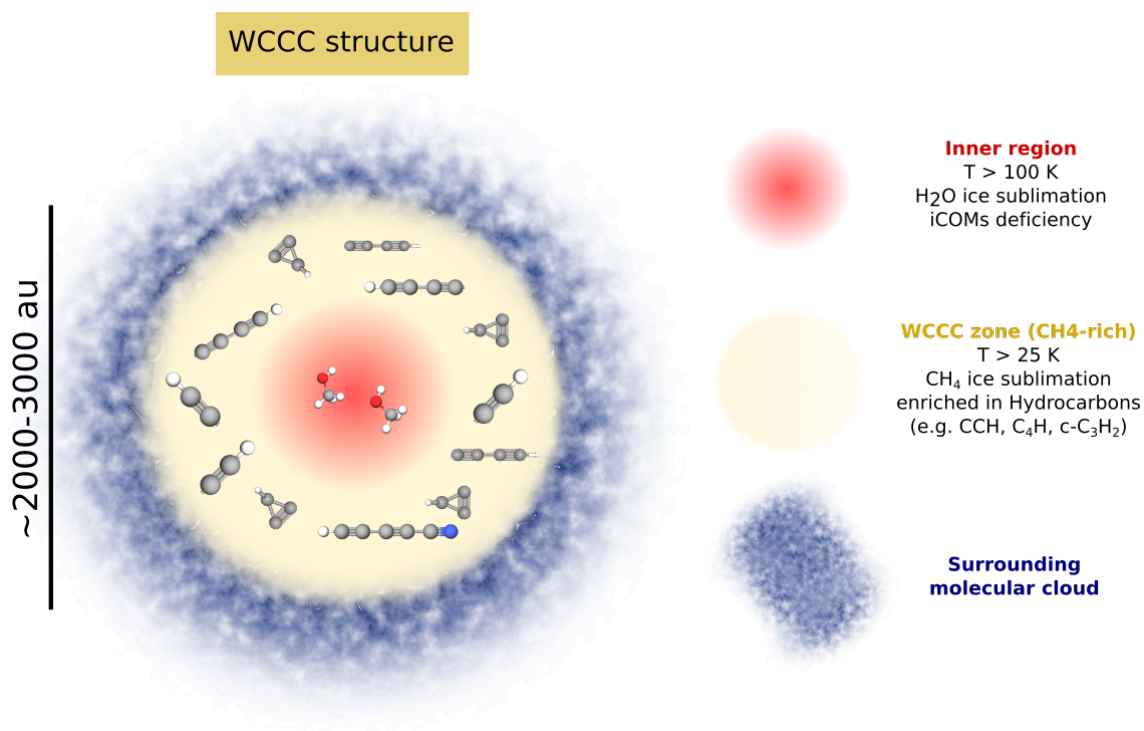


Figure 13: Scheme of a WCCC object structure. The central hot component (light red) is deficient in iCOMs whereas the WCCC zone (yellow) is enriched in carbon chain molecules. The cold envelope is not represented here. For simplicity and because I aim to focus on the chemical structure of a Class 0/I protostar, the outflow and disk are not represented. The scheme is not at scale.

emission of carbon chains from a ≈ 1000 au scale around this source has been confirmed by Sakai et al. (2010), as seen in Figure 14.

The molecular content of L1527 is quite different from that of hot corinos. Deuterated species have been detected but with low- to moderate deuterium fractionation levels (e.g. Roberts & Millar 2007; Sakai et al. 2009b; Yoshida et al. 2019). Several N- and S-bearing species have been detected (e.g. Sakai et al. 2008b; Sakai & Yamamoto 2013; Lefloch et al. 2018; Yoshida et al. 2019). Ions are also detected (Sakai et al. 2008b,c; Yoshida et al. 2019), including the first anion, C_6H^- , that has been detected toward a star-forming region (Sakai et al. 2007) followed by C_4H^- (Agúndez et al. 2008). As for iCOMs, a few of them have been detected with abundances of about one order of magnitude less than in hot corinos (e.g. CH_3OH , CH_3CHO ; Sakai et al. 2009a; Yoshida et al. 2019).

3.3.3 WCCC chemistry

Carbon chain molecules were initially thought to be abundant only in the early phases of the star formation process and deficient in the later stages, in particular at the protostellar stage, (Suzuki et al. 1992; Hirota et al. 2009) where carbon atoms are supposed to be locked onto CO molecules with a conversion timescale comparable to the dynamical timescale of molecular clouds (Sakai & Yamamoto 2013). In fact, carbon chain molecules of the form C_nH , C_nH_2 and HC_2nN are usually associated with cold dark clouds (e.g. Suzuki et al. 1992; Markwick et al. 2000; Fossé et al. 2001; Hirota et al. 2004; Kaifu et al. 2004; Hirota et al. 2009; Gratier et al. 2016; Cernicharo et al. 2021; Loomis et al. 2021).

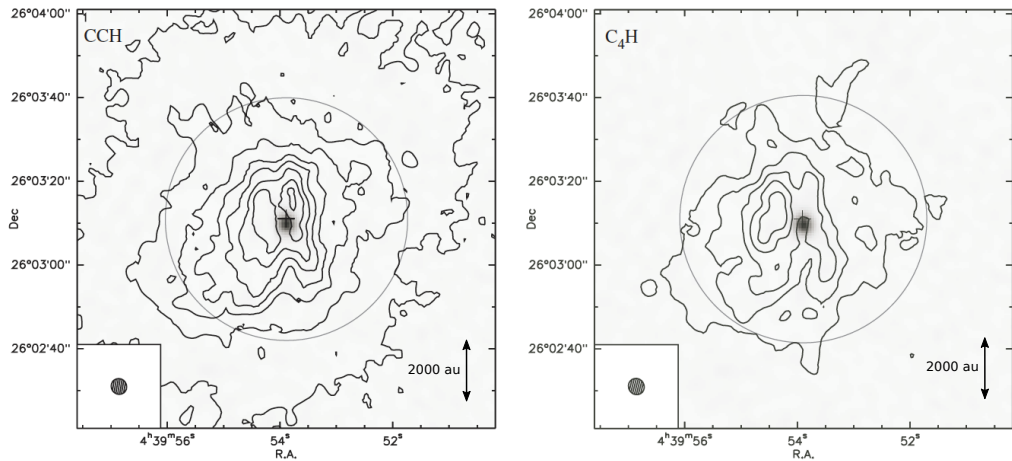


Figure 14: Intensity maps of CCH (left) and C₄H (right) lines in L1527 taken from Sakai et al. (2010). Levels are every 3.0×10^{-2} Jy/beam.km/s. The 3 mm continuum is represented with a grey-scale image. The strapped oval is the synthesised beam and the circle the field of view. The binary is not resolved here. The large extension of carbon chains around the protostar is well seen here.

However, the detection of carbon chains in protostellar envelopes led to the proposal of a new mechanism of carbon chains production in the lukewarm region of solar-type protostars envelope called the WCCC zone (Sakai et al. 2008a). The proposed WCCC mechanism has then subsequently been confirmed by chemical model calculations (e.g. Aikawa et al. 2008, 2012; Hassel et al. 2008, 2011; Wang et al. 2019).

In protostars lukewarm envelope, the temperature reaches easily at least 25 K, the sublimation temperature of CH₄ (Collings et al. 2004; Ferrero et al. 2020). Once CH₄ desorbs into the gas phase, it reacts with the other species already present there, triggering the WCCC mechanism. In the gas phase, CH₄ reacts with C⁺ and H₃⁺. The first carbon chains subsequently formed after a few reactions are CCH and C₂H₂. Further reactions involving C⁺ will lead to the formation of long carbon chains. On the other hand, C₂H₃⁺ formed via the reaction CH₄ + C⁺ can react with H₂, C, CH₄ and C₂H to produce longer carbon chains. A scheme of the basic WCCC chemistry mechanism is shown in Figure 15. To trigger the WCCC mechanism, large amounts of CH₄ (abundance at least several times 10⁻⁷; Sakai & Yamamoto 2013) need to be present in the grain ice mantles. The CH₄ region of desorption corresponds to a distance of a few thousands of au around $\sim 1 L_{\odot}$ protostar where most carbon chains are distributed (Sakai et al. 2010).

The WCCC feature is not found solely towards solar-type protostars. Wu et al. (2019) found WCCC characteristic towards the starless core called the eastern molecular core of L1489 IRS. Indeed, they found abundances of C₄H and CH₃CCH similar to that found in L1527. The core appears to be warmer (heated probably by the nearby protostars L1489 IRS) and at a late evolutionary stage, allowing the WCCC chemistry to occur. WCCC mechanisms have been also found towards massive star-forming regions where the chemistry in the envelope of protostars resembles that of low-mass WCCC sources (Mookerjee et al. 2012; Saul et al. 2015; Taniguchi et al. 2018a,b, 2021a).

WCCC chemistry
T > 25 K

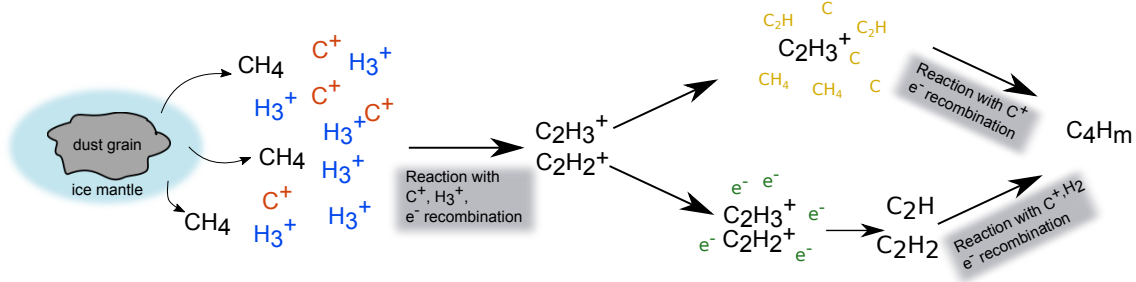


Figure 15: Simplified scheme of the formation of carbon chains in a lukewarm environment (WCCC zone) of a protostellar envelope. Adapted from Sakai & Yamamoto (2013).

3.4 Hot corino and WCCC objects: an exclusive nature ?

In Table 3, the characteristics of hot corinos and WCCC sources, as we know them so far, are summarised. From this table, it seems that hot corinos and WCCC objects have completely opposite characteristics, implying an exclusive nature. Moreover, if we compare the spectra of the hot corino prototype IRAS 16293 with the WCCC prototype L1527 (see Figure 16), we can see a significantly different spectrum pattern.

Table 3: Characteristics of hot corinos and WCCC sources

Characteristics	Hot corinos	WCCC source
Size	≤ 100 au	≈ 1000 – 3000 au
Temperature	≥ 100 K	≥ 25 K
Density	≥ 10 ⁷ cm ³	≈ 10 ⁶ cm ³
Molecular content	iCOMs enrichment, deficiency in carbon chain molecules rich in S-bearing species	deficiency in iCOMs, various and long carbon chain molecules poor in S-bearing species
deuterium fractionation	heavy deuteration level	moderate deuteration level
Location ^a	deep within proto-clusters?	in isolation/near the edge of a molecular cloud?

^a Higuchi et al. 2018

However, chemical models predict the existence of hybrid objects, with the simultaneous enrichment in iCOMs near the central object (~ 100 au), and enrichment in carbon chains at a larger scale (≈ 1000 au)(Aikawa et al. 2008, 2020). Hybrid objects are thus hot corinos surrounded by a WCCC zone. As chemical models efficiently reproduce these types of objects, their observations are rare. As of today, only two hybrids have been clearly identified: the solar-type protostars L483 and B335. Observations are however biased towards the search for hot corinos, because of their enrichment in iCOMs, and their interest in the context of life. Observations towards solar-mass protostars are performed with an angular resolution that is enough to observe hot corinos but too high to observe possible WCCC features because the latter are being resolved out at high angular resolutions.

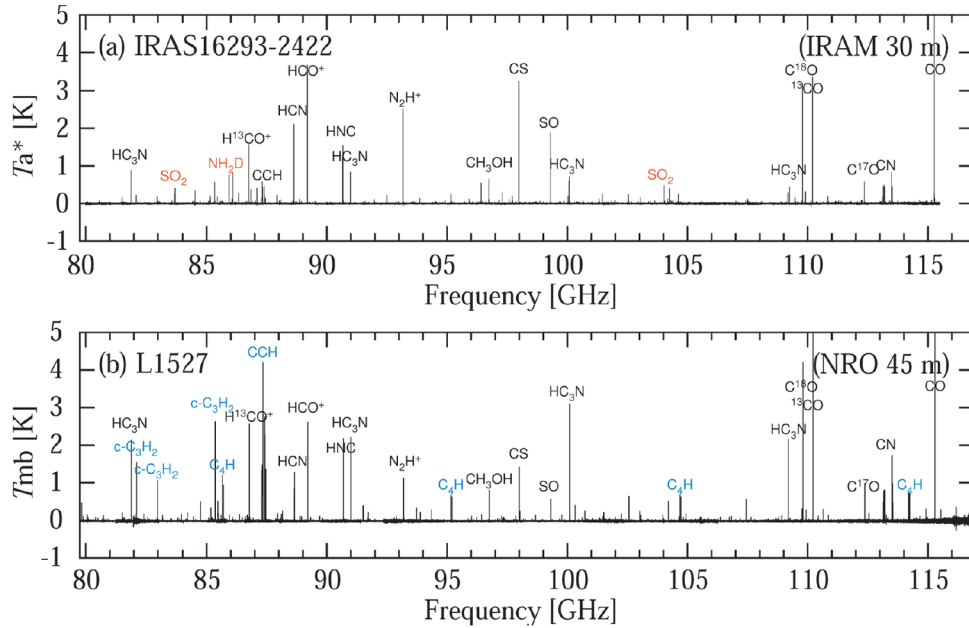


Figure 16: Comparison of spectrum obtained towards a) IRAS 16293 (Caux et al. 2011) and b) L1527 (Sakai & Yamamoto 2013). The two spectra are issued from 3mm spectral line surveys at IRAM-30m and Nobeyama-45m, respectively.

3.4.1 Hybrids: hot corino falafel wrapped in WCCC bread

There are two unambiguously identified hybrids: IRAS 18140-0440 (hereafter L483) and IRAS 19347+0727 (hereafter B335). L483 is a Class 0 to Class I protostar (e.g. Tafalla et al. 2000) located in the Aquila Rift filament at 436 ± 9 pc from us (Ortiz-León et al. 2018) while B335 is a Class 0 protostar located in the Bok Globule B335, ~ 100 pc away from us (Olofsson & Olofsson 2009).

L483 has first been considered a carbon chain rich core, as bright lines of $c\text{-C}_3\text{H}_2$, HC_3N , HC_5N were detected (Benson et al. 1998; Hirota et al. 2009). Then, Sakai et al. (2009a) classified this source as a WCCC candidate due to the detection of the rare carbon chain $l\text{-C}_3\text{H}_2$, which was previously detected only in the two confirmed WCCC sources L1527 and IRAS15398-3359, as well as the derivation of a relatively high abundance of C_4H . The detection of HCCO by Agúndez et al. (2015) toward the source supported its possible WCCC nature, but it is only in 2017, thanks to ALMA observations showing CCH emission at a few hundred au scale around the protostar, that the WCCC nature of the source was confirmed (Oya et al. 2017). For B335, its WCCC nature has been demonstrated more straightforwardly since Imai et al. (2016) detected CCH and $c\text{-C}_3\text{H}_2$ with relatively compact spatial distribution around the protostar (within a few 100 au), awarding its WCCC nature.

Concerning the hot corino nature of protostars, the detection of iCOMS such as NH_2CHO and HCOOCH_3 concentrated around the continuum peak of L483 and B335 implies the presence of a hot corino in the inner region (Imai et al. 2016; Oya et al. 2017). For L483, the presence of a hot corino with a radius of $\sim 40 - 60$ au has been further supported by the detection of other iCOMs such as CH_3OH , CH_3OCH_3 , $\text{C}_2\text{H}_5\text{OH}$ (Jacobsen et al. 2019). For B335, the iCOMs emission lines are marginally resolved and the hot corino

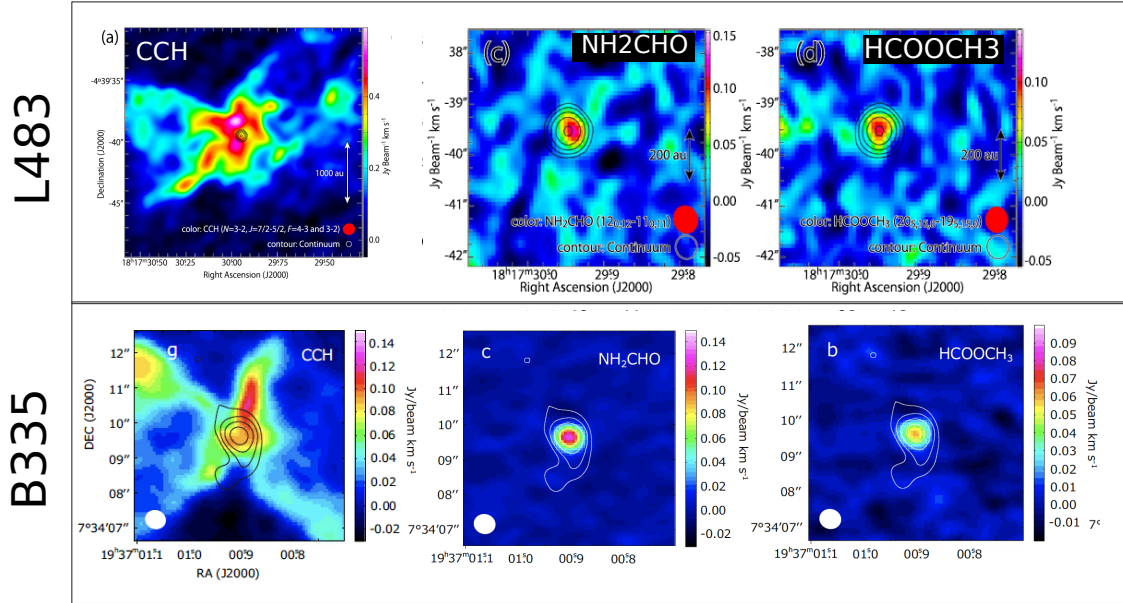


Figure 17: Intensity maps of CCH, NH_2CHO and HCOOCH_3 towards L483 (taken from [Oya et al. 2017](#)) and B335 (taken from [Imai et al. 2016](#)). In both sources, the 1.2mm continuum maps are represented by the black or white contours while the molecular species emission is on a coloured scale. We see that the two iCOMs originate from a compact region around the protostar, the hot corino, whilst the carbon chain molecule originates in a more extended region, the WCCC zone.

size is within a few 10 au. Finally, the mixed nature of L483 is also seen in the 3mm line survey by [Agúndez et al. \(2019\)](#), where both a handful of carbon chain molecules and iCOMs are detected. Figure 17 shows the moment 0 maps of some of the detected iCOMs and carbon chains.

3.4.2 Potential hybrid candidates

There are some other hybrid candidates but further interferometric observations are needed to confirm it.

IRAS11590-6452 (BHR71 IRS1 hereafter) is a class 0 protostar ([Froebrich 2005](#); [Green et al. 2013](#); [Yang et al. 2018](#)) which has been classified as a potential WCCC source by [Sakai et al. \(2009a\)](#), due to the detection of C_4H_2 lines, as in the confirmed WCCC source IRAS 15398-3359, and to the relatively high abundance of C_4H . On the other hand, [Yang et al. \(2020\)](#) discovered the presence of a hot corino within a radius of 100 au around the protostar. Even though the hot corino nature of this source has been confirmed, its WCCC nature still needs to be confirmed by interferometric observations. Hence, BHR71 IRS1 is a candidate hybrid source.

L1448C (also known as L1448-mm) is a Class 0 protostar ([Anglada et al. 1989](#)). L1448C is one of the sources mentioned as potentially having a WCCC zone by ([Sakai et al. 2009a](#)), as a high abundance of C_4H is measured towards the source. However, interferometric observations are still needed to confirm the WCCC nature of this source. There exist hints of the hot corino nature of this source, such as a large jump in H_2CO in its hot region ($T \geq 100$ K; [Maret et al. 2004](#)), the relatively high abundance of CH_3OH , and the detection of three other iCOMs possibly originating from a hot corino ([Belloche](#)

et al. 2020). Although there are strong evidences that L1448C is a hot corino, both natures (hot corino and WCCC) still need to be confirmed. L1448C is thus a hybrid candidate.

Two main large surveys in the Perseus molecular cloud, aiming to characterise the chemical nature of solar-type protostars, have been performed (Higuchi et al. 2018; Yang et al. 2021). Among the surveyed sources, three protostars can be classified as hybrid candidates: the Class I protostars NGC1333 IRAS 1 (Per-emb 35 A) and B5 IRS 1 (Per-emb 53), and the Class 0/I protostar L1455 IRS 4 (Per-emb 20). Their WCCC nature is based on results of single-dish observations of carbon chains and methanol (Higuchi et al. 2018). The spatial distribution of carbon chains being therefore unknown, interferometric observations are mandatory to confirm their WCC nature. On the other hand, Yang et al. (2021) detected methanol towards the three sources as well as formic acid (HCOOH) and methyl formate (CH₃OCHO) towards NGC1333- IRAS 1. The compact distribution of those species as well as the derived high excitation temperature are compatible with a hot corino origin.

Finally, IRAS 03245+3002 (Per-emb 17; L1455 IRS1) is a potential Class 0/I hybrid. Methanol, as well as its deuterated form CH₂DOH and its ¹⁸O isotopologue, methyl formate and dimethyl ether, have been detected towards the source (Yang et al. 2021). On the other hand, HC₃N has been observed with ALMA by Taniguchi et al. (2021b). The spatial extend of HC₃N (~ 3000 au) is similar to the spatial distribution of carbon chains in L1527 and can be explained by the WCCC mechanism. The detection of other long carbon chains is however required to confirm the WCCC nature of the source.

3.4.3 The chemical nature of solar-mass protostars: is everyone special?

The fraction of hot corinos, WCCC sources and hybrids is ridiculous compared to the number of solar-mass protostars. The majority of solar-mass protostars seem to show *transitional* chemical composition, revealing a full range of chemical possibilities lying between the two distinct chemistries. When comparing the abundances of C₄H and CH₃OH, two molecules abundant in WCCC sources and hot corinos respectively, Graninger et al. (2016) and Lindberg et al. (2016) showed that all the protostars from their sample had intermediate abundances between those for WCCC sources and those for hot corinos. Higuchi et al. (2018) came to the same conclusion in their surveys of CCH and CH₃OH toward 36 Perseus solar-type protostars, most of which presented intermediate characters between hot corinos and WCCC sources. Then, surveys from De Simone et al. (2017) and Belloche et al. (2020), detected emissions of at least three iCOMs towards about 30% of solar-mass protostars.

In conclusion, for a long time, only a few hot corinos and WCCC objects were known. Thanks to the high-angular resolutions provided by powerful interferometers such as ALMA and NOEMA, the number of hot corinos, WCCC objects and hybrids (recognised or candidates) significantly increased in the last three years. Yet, what causes this chemical diversity is still not clear, although recent results start to shed light on this subject. I address this point in the following section.

3.5 On the origin of the chemical differentiation

Both the hot corino and the WCCC chemistry are triggered by the sublimation of molecules trapped within the ice mantles of dust grains. There seems to be a significant amount of CH₄ ice in the grain mantles of WCCC objects when there seems to be a large amount

of CH_3OH in the grain mantles of hot corino sources. The difference in the chemical composition of protostars is thus due to the different grain mantles compositions. What could cause this chemical different composition? The answer hides in how grains formed, evolved and under which circumstances in their history. Today, the origin of the various grain mantles chemical compositions in hot corinos and WCCC objects is still an open question. I present here two major hypotheses.

3.5.1 Pre-stellar core phase timescale: an evolutionary cause

A first explanation involves the difference of timescales during the prestellar core phase (Sakai et al. 2008a, 2009a) and is represented in Figure 18. The typical timescale during which atomic carbon in the gas is locked onto the CO molecule is about 3×10^5 yr (Sakai & Yamamoto 2013). In the case of the formation of a hot corino, the duration of the prestellar phase would exceed this timescale. Molecules of CO freeze-out onto the dust grain mantles, where they undergo hydrogenation processes resulting in the formation of CH_3OH and H_2CO , key molecules to form other iCOMs (see Section 3.2.3).

On the other hand, if the duration of the prestellar core phase is faster or similar to the chemical timescale given above, carbon atoms do not have time to lock onto CO molecules and are depleted onto the grains in atomic form. The result of the carbon atom hydrogenation leads to the formation of methane. Once CH_4 is released into the gas phase, it will mainly produce carbon chains molecules, leading to the formation of a WCCC object as explained in Section 3.3.3.

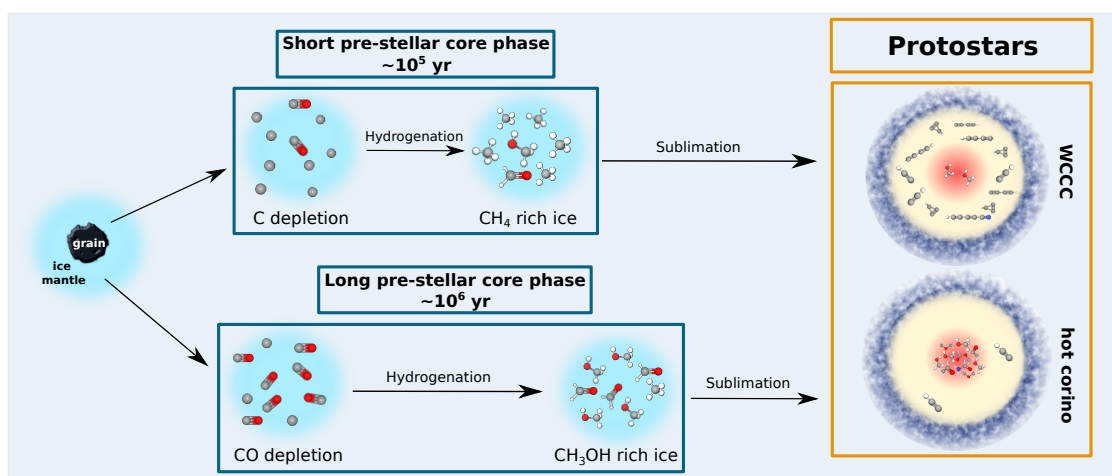


Figure 18: Scheme representing the formation of hot corino vs WCCC objects depending on the duration of the pre-stellar core phase. The outermost layer of the ice mantle is represented by the blue circles. For simplicity, the dust grain core is not represented in the pre-stellar core phase. Adapted from Sakai & Yamamoto (2013).

This theory works only if we consider a layered structure of the grain mantle (Taquet et al. 2012). In the case of the long starless core phase, the solid CH_4 formed earlier is trapped into most inner layer than CH_3OH and H_2CO . Thus, at temperatures reaching the CH_4 sublimation temperature, CH_4 cannot desorb and stays trapped. When the whole mantle sublimates at $T \geq 100$ K, CH_4 can then desorb, but it cannot react with C^+ to form carbon chains, as the ion has a very low abundance. Inversely, in the case of a short pre-stellar core phase, the outer layer has substantial amounts of CH_4 as CH_3OH and H_2CO

could not form in great amounts. Thus, CH_4 will be able to desorb earlier than in the previous case ($T=25\text{K}$) and trigger the WCCC chemistry.

Finally, this theory has recently been disproved by chemical model calculations. [Aikawa et al. \(2020\)](#) tested the dependence of hot corino and WCCC chemistry on the duration of the prestellar core phase. They varied several physical parameters of the static phase such as temperatures, visual extinction and duration of the static phase. They found that the variation of the parameters could reproduce hot corinos and hybrid sources, where both iCOMs and carbon chains are present, but they could not reproduce prototypical WCCC sources, where iCOMs are deficient.

3.5.2 External illumination: an environmental factor

A second hypothesis for the chemical variation of the dust grain ice mantles is the UV radiation from the Interstellar Radiation Field (ISRF) during the pre-stellar core phase ([Spezzano et al. 2016, 2020](#); [Lattanzi et al. 2020](#)).

[Spezzano et al. \(2016\)](#) mapped the emission of methanol and the carbon chain $c\text{-C}_3\text{H}_2$ across the pre-stellar core L1544. They found a chemical differentiation throughout the cloud due to its exposure to the ISRF. The part of the cloud more exposed to the latter presents a maximum in $c\text{-C}_3\text{H}_2$ emission whereas the part of the cloud more shielded from the ISRF presents a maximum in methanol. More recently, [Spezzano et al. \(2020\)](#) mapped the same species towards a sample of 6 dense cores, located in different environments and with different evolutionary ages (starless and pre-stellar cores). The cores embedded in a non-homogenous ISRF show the same trend as in L1544: active carbon chemistry is seen where the cloud is more exposed to the ISRF while methanol emission peaks where the cloud is more shielded. Likewise, [Lattanzi et al. \(2020\)](#) compared the chemical composition of L1544 with that of L183. The two PSCs are located in different environments. On one hand, L1544 lies at the edge of the Taurus Molecular Cloud and is more exposed to the ISRF than L183, which is, on the other hand, more embedded in the surrounding cloud. Their results showed that L1544 is richer in carbon-bearing species while L183 is richer in oxygen-bearing species.

All the above studies conclude that the chemical differences within/between the dense cores are due to their non-homogeneous exposition to the ISRF. Far Ultra-Violet (FUV) photons break small molecules in a process called photochemistry. Photochemistry prevents atomic carbon to lock onto the CO molecules. Carbon atoms thus freeze out onto grains and form CH_4 ices leading to the formation of WCCC objects in the protostellar stage. The regions exposed to the ISRF UV field are called Photo-Dissociation Regions. On the other hand, in regions shielded from the ISRF, the absence of photochemistry allows carbon atoms to be locked into CO molecules, enriching ices in CH_3OH and H_2CO and thus leading to the formation of a hot corino through iCOMs production. This scenario works only for uniform illumination cases. If the illumination is not homogeneous, the ices formed can present a mix of CH_3OH and CH_4 molecules ([Spezzano et al. 2016](#)).

This hypothesis is consistent with results from [Higuchi et al. \(2018\)](#) and [Lefloch et al. \(2018\)](#), who showed that hot corinos would tend to be located at the centre of molecular clouds whilst WCCC objects are more exposed to the ISRF, as they are located at the edge of molecular clouds or in isolation. Recently, [Kalvans \(2021\)](#) performed chemical simulations of a gas parcel in a protostar with different irradiation levels to investigate the carbon chain chemistry in WCCC sources. They found that WCCC chemistry can be reproduced under interstellar irradiation or cosmic rays. In conclusion, the environment

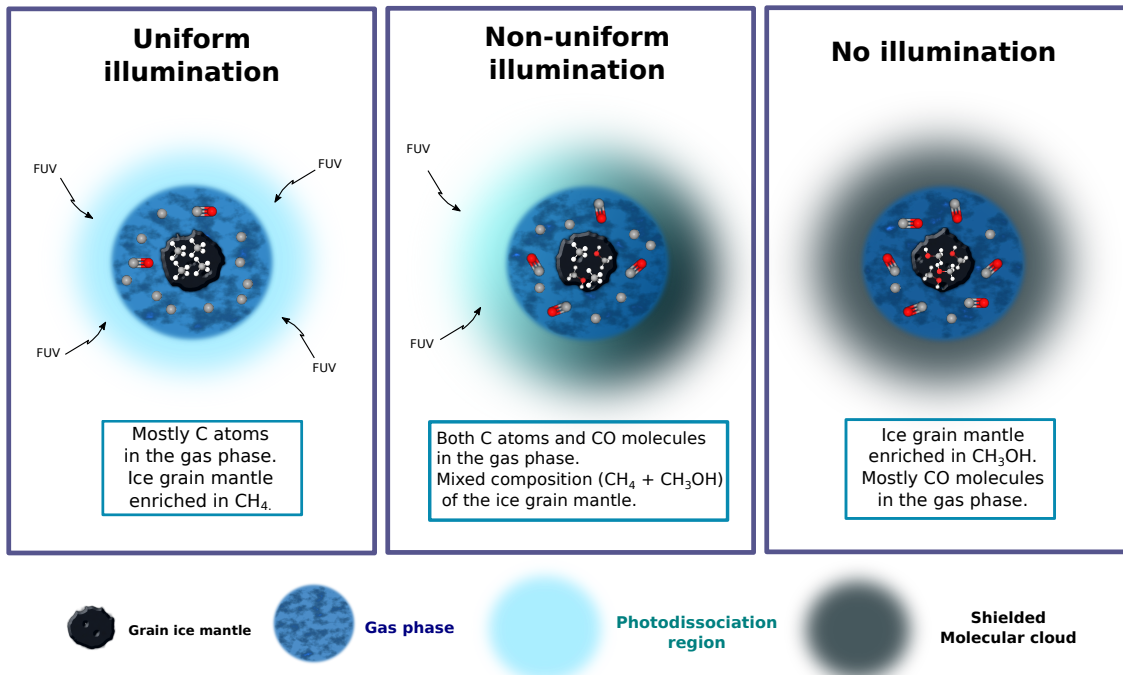


Figure 19: Scheme showing the effect of a uniform, a non-uniform and no illumination of a pre-stellar core on the chemistry of the grain surfaces. A uniform illumination will lead to a grain mantle enriched in methane (CH_4) whereas the absence of illumination will result in a grain mantle rich in methanol (CH_3OH). A non-uniform illumination will lead to ice mantles with a mixed composition ($\text{CH}_4 + \text{CH}_3\text{OH}$). Adapted from [Spezzano et al. \(2016\)](#).

could be the main parameter in the chemical diversity of solar-mass protostars. We need to increase the statistics of hot corinos and WCCC sources and study their environment to confirm this hypothesis.

Finally, from hot corinos to WCCC sources passing through hybrid objects, we face a broad range of possible chemical pasts for our Sun. It is thus legitimate to ask ourselves the following questions: What is our Sun's birth environment? Can we find hot corinos, WCCC objects and/or mixed objects there? If so, which one prevails?

4 The Sun's birth environment: A lively nursery

In Section 1, we saw that stars are born in the densest part of giant molecular clouds. Observations of those molecular clouds showed that we can distinguish between two different types of star-forming regions (e.g. [Lada 1987](#); [Shu et al. 1987](#); [Allen et al. 2007](#); [Evans et al. 2009](#)): isolated dense cores that form only low-mass ($\leq 8 M_\odot$) protostars (e.g. Taurus Molecular Cloud) versus single massive concentration of gas (e.g. OMC complex; also called clusters), in which both high-mass and low-mass protostars are formed. In which of those environments was our Sun born? Is it the same region where hot corinos and WCCC objects are found? If we want to understand whether our Sun underwent a

hot corino phase, a WCCC phase or neither, we should look into analogues of the Sun's birth environment. In this section, I first present the birth environment of our Sun, based on what is currently known. Then, I present the closest and best analogue to the Sun's birth environment, targeted in this thesis.

4.1 On the trail of our Sun's past

Most of stars form within groups or clusters of stars (e.g. [Carpenter 2000](#); [Lada & Lada 2003](#); [Porrás et al. 2003](#); [Evans et al. 2009](#)). Those clusters usually dissolve in a few tens of Myr or even less (e.g. [Hartmann et al. 2001](#); [Engargiola et al. 2003](#); [Kawamura et al. 2009](#); [Meidt et al. 2015](#); [Corbelli et al. 2017](#); [Chevance et al. 2020](#), and references therein). Thus, our Sun being 4.6 Gyr old ([Bonanno et al. 2002](#); [Amelin et al. 2002](#); [Baker et al. 2005](#)), its birth environment has long been dissipated. How then can we know what it looked like? Hopefully, not every piece of this past birthplace is gone: some characteristics of the present-day Solar System give us some clues about the early phases of its formation. Three main characteristics are powerful constraints on the Solar System formation process ([Pfalzner 2013](#)):

1. Presence of Short-lived radioactive species precursors of ^{26}Al and ^{60}Fe in meteorites
2. Planetary system outer boundary located at ~ 30 au and Kuiper belt inner boundary at 45 au
3. Higher eccentricities and higher inclination angles for the Kuiper belt objects than for the planets

All of those characteristics indicate that our Sun was likely born in a clustered environment (e.g. [Adams 2010](#); [Pfalzner & Vincke 2020](#)). I will explain why in the next two subsections.

4.1.1 Short-lived radioactive species and their origin

Short-lived radioactive species (SLRs) are species for which the half-life time is less than about 10 Myr. Therefore, they must have been incorporated into the early Solar System soon (~ 1 Myr) after their production which provides constraints on the conditions where they were produced (e.g. [Gounelle et al. 2006](#); [Adams 2010](#); [Diehl et al. 2021](#)). Hence, SLRs are great tools to trace back the link between the Sun and other stars born in the same molecular cloud and are used to estimate the number of stars/mass of the solar birth cluster (e.g. [Dauphas & Chaussidon 2011](#); [Gounelle & Meynet 2012](#); [Parker et al. 2014](#); [Nicholson & Parker 2017](#); [Portegies Zwart 2019](#)) and/or to estimate the types of stars present in the neighbourhood of the early Solar System, hence the astrophysical environment in which the Sun has evolved (e.g. [Meyer & Clayton 2000](#); [Looney et al. 2006](#); [Gounelle et al. 2006](#); [Gounelle & Meynet 2012](#); [Huss et al. 2009](#); [Lugaro et al. 2018](#); [Kaur & Sahijpal 2019](#); [Portegies Zwart 2019](#)).

The former presence of SLRs in the early Solar System can be inferred by measuring their daughter isotopes in meteoritic materials such as ^{26}Mg for ^{26}Al and ^{60}Ni for ^{60}Fe . The relation SLR-daughter isotope, called short-lived chronometers, can help determine the time at which the SLRs have been formed with a resolution of 1 Myr or less (e.g. [Wadhwa & Russel 2000](#); [Kita et al. 2005](#); [Gounelle & Russel 2005](#); [Wadhwa et al. 2007](#)). Some

SLRs show peculiar abundances: ^{26}Al is overabundant whereas ^{60}Fe is underabundant. These abnormal abundances can be explained by the presence of a windy Wolf-Rayet star or nearby supernovae (SN) explosions (e.g. [Looney et al. 2006](#); [Williams & Gaidos 2007](#); [Gounelle et al. 2009](#); [Gounelle 2015](#); [Young 2014](#); [Dwarkadas et al. 2017](#); [Portegies Zwart 2019](#)). Having a Wolf-Rayet star and a succession of SN explosions in the same birth environment seems to be quite a rare association unless we consider that our Sun is born in a large cluster. The origin of the SLRs is still debated today (see [Diehl et al. 2021](#) for a review). However, the cluster in which our Sun was born needs to be relatively massive to explain the presence of SLRs at an early stage of the Sun's formation.

4.1.2 Present Solar System structure constraints

For solar-type protostars, the observed sizes (radii) for protoplanetary disks range from ~ 10 au to a few 100 au, with the majority of disks between 100 and 200 au (e.g. [McCaughrean & O'dell 1996](#); [Vicente & Alves 2005](#); [Eisner et al. 2008](#); [Andrews & Williams 2007](#); [Andrews et al. 2009, 2010](#); [Williams & Cieza 2011](#)). The present boundaries of the Solar System located at 30 au for the planets, and at 45 au for the Kuiper belt, probably imply that the protoplanetary disk of the early Solar System has been truncated at some point by one (or more) process(es). Different processes could lead to the disk truncation such as close encounters (e.g. [Pfalzner et al. 2005](#); [Rosotti et al. 2014](#); [Vincke et al. 2015](#); [Portegies Zwart 2016](#); [Pfalzner et al. 2018](#)), photoevaporation by nearby massive stars (e.g. [Smith et al. 2003](#); [Mitchell & Stewart 2011](#); [Wright et al. 2012](#); [Mann et al. 2014](#); [Kim et al. 2016](#); [Winter et al. 2018](#); [Haworth et al. 2017](#); [Eisner et al. 2018](#)) or SN explosion ([Chevalier 2000](#); [Pelupessy & Portegies Zwart 2012](#); [Close & Pittard 2017](#)) although the last hypothesis is controversial ([Ansdell et al. 2020](#)). However, the most probable process at the origin of the supposed disk truncation and also explaining the high eccentricities and inclinations of the Kuiper belt objects is the close encounter (e.g. [Ida et al. 2000](#); [Morbidelli & Levison 2004](#); [Kenyon & Bromley 2004](#); [Jílková et al. 2015](#); [Pfalzner et al. 2018](#)). Hence, the physical and dynamical properties of the Solar System could be a natural consequence of a dense birth cluster.

Finally, to explain the meteoritic enrichment in SLRs daughter species, the disk truncation or the dynamical properties of the Kuiper belt objects, we need a birth cluster which is massive and dense. However, there exist two different types of massive clusters: starburst clusters or leaky clusters (also called OB associations). Starburst clusters are compact clusters (0.1pc) with high initial densities ($10^5 - 10^6 \text{ M}_{\odot} \text{ pc}^{-3}$) that will extend to over a few parsecs (1-3 pc) in 10 Myr or longer without losing their mass. On the other hand, leaky clusters are more diffuse clusters ($\sim 5\text{pc}$) which expand up to sizes of a few tens of pc while losing mass during the process ([Pfalzner 2009](#)). The Solar System probably formed in one of these two environments, but which one? [Pfalzner \(2013\)](#) showed that starburst clusters as the Sun birth cluster would lead to a disk too small compared to the present geometry of the Solar System and that the high concentration of massive stars would lead to further destruction of the disk. Therefore, the Sun is more likely to have been born in a large cluster with high-mass stars in its vicinity ([Adams 2010](#); [Portegies Zwart 2009](#); [Brasser et al. 2012](#); [Pfalzner 2013](#); [Pfalzner et al. 2015](#); [Pfalzner & Vincke 2020](#); [Winter et al. 2020b](#)). A scheme representing this type of environment is shown in [Figure 5.1](#).

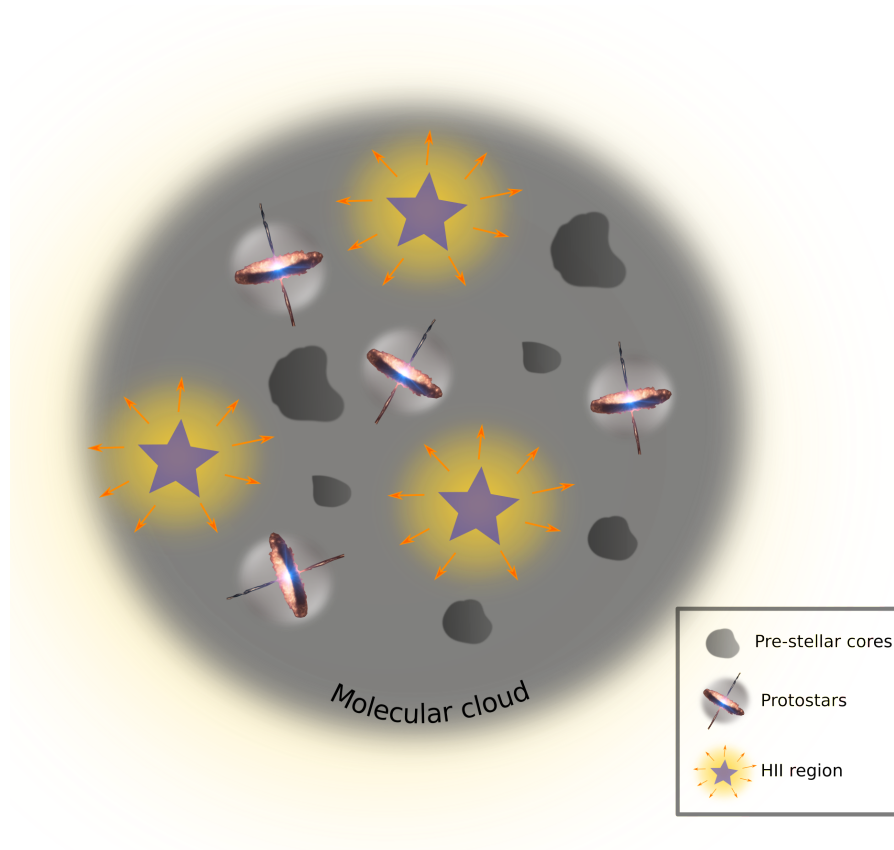


Figure 20: Scheme of a large cluster, which was very likely the birth environment of our Sun. The HII regions are formed by massive (O/B-type) stars that are important sources of UV radiation. The Photodissociation Region (PDR) is the region surrounding the molecular cloud and is created by the nearby HII regions. The molecular cloud contains Class 0 and I protostars, as well as pre-stellar cores. These are cold and dense fragments of the molecular clouds that will give birth to protostars.

4.2 The OMC-2/3 filament: The closest analogue to our Sun’s birth environment

Are there hot corinos and/or WCCC objects in Solar-like birth environments? Before the beginning of this thesis, almost all known hot corinos and WCCC objects were located in low-mass star-forming regions such as Perseus, Serpens, Taurus among others. The hot corino located in the Orion Molecular Cloud (OMC), HH212-MM1 (Codella et al. 2016, 2018; Lee et al. 2017; Lee et al. 2019), is quite isolated from massive stars. Its environment does not fulfil all criteria to be considered as analogue to that of the Sun. On the WCCC side, no solar-mass WCCC object located in high-mass star-forming regions were detected. Hence, we did not know whether hot corinos and/or WCCC objects were present in an environment that is analogue to that in which our Sun was born. In order to determine whether the Sun experienced a hot corino phase, a WCCC phase, or neither, we need to search for hot corinos and WCCC objects in Solar-like birth environments, which is one of the goals of this thesis.

So far, the best-known analogue is the OMC-2/3 filament. The filament is located in the Orion A molecular cloud at a distance of (393 ± 25) pc (Großschedl et al. 2018) and

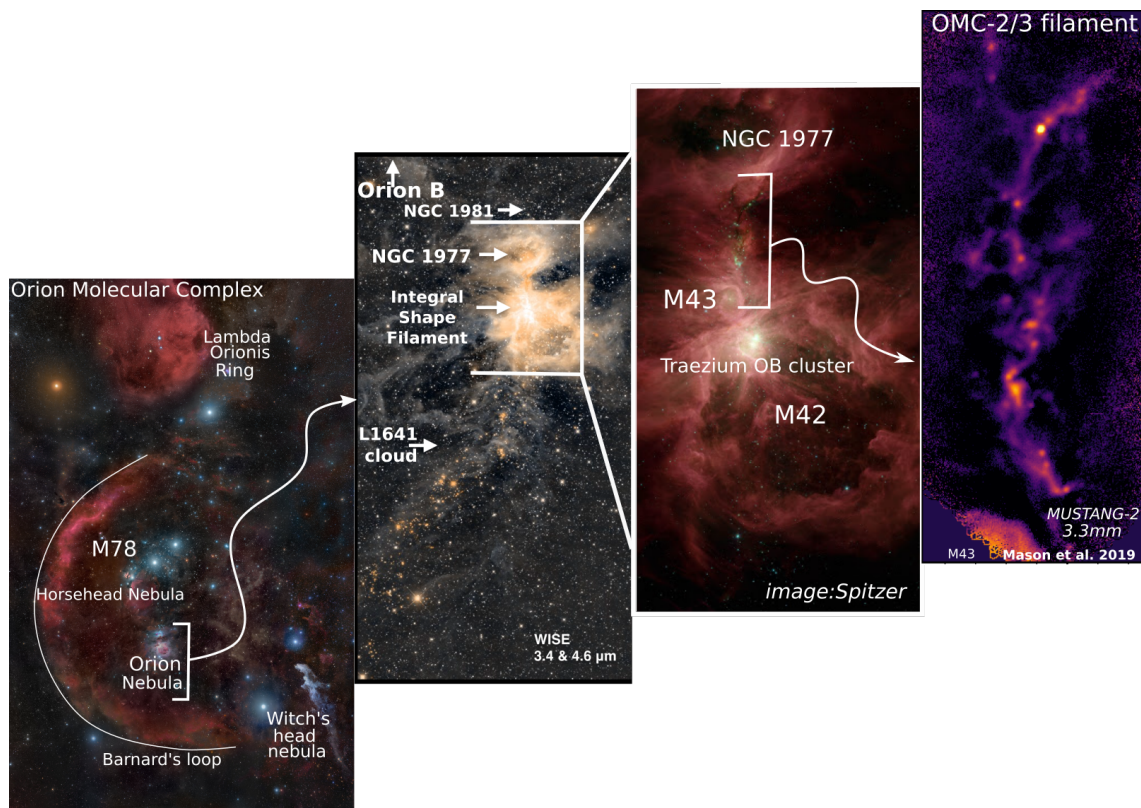


Figure 21: The Orion Molecular Complex contains the Orion A molecular cloud, itself contained in the 1° (7.3 pc) long Integral Shape Filament (ISF). The OMC-2/3 filament is located in the northern part of the ISF, between the HII regions NGC 1977, The Trapezium OB cluster and M43.

is part of the 1° long Integral Shape Filament (ISF; [Bally et al. 1987](#)). OMC-2/3 is located in the northern part of the ISF, north of OMC-1, the known "hot core" ([Batria et al. 1983](#)) which is associated with the Orion Nebula (see [Figure 21](#)). The OMC-2/3 filament is composed of two molecular clouds, OMC-2 and OMC-3. OMC-2 is the southern cloud and has been first identified by [Gatley et al. \(1974\)](#) whereas OMC-3 is the northern cloud and has been clearly labelled in 1997 by [Chini et al.](#) (although the very first reference to OMC-3 appears in [Kutner et al. 1976](#)). The two clouds are bounded by two major HII regions, NGC1977 to the North (powered by B stars) and the Trapezium OB cluster to the South (powered by O and B stars). Additionally, three B stars are located to the East of the OMC-2/3 filament (M43). The two OMC clouds seem to have different evolutionary stages, with OMC-3 being younger than OMC-2 (e.g. [Castets & Langer 1995](#); [Chini et al. 1997](#); [Lis et al. 1998](#)).

OMC-2/3 is one of the most known active sites of star-forming regions (e.g. [Rayner et al. 1989](#); [Bally et al. 1991](#); [Jones et al. 1994](#); [Ali & Depoy 1995](#)) and has been extensively studied since its discovery. A wealth of pre-stellar, Class 0, Class I objects and PMS stars have been detected towards the region thanks to submillimeter and IR observations (e.g. [Rayner et al. 1989](#); [Mezger et al. 1990](#); [Jones et al. 1994](#); [Chini et al. 1997](#); [Lis et al. 1998](#); [Johnstone & Bally 1999](#); [Nielbock et al. 2003](#); [Megeath et al. 2012](#); [Stutz et al. 2013](#); [Furlan et al. 2016](#); [Kainulainen et al. 2017](#); [Tobin et al. 2020](#)). Thanks to the high-angular resolution achieved by interferometers such as VLA and ALMA, the number of detected sources in the OMC-2/3 filament is far from the original six sources

detected in OMC-2 by [Mezger et al. \(1990\)](#) (labelled FIR1-6). An overview of the stellar content is shown in [Figure 22](#). The relatively young population of the OMC-2/3 filament is comforted by the presence of several molecular outflows, H₂ knots and Herbig-Haro objects (e.g. [Castets & Langer 1995](#); [Yu et al. 1997, 2000](#); [Aso et al. 2000](#); [Williams et al. 2003](#); [Takahashi et al. 2008](#); [Gómez-Ruiz et al. 2019](#); [Feddersen et al. 2020](#)) as well as radio and X-rays emissions towards some of the sources (e.g. [Reipurth et al. 1999](#); [Tsuboi et al. 2001](#); [Tobin et al. 2020](#)). Other types of objects, such as young brown dwarfs, have also been detected towards OMC-2/3 ([Peterson et al. 2008](#)).

The OMC-2/3 filament is particularly interesting because it is the nearest region containing low- to high-mass forming stars, and it is surrounded by bright OB stars. Hence, this region fulfil all the requirements to be labelled as a Sun's birth-like environment. Additionally, OMC-2/3 is a unique target to probe the effect of a highly illuminated environment on a possible chemical diversity among the OMC-2/3 solar-type protostars.

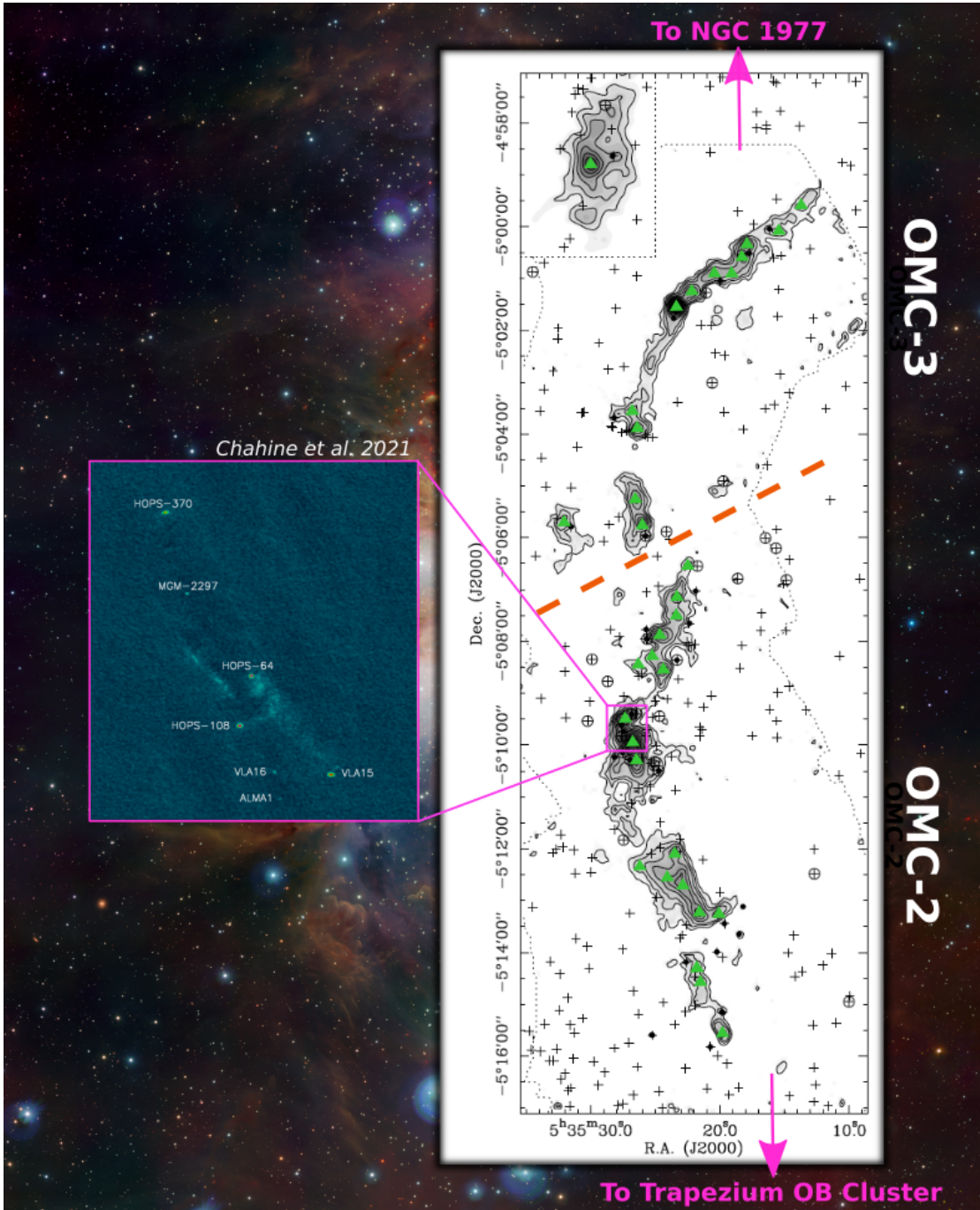


Figure 22: Overview of the stellar content of OMC-2/3 at a large scale (≤ 10000 au). Image adapted from [Nielbock et al. \(2003\)](#). The upper left insert (square grid) is taken from the SIMBA map of [Nielbock et al. \(2003\)](#). The 1.3mm map in grey-scale is from [Chini et al. \(1997\)](#) whose limits are represented by dotted lines. Contours are increased linearly from a 3σ noise level ($1\sigma = 25\text{mJy/beam}$). The filled dots represent the MIR sources, the crosses represent the 2MASS sources, open circles represent objects with a colour excess ([Nielbock et al. 2003](#)), and the green triangles represent the sources previously detected by [Chini et al. \(1997\)](#) and [Lis et al. \(1998\)](#). New high-angular resolution observations reveal the multiplicity of solar-mass stars as seen in the magenta framing, which shows the 1.3mm dust continuum map of OMC-2 FIR3 and FIR4 (image taken from [Chahine et al. 2021](#)). The beam of the observations is depicted in the lower-left corner. The separation between OMC-2 and OMC-3 is represented by the orange dashed line.

5 Context and Objectives

5.1 The DOC (Dawn of Organic Chemistry) project



This thesis is part of the DOC (Dawn of Organic Chemistry) project (P.I. Cecilia Ceccarelli), funded by the ERC (European Research Council) under grant No 741002. The project aims to understand the start of organic chemistry in systems similar to the Sun's progenitor, how organic chemistry evolves in these systems and, consequently, whether the chemical seeds of life are universal, and to what extent. In practice, the goal of DOC is to provide a reliable theory for organic chemistry in nascent solar-type systems.

The DOC project combines astronomical observations, theoretical quantum chemistry computations, and astrophysical/physical modelling, corresponding to three Work Packages (WPs). The first work package (WP 1) corresponds to astronomical observations. It aims to obtain the abundance and distribution of iCOMs in a large sample of prestellar cores, hot corinos and outflow shocks. The second work package (WP 2) concerns quantum chemistry computations. In this WP, theoretical quantum chemistry computations of the reactions on the grain surfaces and in the gas phase are performed. They will give new insights into the feasibility of gas and grain formation routes of iCOMs that are commonly found in astrochemical network databases. Finally, the last work package (WP 3) concerns models and tools. Work package 3 aims to build up astrochemical models and tools to compare observations with model predictions, using the results from the theoretical calculations obtained within DOC (i.e. from WP 2). Therefore, the three WPs are complementary and need to work in synergy to get a comprehensive picture of iCOMs chemistry in the early stages of the low-mass star formation process.

From Figure 23, my thesis belongs to WP 1 and aims to address question 2, i.e. whether all Solar-type protostars have a hot corino and how it depends on the prestellar core phase. The main task associated is to classify the diversity of organic richness in solar-type stars. I describe more in detail the objectives of the thesis in the next section.

WP 1: ASTRONOMICAL OBSERVATIONS		
<i>Objective:</i> Provide a framework of observations, from which we can derive the COMs abundances and distribution, and learn which organic molecules are present, in which protostars, at which scales, and what affects them.		
<i>Questions to answer</i>	<i>Tasks</i>	<i>DOC team</i>
Q1: What is the organic molecular complexity in Solar type pre- and proto- stellar sources?	T1.1: Inventory of the organic and molecular content	SR1, PhD1
Q2: Do all Solar type protostars have a hot corino and how does it depend on the prestellar phase?	T1.2: Classification of the diversity of organic richness in Solar type forming stars	SR3, PhD2
Q3: Is organic enrichment of hot corinos transferred at planet-formation scales?	T1.3: Determination of organic enrichment from the collapsing envelope to planet formation zone	PD1
Q4: What is the ionization and how does it affect the COMs formation and evolution?	T1.4: Gas ionization constraints	PhD3

Figure 23: Extract from the ERC DOC proposal showing a brief description of WP1 with the list of questions and tasks associated with this WP. SR stands for Senior Researcher and PD for Postdoc. Extract taken from the ERC DOC proposal led by Cecilia Ceccarelli.

5.2 Shedding light on the Sun’s chemical past: Objectives of the thesis

From Sec. 3, it is clear that not all solar-mass protostars share the same chemical content. This fact does not make it easier to understand the chemical past of our Sun. Because of the correlation found between the abundance of iCOMs in hot corinos and those found in comets, it is suspected that our Sun experienced a hot corino phase (e.g. Ceccarelli et al. 2014a; Drozdovskaya et al. 2019; Bianchi et al. 2019). Is it truly the case? Could our Sun, instead, undergo a WCCC phase, or even a hybrid phase? Until recently, most of the solar-mass protostars that have been targeted for astronomical studies are located in low-mass star-forming regions. These regions are relatively nearby (≤ 300 pc) and are thus easy to observe. Nonetheless, our Sun was more likely born in a large stellar cluster, with high-mass stars in its vicinity (Sec. 4). Efforts to characterise the chemical nature of solar-mass protostars located in these types of regions are needed to make a step forward in the comprehension of our Sun’s chemical history.

Before starting this thesis, there existed no systematic study of the chemical nature of solar-mass protostars located in a region similar to the one in which our Sun was born. Additionally, there was no detection of either hot corinos or WCCC sources in such regions. The ultimate goal of my thesis was (and still is) to shed light on the chemical nature of solar-mass protostars in a region analogue to the Sun’s birth environment. I also aim to bring new pieces of evidence to complete the puzzle of the Sun’s chemical past. This thesis also aims to comprehend what could cause the chemical diversity seen in the protostellar stage.

The first immediate goal of the thesis is to understand the influence of an enhanced UV radiation field within a star-forming region and the increased temperature of the natal cloud, which are both parameters likely playing a role in the chemical outcome on the proto-Solar environment. I, therefore, aim to understand what type of objects are present in a region similar to the one in which our Sun was likely born (Sect. 4). Are there predominantly hot corinos, WCCC or hybrid objects in this type of region? To address this question, I investigated the chemical nature of several solar-mass protostars located in the OMC-2/3 filament, the closest best analogue to the Sun’s birth environment. If one type of object is more abundant than the other ones, it can be a first hint on the former chemical nature of the Sun: if hot corinos are prevailing, then this would point towards the ancient hot corino nature of our Sun. If, on the other hand, WCCC objects are

predominant in this region, then the former chemical nature of our Sun could have been more related to a WCCC type chemistry.

The second goal of this thesis concerns the chemical diversity of solar-mass protostars. I present the two major hypotheses about what could cause the chemical diversity among low-mass protostars in Sec. 3.5: the pre-stellar core phase timescale and the external UV-illumination. In this thesis, I investigated the external UV-illumination, i.e. the environmental factor. The targeted region, the OMC-2/3 filament, is bounded by several HII regions, which makes it particularly UV-illuminated. I compared the chemical content of solar-mass protostars located in the OMC-2/3 filament and the Perseus Molecular Cloud. The former is a low- to high-mass star-forming region that is highly UV-illuminated, while the latter is a star-forming region hosting only low-mass protostars and is significantly less UV-illuminated compared to OMC-2/3. Comparing these two regions is useful to understand whether, and how, the environment plays a role in the chemical diversity seen at the protostellar stage. If hot corinos prevail in one of the two regions and WCCC sources prevail in the other one, this would suggest that UV-illumination can play a role in shaping the chemical nature of protostars. On the other hand, if the two regions show similar content in terms of hot corinos, WCCC objects or hybrid sources, then the environment may not be at the origin of the chemical diversity seen among solar-mass protostars.

The thesis structure is the following. First, the tools and methodology I used to achieve the goals cited above are described in Chapter 1. In particular, I focus on single-dish telescopes and interferometers for the tools, and molecular line analysis for the methodology. Then, the results of the thesis are divided into two chapters, Chapters 2 and 3. Chapter 2 presents the results of the large-scale (≤ 10000 au) study performed with single-dish telescopes. Chapter 3 presents the results of the small-scale (~ 100 au) study, which are the first results of the Orion ALMA New Generation Survey (ORANGES). First, the dust continuum analysis performed towards the OMC-2/3 filament protostars using a combination of ALMA and VLA observations is presented in Sec. 3.1. Then, the results of the hot corino and WCCC sources hunt using ALMA observations are given in Sections 3.2 and 3.3. Finally, the ongoing project which concerns the organic chemistry associated with an intriguing molecular outflow driven by one of the protostellar sources in the OMC-2/3 filament is described in Chapter 4 with the presentation of preliminary results. The manuscript ends with the conclusion and prospects of the thesis.

Observing Tools and Methodology

This chapter is dedicated to the observing tools and the methodology I used during my thesis. The first part of this chapter concerns the observing tools whilst the second part concerns the methodology. I based the explanations mostly on Master 2 courses of the University of Grenoble Alpes, the 10th IRAM mm Interferometry school (Grenoble, France 2018), the first ACO Network School (Perugia, Italy 2019), the Book of Wilson et al. 2009 and the NRAO Essential Radio Astronomy course website.

1 Observing Tools: Radio Telescopes

All of the data I have been working on during this thesis were obtained with radio telescopes, both single-dish telescopes and radio interferometers. In the following, I will first describe some concepts of radio astronomy that are useful to know as an observer. I will then describe some important aspects of single-dish telescopes and radio interferometers and present the instruments from which the data were acquired.

1.1 The radio window

The Earth's atmosphere absorbs most part of the electromagnetic spectrum. Only optical/near-infrared and radio observations can be made from the ground as seen in Figure 1.1. Atmospheric windows delimited parts of the electromagnetic spectrum that are not totally blocked by the Earth's atmosphere. There are thus two windows, the visible and the radio windows. Within the thesis framework, we are interested in the radio window. I will, therefore, focus on it.

The radio band concerns frequencies between $\nu \sim 15$ MHz ($\lambda \sim 20$ m) and $\nu \sim 1.5$ THz ($\lambda \sim 0.2$ mm). Even though we can observe from the ground in the radio wavelengths, we need to avoid frequencies longwards of $\lambda = 1$ m (ionospheric effects) and shortwards $\lambda = 2$ cm, because of some atmospheric molecular lines that are dominating (in particular H₂O, O₂, O₃). The water vapour (H₂O) has a band at 22 GHz ($\lambda = 1.35$ cm) and 183 GHz (1.63 mm), molecular oxygen (O₂) has an intense band at 60 GHz (5 mm) and a line near 119 GHz (2.52 mm). Ozone (O₃), which is a minor species, has a several lines in the mm wavelengths. Finally, N₂, and CO₂ are also species composing the atmosphere, but they do not have rotational lines (they do not have a permanent dipole). Their lines (vibrational transitions) occur at frequencies longwards of 300 GHz. It is possible to

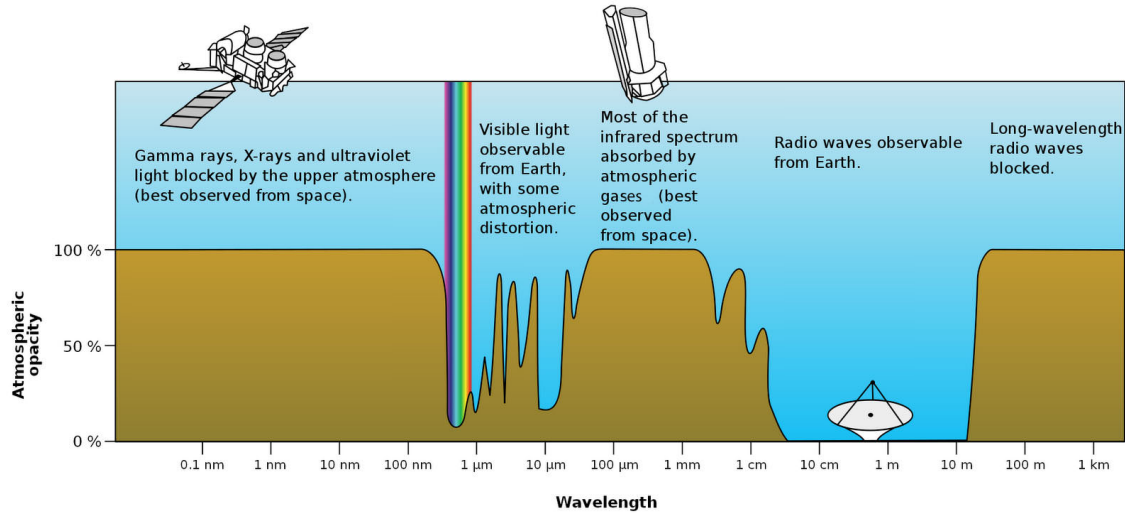


Figure 1.1: Schematic view of the electromagnetic radiation absorption by the Earth's atmosphere. Only a fraction of the radio window is totally transparent. Credit: NASA

minimize the atmosphere effects by observing at a high altitude, from a dry site and with stable atmospheric conditions.

1.2 Black-body radiation and Brightness temperature

In radioastronomy, the observed signal is obtained comparing a reference black-body of a given temperature with the source in the sky and is measured in units of temperatures. I introduce here the black-body radiation and the brightness temperature. These concepts are also useful for molecular line analysis (Sec. 2).

Black-body radiation A black body is an idealised body that is completely opaque and absorbs all the incident radiation. The specific intensity of the radiation of a black-body in thermodynamic equilibrium is given by the Planck function:

$$B_\nu(T) = \frac{2h\nu^3}{c^2} \frac{1}{e^{\frac{h\nu}{k_B T}} - 1} \quad (1.1)$$

The units are $\text{erg s}^{-1} \text{cm}^{-2} \text{Hz}^{-1} \text{sr}^{-1}$. The Planck function depends on the temperature and we can distinguish two limiting cases :

1. $h\nu \ll k_B T$, The Rayleigh-Jeans (R-J) approximation
2. $h\nu \gg k_B T$, The Wien's law

Only the R-J approximation is interesting here as Wien's law does not generally apply at radio frequencies. The Rayleigh-Jeans approximation is defined as the classical limit of the Planck law as the Planck function becomes:

$$I_\nu(T) = \frac{2k_B \nu^2}{c^2} T \quad (1.2)$$

Brightness temperature: The brightness temperature is the temperature of a black body producing the same specific intensity as the emitting source, I_ν . For any value of I_ν , T_B is defined as:

$$I_\nu = B_\nu(T_B) \quad (1.3)$$

To measure the radiation of a source, we can use several quantities such as the luminosity, flux density, F_ν , or the specific intensity (or brightness), I_ν . The flux density is the amount of energy per unit frequency in the observed spectral range. The units usually used are Janskys ($1 \text{ Jy} = 10^{-23} \text{ erg s}^{-1} \text{ cm}^{-2} \text{ Hz}^{-1}$). The flux density is given by:

$$F_\nu = \frac{F}{\Delta_\nu} \quad (1.4)$$

where F is the amount of radiation energy per unit time and per unit area.

The specific intensity, I_ν , is the energy flux at a frequency ν in one direction per unit area, unit solid angle and unit frequency. Both quantities are linked as:

$$F_\nu = \int I_\nu d\Omega \quad (1.5)$$

When approximating a source as a Gaussian source, $\Omega = \frac{\pi \theta_{maj} \times \theta_{min}}{4 \ln 2}$. We have then the relation:

$$\left[\frac{F_\nu}{\text{mJy}} \right] = 0.735 T_B \left[\frac{\theta_{maj} \times \theta_{min}}{\text{arc seconds}^2} \right] \left[\frac{\lambda}{\text{cm}} \right]^{-2} \quad (1.6)$$

This formula is valid in the R-J limit.

1.3 Single-dish telescopes

1.3.1 Telescope structure and elements

Figure 1.2 shows the structure of a radio telescope. The most common type of radio telescope is the steerable parabolic antenna (also called a *dish*). The incoming source radiation is first collected by the antenna, before being amplified and detected by a receiver. The receivers are kept to a very low temperature to minimize the instrumental noise. At radio frequencies, thermal noise dominates. The conversion of the frequency is done by the mixer that combines the incoming signal, ν_s , with a monochromatic signal at the nearest frequency generated in the local oscillator (LO), ν_{LO} , as shown in Fig. 1.3. The receivers are composed of two elements, (1) a *frontend* that amplifies the incoming signal and convert it to an intermediate frequency (IF), and (2) a *backend*, that extracts information about polarisation, (polarimeter) spectral line profiles (spectrometer) or pulse (pulse backends).

In radio telescopes, two main types of receivers are used: heterodyne receivers and bolometers. Heterodyne receivers are coherent radiometers. Both amplitude and phase information is kept from the incoming signal, which is why they are used for spectral line observations. They typically have a large tunable instantaneous bandwidth (up to 32 GHz) and an extremely high spectral resolution $\nu/\delta\nu \sim 10^6 - 10^7$. On the other hand, bolometers are incoherent receivers, the phase information is lost. Like a thermometer, the bolometer will detect a temperature change which is a measure of the intensity of

the incident radiation. They have a very large bandwidth (~ 50 GHz) because the thermal effect is independent of the frequency of the absorbed radiation. They are used for continuum observations.

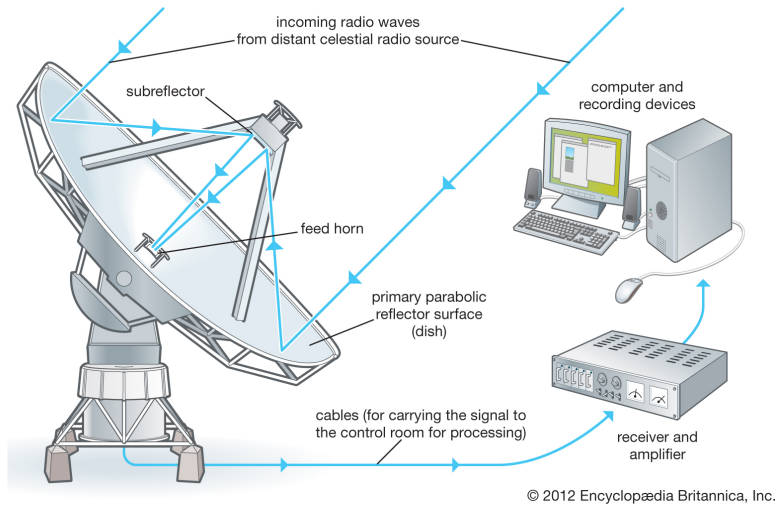


Figure 1.2: Scheme of a single-dish radio telescope. Credit: Encyclopedia Britannica, Inc.

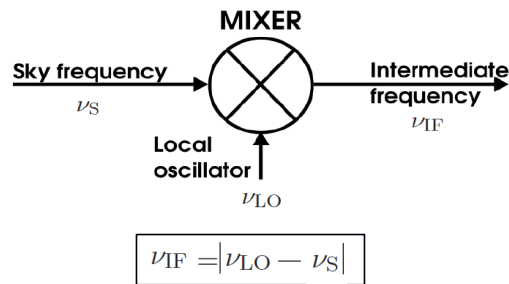


Figure 1.3: Scheme of the conversion of the sky frequency into an intermediate frequency by a mixer. Image adapted from a M2 course.

1.3.2 Antenna parameters

In an antenna, the electromagnetic radiation is converted into electrical currents. The antenna is therefore a passive device. Radio telescopes are functioning as receiving antennas. The coupling between the incident radiation with the telescope must be taken into account. We can measure several of the antenna properties described below.

Beams The beam power pattern $P(\theta, \phi)$ is the response of the antenna as a function of the direction. The beam power pattern function is composed of one main lobe and several side lobes as shown in Fig. 1.4. The quantity that is however usually measured is the normalised beam power pattern, $P_n(\theta, \phi)$:

$$P_n(\theta, \phi) = \frac{P(\theta, \phi)}{P_{\max}} \quad (1.7)$$

The beam solid angle Ω_A of an antenna is measured in steradian (sr) and is given by:

$$\Omega_A = \int \int_{4\pi} P_n(\theta, \phi) d\Omega \quad (1.8)$$

For most antennas, the normalised power pattern has larger values for a certain range of θ and ϕ than for the rest of the sphere. This range is the main beam of the antenna (also called the main lobe). The rest are the side lobes (or also called minor lobes). The main beam solid angle Ω_{MB} is defined as:

$$\Omega_{MB} = \int \int_{\text{main lobe}} P_n(\theta, \phi) d\Omega \quad (1.9)$$

The angular extent of the main beam is measured by the half-power beamwidth (HPBW). It is the angle between points of the main beam where the normalised power pattern is half of the maximum. The first null beamwidth is the angle between the first nulls on either side of the main beam. Usually, neglecting small imperfections, radio telescopes are axially symmetric and the beam pattern can be approximated as Gaussian. The main beam solid angle is then:

$$\Omega_{MB} = 1.133\theta_{MB}^2 \quad (1.10)$$

where θ_{MB} is the HPBW in radians. The HPBW of a typical radio-telescope with an antenna diameter D , is:

$$\theta_{MB} \sim \frac{\lambda}{D} \quad (1.11)$$

The main beam efficiency, η_B , indicates the fraction of the power that is concentrated into the main beam:

$$\eta_B = \frac{\Omega_{MB}}{\Omega_A} \quad (1.12)$$

Temperatures The antenna temperature, T_A , is defined as the temperature of the black body whose flux is equal to that measured by the antenna of the telescope, corrected for the atmospheric absorption. It is thus a measured quantity that is linked to the source temperature but also the telescope. The antenna temperature is defined by the Nyquist formula (Nyquist 1928):

$$T_A = \frac{P_v}{k_B} \quad (1.13)$$

where P_v is the power extracted by an antenna:

$$P_v = \frac{1}{2} A_e F_v \quad (1.14)$$

with F_v the observed flux density in jansky (Jy), and A_e is the effective aperture in m^2 .

However, the above definition of the antenna temperature does not take into account the sidelobes of the real beam pattern. What we want to measure is what is coming from

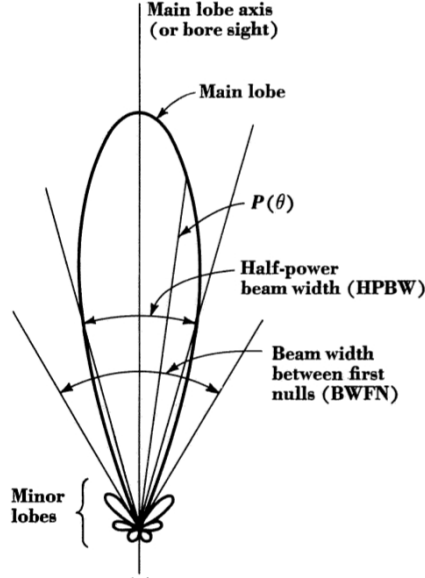


Figure 1.4: Scheme of the beam power pattern. The main lobe and side lobes (also called minor lobes) are represented. The half-power beamwidth (HPBW) and first null beamwidth (FNBW) are labelled. The image is taken from the M2 course given by Prof. Hily-Blant.

the $2\pi sr$ in front of the telescope, therefore excluding any contribution coming from the ground, the telescope etc. We thus define the corrected antenna temperature T_A^* as:

$$T_A^* = \frac{T_A}{F_{\text{eff}}} \quad (1.15)$$

where $F_{\text{eff}} = \Omega_{2\pi}/\Omega_A$ is called the *forward efficiency*.

Another useful quantity is the main-beam temperature, T_{MB} , which is a measure of the observed intensity of the studied source in the main-beam. The main-beam temperature is defined as:

$$T_{\text{MB}} = \frac{T_A}{B_{\text{eff}}} = \frac{F_{\text{eff}}}{B_{\text{eff}}} T_A^* \quad (1.16)$$

where $B_{\text{eff}} = \Omega_{\text{MB}}/\Omega_A$ is called the *beam efficiency*.

The main-beam temperature, T_{MB} , is thus still antenna dependent and is not directly the source temperature, T_B . The two quantities, T_{MB} and T_B are however linked, as T_{MB} is the convolution of the source temperature with the normalised beam pattern of the telescope. If both the telescope beam pattern and the source emission function are gaussian, the two temperatures are related as follows:

$$T_B = \frac{\theta_s^2 + \theta_{\text{MB}}^2}{\theta_s^2} T_{\text{MB}} \quad (1.17)$$

where $\frac{\theta_s^2}{\theta_s^2 + \theta_{\text{MB}}^2}$ is called the *filling factor* (ff). The observed source size, θ_{obs} , the true source size, θ_s and the main beam size, θ_{MB} are also related:

$$\theta_{\text{obs}}^2 = \theta_s^2 + \theta_{\text{MB}}^2 \quad (1.18)$$

Two extreme cases can be considered.

1. The source is larger than the beam, i.e. the source is *resolved*
2. The source is smaller than the beam, i.e. the source is *unresolved*

We can thus simplify Eq. 1.17 as:

$$\begin{aligned}
 T_B &\simeq T_{MB}; \theta_s \gg \theta_{MB} \text{ (Case 1)} \\
 T_B &\simeq \frac{\theta_{MB}^2}{\theta_s^2} T_{MB}; \theta_s \ll \theta_{MB} \text{ (Case 2)}
 \end{aligned}
 \tag{1.19}$$

1.3.3 Noise considerations

Noise powers are represented by temperatures, which add linearly. The power per unit bandwidth entering a receiver can be characterized by a temperature, as given by $P_\nu = k_B T$. The total noise of a receiving radio telescope is called system temperature, T_{sys} . Additionally to the antenna temperature, the system temperature is composed of several other contributions. The main ones are described here.

$$T_{sys} = T_{bg} + T_{atm} + T_{sca} + T_{rec} + T_A + T_s + \dots \tag{1.20}$$

with

- T_{bg} , the noise contribution from the cosmic microwave ($T \sim 2.73\text{K}$) and galactic backgrounds.
- T_{atm} , the atmosphere contribution which depends on the frequency. The main contribution at millimetre wavelengths comes from the water vapour
- T_{sca} , the contribution from the surroundings (ground and telescope) which is around 300 K, also known as *spillover*
- T_{rec} , the noise contribution from the receiver
- T_s is the contribution from the astrophysical source

The antenna temperature and system temperature are linked by the radiometer formula:

$$S/N = \frac{T_A}{T_{sys}} \sqrt{\Delta\nu t} \tag{1.21}$$

with S/N the signal-to-noise ratio, $\Delta\nu$ the frequency bandwidth of the signal and t is the integration time on source.



Figure 1.5: The IRAM-30m telescope. Credits: IRAM

1.3.4 The IRAM 30-m telescope

The IRAM-30m is located on Pico Veleta, in the Spanish Sierra Nevada, at 2850m of altitude (Fig. 1.5). The telescope has a single-dish parabolic antenna of 30m, which ensures the best sensitivity achieved among the other single-dish radio telescopes. Observations can be carried out at 3, 2, 1 and 0.87mm. It is one of the two observatories managed by the international research institute for radio astronomy, the "Institut de RadioAstronomie Millimétrique" (IRAM). IRAM has been founded in 1979 by the French CNRS (Centre National de la Recherche Scientifique), the German MPG (Max Planck Gesellschaft), and the Spanish IGN (Instituto Geográfico Nacional). Its main headquarters are located in Grenoble, France.

Receivers and backends There are currently two heterodyne receivers on the IRAM-30m, EMIR (Eight MIXer Receiver) and HERA. EMIR is a spectral line receiver available since 2009 that operates at 3mm (E 090), 2mm (E 150), 1.3mm (E 230) and 0.87mm (E 330). The EMIR bands are equipped with dual sideband (DSB) mixers offering 8GHz of instantaneous bandwidths per sideband and polarisation. HERA (HEterodyne Receiver Array) consists of 2 arrays of 3x3 pixels separated by 24". HERA works only at 1.2mm and provides a bandwidth of 1 GHz. The receiver bands available at the IRAM-30m compared to the atmospheric transmission are shown in Fig. 1.6. There is also one continuum camera, NIKA-2 (New IRAM Kid Array 2). NIKA-2 is available since 2017 and operates simultaneously at 150 and 260 GHz with a field-of-view of 6.5'. It is a dual-band camera. Testing and commissioning of polarimetry at 1mm are still ongoing. There are several backends available to combine with the EMIR and HERA receivers. The list of backends for the two receivers is shown in Table 1.1.

Softwares All data acquired with the IRAM-30m telescope are reduced with the Grenoble Image and Line Data Analysis System (GILDAS) software package developed at IRAM (<https://www.iram.fr/IRAMFR/GILDAS>). Several interactive programs are available, to prepare observations (ASTRO), prepare plots of data or results (GREG), reduce and process single-dish data (CLASS), calibrate the NOEMA interferometric data

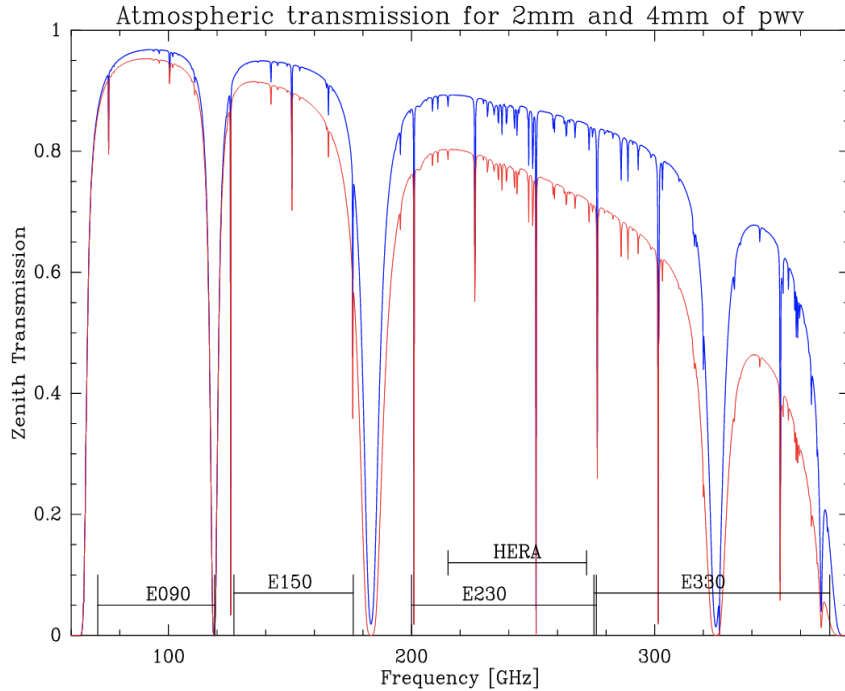


Figure 1.6: The IRAM-30m atmospheric transmission between 60 and 400 GHz for 2 and 4 mm of precipitable water vapor. The receiver bands are indicated. Credits: IRAM

Table 1.1: EMIR and HERA available backends

Backend	Channel width	Bandwidth	Receiver
FTS	50 or 195 kHz	8×4 GHz	EMIR, HERA
WILMA	2 MHz	16 MHz or 18×930 MHz	EMIR, HERA
VESPA	3.3 kHz - 1.25 MHz	10-512 MHz	EMIR, HERA
XPOL	40 kHz - 2.5 MHz	20-640 MHz	EMIR
BBC	8 GHz		EMIR
4 MHz	4 MHz	8 or 9 × 1 GHz	EMIR, HERA



Figure 1.7: The Nobeyama-45m single-dish telescope. Credits: NAOJ.

(CLIC), to image and deconvolute data (MAPPING) and to observe with the 30m telescope (PAKO and MIRA).

1.3.5 The Nobeyama-45m telescope

The Nobeyama-45m is located at Minamimakimura, Minamisaku, Nagano in Japan, at an altitude of 1350m (Fig. 1.7). The antenna has a diameter of 45m and operates between 20 and 116 GHz (~ 3 -15mm). It is one of the largest single-dish radio telescopes in the 3mm band. The observatory is managed by the Nobeyama Radio Observatory (NRO), a section of the National Astronomical Observatory of Japan (NAOJ).

Receivers and backends There are several receivers, H22, H40, Z45, T70 and FOREST. H22, H40 and Z45 are single sidebands of 2 (H22, H40) and 4 GHz (Z45) bandwidth. while T70 is a dual sideband receiver of 8 GHz bandwidth. FOREST (FOur-beam REceiver System on the 45-m telescope) is a dual sideband receiver of 8 GHz bandwidth. The configuration of the four beams is a 2×2 with a separation of $50''$. There are two backends, one for spectroscopic observations, SAM45 (Spectral Analysis Machine for the 45-m telescope) and one for continuum observations, Continuum BE.

Softwares Two software are available for spectral line data reduction, Java NEWSTAR (<https://www.nro.nao.ac.jp/~jnewstar/html/>) for single pointing observations (PoSW, ON-ON) and NOSTAR (https://www.nro.nao.ac.jp/~nro45mrt/html/obs/otf/reduction_en.html) for mapping (OTF). The software are developed at NRAO and are based on AIPS (Astronomical Image Processing System).

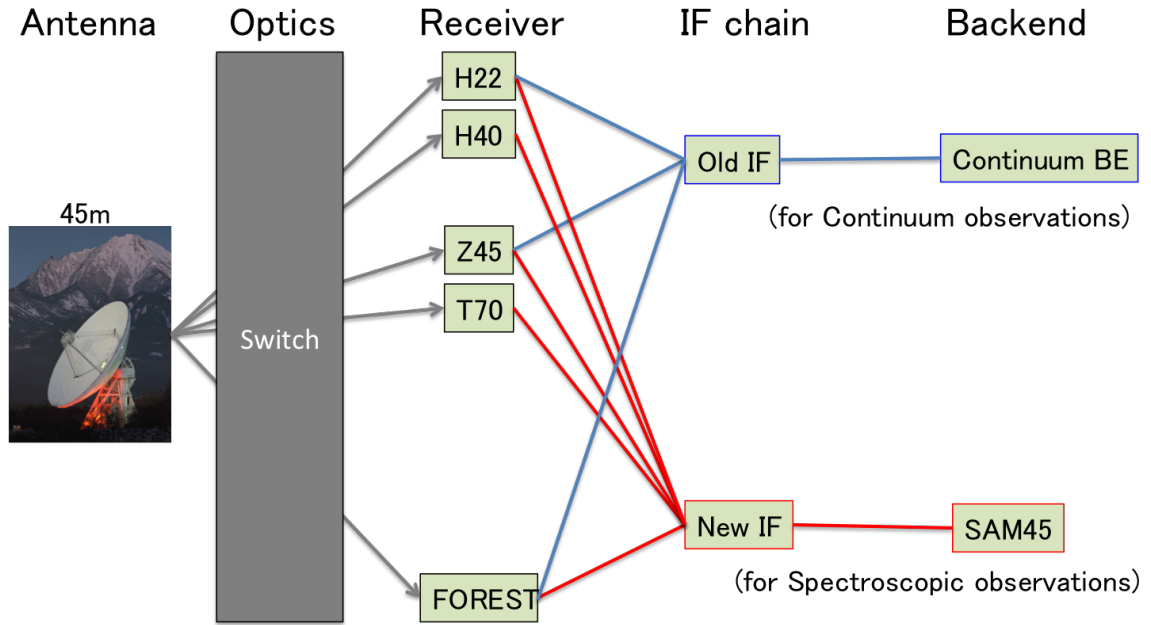


Figure 1.8: Schematic diagram of the Nobeyama-45m single-dish telescope. Credits: NRO

1.4 Radio interferometers

1.4.1 Beyond the diffraction limit

The diffraction limit theory predicts that the angular resolution of a radio telescope, i.e. the smallest angle for which two objects can be separated, is $\theta \sim \lambda/D$. If we take the example of the IRAM-30m with $D=30$ m and $\lambda=1$ mm, we have an angular resolution of $\theta \sim 10''$. The objects of interest of this thesis are solar-mass protostars. Are single-dish telescopes such as the IRAM-30m sufficient to resolve them? If we consider the relation $1\text{au}@1\text{pc} = 1''$ and that $1\text{pc}=2 \times 10^5\text{au}$, the angular size of a protostar located at 150 pc with an envelope diameter of a few 1000 au is $\sim 6''$. If we consider protostars located at about 400 pc as this is the case for Orion protostars, their angular size is $\sim 2.5''$. We are thus largely limited with single-dish telescopes. To improve the spatial resolution, we can either increase D or decrease λ . We are naturally limited for the wavelengths, especially when observing embedded sources that are rather cold objects emitting most intensely at long wavelengths. Therefore, we need to increase D . Building stable and easily steerable dishes with diameters larger than about 300m is technologically challenging. The solution to bypass this problem is interferometry (or aperture synthesis).

Interferometry consists of combining many small single-dishes placed far apart to *synthesise* a giant dish. In practice, each dish receives radiation from the same object. All the signals are combined by pairs of antennas, called baselines. For each baseline, the angular resolution is $\theta \sim \lambda/d$ where d is the distance between the antennas. A short baseline will provide a low resolution whilst a long baseline will provide a high resolution. The field of view of an interferometer is called the primary beam and is defined as $\theta_{PB} \sim \lambda/D$ with D the diameter of each dish of the array.

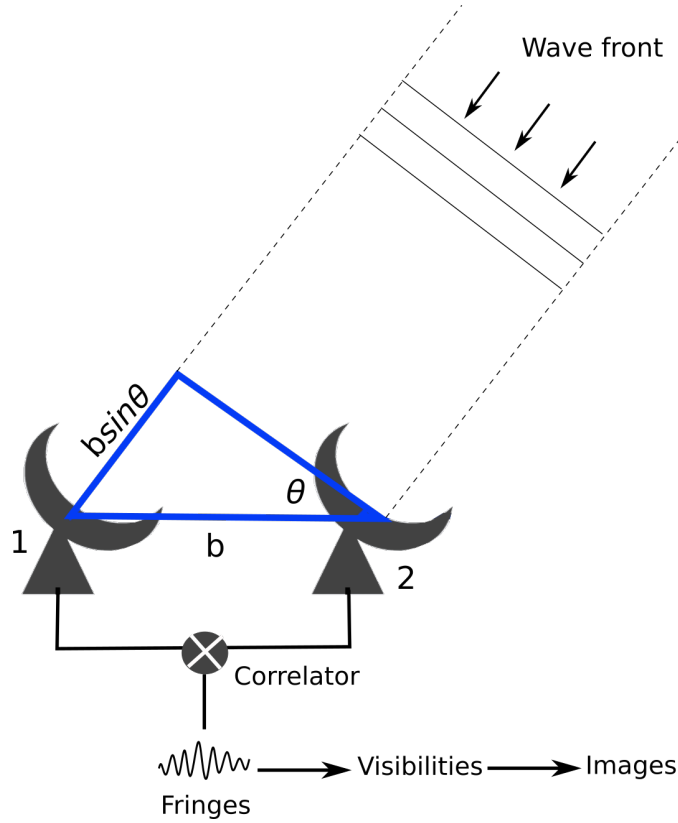


Figure 1.9: Scheme of a 2-elements interferometer. Image adapted from A. López-Sepulcre’s presentation at the first ACO Network School (Perugia, Italy, 2019).

1.4.2 Basic principles of interferometry

The best way to explain the functioning of an interferometer is to look at a two-element interferometer. Two antennas of diameters D are separated by a distance b (called baseline) as represented in Fig. 1.9. The radio signal from the observed astronomical source approaches the antennas along parallel paths which generates a time delay in the arrival of the wavefront to antenna 1. We assume that the incoming radiation is a plane electromagnetic wave of amplitude E . The output voltage of the two antennas are:

$$\begin{aligned} U_1 &\propto E e^{i\omega t} \\ U_2 &\propto E e^{i\omega(t-\tau)} \end{aligned} \quad (1.22)$$

where τ is the time delay of formula $\tau = b \sin \theta / c$ and $\omega = 2\pi\nu$ is the angular frequency (in $\text{rad}\cdot\text{s}^{-1}$). This time delay causes a phase difference between the two signals at their arrival which is $\Delta\psi = 2\pi \frac{b}{\lambda} \sin \theta$. The correlator multiplies the signals from each pair of antennas and averages them over a time called the integration time. If the time is sufficiently long compared to a single full oscillation, i.e. $t \gg 2\pi/\omega$. The correlator output is:

$$R(\tau) \propto \frac{1}{2} E^2 e^{i\omega\tau} \quad (1.23)$$

The correlator output thus depends on the time delay τ . Because the source is moving across the sky (due to the Earth’s rotation), τ varies. This results in an oscillatory function,

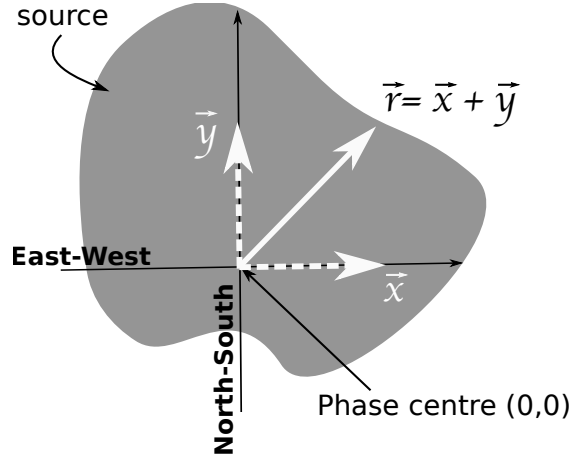


Figure 1.10: Scheme of the coordinate system used to project the baseline plane onto the sky plane. Adapted from A. López-Sepulcre’s presentation during the first ACO Network School (Perugia, Italy 2019).

the fringes, that are the response pattern of an interferometer. From the antenna position, the source direction and time, we know τ . We can thus correct the fringes or *remove* them by correcting the delay for the phase centre. The wavefront arrives then in phase to the antennas.

We also need to take into account the fact that the observed source may not be a point source and could be offset from the phase centre. The correlator output integrated over the source is the complex visibilities, V . It is an output for a given pair of antennas after fringe removals and contains information about the source position, structure, and multiplicity. There is an extra phase difference at points of the source that is offset from the phase centre $\Phi = 2\pi \frac{\vec{b} \cdot \vec{r}}{\lambda}$. We project the baseline plane onto the sky plane (x, y) in the coordinate system shown in Fig. 1.10. Complex visibilities are then defined as:

$$V = \iint I(x, y) e^{i2\pi(b_x x + b_y y)/\lambda} dx dy \quad (1.24)$$

The visibilities can be expressed as complex numbers with a real and an imaginary part, measured separately. We have then $V = A e^{i\Phi_V}$ with A the visibility amplitude, which contains information about the amount of radiation from the source, and Φ_V the visibility phase that contains information about the position of the source.

$$A = \sqrt{Re^2 + Im^2} \quad (1.25)$$

$$\Phi_V = \tan^{-1}(Im/Re) \quad (1.26)$$

We note that complex visibilities (Eq. 1.24) look like a 2D inverse Fourier Transform (FT). The Fourier transform is the decomposition of a time-dependent signal into a sum of frequencies. Figure 1.11 shows some examples of Fourier transforms.

$$F(\nu) = \int f(t) e^{-i2\pi\nu t} dt; \text{ Fourier Transform (FT)} \quad (1.27)$$

$$f(t) = \int F(\nu) e^{i2\pi\nu t} d\nu; \text{ Inverse Fourier Transform (FT}^{-1}\text{)} \quad (1.28)$$

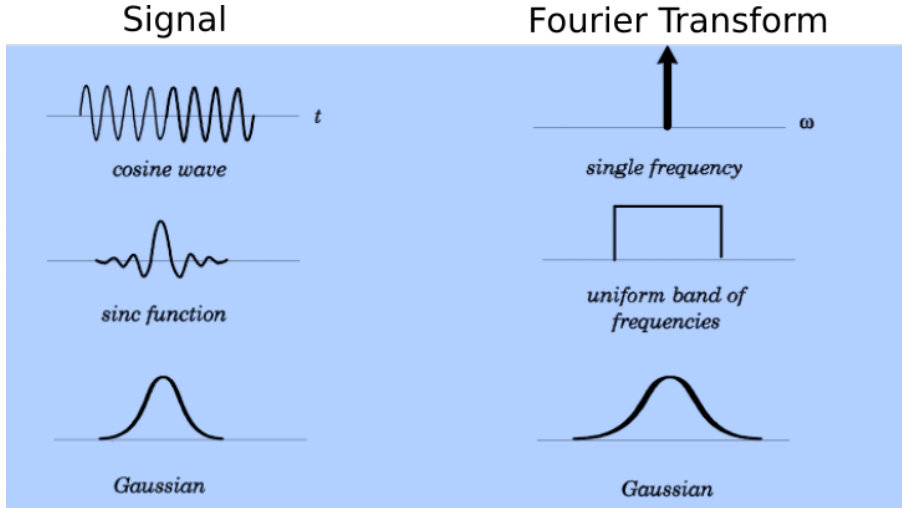


Figure 1.11: Examples of Fourier transforms on different functions. Only the real parts of the transforms are shown. Adapted from an image taken on mri-q.com website.

The visibility is a function of the spacing:

$$\begin{aligned} \frac{b_x}{\lambda} &\rightarrow u \\ \frac{b_y}{\lambda} &\rightarrow v \end{aligned} \quad (1.29)$$

We use u and v for the spacing, which define the uv plane. The uv plane is a projection of the baseline plane (Earth) onto the sky. In Eq.1.24, x and y have units of angles (radians). Therefore, we can consider u and v having units of *inverse angle*.

The output of the interferometer is thus a collection of visibilities obtained throughout the observations, each corresponding to a given pair of antennas (i.e. baselines) in the interferometer at a given time. The intensity distribution $I(x, y)$, is the image we want to obtain. *Imaging* is simply the recovery of the intensity distribution by the inverse Fourier Transform of the measured visibility function:

$$I(x, y) = \iint V(u, v) e^{-i2\pi(ux+vy)} dudv \quad (1.30)$$

In practice, performing a true analytical integral as in Eq.1.27 is not possible because we do not have a continuous sampling of the variables u and v . The integral becomes then a summation We need to measure the visibility function in the uv plane several times to get a complete sampling of the visibility function or "a good uv coverage". Good uv coverage is essential to get a good image quality. Each antenna pair (baseline) gives a *view* of the source differently since one projected baseline is one sample in the Fourier uv plane. The more visibilities we have, the better the source image. For a given array configuration, there are two ways of improving the uv coverage. First, we can increase the number of baselines: for N number of antennas, there are $N(N-1)/2$ independent baselines. Second, we can use the Earth rotation: visibilities corresponding to different (u, v) values are recorded as the source is followed along its track in the sky. The antennas can also be arranged in different configurations to change the final angular resolution.

1.4.3 Data calibration

Data calibration is essential to derive the response of the instrument. Therefore, during the observations and in addition to the observed target, sources in the sky called calibrators must be observed. These calibrators are used to perform three main types of visibility calibration during data reduction.

Bandpass calibration The bandpass calibration compensates for the changes of instrumental gain in phase and amplitude, with frequency. It is important for spectral line observations because frequency dependent amplitude errors can limit the detection of weak spectral features and imitate changes in the line structures, and frequency dependent phase errors can lead to spatial offsets between spectral features. The bandpass calibrator is ideally a strong source (usually a quasar) with a flat spectrum. Bandpass calibration is stable during the track for a given tuning which is why it is observed only once, at the beginning or end of the observation track.

Phase and amplitude calibration This calibration compensates for relative temporal variations of the phase of the correlated signal on different antennas or baselines, due to the atmosphere. The calibrator is a sufficiently strong source, preferably a point source. The calibrator needs to be observed regularly (every 20min for NOEMA). If the calibrator is a point source, the gain is derived assuming an intrinsic phase of 0. The phase calibration is critical for the final image quality.

Absolute flux calibration The absolute flux calibration is needed to scale the amplitudes of both the science target and calibrators to correct the flux density. To do so, a source with known flux density, spectral index, and structure (typically a regularly monitored source) is used. The derived scaling factor applies to the other calibrators and the targeted source.

1.4.4 Self-calibration

The noise in the image can be higher than the thermal noise due to amplitude and phase errors that remain after performing the data calibrations cited above. The phase calibration performed is not always sufficient to calibrate the atmospheric phase. Self-calibration is one possible solution and consists of calibrating the instrument on the source itself if the latter is sufficiently intense. Self-calibration can improve both amplitude and phase, but it is usual to improve only the phase, as there are not many residuals in the amplitude. The resulting SNR of the image is usually largely improved. Self-calibration is typically carried out in the uv plane, on the continuum of the source. The corrections obtained after self-calibrating need to be applied to the spectral line data afterwards.

1.4.5 Sensitivity

The random noise limit to an interferometer system is calculated with the same method as for a single-dish telescope. The rms fluctuations in antenna temperature are:

$$\Delta T_A \propto \frac{T_{\text{sys}}}{\sqrt{t\Delta\nu}} \quad (1.31)$$

When applying the definition of the flux density, F_ν in terms of antenna temperature in an N-element system, we obtain:

$$\Delta F_\nu = 2k_B \frac{T_{\text{sys}} e^\tau}{A_e \sqrt{2Nt\Delta\nu}} \quad (1.32)$$

where τ is the atmospheric optical depth, A_e the effecting area of a single-dish telescope of diameter D . The quantity $T_{\text{sys}} e^\tau$ is the system temperature corrected for the atmospheric absorption. Because flux density and brightness temperature of a source are linked, we can derive the rms brightness temperature due to random noise in an interferometric image as:

$$\Delta T_b = 2k_B \lambda^2 \frac{T_{\text{sys}} e^\tau}{A_e \Omega_b \sqrt{2Nt\Delta\nu}} \quad (1.33)$$

1.4.6 A quick view of some radio interferometers

There are several radio interferometers but I present here three of them, as I use data issued from those interferometers in this thesis. Table 1.2 summarises the main characteristics of the three interferometers.

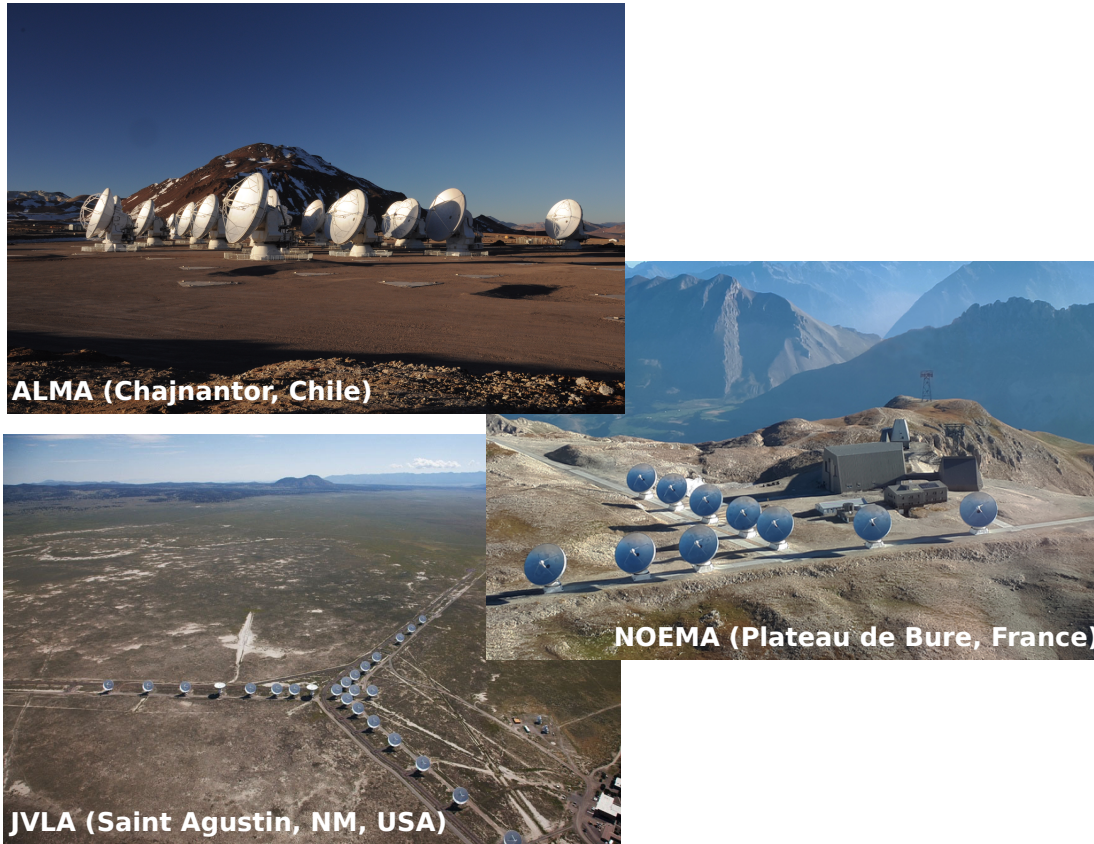


Figure 1.12: ALMA, NOEMA and JVLA radio interferometers. Image credits: NRAO for ALMA and JVLA and IRAM for NOEMA.

ALMA The Atacama Large Millimeter/sub-mm Array (ALMA) is operated by the National Radio Astronomy Observatory (NRAO) and is issued from a collaboration between North America, East Asia and Europe. The ALMA interferometer is located on the Chajnantor plateau in the Atacama desert, in Chile, and at an altitude of 5000m.

The array is composed of 66 antennas, 50 of them being 12-m antennas and 12 of them being 7-m antennas. The last four antennas are used as single-dishes. The baselines range between 160m in the most compact configuration up to 16 km in the most extended one. The frequency range available is divided into several receiver bands, from Band 3 to Band 10. Band 3 starts at 84 GHz and band 10 at 950 GHz. Two additional bands will be added, Band 1 around 40 GHz which will, in principle, be ready for cycle 10 (2023), and Band 2 with frequencies in the range 67-90 GHz (Yagoubov et al. 2020) has been recently approved for construction.

The spatial resolution achieved by ALMA ranges from 0.5'' at 950 GHz to 4.8'' at 110 GHz in the most compact configuration whilst it ranges between 20mas at 230 GHz to 43mas at 110 GHz, in the most extended one. The spectral resolution can vary between 3.8 kHz and 15.6 MHz for the channel spacing. The instantaneous total bandwidth is 8 GHz.

NOEMA The NOrthern Extended Millimetre Array (NOEMA) is operated by IRAM. NOEMA is located on the Plateau de Bure in the French Alps at 2560m altitude and it is the successor of the Plateau de Bure Interferometer.

Historically, the Plateau de Bure interferometer started with 3 antennas with 15-m diameter in 1988 and reached 6 antennas in 2001. It was then replaced by NOEMA with the addition of the 7th antenna in 2014. Today, the array is composed of 11 antennas arranged in a "T" shape, with a maximum baseline of 760m. A 12th antenna is planned as well as the baseline extension up to 1700m. The frequency range covered by NOEMA is divided into 4 bands. Band 1 (3mm) covers frequencies between 71 and 119 GHz, Band 2 between 127 and 182 GHz (2mm), Band 3 (1.3mm) between 197 and 276 GHz, and Band 4 (0.8mm) between 275 and 373 GHz will be available in the future.

The most compact configuration has a resolution of 3.9'' at 100 GHz and 1.7'' at 230 GHz. The best spatial resolution is reached for the most extended configuration, with 1'' at 100 GHz and 0.4'' at 230 GHz. NOEMA has a high-performance wide-band correlator named PolyFix allowing an instantaneous bandwidth up to 32 GHz for up to twelve antennas and per polarization. The spectral resolution is 2 MHz but two higher spectral resolution modes with spacing of 250 and 62.5 kHz are also available. Further spectral modes will be added in the future.

JVLA The Karl G. Jansky Very Large Array (JVLA) is a centimetre wavelength radio astronomy observatory, operated by NRAO. The JVLA is located in the Plains of San Agustin in New Mexico, USA, at 2120m in altitude. Its construction started in 1973 and the first observations were performed in 1976.

The array is composed of 28 antennas of 25-m in size (27 effective antennas, 1 spared for maintenance) that are organised in an iconic "Y" shape. The most compact configuration (configuration D) has a baseline of ~ 1 km whilst the most extended one has a baseline of 36.4 km (configuration A). The frequency range available ranges from 74 MHz to 50 GHz. At 50 GHz, the highest spatial resolution achieved ranges from 1.4'' (configuration D) down to 0.04'' (configuration A). The total instantaneous bandwidth

Table 1.2: Some characteristics of NOEMA, ALMA and JVLA.

Characteristics	NOEMA	ALMA	VLA
Wavelength domain	Millimetre	Millimetre/sub-millimetre	centimetre
Number of antennas	11 × 15-m	66 (54 × 12-m + 12 × 7-m)	28 × 25-m
Frequency range [GHz]	71 – 373	84 – 950	0.074 – 50
Baseline range	24 – 760m	150m – 16 km	1 km– 36.4 km
Angular resolution ["]	0.4 – 3.9	0.02 – 4.8	0.04 – 1.4
Bandwidth per polarization	2 × 8 GHz	2 × 4 GHz	2 × 4 GHz

available is up to 8 GHz and the channel width varies between 15.6 kHz and 2 MHz.

2 Molecular line analysis

The work in this thesis mostly relies on the analysis of molecular lines which are due to the emission/absorption of photons at specific frequencies in the gas. Understanding the basics of radiative transfer is thus important to be able to analyse the molecular lines. This section gives, therefore, some radiative transfer basics, and presents methods to extract the physical properties of the gas emitting a molecular species.

2.1 The radiative transfer equation

We consider an illuminating source emitting photons at a frequency ν , an observer, and in between a cloud composed of dust and gas at a temperature T and a density n . Photons emitted by the illuminating source can be either absorbed by the dust and gas of the cloud, or emitted, absorbed, and scattered by both dust and gas at each position in the cloud. If we want to know what is the energy flux at a frequency ν that reaches the observer at a distance d from the cloud, we need to understand how a photon *travels* through a medium to its border. Figure 1.13 is a scheme of this situation. The intensity of light is not constant when propagating through an emitting or an absorbing medium. In the following, the scattering of photons is neglected as it is not a dominant source of radiation in the FIR to radio wavelength range. The change then in intensity is described by the radiative transfer equation, the main equation in the treatment of radiations in astrophysics:

$$\frac{dI_\nu}{d\tau(\nu)} = S_\nu - I_\nu \quad (1.34)$$

where I_ν is the specific intensity, S_ν is the source function (i.e. the intensity emitted over the mean free path of photons) and $d\tau(\nu)$ is the optical depth. The mean free path is the average distance (units of cm) travelled by photons before their absorption by the medium. The source function is defined as the ratio of the emission coefficient (also called emissivity; in $\text{ergs}\cdot\text{s}^{-1}\text{cm}^{-3}\text{sr}^{-1}\text{Hz}^{-1}$), j_ν , to the absorption coefficient, α_ν (in cm^{-1}):

$$S_\nu = \frac{j_\nu}{\alpha_\nu} \quad (1.35)$$

The optical depth, $\tau(\nu)$, is defined as the difference in the mean free path in the propagation direction and depends on the properties of the absorbing material and of the quan-

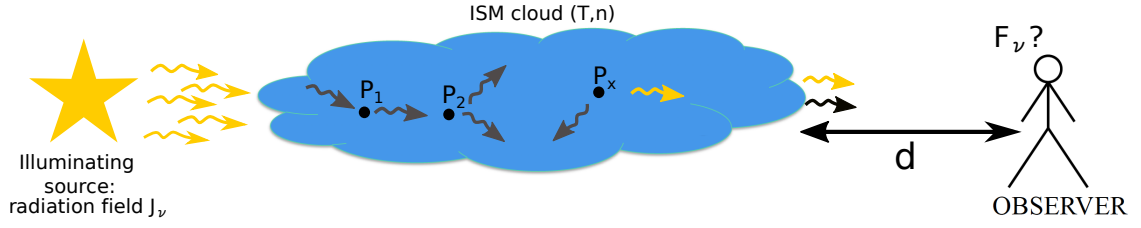


Figure 1.13: Scheme explaining the radiative transfer problem: an illuminated source irradiates an ISM cloud in which the photons from the emitting sources are scattered, absorbed or emitted at different position in the cloud. The observer located at a distance d from the ISM cloud, aims to know what flux F_ν reaches him. Adapted to one of Cecilia Ceccarelli's presentation (ACO Network School, Perugia, Italy).

tity of material the radiation has to go through:

$$d\tau(\nu) = -\alpha_\nu ds \quad (1.36)$$

The optical depth is dimensionless. Usually, $\tau(\nu) > 0$, except in case of masers. There are two extreme cases for the optical depth:

1. Optically thin, where $\tau(\nu) \ll 1$. The medium is transparent and photons can travel through it.
2. Optically thick, where $\tau(\nu) \gg 1$. We see where photons get their last interaction before being absorbed.

If for simplicity, we assume that S_ν is constant inside the region, the solution of the radiative transfer equation (Eq. 1.34) is:

$$I_\nu[\tau(\nu)] = I_\nu(0)e^{-\tau(\nu)} + S_\nu(1 - e^{-\tau(\nu)}) \quad (1.37)$$

where $I_\nu(0)$ is the external (or background) source intensity. In the very optically thick case ($\tau \rightarrow \infty$), the solution of Eq. 1.37 is:

$$I_\nu = S_\nu \quad (1.38)$$

Here, the intensity, I_ν , goes to the source function, S_ν , which means that only the fraction of photons emitted in the medium that is not absorbed can reach the border of the cloud. On the other hand, the solution of the optically thin case is:

$$I_\nu[\tau(\nu)] = I_\nu(0) + \tau_\nu(S_\nu - I_\nu(0)) \quad (1.39)$$

In this situation, most photons can reach the border of the cloud. In case of a spectral line, the source function S_ν depends on the populations of the levels in the upper and lower state of the species. If the levels are thermalized, we are under *Local Thermodynamic Equilibrium* (LTE; see Section 2.2), and we can write $S_\nu = B_\nu(T)$ (Kirchhoff's law). This

means that S_ν is governed by the gas kinetic temperature T through the Planck function. Equation 1.37 then becomes:

$$I_\nu(\tau(\nu)) = I_\nu(0)e^{-\tau(\nu)} + B_\nu(T)(1 - e^{-\tau(\nu)}) \quad (1.40)$$

Under LTE and at long wavelengths, when the R-J limit often holds (see Eq. 1.2), the Equation 1.40 becomes:

$$T_B = T_{bg}e^{-\tau(\nu)} + T(1 - e^{-\tau(\nu)}) \quad (1.41)$$

where T_{bg} corresponds to the temperature of the background emission when it is a black body. The quantity T_B is the brightness temperature defined in Eq. 1.3. With the R-J approximation, it holds:

$$T_B = \frac{\lambda^2}{2k_B} I_\nu = \frac{c^2}{2\nu^2 k_B} I_\nu \quad (1.42)$$

Again, taking the two limiting cases for the optical depth, we have:

$$\begin{aligned} T_B &= T_{bg} + T\tau(\nu); \text{ if } \tau(\nu) \ll 1 \\ T_B &= T; \text{ if } \tau(\nu) \gg 1 \end{aligned} \quad (1.43)$$

2.2 Level populations and Local Thermodynamic Equilibrium

In the gas, the emission and absorption of photons can only occur at given frequencies, which are equal to the energy difference of the final and initial state of the system (atom or molecule). As the gas is composed of several species (atoms/molecules), the line spectrum is the result of all the transitions of all the species in all the various energy levels. To understand the line spectrum, we need to know the statistical distribution of the species in each energy level. The level population of an observed molecule depends on the environment in which the molecule is located.

2.2.1 Statistical equilibrium equation

Let us assume a 2-level system (i.e. a single species with 2 levels of energy only), with l the lower energy level and u the upper energy level. The system can be excited or de-excited via various processes, such as collision with other species, or absorption/emission of a photon at the frequency ν_{ul} . At equilibrium, the rate of excitation of the lower level l is equal to the rate of the de-excitation of the upper level u . This is formulated by the statistical equilibrium equation:

$$n_l n_{coll} \gamma_{lu} + n_l B_{lu} J_\nu = n_u n_{coll} \gamma_{ul} + n_u A_{ul} + n_u B_{ul} J_\nu \quad (1.44)$$

where γ_{lu} and γ_{ul} are respectively the excitation and de-excitation collisional coefficients, n_{coll} is the number density of the collisors, B_{lu} , B_{ul} and A_{ul} are the Einstein coefficients, J_ν is the specific intensity of the radiation field at frequency ν_{ul} , and n_l and n_u are

the number density of the levels l and u , respectively. The Einstein coefficients are related as:

$$\begin{aligned} B_{lu} &= \frac{g_u}{g_l} B_{ul} \\ B_{ul} &= \frac{A_{ul} c^2}{2h\nu^3} \end{aligned} \quad (1.45)$$

where g_u and g_l are the statistical weight of the levels u and l , respectively. For a multi-level system, the Eq. 1.44 can be generalized by adding all the excitation and de-excitation transitions between the levels. This results in a system of N_{lev} (N number of levels) equations:

$$\sum_{l=1}^{u-1} (n_l n_{coll} \gamma_{lu} + n_l B_{lu} J_{\nu_{ul}}) = n_u \sum_{l=u+1}^{N_{lev}} (n_{coll} \gamma_{ul} + A_{ul} + B_{ul} J_{\nu_{ul}}) \quad (1.46)$$

Solving the statistical equilibrium equation is not straightforward. For simplicity, we assume *Local Thermal Equilibrium* (LTE). This means that all atoms/molecules have the same internal energy distribution, which depends only on the kinetic gas temperature, T . All level populations are thermalized and follow the Boltzmann distribution. If n_x is the total number density of the species x , the Boltzmann distribution is:

$$n_i = \frac{g_i n_x}{Q(T)} e^{-\frac{E_i}{k_B T}} \quad (1.47)$$

where n_x is written as:

$$n_x = \sum_{i=1}^{N_{lev}} n_i \quad (1.48)$$

and where $Q(T)$ is the partition function, defined as:

$$Q(T) = \sum_{i=1}^{N_{lev}} g_i e^{-\frac{E_i}{k_B T}} \quad (1.49)$$

where g_i is the statistical weight of level i .

2.2.2 Detailed balance

If we consider again a 2-level system and suppose that (1) the excitations/de-excitations from the radiation are negligible, and (2) LTE holds, the statistical equilibrium equation (Eq. 1.44) becomes:

$$n_u \gamma_{ul} = n_l \gamma_{lu} \quad (1.50)$$

The levels are thermalized and follow the Boltzmann distribution. Therefore, there is a relation between the two collisional coefficients called the detailed balance, written as:

$$\gamma_{ul} = \gamma_{lu} \frac{g_l}{g_u} e^{-\frac{E_u - E_l}{k_B T}} \quad (1.51)$$

Even though we assume that LTE holds to derive this relation, Eq. 1.51 is always true because the γ_{ul} and γ_{lu} coefficients only depend on the transition and on the system structure.

2.2.3 Critical density

If the collisions between atoms/molecules are not frequent enough to reach LTE, the number of collisions, the collisional and the spontaneous emission coefficients govern the energy population level. If for simplicity, we neglect the radiation field J_ν , Eq. 1.44 becomes:

$$n_l n_{coll} \gamma_{lu} = n_u n_{coll} \gamma_{ul} + n_u A_{ul} \quad (1.52)$$

Using the detailed balance of the collisional coefficient given above, it follows:

$$\frac{n_u}{n_l} = \frac{g_u}{g_l} e^{-\frac{E_u - E_l}{k_B T}} \left(1 + \frac{n_{cr}}{n_{coll}} \right)^{-1} \quad (1.53)$$

where n_{cr} is the critical density defined as:

$$n_{cr} = \frac{A_{ul}}{\gamma_{ul}} \quad (1.54)$$

The critical density is the minimum density needed to de-excite a transition faster than the emission of a photon, namely, that collisions dominate both the excitation and the de-excitation. In other words, collisions dominate the level populations, which is the definition of LTE. The critical density depends on the species, the transition, and the gas kinetic temperature. If the density of the cloud is larger than n_{cr} , collisions govern the level population which means that LTE holds and that the level population follow the Boltzmann distribution. On the other hand, if the cloud density is lower than n_{cr} , the level is de-excited by the emission of photons rather than by collisions. The populations of the upper and lower levels depend on the gas kinetic temperature but also on the density of the colliding particles, n_{coll} , (which are mainly H or H₂ densities, the two most abundant species in the neutral ISM). The levels are said to be sub-thermally populated. The critical density definition only applies if $J_\nu = 0$ (source of radiation negligible). We can also generalize the critical density for a multi-level system as follows:

$$n_{cr} = \frac{\sum_{i=0}^{N_{lev}} A_{ui}}{\sum_{i=0}^{N_{lev}} \gamma_{ui}} \quad (1.55)$$

It is the ratio between the upper to lower level de-population rate by photon emission and the upper to lower de-population rate by collisions, from all levels. As for a 2-level system, the population of the levels with respect to the LTE solution depends on the colliding particles density in the gas, the gas temperature, and the energy level. Usually, high energy levels are less populated than low energy levels.

2.2.4 Excitation temperature

In the ISM, the levels are not usually in LTE. It is then useful to introduce the excitation temperature, T_{ex} , which is defined as:

$$T_{ex} = \frac{-E_{ul}}{k_B} \left[\ln \left(\frac{n_u g_l}{n_l g_u} \right) \right]^{-1} \quad (1.56)$$

where $E_{ul} = E_u - E_l$. Using the Eq. 1.53 which defines the critical density, and therefore assuming that the radiation field is negligible, it holds:

$$T_{ex} = T \left[\frac{k_B T}{E_{ul}} \ln \left(1 + \frac{n_{cr}}{n_{coll}} \right) + 1 \right]^{-1} \quad (1.57)$$

where T is the gas kinetic temperature. Two cases can be distinguished:

1. if $n \gg n_{cr}$ then $T_{ex} \sim T$
2. if $n < n_{cr}$ then $T_{ex} < T$

The excitation temperature is the gas kinetic temperature (T) if the levels are thermally populated, i.e. if we are under LTE conditions. This definition is valid for a 2-level system only. In the case of a multi-level system, we define the rotational temperature, T_{ROT} . This is the temperature if all the levels are in LTE. In that case, we would have $T_{ex} = T_{ROT} = T$.

2.3 Line formation and broadening mechanisms

Let us consider a 2-level system. The population of the levels is governed by the statistical equilibrium equation (Eq. 1.44). A fraction of the species in the upper energy level u will decay to the lower energy level l , and a photon of frequency ν_{ul} will be spontaneously emitted. If a strong radiation field illuminates the gas at the same frequency as the transition frequency, there will be also a stimulated emission. The emitted photons will form an emission line at the frequency of the transition. On the other hand, if the excitation of the upper level is dominated by the absorption of the photons rather than collisions, the radiation field at frequency ν_{ul} is strong enough and an absorption line will be formed. Quantitatively, there is absorption when the excitation temperature of the transition is lower than the radiation temperature, specifically when there are both a strong radiation background and a tenuous gas.

The line formed, whether it is in emission or absorption, is not infinitely narrow because the energy levels are not infinitely sharp. Several mechanisms can play a role in the shape of the line but the relevant mechanism in the ISM is the Doppler (thermal) broadening. I note that high optical depth can also affect the shape of the line but I focus here only on the thermal broadening.

Species (atoms or molecules) in the gas are moving with respect to the observer. The photon observed, therefore, does not have the same frequency as when it was emitted: this is due to the Doppler effect. As the atoms/molecules follow the Maxwell distribution, the line is spread over a range in frequency. If we consider a species moving with a velocity v_z long the line of sight of the observer, the Doppler shift is written as $\nu - \nu_0 = \frac{\nu_0 v_z}{c}$, with ν_0 the rest-frame frequency of the line. In this case, the line profile is a Gaussian profile:

$$\Phi_\nu = \frac{1}{\Delta\nu_D \sqrt{\pi}} e^{-\frac{(\nu-\nu_0)^2}{\Delta\nu_D^2}} \quad (1.58)$$

where $\Delta\nu_D$ is the Doppler width defined by $\Delta\nu_D = \frac{\nu_0}{c} b$ with b the Doppler parameter (km/s). The Doppler parameter is linked to the gas kinetic temperature as:

$$b = \sqrt{\frac{2k_B T}{m_x}} = 0.129 \sqrt{\frac{T}{A_x}} \text{ km/s} \quad (1.59)$$

where m_x and A_x are the mass and the atomic number of the species, respectively. We note that b depends on the species mass: the larger the mass of the molecule, the narrower the line. Analogously, b depends on the gas temperature: the larger the gas temperature, the larger the linewidth. The full width at half maximum (FWHM) of the line is defined as:

$$\Delta\nu_{th} = 2\sqrt{\ln(2)}\Delta\nu_D = \frac{\nu_0}{c}\sqrt{\frac{8\ln(2)k_B T}{m_x}} \quad (1.60)$$

2.4 Deriving the physical properties of a gas emitting molecular species

For a given molecule, depending on the number of molecular lines detected and on the availability of the collisional rates for the observed transitions, different methods are available to derive the physical properties of the gas in which the molecule is emitted. In the following, I present the two main spectral analysis methods, the Rotational Diagram (RD) and the Large Velocity Gradient (LVG) method, that are used in this thesis.

2.4.1 Rotational diagram

If we detect enough transition lines from a species, we can perform the rotational diagram (RD) analysis, which is the *step 0* of the molecular line analysis. Two main assumptions are made: LTE and optically thin lines. A supplementary assumption is that the background temperature is negligible. The RD provides an estimate of the average gas kinetic temperature as well as of the column densities of the species from which the lines are emitted.

To construct the RD, we start from the equation for the intensity at a given frequency ν in the case of a constant source, that is reminded here:

$$I_\nu[\tau(\nu)] = I_\nu(0)e^{-\tau(\nu)} + S_\nu(1 - e^{-\tau(\nu)}) \quad (1.61)$$

We assume LTE conditions (i.e. $S_\nu = B_\nu(T)$ with T the gas kinetic temperature). If we also assume the absence of an external source $I_\nu(0)$, the equation becomes:

$$I_\nu[\tau(\nu)] = B_\nu(T)(1 - e^{-\tau(\nu)}) \quad (1.62)$$

The optical depth $\tau(\nu)$ defined in Eq. 1.36 can be defined with useful and measurable parameters. Let us integrate the optical depth over the line profile and the solid angle. We get:

$$\tau = \frac{h\nu}{4\pi} \int d\nu \Phi(\nu) \int n_l B_{lu} \left(1 - \frac{g_l n_u}{g_u n_l}\right) \quad (1.63)$$

Assuming a Gaussian profile for the line, an homogeneous semi-infinite slab (the density and temperature are constant across the slab) for the geometry, the FWHM of the line is $\sqrt{\pi/(4\ln 2)}\Delta\nu \sim \Delta\nu$. Using the relation between the Einstein coefficient given in Eq. 1.45, the optical depth can be expressed as:

$$\tau(z) = \frac{A_{ul}c^3\Delta z}{8\pi\nu^3\Delta\nu} n_u \left(\frac{g_u n_l}{g_l n_u} - 1\right) \quad (1.64)$$

where Δz is the distance from the surface. As we are under the LTE conditions, we can use the Boltzmann distribution and we can, finally, rewrite the optical depth as:

$$\tau = \frac{A_{ul}c^3}{8\pi\nu^3\Delta\nu}N_u\left(e^{E_{ul}/k_B T} - 1\right) \quad (1.65)$$

considering that $N_u = \Delta z n_u$. Now we can use this optical depth formula to insert it in Eq. 1.62. Using the Rayleigh-Jeans approximation and the definition of the brightness temperature (Eq. 1.42), we obtain a formula for the brightness temperature, which is what is measured with the observations:

$$T_B = \frac{hc^3 A_{ul} N_u}{8\pi k_B \nu^2 \Delta\nu} \left(\frac{1 - e^{-(\tau_\nu)}}{\tau_\nu} \right) \quad (1.66)$$

with N_u the column density of the upper energy level. Since we assumed optically thin lines, the equation 1.66 becomes:

$$N_u = \frac{8\pi k_B \nu^2}{hc^3 A_{ul}} W \quad (1.67)$$

where W is the velocity-integrated intensity defined as $W = \int T_B d\nu \approx T_B \Delta\nu$. By definition, at LTE, it holds:

$$\frac{N_u}{N_x} = \frac{g_u}{Q(T)} e^{-\frac{E_u}{k_B T}} \quad (1.68)$$

where N_x is the molecule total column density. By applying the natural logarithm to both terms of Eq. 1.68, we obtain:

$$\ln\left(\frac{N_u}{g_u}\right) = \ln\left(\frac{N_x}{Q(T)}\right) - \frac{E_u}{k_B T} \quad (1.69)$$

We can thus construct the rotational diagram by plotting $\ln(N_u/g_u)$ as a function of E_u . The slope to the best linear fit is proportional to $1/T_{\text{ROT}}$ and its intercept gives us the quantity $\ln(N_x/Q)$. From the RD, we can therefore extract the rotational temperature, T_{ROT} , and the total column density of the molecule, N_x , which are estimates of the average temperature of the emitting gas and the column density of the species emitting the lines, respectively. If we are truly under LTE conditions and lines are all optically thin, we should obtain a perfectly straight line. In this case, the derived rotational temperature is then equal to the gas kinetic temperature and the total column density of the species is accurate. But this is rarely the case and what we usually obtain are non-aligned points as shown in Fig. 1.14. This means that non-LTE effects and/or optically thick lines are present. The RD will therefore provide only an approximate (or even wrong) value of the average gas temperature and of the species column density. This method has thus a limited range of validity. Note that a correction for opacity is possible with the *Population Diagram* method (Goldsmith & Langer 1999).

Finally, the column density of the upper energy level u , N_u , derived by the velocity-integrated intensity is averaged over the telescope beam. Two configuration cases are thus defined: either the emitting source size is smaller than the beam telescope, or it is larger. We thus need to apply the filling factor, f , defined in Sec. 1.3.2 to get the correct total column density of the species, N_x . As the size of the telescope beam depends on the frequency, so does the filling factor. Thus, in the case where we have a large range of frequencies used in the RD, we need to apply the filling factor to the different lines.

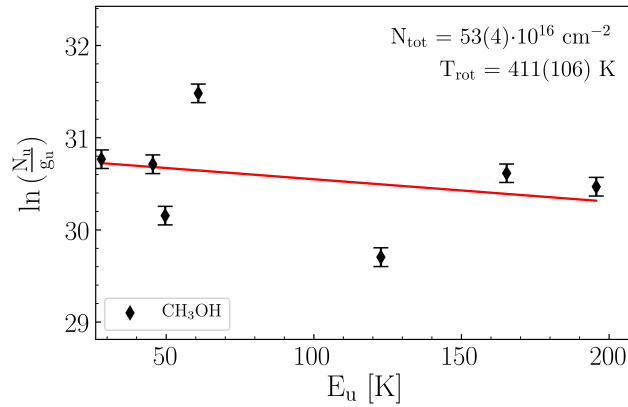


Figure 1.14: Example of a rotational diagram. The points are not perfectly aligned because of the presence of non-LTE effects and/or optically thick lines.

2.4.2 The large velocity gradient (LVG) method

The large velocity gradient (LVG) method is a step further in the interpretation of the observed lines compared to the rotational diagram. It is the application of the escape probability method to the problem of a gas with a systemic large velocity gradient. This method is often used in interpreting molecular spectra. I will first quickly introduce the escape probability method and then its application to the LVG method.

Escape probability method In Sec. 2.1, I introduced the radiative transfer equation. The latter is not easy to solve as there is a coupling between the level populations and the averaged field intensity, J_ν . The radiative transfer equation is then non-linearly coupled with the statistical equilibrium equations and a complete solution of the radiative transfer is difficult to obtain. However, the situation can be simplified if we consider the absorption of the photons to be local. In this case, the different regions of the medium are not radiatively coupled and the statistical equilibrium equations can be decoupled from the radiative transfer equation.

The escape probability method has been first formulated by Sobolev (1960) for stellar atmospheres, before being extended to other physical problems. The method is thus also known as the Sobolev method. The basic idea of this method is to introduce a local multiplicative factor that describes the probability that a photon will escape the medium after it is emitted. If we assume that there is no external source of radiation and that the source is completely opaque to its own radiation, J_ν would approach the local value of S_ν . A deviation of J_ν from S_ν reflects then the photons escaping the medium and the fraction of photons locally trapped is represented by the quantity J_ν/S_ν . If we define β_{esc} as the probability for a photon to escape, then the quantity $(1 - \beta_{esc})$ is the fraction of non-escaped photons.

Let us consider a two-level system. We make the following assumptions: the density and temperature are constant across the slab and the source function is constant across the slab. With the escape probability method, J_ν and β_{esc} can be expressed as:

$$J_\nu = S_\nu(1 - \beta_{esc}),$$

$$\beta_{esc} = \frac{1}{4\pi} \int d\Omega \int \Phi(\nu) e^{-\tau(\nu)} d\nu \quad (1.70)$$

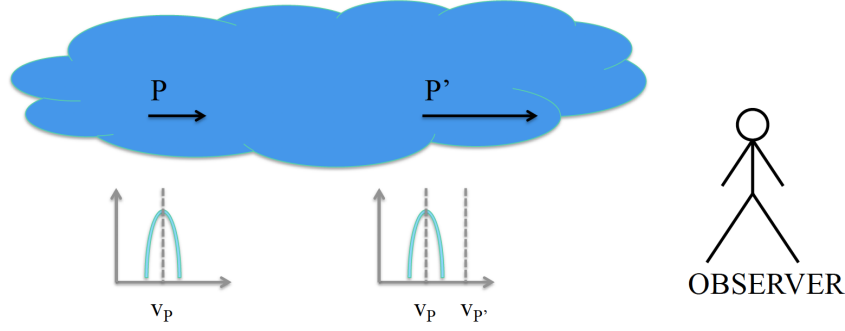


Figure 1.15: Scheme illustrating the LVG method. Taken from C. Ceccarelli's presentation of a M2 course.

where $\Phi(\nu)$ is the Gaussian line profile. The probability β_{esc} depends on the source geometry and the optical depth. For a semi-infinite slab (Scoville & Solomon 1974; de Jong et al. 1975), β_{esc} is defined as:

$$\beta_{esc} = \frac{1 - e^{-3\tau(\nu)}}{3\tau(\nu)} \quad (1.71)$$

For a uniform sphere (Osterbrock 1974), β_{esc} is defined as:

$$\beta_{esc} = \frac{3}{4\tau(\nu)} \left[1 - \frac{1}{2\tau(\nu)^2} + \left(\frac{1}{\tau(\nu)} + \frac{1}{2\tau(\nu)^2} \right) e^{-2\tau(\nu)} \right] \quad (1.72)$$

From the definition of the source function (Eq.1.35), the latter can be expressed in terms of Einstein coefficients such as:

$$S_\nu = \frac{n_u A_{ul}}{n_l B_{lu} - n_u B_{ul}} \quad (1.73)$$

Using Eq. 1.70 for J_ν and substituting it in the statistical equilibrium equation (Eq.1.44) for a two-level system, we obtain:

$$\frac{n_u}{n_l} = \frac{g_u}{g_l} e^{-h\nu/k_B T} \frac{1}{1 + \beta \frac{n_{cr}}{n_{coll}}} \quad (1.74)$$

As desired, the radiative intensity is decoupled from the statistical equilibrium equation. From Eq.1.74, we see that photons trapping scales down the spontaneous emission rate (as the critical density is linked to this coefficient: Eq. 1.54) which corresponds to the fact that a photon is *emitted* only if it escapes the medium.

Large velocity gradient code Let us consider a medium in which a photon of frequency ν is emitted at a point P with a velocity v_p . If the gas is moving with respect to the position P with its own velocity, the photon emitted in P cannot be absorbed in P'. The photon frequency is Doppler-shifted outside the $h\nu + \Delta\nu_{th}$, where ν_{th} is the thermal width of the line defined in Eq.1.60. The situation is represented in Fig.1.15.

The photon has two possibilities: either it is absorbed close to where it is emitted, or it escapes the medium. We saw in the previous paragraph that the probability of the photon to escape, β_{esc} , depends on the source geometry and the optical depth. Since the optical depth is linked to the radiative mean free path of the photon, the denser the medium, the

smaller the distance travelled by the photon and, thus, the less probability the photon has to escape.

Any LVG code allows calculating the line flux from a cloud of gas with a systemic gradient of velocity, constant density and temperature, for a given geometry (e.g. semi-infinite slab, uniform sphere). The flux F of a line emitted by a source at a distance d and expressed using the escape probability formalism is:

$$F = \frac{1}{4\pi d^2} \int_{\text{volume}} dV h\nu A_{ul} n_u \beta_{esc} \quad (1.75)$$

where the integral is on the volume of the emitting source. The flux computed by the LVG codes depends thus on the gas density and temperature, the column density of the molecule (for the line opacity), the velocity gradient (calculated from the linewidth), and the size of the emitting region. From the data and the model issued by the LVG code, one can derive the H_2 density, n_{H_2} , the species column density, the gas temperature and the source size if not already known before. The LVG code used for this thesis is that developed by [Ceccarelli et al. \(2003\)](#). The description of the modelling carried out in this thesis is detailed in papers 1 (Chapter 2) and 3 (Chapter 3, Sec. 3.2).

The hunt of hot corinos and WCCC objects in the OMC-2/3 filament: A single-dish approach

The first project I carried out was to find hot corinos and WCCC candidates in the OMC-2/3 filament, using single-dish observations. At the time of this first study, there was only one hot corino detected in the Orion Molecular Cloud (OMC), HH212 ([Codella et al. 2016, 2018](#); [Lee et al. 2017](#); [Lee et al. 2019](#)), and no evidence of WCCC sources. Yet HH212 is isolated and is not considered to be located in an environment similar to the one in which our Sun was born.

A handful of studies have been performed to assess the chemical nature of low-mass protostars and to understand hot corinos and WCCC objects. These works surveyed several low-mass star-forming regions using single-dish observations (scale ~ 10000 au) of small carbon chains (CC) and iCOMs, molecules characteristic of WCCC sources and hot corinos, respectively. They derived the abundance ratio $[\text{CC}]/[\text{iCOMs}]$ (e.g. $[\text{CCH}]/[\text{CH}_3\text{OH}]$, $[\text{C}_4\text{H}]/[\text{CH}_3\text{OH}]$; [Lindberg et al. 2016](#); [Graninger et al. 2016](#); [Higuchi et al. 2018](#)) and two main results came out from these studies: (1) the majority of the sources surveyed presents a chemical content that is transitional between hot corinos and WCCC sources, i.e. $[\text{CC}]/[\text{iCOMs}] \sim 1$ ([Lindberg et al. 2016](#); [Graninger et al. 2016](#); [Higuchi et al. 2018](#)), and (2) hot corinos tend to be located at the centre of the cloud whilst WCCC sources are located near the edges of clouds or in isolation ([Lefloch et al. 2017](#); [Higuchi et al. 2018](#)). These studies present caveats concerning the choice of molecules. First, carbon chains are usually abundant in photodissociation regions (PDRs), which means their spatial distribution can be quite extended (e.g. [Fossé et al. 2001](#); [Fuente et al. 2003](#); [Teyssier et al. 2004](#); [Pety et al. 2005](#); [Gerin et al. 2009](#); [Gúzman et al. 2015](#); [Cuadrado et al. 2015](#)). Second, methanol, the most used iCOMs in these studies, is detected in both PDRs and molecular clouds (e.g. [Leurini et al. 2010](#); [Guzmán et al. 2013](#); [Cuadrado et al. 2017](#); [Punanova et al. 2018](#)). Observations with single-dish telescopes are limited in spatial resolution, and one cannot always disentangle the protostars from their surroundings. Important contributions can, therefore, be attributed to the surrounding PDR or molecular cloud in which the sources are embedded.

The goals of this study were twofold: (1) search for hot corino and WCCC candidates in the OMC-2/3 filament and (2) verify the reliability of using single-dish observations of carbon chains and methanol to determine the chemical nature of solar-mass proto-

stars. To achieve these goals, I derived the abundance ratio $[CCH]/[CH_3OH]$ towards nine (Class 0 and I) solar-mass protostars using three sets of observations. Two of them were single-pointing observations (IRAM-30m at 1.3mm and Nobeyama 45m at 3mm; P.I. Ana López-Sepulcre), and the third one is on-the-fly mapping observations at 3mm, centred on one of the sources. While the first two datasets were obtained before my thesis started, the last dataset was obtained via a Director's Discretionary Time proposal for which I am the PI.

Results of the single-pointing observations showed that the lines of CCH and CH_3OH were both narrower than expected, with linewidths between 0.8 and 1.6 $km.s^{-1}$. The estimated physical parameters, derived with both a local thermal equilibrium (LTE) and non-LTE analysis, showed that all sources have similar gas density and temperature, the latter being low (≤ 30 K) for both CCH and CH_3OH . These two results are incompatible with the hypothesis of the line emission coming from the inner part of the protostars envelopes. In addition, we found the gas emitting methanol having constant temperature and density across the mapped region. We also found a decrease in the $[CCH]/[CH_3OH]$ abundance ratio from the north side, more UV-illuminated, to the south side, more shielded from UV photons, of the cloud. We, therefore, concluded that the observed line emission is not associated with the protostars but rather with the parent cloud gas. Finally, we compared the CCH and CH_3OH column densities derived in this study with those from other WCCC objects, hot corinos, PDRs and molecular clouds. Additionally, this comparison strongly suggests that the line emission from the two species, CCH and CH_3OH , is likely dominated by the PDR surrounding the molecular cloud in which the protostars are embedded.

In conclusion, one needs to be careful when determining the chemical nature of solar-mass protostars using single-dish observations of CH_3OH , CCH, and other small carbon chains by extension. These species can be emitted from external components not directly linked to the protostars. Thus, using the abundance ratio $[CC]/[iCOMs]$ is unreliable, notably in high UV-illuminated regions. As a consequence, we could not find hot corinos or WCCC candidates in the OMC-2/3 filament. The next step is to use interferometry which will allow us to get rid of the external contamination and probe the inner region of the protostars envelope.

The hereafter paper has been published in the *Astronomy & Astrophysics* 2020, 636, A19.

Hunting for hot corinos and WCCC sources in the OMC-2/3 filament

M. Bouvier¹, A. López-Sepulcre^{1,2}, C. Ceccarelli^{1,3}, C. Kahane¹, M. Imai⁴, N. Sakai⁵,
S. Yamamoto^{4,6}, and P. J. Dagdigan⁷

¹ Univ. Grenoble Alpes, CNRS, Institut de Planétologie et d'Astrophysique de Grenoble (IPAG), 38000 Grenoble, France
e-mail: mathilde.bouvier@univ-grenoble-alpes.fr

² Institut de Radioastronomie Millimétrique (IRAM), 300 rue de la Piscine, 38406 Saint-Martin-D'Hères, France

³ CNRS, IPAG, 38000 Grenoble, France

⁴ Department of Physics, The University of Tokyo, 7-3-1, Hongo, Bunkyo-ku, Tokyo 113-0033, Japan

⁵ RIKEN, Cluster for Pioneering Research, 2-1, Hirosawa, Wako-shi, Saitama 351-0198, Japan

⁶ Research Center for the Early Universe, The University of Tokyo, 7-3-1, Hongo, Bunkyo-ku, Tokyo 113-0033, Japan

⁷ Department of Chemistry, The Johns Hopkins University, Baltimore, MD 21218-2685, USA

Received 21 November 2019 / Accepted 3 March 2020

ABSTRACT

Context. Solar-like protostars are known to be chemically rich, but it is not yet clear how much their chemical composition can vary and why. So far, two chemically distinct types of Solar-like protostars have been identified: hot corinos, which are enriched in interstellar Complex Organic Molecules, such as methanol (CH₃OH) or dimethyl ether (CH₃OCH₃), and warm carbon chain chemistry (WCCC) objects, which are enriched in carbon chain molecules, such as butadiynyl (C₄H) or ethynyl radical (CCH). However, none of these have been studied so far in environments similar to that in which our Sun was born, that is, one that is close to massive stars.

Aims. In this work, we search for hot corinos and WCCC objects in the closest analogue to the Sun's birth environment, the Orion Molecular Cloud 2/3 (OMC-2/3) filament located in the Orion A molecular cloud.

Methods. We obtained single-dish observations of CCH and CH₃OH line emission towards nine Solar-like protostars in this region. As in other similar studies of late, we used the [CCH]/[CH₃OH] abundance ratio in order to determine the chemical nature of our protostar sample.

Results. Unexpectedly, we found that the observed methanol and ethynyl radical emission (over a few thousands au scale) does not seem to originate from the protostars but rather from the parental cloud and its photo-dissociation region, illuminated by the OB stars of the region.

Conclusions. Our results strongly suggest that caution should be taken before using [CCH]/[CH₃OH] from single-dish observations as an indicator of the protostellar chemical nature and that there is a need for other tracers or high angular resolution observations for probing the inner protostellar layers.

Key words. astrochemistry – methods: observational – stars: solar-type – ISM: individual objects: OMC-2/3 – stars: formation

1. Introduction

A key aspect of the chemical richness of the protostellar stage is the diversity found among Solar-like protostars. Indeed, two chemically distinct types of Solar-like protostars have been identified. On the one hand, hot corinos (Ceccarelli et al. 2000, 2007) are compact (<100 au), dense (>10⁷ cm⁻³), and hot (>100 K) regions, enriched in interstellar Complex Organic Molecules (hereafter iCOMs; for example, CH₃OH, CH₃CHO, HCOOCH₃; Herbst & Van Dishoeck 2009; Ceccarelli et al. 2017). On the other hand, warm carbon chain chemistry (hereafter WCCC; Sakai et al. 2008, Sakai & Yamamoto 2013) objects have an inner region deficient in iCOMs but a large (≈2000 au) zone enriched in carbon chain molecules (e.g. CCH, c-C₃H₂, C₄H). This dichotomy does not seem to be absolute as at least one source, the protostar L483, presents both hot corino and WCCC characteristics (Oya et al. 2017). Understanding what causes this chemical diversity is a fundamental step in understanding the formation and the evolution of a planetary system like our own and, perhaps, to understand the appearance of life on Earth. Furthermore, given our Sun was formerly a protostar, it is natural to consider whether it may have experienced a hot corino phase, a

WCCC phase, or neither of the two in its youth. In this respect, we recall that the Solar System formed in a large stellar cluster in proximity to high-mass stars ($M_* \geq 8 M_\odot$; Adams 2010, Pfalzner et al. 2015).

So far, there have been only a few hot corinos and WCCC objects identified and almost all of them are located in low-mass star forming regions (e.g. Cazaux et al. 2003; Sakai et al. 2008; Taquet et al. 2015). Besides the relatively small number of WCCC objects in low-mass star-forming regions, WCCC characteristics have also been seen in other environments, such as the starless core L1489 (Wu et al. 2019) and in the giant HII region NGC 3576 (Saul et al. 2015). A hot corino was also found in the high-mass star-forming region of Orion, HH212-MM1 (Codella et al. 2016), but as with the other hot corinos, it is located far from massive stars. Previous observational studies have been carried out towards hot corinos and WCCC objects in an effort to better understand them. Some studies have been targeted on just one type of object (either hot corino or WCCC object; e.g. Caux et al. 2011; Jørgensen et al. 2016; López-Sepulcre et al. 2017; Oya et al. 2017; Ospina-Zamudio et al. 2018; Agúndez et al. 2019; Bianchi et al. 2019; Yoshida et al. 2019), or one type of molecular tracer (Carbon-chain or iCOMs; e.g. Law et al. 2018;

Table 1. Summary of the excitation temperatures (T_{ex}) and column densities (N_{tot}) of the different tracers of hot corinos (CH_3OH) and WCCC objects (CCH and C_4H) derived in previous surveys obtained with single-dish telescope observations.

Object type	Molecule	Graninger et al. (2016)		Lindberg et al. (2016)		Higuchi et al. (2018)		L1527 ^(b)		IRAS 16293-2422 ^(c)	
		T_{ex} [K]	N_{tot} [$\times 10^{13}\text{cm}^{-2}$]	T_{ex} [K]	N_{tot} [$\times 10^{13}\text{cm}^{-2}$]	T_{ex} [K]	N_{tot} [$\times 10^{13}\text{cm}^{-2}$]	T_{ex} [K]	N_{tot} [$\times 10^{13}\text{cm}^{-2}$]	T_{ex} [K]	N_{tot} [$\times 10^{13}\text{cm}^{-2}$]
WCCC tracers	CCH	8 – 21	≤ 52	8 ± 1	33 ± 3	18 ± 6	9 ± 6
	C_4H	7 – 15	< 4	7 – 16.5 ^(a)	< 1	12.3	20 ± 4	12.3	1.2 ± 0.3
Hot corino tracer	CH_3OH	4 – 7	0.2 – 11	< 123 ^(a)	0.2 – 95	8 – 21	0.5 – 16	8 ± 1	8 ± 1	84 ± 6	90 ± 10
Resolution (au)		4100–13 000		7800–8200		2400–4900		2400–4900		500–2000	

Notes. ^(a)Excitation temperatures taken from $\text{c-C}_3\text{H}_2$ and H_2CO APEX observations for C_4H and CH_3OH respectively (Lindberg et al. 2016).

References. ^(b)Higuchi et al. (2018), Sakai et al. (2008). ^(c)Van Dishoeck et al. (1995), Sakai et al. (2009).

Wu et al. 2019) whereas other studies targeted all kinds of protostars and selected tracers to evaluate their chemical nature (i.e. comparative statistical studies of chemical diversity; e.g. Graninger et al. 2016, Lindberg et al. 2016, Higuchi et al. 2018). For the latter, the method employed is based on observations with single-dish telescopes (scale of $\approx 10\,000$ au) of small carbon chains (e.g. CCH, C_4H) and methanol (CH_3OH) as tracers of WCCC objects and hot corinos, respectively. However, this method presents some caveats. Indeed, emission of small carbon chains are usually extended and present in the Photo-Dissociation Regions (hereafter PDRs) surrounding the molecular clouds (e.g. Pety et al. 2005; Cuadrado et al. 2015). As for CH_3OH , it is also a species that has been found in PDRs as well as in molecular clouds (e.g. Leurini et al. 2010; Guzmán et al. 2013; Cuadrado et al. 2017; Punanova et al. 2018). Thus, an important contribution from the parental molecular cloud or from the surrounding PDR may occur when observing those molecules with single-dish telescopes.

In this context, the goal of the present work is twofold: (1) to identify the nature of several protostars, hot corinos, or WCCC objects in a region containing high-mass stars and whether it depends on the object position in the cloud; this will help us to understand whether the Sun passed through a hot corino or a WCCC object phase. Indeed, if only hot corinos are found in Orion Molecular Cloud 2/3 (OMC-2/3), this would strongly suggest that our Sun also underwent a hot corino phase during its youth and vice versa; (2) to verify the reliability of using single-dish observations of small hydrocarbons and methanol to classify the chemical nature of the protostars.

To reach these two goals, we obtained new IRAM-30 m and Nobeyama-45 m observations of ethynyl radical (CCH) and methanol towards a sample of nine known protostars in the closest high- and low- mass star forming region, OMC-2/3, and a map of a portion of it. Following Higuchi et al. (2018), we used the $[\text{CCH}]/[\text{CH}_3\text{OH}]$ abundance ratio to make a first assessment of the chemical nature of the targeted sources: a small (≤ 0.5) ratio would be suggestive of a hot corino candidate whereas a large (≥ 2) ratio would rather be suggestive of a WCCC candidate, as we will discuss in detail in Sect. 3. Moreover, this abundance ratio is about one order of magnitude different when comparing the hot corino and WCCC templates sources (see Table 1), which would a priori justify the use of this initial criterion.

This paper is structured as follows. In Sect. 2, we briefly review the previous surveys with single-dish observations aimed to study the chemical nature of low-mass protostars. In Sect. 3, we briefly describe the OMC-2/3 region, the selected source sample and explain the choice of the molecular species that we

targeted. A description of the observations are presented in Sect. 4. In Sect. 5, we show the results of the analysis of the observed lines. In Sect. 6, we present the derived physical conditions (temperature and density) of the gas which emits the detected CCH and CH_3OH lines and their column densities. In Sect. 7, we discuss our findings. We finally end with some concluding remarks in Sect. 8.

2. Prior surveys of protostellar chemical diversity with carbon chain-iCOM ratios

The first efforts aimed at improving statistics on the chemical nature and diversity of low-mass protostars were only recently begun. The chemical tool used is the abundance ratio between carbon chains (e.g. CCH, C_4H) and iCOMs (e.g. CH_3OH). Those families of molecules are abundant in WCCC objects and in hot corinos, respectively. We present in this section only surveys that used the chemical tool cited above to identify hot corinos and WCCC sources.

Graninger et al. (2016) investigated the relationship between C_4H and CH_3OH in 16 embedded protostars located in the northern hemisphere. The abundance ratio $[\text{C}_4\text{H}]/[\text{CH}_3\text{OH}]$ for a typical WCCC is 2.5 and for typical hot corinos (IRAS 16293-2422, IRAS 4A, IRAS 4B, Serpens MMS4), < 0.15 . With this definition, among their 16 sources, there would be five WCCC sources and at most two hot corinos. However, the temperatures derived are likely too low (≤ 15 K) to correspond to the lukewarm envelope of the protostars. Their main results are: (1) there is a positive correlation between the column densities of C_4H and CH_3OH , indicating that the two species are present in a lukewarm environment in the protostellar envelopes; and (2) they found a lower amount of CH_3OH than in hot corinos and a lower amount C_4H than in WCCC sources. The under-abundance of carbon chains in this source sample has been confirmed by Law et al. (2018).

Similarly, Lindberg et al. (2016), observed 16 low-mass protostars in the southern hemisphere and, including the results from Graninger et al. (2016), they investigated the origin of C_4H and CH_3OH in the protostellar envelopes. Using the same abundance ratio, two sources would be labelled as WCCC protostars and about six as hot corinos. Contrary to Graninger et al. (2016), they did not observe evidence of a correlation between the column densities of the two species and they concluded that CH_3OH would reside in the warmer inner regions of the protostellar environment, whereas C_4H would reside rather in the cooler outer regions of the protostellar environment. However, the derived excitation temperature for CH_3OH never exceeds 36 K, except in the well-known hot corino IRAS 16293-2422.

Table 2. Selected sources and their properties.

Source	RA J2000	Dec J2000	Mass M_{\odot}	Radio (Y/N)	Outflow (Y/N)	Notes	Reference
CSO33	05:35:19.50	-05:15:35.0	6	N	Y?	Near HII region (M42)	1
FIR6c ^(a)	05:35:21.60	-05:13:14.0	5–9	N	Y	Class 0	2
FIR2 ^(a)	05:35:24.40	-05:08:34.0	4–10	N	Y	Class I	2
FIR1a	05:35:24.40	-05:07:53.0	12	Y	N	Class 0?	2
MMS9	05:35:26.20	-05:05:44.0	4.7	Y	Y	Class 0	2
MMS5	05:35:22.50	-05:01:15.0	4.5	N	Y	Class 0, part of the OTF map	2
MMS2	05:35:18.50	-05:00:30.0	2.8	Y	Y	Class I, binary, part of the OTF map	2
CSO3	05:35:15.80	-04:59:59.0	12	N	N	Binary, part of the OTF map	1
SIMBA-a ^(b)	05:35:29.80	-04:58:47.0	6.5	...	Y	Class 0, isolated, near HII region (NGC 1977)	3

Notes. The envelope mass of the protostars are taken from Li et al. (2013) and Takahashi et al. (2008). The data for the radio component are taken from VLA cm-radio emission (Reipurth et al. 1999). The data on the outflows are from Takahashi et al. (2008). ^(a)Left out of the analysis due to prominent non-Gaussian line wings. ^(b)Data from the 3mm only, as there was emission contamination from the wobbler off position for the 1mm data set.

References. (1) Lis et al. (1998); (2) Chini et al. (1997); (3) Nielbock et al. (2003).

Those temperatures seem too low for CH₃OH to originate in the hot corinos. Indeed, for hot corinos ($T \geq 100$ K; Ceccarelli et al. 2007), we expect excitation temperatures of at least 50 K to support an origin of emission dominated by the hot corino.

Finally, Higuchi et al. (2018), performed a survey of 36 low-mass protostars in the Perseus region. They compared the abundance ratio [CCH]/[CH₃OH] of each source to that of L1527, the prototypical WCCC source, to characterise their chemical nature. From this criterion, at most four sources can be WCCC protostars and 14 sources seem to be hot corinos. Two main results of their work are: (1) the majority of the sources have intermediate chemical composition between hot corinos and WCCC types; and (2) WCCC objects tend to be found at the edge of molecular clouds or in relative isolation, whereas the hot corinos tend to be located in the centre of molecular clouds. Also in this case, the derived excitation temperatures are low (in the range of 8–21 K), so it is not entirely clear whether the observed molecular emission is contaminated by the molecular cloud.

Table 1 summarises the derived excitation temperatures and column density of CCH, C₄H and CH₃OH in the three surveys, as well as those derived for L1527 (the WCCC prototype) and IRAS 16293-2422 (the hot corino prototype). Based on these surveys and their definition of hot corinos and WCCC objects, about 33% of the low-mass protostars are hot corinos, 17% can be classified as WCCC sources and the rest (50%) do not seem clearly to belong to any of the two categories. We note that the definition of hot corino and WCCC object varies from one survey to another. Overall, 66 low-mass protostars have been surveyed upon adding up all of these studies, but all of them concern regions with no massive stars nearby, which is basis of the next step and overall goal of our study.

3. Targeted sources and molecular tracers

3.1. Target selection

OMC-2/3 is part of the Orion A molecular complex and is composed of two major molecular clouds, OMC-2 and OMC-3. Those two clouds form a filament-shaped region located between the Trapezium OB stellar cluster and the NGC 1977 HII region, at a distance of (393 ± 25) pc from the Sun (Großschedl et al. 2018). OMC-2 lies to the north of OMC-1, which is the

molecular cloud associated with the Orion Nebula, and was identified by Gatley et al. (1974). The cloud OMC-3, located further north, was labelled later by Chini et al. (1997). OMC-2/3 has been extensively studied since its discovery and multiple protostars, in particular Class 0 protostars, have been identified (e.g. Chini et al. 1997), as well as multiple molecular outflows (e.g. Reipurth et al. 1999; Williams et al. 2003; Takahashi et al. 2008), and H₂ shocks and jets (Yu et al. 1997).

What makes OMC-2/3 particularly interesting is that it is the nearest region containing both low- and high-mass forming stars. In addition, it is surrounded by bright OB stars which create HII regions and PDR. Thus, OMC-2/3 is unique target for the study of a region similar to the one in which the Solar System was born, as well as to probe the effect of different environments. For this reason we carried out a systematic study of several sources with the goal of characterising their chemical nature, that is, hot corino versus WCCC objects, and how this depends on the location of the source within OMC-2/3 and its immediate surroundings.

With this in mind, we selected a sample of low-mass protostellar sources which satisfy the following three criteria: (1) detection in the (sub-)mm continuum emission; (2) estimation (based on the continuum) masses $\leq 12 M_{\odot}$; (3) bona fide Class 0 and I protostars (which excludes pre-stellar cores that may also be present in this region). The resulting sample consists of nine sources, whose coordinates as well as some of their known properties, are listed in Table 2. Their masses (dust+gas) cover from 2.8 to $12 M_{\odot}$ (Takahashi et al. 2008; Li et al. 2013), constituting, therefore, a rather homogeneous sample in this respect. Most of the sources are known to possess outflows, which is in line with their protostellar nature, and one third of them have detected cm-radio emission (Reipurth et al. 1999), which is again a sign of a protostellar nature (e.g. Anglada 1995, 1996). Finally, Fig. 1 shows the distribution along the OMC-2/3 filament of the selected targets: they cover the whole filament from the north end (CSO3 source) to the south one (CSO33 source). Some of them are close to the border of the molecular cloud whereas others lie well inside, where the UV radiation field from the nearby OB stars is expected to be as much as 3 orders of magnitude lower than at the edge of the filament (see López-Sepulcre et al. 2013). This will thus allow us, as we aim, to probe different environments across the filament. We note that we did not add to

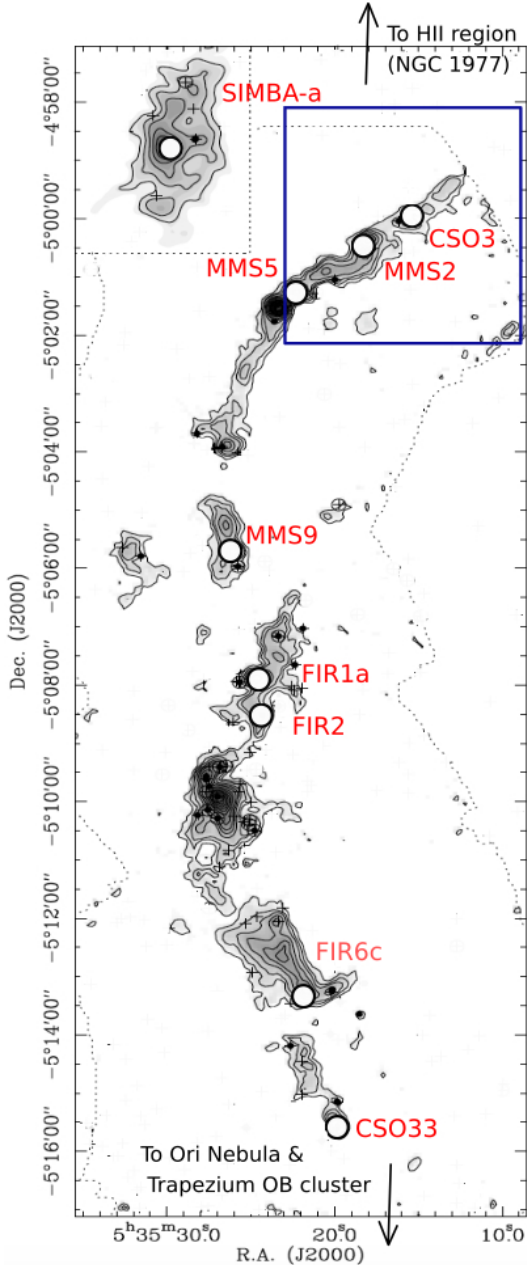


Fig. 1. Map of the continuum at 1.3 mm towards the OMC-2/3 filament, adapted from Chini et al. (1997) and Nielbock et al. (2003). The upper left insert (square grid) is taken from the SIMBA map of Nielbock et al. (2003) and added on the 1.3 mm map of Chini et al. (1997) whose limits are represented by the dotted lines. Contours rise linearly from a 3σ rms noise level (Nielbock et al. 2003), the rms noise of the map being 25 mJy (Chini et al. 1997). The selected targets of the present study are marked with white circles, which have the size of the IRAM-30 m beam at 1.3 mm. The names of the sources are reported in red (see Table 2). Please note that some black crosses and filled dots are present throughout the figure. They represent some of the 2MASS sources and MIR sources from TIMMI 2 observed by Nielbock et al. (2003). The blue square indicates the region mapped with IRAM-30 m at 3 mm. The two arrows show the direction of the HII region NGC 1977 (top) and the Ori Nebula and Trapezium OB cluster (bottom).

the study the famous FIR4, the brightest sub-mm source in the OMC-2 cloud, because it is already the focus of several past and future studies (e.g. López-Sepulcre et al. 2013; Kama et al. 2013; Ceccarelli et al. 2014; Fontani et al. 2017; Favre et al. 2018).

Finally, in order to be able to disentangle the contamination of the protostar from the cloud, we also mapped the northern region around MMS5, MMS2, and CSO3 (see Fig. 1). We chose the area to be mapped considering three main criteria. Firstly, the area has to contain both a part of the filament, with at least one protostar from our sample, and a part outside of the filament to see whether the abundance ratio varies across the map and if so, then how. Secondly, we aimed to target the most quiescent environment possible, excluding regions with sources associated with known outflows or jets (Yu et al. 1997; Reipurth et al. 1999; Williams et al. 2003; Takahashi et al. 2008). These two criteria lead us to select OMC-3, which is more quiescent than OMC-2 from this point of view. Finally, we aimed to target more than one protostar from our sample to understand whether the abundance ratio $[CCH]/[CH_3OH]$ varies among the sources and how. Thus, the region centred on CSO3, which includes three of our protostellar targets, was selected as the best area to map.

3.2. Selected molecules

In order to identify whether the targeted sources belong to the hot corino, WCCC sources classes, or none of them, we targeted lines from CCH and CH_3OH , two molecules that are characteristic of WCCC and hot corinos sources, respectively (Maret et al. 2005; Sakai & Yamamoto 2013). As in previous similar works (Sect. 2), we used their relative abundance ratio, $[CCH]/[CH_3OH]$, to assess their chemical nature. Specifically, based on the values measured in the two prototypes of hot corinos and WCCC sources (IRAS 16293-2422 and L1527: see Table 1), a $[CCH]/[CH_3OH]$ abundance ratio larger than about 2 would roughly identify a WCCC source while a value lower than about 0.5 would testify for a hot corino nature; sources with values in between may be intermediate cases.

We selected two bands, at 3 and 1 mm, of the hyperfine structure lines of CCH, and several CH_3OH rotational lines which cover a large range (~ 7 to ~ 100 K) of transition upper level energy, in order to derive column densities and temperatures of CCH and CH_3OH . The list of the targeted lines as well as their spectroscopic parameters is reported in Table 3.

4. Observations

We obtained single-pointing observations towards the nine sources of Table 2 with the single-dish telescopes IRAM-30 m, targeting the CCH and CH_3OH lines in the 3 and 1 mm bands, and Nobeyama-45 m, for additional 3mm CCH lines. In addition, in order to disentangle the inner protostellar emission from that originating from the more external parental cloud, we obtained a $3' \times 3'$ arcmin² map of the north end of OMC-3 with the IRAM-30 m (see Fig. 1) in both CCH and CH_3OH lines. In the following, we individually describe the observations obtained at the two telescopes.

4.1. IRAM-30 m telescope

Single-pointing observations were carried out on January 13th and 17th 2016, and on February 24–25th and 29th 2016. The EMIR receiver E2 (1.3 mm) was used in order to cover the chosen spectral windows from 239.14 to 246.92 GHz and from 254.82 to 262.6 GHz. The Fourier Transform Spectrometer (FTS), providing a spectral resolution of 195 kHz (0.26 km.s^{-1}), was connected to the receiver. For each source, single-pointing observations in wobbler mode were made, with a wobbler throw of $120''$. The resulting beam size is $10''$. Focus and pointing were

Table 3. Targeted lines and their spectroscopic properties.

Molecule	Transition	Freq. [GHz]	E_{up} [K]	A_{ij} [s ⁻¹]	Observation mode Single-point (S)/Map (M)	Telescope
CH ₃ OH	5 ₋₁ -4 ₀ E	84.521	40.4	1.97E-06	S and M	IRAM-30 m + Nobeyama-45 m
	2 ₋₁ -1 ₋₁ E	96.739	12.5	2.56E-06	M	IRAM-30 m
	2 ₀ -1 ₀ A	96.741	6.9	3.41E-06	M	IRAM-30 m
	2 ₀ -1 ₀ E	96.745	20.0	3.42E-06	M	IRAM-30 m
	2 ₁ -1 ₁ E	96.755	28.0	2.62E-06	M	IRAM-30 m
	5 ₁ -4 ₁ A	239.746	49.1	5.66E-05	S	IRAM-30 m
	5 ₀ -4 ₀ E	241.700	47.9	6.04E-05	S	IRAM-30 m
	5 ₋₁ -4 ₋₁ E	241.767	40.4	5.81E-05	S	IRAM-30 m
	5 ₀ -4 ₀ A	241.791	34.8	6.05E-05	S	IRAM-30 m
	5 ₃ -4 ₃ A	241.832 ^(a)	84.6	3.87E-05	S	IRAM-30 m
	5 ₃ -4 ₃ A	241.833 ^(a)	84.6	3.87E-05	S	IRAM-30 m
	5 ₂ -4 ₂ A	241.842	72.5	5.11E-05	S	IRAM-30 m
	5 ₃ -4 ₃ E	241.843	82.5	3.88E-05	S	IRAM-30 m
	5 ₃ -4 ₃ E	241.852	97.5	3.89E-05	S	IRAM-30 m
	5 ₁ -4 ₁ E	241.879	55.9	5.96E-05	S	IRAM-30 m
	5 ₂ -4 ₂ A	241.887	72.5	5.12E-05	S	IRAM-30 m
	5 ₂ -4 ₂ E	241.904 ^(a)	57.1	5.03E-05	S	IRAM-30 m
	5 ₂ -4 ₂ E	241.904 ^(a)	60.7	5.09E-05	S	IRAM-30 m
	5 ₁ -4 ₁ A	243.915	49.7	5.97E-05	S	IRAM-30 m
	2 ₁ -1 ₀ E	261.805	28.0	5.57E-05	S	IRAM-30 m
CCH	$N=1-0, J=3/2-1/2, F=1-1$	87.284	4.2	2.60E-07	S and M	IRAM-30 m + Nobeyama-45 m
	$N=1-0, J=3/2-1/2, F=2-1$	87.316	4.2	1.53E-06	S and M	IRAM-30 m + Nobeyama-45 m
	$N=1-0, J=3/2-1/2, F=1-0$	87.328	4.2	1.27E-06	S and M	IRAM-30 m + Nobeyama-45 m
	$N=1-0, J=1/2-1/2, F=1-1$	87.402	4.2	1.27E-06	S and M	IRAM-30 m + Nobeyama-45 m
	$N=1-0, J=1/2-1/2, F=0-1$	87.407	4.2	1.54E-06	S and M	IRAM-30 m + Nobeyama-45 m
	$N=1-0, J=1/2-1/2, F=1-0$	87.446	4.2	2.61E-07	S and M	IRAM-30 m + Nobeyama-45 m
	$N=3-2, J=7/2-5/2, F=3-3$	261.978	25.1	1.96E-06	S	IRAM-30 m
	$N=3-2, J=7/2-5/2, F=4-3$	262.004	25.1	5.32E-05	S	IRAM-30 m
	$N=3-2, J=7/2-5/2, F=3-2$	262.006	25.1	5.12E-05	S	IRAM-30 m
	$N=3-2, J=5/2-3/2, F=3-2$	262.064	25.2	4.89E-05	S	IRAM-30 m
	$N=3-2, J=5/2-3/2, F=2-1$	262.067	25.2	4.47E-05	S	IRAM-30 m
	$N=3-2, J=5/2-3/2, F=2-2$	262.078	25.2	6.02E-06	S	IRAM-30 m
	$N=3-2, J=5/2-5/2, F=3-3$	262.208	25.2	3.96E-06	S	IRAM-30 m
	$N=3-2, J=5/2-5/2, F=3-2$	262.236	25.2	4.04E-07	S	IRAM-30 m
$N=3-2, J=5/2-5/2, F=2-2$	262.250	25.2	2.27E-06	S	IRAM-30 m	

Notes. The last two columns indicate whether the line is observed in the single-pointing observations (S) or in the OTF map (M), and the used telescope. The spectroscopic data for CCH are from [Padovani et al. \(2009\)](#) through the CDMS (Cologne Database for Molecular Spectroscopy: [Müller et al. 2005](#)) and for CH₃OH, from [Xu et al. \(2008\)](#) through the JPL molecular spectroscopy database (Jet Propulsion Laboratory: [Pickett et al. 1998](#)) databases. ^(a) Lines blended, they are not used in the LTE and LVG analysis.

checked every 1.5 h and every six hours respectively throughout the observations and with a pointing accuracy of ≤ 2 arcsec at 1 mm and of ≤ 5 arcsec at 3 mm.

Additionally, an on-the-fly (OTF) map of size $3' \times 3'$ arcmin², centred on the source CSO3 was observed on October 22nd 2018 (see Fig. 1) with a beam size of $30''$. The dump time was 1 s and the sampling interval $10''$. The map was repeatedly scanned both along the right ascension (RA) and the declination (Dec) directions until the required root mean square (rms) was reached. We used the EMIR receiver and the FTS units to cover the frequencies from 80.2 to 87.8 GHz and from 95.7 to 103.3 GHz. The spectral resolution obtained is 0.7 km s^{-1} .

We used the Continuum and Line Analysis Single-dish Software (CLASS) from the GILDAS package¹ to reduce the two sets

of data. For the single-pointing observations, a baseline of a first-order polynomial was subtracted for each scan. Then all spectral scans were stitched together to get a final spectrum for each source. Finally, the intensity was converted from antenna temperature (T_A^*) to main beam temperature (T_{mb}) using the Ruze's formula $B_{\text{eff}} = B_0 \cdot \exp[-(4\pi\sigma/\lambda)^2]$, the scaling factor $B_0 = 0.863$ and the width factor $\sigma = 66 \mu\text{m}$ (from the IRAM website²). For the OTF map, the baseline was corrected before conversion from T_A^* to T_{mb} .

Through an inspection of individual scans, the calibration uncertainties were estimated to be better than 20 and 15% for the single-pointing and the OTF observations, respectively. The rms sensitivity for a channel width of 195 kHz is in the range

¹ <http://www.iram.fr/IRAMFR/GILDAS>

² <http://www.iram.es/IRAMES/mainWiki/Iram30mEfficiencies>

Table 4. All detected and non-detected lines for each source for the single-pointing observations.

Molecule	Freq. (GHz)	CSO33	SIMBA-a	MMS5	FIR2 ^(a)	FIR6c ^(b)	FIR1a	MMS9	MMS2	CSO3
CH ₃ OH	84.521	Y	Y	Y	Y	O	Y	Y	Y	Y
	239.746	Y	...	Y	O	O	Y	Y	Y	N
	241.700	Y	...	Y	O	O	Y	Y	Y	Y
	241.767	Y	...	Y	O	O	Y	Y	Y	Y
	241.791	Y	...	Y	O	O	Y	Y	Y	Y
	241.832	N	...	N	O	O	N	N	N	N
	241.833	N	...	N	O	O	N	N	N	N
	241.842	N	...	N	O	O	N	N	N	N
	241.879	Y	...	Y	O	O	Y	Y	Y	Y
	241.887	N	...	Y	N	O	N	N	N	N
	241.904	Y	...	Y	O	O	Y	Y	Y	Y
	241.904	Y	...	Y	O	O	Y	Y	Y	Y
	243.915	Y	...	Y	Y	O	Y	Y	Y	N
	261.805	Y	...	Y	Y	O	Y	Y	Y	Y
CCH	87.284	Y	Y	Y	O	Y	Y	Y	Y	Y
	87.316	Y	Y	Y	O	Y	Y	Y	Y	Y
	87.328	Y	Y	Y	O	Y	Y	Y	Y	Y
	87.402	Y	Y	Y	O	Y	Y	Y	Y	Y
	87.407	Y	Y	Y	O	Y	Y	Y	Y	Y
	87.446	Y	Y	Y	O	Y	Y	Y	Y	Y
	261.978	Y	...	Y	O	Y	Y	Y	Y	Y
	262.004	Y	...	Y	O	Y	Y	Y	Y	Y
	262.006	Y	...	Y	O	Y	Y	Y	Y	Y
	262.064	Y	...	Y	O	Y	Y	Y	Y	Y
	262.067	Y	...	Y	O	Y	Y	Y	Y	Y
	262.078	Y	...	Y	O	Y	Y	Y	Y	Y
	262.208	Y	...	Y	Y	Y	Y	Y	Y	Y
	262.236	N	...	Y	Y	N	N	N	N	N
262.250	Y	...	Y	Y	Y	Y	Y	Y	Y	

Notes. Y stands for detected ($\text{SNR} \geq 3$) and N for non-detected. The symbol “O” indicates that the line is contaminated by the emission of the outflow wing of an adjacent line making the assessment of a detection impossible. ^(a)Source left out of analysis due to prominent outflow features (see Table 2). ^(b)Source left out of analysis due to non-Gaussian shapes in the line profile (see Table 2).

of 9.2–9.6 mK [T_A^*] for single-pointing and is 20 mK [T_A^*] for the OTF map. The spectra of the source SIMBA-a showed emission at the offset position thus contaminating the final spectrum. This source has thus been left out from any further analysis concerning the IRAM-30 m observations.

4.2. Nobeyama-45 m telescope

The observations were carried out between the 10th and the 17th of January 2016. The T70 receiver was used in order to cover the chosen spectral windows from 72 to 76 GHz and from 84 to 88 GHz in the 3mm band. A bank of 16 SAM45 auto-correlators were used with a spectral resolution of 244 kHz. The resulting beam size is 20". For each source, position-switch observations were made. Pointing of the telescope was checked by using Orion KL SiO maser emission (Snyder & Buhl 1974; Wright & Plambeck 1983) every 1.5 h throughout the observations with a pointing accuracy of about 4 arcsec.

After inspection of individual scans, the calibration uncertainties were estimated to be better than 40%. The main-beam temperature (T_{mb}) was derived using the telescope main beam efficiency, which is obtained by comparing the CCH (87.316 GHz) and H₂CO (72.84 GHz) lines observed towards Orion KL, the reference source. We used the software JNewstar³

³ <https://www.nro.nao.ac.jp/~jnewstar/html>

developed by the Nobeyama Radio Observatory to reduce the data. The rms sensitivity acquired for a channel width of 244 kHz is 5 mK [T_A^*].

5. Results

In all three data sets, the two single-pointing observations with IRAM-30 m and Nobeyama-45 m plus the map with IRAM-30 m, we extracted the spectra of the lines in Table 3 and fitted the detected ones with Gaussian functions in order to derive the usual parameters, the velocity-integrated intensity, rest velocity, and line full width at half maximum (FWHM).

5.1. Single-pointing

The intensity threshold set for the line detection is 3σ on the peak intensity of the line for a channel width of $\approx 0.2 \text{ km s}^{-1}$ and of $\approx 0.4 \text{ km s}^{-1}$ for the IRAM-30 m and Nobeyama-45 m data, respectively. A summary of all transitions of CCH and of CH₃OH that have been detected in the source sample is shown in Table 4. Samples of the observed spectra are shown in Fig. 2. The Local Standard Rest velocities V_{lsr} derived are in the range 10.5–11.6 km s^{-1} for both species. We find line widths in the range from 0.8 to 1.6 km s^{-1} for CCH and CH₃OH both at 1 mm and 3 mm, as shown in Fig. 3. Furthermore, when superimposing

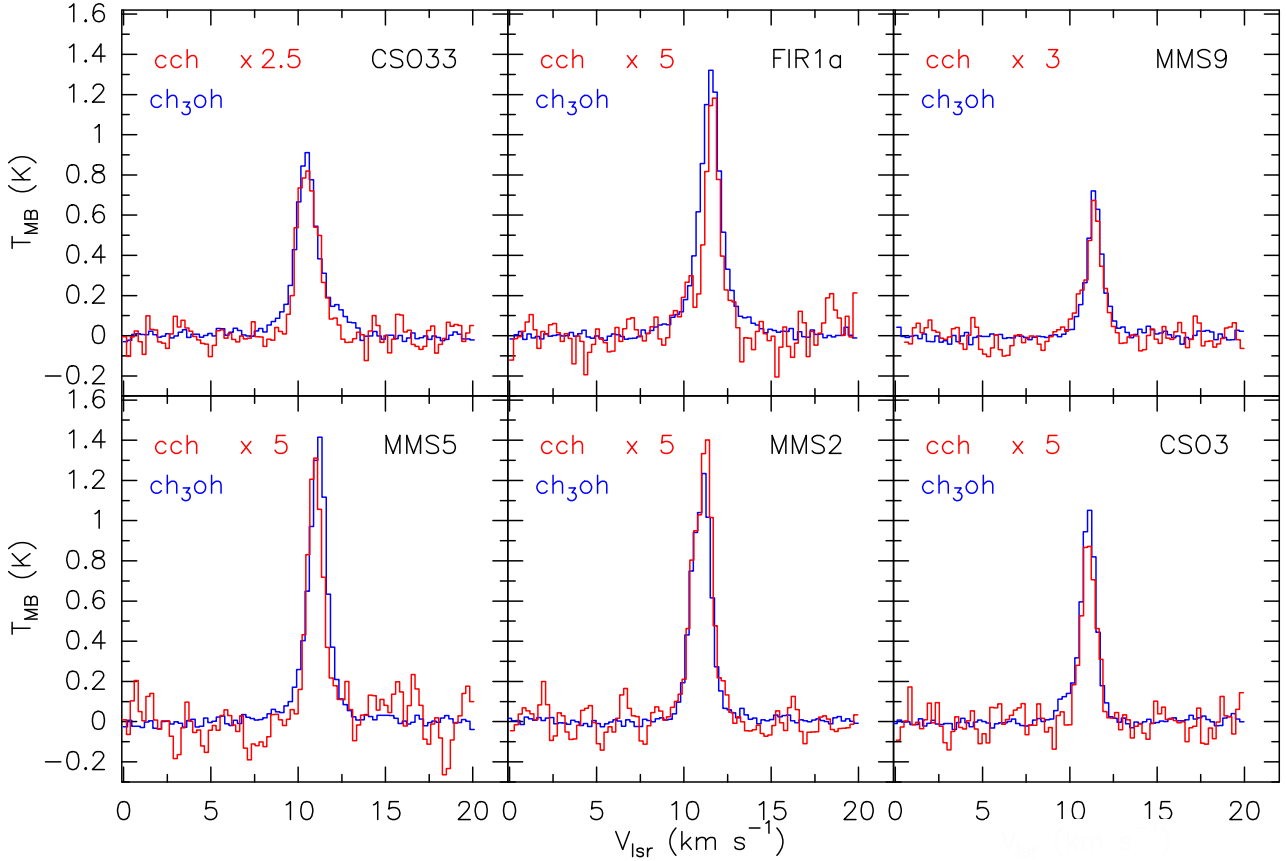


Fig. 2. Spectra of the CCH ($N=3,2$, $J=5/2-3/2$, $F=2-2$; red) and CH_3OH (5_0-4_0 A; blue) lines observed with the IRAM-30 m telescope towards six sources of the sample that show well-constrained line profiles suitable for the analysis (see Sect. 5.1) and for which 1mm data are available (see Table 2). For the purposes of visibility, the spectra of CCH has been increased by various scale factors in order to match the size of the CH_3OH lines.

the most intense⁴ lines of CCH and CH_3OH from the IRAM-30 m data, as shown in Fig. 2, the similarity of the shape of the lines is evident. The detected lines of each species for each source are reported in Appendix A.

In FIR2, high-velocity components suggestive of outflows have been detected around multiple lines. In particular, CH_3OH lines display a prominent high-velocity component that blends with the ambient component at the V_{lsr} of the source. Disentangling the ambient from the high-velocity component of CH_3OH lines with the current data set was thus impossible. Similarly, in FIR6c, important high-velocity emission is present and as a consequence, the lines of CH_3OH have non-Gaussian shapes. We could not isolate the component tracing the ambient envelope. These two sources have been left out from further analysis. The $N=5-4$ transition of CH_3OH for those two sources is shown in Appendix A.

Table 5 presents the statistics results from the Gaussian fits. The fit parameters for each molecule and for each source are presented in Appendix B.1. In most cases, we could fit the lines with a single Gaussian component. The most intense lines of CH_3OH and CCH show a broad ($\sim 4 \text{ km s}^{-1}$) component and could be fitted with two Gaussian curves. However, due to the small number of broad components clearly detected for each source, we do not have enough data to characterise this second component which could be associated with outflowing motions. We will thus

focus on the narrow component ($\leq 2 \text{ km s}^{-1}$) of the lines in what follows.

5.2. Maps

The intensity threshold set for the line detection is 3σ on the peak intensity of the line and for a channel width of $\approx 0.7 \text{ km s}^{-1}$. Figure 4 shows velocity-integrated maps of the CCH ($N=1-0$, $J=3/2-1/2$, $F=1-0$) and of the CH_3OH ($2_{-1}-1_{-1}$ E) lines. The integration has been done in the velocity range of $7.9-12.8 \text{ km s}^{-1}$ for both lines. The sources MMS5, MMS2, and CSO3 are in the field of the mapped region. In Fig. 4, we can see that the two lines peak at the position near the sources MMS2 and CSO3. In addition, CH_3OH shows two other peaks, south and west of the protostars. The emission of CCH is more extended than that of the CH_3OH . For clarity, we will refer to the West peak of methanol as the position “W”. Based on the CH_3OH observations, the peak which is located south of the sources can be explained by the presence of outflows that are driven by MMS5 and MMS2 (also seen in CO by Takahashi et al. 2008). The methanol peak at position “W” does not seem to correspond with any outflow. The reason of this peak is thus unknown and we will not discuss any further its origin as it is not the goal of this paper. All the lines presented in Table 3 have been detected. For CCH, the most intense line at 87.316 GHz is detected in 99% of the map. The next two most intense lines (87.328 and 87.402 GHz) are detected in 90% of the map. The line at 87.407 GHz is detected in 85% of the map. Finally, the

⁴ The most intense lines of CCH being blended, we chose the next intense one.

Table 5. Mean derived properties from Gaussian fits for each source and for each set of observations.

Source	IRAM		Nobeyama		IRAM		Nobeyama	
	$V_{\text{lsr CH}_3\text{OH}}$ [km s ⁻¹]	$V_{\text{lsr CCH}}$ [km s ⁻¹]	$V_{\text{lsr CH}_3\text{OH}}$ [km s ⁻¹]	$V_{\text{lsr CCH}}$ [km s ⁻¹]	$FWHM_{\text{CH}_3\text{OH}}$ [km s ⁻¹]	$FWHM_{\text{CCH}}$ [km s ⁻¹]	$FWHM_{\text{CH}_3\text{OH}}$ [km s ⁻¹]	$FWHM_{\text{CCH}}$ [km s ⁻¹]
CSO33	10.5 ± 0.1	10.5 ± 0.1	10.7 ± 0.2	10.6 ± 0.2	1.6 ± 0.2	1.4 ± 0.1	1.4 ± 0.2	1.3 ± 0.2
FIR1a	11.6 ± 0.1	11.6 ± 0.1	11.3 ± 0.2	11.3 ± 0.2	1.2 ± 0.1	1.0 ± 0.1	1.4 ± 0.2	1.2 ± 0.2
MMS9	11.4 ± 0.1	11.4 ± 0.1	11.5 ± 0.2	11.6 ± 0.2	1.0 ± 0.1	0.8 ± 0.1	1.3 ± 0.2	1.0 ± 0.2
MMS5	11.1 ± 0.1	11.0 ± 0.1	11.4 ± 0.2	11.2 ± 0.2	1.2 ± 0.1	1.0 ± 0.1	1.1 ± 0.2	1.0 ± 0.2
MMS2	11.1 ± 0.1	11.2 ± 0.1	11.1 ± 0.2	10.8 ± 0.2	1.2 ± 0.1	1.4 ± 0.1	1.2 ± 0.2	1.6 ± 0.2
CSO3	11.1 ± 0.1	11.1 ± 0.1	11.2 ± 0.2	10.9 ± 0.2	0.8 ± 0.1	0.9 ± 0.1	1.0 ± 0.2	1.0 ± 0.2
SIMBA-a	10.5 ± 0.2	10.5 ± 0.2	0.9 ± 0.2	1.1 ± 0.2

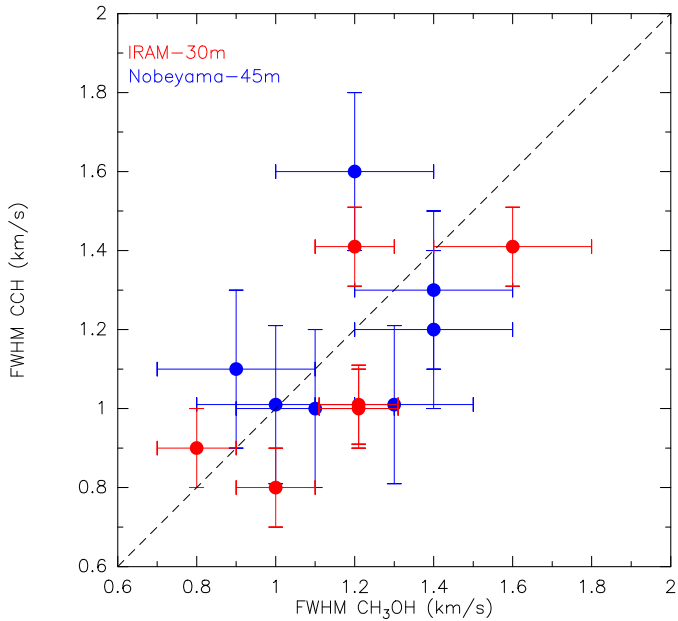


Fig. 3. Average widths (FWHM) of the CCH (y-axis) and CH₃OH (x-axis) lines observed in each source of Table 2, using the IRAM-30 m (red) and the Nobeyama-45 m (blue), respectively. The errors are 1 σ of the average values. This shows that the two molecules are emitted in a similar and quiescent region (Sect. 5.1). We note that only six sources are reported for the IRAM-30 m observations and seven for the Nobeyama-45 m: this is because the sources FIR6c and FIR2 have been left out from the analysis in both set of observations, the lines being blended with outflows (see Table 2). The source SIMBA-a is contaminated by the wobbler off position only in the IRAM-30 m data set. We could thus perform the analysis with Nobeyama-45 m (see Table 2).

two least intense lines (87.284 and 87.446 GHz) are detected in 58% of the map. For CH₃OH, the most intense lines (96.741 and 96.739 GHz) are present on 65% of the map on average. Then the lines at 84.521 and 96.445 GHz are present on 30% of the map. Finally, the least intense line at 96.755 GHz is present on 6% of the map and its emission is concentrated at the methanol peak at position “W”.

Moments 1 and 2 for those same lines are shown in Fig. B.1. From the moment maps, we see that the velocities are rather constant throughout the map with a low-velocity region at the location of the second peak of CH₃OH. The line widths of CH₃OH are slightly larger (1.5 km s⁻¹ instead of 1 km s⁻¹ in the rest of the filament) where the methanol peaks, south-east of the sources. Considering that the sources MMS5 and MMS2

drive outflows, this may be the reason of this slight increase. For CCH, the line width is on average 1 to 1.5 km s⁻¹ towards the centre and gets larger (>2.0 km s⁻¹) to the North West. From the line shapes, we find that the CCH is double peaked in the north of the region, explaining the increase of the line width. A further analysis of the line shape shows that there is a second component located at a rest velocities at 10 km s⁻¹ in the North west of the filament and 9 km s⁻¹ where there is the CH₃OH peak. This specific line shape is only seen in the CCH and not in the CH₃OH lines suggesting an even more external component with mainly CCH in the north of the filament. This could be explained by the fact that CCH is more enhanced by the UV photons than CH₃OH. This CCH component would thus probe the outer layers of the cloud, an area that is more exposed to the interstellar field. In the following, we will consider only the component of CCH that is common with the CH₃OH, as the second component of CCH does not coincide with the position of the sources and as our goal is solely to place constraints on the region of emission in which both CCH and CH₃OH are present.

6. Physical parameters and [CCH]/[CH₃OH] abundance ratios

6.1. Description of the modelling

We used two methods to derive the physical parameters of the emitting gas and the [CCH]/[CH₃OH] abundance ratios. We first used an approach based on the local thermal equilibrium (LTE) approximation (as a consistency check) and then we carried out a non-LTE analysis.

In the LTE approach, we used the usual rotational diagram for the CH₃OH lines and the fitting of the hyperfine structure for the CCH lines. Both methods allow us to derive the rotational or excitation temperature and the beam-averaged column density, assuming that the emission is extended, as shown by the maps (Sect. 5). In addition, the rotational diagram approach assumes that the lines are optically thin, an assumption which we verified a posteriori to be correct (see below).

For the non-LTE analysis, we used the large velocity gradient (LVG) model developed by Ceccarelli et al. (2003). For CH₃OH, we used the CH₃OH-H₂ collisional rates from Flower et al. (2010) through the BASECOL database⁵ (Dubernet et al. 2013). Please note that for the LVG analysis, we used the CH₃OH-E species and assumed a ratio CH₃OH-E/CH₃OH-A equal to 1 to retrieve the total column density of CH₃OH and thus calculate the abundance ratio [CCH]/[CH₃OH]. For CCH, we used

⁵ <https://basecol.vamdc.eu>

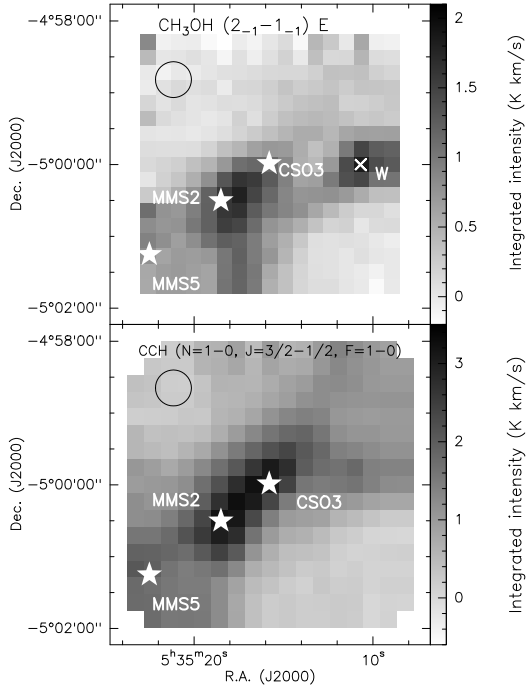


Fig. 4. Map of $\text{CH}_3\text{OH}(2_{-1-1-1})\text{E}$ and $\text{CCH}(N=1-0, J=3/2-1/2, F=1-0)$ lines, integrated between 7.9 and 12.8 km s^{-1} . The stars represents the sources MMS5, MMS2 and CSO3. The West peak of methanol is represented by a white cross. The filled circle represent the IRAM-30 m beam size of $30''$.

the CCH-H_2 collisional rates, from [Dagdigian \(2018\)](#). For each source, we ran large grids of models varying the model parameters: the $\text{CH}_3\text{OH-E}$ and CCH column density, $N_{\text{CH}_3\text{OH-E}}$ and N_{CCH} , from 5×10^{11} to $1 \times 10^{17}\text{ cm}^{-2}$ the kinetic temperature, T_{kin} , from 2 to 200 K; the gas density, $n(\text{H}_2)$, from 5×10^3 to $1 \times 10^{10}\text{ cm}^{-3}$. Those ranges of parameters have been chosen according to the values typically found in molecular cores, PDRs, and protostellar envelopes, as we expect the emission to come from those types of environments. The source size was fixed and set as extended. We ran beforehand the LVG model for the source MMS2, present in the OTF map, with the source size set as a free parameter. The result gave a source size significantly larger than the beam size ($\geq 150''$), confirming the extended characteristic of the source. We thus fixed the source size as extended (the filling factor is thus equal to 1) for the LVG analysis. Finally, the line width was taken equal to the measured FWHM for each source (Table 5).

In the following, we present the non-LTE analysis results of both the single pointing observations towards six out of the nine target sources (Table 2) and the map of the northern cloud (Fig. 4). The results of the LTE analysis for both single pointing observations and for the OTF map are presented in Appendix C.

6.2. Physical parameters and abundance ratio towards the sources

We analysed the line emission towards six out of the nine sources of Table 2. In SIMBA-a, the number of detected lines is too small to obtain meaningful results, while in FIR2 and FIR6c, the line emission is dominated by the outflow.

For each source, the best fit values were found by comparing the LVG model predictions with the observations as follows: for each column density, the minimum χ^2 was found with respect

to the density-temperature parameter space, and then the best fit values of density and temperature were derived. The error on each fitted parameter was defined by the 1σ distribution. The results of the analysis are summarised in Table 6 and the density-temperature χ^2 contour plots obtained for each source are shown in Figs. 5 and 6 (source CSO33).

The following results are immediately evident, when one excludes CSO33, the source of the sample closest to the Trapezium OB stars cluster:

1. All sources have similar gas density and temperature.
2. While the density and temperature of the gas emitting the methanol lines are well constrained, the density and temperature values are degenerate for the gas emitting CCH. This is because the CCH lines cover a relatively smaller transition upper level energy range with respect to the methanol lines.
3. The gas emitting methanol and CCH do not have the same density and temperature. Either CCH originates in a less dense or a colder gas, or both, than the gas emitting methanol. The case of MMS9 would suggest that CCH is emitted in a colder gas than methanol.
4. The gas emitting methanol lines has a temperature that is relatively similar, between 12 and 30 K (considering the errors), and a density also rather similar among the different sources, $(1-3) \times 10^6\text{ cm}^{-3}$. These low temperatures are incompatible with the hypothesis that methanol lines originate in a hot corino like region, as we will discuss in more detail in Sect. 7.
5. In the same vein, the relatively low temperatures, $\leq 30\text{ K}$, of the gas emitting CCH are compatible with an origin from the cold envelopes of the sources or their parental molecular cloud.
6. What is particularly relevant to the goal of this work is that the $[\text{CCH}]/[\text{CH}_3\text{OH}]$ abundance ratio is similar in all sources, within the errors, and equal to about 6 (with a range from 1.5 to 13.5 considering the errors).

6.3. Temperature and density of the extended gas

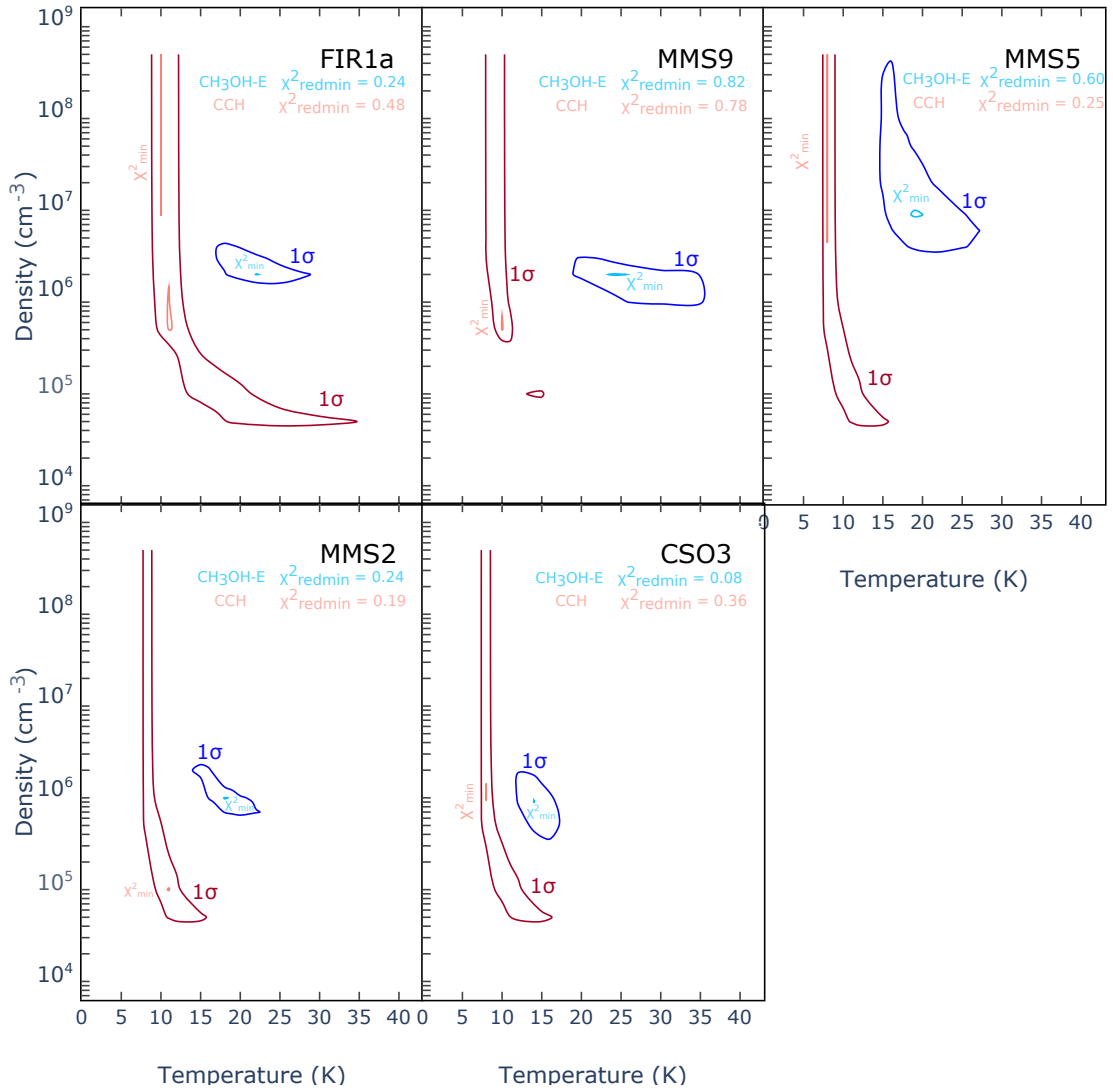
We also ran the LVG model for the map. However, considering that for CCH we have only the $N=1-0$ transition, it was not possible to do an LVG analysis with this species. For $\text{CH}_3\text{OH-E}$, we took into account positions with at least three lines to perform the LVG analysis. As for the single-pointing, the gas temperature and gas density derived for each position are based on the best fit for the column density.

The results of the LVG analysis of $\text{CH}_3\text{OH-E}$ are shown in Fig. 7. Within the error bars (about 5–10 K), the temperature of the gas emitting the methanol is rather constant across the cloud, around 15–20 K, with a slightly lower temperature, between 12–10 K, at the border of the cloud. Again within the error bars (a factor two), the H_2 density is also relatively constant across the cloud, with the bulk of the emission originating from a gas at density $(5-9) \times 10^6\text{ cm}^{-3}$ and possibly a slightly less dense halo surrounding it. We verified the non-variation of the properties of the CH_3OH emitting gas throughout the filament by deriving the intensity ratio of two optically thin lines of methanol (see Appendix B.2). When considering the error bars, both the temperature and the density are very similar to those derived towards the three sources in the field: CSO3, MMS2, and MMS5. In other words, there is no clear evidence that the detected methanol emission originates in the three sources rather than in the parent cloud gas belonging to the cloud.

Finally, also the methanol column density is, within a factor of 3, constant across the cloud and no obvious increase is seen

Table 6. Kinetic temperature (T_{kin}), total column densities (N_{tot}) and abundance ratio $[\text{CCH}]/[\text{CH}_3\text{OH}]$ derived from $\text{CH}_3\text{OH-E}$ and CCH.

Source	$T_{\text{kin}}(\text{CH}_3\text{OH})$ [K]	$N_{\text{CH}_3\text{OH-E}}$ [$\times 10^{13} \text{ cm}^{-2}$]	$n(\text{H}_2)$ [$\times 10^6 \text{ cm}^{-3}$]	$T_{\text{kin}}(\text{CCH})$ [K]	N_{CCH} [$\times 10^{14} \text{ cm}^{-2}$]	$n(\text{H}_2)$ [$\times 10^4 \text{ cm}^{-3}$]	$[\text{CCH}]/[\text{CH}_3\text{OH}]$
CSO33	70^{+40}_{-28}	$2^{+3}_{-0.5}$	5^{+7}_{-2}	15^{+105}_{-4}	$3^{+1}_{-1.5}$	>5	7.5^{+6}_{-4}
FIR1a	22^{+6}_{-6}	3^{+1}_{-1}	$2^{+2}_{-0.5}$	11^{+24}_{-2}	2^{+1}_{-1}	>4	3.5^{+2}_{-2}
MMS9	24^{+11}_{-6}	$1.5^{+0.5}_{-0.5}$	2^{+1}_{-1}	10^{+5}_{-2}	2^{+1}_{-1}	>8	$6.5^{+3.5}_{-3.5}$
MMS5	19^{+9}_{-5}	$3^{+1.5}_{-1}$	9^{+400}_{-6}	8^{+8}_{-1}	4^{+3}_{-2}	>4	$6.5^{+5}_{-3.5}$
MMS2	19^{+4}_{-4}	$4^{+2}_{-1.5}$	$1^{+1.5}_{-0.3}$	11^{+5}_{-3}	$6^{+4}_{-3.5}$	>4	7.5^{+5}_{-3}
CSO3	14^{+3}_{-2}	$3^{+1.5}_{-1}$	$1^{+1}_{-0.6}$	8^{+8}_{-1}	$3^{+2.5}_{-1.5}$	>4	5^{+4}_{-3}


Fig. 5. Density versus temperature contour plot for all the sources except CSO33 (see Fig. 6). The minimum χ^2 and the 1σ contour plot are obtained for a minimum value of the χ^2 in the column density parameter. The values of the reduced χ^2_{redmin} are quoted in the upper corner of each panel.

in correspondence with CSO3, and only by a factor of 5 towards MMS2 and MMS5 (which lies at the border of the map, so the result has to be taken with caution).

6.4. $[\text{CCH}]/[\text{CH}_3\text{OH}]$ abundance ratio across the northern cloud

As we stated in the previous section, in the map of the northern cloud, we could not derive the $[\text{CCH}]/[\text{CH}_3\text{OH}]$ abundance

ratio via a non-LTE analysis because of the limited number of CCH lines observed. We therefore used the LTE approach for deriving the CCH and methanol column density in each pixel, which is sampled every half beam. In order to derive the abundance ratio, we assume that CCH and CH_3OH are emitted in the same region. In total, 81 positions throughout the map were extracted and analysed. Of those, we took into account positions with at least three lines for both CCH and CH_3OH . For CCH we used the hyperfine line structure whereas for CH_3OH we used the

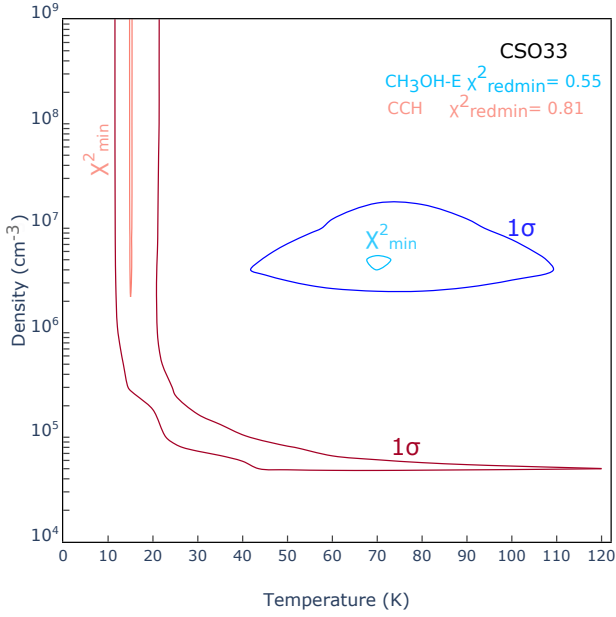


Fig. 6. Density versus temperature contour plot for the source CSO33. The source CSO33 represents an extreme case, with the largest temperature of the analysed sample. This is probably because CSO33 is the closest to the Trapezium OB stars cluster. The minimum χ^2 and the 1σ contour plot are obtained for a minimum value of the χ^2 in the column density parameter. The values of the reduced χ^2_{redmin} are quoted in the upper corner of the panel.

rotational diagram method, as described in Sect. 6.1. The results of the LTE analysis are reported in Table C.3.

The derived total column densities are in the range $(2\text{--}11) \times 10^{14} \text{ cm}^{-2}$ for CCH and in the range $(2\text{--}16) \times 10^{13} \text{ cm}^{-2}$ for CH_3OH , which is in quite good agreement with the values derived by the non-LTE analysis. The map of the $[\text{CCH}]/[\text{CH}_3\text{OH}]$ abundance ratio is shown in Fig. 8. It shows an overall gradient from north to south, with the northern part of the cloud more enriched in CCH with respect to CH_3OH than the southern part. On the other hand, we do not see any significant variation of the abundance ratio in correspondence of the positions of the protostars in the field. In other words, the $[\text{CCH}]/[\text{CH}_3\text{OH}]$ abundance ratio is more associated with the parent cloud gas in the cloud than with the protostars themselves.

7. Discussion

7.1. The ambiguous origin of the CCH and CH_3OH line emission towards the targeted sources

The first goal of this work is to identify the nature of the surveyed sources, whether they are hot corinos or WCCC objects (Sect. 1). As done in previous surveys (Sect. 2), we observed several CCH and CH_3OH lines in order to derive their relative abundance ratio and, consequently, to assess the sources chemical nature: it is a hot corino if $[\text{CCH}]/[\text{CH}_3\text{OH}]$ is less than about 0.5 and WCCC object if larger than about 2. Based on this definition and the derived $[\text{CCH}]/[\text{CH}_3\text{OH}]$ abundance ratios (~ 6 ; Table 6), we could argue that all the sources in OMC-2/3 are WCCC objects. However, before taking this conclusion as final, we have to be sure that the emission towards the sources is due to the sources themselves and that it is not polluted, nor dominated, by the emission from the cloud to which the sources belong – which is the second goal of this study. We therefore start the discussion on this point first.

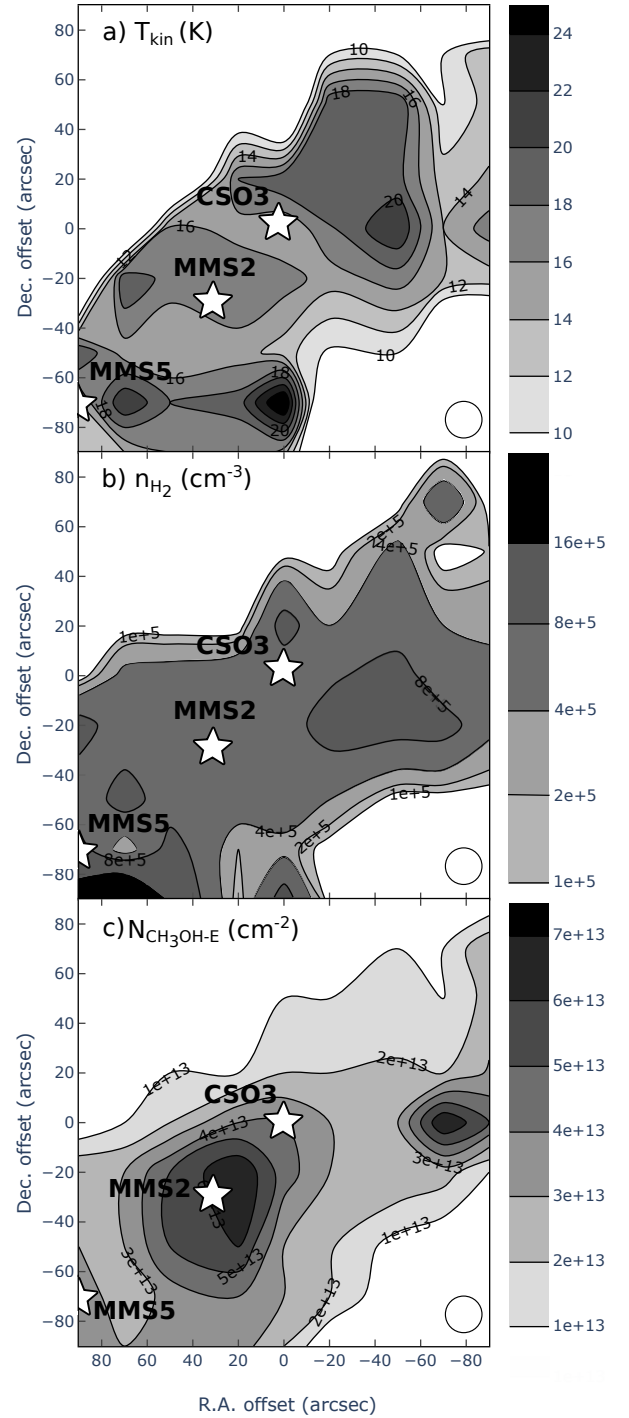


Fig. 7. Map of the $\text{CH}_3\text{OH-E}$ column density (*bottom panel*), temperature (*top panel*), and density (*central panel*) of the gas emitting the methanol lines in the northern cloud, which is shown in Fig. 1, as derived by the non-LTE analysis described in Sect. 6.4. The size of the beam ($30''$) is shown by a white filled circle at the bottom right of each map, the position of the protostars are represented by white stars. We note that the average error bar in the derived temperature is 5–10 K; in the density, it is a factor of two and in the $\text{CH}_3\text{OH-E}$ column density, it is $3 \times 10^{13} \text{ cm}^{-2}$.

We begin by summarising the results of our analysis of the observations towards the sources:

1. The CCH and CH_3OH line widths are narrow ($0.8\text{--}1.6 \text{ km s}^{-1}$; Fig. 2) and their spectral shapes (Fig. 3) are very similar between them and among the sources: this first result

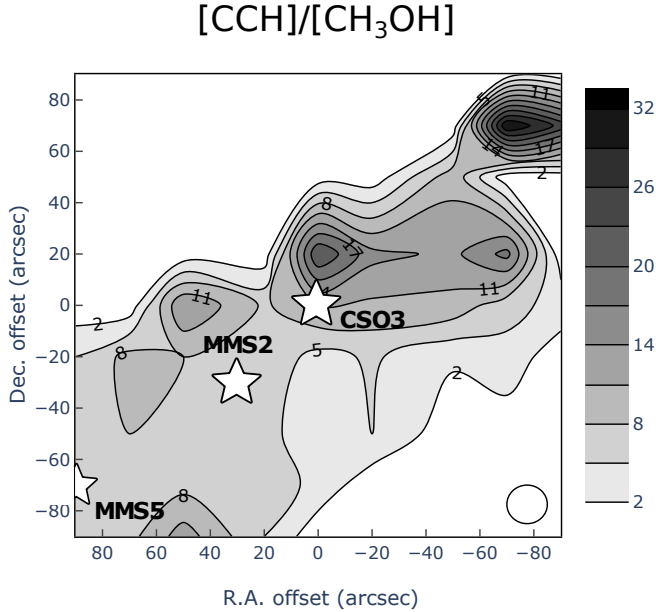


Fig. 8. Map of the $[\text{CCH}]/[\text{CH}_3\text{OH}]$ abundance ratio as derived via the LTE analysis described in Sect. 6.4. The sources MMS5, MMS2, and CSO3 are represented by white stars. The beam size is the white circle at the bottom right of the figure. We note that the error bar in the derived $[\text{CCH}]/[\text{CH}_3\text{OH}]$ abundance ratio is about 4 (see Table C.3 of Appendix C).

suggests that the lines are emitted approximately in the same region and that this region is rather quiescent.

2. The temperature of the gas emitting methanol is always lower than 30 K (with the exception of CSO3; see text above: Fig. 5 and Table 6), which certainly does not support the hypothesis of an origin in the sources' hot corino. However, the methanol could be associated with the cold envelope of the sources (e.g. Maret et al. 2005; Vastel et al. 2014) or the parental cloud.
3. The CCH and CH_3OH lines probe a gas at likely different temperatures: The CCH lines trace a gas at about 10 K while CH_3OH traces a slightly warmer gas, at about 20 K (Table 6). This could be consistent with the emission arising from the two molecules in the source envelopes, where methanol originates slightly deeper in the envelope (larger density and higher temperature) than CCH. However, the uncertainty on the CCH density-temperature values (Figs. 5 and 6) also makes it possible that the two molecules lie in the cloud and, specifically, in its surrounding (chemically stratified) PDR.
4. The CCH and CH_3OH -E derived column densities are rather similar among the sources: either the envelopes have all the same characteristics or the emission is associated with the cloud or its PDR.
5. To give an idea of the behaviour of the targeted sources over the full OMC-2/3 filament, in Fig. 9 we show the gas temperature and density, CCH and CH_3OH -E column densities, and the $[\text{CCH}]/[\text{CH}_3\text{OH}]$ abundance ratio derived towards each source from the non-LTE analysis as a function of the source projected distance from the Trapezium OB cluster. We do not see any variation of any of those quantities along the filament. The only exception is CSO33, which stands out from the other sources as it has a larger gas temperature; however, the difference is not significant and it is probably due to the fact that this source is the closest to the Trapezium

OB cluster. This uniformity of the various derived quantities towards the sources regardless of their position in the filament favours the hypothesis that the emission is dominated by the cloud and/or PDR rather than the sources' envelopes.

In summary, based on the single-dish observations, we conclude that the CCH and CH_3OH lines are either associated with the cold envelopes of the sources or the cloud to which they belong to or the PDR encircling the cloud, with hints that the first hypothesis for the source envelope origin is likely to be incorrect.

7.2. The emission from the cloud and its surrounding PDR

The analysis of the CCH and CH_3OH line maps of the northern portion of OMC-3/3 filament (Sect. 6.4) allow us to disentangle the ambiguity described above. We start by summarising the results from the OTF map observations analysis.

1. The maps of the gas temperature and density, derived by our non-LTE analysis of the CH_3OH -E lines and shown in Fig. 7, clearly indicate that there is no increase (or decrease) of these physical parameters in coincidence with the three sources in the field. The density map shows a sharp increase of the cloud density at its borders and then a ridge with a rather constant density at $(4\text{--}8) \times 10^5 \text{ cm}^{-3}$. The temperature map also shows a sharp increase at the cloud border and then a rather constant value, 14–16 K, across the ridge.
2. The CH_3OH -E column density shows a gradient which, however, seems associated, rather, with the penetration into the cloud rather than with the sources themselves (Fig. 7): the CH_3OH -E column density increases going inwards the central regions of the filament, the ones more shielded by the external photons illumination. There is a marginal increase of the CH_3OH -E column density in correspondence of MMS2, from 2×10^{13} to $6 \times 10^{13} \text{ cm}^{-2}$, namely, about a factor of three with respect to the value in the ridge.
3. The map of the $[\text{CCH}]/[\text{CH}_3\text{OH}]$ abundance ratio (Fig. 8) does not show any variation caused by the presence of the sources: the $[\text{CCH}]/[\text{CH}_3\text{OH}]$ abundance ratio is relatively constant across the region with a possible gradient in the north-east to south-west direction, which could be due to the UV illumination from the nearby HII region NGC 1977 (located at $\leq 10''$ from CSO3, so $\leq 2 \text{ pc}$), located to the north-east of the map.

When considering the map observations and the derived values (gas temperature and density, CCH and CH_3OH -E column densities, and the $[\text{CCH}]/[\text{CH}_3\text{OH}]$ abundance ratio) of all the sources along the filament OMC-2/3 (Fig. 9), it seems inevitable to conclude that the observed CCH and CH_3OH line emission is dominated by the cloud in which the sources are embedded or the PDR that surrounds it.

7.3. What does the $[\text{CCH}]/[\text{CH}_3\text{OH}]$ abundance ratio probes? - WCCC objects, hot corinos, molecular clouds, or PDRs

Figure 10 reports a compilation of the CCH and CH_3OH total column densities observed towards WCCC objects, hot corinos, molecular clouds, and PDRs, all derived with single-dish telescopes observations. We label as a “molecular cloud” every object where we think the emission CCH and CH_3OH is dominated by the non-PDR, such as pre-stellar cores, even though we know it might be not completely true. Nonetheless, they give an indication how a possible emission from the bulk or parts not illuminated by the UV would position the object on the diagram.

The figure immediately shows that the sources in OMC-2/3 have CCH and CH_3OH total column densities similar to those of

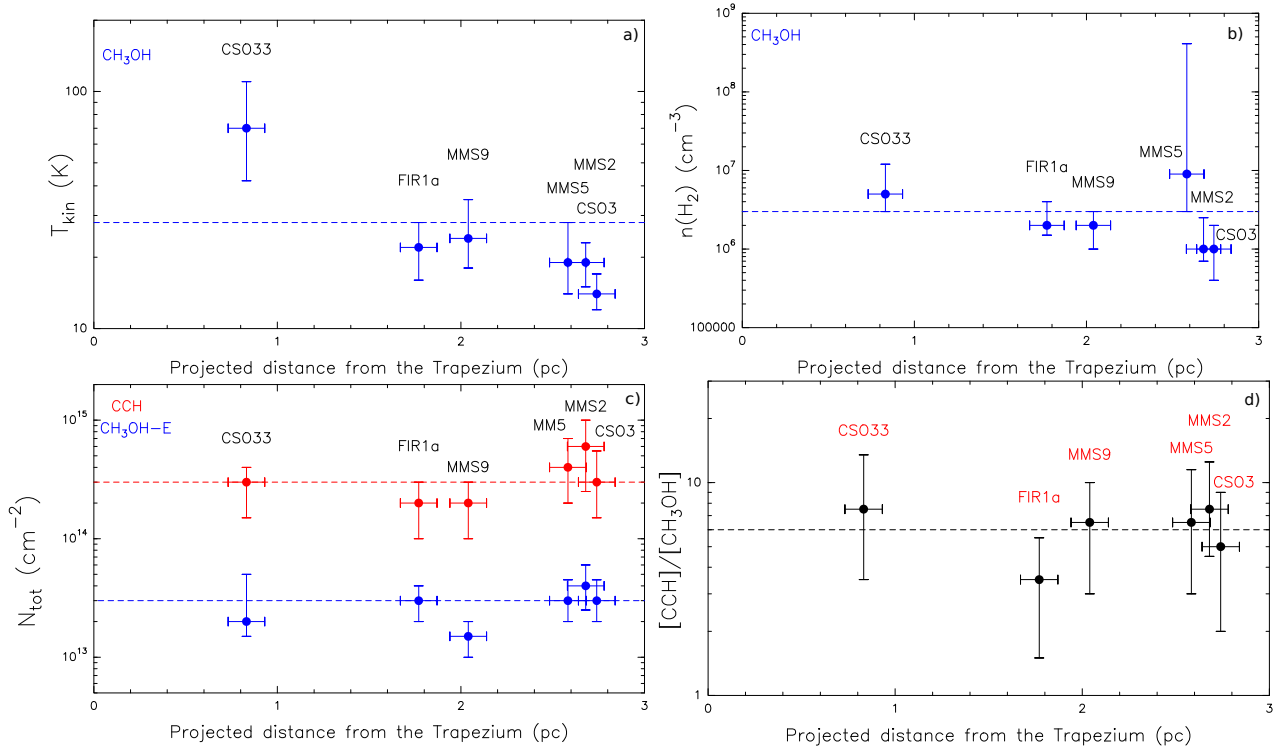


Fig. 9. Results of the LVG analysis for each source. (a) kinetic temperatures (T_{kin}) of CH_3OH as a function of the distance to the Trapezium; (b) column densities (N_{tot}) of CCH and of $\text{CH}_3\text{OH-E}$ as a function of the distance to the Trapezium; (c) derived gas density (n_{H_2}) for CH_3OH and CCH; (d) abundance ratio $[\text{CCH}]/[\text{CH}_3\text{OH-E}]$ as a function of the distance to the Trapezium. The red- and blue- dashed lines are the derived averaged values for each parameter for CCH and $\text{CH}_3\text{OH-E}$ respectively. The error bars are at 1σ .

Table 7. Comparison of the results derived from the LTE analysis of the Higuchi et al. (2018) survey with the results derived in the present work (both LTE and non-LTE LVG results).

Paper	T_{CCH} [K]	N_{CCH} [$\times 10^{13} \text{cm}^{-2}$]	$T_{\text{CH}_3\text{OH}}$ [K]	$N_{\text{CH}_3\text{OH-E}}$ [$\times 10^{14} \text{cm}^{-2}$]	$[\text{CCH}]/[\text{CH}_3\text{OH}]$
Higuchi et al. (2018)	8–21	0.5–16	8–21	<5.2	0.04–3.9
This work, LTE	5–17	60–110	10–17	0.1–0.7	14–50
This work, LVG	8–15	20–60	14–70	0.2–0.4	3.5–7.5

the WCCC prototype L1527 and the PDRs. Since we demonstrated in Sects. 7.1 and 7.2 that the CCH and CH_3OH line emission is dominated by the extended emission rather than the source envelopes; this similarity leads us to conclude that in the specific case of OMC-2/3, the emission is in fact dominated by the PDR encircling the molecular cloud. This is fully consistent with the fact that the OMC-2/3 filament is surrounded by luminous OB stars, the Trapezium cluster and NGC 1799 HII region, namely exposed to an intense UV illumination.

On the other hand, the CCH and CH_3OH total column densities observed towards the sources in Perseus surveyed by Higuchi et al. (2018) are definitively different from those of the PDRs, perhaps close to those in molecular clouds, and in between the PDRs and the IRAS 16293-2224 hot corino. Given the observed (rotational) temperatures measured towards the Perseus sources by Higuchi et al. (2018), similar to those measured in our OMC-2/3 sample (see Table 7), it remains to be verified whether the emission is not polluted or dominated by the surrounding cloud emission. In Table 7, we note that the small difference observed in the derived column densities of CCH with the two different

methods can be due to the sensitivity of the input parameters of the Hyperfine fitting structure Tool used for the LTE analysis (see Appendix C.1.2). Moreover, four of the Perseus sources, namely, SVS 13A, IRAS 2A, IRAS 4A and IRAS 4B, are confirmed hot corinos by interferometric observations (Bottinelli et al. 2004, 2007; Jørgensen et al. 2005; Sakai et al. 2006; Taquet et al. 2015; De Simone et al. 2017; López-Sepulcre et al. 2017). In Fig. 10, these sources are scattered from the hot corino prototype and their hot corino nature is not always obvious (e.g. SVS 13A, IRAS 2A) if we refer to this plot only.

Finally, a similar word of caution may apply to the surveys by Graninger et al. (2016) and Lindberg et al. (2016), given, again, the measured low (rotational) temperatures (Table 1). Besides, the methanol column densities in their sources are lower than $\sim 10^{13} \text{cm}^{-2}$, namely less than for the Perseus sources (see Fig. 10), which would suggest, again emission from dense cold cloud gas.

In conclusion, our results strongly suggest that the $[\text{CCH}]/[\text{CH}_3\text{OH}]$ abundance ratio derived by single-dish observations is not reliable enough to trace the envelope of the protostars.

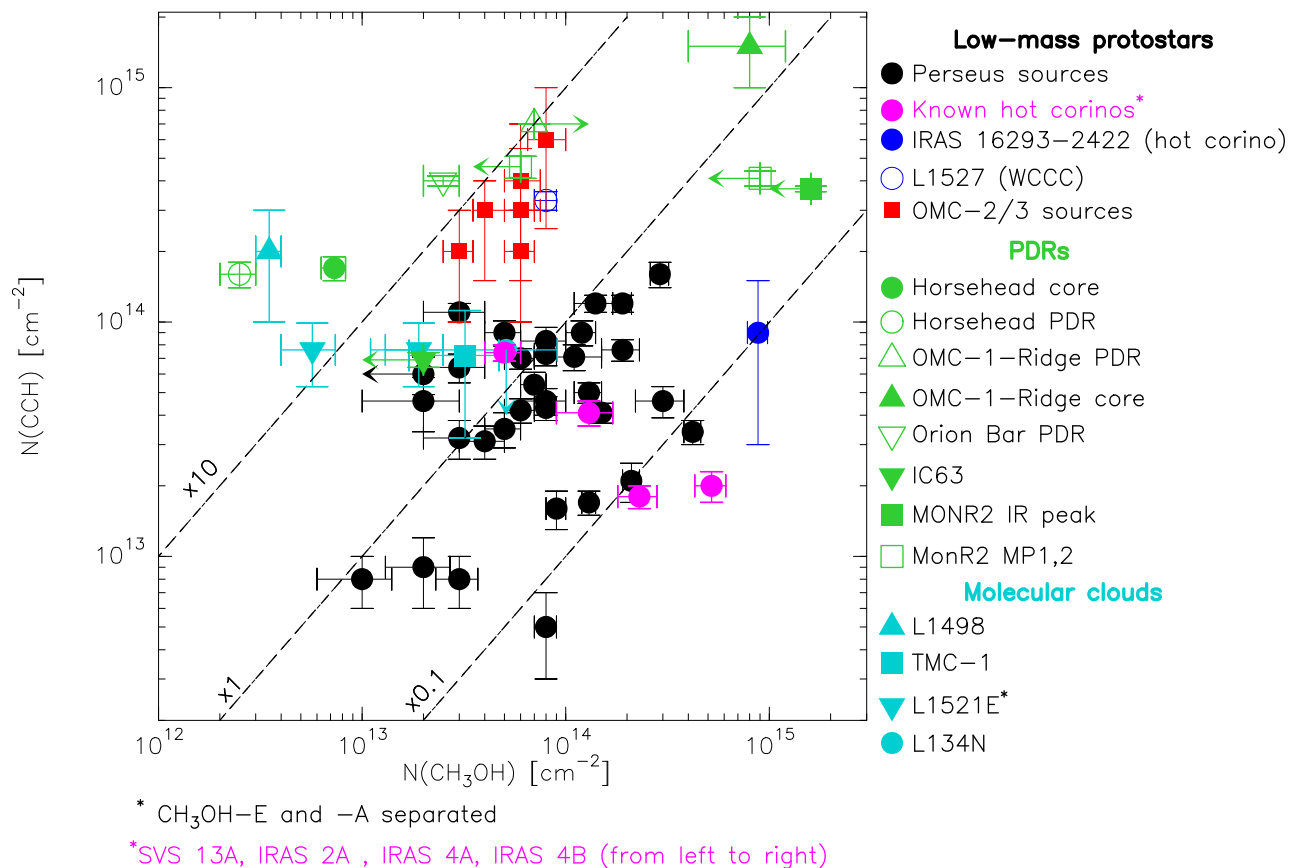


Fig. 10. Compilation of the CCH (y-axis) and CH₃OH (x-axis) total column densities, derived with single-dish observations towards WCCC objects, hot corinos, molecular clouds, and PDRs. The points refer to measurement towards: the WCCC object prototype L1527 (blue open circle: Sakai et al. 2008); the hot corino prototype IRAS 16293-2422 (filled blue circle: Van Dishoeck et al. 1995); the sources in the Perseus cloud (black: Higuchi et al. 2018); the known hot corinos among the Perseus sources (filled pink circle: Higuchi et al. 2018), the sources in OMC-2/3 (red: this work); various PDRs (green): Horsehead nebula (Teyssier et al. 2004; Guzmán et al. 2013), OMC-1 Ridge PDR and core (Ungerechts et al. 1997), Orion Bar (Cuadrado et al. 2015, 2017), IC63 (Jansen et al. 1994; Teyssier et al. 2004), and Mon R2 (Ginard et al. 2012); various pre-stellar cores (light blue): L1498 (Padovani et al. 2009, Daprà et al. 2017), TMC-1 (Friberg et al. 1988, Pratap et al. 1997, Soma et al. 2015), L1521E (Nagy et al. 2019) and L134N (Dickens et al. 2000) as representatives of cold molecular clouds. Upper limits are represented by arrows.

Since several WCCC objects and hot corinos have been classified solely based on single-dish observations of small carbon chains and CH₃OH (see Sect. 2), we suggest those classifications be verified by better spatial resolution or higher excitation lines observations that would be capable of focusing on the inner protostellar envelopes and getting rid of the extended emission from the cloud and the PDR necessarily associated with the targeted sources.

8. Conclusions

We carried out CCH and CH₃OH observations with the single-dish IRAM-30 m and the Nobeyama-45 m telescopes of nine Solar-like protostars located in the OMC-2/3 filament in order to determine their chemical nature. Here are our main conclusions:

1. The derived gas temperatures and gas densities of CCH and CH₃OH towards the six sources out of the nine sources and the results from the map observations indicates that the two species are emitted from an external layer not associated with the protostars.
2. The column density ratios [CCH]/[CH₃OH], from 1.5 to 13.5 within the error bars, derived for our source sample specify that this external layer is likely the PDR.
3. We could not achieve the first goal of our study that is finding hot corino or WCCC candidates in the OMC-2/3

filament. The abundance ratio used is not reliable for single-dish observations. We thus need to choose other tracers for single-dish observations or to employ interferometric observations to avoid contamination from the cloud and/or the associated PDR.

Acknowledgements. We thank the referee for the careful reading and the constructive remarks that helped to improve the paper. This project has received funding from the European Research Council (ERC) under the European Union’s Horizon 2020 research and innovation programme, for the Project “The Dawn of Organic Chemistry” (DOC), grant agreement No 741002 and from the European Union’s Horizon 2020 research and innovation programme under the Marie Skłodowska-Curie grant agreement No 811312. This work is based on observations carried out under the project numbers D01-18 and p279673 with the IRAM-30 m telescope and based on observations carried out with the Nobeyama-45 m. IRAM is supported by INSU/CNRS (France), MPG (Germany) and IGN (Spain). The Nobeyama 45-m radio telescope is operated by Nobeyama Radio Observatory, a branch of National Astronomical Observatory of Japan.

References

- Adams, F. C. 2010, *ARA&A*, 48, 47
- Agúndez, M., Marcelino, N., Cernicharo, J., Roueff, E., & Tafalla, M. 2019, *A&A*, 625, A147
- Anglada, G. 1995, *Rev. Mex. Astron. Astrofis.*, 1, 67
- Anglada, G. 1996, *ASP Conf. Ser.* 93, 3
- Bianchi, E., Codella, C., Ceccarelli, C., et al. 2019, *MNRAS*, 483, 1850
- Bottinelli, S., Ceccarelli, C., Lefloch, B., et al. 2004, *ApJ*, 615, 354

- Bottinelli, S., Ceccarelli, C., Williams, J. P., & Lefloch, B. 2007, *A&A*, **463**, 601
- Caux, E., Kahane, C., Castets, A., et al. 2011, *A&A*, **532**, A23
- Cazaux, S., Caux, E., Parise, B., & Teyssier, D. 2003, *ApJ*, **593**, 51
- Ceccarelli, C., Loinard, L., & Castets, A. 2000, *A&A*, **357**, L9
- Ceccarelli, C., Maret, S., Tielens, A. G. G. M., Castets, A., & Caux, E. 2003, *A&A*, **410**, 587
- Ceccarelli, C., Caselli, P., Herbst, E., Tielens, A. G. G. M., & Caux, E. 2007, *Protostars and Planets V*, eds. B. Reipurth, D. Jewitt & K. Keil (Tucson: University of Arizona Press)
- Ceccarelli, C., Dominik, C., López-Sepulcre, A., et al. 2014, *ApJ*, **790**, L1
- Ceccarelli, C., Caselli, P., Fontani, F., et al. 2017, *ApJ*, **850**, 176
- Chini, R., Reipurth, B., Ward-Thompson, D., et al. 1997, *ApJ*, **474**, L135
- Codella, C., Ceccarelli, C., Cabrit, S., et al. 2016, *A&A*, **586**, A3
- Cuadrado, S., Goicoechea, J. R., Pilleri, P., et al. 2015, *A&A*, **575**, A82
- Cuadrado, S., Goicoechea, J. R., Cernicharo, J., et al. 2017, *A&A*, **603**, A124
- Daghdigian, P. J. 2018, *MNRAS*, **479**, 3227
- Dapra, M., Henkel, C., Levshakov, S. A., et al. 2017, *MNRAS*, **472**, 4434
- De Simone, M., Codella, C., Testi, L., et al. 2017, *A&A*, **599**, A121
- Dickens, J. E., Irvine, W. M., Snell, R. L., et al. 2000, *ApJ*, **542**, 870
- Dubernet, M.-L., Alexander, M. H., Ba, Y. A., et al. 2013, *A&A*, **553**, A50
- Favre, C., Ceccarelli, C., López-Sepulcre, A., et al. 2018, *ApJ*, **859**, 136
- Flower, D. R., Pineau des Forêts, G., & Rabli, D. 2010, *MNRAS*, **409**, 29
- Fontani, F., Ceccarelli, C., Favre, C., et al. 2017, *A&A*, **605**, A57
- Friberg, P., Madden, S., Hjalmarson, A., & Irvine, W. 1988, *A&A*, **195**, 281
- Gatley, I., Becklin, E. E., Matthews, K., et al. 1974, *ApJ*, **191L**, 121
- Ginard, D., González-García, M., Fuente, A., et al. 2012, *A&A*, **543**, A27
- Graninger, D. M., Wilkins, O. H., & Öberg, K. I. 2016, *ApJ*, **819**, 140
- Großschedl, J. E., Alves, J., Meingast, S., et al. 2018, *A&A*, **619**, A106
- Guzmán, V. V., Goicoechea, J. R., Pety, J., et al. 2013, *A&A*, **560**, A73
- Herbst, E., & Van Dishoeck, E. F. 2009, *ARA&A*, **47**, 427
- Higuchi, A. E., Sakai, N., Watanabe, Y., et al. 2018, *ApJS*, **236**, 52
- Jansen, D. J., Van Dishoeck, E. F., & Black, J. H. 1994, *A&A*, **282**, 605
- Jørgensen, J. K., Bourke, T. L., Myers, P. C., et al. 2005, *ApJ*, **632**, 973
- Jørgensen, J. K., van der Wiel, M. H. D., Coutens, A., et al. 2016, *A&A*, **595**, A117
- Kama, M., López-Sepulcre, A., Dominik, C., et al. 2013, *A&A*, **556**, A57
- Law, C., Öberg, K. I., Bergner, J. B., & Graninger, D. 2018, *ApJ*, **863**, 88
- Leurini, S., Parise, B., Schilke, P., Pety, J., & Roloffs, R. 2010, *A&A*, **511**, A82
- Li, D., Kauffmann, J., Zhang, Q., & Chen, W. 2013, *ApJ*, **768**, L5
- Lindberg, J. E., Charnley, S. B., & Cordiner, M. A. 2016, *ApJ*, **833**, L14
- Lis, D. C., Serabyn, E., Keene, J., et al. 1998, *ApJ*, **509**, 299
- López-Sepulcre, A., Taquet, V., Sánchez-Monge, A., et al. 2013, *A&A*, **556**, A62
- López-Sepulcre, A., Sakai, N., Neri, R., et al. 2017, *A&A*, **606**, A121
- Maret, S., Ceccarelli, C., Tielens, A. G. G. M., et al. 2005, *A&A*, **442**, 527
- Müller, H. S. P., Schlöder, F., Stutzki, J., et al. 2005, *IAU Symp.*, **235**, 62
- Nagy, Z., Spezzano, S., Caselli, P., et al. 2019, *A&A*, **630**, A136
- Nielbock, M., Chini, R., & Müller, S. A. H. 2003, *A&A*, **408**, 245
- Ospina-Zamudio, J., Lefloch, B., Ceccarelli, C., et al. 2018, *A&A*, **618**, A145
- Oya, Y., Sakai, N., Watanabe, Y., et al. 2017, *ApJ*, **837**, 174
- Padovani, M., Walmsley, C. M., Tafalla, M., Galli, D., & Müller, H. S. P. 2009, *A&A*, **505**, 1199
- Pety, J., Teyssier, D., Fosse, D., et al. 2005, *A&A*, **435**, 885
- Pfalzner, S., Davies, M. B., Gounelle, M., et al. 2015, *PhysS*, **90f8001P**, 068001
- Pickett, H. M., Poynter, R. L., Cohen, E. A., et al. 1998, *J. Quant. Spectr. Rad. Transf.*, **60**, 883
- Pratap, P., Dickens, J. E., Snell, R. L., et al. 1997, *ApJ*, **486**, 862
- Punanova, A., Caselli, P., Feng, S., et al. 2018, *ApJ*, **855**, 112
- Reipurth, B., Rodríguez, L. F., & Chini, R. 1999, *ApJ*, **118**, 983
- Sakai, N., & Yamamoto, S. 2013, *Chem. Rev.*, **113**, 8981
- Sakai, N., Sakai, T., & Yamamoto, S. 2006, *PASJ*, **58**, 1
- Sakai, N., Sakai, T., Hirota, T., & Yamamoto, S. 2008, *ApJ*, **672**, 371
- Sakai, N., Sakai, T., Hirota, T., Burton, M., & Yamamoto, S. 2009, *ApJ*, **697**, 769
- Saul, M., Tothill, N. F. H., & Purcell, C. R. 2015, *ApJ*, **798**, 36
- Snyder, L. E., & Buhl, D. 1974, *ApJ*, **189**, L31
- Soma, T., Sakai, N., Watanabe, Y., & Yamamoto, S. 2015, *ApJ*, **802**, 74
- Takahashi, S., Saito, M., Ohashi, N., et al. 2008, *ApJ*, **688**, 244
- Taquet, V., López-Sepulcre, A., Ceccarelli, C., et al. 2015, *ApJ*, **804**, 81
- Teyssier, D., Fossé, D., Gerin, M., et al. 2004, *A&A*, **417**, 135
- Ungerechts, H., Bergin, E. A., Goldsmith, P. F., et al. 1997, *ApJ*, **482**, 245
- Van Dishoeck, E. F., Blake, G. A., Jansen, D. J., & Groesbeck, T. D. 1995, *ApJ*, **447**, 760
- Vastel, C., Ceccarelli, C., Lefloch, B., & Bachiller, R. 2014, *ApJ*, **795**, L2
- Williams, J. P., Plambeck, R. L., & Heyer, M. H. 2003, *ApJ*, **591**, 1025
- Wright, M. C. H., & Plambeck, R. L. 1983, *ApJ*, **267**, L115
- Wu, Y., Liu, X., Chen, X., et al. 2019, *MNRAS*, **488**, 495
- Xu, L.-H., Fisher, J., Lees, R. M., et al. 2008, *J. Mol. Struct.*, **251**, 305
- Yoshida, K., Sakai, N., Nishimura, Y., et al. 2019, *PASJ*, **71**, 18
- Yu, K. C., Bally, J., & Devine, D. 1997, *ApJ*, **485**, 45
- Ziurys, L. M., Saykally, R. J., Plambeck, R. L., & Erickson, N. R. 1982, *ApJ*, **254**, 94

Appendix A: Sample of lines

Sample of CCH and CH₃OH lines detected at 1.3 mm (IRAM-30 m) and at 3 mm (Nobeyama-45 m) for each source (except for SIMBA-a, FIR6c and FIR2 as explained in Sects. 4.1 and 5.1).

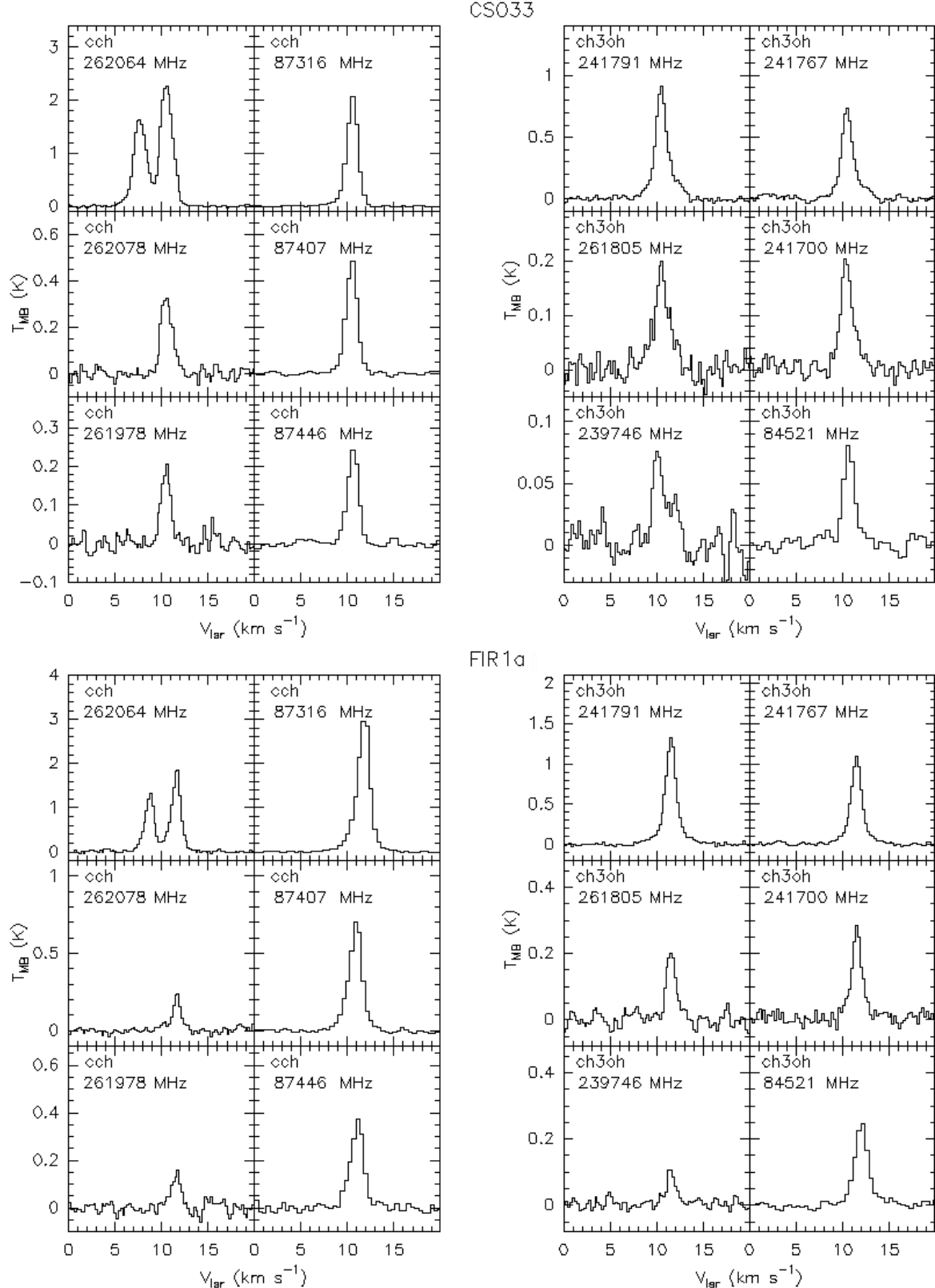


Fig. A.1. Sample of CCH and CH₃OH lines of the sources CSO33 (*top*) and FIR1a (*bottom*).

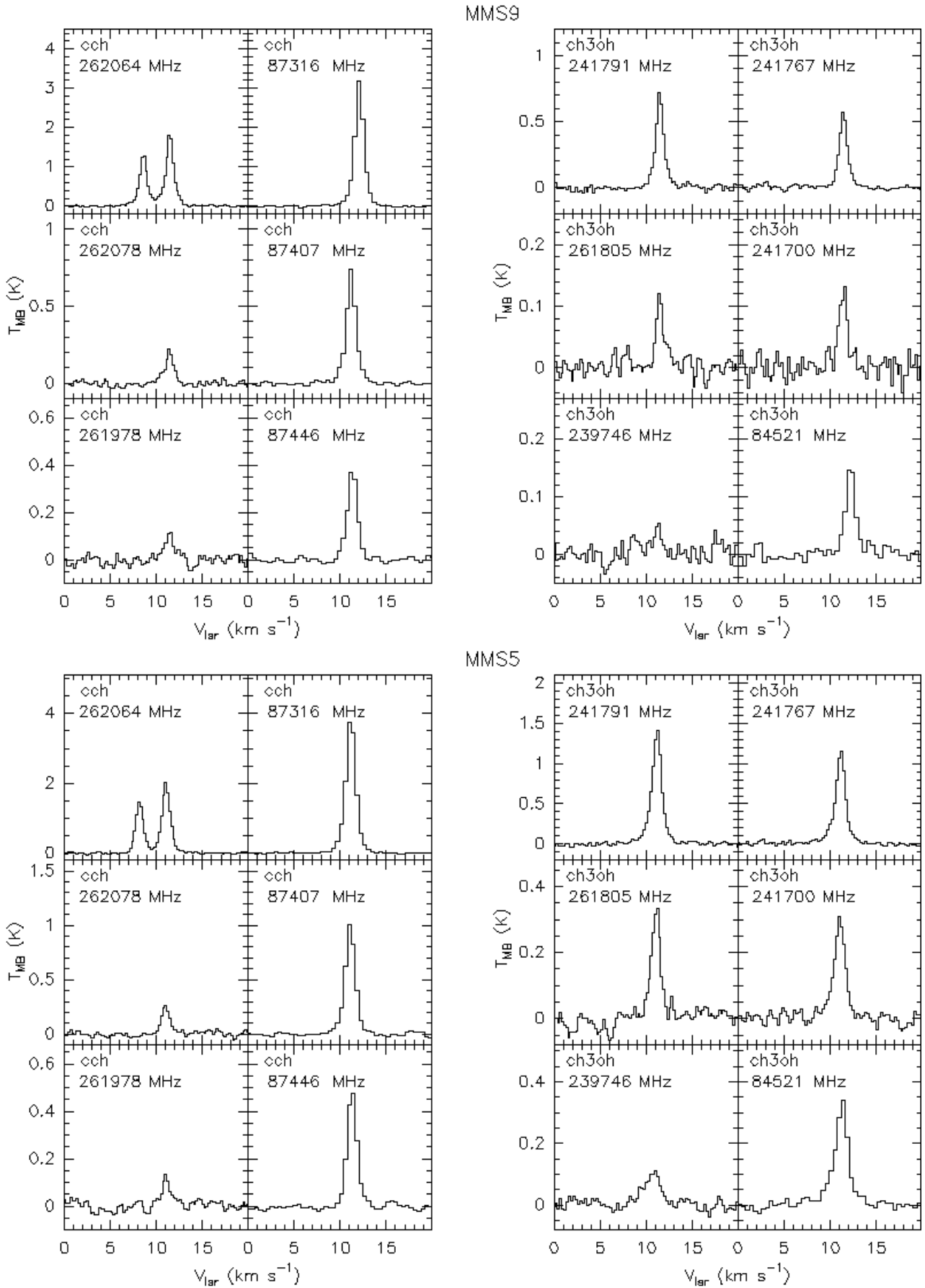


Fig. A.2. Sample of CCH and CH₃OH lines of the sources MMS9 (top) and MMS5 (bottom).

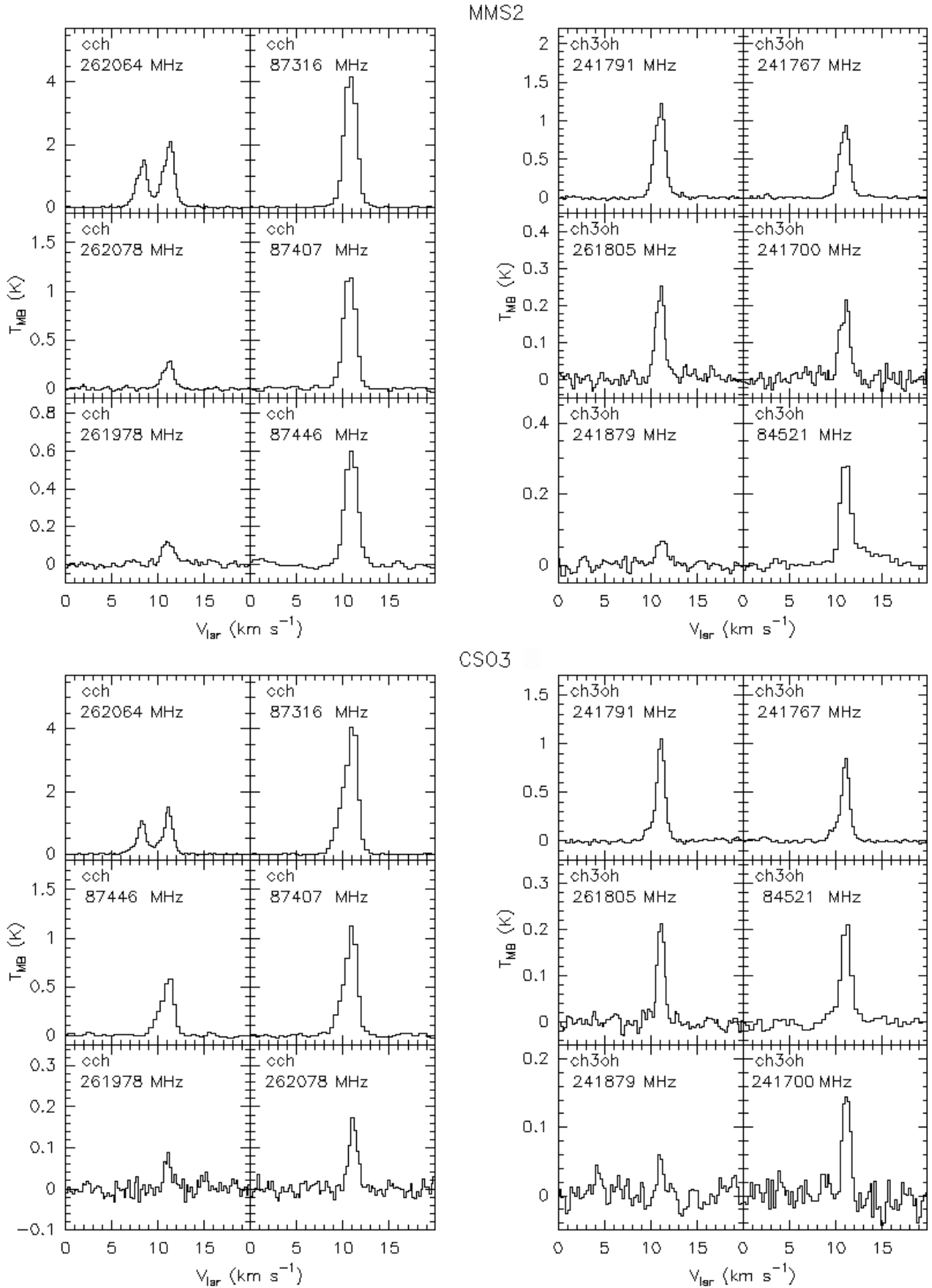


Fig. A.3. Sample of CCH and CH_3OH lines of the sources MMS2 (top) and CSO3 (bottom).

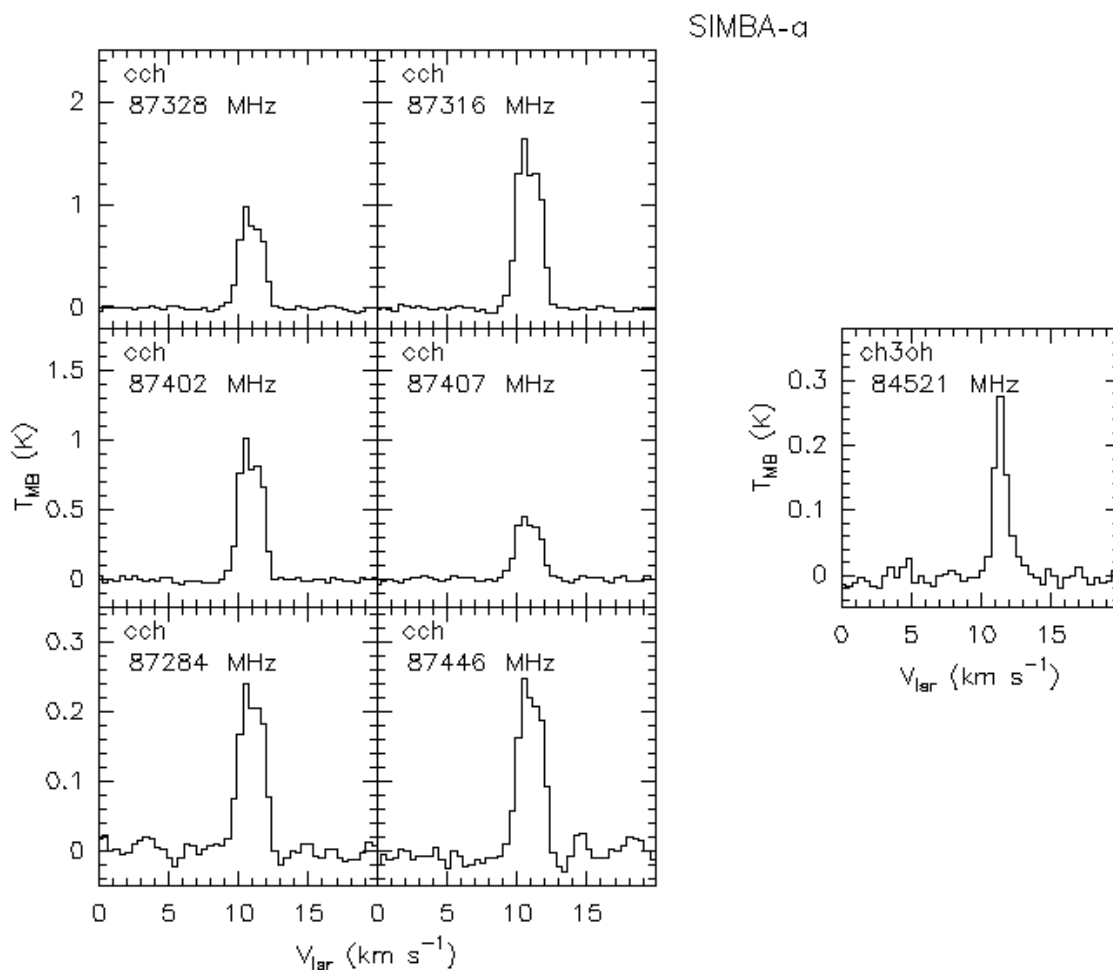


Fig. A.4. Sample of CCH and CH₃OH lines of the source SIMBA-a.

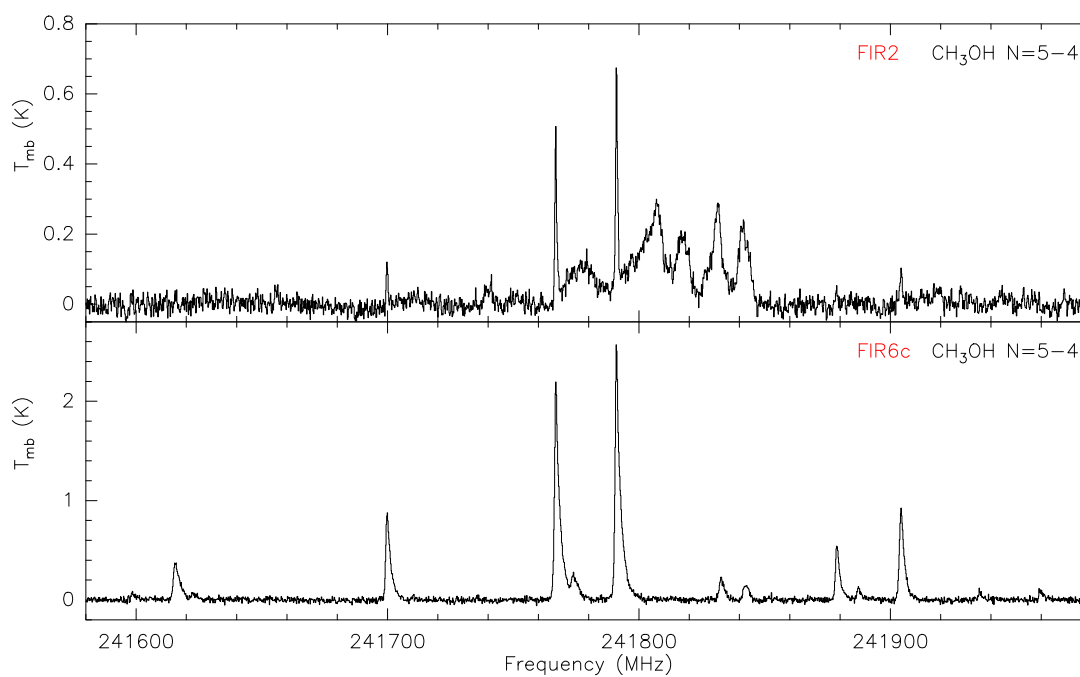


Fig. A.5. Lines of the $N=5-4$ transition of CH₃OH for FIR2 (top) and FIR6c (bottom). In both spectra, broad shoulders indicating the presence of outflows are present.

Appendix B: Gaussian fit results

B.1. Single-pointing

Here we present the Gaussian fits performed on each of the detected lines of CCH and CH₃OH for each source. Calibration errors of 20% and 40% for the IRAM-30 m and Nobeyama-45 m observations have not been included.

B.2. OTF Map

Maps of moments 1 and 2 of the lines CCH ($N=1-0$, $J=3/2-1/2$, $F=1-0$) and CH₃OH($2_{-1}-1_{-1}$ E) with a threshold of 3σ . Here we also show the intensity ratio map of two optically thin lines of methanol, ($2_{-1}-1_{-1}$) E and (2_0-1_0)E.

Table B.1. Gaussian fit parameters for narrow component in CSO33.

Molecule	Frequency	Area [mK.km s ⁻¹]	V_{lsr} [km s ⁻¹]	$FWHM$ [km s ⁻¹]	T_{peak} [mK]	
CH ₃ OH	84.521	122 ± 10	10.7 ± 0.2	1.4 ± 0.2	80 ± 10	
	239.746	146 ± 18	10.6 ± 0.1	2.5 ± 0.3	74 ± 14	
	241.700	114 ± 40	10.3 ± 0.1	0.9 ± 0.2	202 ± 13	
	241.767	668 ± 44	10.5 ± 0.1	1.1 ± 0.1	569 ± 17	
	241.791	740 ± 42	10.4 ± 0.1	1.1 ± 0.1	656 ± 15	
	241.879	171 ± 16	10.3 ± 0.1	1.4 ± 0.2	117 ± 16	
	243.915	155 ± 14	10.4 ± 0.1	2.1 ± 0.2	70 ± 13	
	261.805	268 ± 20	10.5 ± 0.1	1.9 ± 0.1	198 ± 19	
	CCH	87.284	333 ± 10	10.6 ± 0.2	1.4 ± 0.2	224 ± 10
		87.316	2614 ± 30	10.6 ± 0.2	1.3 ± 0.2	1910 ± 10
87.328		1397 ± 10	10.6 ± 0.2	1.3 ± 0.2	1030 ± 10	
87.402		1405 ± 60	10.6 ± 0.2	1.3 ± 0.2	1050 ± 10	
87.407		599 ± 90	10.6 ± 0.2	1.3 ± 0.2	430 ± 10	
87.446		367 ± 10	10.6 ± 0.2	1.4 ± 0.2	244 ± 10	
261.978		256 ± 14	10.5 ± 0.1	1.2 ± 0.1	195 ± 18	
262.004		4868 ± 50	10.5 ± 0.1	1.5 ± 0.1	3020 ± 17	
262.006		3902 ± 70	10.5 ± 0.1	1.5 ± 0.1	2470 ± 19	
262.064		3677 ± 34	10.5 ± 0.1	1.5 ± 0.1	2260 ± 14	
262.067		2334 ± 15	10.5 ± 0.1	1.4 ± 0.1	1520 ± 17	
262.078		504 ± 18	10.5 ± 0.1	1.4 ± 0.1	332 ± 21	
262.208		526 ± 16	10.5 ± 0.1	1.5 ± 0.1	332 ± 18	
262.250		180 ± 14	10.5 ± 0.1	1.3 ± 0.1	137 ± 16	

Table B.2. Gaussian fit parameters for narrow component in FIR1a.

Molecule	Frequency	Area [mK.km s ⁻¹]	V_{lsr} [km s ⁻¹]	$FWHM$ [km s ⁻¹]	T_{peak} [mK]	
CH ₃ OH	84.521	411 ± 10	11.7 ± 0.2	1.7 ± 0.2	229 ± 10	
	239.746	123 ± 13	11.6 ± 0.1	1.1 ± 0.2	102 ± 13	
	241.700	290 ± 14	11.6 ± 0.1	1.1 ± 0.1	230 ± 16	
	241.767	1020 ± 60	11.5 ± 0.1	1.1 ± 0.1	853 ± 17	
	241.791	1260 ± 50	11.5 ± 0.1	1.1 ± 0.1	1050 ± 14	
	241.879	162 ± 12	11.6 ± 0.1	1.3 ± 0.1	119 ± 14	
	243.915	182 ± 18	11.7 ± 0.1	1.6 ± 0.2	105 ± 16	
	261.805	265 ± 16	11.5 ± 0.1	1.2 ± 0.1	203 ± 20	
	CCH	87.284	346 ± 116	11.4 ± 0.2	1.3 ± 0.2	131 ± 10
		87.316	2910 ± 33	11.3 ± 0.2	1.2 ± 0.2	2260 ± 11
87.328		1210 ± 103	11.3 ± 0.2	1.1 ± 0.2	1030 ± 11	
87.402		1597 ± 10	11.1 ± 0.2	1.2 ± 0.2	1270 ± 14	
87.407		890 ± 88	11.1 ± 0.2	1.0 ± 0.2	388 ± 10	
87.446		312 ± 18	11.3 ± 0.2	1.2 ± 0.2	249 ± 13	
261.978		140 ± 17	11.6 ± 0.1	1.1 ± 0.1	147 ± 21	
262.004		2435 ± 28	11.5 ± 0.1	1.0 ± 0.1	2230 ± 23	
262.006		1714 ± 35	11.5 ± 0.1	1.0 ± 0.1	1560 ± 20	
262.064		1841 ± 31	11.6 ± 0.1	1.0 ± 0.1	1680 ± 28	
262.067		1184 ± 36	11.5 ± 0.1	1.0 ± 0.1	1060 ± 25	
262.078		210 ± 42	11.6 ± 0.1	1.0 ± 0.2	235 ± 54	
262.208		181 ± 18	11.6 ± 0.1	1.2 ± 0.1	199 ± 21	
262.250		90 ± 10	11.8 ± 0.2	0.8 ± 0.1	103 ± 21	

Table B.3. Gaussian fit parameters for narrow component in MMS9.

Molecule	Frequency	Area [mK.km s ⁻¹]	V_{lsr} [km s ⁻¹]	$FWHM$ [km s ⁻¹]	T_{peak} [mK]	
CH ₃ OH	84.521	213 ± 10	11.5 ± 0.2	1.3 ± 0.2	154 ± 10	
	239.746	47 ± 9	11.2 ± 0.1	0.8 ± 0.2	52 ± 13	
	241.700	150 ± 15	11.4 ± 0.1	1.1 ± 0.1	132 ± 19	
	241.767	220 ± 12	11.4 ± 0.1	0.7 ± 0.1	308 ± 15	
	241.791	300 ± 60	11.4 ± 0.1	0.7 ± 0.1	430 ± 19	
	241.879	57 ± 9	11.4 ± 0.1	0.7 ± 0.1	74 ± 13	
	243.915	105 ± 12	11.5 ± 0.1	1.8 ± 0.2	55 ± 12	
	261.805	115 ± 12	11.4 ± 0.1	0.8 ± 0.1	130 ± 16	
	CCH	87.284	471 ± 15	11.6 ± 0.2	1.3 ± 0.2	343 ± 13
		87.316	2046 ± 10	11.6 ± 0.2	0.9 ± 0.2	2230 ± 12
87.328		1128 ± 118	11.6 ± 0.2	0.9 ± 0.2	1200 ± 12	
87.402		1494 ± 32	11.6 ± 0.2	0.9 ± 0.2	1510 ± 13	
87.407		463 ± 79	11.6 ± 0.2	0.9 ± 0.2	483 ± 12	
87.446		519 ± 11	11.5 ± 0.2	1.3 ± 0.2	378 ± 11	
261.978		70 ± 30	11.5 ± 0.1	0.6 ± 0.2	123 ± 16	
262.004		1830 ± 24	11.4 ± 0.1	0.8 ± 0.1	2030 ± 21	
262.006		1370 ± 16	11.4 ± 0.1	0.9 ± 0.1	1520 ± 17	
262.064		1500 ± 12	11.5 ± 0.1	0.9 ± 0.1	1610 ± 19	
262.067		990 ± 10	11.4 ± 0.1	0.9 ± 0.1	1100 ± 16	
262.078		214 ± 13	11.4 ± 0.1	1.0 ± 0.1	210 ± 18	
262.208		197 ± 12	11.4 ± 0.1	0.8 ± 0.1	235 ± 17	
262.250		68 ± 11	11.5 ± 0.1	0.7 ± 0.1	91 ± 18	

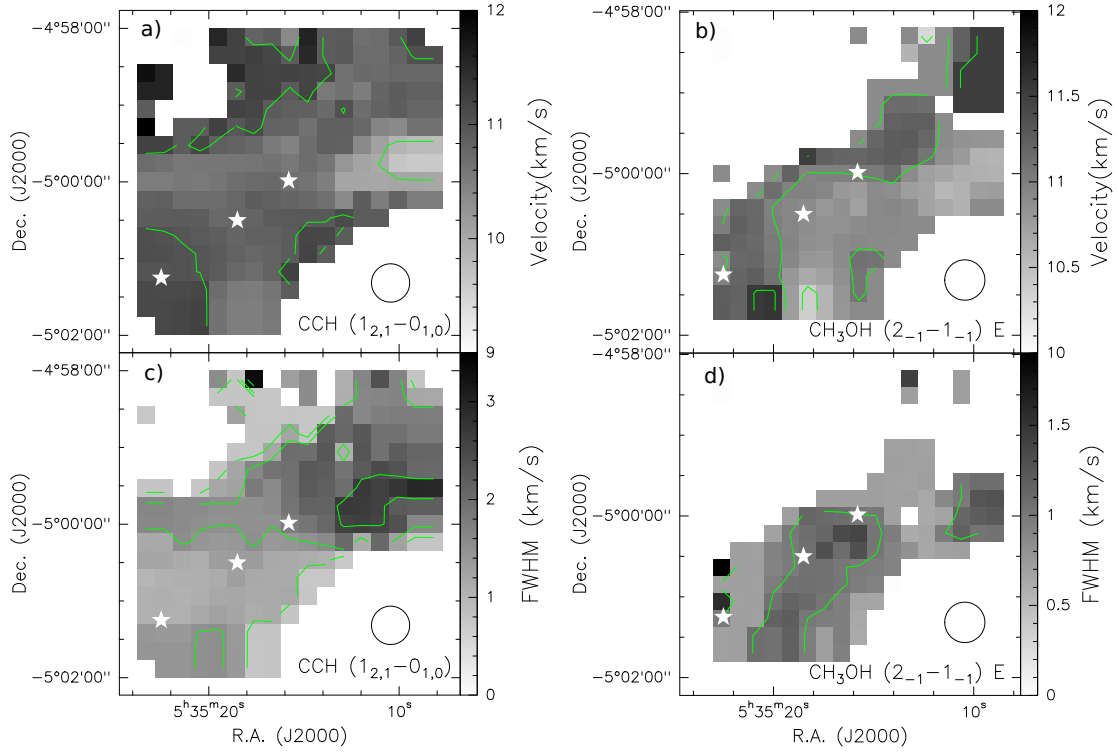


Fig. B.1. Moment maps of CCH and CH₃OH; (a) and (c) moments 1 and 2 of the line CCH ($N=1-0$, $J=3/2-1/2$, $F=1-0$) (a),(c), respectively; (b) and (d) moments 1 and 2 of the line CH₃OH($2_{-1}-1_{-1}$ E) respectively. The velocity integration is between 7.9 and 12.8 km s⁻¹ and the threshold has been set at 3σ for both lines. Contour levels for Moment 1 are 10 and 11 km s⁻¹ for CCH and 10.5, 11 and 11.5 km s⁻¹ for CH₃OH. Contour levels for Moments 2 are 1, 1.5 and 2.5 km s⁻¹ for CCH and 1 km s⁻¹ for CH₃OH.

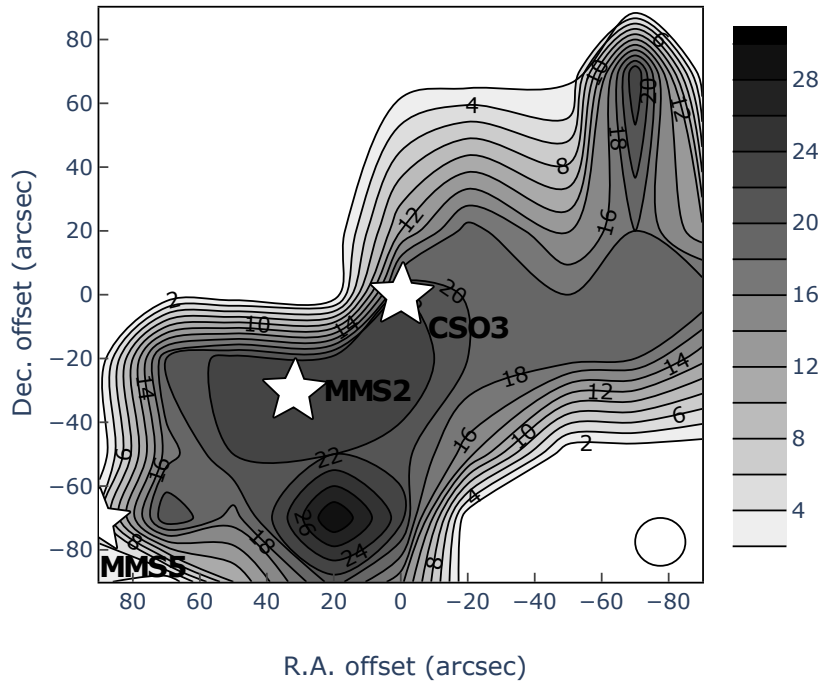


Fig. B.2. Intensity ratio of the CH₃OH lines $2_{-1}-1_{-1}$ E and 2_0-1_0 E. The lines chosen are optically thin. We see clearly that the ratio is constant throughout the filament. Error on the line intensity ratio is less than 3.

Table B.4. Gaussian fit parameters for narrow component in MMS5.

Molecule	Frequency	Area [mK.km s ⁻¹]	V_{lsr} [km s ⁻¹]	$FWHM$ [km s ⁻¹]	T_{peak} [mK]
CH ₃ OH	84.521	245 ± 60	11.4 ± 0.2	1.1 ± 0.2	216 ± 10
	239.746	207 ± 19	10.8 ± 0.1	1.8 ± 0.2	108 ± 17
	241.700	250 ± 90	11.1 ± 0.1	1.1 ± 0.1	216 ± 17
	241.767	880 ± 70	11.2 ± 0.1	0.9 ± 0.1	880 ± 21
	241.791	1020 ± 40	11.2 ± 0.1	0.9 ± 0.1	1020 ± 19
	241.879	280 ± 20	11.0 ± 0.1	1.6 ± 0.1	163 ± 20
	241.887	60 ± 10	11.2 ± 0.1	0.9 ± 0.2	60 ± 16
	243.915	264 ± 17	11.0 ± 0.1	1.6 ± 0.1	151 ± 18
	261.805	416 ± 33	11.1 ± 0.1	1.2 ± 0.1	320 ± 27
	87.284	670 ± 11	11.2 ± 0.2	1.1 ± 0.2	477 ± 10
87.316	4184 ± 12	11.2 ± 0.2	1.0 ± 0.2	3450 ± 13	
87.328	2334 ± 20	11.2 ± 0.2	1.0 ± 0.2	1930 ± 11	
87.402	2132 ± 26	11.2 ± 0.2	0.9 ± 0.2	1910 ± 17	
87.407	1041 ± 90	11.1 ± 0.2	1.1 ± 0.2	862 ± 15	
87.446	654 ± 13	11.3 ± 0.2	1.1 ± 0.2	488 ± 12	
261.978	130 ± 16	11.0 ± 0.1	1.0 ± 0.2	124 ± 19	
CCH	262.004	2582 ± 36	11.0 ± 0.1	1.0 ± 0.1	2360 ± 21
262.006	2104 ± 22	11.0 ± 0.1	1.0 ± 0.1	1970 ± 21	
262.064	1601 ± 10	11.0 ± 0.1	0.9 ± 0.1	1610 ± 23	
262.067	1556 ± 70	11.0 ± 0.1	1.0 ± 0.1	1410 ± 23	
262.078	289 ± 15	11.0 ± 0.1	1.1 ± 0.1	258 ± 20	
262.208	274 ± 13	11.0 ± 0.2	1.0 ± 0.1	252 ± 18	
262.236	79 ± 15	10.7 ± 0.1	1.0 ± 0.2	73 ± 16	
262.250	86 ± 17	11.0 ± 0.1	0.7 ± 0.2	118 ± 24	

Table B.5. Gaussian fit parameters for narrow component in MMS2.

Molecule	Frequency	Area [mK.km s ⁻¹]	V_{lsr} [km s ⁻¹]	$FWHM$ [km s ⁻¹]	T_{peak} [mK]
CH ₃ OH	84.521	362 ± 15	11.1 ± 0.2	1.2 ± 0.2	273 ± 9
	239.746	86 ± 13	11.0 ± 0.1	1.7 ± 0.3	48 ± 12
	241.700	269 ± 13	11.0 ± 0.1	1.3 ± 0.1	199 ± 16
	241.767	1220 ± 20	11.0 ± 0.1	1.3 ± 0.1	901 ± 13
	241.791	1603 ± 10	11.0 ± 0.1	1.3 ± 0.1	1160 ± 13
	241.879	97 ± 12	11.2 ± 0.1	1.3 ± 0.2	72 ± 14
	243.915	139 ± 11	11.2 ± 0.1	1.5 ± 0.2	71 ± 12
	261.805	298 ± 12	11.0 ± 0.1	1.2 ± 0.1	239 ± 15
	87.284	957 ± 16	10.9 ± 0.2	1.6 ± 0.2	578 ± 11
	87.316	7084 ± 15	10.8 ± 0.2	1.6 ± 0.2	4290 ± 12
87.328	3981 ± 17	10.9 ± 0.2	1.5 ± 0.2	2480 ± 14	
87.402	4165 ± 18	10.8 ± 0.2	1.5 ± 0.2	2610 ± 15	
87.407	1930 ± 15	10.7 ± 0.2	1.5 ± 0.2	1190 ± 15	
87.446	1021 ± 16	10.9 ± 0.2	1.6 ± 0.2	608 ± 11	
CCH	261.978	188 ± 13	11.1 ± 0.1	1.5 ± 0.1	120 ± 16
262.004	3927 ± 21	11.1 ± 0.1	1.4 ± 0.1	2570 ± 23	
262.006	3334 ± 16	11.2 ± 0.1	1.6 ± 0.1	2000 ± 16	
262.064	2996 ± 16	11.2 ± 0.1	1.4 ± 0.1	1940 ± 18	
262.067	2203 ± 15	11.2 ± 0.1	1.5 ± 0.1	1360 ± 16	
262.078	360 ± 20	11.1 ± 0.1	1.3 ± 0.1	257 ± 14	
262.208	353 ± 12	11.1 ± 0.1	1.4 ± 0.1	241 ± 14	
262.250	129 ± 13	11.2 ± 0.1	1.3 ± 0.1	91 ± 17	

Table B.6. Gaussian fit parameters for narrow component in CSO3.

Molecule	Frequency	Area [mK.km s ⁻¹]	V_{lsr} [km s ⁻¹]	$FWHM$ [km s ⁻¹]	T_{peak} [mK]
CH ₃ OH	84.521	192 ± 32	11.2 ± 0.2	1.0 ± 0.2	179 ± 8
	241.700	160 ± 13	11.2 ± 0.1	1.0 ± 0.1	157 ± 17
	241.767	700 ± 10	11.1 ± 0.1	0.9 ± 0.1	725 ± 11
	241.791	820 ± 40	11.1 ± 0.1	0.9 ± 0.1	898 ± 16
	241.879	42 ± 9	11.1 ± 0.1	0.6 ± 0.2	62 ± 15
	261.805	205 ± 9	11.1 ± 0.1	0.9 ± 0.1	220 ± 13
	87.284	470 ± 15	11.2 ± 0.2	1.0 ± 0.2	320 ± 12
	87.316	2578 ± 50	11.2 ± 0.2	0.9 ± 0.2	2560 ± 15
	87.328	1745 ± 14	11.2 ± 0.2	1.0 ± 0.2	1600 ± 11
	87.402	1647 ± 29	11.1 ± 0.2	1.0 ± 0.2	1620 ± 18
87.407	991 ± 18	11.1 ± 0.2	1.1 ± 0.2	851 ± 13	
87.446	438 ± 153	11.3 ± 0.2	1.0 ± 0.2	401 ± 12	
CCH	261.978	72 ± 11	11.0 ± 0.1	0.8 ± 0.1	83 ± 14
262.004	1900 ± 40	11.1 ± 0.1	1.0 ± 0.1	1890 ± 16	
262.006	1840 ± 11	11.1 ± 0.1	0.8 ± 0.1	1040 ± 12	
262.064	1510 ± 10	11.1 ± 0.1	1.0 ± 0.1	1390 ± 14	
262.067	680 ± 10	11.1 ± 0.1	0.8 ± 0.1	775 ± 10	
262.078	193 ± 10	11.1 ± 0.1	1.0 ± 0.1	177 ± 13	
262.208	187 ± 12	11.1 ± 0.1	1.0 ± 0.1	177 ± 17	
262.250	72 ± 11	11.1 ± 0.1	1.2 ± 0.2	56 ± 13	

Table B.7. Gaussian fit parameters for narrow component in SIMBA-a.

Molecule	Frequency	Area [mK.km s ⁻¹]	V_{lsr} [km s ⁻¹]	$FWHM$ [km s ⁻¹]	T_{peak} [mK]
CH ₃ OH	84.521	226 ± 71	10.5 ± 0.2	0.9 ± 0.2	241 ± 8
CCH	87.284	327 ± 40	10.5 ± 0.2	1.3 ± 0.2	233 ± 13
	87.316	2000 ± 50	10.4 ± 0.2	1.1 ± 0.2	1630 ± 16
	87.328	1165 ± 49	10.5 ± 0.2	1.2 ± 0.2	950 ± 15
	87.402	1147 ± 46	10.4 ± 0.2	1.1 ± 0.2	1000 ± 16
	87.407	554 ± 64	10.4 ± 0.2	1.2 ± 0.2	442 ± 14
	87.446	324 ± 45	10.6 ± 0.2	1.2 ± 0.2	247 ± 11

Appendix C: LTE methods & results

Here we present the methods used to perform the LTE analysis and the results obtained.

C.1. Single-pointing

C.1.1. CH₃OH lines

In the case of the methanol lines, we used the usual rotational diagram approach, which assumes optically thin lines and LTE level populations. To this end, we included all lines with a detection threshold of 3σ and assumed extended emission. We note

that we verified a posteriori that the optically thin lines approximation is valid: we used the ULSA (Unbiased Line Spectral Analysis) package developed at IPAG, which is a LTE radiative transfer code to verify a posteriori this assumption. The opacity values of the CH₃OH lines given were less than 0.1. The rotational diagrams are presented in Fig. C.1 and the mean derived parameters are listed in Table C.1. In the six sources, the mean derived rotational temperatures and methanol beam-averaged column densities are 13.0 ± 1.5 K and $(4 \pm 2) \times 10^{13}$ cm⁻², respectively. However, we observe a scatter of the points from the linear fit in every rotational diagram, probably due to non-LTE effects.

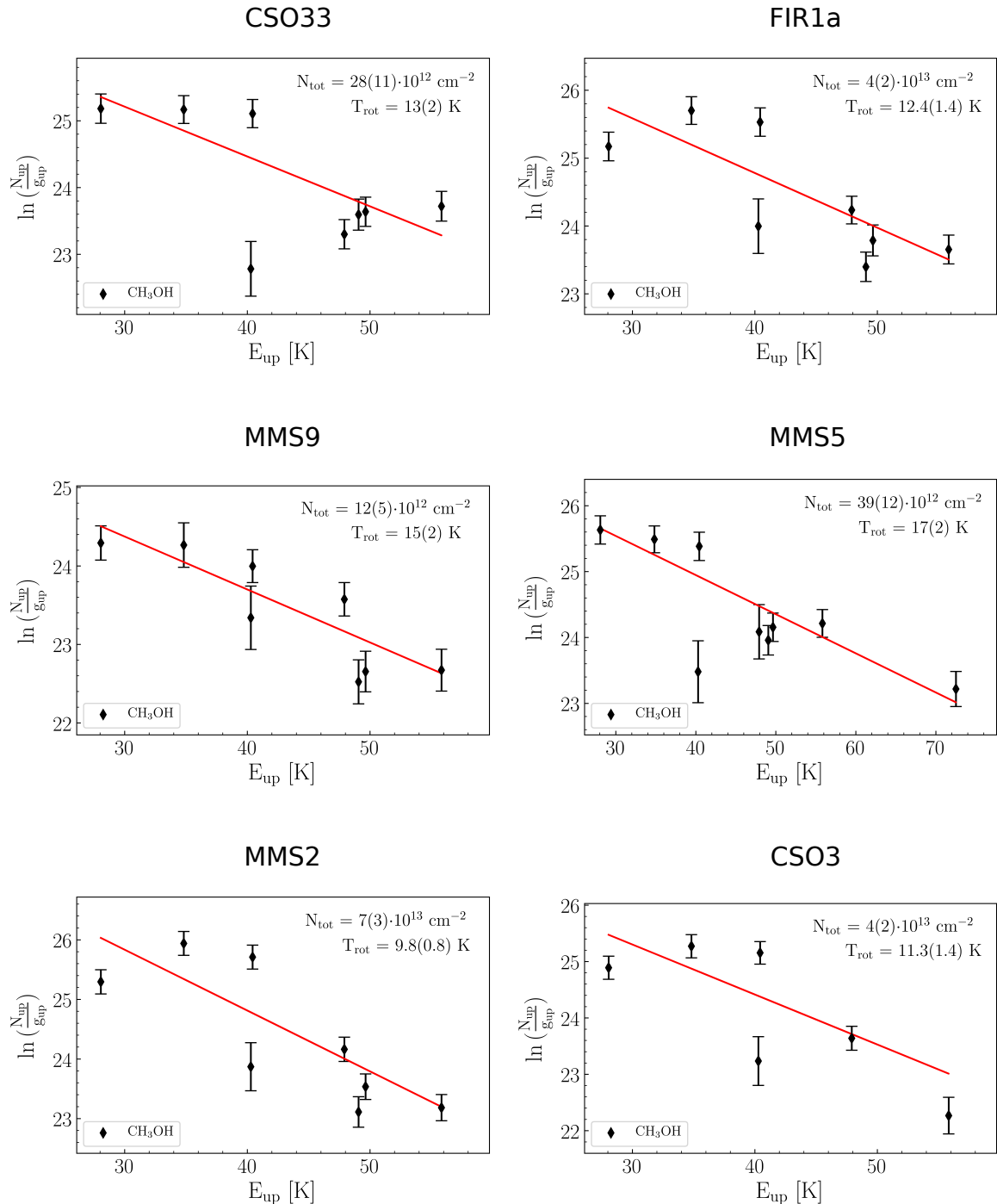


Fig. C.1. Rotational diagrams of CH₃OH for each source.

Table C.1. Rotational temperatures and beam-averaged column densities of CH₃OH and CCH towards seven out of the nine target sources (Table 2).

Source	IRAM 1 mm + Nobeyama 3 mm		IRAM 1 mm		Nobeyama 3 mm		Mean CCH		Ratio [CCH]/[CH ₃ OH]
	$T_{\text{CH}_3\text{OH}}$ [K]	$N_{\text{CH}_3\text{OH}}$ [$\times 10^{13}$ cm ⁻²]	T_{CCH} [K]	N_{CCH} [$\times 10^{14}$ cm ⁻²]	T_{CCH} [K]	N_{CCH} [$\times 10^{14}$ cm ⁻²]	T_{CCH} [K]	N_{CCH} [$\times 10^{14}$ cm ⁻²]	
CSO33	13 ± 2	3 ± 1	11 ± 1	11.6 ± 3.5	11 ± 3	5 ± 2	11.0 ± 2.5	8.0 ± 1.5	22 ± 10
FIR1a	12 ± 1	4 ± 2	17 ± 3	4 ± 1	17 ± 6	11 ± 9	17.0 ± 4.5	7.5 ± 5.0	19 ± 16
MMS9	15 ± 2	1.2 ± 0.5	14 ± 2	4 ± 1	15 ± 5	7 ± 5	14.5 ± 3.5	6 ± 3	50 ± 33
MMS5	17 ± 2	4 ± 1	14 ± 2	4.5 ± 1.4	13 ± 4	10 ± 6	13.5 ± 3.0	7.0 ± 3.5	17 ± 10
MMS2	10 ± 1	7 ± 3	11 ± 1	8.2 ± 2.5	10 ± 3	13.7 ± 6.5	10.5 ± 2.0	11 ± 5	14 ± 8
CSO3	11 ± 1	4 ± 2	23 ± 4	3 ± 1	11 ± 3	13 ± 7	17 ± 8.5	8 ± 4	20 ± 14
SIMBA-a	5 ± 1	11 ± 2	5 ± 1	11 ± 2	...

C.1.2. CCH lines

We clearly detect all the components from the CCH ($N=1-0$) transition and around eight to nine (out of 11) hyperfine components of the CCH ($N=3-2$) transition depending on the source. In order to derive excitation temperatures and column densities for the hyperfine structure of CCH, we used the Hyperfine fitting Structure (HfS) Tool in the CLASS software package. We derived the parameters separately for the data at 1mm and at 3mm because the HfS routine treats only one hyperfine transition at a time. By doing the analysis for the two transitions, we verified that we obtained the same physical parameters for the two transitions. The opacities derived show that most of the sources are moderately optically thick with values ranging from 0.8 to 2.2 at 1 mm and from 0.6 to 3.3 at 3 mm. The derived line widths, FWHM, and rest velocities, V_{lsr} , are similar to those derived from the Gaussian fits for most sources. The line widths may be larger for sources in which the line profile shows two components, such as the source SIMBA-a (see Appendix A).

The routine reads an input file containing the number of the components of the multiplet and their relative velocities, with respect to a chosen hyperfine component (here we chose the line at 262.004 GHz), as well as their relative intensities. We used the predicted frequencies and intensities of the CCH lines for the $N=3-2$ transition, taken from Ziurys et al. (1982). In order to check the results and the predicted values, we used all the components of the multiplet, detected or not. The outputs given by the routine are the following: $p_1 = T_{\text{mb}} \times \tau$, the rest velocity V_{lsr} , the width of the lines ΔV (labelled here as FWHM) and the total opacity of the multiplet $p_4 = \tau$. From those parameters, we can extract the excitation temperature, T_{ex} , and the total column density of CCH, N_{tot} , for each source thanks to Eqs. (C.1), (C.2), and (C.4).

$$J_{T_{\text{ex}}} = J_{T_{\text{bg}}} + \frac{p_1}{p_4} \quad (\text{C.1})$$

where $J(T)$, the intensity in units of temperature, is defined as:

$$J(T) = \frac{h\nu}{k_{\text{B}}T} \frac{1}{e^{h\nu/k_{\text{B}}T} - 1}, \quad (\text{C.2})$$

where h , ν , k_{B} and T are the Planck constant, the frequency, the Boltzmann constant and the temperature respectively.

This leads to:

$$T_{\text{ex}} = \frac{h\nu/k_{\text{B}}}{\ln\left(1 + \frac{h\nu/k_{\text{B}}}{J_{T_{\text{bg}}} + \frac{p_1}{p_4}}\right)}. \quad (\text{C.3})$$

We then can calculate the total column density N_{CCH} :

$$N_{\text{CCH}} = \frac{8\pi\nu^3\tau\Delta V Q(T_{\text{ex}})}{A_{ij}g_j c^3} \frac{e^{E_u/T_{\text{ex}}}}{e^{hc/\nu T_{\text{ex}}} - 1}, \quad (\text{C.4})$$

where E_u , A_{ij} , g_j , $Q(T_{\text{ex}})$, c and T_{ex} are the upper level energy, the Einstein coefficient, the statistical weight of the upper level energy, partition function of the excitation temperature, the celerity and the excitation temperature, respectively.

The results of the hyperfine fit and of the LTE analysis are shown in Tables C.2 and C.1 respectively. The excitation temperatures derived at 1mm and at 3mm are similar, as well as the total column densities. We thus averaged the results for the two transitions. The mean excitation temperature ranges from 5 to 17 K and the column density from 6×10^{14} to 11×10^{14} cm⁻².

C.2. OTF Map

To derive the excitation temperatures and the column densities of each position of the map, we used the same methods as for the single-pointing. We took into account only positions with at least 3 detected lines of each molecules. The derived parameters are shown in Table C.3 and the results in Fig. C.2. The rotational temperatures range from 5 to 33 K and the column densities range from 2×10^{13} to 16×10^{13} cm⁻² for CH₃OH. For CCH, temperatures ranges from 4 to 15 K and column densities ranges from 1×10^{14} to 11×10^{14} cm⁻².

Table C.2. Results of the hyperfine structure fit of CCH for each source, at 1 mm and 3 mm.

Telescope	Source	$T_{\text{mb}} * \tau$ [K]	V_{lsr} [km s ⁻¹]	$FWHM$ [km s ⁻¹]	τ_{main}
IRAM	CSO33	13 ± 6	10.4 ± 0.1	1.5 ± 0.1	2.2
	FIR1a	9 ± 5	11.5 ± 0.1	1.2 ± 0.1	0.8
	MMS9	8 ± 4	11.4 ± 0.1	1.0 ± 0.1	1.0
	MMS5	9 ± 7	11.0 ± 0.1	1.1 ± 0.1	1.0
	MMS2	10 ± 4	11.1 ± 0.1	1.4 ± 0.1	1.7
	CSO3	7 ± 5	11.0 ± 0.1	1.1 ± 0.1	0.4
Nobeyama	CSO33	6 ± 2	10.6 ± 0.2	1.3 ± 0.2	0.8
	FIR1a	8 ± 3	11.8 ± 0.2	1.6 ± 0.2	0.6
	MMS9	9.0 ± 3.5	11.6 ± 0.2	1.1 ± 0.2	0.7
	MMS5	12 ± 5	11.2 ± 0.2	1.2 ± 0.2	1.2
	MMS2	15 ± 6	10.8 ± 0.2	1.4 ± 0.2	2.1
	CSO3	13 ± 5	10.9 ± 0.2	1.6 ± 0.2	1.5
	SIMBA-a	7 ± 3	10.8 ± 0.2	1.7 ± 0.2	3.3

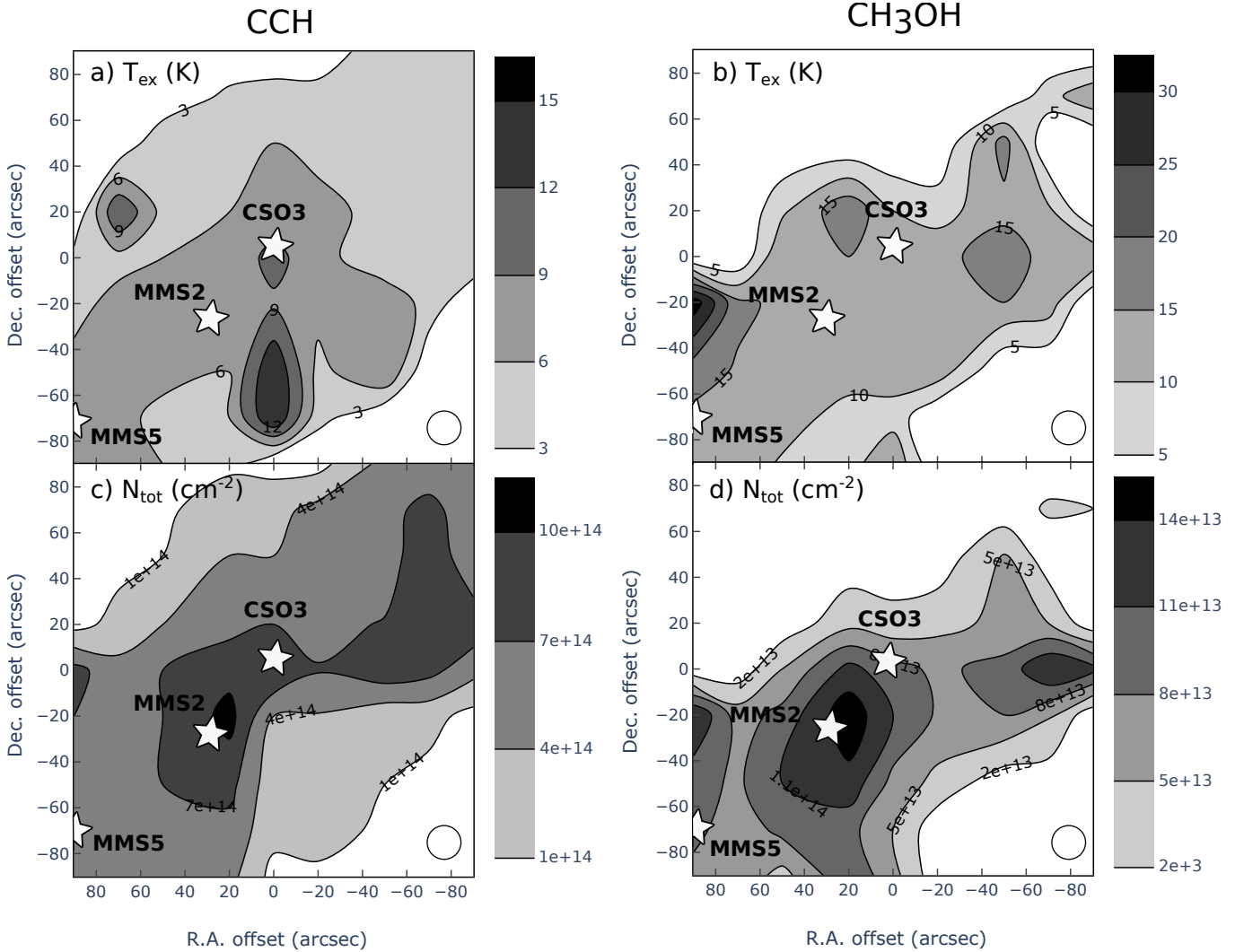

Fig. C.2. LTE results for the OTF map. The size of the beam is shown by a white filled circle at the bottom right of each map. (a and b): derived excitation temperature, T_{ex} , of CCH and CH_3OH respectively. (c and d): derived total column density, N_{tot} , of CCH and CH_3OH , respectively.

Table C.3. Derived excitation temperatures and column densities of CCH and CH₃OH from the LTE analysis.

Coordinates		CH ₃ OH		CCH		Ratio
Offset RA [arcsec]	Offset Dec [arcsec]	T_{ex} [K]	N_{tot} [$\times 10^{13}$ cm ⁻²]	T_{ex} [K]	N_{tot} [$\times 10^{14}$ cm ⁻²]	[CCH]/[CH ₃ OH]
+90	-90	14 ± 10	7 ± 3	8.5 ± 0.5	5 ± 2	7 ± 4
+90	-70	14 ± 2	9 ± 2	7 ± 1	7 ± 2	8 ± 3
+90	-50	17 ± 3	9 ± 2	7 ± 1	6 ± 2	7 ± 3
+90	-20	33 ± 11	14 ± 3	5 ± 1	7 ± 1	5 ± 1
+90	0	4 ± 1	8 ± 1	...
+70	-90	15 ± 2	7 ± 1	7 ± 1	5 ± 2	7 ± 3
+70	-70	14 ± 1	6 ± 1	7 ± 1	5 ± 1	8 ± 2
+70	-50	14.5 ± 1.5	7.5 ± 1.0	7 ± 1	6 ± 2	8 ± 3
+70	-20	16 ± 2	6.5 ± 1.0	7 ± 1	6 ± 2	9 ± 3
+70	0	5 ± 1	5 ± 1	...
+70	+20	12 ± 4	2 ± 1	...
+50	-90	9 ± 2	4 ± 1	6 ± 1	5 ± 1	12.5 ± 4
+50	-70	14 ± 1	9 ± 1	5 ± 1	6 ± 1	7 ± 1
+50	-50	13 ± 1	11 ± 2	7 ± 1	7 ± 2	6 ± 2
+50	-20	14 ± 1	9 ± 1	8 ± 1	7 ± 3	8 ± 3
+50	0	15 ± 3	5 ± 1	6 ± 1	7 ± 1	14 ± 2
+50	+50	6 ± 1	1.0 ± 0.2	...
+20	-90	8 ± 2	10.5 ± 1.0	4.5 ± 1.0	5 ± 1	5 ± 1
+20	-70	6.5 ± 1.0	9 ± 2	6 ± 1	6 ± 1	7 ± 2
+20	-50	14 ± 1	13 ± 2	6 ± 1	8 ± 2	6 ± 2
+20	-20	15 ± 2	16 ± 2	8.5 ± 1.0	11 ± 4	7 ± 3
+20	0	15 ± 2	12 ± 2	7 ± 1	9 ± 3	7.5 ± 3
+20	+20	6 ± 1	6 ± 1	...
+20	+50	4 ± 1	4 ± 1	...
+20	+70	4 ± 1	4 ± 1	...
0	-90	14 ± 2	6 ± 1
0	-70	8 ± 1	5 ± 1	15 ± 6	2 ± 1	4 ± 2
0	-50	12.5 ± 1.0	7 ± 1	15 ± 4	2 ± 2	3 ± 2
0	-20	14 ± 1	11 ± 2	8.5 ± 1.0	4 ± 2	4 ± 2
0	0	13 ± 1	9 ± 1	10 ± 2	10 ± 5	11 ± 6
0	+20	10 ± 2	3 ± 1	7 ± 1	7 ± 2	23 ± 10
0	+50	6 ± 1	4 ± 1	...
0	+70	5 ± 1	3 ± 1	...
-20	-70	4 ± 1	3 ± 1	...
-20	-50	13 ± 1	4 ± 1	5 ± 1	2 ± 1	5 ± 3
-20	-20	12 ± 1	6 ± 1
-20	0	5.5 ± 1.0	7 ± 1	...
-20	+20	8 ± 2	4 ± 1	7 ± 1	6 ± 2	15 ± 6
-20	+50	5 ± 1	5 ± 1	...
-20	+70	5 ± 1	5 ± 1	...
-50	-50	9 ± 1	1.0 ± 0.2	...
-50	-20	15 ± 2	8 ± 1	8 ± 1	2 ± 1	2.5 ± 1.0
-50	0	18 ± 2	9 ± 1	4 ± 1	9 ± 1	10 ± 2
-50	+20	5 ± 1	6 ± 1	...
-50	+50	17 ± 3	5 ± 1	5 ± 1	5 ± 1	10 ± 3
-50	+70	4 ± 1	6 ± 1	...
-50	+90	6 ± 1	5 ± 1	...
-70	-20	13 ± 1	5.5 ± 1	5 ± 1	2 ± 2	4 ± 4
-70	0	13 ± 1	14 ± 2	5 ± 1	8 ± 1	6 ± 1
-70	+20	11 ± 1	5 ± 1	4 ± 1	9 ± 1	18 ± 4
-70	+50	4 ± 1	10 ± 9	...
-70	+70	8 ± 2	2.5 ± 1	4 ± 1	8 ± 1	32 ± 13
-70	+90	5 ± 1	5 ± 4	...
-90	0	14.5 ± 1.0	12 ± 2	5.5 ± 1.0	5 ± 1	4 ± 1
-90	+20	4 ± 1	9 ± 1	...
-90	+50	6 ± 1	4 ± 1	...
-90	+70	14 ± 11	2 ± 1	5 ± 1	5 ± 1	25 ± 13
-90	+90	6 ± 1	4 ± 4	...

Notes. Only positions with results (at least three lines) are shown here.

ORion Alma New GEneration Survey (ORANGES)

The previous study showed that, for the highly UV-illuminated OMC-2/3 filament, single-dish observations of ethynyl radical (CCH) and methanol (CH_3OH) are not reliable to detect hot corino and WCCC candidates. We need to probe smaller scales to limit the contamination by the ubiquitous PDR surrounding the region. Interferometry is the best means, and the following two studies are based on interferometric observations.

The ORion Alma New GEneration Survey (ORANGES) aims to study the molecular content of solar-mass protostars located in the OMC-2/3 filament. It is the follow-up of the single-dish study (see Chapter 2). To determine the chemical nature of Orion solar-mass protostars, we need a high enough angular resolution to probe the inner part of their envelope. The ORANGES project consists of ALMA observations at 1.3mm with $0.25''$ (~ 100 au) angular resolution (P.I. Ana López-Sepulcre). A noteworthy fact about ORANGES is that this project has been designed to be directly comparable to the PERseus Alma CHEmistry Survey (PEACHES; P.I. N. Sakai). PEACHES is a follow-up project from the single-dish study of solar-mass protostars located in the Perseus Molecular Cloud (Higuchi et al. 2018) probing the complex chemistry towards the embedded protostars. The projects ORANGES and PEACHES are complementary as they target two very different environments. On the one hand, the Perseus Molecular Cloud is a loose protocluster devoid of massive stars, where only low-mass stars are forming. On the other hand, the OMC-2/3 filament is a dense cluster with high-mass ($\geq 8 M_{\odot}$) stars in its vicinity. Comparing the chemical nature of solar-mass protostars located in these two environments can give constraints to the role of the environment on the chemistry of the inner protostellar regions. The distance of the two clouds (between 234 and 331 pc for Perseus and ~ 400 pc for Orion) has been taken into account in the choice of both the sensitivity and the spatial resolution to avoid any biases. The ORANGES project thus probes the same angular scales (~ 100 au) and reach the same sensitivity as the PEACHES project (~ 22 mJy/beam for PEACHES and ~ 24 mJy/beam for ORANGES).

This chapter is divided into three sections. In Sect. 3.1, the ORANGES project is presented with the analysis of the dust continuum towards 16 OMC-2/3 solar-mass protostars. Several dust parameters and free-free emission are extracted towards the protostars and the main goal of the study is to understand whether the high UV-illumination of the filament impacts the dust properties of the embedded cores. The second ORANGES-based study is presented in Sec. 3.2 and focuses on the analysis of methanol. The study

aims to determine how many hot corinos are located in the OMC-2/3 filament and if the chemical nature of solar-mass protostars is affected by the environment in which they are located.

Finally, Sec. 3.3 concerns the hunt for WCCC in OMC-2/3. I mapped the CCH emission towards my source sample. As explained in the Section, the currently available ALMA data are insufficient to search for WCCC objects and we, therefore, need to ask for more observations. We describe in more detail the first two works which have been published (3.1) or have been submitted to be published (3.2).

3.1 ORANGES I. Dust continuum and free-free emission of OMC-2/3 filament protostars

Several physical properties can be extracted from the dust continuum analysis of protostellar sources. Specifically, the Spectral Energy Distributions (SEDs) (Sec. 2) are a powerful tool to classify Young Stellar Objects (YSOs) and derive their physical parameters (e.g. evolutionary age, bolometric luminosity), as well as several dust parameters (dust temperature, dust emissivity spectral index, mass). In particular, the dust emissivity spectral index is useful to probe dust properties and gives information on the dust grains size, shape and composition (e.g. [Draine 2006](#); [Compiègne et al. 2011](#); [Jones et al. 2017](#)). Values for the dust emissivity spectral index can vary from the commonly adopted value of 2 ([Hildebrand 1983](#); [Draine & Lee 1984](#)) and can be lower due to large optical depths, grain growth or a change in the grain composition (e.g. [Beckwith & Sargent 1991](#); [Ossenkopf & Henning 1994](#); [Draine 2006](#); [Guilloteau et al. 2011](#); [Testi et al. 2014](#); [Ysard et al. 2019](#)). The presence of thermal free-free emission can also be extracted from the SEDs. To do so, we need data points in the centimetre, where thermal free-free emission can dominate. Determining the presence (or absence) of free-free emission can provide hints on the youth of the source (e.g. [André et al. 1988](#); [Anglada 1995](#); [Anglada et al. 2018](#); [Shirley et al. 2007](#)). If we do not consider this free-free contribution, it can lead to an underestimation of spectral indices. Disentangling dust from free-free emission is therefore essential.

Studies on solar-mass protostars in low- to high-mass star-forming regions such as the OMC-2/3 filament are scarcer than in low-mass star-forming regions because they are farther and thus, more difficult to observe. The only studies available towards the OMC-2/3 region are those from the *Herschel* Orion Protostar Survey (HOPS; e.g. [Megeath et al. 2012](#); [Fischer et al. 2013](#); [Furlan et al. 2016](#)) and from the VANDAM survey (e.g. [Tobin et al. 2019, 2020](#)). The former aimed to classify and characterise the Orion protostars population, whilst the latter aimed to investigate the protostellar disks of Class 0 and I protostars.

The first ORANGES study reported in this section aims to characterise the dust properties of the OMC-2/3 sources, and to understand whether the small scale (≤ 100 au) dust properties are affected by the nearby HII regions, as this is the case for the line emission at larger scales (≤ 10000 au; see Chapter 2). To reach these goals, I have constructed millimetre to centimetre SEDs using archival ALMA (0.87mm) and VLA (9mm) data from the VANDAM survey ([Tobin et al. 2020](#)). I could derive basic properties for each source: multiplicity, constraints on the dust temperature and mass of the immediate region around the protostar (scale of 100-1000 au), dust emissivity spectral index and free-free emission.

The observations are centred on the nine solar-mass protostars detected with single-dish observations. Thanks to the high angular resolution of our ALMA observations, several sources showed multiplicity. Overall I detected 28 sources with 18 of them inside the primary beam. Not enough data were available for 2 of the 18 sources, so only 16 sources were analysed. Continuum maps of the sources show that most of them are well centrally peaked and have weaker dust emission extending asymmetrically. We found that 67% of our sources are multiple systems which is consistent with what was found in other studies (e.g. [Looney et al. 2000](#); [Maury et al. 2010](#); [Enoch et al. 2011](#); [Tobin et al. 2013](#)). We also found a marginal anticorrelation (Pearson coefficient of -0.58) between the number of protostars in each system and the distance of the system in the OMC-2/3 filament. The source multiplicity seems to be higher in the south of the filament, but the statistics are too poor to confirm this result.

From the SEDs, we could constraint several dust parameters. For sources showing no multiplicity at the resolution of our observations, we used their bolometric luminosity (from HOPS) to calculate the dust radiation temperature. This temperature can be used as an approximation of the dust temperature and provides additional constraints on this parameter. We could constraint the dust temperature in 11 out of the 16 sources. We classified six sources as hot ($T \geq 90$ K), three sources as warm ($T \geq 50$ K) and two sources as cold ($T < 50$ K).

Once the dust temperature is constrained, we could constrain all of the other parameters. The results are summarized below.

Dust emissivity spectral indexes For the dust emissivity spectral indexes, the majority of the sources (9/16) have low indexes (< 1). Different interpretations can explain the low index, such as grain growth (contribution from the disk), large optical depth and/or dust self-scattering, and dust grain composition (e.g. [Aannestad 1975](#); [Miyake & Nakagawa 1993](#); [Ossenkopf & Henning 1994](#); [Agladze et al. 1996](#); [Draine 2006](#); [Coupeaud et al. 2011](#); [Jones et al. 2013, 2017](#); [Wong et al. 2016](#); [Ysard et al. 2019](#)). Additionally, the intrinsic dependence between the dust temperature and the dust emissivity spectral index could also account for the low values of β (e.g. [Mennella et al. 1998](#); [Boudet et al. 2005](#)). We took into account the dust optical depth when constructing the SEDs so this parameter should not be the main explanation for the low dust emissivity spectral indexes.

Masses The derived (envelope+disk) masses range between 2×10^{-4} and $0.1 M_{\odot}$. They are for most cases in good agreement with those derived in [Tobin et al. \(2020\)](#).

Free-free emission Then, $\sim 31\%$ of the source sample show evidence of free-free emission. By comparing with the previous survey from [Reipurth et al. \(1999\)](#), we found some discrepancies. They detected free-free emission towards MMS2 while we did not and they did not detect free-free emission towards FIR2 and MMS5 while we did. This can be due to either a difference of sensitivity between the VANDAM survey observations and those of [Reipurth et al. \(1999\)](#) or the difference of frequency at which the observations were performed.

Evolutionary status Finally, we could confirm or correct the classification of the OMC-2/3 protostars from the extracted dust emissivity spectral indexes, the dust and bolometric temperature, and the presence of outflow from previous studies (e.g. [Williams et al. 2003](#);

[Takahashi et al. 2008](#); [Tobin et al. 2016b](#); [Tanabe et al. 2019](#); [Feddersen et al. 2020](#)). We confirm and corrected the evolutionary status for 10 and 6 sources, respectively.


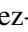



One of the goals of this study is also to understand whether the nearby HII regions affect the dust properties of the OMC-2/3 solar-mass protostars. First, our results show that colder sources seem to be located at the centre of the OMC-2/3 filament whilst the warmest sources seem to be located at the edges. However, due to the poor statistics and because we could not constraint enough the temperature for 5 sources, we cannot conclude whether the dust temperature of the sources is affected by the nearby HII regions.

In addition, we did not find any correlation between the (envelope+disk) mass and the position of the sources in the filament nor between the dust emissivity spectral index and the position of the sources in the filament. Our results show, therefore, that the small-scale dust properties of the OMC-2/3 solar-mass protostars are likely not affected by the nearby HII regions and that the formation of protostars takes place simultaneously throughout the filament. Evidently, larger statistical studies are needed to conclude whether the presence of external, nearby UV sources has any impact on the forming protostars.

The hereafter paper has been published in the *Astronomy & Astrophysics* 2021, 653, A117.

ORion Alma New GEneration Survey (ORANGES)

I. Dust continuum and free-free emission of OMC-2/3 filament protostars

M. Bouvier¹ , A. López-Sepulcre^{1,2} , C. Ceccarelli^{1,3} , N. Sakai⁴, S. Yamamoto^{5,6} , and Y.-L. Yang^{4,7} 

¹ Univ. Grenoble Alpes, CNRS, IPAG, 38000 Grenoble, France
e-mail: mathilde.bouvier@univ-grenoble-alpes.fr

² Institut de Radioastronomie Millimétrique (IRAM), 300 rue de la Piscine, 38406 Saint-Martin-D'Hères, France

³ CNRS, IPAG, 38000 Grenoble, France

⁴ RIKEN, Cluster for Pioneering Research, 2-1, Hirosawa, Wako-shi, Saitama 351-0198, Japan

⁵ Department of Physics, The University of Tokyo, 7-3-1, Hongo, Bunkyo-ku, Tokyo 113-0033, Japan

⁶ Research Center for the Early Universe, The University of Tokyo, 7-3-1, Hongo, Bunkyo-ku, Tokyo 113-0033, Japan

⁷ Department of Astronomy, University of Virginia, Charlottesville, VA 22904-4235, USA

Received 23 April 2021 / Accepted 28 June 2021

ABSTRACT

Context. The spectral energy distribution (SED) in the millimetre to centimetre range is an extremely useful tool for characterising the dust in protostellar envelopes as well as free-free emission from the protostar and outflow. Actually, the evolutionary status of solar-type protostars is often based on their SED in the near-infrared to millimetre range. In addition, the presence or absence of free-free emission can be considered an indicator of the source evolutionary stage (Class 0/I versus Class II/III). While many studies have been carried out towards low- and high-mass protostars, little exists so far about solar-type protostars in high-mass star-forming regions, which are likely to be representatives of the conditions where the Solar System was born.

Aims. In this work, we focus on the embedded solar-type protostars in the Orion Molecular Cloud (OMC) 2 and 3 filaments, which are bounded by nearby HII regions and which are, therefore, potentially affected by the high-UV illumination of the nearby OB stars. We use various dust parameters to understand whether the small-scale structure (≤ 1000 au) and the evolutionary status of these solar-type protostars are affected by the nearby HII regions, as is the case for the large-scale ($\leq 10^4$ au) gas chemical composition.

Methods. We used the Atacama Large (sub-)Millimeter Array (ALMA) in the 1.3 mm band (246.2 GHz) to image the continuum of 16 young (Class 0/I) OMC-2/3 solar-type protostars, with an angular resolution of $0.25''$ (100 au). We completed our data with archival data from the ALMA and VLA VANDAM survey of Orion Protostars at 333 and 32.9 GHz, respectively, to construct the dust SED and extract the dust temperature, the dust emissivity spectral index, the envelope plus disk mass of the sources and to assess whether free-free emission is contaminating their dust SED in the centimetre range.

Results. From the millimetre to centimetre range dust SED, we found low dust emissivity spectral indexes ($\beta < 1$) for the majority of our source sample and free-free emission towards only 5 of the 16 sample sources. We were also able to confirm or correct the evolutionary status of the source sample reported in the literature. Finally, we did not find any dependence of the source dust parameters on their location in the OMC-2/3 filament.

Conclusions. Our results show that the small-scale dust properties of the embedded OMC-2/3 protostars are not affected by the high-UV illumination from the nearby HII regions and that the formation of protostars likely takes place simultaneously throughout the filament.

Key words. dust, extinction – methods: observational – stars: protostars – stars: solar-type

1. Introduction

Spectral energy distributions (SEDs) from young stellar objects has historically been the main means for classifying their evolutionary status. Notably, the currently used classification in pre-stellar cores and Class 0 to II protostars is largely based on the source SED (e.g. Lada & Wilking 1984; Adams et al. 1987; Lada 1987; André et al. 1993; André & Montmerle 1994; Evans et al. 2009; Dunham et al. 2014). Although studies of gaseous species can provide invaluable informations on the physical, dynamical, and chemical structures of young protostars, the SED remains an important tool for assessing the protostar evolutionary status for several reasons. First, only the measure of the SED from millimetre (mm) to infrared (IR) wavelengths can provide the luminosity of the young accreting protostar: the smaller the luminosity, the smaller the mass of the central object and

its evolutionary age (André et al. 1993; Saraceno et al. 1996). Second, the mm–IR SED can provide the averaged temperature of the dusty envelope plus disk system surrounding the central future star: the lower the temperature the younger the protostar (e.g. Myers & Ladd 1993; Chen et al. 1995; Dunham et al. 2014). Third, the mass of the envelope plus disk system can be estimated by the mm SED once the dust temperature is constrained: the smaller the mass with respect to the guessed central object mass, the more evolved the protostar (e.g. André et al. 1993; Terebey et al. 1993; André & Montmerle 1994; Greene et al. 1994).

Furthermore, dust grains evolve along with the host protostar, both because of the appearance and evolution of icy mantles coating the dust grains (made up of silicates and carbonaceous material: Hoyle & Wickramasinghe 1969; Jones et al. 2013, 2017) and because of the coagulation process in the cold and

dense regions of the protostar (e.g. Ossenkopf & Henning 1994; Ormel et al. 2009; Boogert et al. 2015). The SED is, again, a major means of studying the grain evolution in protostars and, more relevant to the present work, the coagulation process (e.g. Miyake & Nakagawa 1993; Ossenkopf & Henning 1994; Draine 2006; Jones et al. 2017). Specifically, very often the average grain sizes are estimated by the measurement of the dust emissivity spectral index, β , in the radio to millimetre wavelength range (e.g. Weintraub et al. 1989; Beckwith & Sargent 1991).

Finally, free-free emission is a mechanism that can dominate the radio emission. It can be extracted from the SED, providing precious information on the evolutionary status of protostars. It probes the ionised gas close to the central object, due to the presence of ionised jets, compact HII regions, or photoevaporating winds, phenomena linked with young protostars (i.e. Class 0 and I sources; e.g. André et al. 1988; Anglada 1995; Anglada et al. 2018; Shirley et al. 2007; Pascucci & Gorti 2012). As a consequence, the radio–mm SED is necessary to disentangle the dust from the free-free emission.

In the past such studies have focused on nearby (≤ 300 pc) low-mass star-forming regions, both because they are easier to obtain from an observational point of view and because they potentially tell us what could have been the first phases of the Solar System birth (e.g. Li et al. 2017; Murillo et al. 2018; Hernández-Gómez et al. 2019). As now recognised by several authors, the Solar System was actually born in a region containing numerous low-, intermediate-, and high-mass stars (e.g. Adams 2010; Pfalzner et al. 2015). The high-mass stars may have an effect on the physico-chemical conditions of the dusty protostellar envelopes lying nearby, through e.g. higher temperatures, UV radiation, or winds. In particular, several studies have shown an influence of the external UV irradiation from massive stars on the dust temperature of cores or disks (Walsh et al. 2013; Brand et al. 2021; Haworth 2021). Studies of solar-mass protostars in this type of star-forming regions are scarcer because they are more distant, and therefore observations are more difficult.

The closest (about 400 pc) low- to high-mass star-forming region is the Orion Molecular Cloud (OMC) complex. In particular, OMC-2 and OMC-3 (also known as OMC-2/3; Mezger et al. 1990) are very active sites of star formation. They are distributed along a filament to the north of the famous BN-KL object. A few studies of OMC-2/3 have appeared in the literature aiming to classify and characterise the population of Orion protostars, which is the case of the *Herschel* Orion Protostar Survey (e.g. Megeath et al. 2012; Fischer et al. 2013; Furlan et al. 2016), and to investigate the protostellar disk towards the Class 0 and I protostars of the Orion A and B molecular clouds, which is the case for The VLA/ALMA Nascent Disk and Multiplicity (VANDAM) Survey of Orion Protostars (e.g. Tobin et al. 2019, 2020).

In this work, we focus on the small-scale structure (≤ 1000 au) of more than a dozen embedded protostars in OMC-2/3, more specifically on their evolutionary status, and we aim to understand whether there is an evolutionary trend along the filament and whether the nearby massive star can affect the dust properties of the protostars. To this end, we used new Atacama Large (sub-)Millimetre Array (ALMA) observations, part of our project ORANGES, and archival data from both ALMA and the Very Large Array (VLA) to obtain the dust SED and basic properties of each source: multiplicity, constraints on the dust temperature at 100–1000 au, dust emissivity spectral index β , free-free emission. Putting together these properties, we were able to constrain the evolutionary status of the targeted protostars and whether the position along the OMC-2/3 filament impacts it.

This paper is organised as follows. We first report a literature review of the dust temperature, dust emissivity spectral index β , envelope plus disk (envelope + disk) mass, and free-free emission as a function of the evolutionary status in Sect. 2. In Sect. 3, we describe the ORANGES survey and the selected source sample, and we report a review of what is known about them in terms of dust properties and what is still missing from these previous studies. The observations and archival data used are presented in Sect. 4. The results of the new ALMA observations, with the source maps, and the source sizes and flux densities extracted, are presented in Sect. 5. The source multiplicity and properties derived by the dust SED analysis (dust temperature, dust emissivity spectral index, and masses), as well as the construction of the dust SEDs, are reported in Sect. 6. Finally, we discuss the results in Sect. 7 before concluding in Sect. 8.

2. Review of protostar properties versus evolutionary status

Several parameters have an impact on the shape of SEDs, such as the dust temperature and emissivity spectral index across the protostar, the (envelope + disk) mass of the source and the presence of free-free emission. We present here the parameters we focus on in this work and how they evolve with the different evolutionary stages.

Dust temperature. The dust temperature, T_d , has an impact on the shape of the SED by setting the position of its peak. We can use the dust temperature to distinguish between pre-stellar cores ($T_d \leq 10$ K) and more evolved stages (i.e. Class 0/I/II, $10 \leq T_d \leq 100$ K; e.g. Ceccarelli et al. 2000; Jørgensen et al. 2002; Bergin et al. 2007; Dullemond & Monnier 2010; Crimier et al. 2010); however, it is hard to distinguish between each of the protostellar stages (Classes 0, I, and II). In that case the bolometric temperature, T_{bol} , defined as the temperature of a black body with the same mean frequency as the observed SED (Myers & Ladd 1993; André et al. 2000) is more useful. Chen et al. (1995, 1997), among others, showed that young stellar objects (YSOs) have different bolometric temperatures depending on their stages. Roughly speaking, Class 0 sources have $T_{bol} < 70$ K, Class I sources have $70 < T_{bol} < 650$ K, and Class II and III sources have $T_{bol} > 650$ K.

Dust emissivity spectral index. The dust emissivity spectral index, β , is useful to probe dust properties such as grain size, composition, and shape (e.g. Draine 2006; Compiègne et al. 2011; Jones et al. 2017). While a fixed value of $\beta = 2$ is commonly adopted in the literature (Hildebrand 1983; Draine & Lee 1984), a change in the composition of the dust grains, large optical depths, or grain growth are usually responsible for lower values of β (e.g. Beckwith & Sargent 1991; Ossenkopf & Henning 1994; Draine 2006; Guilloteau et al. 2011; Testi et al. 2014; Ysard et al. 2019). On the other hand, the growth of the icy grain mantle can explain higher values ($\beta \geq 2$; e.g. Kuan et al. 1996; Lis & Menten 1998). In this context, the dust emissivity spectral index can change depending on the evolutionary stage of the sources: The highest values have been measured towards pre-stellar cores ($1 \leq \beta \leq 2.7$; e.g. Lis et al. 1998; Shirley et al. 2005, 2011; Schnee et al. 2010; Sadavoy et al. 2013; Bracco et al. 2017), while the lowest values have been measured towards Class II protostars ($0 \leq \beta \leq 1$; e.g. Ricci et al. 2010; Bracco et al. 2017; Tazzari et al. 2021). Class 0 and I protostars show intermediate values ($\beta \sim 1.7$ –2; e.g. Natta et al. 2007).

Dust mass. In young protostars, the envelope mass dominates over that of the disk. Considering that our observations are not sensitive enough to distinguish between the two components, we focus here only on how the envelope mass evolves with the evolutionary stage of protostars. First during the Class 0 phase, the envelope mass dominates the object mass ($M_{\text{env}} \geq M_*$), whilst for Class I sources the envelope mass is lower ($M_{\text{env}} \leq M_*$ and $M_{\text{env}} \geq 0.1 M_\odot$; André et al. 1993; Enoch et al. 2009). Then, in Class II and III objects the envelope has almost entirely dissipated ($M_{\text{env}} \leq 0.1 M_\odot$; Greene et al. 1994; Crapsi et al. 2008) and the mass is dominated by that of the central object.

Free-free emission. Finally, the presence of thermal (free-free) emission results in a shallower slope of the SED in the millimetre to centimetre domain and can be used to determine the evolutionary status of the object. This free-free emission is thought to be produced by jets or winds associated with the outflows driven by Class 0 and I sources (Anglada 1996; Pech et al. 2016; Tychoniec et al. 2018a) or could be associated with the photoevaporation region of Class I disks (e.g. Pascucci & Gorti 2012; Anglada et al. 2018). At later stages (Class II/III sources), radio continuum emission due to gyrosynchrotron radiation can be detected, but is characterised by a different spectral index (Feigelson & Montmerle 1985; André et al. 1988; Pech et al. 2016). Finally, the absence of such compact radio emission in a source indicates that the latter is likely a pre-stellar core (Yun et al. 1996).

3. The ORANGES project

3.1. Description of the project

The Orion ALMA New Generation Survey (ORANGES) is a project aiming to study the molecular content, on small scales (≤ 1000 au), of the solar-type protostars located in the OMC-2/3 filament. It follows a large-scale ($\leq 10^4$ au) study of these same protostellar cores (Bouvier et al. 2020). The focus of this previous study, carried out with the single-dish telescopes IRAM-30m¹ and Nobeyama-45m², was to identify Warm Carbon Chain Chemistry (WCCC) protostars and hot corino candidates using observations of two species, CCH and CH₃OH. Briefly, these two molecules are expected to be abundant in WCCC protostars and hot corinos, respectively. Therefore, the use of the relative abundance of these two species is thought to be a good indicator of the chemical nature of solar-type protostars (e.g. Higuchi et al. 2018). However, given the relatively large spatial scales probed by the single-dish observations ($\sim 10^4$ au) and the highly UV illuminated OMC-2/3 region, we found that the line emission from the two species is dominated by the photodissociation region (PDR), and not by the protostars. Therefore, in order to assess the chemical nature of the OMC-2/3 solar-type protostars, small-scale (≤ 1000 au) interferometric observations are mandatory to get rid of the PDR contamination.

The ORANGES project consists of new ALMA observations at 246.2 GHz towards the same sample of sources studied in Bouvier et al. (2020). The spatial resolution is about 0."25 equivalent to about 100 au at the OMC-2/3 distance. As said, our ultimate goal is to assess the number of WCCC sources versus hot corinos in the OMC-2/3 region, which is the best known analogue of the Solar System progenitor. To achieve this goal

we designed the spectral setup to make the distinction between hot corinos and WCCC objects, which will be presented in a forthcoming paper on the molecular content.

In the following we briefly present the OMC-2/3 region and then introduce the ORANGES source sample (Sect. 3.2). We then review the previous continuum studies obtained towards the sample sources (Sect. 3.3), and finally we summarise what is still poorly or totally unknown of them with respect to the dust (Sect. 3.4).

3.2. Source sample

The OMC-2/3 filament is located at a distance of (393 ± 25) pc from the Sun (Großschedl et al. 2018) and it is bounded by three HII regions: NGC1977 to the north, the Trapezium OB cluster to the south, and M43 to the southeast. It is the closest analogue to our Sun's birth environment, hence the high interest to study this region. OMC-2/3 is one of the most active star-forming regions (e.g. Rayner et al. 1989; Bally et al. 1991; Jones et al. 1994; Ali & Depoy 1995) in which a wealth of low-mass protostars have been detected (e.g. Mezger et al. 1990; Chini et al. 1997; Lis et al. 1998; Nielbock et al. 2003). From these studies we previously selected nine bona fide solar-type protostars to study their molecular content (see above; Bouvier et al. 2020). We applied three criteria to select the sources: (1) detection in the (sub-)mm continuum emission; (2) estimated (from the large-scale continuum) envelope masses $\leq 12 M_\odot$; (3) bona fide Class 0 and I protostars, based on their estimated bolometric temperature. In ORANGES we targeted the nine sources, centring the observations on the protostar coordinates (Table 1) derived from previous single-dish observations (Chini et al. 1997; Lis et al. 1998; Nielbock et al. 2003).

3.3. Previous continuum studies on the sample sources

All the properties previously known and described below are summarised in Table 2 (see also Sect. 6).

Source classification. The nine selected sources are also part of the HOPS survey (e.g. Megeath et al. 2012; Fischer et al. 2013; Furlan et al. 2016), which used *Herschel*³ observations. We therefore already have some information on those protostars, even though the *Herschel* observations cannot disentangle multiple sources in the *Herschel* beam ($5.2\text{--}12''$). HOPS provided estimates of the sources evolutionary classification based on their bolometric luminosity, L_{bol} ; bolometric temperature, T_{bol} ; and envelope masses, M_{env} . From the HOPS survey, six of our nine sources were classified as Class 0, two as Class I, and one as a Flat spectrum source. The derived bolometric luminosities and temperatures range from $5.7 L_\odot$ to $23.2 L_\odot$ and from 28.4 K to 186.3 K, respectively, and the envelope masses range from $\sim 0.1 M_\odot$ to $\sim 5.6 M_\odot$.

Dust temperature. Large-scale (> 1000 au) studies were performed to derive the dust temperature and dust emissivity spectral index, and to determine whether free-free emission is present towards those sources. First, the previously derived dust temperature from continuum emission along the filament is typically about 20–30 K (Chini et al. 1997; Lis et al. 1998; Johnstone & Bally 1999; Schuller et al. 2021), and similar values were found for the kinetic temperature using molecular lines (e.g. Li et al. 2013; Hacar et al. 2018), although Shimajiri et al. (2009) found a warmer temperature up to 50 K towards the FIR6 region.

¹ <https://www.iram-institute.org/>

² <https://www.nro.nao.ac.jp/~nro45mrt/html/index-e.html>

³ <https://sci.esa.int/web/herschel>

Dust emissivity spectral index. Several studies, covering wavelengths between 350 μm and 2 mm, found values for the dust emissivity spectral index ranging from 1 to 2 (Chini et al. 1997; Lis et al. 1998; Johnstone & Bally 1999). Later, Schnee et al. (2014) measured the dust emissivity spectral index of the OMC-2/3 sources between 1.2 and 3.3 mm. They found a median value for the index of 0.9 on 0.1 pc scales, lower than what was previously measured. On the other hand, Sadavoy et al. (2016) used *Herschel* data between 160 and 550 μm with their IRAM-30m data at 2 mm (150 GHz) and derived indexes around 1.6–1.8. Recently, Mason et al. (2020) found that the discrepancy between the values from Schnee et al. (2014) and Sadavoy et al. (2016) was due to abnormally high 3.3 mm (90.9 GHz) emission in OMC-2/3. The reason of the excess emission at 90.9 GHz is not entirely clear, although the possibility of the presence of amorphous dust grains could be an explanation (e.g. Mény et al. 2007; Coupeaud et al. 2011; Paradis et al. 2011).

Free-free emission. Finally, using VLA, Reipurth et al. (1999) detected 8.3 GHz emission towards 11 sources associated with the OMC-2/3 filament, among which there are three of our protostars: MMS2, MMS9, and FIR1a. They attributed the 8.3 GHz free-free emission as probably due to shocks caused by the out-flowing material.

3.4. Limits of the previous studies and novelty of ORANGES

Tobin et al. (2020) published high-resolution continuum observations towards our source sample as part of the VANDAM survey. The two surveys, VANDAM and ORANGES, are complementary; the VANDAM survey aims to characterise the dust physical properties of the protostellar disks of the Orion protostars (masses, radii), whereas ORANGES focuses on the dust physical properties of the protostars (inner envelope+disk), specifically of the sources on a larger scale. The different objectives of the two surveys make them highly complementary, and also means that the ORANGES survey provides novel important information. We describe the specific differences and the ORANGES novelties below.

First, in order to derive the disk masses, Tobin et al. (2020) used the bolometric luminosity of each system to derive the dust temperature. However, several of our sources being multiple systems, the bolometric luminosity is not accurate for each of the objects in each system. We therefore aim to constrain the dust temperature for each of our sources without using bolometric luminosities.

Second, based on the study from Tychoniec et al. (2018b) in the Perseus region, they assumed the 32.9 GHz continuum emission to be dominated by the dust emission even though they mention the possibility of free-free contamination at this wavelength. Therefore, the spectral indexes they provide between 333 and 32.9 GHz might not be accurate if the 32.9 GHz emission is contaminated by free-free emission. We thus aim to provide a more reliable dust emissivity spectral index for each of our sources, and use these indexes to confirm or correct the evolutionary stages of the sources.

Finally, Tobin et al. (2020) provide the disk masses assuming optically thin dust emission at 333 GHz. Therefore, the derived disk masses can be considered only as lower limits if the assumption does not hold and we aim to better constrain the (envelope + disk) masses of our source sample.

In order to better constrain the physical properties of the ORANGES sample, we chose to complete our 246.2 GHz

ALMA data with the archived data from the VANDAM survey (Tobin 2019a,b). The different sets of observations are described in the next section.

4. Observations and data reduction

4.1. ALMA observations at 246.2 GHz

The ALMA ORANGES observations were performed on October 27–29, 2016, during Cycle 4, in Band 6 (~ 250 GHz), under the ALMA project 2016.1.00376.S. A total of 42 antennas of the 12m array were used with a baseline length range of 18.6m–1100m. The integration time on source is ~ 19 min for each source. As the present study concerns the dust continuum analysis, we present only the setup of the continuum spectral window. With a total bandwidth of ~ 2 GHz, the continuum spectral window was centred at 246.2 GHz and with a spectral resolution of 0.977 MHz (~ 1.2 km s $^{-1}$). The band-pass and flux calibrators used were J0510+1800 and J0522-3627, and the phase calibrators used were J0607-0834 and J0501-0159. The flux calibration error is estimated to be better than 10%. The precipitable water vapour (PWV) was typically less than 1 mm, the system temperatures less than 200 K, and the phase root mean square (rms) less than 50°.

We used the Common Astronomy Software Application (CASA; McMullin et al. 2007) for the data calibration. We then exported the calibrated visibility tables to the GILDAS⁴ format, and performed the imaging in MAPPING. We produced continuum images by averaging line-free channels in the visibility plane. We produced the continuum images using natural weighting (via the CLEAN procedure). Phase self-calibration was performed for all sources with a signal-to-noise ratio (S/N) > 100 . Only CSO3 did not fulfil the criteria. We applied three successive rounds of calibration with solution intervals in the range 300–60 s. Solution intervals were adjusted from one source to another, depending on the S/N and of the number of flagged solutions. This resulted in a significant improvement in the S/N for the continuum images, from 24% (FIR1a) to 293% (SIMBA-a). The maps shown in this paper are not corrected for the primary beam, but we took into account the correction to measure the flux densities. The resulting synthesised beam for each field, as well as the noise rms, are presented in Table 1. The half power primary beam size is 25.6''.

4.2. Archival data at 333 and 32.9 GHz

Our source sample is part of the VLA/ALMA Nascent Disk and Multiplicity (VANDAM) Survey of Orion Protostars. In order to be able to construct the dust SED of the sources in the centimetre to millimetre range, we used archival data from the VANDAM Survey (Tobin et al. 2020) at 333 GHz (0.87mm) from ALMA, and we used the data at 32.9 GHz (9mm) from the VLA observations.

We used the *robust*=2 (equivalent to natural weighting) cleaned images, for both the ALMA and the VLA data. Both sets of archival data are taken from the Harvard Dataverse⁵ (Tobin 2019a,b). The angular resolutions are 0.1'' (~ 39 au) and 0.08'' (~ 31 au) at 333 GHz and at 32.9 GHz respectively. The baseline length ranges are 15–3700 m for ALMA and 0.68–36.4 km for VLA (A-configuration). The resulting synthesised beam for each

⁴ <http://www.iram.fr/IRAMFR/GILDAS>

⁵ <https://dataverse.harvard.edu>

Table 1. Continuum beam parameters at 246.2 GHz, 333 GHz, and 32.9 GHz, as well as rms and centre of observations used.

Field	Beam size ($''$)	PA ($^\circ$)	rms ($\mu\text{Jy beam}^{-1}$)	RA (J2000)	Dec (J2000)
ALMA 246.2 GHz					
CSO33	0.32×0.27	-77	44	05:35:19.5	-05:15:35.0
FIR6c	0.32×0.28	90	60	05:35:21.6	-05:13:14.0
FIR2	0.32×0.27	-76	54	05:35:24.4	-05:08:34.0
FIR1a	0.32×0.27	-76	58	05:35:24.4	-05:07:53.0
MMS9	0.32×0.27	-74	50	05:35:26.2	-05:05:44.0
MMS5	0.32×0.28	-76	80	05:35:22.5	-05:01:15.0
MMS2	0.32×0.27	-77	60	05:35:18.5	-05:00:30.0
CSO3	0.32×0.27	-74	49	05:35:15.8	-04:59:59.0
SIMBA-a	0.32×0.27	-77	50	05:35:29.8	-04:58:47.0
ALMA 333 GHz					
CSO33	0.12×0.12	29	580	05:35:19.465	-05:15:32.72
FIR6c	0.13×0.12	86	710	05:35:21.400	-05:13:17.50
FIR2	0.12×0.12	26	277	05:35:24.306	-05:08:30.58
FIR1a-a	0.12×0.12	25	518	05:35:25.607	-05:07:57.32
FIR1a-b	0.13×0.12	84	640	05:35:23.927	-05:07:53.47
MMS9	0.12×0.12	23	590	05:35:25.824	-05:05:43.65
MMS5	0.12×0.12	21	335	05:35:22.430	-05:01:14.15
MMS2	0.12×0.12	17	296	05:35:18.317	-05:00:32.97
SIMBA-a	0.12×0.12	13	280	05:35:29.720	-04:58:48.79
VLA 32.9 GHz					
CSO33	0.11×0.08	-31	11	05:35:19.466	-05:15:32.72
FIR6c	0.10×0.07	-15	17	05:35:21.400	-05:13:17.50
FIR2	0.09×0.07	31	8	05:35:24.299	-05:08:30.73
FIR1a	0.09×0.06	14	11	05:35:23.926	-05:07:53.47
MMS9	0.12×0.07	35	8	05:35:25.823	-05:05:43.65
MMS5	0.11×0.06	0	11	05:35:22.891	-05:01:24.21
MMS2	0.11×0.08	-33	10	05:35:18.915	-05:00:50.86
CSO3	0.12×0.07	42	14	05:35:16.152	-05:00:02.26
SIMBA-a	0.09×0.06	-1	8	05:35:29.720	-04:58:48.79

Notes. Information on the beam size and rms at 333 and 32.9 GHz are issued from the archived images used (Tobin 2019a,b), whilst information on the centre of observations for the two sets of data are from Tobin et al. (2020).

field and each interferometer, as well as the rms noise, are presented in Table 1. More observational details are given in Tobin et al. (2020).

5. Results

5.1. Maps

We observed nine fields centred on the nine protostars of Table 1. Thanks to the achieved angular resolution of $0.25''$ (~ 100 au), many multiple sources could be disentangled. The complete list of detected sources in each field is listed in Table A.1. In total, we detected 28 sources, of which 18 are located inside the primary beam (see Fig. A.1). The following analysis focuses on the latter, with the exception of FIR6c-c and MIR4. For FIR6c-c, no clear counterparts were found in the 333 and 32.9 GHz data. For MIR4, the source is not included in the 333 GHz maps and we did not find any counterpart at 32.9 GHz. Therefore, we analysed 16 protostars in this work. Their coordinates and previously attributed parameters are listed in Table 2.

The ORANGES 246.2 GHz continuum maps of the 16 sources are shown in Fig. 1, where the archival 333 GHz ALMA and 32.9 GHz VLA data are superposed. Most of the sources that appeared to be single sources with single-dish observations are multiple systems. Some sources are separated by about 1000 to ~ 5500 au in the plane of the sky (e.g. CSO33, FIR6c, FIR1a, MMS9); others have smaller projected separations of less than ~ 700 au, (MMS2-a with MMS2-b, and MMS9-b with MMS9-c) or even less than ~ 100 au (CSO33-b and MMS2-a). Finally, one source, CSO3-b, is part of a binary system, whose other component, CSO3-a, is about 7000 au away and out of the primary beam (see Fig. A.1).

All the sources are detected at a $\geq 10\sigma$ level. We resolve all the sources at 246.2 GHz, except CSO33-c and MMS9-c, which we only marginally resolve. All of the sources are clearly centrally peaked, except CSO3-b for which the continuum is more diffuse. For most of the sources the dust emission at 246.2 GHz always extends asymmetrically, and in some cases neighbouring sources are ‘linked’ by the dust emission (CSO33-a with CSO33-b, MMS9-a with MMS9-b and MMS9-c, and MMS2-a with MMS2-b). MMS9-d and CSO33-c are the only two sources of the sample that are compact with no dust emission extension around them. Some sources are clearly elongated at 246.2 GHz, such as FIR6c-a, CSO33-a, MMS9-a, and FIR1a-b. For the first two sources, this is due to the fact that we resolve the protostellar disk emission (Tobin et al. 2020; Sheehan et al. 2020). The protostellar disk of MMS9-a is also resolved, but it is more obvious when looking at the 333 GHz emission. CSO3-b is the only source for which the 333 GHz emission is not detected, whilst MMS9-d is the only source for which the 32.9 GHz emission is not detected.

Finally, the 333 and 32.9 GHz emission are always more compact than the 246.2 GHz emission. This may be due to several factors. The first factor would be that VLA observations are more sensitive to larger grains than ALMA observations, therefore tracing a slightly different region than with ALMA observations. Another factor could be the difference in sensitivity: VANDAM ALMA data at 333 GHz are ten times less sensitive than our ALMA data at 246.2 GHz. Finally, the maximum recoverable scale (MRS) of the different observations can also play a role. Whilst the MRS of our ALMA observations is $\sim 9''$ (3500 au), the MRS of the VANDAM observations are $\sim 7''$ (2700 au) at 333 GHz and $\sim 5''$ (2100 au) at 32.9 GHz. Our 246.2 GHz data are thus likely filtering less emission compared to those at 333 and 32.9 GHz. In summary, the sources have very different morphologies, therefore constituting a very interesting zoo.

5.2. Flux densities and source size derivation

In order to derive a meaningful dust SED, the flux density at each frequency (333, 246.2, and 32.9 GHz) has to be measured with the same source size. Considering that we have different sets of observations with different angular resolutions and in order to remain consistent in the size choice when measuring the flux density at each wavelength and for each source, we used the method described below.

We used the ORANGES data set to perform a fit of the 16 sources in the visibility plane with the task *uv_fit* in MAPPING from the GILDAS package. We chose to fit each source with either a point source or a simple 2D Gaussian function, circular or elliptical depending on what was the best fit. The source size (i.e. the size of the fitted component) is given as an output of the fit, except when using the point source function. All

Table 2. 16 analysed sources, their coordinates, and the known parameters from the *Herschel* HOPS observations.

Source	RA (J2000)	Dec (J2000)	HOPS name ^(a,b)	<i>Herschel</i> classification ^(b)	$L_{\text{bol}}^{(b)}$ (L_{\odot})	$T_{\text{bol}}^{(b)}$ (K)	$M_{\text{env}}^{(b)}$ (M_{\odot})	Notes
CSO33-a	05:35:19.41	-05:15:38.41	HOPS-56-B	0	23.3	48.1	0.8	
CSO33-b	05:35:19.48	-05:15:33.08	HOPS-56-A-A/B/C	0	23.3	48.1	0.8	triple system
CSO33-c	05:35:19.81	-05:15:35.22	V2358 Ori	0	23.3	48.1	0.8	
FIR6c-a	05:35:21.36	-05:13:17.85	HOPS-409	0	8.2	28.4	1.8	
FIR2	05:35:24.30	-05:08:30.74	HOPS-68	I	5.7	100.6	1.0	
FIR1a-a	05:35:24.87	-05:07:54.63	HOPS-394-B	0	6.6	45.5	0.2	
FIR1a-b	05:35:24.05	-05:07:52.07	HOPS-394-A	0	6.6	45.5	0.2	
MMS9-a	05:35:25.97	-05:05:43.34	HOPS-78-A	0	8.9	38.1	0.2	
MMS9-b	05:35:26.15	-05:05:45.80	HOPS-78-B	0	8.9	38.1	0.2	
MMS9-c	05:35:26.18	-05:05:47.14	HOPS-78-C	0	8.9	38.1	0.2	
MMS9-d	05:35:25.92	-05:05:47.70	HOPS-78-D	0	8.9	38.1	0.2	no VLA counterpart
MMS5	05:35:22.47	-05:01:14.34	HOPS-88	0	15.8	42.4	0.4	
MMS2-a	05:35:18.34	-05:00:32.96	HOPS-92-A-A/B	Flat ^(d)	20.1	186.3	5.6	binary ^(c)
MMS2-b	05:35:18.27	-05:00:33.95	HOPS-92-B	Flat	20.1	186.3	5.6	
CSO3-b	05:35:16.17	-05:00:02.50	HOPS-94	I	6.7	123	0.1	no 333 GHz counterpart
SIMBA-a	05:35:29.72	-04:58:48.60	HOPS-96	0	6.2	35.6	1.9	

Notes. ^(a)Fischer et al. (2013). ^(b)Furlan et al. (2016). ^(c)Tobin et al. (2020). ^(d)Protostars characterised by a flat spectral energy distribution (SED) in λF_{λ} from $\sim 2 \mu\text{m}$ to $24 \mu\text{m}$.

visibilities are considered, but a single-component fit corresponds to the most compact and intense emission component of the sources. The nature of the fitted component is likely the disk + inner envelope (warmest and densest part of the envelope). The extended envelope, which makes only a small contribution, remains thus in the fit residuals. For the sources fitted with a point source function we used the deconvolved size given at 333 GHz (or 32.9 GHz if not available at 333 GHz) in Tobin et al. (2020) since these observations have a smaller beam than ours. Once the size for each source is determined, we convolved it with the beam size of each data set (333 GHz, 246.2 GHz and 32.9 GHz; see Table 1 using the formula $\theta_{\text{obs}} = \sqrt{\theta_{\text{beam}}^2 + \theta_{\text{source}}^2}$; this resulted in an ellipse of size $\theta_{\text{obs-MAJ}} \times \theta_{\text{obs-MIN}}$ that we used on the image plane to measure the flux density with the procedure *flux* in MAPPING. An example of *uv* fit result for one of the source samples is shown in Fig. B.1. We verified a posteriori that the flux density given by the *uv* fit and the one measured on the image plane are consistent within 30% at 246.2 GHz. This is due to the difference between the area under the full width at half maximum (FWHM) of a Gaussian and the area under a total Gaussian, in which the flux densities are measured on the image plane and in the visibility plane respectively. Some of our sources show a difference of up to 50%, likely because those sources have the most extended continuum emission.

The flux density uncertainties include a 10% amplitude calibration error. For the derived source sizes, we used the 10% calibration error even if the size was taken from Tobin et al. (2020) since they estimated their calibration to be better than 10% as well. The errors given by the fit in the visibility plane are negligible as they tend to be less than 1%. The derived flux densities at 333, 246.2, and 32.9 GHz, the derived source sizes, and the fitting results are summarised in Table 3.

5.3. Specific cases

Several specific cases arose during the source fitting. First, for CSO33-a, FIR1a-b, MMS9-a, and MMS9-b we could not get a satisfactory fit for the sources. We thus used the

deconvolved sizes given in Tobin et al. (2020). Second, the source FIR1a-a could be fitted only with a point source function. However, no deconvolved size was available in Tobin et al. (2020). We then fitted the source with an arbitrary chosen size, covering the whole compact emission at 246.2 GHz (corresponding to about a 50σ contour). Last, CSO33-b is a marginally resolved triple system at 246.2 GHz, whilst it is resolved at 333 GHz. We chose to fit the triple system with an arbitrary size that was large enough to include the three components of the system. Hence, for FIR1a-a and CSO33-b, caution was taken for the analysis of their results as the sizes chosen were very likely overestimated, which would therefore lead to underestimating the dust optical depths, H_2 column densities, and the (envelope + disk) masses. For the same reason, the dust emissivity spectral indexes for those two sources do not necessarily represent the real values.

6. Physical parameters of the sources

6.1. Source multiplicity

In the nine initially targeted fields, we found six multiple systems at a spatial resolution of $0.25''$ (~ 100 au), which is 67% of the source sample (with a statistical error of 33%). Among these multiple systems, there are three binaries (CSO3, MMS2, and FIR1a), two triple systems (CSO33 and FIR6c), and one quadruple system (MMS9). Our resolution does not allow us to disentangle the triple system of CSO33-b and the binary system of MMS2-a (linear separation less than 100 au), which are both resolved in the VANDAM survey with $0.1''$ resolution (Tobin et al. 2020).

Other studies have been performed in order to assess the multiplicity of Class 0 and I sources. On average, a multiplicity percentage of 64% is found among Class 0 protostars with linear separations in the range 50–5000 au (e.g. Looney et al. 2000; Maury et al. 2010; Enoch et al. 2011; Tobin et al. 2013), whilst it is between 18% and 47% for Class I sources with linear separations in the range 45–5000 au (Haisch et al. 2004; Duchêne et al. 2004, 2007; Connelley et al. 2008a,b).

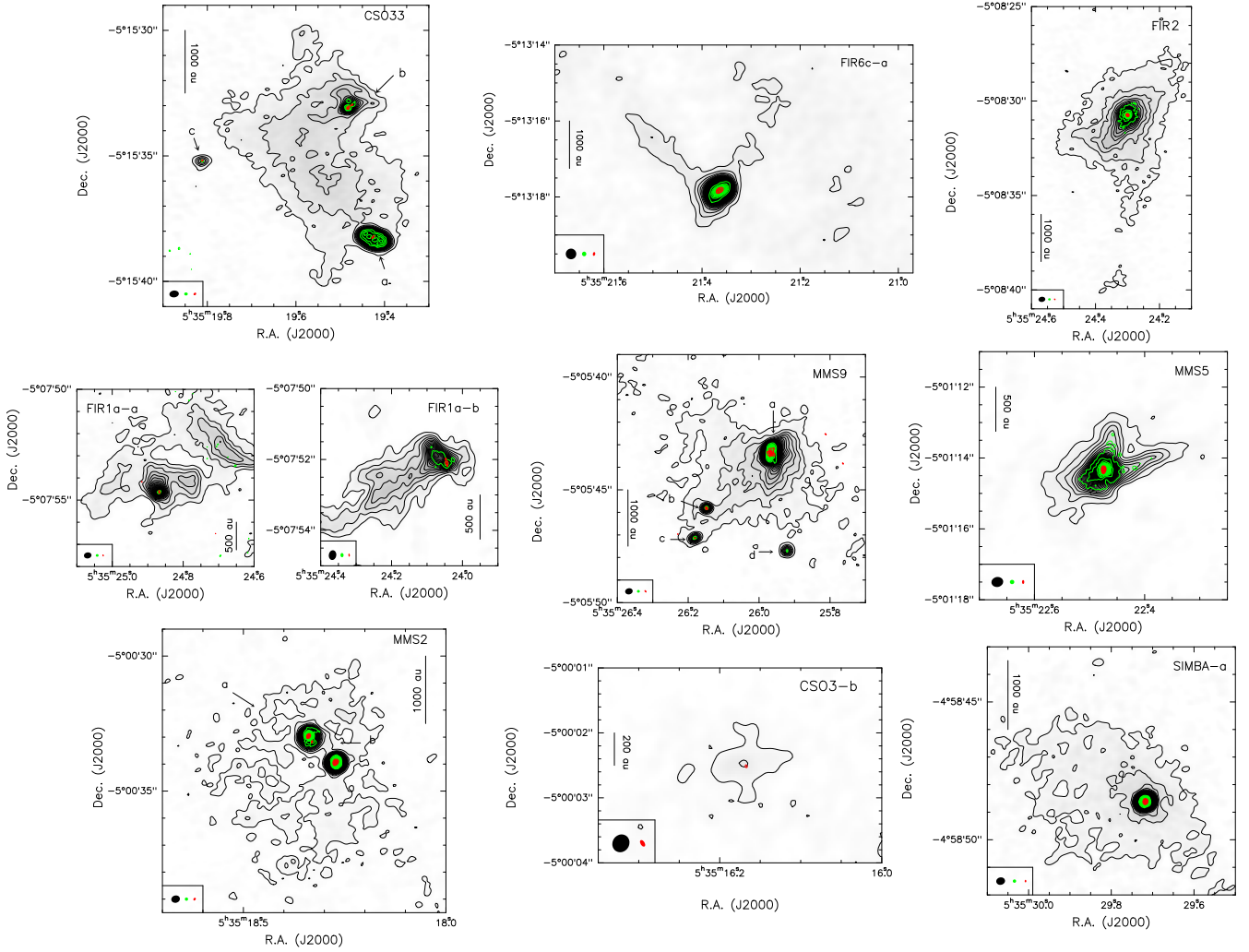


Fig. 1. Continuum maps of the nine fields in Table 1, resolved into several cores, listed in Table 2. Each panel shows the superposition of the ORANGES 246.2 GHz dust continuum (ALMA, grey shaded area + black contours) with 333 GHz continuum (ALMA, green contours) and 32.9 GHz continuum (VLA, red contours), the latter retrieved from the ALMA archive. For the continuum at 246.2 GHz, levels start from 3σ with steps of 5σ , except for FIR6c for which levels start at 5σ and for CS033, MMS9 and CS03 for which level steps are of 7σ . Contours for the 333 GHz data start at 5σ with steps of 5σ , except for CS033 and FIR1a-a for which contours start respectively at 3σ with steps of 3σ and at 10σ with steps of 5σ . Contours for the 32.9 GHz data start at 5σ with steps of 5σ , except for FIR1a-a, FIR1a-b, and CS03-b for which contours start at 3σ with steps of 5σ and for MMS9 for which contours start at 4σ with steps of 5σ . Table 1 reports the 1σ values at each wavelength. The synthesised beams at 246.2 GHz (black), 333 GHz (green), and 32.9 GHz (red) are depicted in the lower left corner of each panel.

Therefore, if we take into account only systems with linear separations in the range 45–5000 au, we find a multiplicity of 67% (with a statistical error of 40%) for Class 0 sources, consistent with that of the other studies. However, for Class I sources, since we do not consider the source CS03 because the projected separation between the two components is larger than 5000 au, our sample of two sources is statistically too poor to be compared with the other studies.

Finally, we found a marginal anti-correlation between the number of protostars in each system and the distance of the system in the OMC-2/3 filament from the Trapezium OB cluster, with a Pearson correlation coefficient of -0.58 (or 34% probability) as shown in Fig. 2. The multiplicity of the sources seems thus to be higher in the southern part of the filament than in the northern part. However, our source sample is rather small, which leads to high statistical uncertainties. Obviously, a study with a larger sample of sources is needed to confirm or disprove these two results.

6.2. Method to derive the dust properties and free-free emission

From the measured flux densities and source size in Sect. 5.2, we derived the dust emissivity spectral index (β) and the free-free contribution, the dust optical depth, the H_2 column density, and the (envelope + disk) mass using the SED method as follows.

The flux density per beam (i.e. each dust SED point) is given by the equation

$$F_\nu = B_\nu(T_d) (1 - e^{-\tau_\nu}) \Omega_s, \quad (1)$$

where F_ν is the flux density, Ω_s is the source solid angle, and $B_\nu(T_d)$ is the Planck function which depends on the dust temperature, T_d , as follows:

$$B_\nu(T_d) = \frac{2h\nu^3}{c^2} \frac{1}{e^{\frac{h\nu}{k_B T_d}} - 1}. \quad (2)$$

Table 3. Measured flux densities and source sizes of the 16 sources in Table 2.

Source	F_ν (333 GHz) (mJy)	F_ν (246.2 GHz) (mJy)	F_ν (32.9 GHz) (mJy)	Decon. size at 246.2 GHz ($''$)	Decon. PA ($^\circ$)	Notes
CSO33-a	70	32	0.23	$0.79 \times 0.39^{(a)}$	61.1	
CSO33-b	31.0	10	0.12	0.60×0.60	...	The flux densities include the triple system
CSO33-c	1.5	0.9	0.044	0.07×0.07	...	
FIR6c-a	93	44	0.7	0.31×0.13	-64	
FIR2	65	28	0.41	0.17×0.17	...	
FIR1a-a	14	7	0.09	0.23×0.20	36.2	The flux densities correspond to a $\sim 50\sigma$ contour at 1.3mm
FIR1a-b	11	4.7	0.20	$0.25 \times 0.13^{(a)}$	80.7	
MMS9-a	164	72	0.8	$0.44 \times 0.14^{(a)}$	171.1	
MMS9-b	4.6	2.4	0.05	$0.05 \times 0.05^{(a)}$	179.4	
MMS9-c	4.6	2.0	0.031	0.10×0.10	...	
MMS9-d	3.5	2.0	$\leq 0.02^{(b)}$	0.13×0.13	...	
MMS5	90	39	0.6	0.15×0.13	-26.3	
MMS2-a	74	33	0.24	0.13×0.13	-40.0	The flux densities include the binary system
MMS2-b	86	43	0.5	0.17×0.12	-6.7	
CSO3-b	$\leq 1^{(b)}$	0.6	0.05	$0.03 \times 0.02^{(c)}$	49.2	
SIMBA-a	108	53	0.6	0.13×0.11	-47.2	

Notes. Flux density uncertainties are 10%. ^(a)Deconvolved size at 333 GHz and associated PA are from Tobin et al. (2020). ^(b) 3σ upper limit. ^(c)Deconvolved size at 32.9 GHz and associated PA are from Tobin et al. (2020).

Table 4. Definition of each of the temperatures used in this study.

Temperature	Symbol	Definition
SED temperature	T_{SED}	Dust temperature constrained from the SED method over the frequency range 32.9–333 GHz.
Bolometric temperature	T_{bol}	Temperature of a blackbody with the same mean frequency as the observed SED.
Dust radiative temperature	T_{rad}	Dust temperature of a dust grain radiatively heated by a L_{bol} source and at a distance r from the heating source.

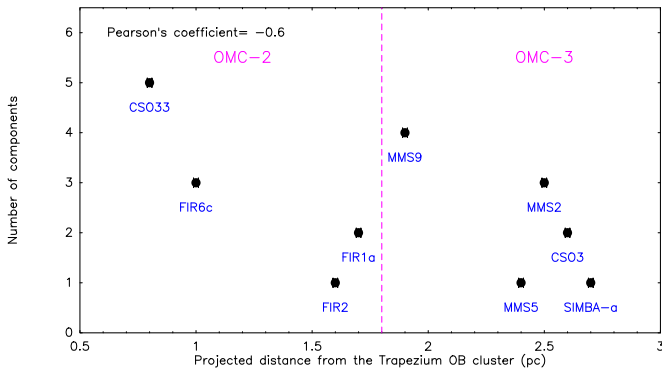


Fig. 2. Number of protostars in each of the nine targeted fields (Table 1) as a function of the projected distance from the Trapezium OB cluster in pc. The magenta line separates the sources in the OMC-2 and OMC-3 filaments.

The dust optical depth τ_ν is defined as

$$\tau_\nu = \mu m_{\text{H}} N_{\text{H}_2} R \kappa_0 \left(\frac{\nu}{\nu_0} \right)^\beta, \quad (3)$$

where $\mu = 2.8$ is the mean molecular weight of the molecular cloud per hydrogen molecule (Kauffmann et al. 2008), m_{H} is the mass of the hydrogen atom, $R = 0.01$ is the mass dust-to-gas

ratio, and $\kappa_0 = 0.9 \text{ cm}^2 \text{ g}^{-1}$ is the emissivity of the dust grain at the reference frequency of $\nu_0 = 230 \text{ GHz}$ (Ossenkopf & Henning 1994).

In the following we indicate as T_{SED} the dust temperature derived from the SED method, according to Eqs. (1) to (3), to distinguish it from other ways to derive T_d , described below at Step 6 (see also Table 4).

Step 1, derivation of β and T_{SED} . From Eq. (1), we derived the dust emissivity spectral index between 333 and 246.2 GHz ($\beta_{333-246.2}$), 333 and 32.9 GHz ($\beta_{333-32.9}$), and 246.2 and 32.9 GHz ($\beta_{246.2-32.9}$) using Eq. (4). As we do not know the sources dust temperature, we derived the indexes for T_{SED} ranging from 10 to 200 K, with steps of 10 K between 10 and 100 K and steps of 20 K between 100 and 200 K:

$$\left(\frac{\nu_1}{\nu_2} \right)^\beta = \frac{\ln \left(1 - \frac{F_{\nu_1}}{B_{\nu_1}(T_{\text{SED}})\Omega_s} \right)}{\ln \left(1 - \frac{F_{\nu_2}}{B_{\nu_2}(T_{\text{SED}})\Omega_s} \right)}. \quad (4)$$

For sources without clear free-free emission (see Step 2), we calculated the weighted mean between $\beta_{333-32.9}$ and $\beta_{246.2-32.9}$ for each T_d to derive the final used β . We note that we did not use $\beta_{333-246.2}$ because of its fairly large uncertainty. For sources with free-free emission, we adopted β equal to $\beta_{333-246.2}$. In some cases we were able to constrain the dust temperature to be larger than a minimum temperature because the observed flux density

would become lower than the predicted value, $F_\nu \leq B_\nu(T_d) \Omega_s$, at lower temperatures.

Step 2, presence of free-free emission. From the dust emissivity spectral index derived in Step 1 we can assess whether there is free-free emission. The derived $\beta_{333-32.9}$, $\beta_{333-32.9}$, and $\beta_{246.2-32.9}$ only differ when free-free emission at 32.9 GHz is present (where we assume that free-free emission is not present at 246.2 and 333 GHz). In that case, $\beta_{333-246.2}$ is expected to be larger than $\beta_{333-32.9}$ and $\beta_{246.2-32.9}$ since a free-free contribution leads to smaller β values. Therefore, sources presenting a variation in β in the different frequencies are those with free-free emission.

Step 3, derivation of τ_ν . We derived the dust optical depth, τ_ν , as a function of (T_{SED}) by inverting Eq. (1):

$$\tau_\nu = -\ln\left(1 - \frac{F_\nu}{B_\nu(T_{\text{SED}})\Omega_s}\right). \quad (5)$$

For sources with no free-free emission at 32.9 GHz, we calculated the dust optical depth at each frequency. For sources with free-free contribution at 32.9 GHz we did not calculate the optical depth at this frequency.

Step 4, derivation of N_{H_2} and $M_{\text{env+disk}}$. We derived the H_2 column density, N_{H_2} , as a function of the SED temperature using Eq. (3). For sources without free-free contribution we calculated N_{H_2} at each frequency; we used the weighted mean of β derived in Step 1, which is a function of (T_{SED}). We then averaged the derived N_{H_2} values between the three frequencies to get a final N_{H_2} as a function of the SED temperature. For sources with centimetre excess we did not calculate N_{H_2} at 32.9 GHz, and we used $\beta_{333-246.2}$. We then averaged the N_{H_2} values between 333 and 246.2 GHz to get a final N_{H_2} as a function of the SED temperature.

Finally, we derived the (envelope + disk) mass of the sources, $M_{\text{env+disk}}$. We note that following the derivation of the source size, (envelope + disk) mass refers to the mass of the disk and of the immediate and warm envelope (densest and most compact component of the envelope). We used the equation

$$M_{\text{env+disk}} = \mu m_{\text{H}} N_{\text{H}_2} d^2 \Omega, \quad (6)$$

where d is the distance of the OMC-2/3 filament.

Step 5, derivation of the fraction of free-free emission at 32.9 GHz, FF. Having derived the dust emissivity spectral index (Step 1) and N_{H_2} (Step 4) and using Eqs. (1) and (3), we can quantify the percentage of free-free emission FF as a function of the SED temperature for each source. To that end, we calculated the flux density at 32.9 GHz that we should have measured if the emission were only due to thermal dust emission, and then compared it to the flux density we actually measured. We therefore derived the percentage of free-free emission at 32.9 GHz as a function of the SED temperature for each source.

Step 6, derivation of the dust radiative temperature T_{rad} . For the sources that are not multiple systems and for which the bolometric luminosity L_{bol} can be trusted, we computed the dust radiative temperature, T_{rad} , defined as the temperature of a dust grain radiatively heated by a L_{bol} source and at a distance r from the heating source. The following formula, roughly valid for an optically thick dust spherical envelope, provides a good

approximate value of T_{rad} (Ceccarelli et al. 2000, Eq. (1)):

$$T_{\text{rad}} = 101 \text{ K} \left(\frac{L_{\text{bol}}}{10 L_\odot}\right)^{1/4} \left(\frac{r}{50 \text{ au}}\right)^{-1/2}. \quad (7)$$

In our case, r is the radius of the dust continuum emission source (Table 3). In the case of elliptical sources, we did the calculations for both the major and minor axis to get a range of possible values for T_{rad} .

The T_{rad} computed in this way provides an approximate value of the dust temperature at the border of the continuum emission source and, if the emission is optically thick, it would be approximately the measured dust temperature. Therefore, it can be used to have an approximate value of the dust temperature in the cases where it could not be otherwise constrained (see Step 1).

Step 7, construction of dust SEDs from the derived dust parameters. Once we have constrained the dust temperature, the dust emissivity spectral index, and the H_2 column density ranges for each of our source samples, we can plot the dust SEDs corresponding to those derived parameters. To this end, we used Eqs. (1), (2), and (3) to calculate the flux density associated with these parameters as a function of frequency, within the dust temperature range derived from the Step 1. When they were available we also used T_{rad} and T_{bol} . We used frequencies in the range [10, 340] GHz, with steps of 10 GHz between 10 and 100 GHz and with steps of 20 GHz between 100 and 340 GHz. This results in a range of possible dust SEDs for a given set of dust parameters (T_d , β , and N_{H_2}). To compare the calculated flux densities with those we measured, and as a self-consistency check, we added the latter on the dust SED plots.

Summary. We used the SED method to derive β (Step 1), τ_ν (Step 3), N_{H_2} and $M_{\text{env+disk}}$ (Step 4), and FF (Step 2 and 5). In the analysis, we used two additional temperatures (see Table 4): the bolometric temperature, T_{bol} , derived by Furlan et al. (2016), and the dust radiative temperature, T_{rad} , derived from the bolometric luminosity of each source and its size (Step 6). Finally, we used these derived parameters to build the associated SEDs (Step 7). All uncertainties in the derivation of β , τ_ν , N_{H_2} , and $M_{\text{env+disk}}$ are detailed in Appendix C.2. In the following subsections, we report the results from this SED fitting technique.

6.3. Dust temperature

T_{SED} . In order to constrain the dust temperature range we took into account that β should range between 0 and 2, as discussed in Sect. 2. We thus constrained the range of dust temperatures for which β respects this condition (see Fig. 3). The derived temperature range, T_{SED} , in each source is reported in Table C.1.

T_{bol} and T_{rad} . Five sources of our sample possess an estimate of the bolometric luminosity and are single systems within the spatial resolution of 0."1 (~40 au): FIR2, MMS5, SIMBA-a, CSO3-b, and FIR6c-a. Although three sources lie in the FIR6c-a *Herschel* beam, from which the bolometric luminosity is derived, we note that the other two are supposedly pre-stellar cores (Kainunlainen et al. 2017). Therefore, the bolometric luminosity is reliably attributable only to FIR6c-a.

For these five sources we derived the bolometric and radiative temperatures, reported in Table C.2, and the other dust properties at these temperatures. Figures 3 and C.1 to C.4 show how these temperatures compare with the dust temperature derived from the SED. In FIR2 and CSO3-b, T_{bol} lies within the

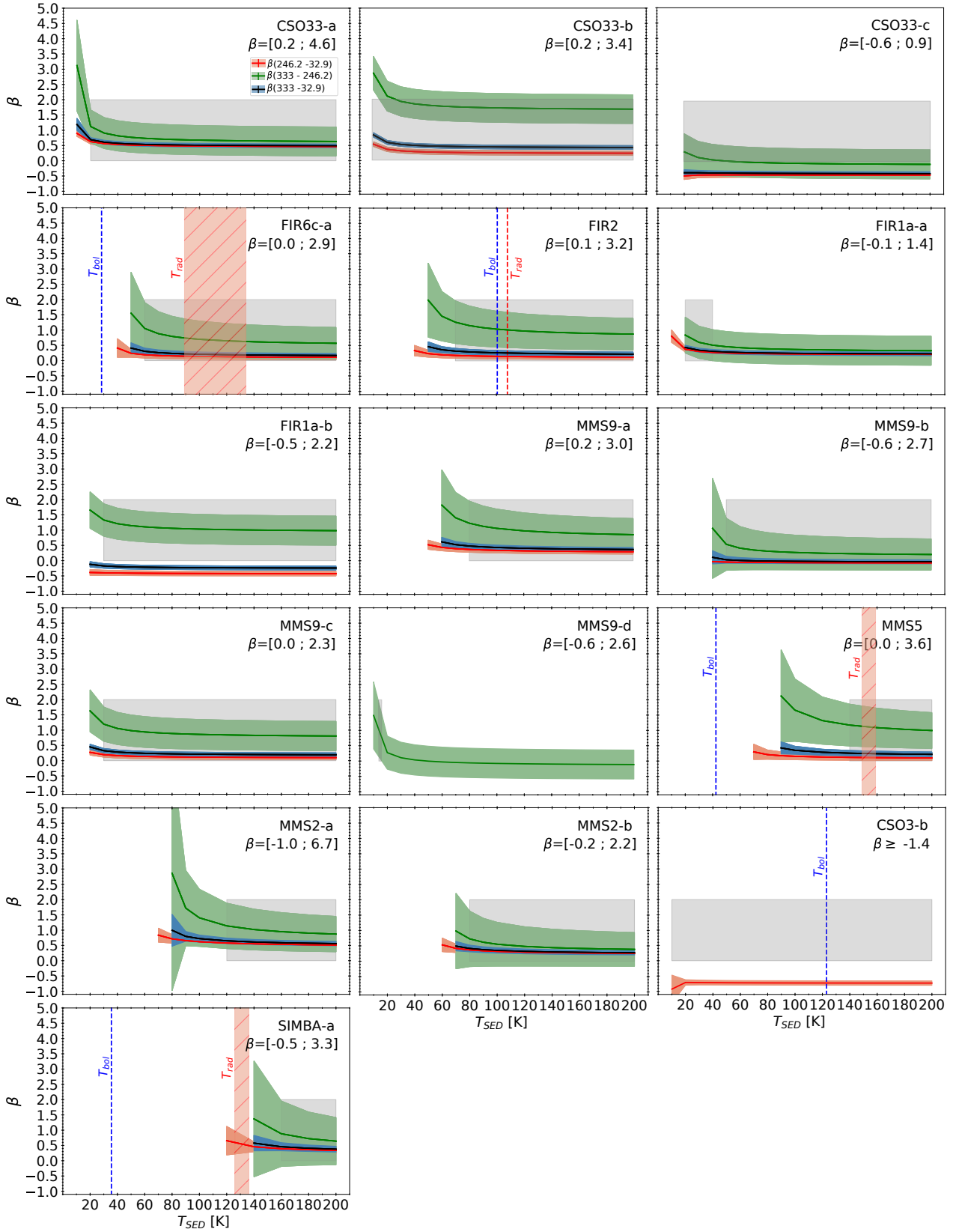


Fig. 3. Dust emissivity spectral indexes, β , as a function of the SED temperature for each source. The indexes were derived between 333 GHz and 32.9 GHz (black lines), 333 GHz and 246.2 GHz (green lines), and 246.2 GHz and 32.9 GHz (red lines). The shaded grey area indicates the authorised range of β values (0–2) provided by theoretical works (see Sect. 2). Applying these limits on β constrains the possible range of T_{SED} values. For each source, the minimum and maximum values of β derived over the full temperature range are indicated at the top right of the plots. For single systems, the bolometric temperature, T_{bol} , derived from *Herschel* (Furlan et al. 2016), and the radiative temperature, T_{rad} , are indicated by a vertical blue dashed line and red shaded area, respectively.

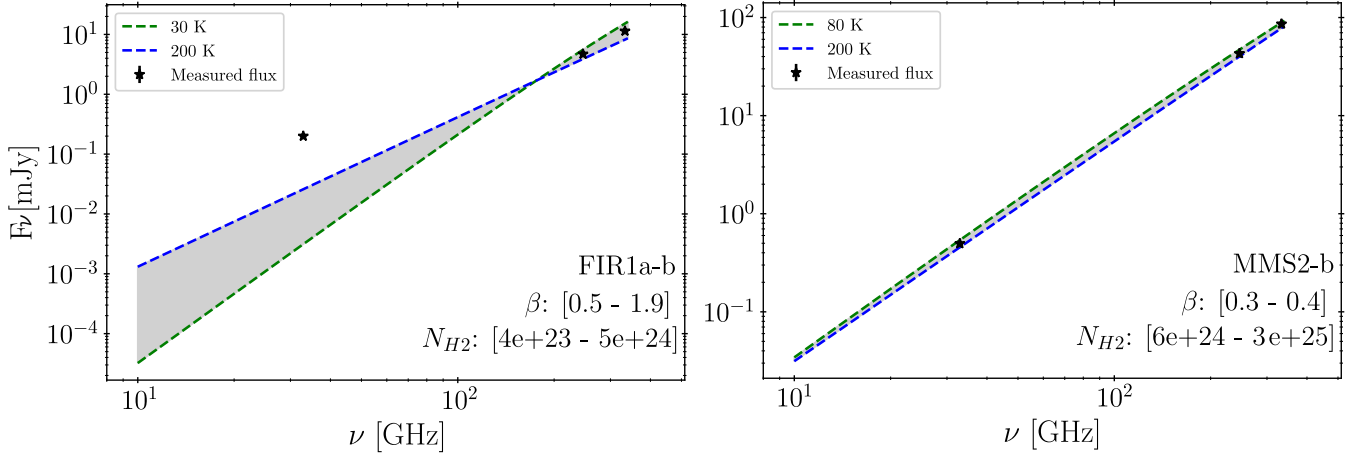


Fig. 4. Example of dust SEDs obtained for two sources, FIR1a-b (*left*) and MMS2-b (*right*). The dust SEDs, calculated for the corresponding dust temperature range of each source and from the final parameters derived for each source (β , N_{H_2} , are shown by the grey shaded area. These parameters are indicated on the lower right side of the plot. Measured flux densities are represented by black filled stars. The dust SEDs corresponding to the two extreme values of the dust temperature range are represented by the blue and green dashed lines.

range of dust temperatures that we derived from the SED. However, in the other three sources, FIR6c-a, MMS5, and SIMBA-a, T_{bol} is lower. This can be explained by the fact that these objects have high dust millimetre optical depths τ . At the mid-infrared (MIR) wavelengths of *Herschel* and *Spitzer* the dust becomes optically thick at a larger radius than that at millimetre wavelengths; consequently, the dust probed by the MIR is colder than that probed by millimetre wavelengths.

On the contrary, with the exception of SIMBA-a and CSO3-b, the radiative temperatures are consistent with the range derived from the SED. They are reported in Table C.2, as are the corresponding dust properties and free-free excess. For CSO3-b we used the bolometric temperature and the associated dust parameters for the analysis. Finally, SIMBA-a possess a radiative temperature that is lower than that derived from the SED; in this case we could not further constrain the temperature and we used the results from the SED.

Hot, warm, and cold sources. We classified the sources in four categories: (1) cold ($T_d < 50$ K), (2) warm ($T_d \geq 50$ K), (3) hot ($T_d \geq 90$ K), and (4) unknown (sources for which the range spans from ≤ 50 K to ≥ 90 K). Following this classification, FIR6c-a, FIR2, MMS5, MMS2-a, CSO3-b, and SIMBA-a are hot sources, while FIR1a-a and MMS9-d are cold sources. In between, MMS9-a,b and MMS2-b are classified as warm sources. Finally, for CSO33-a,-b,-c, FIR1a-b, and MMS9-c, the range of dust temperatures could not be constrained.

6.4. Dust emissivity spectral index and free-free presence

Figure 3 shows the derived β as a function of the SED temperature for each of the sources. Table C.1 lists the dust emissivity spectral indexes derived between 333 and 246.2 GHz, 333 and 32.9 GHz, and 246.2 and 32.9 GHz within the constrained range of dust temperatures. As discussed in the previous subsection, we only consider the indexes lying in the range [0;2] in the following analysis. The final range of β values of each source used in the following are reported in Tables 5 and C.1. The majority of the sources (9/16) have a dust emissivity spectral index < 1 .

In five sources (CSO33-b, FIR2, FIR1a-b, MMS9-c, and MMS5), the index between 333 and 246.2 GHz (green) is larger than the indexes between 246.2 and 32.9 GHz (red) and 333

and 32.9 GHz (black) across the derived SED temperature range. Those sources thus present free-free emission. For FIR6c-a and MMS9-a, uncertainties on $\beta_{333-246.2}$ are too large to definitively assess the presence of free-free emission at 32.9 GHz.

For the remaining sources, the three derived β are consistent with each other within the error bars and are thus considered as sources without free-free emission. The results are reported in Table 5.

6.5. Opacities and envelope plus disk masses

The derived dust optical depths vary between 0.01 and 2.4 at 333 GHz, between 0.004 and 1.6 at 246.2 GHz, and between 0.01 and 1.3 at 32.9 GHz respectively. The derived H_2 column densities range between 1×10^{23} cm $^{-2}$ and 3.8×10^{25} cm $^{-2}$. Finally, the derived (envelope + disk) masses range between $2 \times 10^{-4} M_\odot$ and $0.1 M_\odot$. All the derived values are reported in Table 5, while the plots of these parameters as a function of the dust temperature are shown in Figs. C.2, C.3, and C.4.

6.6. Dust SEDs

The final dust SEDs corresponding to the derived dust parameters for each source are shown in Fig. C.5. We show in Fig. 4 an example of two dust SED plots, for FIR1a-b and MMS2-b. In FIR1a-b we see that the flux density at 32.9 GHz is above the dust SEDs lines, indicating the presence of free-free emission, while this is not the case in MMS2-b.

6.7. Fraction of free-free emission at 32.9 GHz

As said in Sect. 6.4, a $\beta_{333-246.2}$ larger than the other two derived values of beta implies the presence of free-free emission at 32.9 GHz. In the five sources where this happens (CSO33-b, FIR2, FIR1a-b, MMS9-c, and MMS5) we calculated the percentage fraction of the 32.9 GHz emission from free-free with respect to the dust continuum emission. The derived values are reported in Table 5 and shown in Fig. C.1. We can see that for these sources the derived free-free emission ranges between 47% and 100%, whilst in sources with a priori no free-free emission, the largest percentage that can be attributed to free-free emission is 24%. We note that no 333 GHz emission is detected towards

Table 5. Results for the dust parameters derived for each source.

Source	Size (au × au)	T_d (K)	Category	β	τ_{333} $\tau_{246.2}$ $\tau_{32.9}$	$N_{\text{H}_2\text{-mm}}$ ($\times 10^{24} \text{ cm}^2$)	$M_{\text{env+disk}}$ ($\times 10^{-2} M_{\odot}$)	FF (%)	New classification
CSO33-a	310 × 153	20–200	Unknown	0.5–0.7	0.02–0.4 0.01–0.3 0.01–0.1	0.4–6	1–13	0–24	Class 0 or I
CSO33-b	236 × 236	10–200	Unknown	1.2–2.0	≥0.01 ≥0.004 ...	≥0.08	≥0.2	88–100	Class 0
CSO33-c	27.5 × 27.5	20–200	Unknown	0	0.02–0.6 0.02–0.5 0.1–1.5	0.7–13	0.02–0.5	0–21	Class II
FIR6c-a	122 × 51	89–134	Hot	0.1–0.3	0.3–0.7 0.2–0.6 0.2–0.4	7–15	1.5–4	0–21	Class 0
FIR2	67 × 67	101–108	hot	0.4–1.6	0.4–0.6 0.3–0.4 ...	7–10	1–2	55–100	Class I
FIR1a-a	90 × 79	20–40	Cold	0.3–0.4	≥0.1 ≥0.1 ≥0.1	≥3	≥1	0–22	Class 0 or I
FIR1a-b	98 × 51	30–200	Unknown	0.5–1.9	0.03–0.3 0.02–0.2 ...	0.4–5	0.1–1	87–100	Class 0
MMS9-a	173 × 55	80–200	Warm	0.3–0.4	0.2–1.0 0.2–0.7 0.1–0.4	5–19	2–7	0–23	Class 0
MMS9-b	20 × 20	50–200	Warm	0	0.1–1.5 0.1–1.3 0.2–1.3	4–31	0.05–0.5	0–22	Class 0 or I
MMS9-c	39 × 39	30–200	Unknown	0.3–1.8	0.03–0.5 0.03–0.3 ...	0.6–7.5	0.03–0.5	47–100	Class 0 or I
MMS9-d	51 × 51	10–20	Cold	0–2.0	0.3–2.4 0.3–1.4 ...	5–38	0.5–4	...	Class II or background object
MMS5	59 × 51	149–159	Hot	0.5–1.8	0.5–0.9 0.4–0.6 ...	10–15	1–2	60–100	Class 0
MMS2-a	51 × 51	120–200	Hot	0.5–0.6	0.4–1.2 0.3–0.9 0.1–0.3	8–20	1–2	0–23	Class I
MMS2-b	51 × 47	80–200	Warm	0.3–0.4	0.3–1.7 0.2–1.3 0.1–0.6	6–30	1–5	0–22	Class I
CSO3-b	...	123 ^(a)	hot	≥0	... ≥0.02 ...	≥0.4	≥0.02	≥0	Class I
SIMBA-a	51 × 43	160–200	Hot	0.4	0.7–2.2 0.6–1.6 0.4–0.7	18–36	1–3	0–23	Class 0

Notes. First, the linear source sizes are reported in the Col. 2. Then, the dust temperature range and the corresponding category are reported in Cols. 3 and 4 respectively. The dust emissivity spectral indexes are reported in Col. 5. The range of dust optical depth values derived at 333 GHz, τ_{333} , 246.2 GHz, $\tau_{246.2}$, and 32.9 GHz, $\tau_{32.9}$, as well as the H_2 column densities, $N_{\text{H}_2\text{-mm}}$, and (envelope + disk) masses, $M_{\text{env+disk}}$, corresponding to the derived range of temperature, are reported in Cols. 6–8. The range of free-free emission percentage at 32.9 GHz is indicated in Col. 9. In the last column we report the new classification of the sources. ^(a) T_{bol} .

CSO3-b and, consequently, we cannot assess whether an excess at 32.9 GHz is present.

7. Discussion

7.1. Dust properties

Dust temperature. From the above analysis (Sect. 6.3) six sources are classified as hot ($T_d \geq 90$ K), three as warm ($T_d \geq 50$ K), and two as cold ($T_d < 50$ K). We could not constrain the temperature range in the remaining five sources. Our derived temperatures are higher than those derived by previous OMC-2/3 surveys, which found temperatures lower than 30 K (e.g. Chini et al. 1997; Lis et al. 1998; Johnstone & Bally 1999) or around 50 K towards the FIR6 region (Shimajiri et al. 2009). The discrepancy can be due to the fact that we do not probe the same region as that of these studies, and that our higher angular resolution allows us to probe a more internal region of the protostar envelope, which is warmer than the outer one.

Dust emissivity spectral index. The derived dust emissivity spectral indexes range between 0 and 2; the majority (9/16) of the sources have values < 1 . Compared to the canonical value expected for protostar envelopes, between 1 and 2 (e.g. Natta et al. 2007; Jørgensen et al. 2007; Planck Collaboration XXIII 2011; Chiang et al. 2012; Sadavoy et al. 2013; Forbrich et al. 2015; Chen et al. 2016; Li et al. 2017; Bracco et al. 2017; Galametz et al. 2019), our range of derived values is lower. However, several other studies at scales of 100–2000 au, such as ours, found $\beta \leq 1$ (e.g. Jørgensen et al. 2007; Kwon et al. 2009; Chiang et al. 2012; Miotello et al. 2014; Li et al. 2017; Galametz et al. 2019). Different explanations supported by theoretical, modelling, and laboratory works are given in the literature.

The presence of large grains (millimetre- or centimetre-sized) due to grain growth, a large optical depth, and/or dust self-scattering can lead to a decrease in the dust emissivity index in the (sub-)millimetre range (e.g. Miyake & Nakagawa 1993; Ossenkopf & Henning 1994; Draine 2006; Jones et al. 2013, 2017; Wong et al. 2016; Ysard et al. 2019). However, since we took into account the optical thickness of the dust in the derivation of the dust emissivity spectral index, large optical depths should not affect our estimates. An example of the first explanation is that inner protostellar and/or protoplanetary disks, if present, can contribute to the decrease in the dust emissivity index, and the measured dust emissivity spectral indexes in those disks are usually $\beta \leq 1$ (e.g. Beckwith & Sargent 1991; Ricci et al. 2012; Pérez et al. 2012; Ubach et al. 2012; Miotello et al. 2014; Bracco et al. 2017; Liu 2019; Nakatani et al. 2020).

Alternatively, several laboratory works found an intrinsic dependence between the dust emissivity spectral index and the dust temperature in the millimetre range: when the dust temperature increases, β decreases (e.g. Dupac et al. 2003; Menella et al. 1998; Boudet et al. 2005). Finally, another possible explanation for the low value of β is the difference in the dust grain composition compared to that of the diffuse ISM (e.g. Aannestad 1975; Agladze et al. 1996; Menella et al. 1998; Coupeaud et al. 2011; Jones et al. 2013, 2017; Ysard et al. 2019).

Envelope+disk mass. Our estimated (envelope+disk) masses are in good agreement with the values derived by the VANDAM survey (Tobin et al. 2020), except for FIR1a-a and MMS9-d. In FIR1a-a, we only could provide lower limits because we could not derive the source size accurately (see Sect. 5.3), and they are higher than the values found in Tobin et al. (2020) by at least a factor of 5. The mass derived for

MMS9-d differs by up to one order of magnitude compared to what is found in Tobin et al. (2020). In both cases, the discrepancy can be explained by the fact that Tobin et al. (2020) assumed an optically thin dust, whilst the dust might actually be optically thick, especially in the case of MMS9-d (see Table C.1). Therefore, the dust mass for those two objects would be underestimated in their study⁶.

Caution should be taken when using the estimated dust masses as they depend on the choice of the dust opacity coefficient in the millimetre wavelengths, which is known within one order of magnitude accuracy. This uncertainty implies about one order of magnitude uncertainty on the disk mass as well (Miyake & Nakagawa 1993; Natta et al. 2004; Ricci et al. 2010; Fanciullo et al. 2020).

7.2. Free-free emission

We clearly found evidence of free-free emission at 32.9 GHz towards 5 out of 16 sources (i.e. $\sim 31\%$ of the source sample). We can compare this result with the previous study from Reipurth et al. (1999), who surveyed the OMC-2/3 filament with the VLA at 8.3 GHz (3.6 cm). They detected 11 sources that were likely either protostars or very young stars. Of these 11 sources, 2 coincide with some of our multiple systems, namely MMS9 and FIR1a. However, they detected free-free emission towards the MMS2 system whilst we did not, and we detected free-free emission towards FIR2 and MMS5 whilst they did not. We also found free-free emission towards CSO33-b, but this source is not included in their mapped area.

The non-detection of 8.3 GHz emission towards FIR2 and MMS5 can be due to a difference in sensitivity between the VANDAM survey observations ($8 \mu\text{Jy beam}^{-1}$ sensitivity) and those of Reipurth et al. (1999) ($\sim 40 \mu\text{Jy beam}^{-1}$ sensitivity). In addition, the difference in the frequency of the two surveys can also explain the discrepancy in the results. Thermal radio jets and/or winds, which are likely to be responsible of the free-free emission in Class 0 and I protostars (Anglada 1995; Anglada et al. 1998; Rodriguez 1997), show a SED with a positive spectral index at centimetre wavelengths. Therefore, if the free-free emission is weak at 32.9 GHz, it will be even weaker at 8.3 GHz, and thus probably not detectable at this wavelength.

Finally, a possible explanation to why we did not detect a centimetre excess towards either of the two sources composing the MMS2 system is that the 8.3 GHz emission traces a non-thermal radio emission associated with a shock in the outflow driven by the system (Yu et al. 1997). Non-thermal emission at centimetre wavelengths have been detected in YSO jets (e.g. Rodriguez et al. 1989; Martí et al. 1993; Garay et al. 1996; Wilner et al. 1999; Anglada et al. 2018) and is usually found in strong radio knots, away from the core, with a negative spectral index at centimetre wavelengths. Therefore, if the emission is seen at 8.3 GHz, it is not necessarily seen at 32.9 GHz. In the MMS2 field we do not see any other clear 32.9 GHz emission apart from that seen towards the centre of the protostars, which strengthens this hypothesis.

7.3. Evolutionary status

Our sample sources have been previously classified into Class 0, Class I and Flat objects based on SEDs from *Herschel*, *Spitzer*,

⁶ For the sake of completeness, we also compared the estimated mass of our sources with those derived by *Herschel* (Furlan et al. 2016) and found our masses to be between one and two orders of magnitude lower than those of *Herschel*. This is most probably due to the fact that our observations probe smaller regions than that of the HOPS survey.

Table 6. Proposed criteria for defining the evolutionary status of our sample sources based on the derived dust emissivity spectral index, β ; the dust and bolometric temperatures, T_d and T_{bol} ; the presence or not of an outflow; and the presence or not of a compact radio continuum source.

Evolutionary status	β	T_d/T_{bol} K	Outflow (Y/N)	Compact radio continuum (Y/(Y)/N)
PSC	1–2	$T_d \leq 10$	N	N
Class 0	≤ 1.5	$T_{bol} < 70$	Y	Y
Class I	≤ 1	$T_{bol} \geq 70$	Y	Y
More evolved (\geq Class II)	0–1	$T_d \in [10–100]$	Y	(Y)

Notes. The range of the dust emissivity spectral index and temperature are based on the discussion in Sect. 2.

and submillimetre APEX photometric observations (see Furlan et al. 2016). However, the angular resolution of these observations does not allow us to disentangle multiple systems where components have close projected separations, as is the case for most of our sources. Hence, cross-correlating information between the different parameters we derived in this work with previous pieces of information (the presence or not of outflow, T_{bol}), we can reassess the nature of our source sample more accurately. Even though historically Class 0 and Class I protostars have been classified based on single-dish observations, we propose here to determine the source’s evolutionary stage, using the criteria summarised in Table 6. We note that two of our sample sources are close multiple systems (CSO33-b and MMS2-a). Since our 246.2 GHz data does not allow us to disentangle those multiple systems, we analyse them as single systems. The evolutionary stage of each source is presented in Table C.1.

7.3.1. Sources whose previous classification is confirmed

Overall, we could confirm the evolutionary stage of ten sources, six confirmed Class I protostars and four confirmed Class I protostars.

Class 0. The presence of an outflow and of a compact radio continuum emission are two characteristics of the Class 0 and I sources (e.g. André et al. 1993; Anglada 1996; Bontemps et al. 1996; Barsony et al. 1998; André 1997). FIR1a-b, MMS5, SIMBA-a, and FIR6c-a are sources for which the two properties are clearly observed as an outflow was detected towards these sources in previous studies (e.g. Aso et al. 2000; Williams et al. 2003; Takahashi et al. 2008; Tobin et al. 2016; Tanabe et al. 2019; Feddersen et al. 2020; Nagy et al. 2020). A large outflow was also detected towards the MMS9 and CSO33 systems, but the angular resolution does not allow us to determine which of the components is actually the driving source (e.g. Williams et al. 2003; Takahashi et al. 2008; Tanabe et al. 2019; Feddersen et al. 2020).

The dust emissivity spectral indexes are consistent with a Class 0 classification, although in the cases of FIR6c-a and SIMBA-a the index could be consistent with a Class I classification. However, for those sources, and for MMS5 and MMS9-a, the derived range of dust temperatures is surprisingly different from the previously derived bolometric temperature. This indicates that these objects have a large optically thick envelope (see Sect. 6.3), testimony of their young age. They have one of the widest ranges of derived (envelope + disk) masses and temperatures. Furthermore, the derived dust optical depths derived in this work are high enough at low temperature to support this hypothesis (see Table C.1). The derived dust temperature of at

least 80 K and the derived range of values of dust emissivity spectral index of MMS9-a is consistent with a Class 0 classification. In the case of FIR1a-b and CSO33-b, the dust temperature is not constrained enough to use this criteria; however, a high percentage of free-free emission is detected, which indicates that the two sources are quite young. In summary, CSO33-b, FIR6c-a, FIR1a-b, MMS9-a, MMS5, and SIMBA-a are very likely Class 0 sources.

Class I/Flat. Four sources (FIR2, MMS2-a, MMS2-b, and CSO3-b) were previously classified as Class I/Flat spectrum sources, and their status is confirmed with this work. However, we note that this work does not allow us to differentiate between a Class I and a Flat spectrum classification. Therefore, we do not make the distinction between the two classifications, and we use the term ‘Class I’ only to designate either of the two possibilities.

The derived dust temperature for MMS2-a and MMS2-b are at least 120 and 80 K respectively, high enough to be consistent with a Class I classification. In the case of CSO3-b and FIR2 the bolometric temperatures of 123 and 108 K, respectively, consistent with the derived dust temperature range, are the reason why these sources are classified as a Class I sources. Then, the derived dust emissivity spectral index for MMS2-a and MMS2-b is ≤ 1 , coherent with this classification. For FIR2 and CSO3-b the dust emissivity spectral index could not be constrained enough.

Free-free excess has been detected only towards FIR2, which could indicate that the source is a bit less evolved than MMS2-a and MMS2-b. An outflow has been detected towards the MMS2 system (e.g. Aso et al. 2000; Williams et al. 2003; Takahashi et al. 2008; Tanabe et al. 2019; Feddersen et al. 2020), but we need high angular resolution studies to understand which of the two sources is the driving source, and thus which of the two sources is younger. Finally, in the case of CSO3-b, we can see that the 32.9 GHz emission is quite weak, but we cannot determine whether free-free emission is present. Additionally, no sign of outflow features has been detected towards CSO3-b (e.g. Williams et al. 2003; Takahashi et al. 2008) and the derived radiative temperature is significantly higher than the other protostars. This could indicate that CSO3-b is more evolved than the three other sources. In summary, FIR2, MMS2-a, MMS2-b, and CSO3-b are very likely Class I/Flat sources.

7.3.2. Sources whose previous classification is modified

FIR1a-a. FIR1a-a was previously classified as a pre-stellar core (Tobin et al. 2015, 2016; Kainunlainen et al. 2017) because no outflow is detected towards this source (e.g. Tobin et al. 2016; Nagy et al. 2020). However, the presence of compact radio emission at 32.9 GHz is incompatible with this classification (Bontemps et al. 1996; Yun et al. 1996). The dust temperature

derived is less than 40 K suggesting a cold source, but the size of the source having been likely overestimated (see Sect. 5.3), the temperature and dust optical thickness could be underestimated. The range of dust emissivity spectral index values is compatible with either a Class 0 or I classification, although it is more consistent with a Class I classification ($\beta \in [0.3; 0.4]$). No free-free emission is detected at 32.9 GHz towards the source which could support this classification. In summary, FIR1a-a could be either a Class 0 or I protostar, but further investigations are needed to decide on one class over the other.

CSO33-a, MMS9-b, and MMS9-c. CSO33-a, and MMS9-b and MMS9-c are part of the Class 0 systems CSO33 and MMS9, respectively. A compact centimetre emission is also detected towards CSO33-a, MMS9-b, and MMS9-c, but whether they drive an outflow is unknown. Outflows have been detected towards CSO33 and MMS9, but the angular resolution of the observations was insufficient to determine which of the sources actually drives them (e.g. Williams et al. 2003; Takahashi et al. 2008; Tanabe et al. 2019; Feddersen et al. 2020). The dust emissivity spectral indexes of these sources are very different, with $\beta \leq 0.7$ for CSO33-a, $\beta = 0$ for MMS9-b, and $\beta \in [0.3; 1.8]$ for MMS9-c. The spectral indexes are consistent with both Class 0 and I, except for MMS9-b for which the spectral index is consistent with a Class I or even Class II classification. However, as seen on the map of the MMS9 field (Fig. 1), extended dust is still present around MMS9-b, which therefore indicates that a Class II classification is not suitable.

Whilst MMS9-b has a derived dust temperature of at least 50 K, which is consistent with a Class 0 source classification, the dust temperature for all the other sources is not sufficiently constrained. For CSO33-a, a recent study from Sheehan et al. (2020) shows evidence of a disk embedded in a massive envelope, which could indicate that the source is quite young and would favour a Class 0 classification. This is consistent with the fact that the derived (envelope+disk) mass for this source is the highest in the source sample. On the other hand, for MMS9-b and MMS9-c, the relatively narrow (envelope+disk) mass range derived would favour a Class I classification. Free-free emission is detected only towards MMS9-c, but in order to determine if the source could be younger than the other two sources, we need more information on the origin of the free-free emission. In summary, further investigations on the gas temperature and the presence or absence of outflows will help us to decide between Class 0 or I for CSO33-a, MMS9-b, and MMS9-c.

CSO33-c. CSO33-c is part of the Class 0 system CSO33. However, several parameters show that the source is more evolved than a Class 0 or Class I protostar. First, the source is extremely compact, is rather isolated, and resembles a disk. The dust emissivity spectral index is about 0, which is consistent with what is found for protoplanetary disks of Class II sources (e.g. Beckwith & Sargent 1991; Ricci et al. 2010, 2012; Pérez et al. 2012; Tazzari et al. 2021). In summary, CSO33-c is very likely a Class II source.

MMS9-d. Finally, MMS9-d is the most puzzling source. This source is cold ($T_d \leq 20$ K) and closely resembles CSO33-c in terms of geometry. The dust emissivity spectral index range is not constrained, which does not help us to understand the status of this source. Thus, it could be a Class II protostar with a disk seen edge-on as it is cold. However, our 246.2 GHz ALMA data include a $C^{18}O$ line. We thus examined the $C^{18}O$ emission towards both CSO33-c and MMS9-d in order to be sure that those objects are associated with the filament. A clear

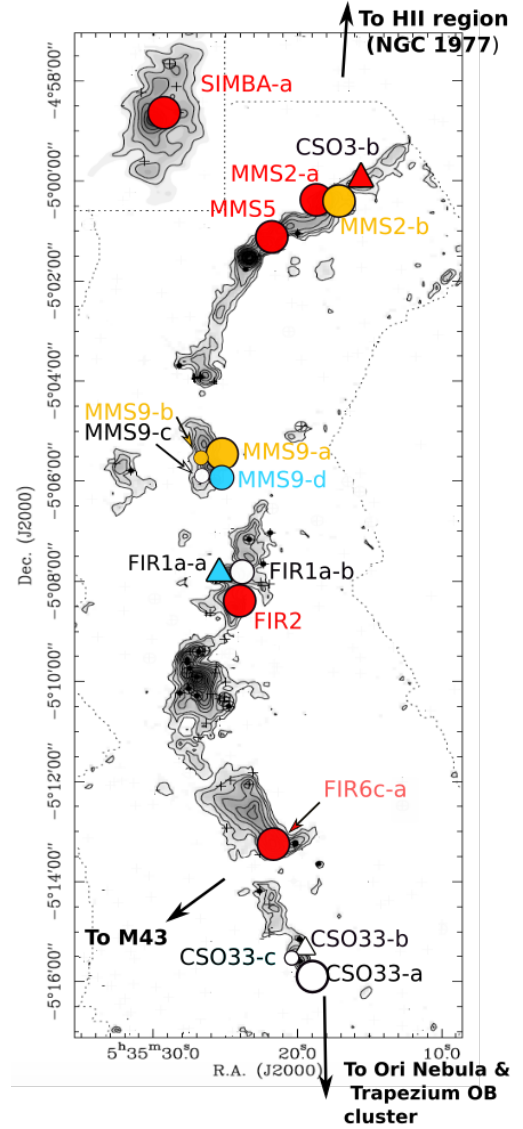


Fig. 5. Map of the continuum at 246.2 GHz towards the OMC-2/3 filament, adapted from Chini et al. (1997) and Nielbock et al. (2003). The upper left insert (square grid) is taken from the SIMBA map of Nielbock et al. (2003). The dotted line indicates the limits of the continuum map at 1.3mm. Contours rise linearly from a 3σ rms noise level, the rms noise of the map being 25 mJy beam^{-1} (Chini et al. 1997). The sources from our sample are shown as coloured circles and triangles, colour-coded depending on the ranges of dust temperature derived in this work: blue means cold ($T_d < 50$ K), yellow means warm ($T_d \geq 50$ K), red means hot ($T_d \geq 90$ K), and white means that the temperature is not constrained enough. The shapes of the symbols are organised from $M_{\text{env+disk}}$ derived values: the smallest circles for sources with a range of values $< 0.01 M_{\odot}$, the largest circles for sources with the highest range of values ($\geq 0.01 M_{\odot}$), medium circles for sources with an intermediate range of values, and triangles for lower limits. The three black arrows pointing outside of the filament show the direction to the different HII regions surrounding OMC-2/3. Some black crosses and filled dots are present throughout the figure, and represent some of the 2MASS sources and MIR sources from TIMMI 2 observed by Nielbock et al. (2003).

$C^{18}O$ emission line is found at the position of CSO33-c, but it is not clear whether the $C^{18}O$ emission is associated with MMS9-d (see Fig. D.1). In addition, the source does not show emission at 32.9 GHz. In summary, the source is either evolved ($>$ Class II) or a background object (perhaps a galaxy).

7.4. Environment influence

One of the goals of this study is to understand whether the environment plays a role in the dust properties of the OMC-2/3 filament protostars. As said before, the filament is bounded by several HII regions which illuminate the region. In a previous work it was shown that the large-scale ($\leq 10^4$ au) chemical composition of the gas around the present source sample is largely governed by the UV photons emitted by the massive stars powering the HII regions (Bouvier et al. 2020). In this work, our aim was to understand whether this highly illuminated environment influences the small-scale (protostellar cores) properties as well. To this end, we studied whether all parameters previously derived (β , T_d , $M_{\text{env+disk}}$, free-free emission) depend on the position of the protostars in the filament.

First, most of the hot sources are located in the north of the filament, in OMC-3, whilst less warm and cold sources tend to be located in the middle of the filament (towards the MMS9 and FIR1a regions), as seen in Fig. 5. The distance between the NGC1977 HII region and SIMBA-a is about the same as the distance between CSO33-a and the Trapezium OB cluster to the south (~ 1 pc in both cases). M43 is closer than the other two HII regions (~ 0.3 pc) from the protostars. Therefore, protostars at the edge of the filament could be warmer due to the nearby HII regions. However, we do not have enough information on the temperature of the southern sources (CSO33-a, CSO33-b, and CSO33-c) in order to draw final conclusions on whether the nearby HII regions play a role in the dust temperature of the sources. Moreover, from Fig. 5, we do not find any correlation between the (envelope + disk) mass of the sources and their position in the filament. These results show a different trend than that found in other systems, where the disk and dust properties of the sources are influenced by nearby sources of UV illumination (e.g. Eisner et al. 2018; Haworth 2021; Brand et al. 2021). This discrepancy is very likely due to the fact that our sources are located further away from the UV illumination source than in those studies, and that they are more shielded from the UV illumination as they are still embedded in the molecular cloud.

Second, we found no correlation between the dust emissivity spectral index, β , and the positions of the sources in the OMC-2/3 filament, as seen in Fig. 6, implying that the environment of the OMC-2/3 filament does not affect the evolutionary status of the sources. This would tend to suggest an almost simultaneous star formation along the OMC-2/3 filament, in agreement with the idea that the latter are structures formed by a relatively fast compression. This result is strengthened by the fact that the more massive protostars ($\geq 0.1 M_{\odot}$) seem to be located throughout the filament with no particular trend, as shown in Fig. 5.

Third, we found a correlation between β and the percentage of free-free emission, with a Pearson correlation coefficient of 0.81 (corresponding to a probability of 66%), as shown in Fig. 6. Therefore, objects with higher dust emissivity spectral index seem to show higher free-free emission percentage. However, the sources with higher free-free emission percentage are not necessarily the youngest ones (i.e. Class 0) since, for instance, we find free-free emission towards Class I (FIR2) and not towards SIMBA-a (Class 0). This result is consistent with other studies showing no substantial evidence of strength variation of the free-free emission from Class 0 to I sources (Pech et al. 2016; Tychonic et al. 2018b).

Evidently, the low statistics and relatively large errors in the parameters of the sources where the dust temperature is not well constrained hamper very strong conclusions on the impact of large-scale UV illumination on low-scale star formation.

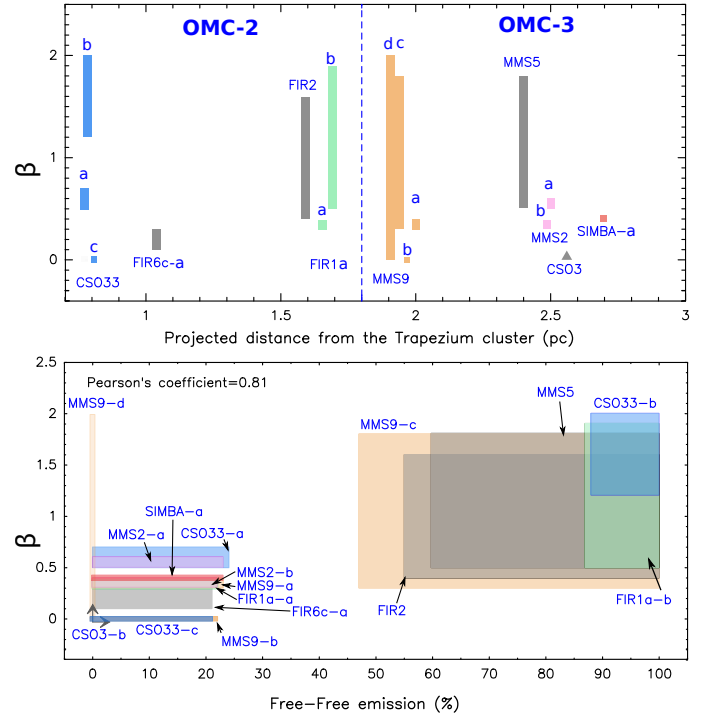


Fig. 6. Main results obtained from the dust parameters derivation of the sources. *Top*: spectral emissivity index, β , for each source as a function of the position in the OMC-2/3 filament. The dashed blue line indicates the separation between the OMC-2 and OMC-3 clouds. *Bottom*: spectral emissivity index, β , as a function of the percentage of free-free emission derived for each source. In both panels, the grey filled rectangles and arrows represent the values of the parameters (β , free-free emission) associated with the bolometric and/or radiative temperatures of the corresponding source. For clarity, a colour is associated with each system (blue for CSO33, green for FIR1a, orange for MMS9, and pink for MMS2). The possible values for these sources are represented with their corresponding coloured area.

Even so, the present work already suggests the potentiality of larger statistical studies towards low-mass star-forming regions to assess whether the presence of external, nearby UV sources has any impact on the forming protostars.

8. Conclusions

Using new 246.2 GHz ALMA data from the ORANGES project complemented with archival 333 GHz ALMA and 32.9 GHz VLA data from the VANDAM survey (Tobin 2019a,b; Tobin et al. 2020), we have constructed the 100 au scale dust SED in the millimetre to centimetre range of 16 protostars located in the OMC-2/3 filament. We have derived several dust parameters, such as the dust temperature, the dust emissivity spectral index, the (envelope+disk) mass of the protostars, and whether free-free emission is present towards the sources. Here are our main conclusions:

- From the dust continuum maps, we detected 28 sources, of which 16 could be analysed in this study. Almost all the sources are detected at 333, 246.2, and 32.9 GHz;
- $(67 \pm 33)\%$ of our fields reveal multiple systems, with average projected separations of at least 1000 au. There is a possible correlation between the number of components of a multiple system and the position of the sources in the filament, with a higher number of components in the south of the filament, but this trend is marginal;

- From the derived dust temperatures, we could classify the sources in four categories: cold ($T_d < 50$ K), warm ($T_d \geq 50$ K), hot ($T_d > 90$ K), and unknown (T_d not constrained). For three sources, *Herschel* likely probes the large gas envelope surrounding the small-scale protostars, which results in bolometric temperatures lower than the dust temperatures derived in this paper, and indicating that these sources are quite young;
- The dust emissivity spectral index of the sources ranges between 0 and 2, with a majority of sources with $\beta < 1$. This range of values coincides with what has been derived in other Class 0 and I sources. Several parameters could lead to a low index, such as grain growth in disks already formed, or the composition of the interstellar grains;
- Our results are consistent with the presence of free-free emission in 5 out of 16 sources, implying that they are relatively young sources. A positive correlation between the dust emissivity spectral index and free-free emission is in agreement with the fact that younger objects (large β) are usually accompanied by free-free emission;
- We were able to confirm or correct the evolutionary stage of our source sample, with six Class 0 sources, four Class I sources, one Class II source, and one source that could be either a Class II or a background object. For the remaining four sources, further investigation is needed to decide between a Class 0 or I evolutionary stage;
- The highly illuminated environment of the OMC-2/3 filament does not seem to affect the small-scale structure and dust properties of the OMC-2/3 protostars, although the sources at the edges of the filament could be warmer due to the nearby HII sources. However, we need to better constrain the dust temperature of the sources in order to confirm this result.

Acknowledgements. We deeply thank the referee for their careful reading and their precise and constructive comments that helped to significantly improve the paper. The authors wish to thank F. Motte, F.-X. Désert and M. Benisty for their fruitful help on the dust continuum method and useful suggestions and discussions. This project has received funding from the European Research Council (ERC) under the European Union’s Horizon 2020 research and innovation programme, for the Project “The Dawn of Organic Chemistry” (DOC), grant agreement No 741 002. This paper makes use of the following ALMA data: ADS/JAO.ALMA#2016.1.00376.S and ADS/JAO.ALMA#2015.1.00041.S. ALMA is a partnership of ESO (representing its member states), NSF (USA) and NINS (Japan), together with NRC (Canada), MOST and ASIAA (Taiwan), and KASI (Republic of Korea), in cooperation with the Republic of Chile. The Joint ALMA Observatory is operated by ESO, AUI/NRAO and NAOJ.

References

- Aannestad, P. A. 1975, *ApJ*, **200**, 30
 Adams, F. C. 2010, *ARA&A*, **48**, 47
 Adams, F. C., Lada, C. J., & Shu, F. H. 1987, *ApJ*, **312**, 788
 Agladze, N. I., Sievers, A. J., Jones, S. A., Burlitch, J. M., & Beckwith, S. V. W. 1996, *ApJ*, **462**, 1026
 Ali, B., & Depoy, D. L. 1995, *AJ*, **109**, 709
 André, P. 1997, *IAUS*, **182**, 483
 André, P., & Montmerle, T. 1994, *ApJ*, **420**, 837
 André, P., Montmerle, T., Feigelson, E. D., Stine, P. C., & Klein, K. L. 1988, *ApJ*, **335**, 940
 André, P., Ward-Thompson, D., & Barsony, M. 1993, *ApJ*, **406**, 122
 André, P., Ward-Thompson, D., & Barsony, M. 2000, in V. Mannings, A. P. Boss, S. S. Russell, eds. *Protostars and Planets IV*, 59
 Anglada, G. 1995, *RMxAC*, **1**, 67
 Anglada, G. 1996, *ASPC*, **93**, 3
 Anglada, G., Villuendas, E., & Estalella, R. 1998, *AJ*, **116**, 2953
 Anglada, G., Rodríguez, L. F., & Carrasco-González, C. 2018, *A&ARv*, **26**, 3
 Aso, Y., Tatematsu, K., Sekimoto, Y., et al. 2000, *ApJS*, **131**, 465
 Bally, J., Langer, W. D., & Liu, W. 1991, *ApJ*, **383**, 645
 Barsony, M., Ward-Thompson, D., André, P., & O’Linger, J. 1998, *ApJ*, **509**, 733
 Beckwith, S. V. W., & Sargent, A. I. 1991, *ApJ*, **381**, 250
 Bergin, E. A., Aikawa, Y., Blake, G. A., & van Dishoeck, E. F. 2007, in *Protostars and Planets V*, eds. Reipurth, B., Jewitt, D., & Keil, K., 751
 Bontemps, S., André, P., Terebey, S., & Cabrit, S. 1996, *A&A*, **311**, 858
 Boogert, A. C. A., Gerakines, P. A., & Whittet, D. C. B. 2015, *ARA&A*, **53**, 541
 Boudet, N., Mutschke, H., Nayral, C., et al. 2005, *ApJ*, **633**, 272
 Bouvier, M., López-Sepulcre, A., Ceccarelli, C., et al. 2020, *A&A*, **636**, A19
 Bracco, A., Palmeirim, P., André, P., et al. 2017, *A&A*, **604**, A52
 Brand, J., Giannetti, A., Massi, F., Wouterloot, J. G. A., & Verdirame, C. 2021, *A&A*, **647**, A154
 Ceccarelli, C., Castets, A., Caux, E., et al. 2000, *A&A*, **355**, 1129
 Chen, H., Myers, P. C., Ladd, E. F., & Woods, D. O. S. 1995, *ApJ*, **445**, 377
 Chen, H., Grenfell, T. G., Myers, P. C., & Hughes, J. D. 1997, *ApJ*, **478**, 295
 Chen, M. C. Y., Di Francesco, J., Johnstone, D., et al. 2016, *ApJ*, **826**, 95
 Chiang, H. F., Looney, L. W., & Tobin, J. J. 2012, *ApJ*, **756**, 168
 Chini, R., Reipurth, B., Ward-Thompson, D., et al. 1997, *ApJ*, **474**, L135
 Compiègne, M., Verstraete, L., Jones, A., et al. 2011, *A&A*, **525**, A103
 Connelley, M. S., Reipurth, B., & Tokunaga, A. T. 2008a, *AJ*, **135**, 2496
 Connelley, M. S., Reipurth, B., & Tokunaga, A. T. 2008b, *AJ*, **135**, 2526
 Coupeaud, A., Demyk, K., Meny, C., et al. 2011, *A&A*, **535**, A124
 Crapsi, A., van Dishoeck, E. F., Hogerheijde, M. R., Pontoppidan, K. M., & Dullemond, C. P. 2008, *A&A*, **486**, 245
 Crimier, N., Ceccarelli, C., Maret, S., et al. 2010, *A&A*, **519**, A65
 Draine, B. T. 2006, *ApJ*, **636**, 1114
 Draine, B. T., & Lee, H. M. 1984, *ApJ*, **285**, 89
 Duchêne, G., Bouvier, J., Bontemps, S., André, P., & Motte, F. 2004, *A&A*, **427**, 651
 Duchêne, G., Bontemps, S., Bouvier, J., et al. 2007, *A&A*, **476**, 229
 Dullemond, C. P., & Monnier, J. D. 2010, *ARA&A*, **48**, 205
 Dunham, M. M., Stutz, A. M., Allen, L. E., et al. 2014, *Protostars and Planets VI*, eds. H. Beuther, R. S. Klessen, C. P. Dullemond and T. Henning, 914, 195
 Dupac, X., Bernards, J. P., Boudet, N., et al. 2003, *A&A*, **404**, 11
 Eisner, J. A., Arce, H. G., Ballering, N. P., et al. 2018, *ApJ*, **860**, 77
 Enoch, M. L., Evans, N. J., I., Sargent, A. I., & Glenn, J. 2009, *ApJ*, **692**, 973
 Enoch, M. L., Corder, S., Duchêne, G., et al. 2011, *ApJS*, **195**, 21
 Evans, N. J., I., Dunham, M. M., K., J. J., et al. 2009, *ApJS*, **181**, 321
 Fanciullo, L., Kemper, F., Scicluna, P., Dharmawardena, T. E., & Srinivasan, S. 2020, *MNRAS*, **499**, 4666
 Feddersen, J. R., Arce, H. G., Kong, S., et al. 2020, *ApJ*, **896**, 11
 Feigelson, E. D., & Montmerle, T. 1985, *ApJ*, **289**, 19
 Fischer, W. J., Megeath, S. T., Stutz, A. M., et al. 2013, *Astron. Nachr.*, **334**, 53
 Forbrich, J., Lada, C. J., Lombardi, M., Román-Zúñiga, C., & Alves, J. 2015, *A&A*, **580**, A114
 Furlan, E., Fischer, W. J., Ali, B., et al. 2016, *ApJS*, **224**, 5
 Galametz, M., Maury, A. J., Valdivia, V., et al. 2019, *A&A*, **632**, A5
 Garay, G., Ramirez, S., Rodriguez, L. F., Curiel, S., & Torrelles, J. M. 1996, *ApJ*, **459**, 193
 Greene, T. P., Wilking, B. A., André, P., Young, E. T., & Lada, C. J. 1994, *ApJ*, **434**, 614
 Großschedl, J. E., Alves, J., Meingast, S., et al. 2018, *A&A*, **619**, A106
 Guilloteau, S., Dutrey, A., Piétu, V., & Boehler, Y. 2011, *A&A*, **529**, A105
 Hacar, A., Tafalla, M., Forbrich, J., et al. 2018, *A&A*, **610**, A77
 Haisch, K. E., J., Greene, T. P., Barsony, M., & Stahler, S. W. 2004, *AJ*, **127**, 1747
 Haworth, T. J. 2021, *MNRAS*, **503**, 4172
 Hernández-Gómez, A., Loinard, L., Chandler, C. J., et al. 2019, *ApJ*, **875**, 94
 Higuchi, A. E., Sakai, N., Watanabe, Y., et al. 2018, *ApJS*, **236**, 52
 Hildebrand, R. H. 1983, *QJRAS*, **24**, 267
 Hoyle, F., & Wickramasinghe, N. C. 1969, *Nature*, **223**, 459
 Johnstone, D., & Bally, J. 1999, *ApJ*, **510**, 49
 Jones, T. J., Mergen, J., Odewahn, S., et al. 1994, *AJ*, **107**, 2120
 Jones, A. P., Fanciullo, L., Köhler, M., et al. 2013, *A&A*, **558**, A62
 Jones, A. P., Köhler, M., Ysard, N., Bocchio, M., & Verstraete, L. 2017, *A&A*, **602**, A46
 Jørgensen, J. K., Schoier, F. L., & van Dishoeck, E. F. 2002, *A&A*, **389**, 908
 Jørgensen, J. K., Bourke, T. L., Myers, P. C., et al. 2007, *ApJ*, **659**, 479
 Kainunlainen, J., Stutz, A. M., Stanke, T., et al. 2017, *A&A*, **600**, A141
 Kauffmann, J., Bertoldi, F., Bourke, T. L., Evans, N. J., I., & Lee, C. W. 2008, *A&A*, **487**, 993
 Kuan, Y. J., Mehringer, D. M., & Snyder, L. E. 1996, *ApJ*, **459**, 619
 Kwon, W., Looney, L. W., Mundy, L. G., Chiang, H. F., & Kemball, A. J. 2009, *ApJ*, **696**, 841
 Lada, C. J. 1987, *IAUS*, **115**, 1
 Lada, C. J., & Wilking, B. A. 1984, *ApJ*, **287**, 610
 Li, D., Kauffmann, J., Zhang, Q., & Chen, W. 2013, *ApJ*, **768**, L5
 Li, J. I.-H., Liu, H. B., Hasegawa, Y., & Hirano, N. 2017, *ApJ*, **840**, 72
 Lis, D. C., & Menten, K. M. 1998, *ApJ*, **507**, 794

- Lis, D. C., Serabyn, E., Keene, J., et al. 1998, *ApJ*, 509, 299
- Liu, H. B. 2019, *ApJ*, 877, L22
- Looney, L. W., Mundy, L. G., & Welch, W. J. 2000, *ApJ*, 529, 477
- Martí, J., Rodríguez, L. F., & Reipurth, B. 1993, *ApJ*, 416, 208
- Mason, B., Dicker, S., Sadavoy, S. I., et al. 2020, *ApJ*, 893, 13
- Maurý, A. J., André, P., Hennebelle, P., et al. 2010, *A&A*, 512, A40
- McMullin, J. P., Waters, B., Schiebel, D., Young, W., & Golap, K. 2007, *ASPC*, 376, 127
- Megeath, S. T., Gutermuth, R., Muzerolle, J., et al. 2012, *AJ*, 144, 192
- Menella, V., Brucato, J. R., Colangeli, L., et al. 1998, *ApJ*, 496, 1058
- Mény, C., Gromov, V., Boudet, N., et al. 2007, *A&A*, 468, 171
- Mezger, P. G., Wink, J. E., & Zylka, R. 1990, *A&A*, 228, 95
- Miotello, A., Testi, L., Lodato, G., et al. 2014, *A&A*, 567, A32
- Miyake, K., & Nakagawa, Y. 1993, *Icarus*, 106, 20
- Murillo, N. M., Harsono, D., McClure, M., Lai, S. P., & Hogerheijde, M. R. 2018, *A&A*, 615, L14
- Myers, P. C., & Ladd, E. F. 1993, *ApJ*, 413, 47
- Nagy, Z., Menechella, A., Megeath, S. T., et al. 2020, *A&A*, 642, A137
- Nakatani, R., Liu, H. B., Zhang, Y., et al. 2020, *ApJ*, 895, L2
- Natta, A., Testi, L., Neri, R., Shepherd, D. S., & Wilner, D. J. 2004, *A&A*, 416, 179
- Natta, A., Testi, L., Calvet, N., et al. 2007, *Protostars and Planets V*, eds. B. Reipurth, D. Jewitt, & K. Keil, 951, 767
- Nielbock, M., Chini, R., & Müller, S. A. H. 2003, *A&A*, 408, 245
- Ormel, C. W., Paszun, D., Dominik, C., & Tielens, A. G. G. M. 2009, *A&A*, 502, 845
- Ossenkopf, V., & Henning, T. 1994, *A&A*, 291, 943
- Paradis, D., Bernard, J. P., Mény, C., & Gromov, V. 2011, *A&A*, 534, A118
- Pascucci, I., Gorti, U., & Hollenbach, D. 2012, *ApJ*, 751, 42
- Pech, G., Loinard, L., Dzib, S. A., et al. 2016, *ApJ*, 818, 116
- Pérez, L. M., Carpenter, J. M., Chandler, C. J., et al. 2012, *ApJ*, 760, 17
- Pfalzner, S., Davies, M. B., Gounelle, M., et al. 2015, *Physica Scripta*, 90, 068001
- Planck Collaboration XXIII. 2011, *A&A*, 536, A23
- Rayner, J., McLean, I., McCaughrean, M., & Aspin, C. 1989, *MNRAS*, 241, 469
- Reipurth, B., Rodríguez, L. F., & Chini, R. 1999, *ApJ*, 118, 983
- Ricci, L., Testi, L., Natta, A., et al. 2010, *A&A*, 512, A15
- Ricci, L., Trotta, F., Testi, L., et al. 2012, *A&A*, 540, A6
- Rodríguez, L. F. 1997, *IAUS*, 182, 83
- Rodríguez, L. F., Curiel, S., Moran, J. M., et al. 1989, *ApJ*, 386, L85
- Sadavoy, S. I., Di Francesco, J., Johnstone, D., Currie, M. J., & Drabek, E. O. 2013, *ApJ*, 767, 126
- Sadavoy, S. I., Stutz, A. M., Schnee, S., et al. 2016, *A&A*, 588, A30
- Saraceno, P., André, P., Ceccarelli, C., Griffin, M., & Molinari, S. 1996, *A&A*, 309, 827
- Schnee, S., Enoch, M., Noriega-Crespo, A., et al. 2010, *ApJ*, 708, 127
- Schnee, S., Mason, B., Di Francesco, J., et al. 2014, *MNRAS*, 444, 2303
- Schuller, F., André, P., Shimajiri, Y., et al. 2021, *A&A* 651, A36
- Sheehan, P. D., Tobin, J. J., Federman, S., Megeath, S. T., & Looney, L. W. 2020, *ApJ*, 902, 196
- Shimajiri, Y., Takahashi, S., Takakuwa, S., Saito, M., & Kawabe, R. 2009, *PASJ*, 61, 1055
- Shirley, Y. L., Nordhaus, M. K., Grcevich, J. M., et al. 2005, *ApJ*, 632, 982
- Shirley, Y. L., Claussen, M. J., Bourke, T. L., Young, C. H., & Blake, G. A. 2007, *ApJ*, 667, 329
- Shirley, Y. L., Huard, T. L., Pontoppidan, K. M., et al. 2011, *ApJ*, 728, 143
- Takahashi, S., Saito, M., Ohashi, N., et al. 2008, *ApJ*, 688, 244
- Tanabe, Y., Nakamura, F., Tsukagoshi, T., et al. 2019, *PASJ*, 71, 8
- Tazzari, M., Testi, L., Natta, A., et al. 2021, *MNRAS*, 506, 2804
- Terebey, S., Chandler, C. J., & André, P. 1993, *ApJ*, 414, 759
- Testi, L., Birnstiel, T., Ricci, L., et al. 2014, *Protostars and Planets VI*, eds. H. Beuther, R. S. Klessen, C. P. Dullemond, & Th. Henning, 914, 339
- Tobin, J., 2019a, ALMA 870 micron Continuum Images, V1 (Harvard Dataverse), <https://doi.org/10.7910/DVN/JETGZC>
- Tobin, J., 2019b, VLA Ka-band (9 mm) Continuum–A–configuration (0.08 arcsec), V1 (Harvard Dataverse), <https://doi.org/10.7910/DVN/ICKYX0>
- Tobin, J. J., Chandler, C. J., Wilner, D. J., et al. 2013, *ApJ*, 779, 93
- Tobin, J. J., Stutz, A. M., Megeath, S. T., et al. 2015, *ApJ*, 798, 128
- Tobin, J. J., Stutz, A. M., Manoj, P., et al. 2016, *ApJ*, 831, 36
- Tobin, J. J., Megeath, S. T., van't Hoff, M., et al. 2019, *ApJ*, 886, 6
- Tobin, J. J., Sheehan, P. D., Megeath, S. T., et al. 2020, *ApJ*, 890, 130
- Tychoniec, L., Tobin, J. J., Karska, A., et al. 2018a, *ApJ*, 852, 18
- Tychoniec, L., Tobin, J. J., Karska, A., et al. 2018b, *ApJS*, 238, 19
- Ubach, C., Maddison, S. T., Wright, C. M., et al. 2012, *MNRAS*, 425, 3137
- Walsh, C., Millar, T. J., & Nomura, H. 2013, *ApJ*, 766, 23
- Weintraub, D. A., Sandell, G., & Duncan, W. D. 1989, *ApJ*, 340, L69
- Williams, J. P., Plambeck, R. L., & Heyer, M. H. 2003, *ApJ*, 591, 1025
- Wilner, D. J., Reid, M. J., & Menten, K. M. 1999, *ApJ*, 513, 775
- Wong, Y. H. V., Hirashita, H., & Li, Z. Y. 2016, *PASJ*, 68, 67
- Ysard, N., Koehler, M., Jimenez-Serra, I., Jones, A. P., & Verstraete, L. 2019, *A&A*, 631, A88
- Yu, K. C., Bally, J., & Devine, D. 1997, *ApJ*, 485, 45
- Yun, J. L., Moreira, M. C., Torrelles, J. M., Afonso, J. M., & Santos, N. C. 1996, *AJ*, 111, 841

Appendix A: Large fields maps

Table A.1 contains the list of all detected sources from the nine fields. The maps of the 246.2 GHz ALMA data showing all the detected sources in each field are shown in Fig. A.1. The field of SIMBA-a is not shown as SIMBA-a is the only source detected within its field.

Table A.1. All detected sources in the nine observed fields, with their coordinates and equivalent name in the HOPS nomenclature.

Field	Source	R.A. (J2000)	Dec. (J2000)	HOPS name ^a
CSO33	CSO33-a	05:35:19.41	-05:15:38.41	HOPS-56-B
	CSO33-b	05:35:19.48	-05:15:33.08	HOPS-56-A-A/B/C
	CSO33-c	05:35:19.81	-05:15:35.22	V2358 Ori
	V1334 Ori	05:35:17.92	-05:15:32.84	HOPS-56-D
FIR6c	FIR6c-a	05:35:21.36	-05:13:17.85	HOPS-409
	FIR6c-c	05:35:21.69	-05:13:12.69	...
	FIR6c-b	05:35:20.78	-05:13:23.24	...
	FIR6d	05:35:20.15	-05:13:15.71	HOPS-59-A
FIR2	FIR2	05:35:24.30	-05:08:30.74	HOPS-68
	MIR18	05:35:25.23	-05:08:23.90	HOPS-69
FIR1-a	FIR1a-a	05:35:24.87	-05:07:54.63	HOPS-394-B
	FIR1a-b	05:35:24.05	-05:07:52.07	HOPS-394-A
	MIR17-A	05:35:25.58	-05:07:57.66	HOPS-71-a
	MIR17-B	05:35:25.54	-05:07:56.83	HOPS-71-b
	MIR16	05:35:25.72	-05:07:46.25	HOPS-72
MMS9	MMS9-a	05:35:25.97	-05:05:43.34	HOPS-78-A
	MMS9-b	05:35:26.15	-05:05:45.80	HOPS-78-B
	MMS9-c	05:35:26.18	-05:05:47.14	HOPS-78-C
	MMS9-d	05:35:25.92	-05:05:47.70	HOPS-78-D
	MIR12	05:35:25.76	-05:05:58.15	HOPS-76
MMS5	MMS6	05:35:23.42	-05:01:30.53	HOPS-87
	MMS5	05:35:22.47	-05:01:14.34	HOPS-88
MMS2	MMS2-a	05:35:18.34	-05:00:32.96	HOPS-92-A-A/B
	MMS2-b	05:35:18.27	-05:00:33.95	HOPS-92-B
	MIR4	05:35:17.74	-05:00:31.06	...
	MMS1	05:35:18.05	-05:00:18.00	J05351805-050017.98
CSO3	CSO3-a	05:35:15.05	-05:00:08.06	HOPS-93
	CSO3-b	05:35:16.17	-05:00:02.50	HOPS-94
SIMBA-a	SIMBA-a	05:35:29.72	-04:58:48.60	HOPS-96

Notes. ^(a)Fischer et al. 2013; Furlan et al. 2016

Appendix B: Fit and residuals

We present here one example of uv fit result towards SIMBA-a. The best fit was obtained for an elliptical Gaussian of size $0.13 \times 0.11''$ with a position angle of -47 . After convolving with the beam, we obtained an ellipse of size $0.35 \times 0.29''$ that we used to measure the associated flux densities.

Appendix C: Dust SED results and uncertainty derivation

C.1. Dust parameters

Plots of the derived free-free emission percentages, the optical depths, the H_2 column densities, and the (envelope + disk)

masses as a function of the SED temperatures. The results are gathered in Tables C.1 and C.2.

C.2. Derivation of uncertainties

In order to derive the uncertainties of the different quantities, we use error propagation. In general, the error of an arbitrary function $q(x_1, \dots, x_n)$ with uncertainties $(\delta x_1, \dots, \delta x_n)$, is

$$\Delta q = \sqrt{\left(\frac{\partial q}{\partial x_1} \delta x_1\right)^2 + \dots + \left(\frac{\partial q}{\partial x_n} \delta x_n\right)^2}. \quad (C.1)$$

The formula used to derive the uncertainties of the dust emissivity spectral index, $d\beta$; dust opacity, $d\tau$; H_2 column density, dN_{H_2} ; and (envelope + disk) mass, $dM_{env+disk}$ are shown below:

$$\begin{aligned} \Delta\beta^2 = & \left(\frac{\delta F_{v1}}{\ln\left(\frac{\nu_1}{\nu_2}\right) \ln\left(1 - \frac{F_{v1}}{\Omega_s B_{v1}}\right) (\Omega_s B_{v1} - F_{v1})} \right)^2 \\ & + \left(\frac{\delta F_{v2}}{\ln\left(\frac{\nu_1}{\nu_2}\right) \ln\left(1 - \frac{F_{v2}}{\Omega_s B_{v2}}\right) (\Omega_s B_{v2} - F_{v2})} \right)^2 \\ & + \left(\frac{\delta\Omega_s}{\ln\left(\frac{\nu_1}{\nu_2}\right)} \right)^2 \left(\frac{F_{v1}}{\Omega_s (B_{v1}\Omega_s - F_{v1}) \ln\left(1 - \frac{F_{v1}}{B_{v1}\Omega_s}\right)} \right. \\ & \left. - \frac{F_{v2}}{\Omega_s (B_{v2}\Omega_s - F_{v2}) \ln\left(1 - \frac{F_{v2}}{B_{v2}\Omega_s}\right)} \right)^2, \quad (C.2) \end{aligned}$$

$$\Delta\tau = \frac{1}{B_v \Omega_s - F_v} \sqrt{\delta F_v^2 + \left(\frac{F_v}{\Omega_s} \delta\Omega_s\right)^2}, \quad (C.3)$$

$$\Delta N_{H_2} = \frac{1}{\mu m_H R \kappa_0 \left(\frac{\nu}{\nu_0}\right)^\beta} \sqrt{\delta\tau_v^2 + \left(\tau_v \ln\left(\frac{\nu}{\nu_0}\right) \delta\beta\right)^2}, \quad (C.4)$$

$$\Delta M_{env+disk} = \mu m_H d \sqrt{(d\Omega \delta N_{H_2})^2 + (2N_{H_2} \Omega \delta d)^2 + (N_{H_2} d \delta \Omega)^2}. \quad (C.5)$$

C.3. Dust SEDs plots

We show here the obtained dust SEDs for each of the source samples, corresponding to the derived dust parameters (β , T_d , and N_{H_2}). We added to each plot the measured flux densities as a self-consistency check.

Appendix D: $C^{18}O$ maps

We present here the $C^{18}O$ ($J=2-1$) maps towards the CSO33 and MMS9 fields.

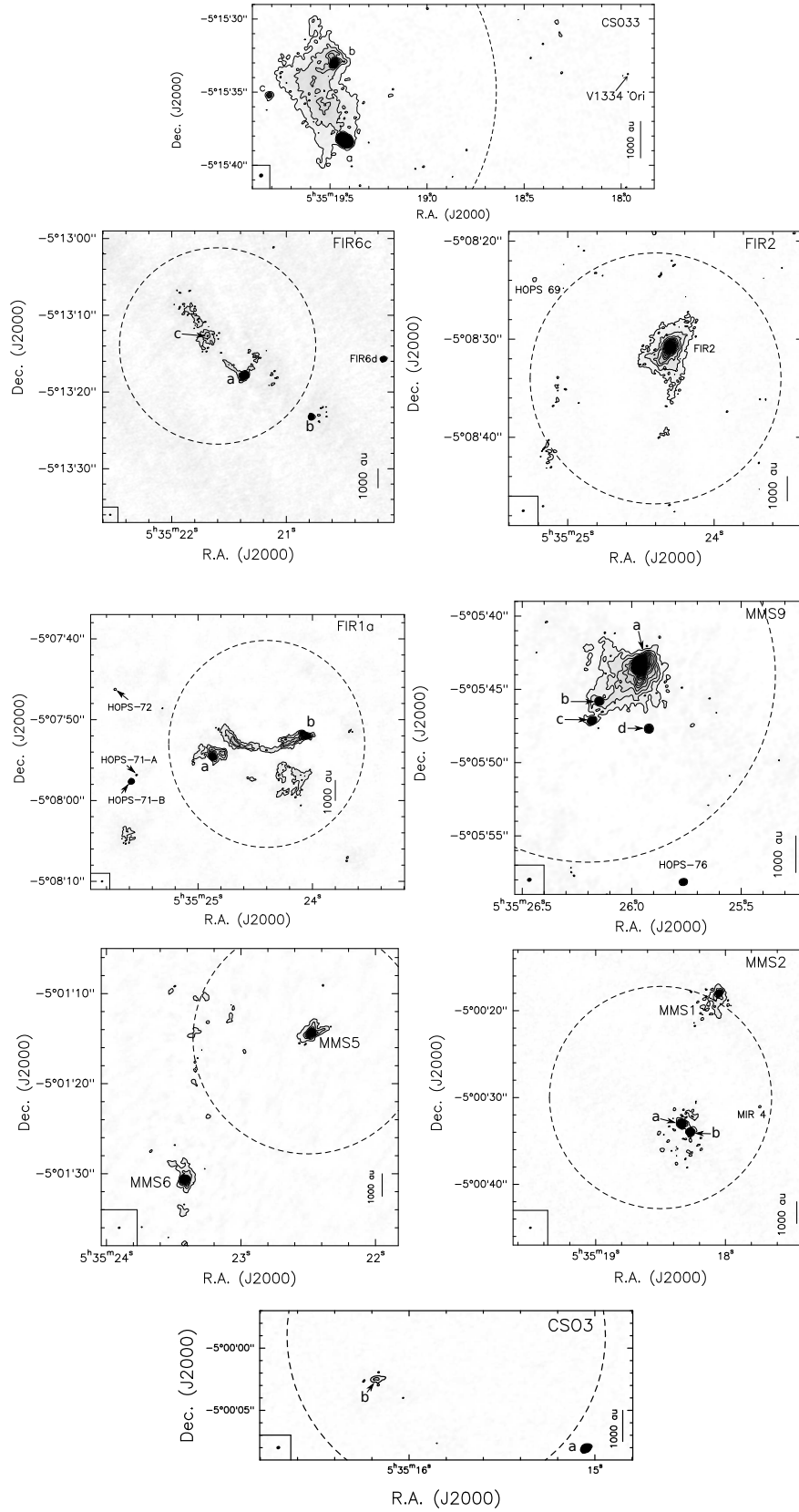


Fig. A.1. 246.2 GHz continuum maps of some of the sample sources with a large field of view to show the detection of the sources located outside the primary beam. Contour levels start at 5σ except for CS033, FIR2 and CS03 for which contour levels start at 3σ . Level steps are 5σ for FIR6c, FIR2, MMS9, MMS2 and CS03, 7σ for CS033 and FIR1a and 10σ for MMS5. The primary beam is indicated by the dashed circles and the beam size is represented at the bottom left of the plots. These maps are not corrected for the primary beam.

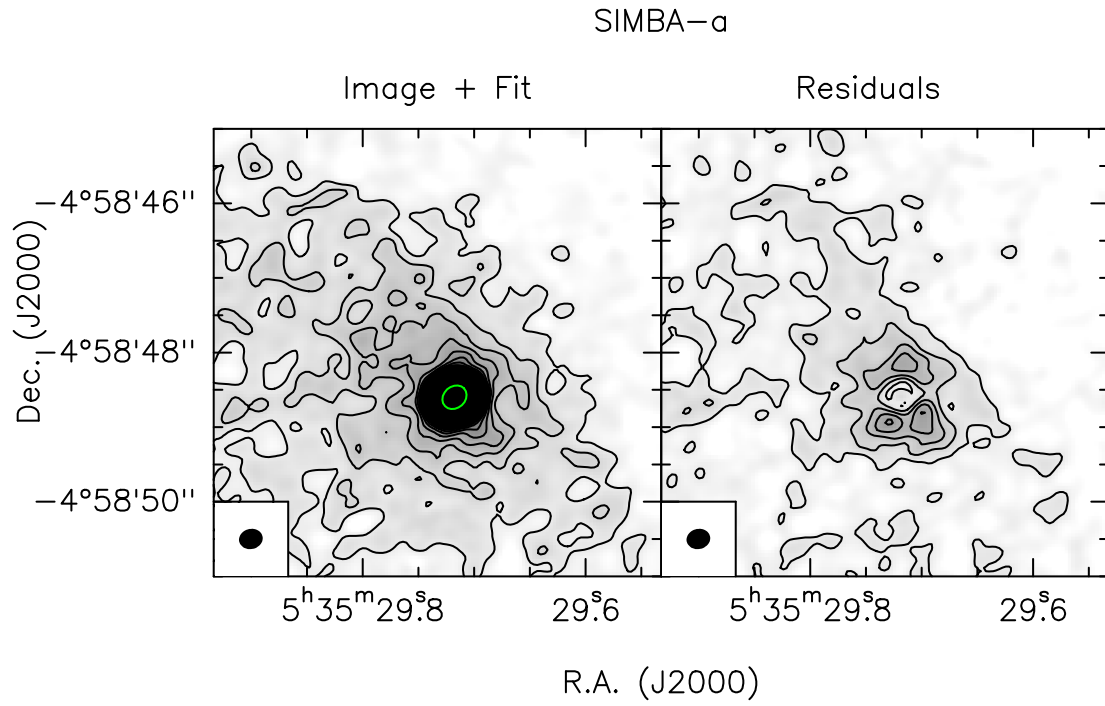


Fig. B.1. Example of a uv fit for SIMBA-a. *Left:* 246.2 GHz continuum map of SIMBA-a with contours starting from 5σ with steps every 5σ (see Table 1 for 1σ values). The source size derived from the fit and convolved by the beam is indicated by the green ellipse. *Right:* Image of the residuals of the uv fit. The synthesised beam is depicted in black in the lower left corner of each panel.

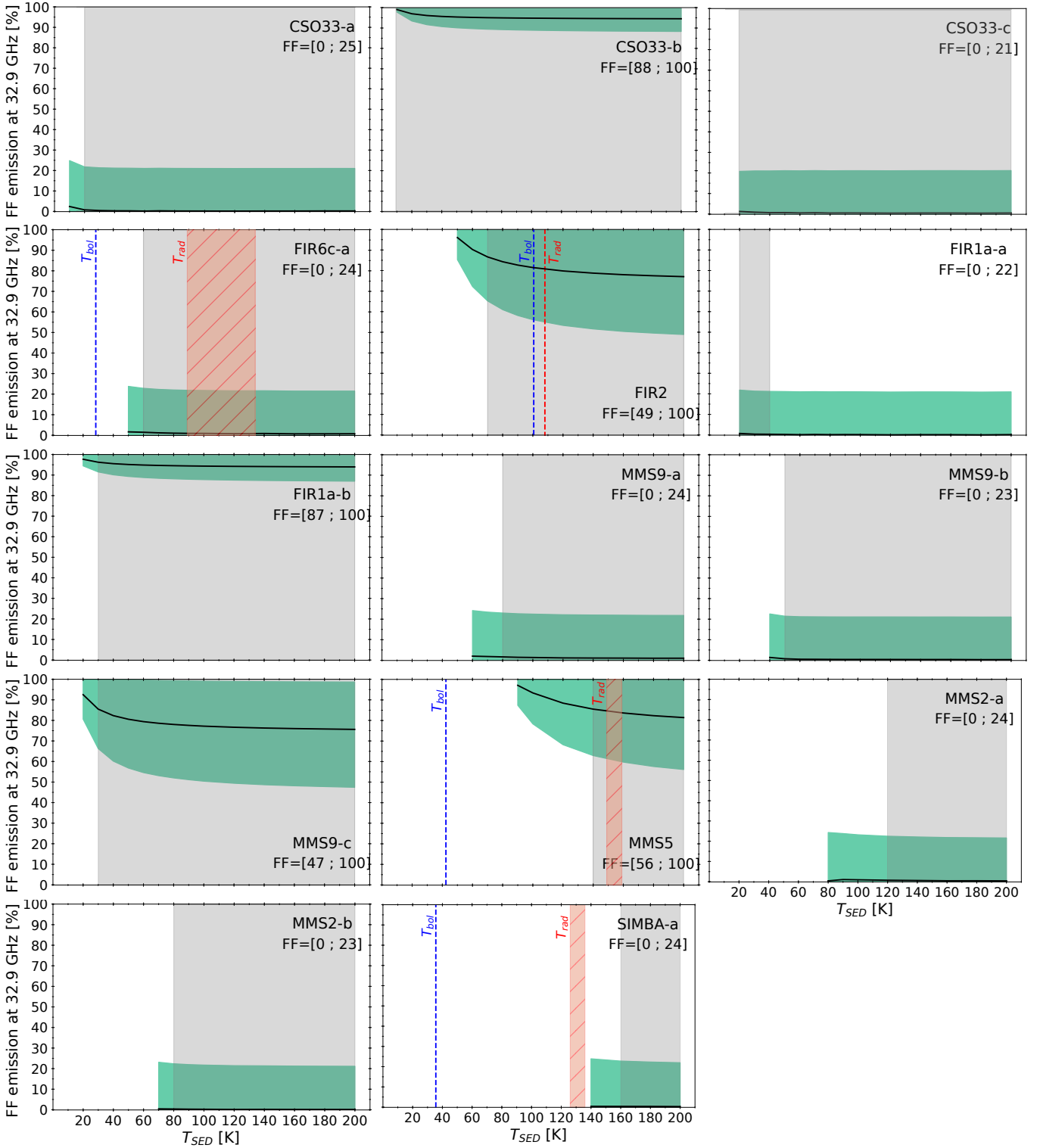


Fig. C.1. Free-free emission at 32.9 GHz as a function of the SED temperature for each source. The shaded grey area corresponds to the range of temperature for which the β values derived are authorised. For each source the minimum and maximum values of the free-free emission percentage derived over the full temperature range are indicated at the top right of the plots. For single systems, the bolometric temperature, T_{bol} , derived from *Herschel* (Furlan et al. 2016) is indicated by a blue dashed line and the radiative temperature, T_{rad} , by a red dashed area or by a red dashed line in the case of FIR2.

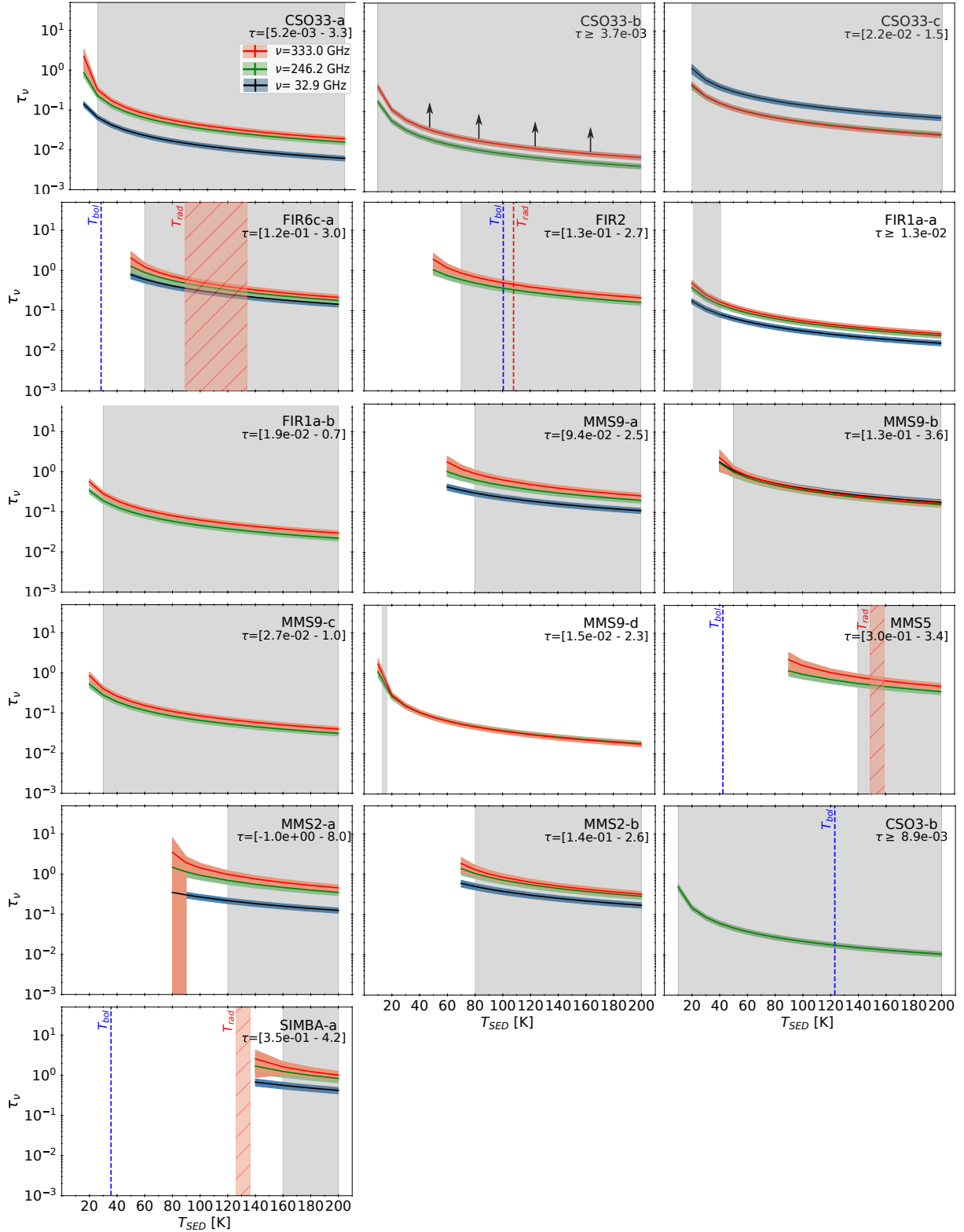


Fig. C.2. Dust optical depths, τ_ν , as a function of the SED temperature at 333 GHz (red lines) and at 246.2 GHz (green lines) for each source. The shaded grey area corresponds to the range of temperature for which the β values derived are authorised. The full range of optical depth values derived over the temperature range for each source is indicated on the top right side of the plot. For single systems, the bolometric temperature, T_{bol} , derived from *Herschel* (Furlan et al. 2016) is indicated by a blue dashed line and the radiative temperature, T_{rad} , by a red dashed area or by a red dashed line in the case of FIR2. Black arrows indicate that the derived values are lower limits.

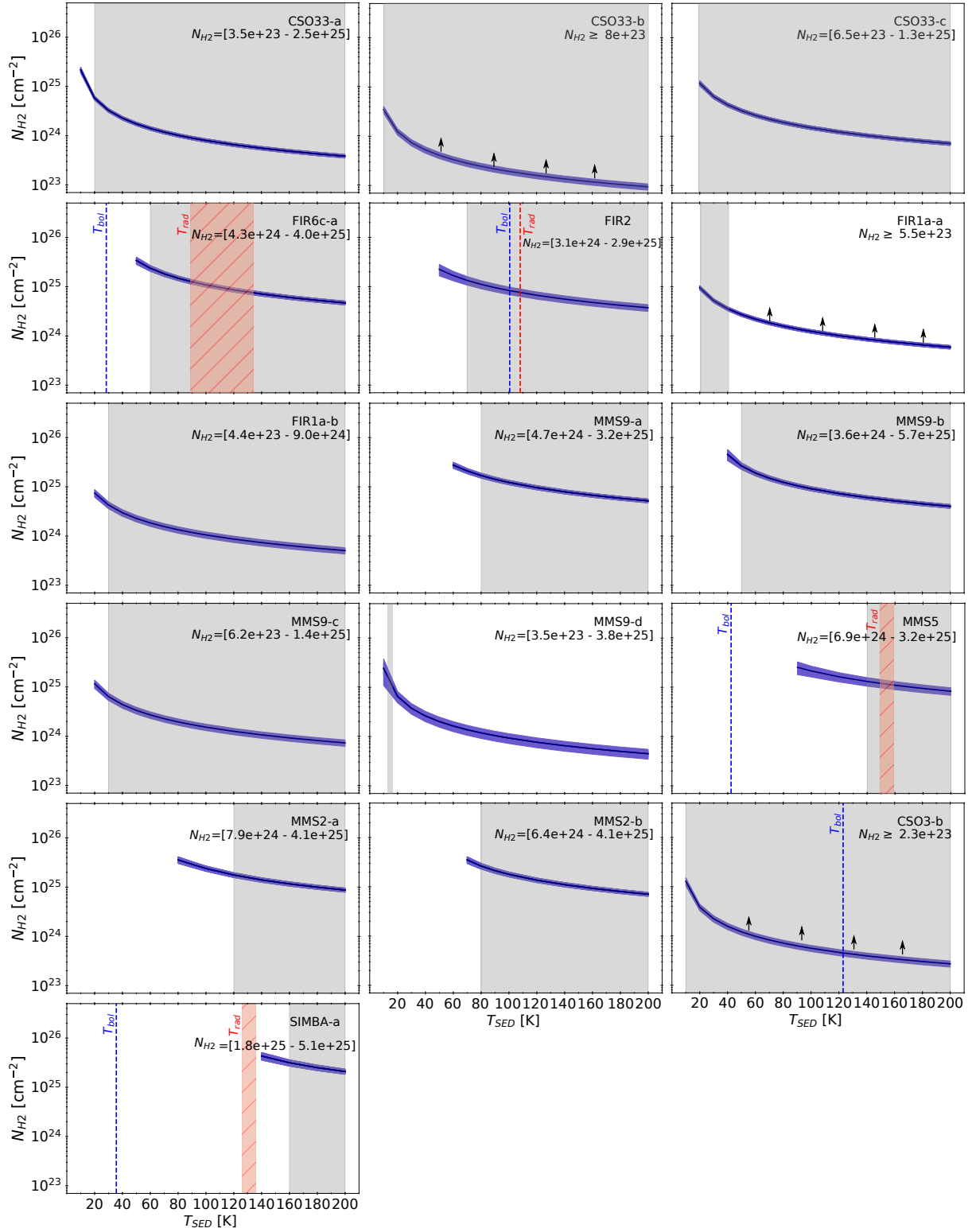


Fig. C.3. H_2 column densities, N_{H_2} , as a function of the SED temperature for each source. The shaded grey area corresponds to the range of temperature for which the β values derived are authorised. For each source the minimum and maximum values of N_{H_2} derived over the full temperature range are indicated at the top right of the plots. For single systems, the bolometric temperature, T_{bol} , derived from *Herschel* (Furlan et al. 2016) is indicated by a blue dashed line and the radiative temperature, T_{rad} , by a red dashed area or by a red dashed line in the case of FIR2. Black arrows indicate that the derived values are lower limits.

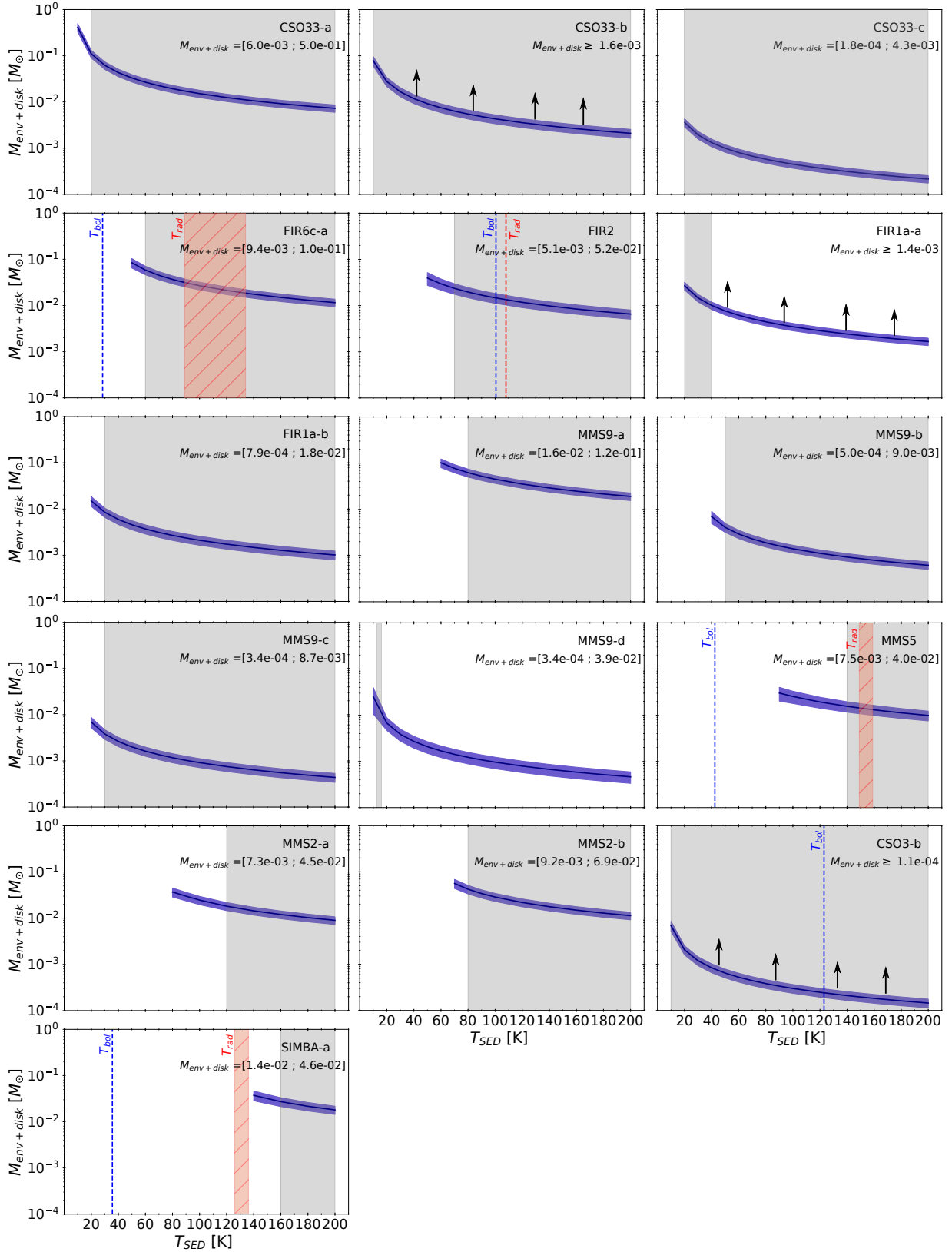


Fig. C.4. Envelope+disk masses, $M_{\text{env} + \text{disk}}$, as a function of the SED temperature for each source. The shaded grey area corresponds to the range of temperature for which the β values derived are authorised, which constrains the possible range of T_{dust} values. The range of (envelope + disk) masses derived over the temperature range for each source is indicated on the top side of the plots. For single systems, the bolometric temperature, T_{bol} , derived from *Herschel* (Furlan et al. 2016), is indicated by a blue dashed line and the radiative temperature, T_{rad} , by a red dashed area or by a red dashed line in the case of FIR2. Black arrows indicate that the derived values are lower limits.

Table C.1. Results of the dust parameter extraction using the SED method for each source. The range of SED temperature derived for each source follows the constraints given by theoretical and observational works on β (see Sect. 2). First, the linear source sizes are reported in the second column. Then, the SED temperature range is reported in Col. 3. The dust emissivity indexes, between 333 GHz and 246.2 GHz ($\beta_{333-246.2}$), 333 GHz and 32.9 GHz ($\beta_{333-32.9}$), and 246.2 GHz and 32.9 GHz ($\beta_{246.2-32.9}$) are reported in Col. 4. The range of dust optical depth values derived at 333 GHz, τ_{333} , 246.2 GHz, $\tau_{246.2}$, and 32.9 GHz, $\tau_{32.9}$, as well as the H₂ column densities, $N_{\text{H}_2\text{-mm}}$, and (envelope + disk) masses, $M_{\text{env+disk}}$, corresponding to the derived range of temperature, are reported in Cols. 5 to 7. The range of free-free emission percentage at 32.9 GHz is indicated in the last column.

Source	Size [au × au]	T_{SED} [K]	$\beta_{333-246.2}$ $\beta_{333-32.9}$ $\beta_{246.2-32.9}$	τ_{333} $\tau_{246.2}$ $\tau_{32.9}$	$N_{\text{H}_2\text{-mm}}$ [$\times 10^{24} \text{ cm}^{-2}$]	$M_{\text{env+disk}}$ [$\times 10^{-2} M_{\odot}$]	FF [%]
CSO33-a	310 × 153	20–200	0.2–1.7 0.4–0.8 0.4–0.7	0.02–0.4 0.01–0.3 0.01–0.1	0.3–25	1–13	0–24
CSO33-b	236 × 236	10–200	1.2–3.4 0.3–0.6 0.2–0.4	≥ 0.01 ≥ 0.004 ...	≥ 0.1	≥ 0.2	88–100
CSO33-c	27.5 × 27.5	20–200	-0.5–0.9 -0.5–-0.3 -0.6–-0.4	0.02–0.6 0.02–0.5 0.1–1.5	1–13	0.02–0.5	0–21
FIR6c-a	122 × 51	60–200	0.1–2.9 0.1–0.6 0.0–0.3	0.2–1.6 0.2–1.1 0.1–0.7	4–27	1–7	0–23
FIR2	67 × 67	70–200	0.4–3.2 0.1–0.6 0.0–0.3	0.2–1.1 0.1–0.7 ...	3–16	0.5–3	49–100
FIR1a-a	90 × 79	20–40	-0.1–1.4 0.2–0.5 0.1–0.5	≥ 0.1 ≥ 0.1 ≥ 0.1	≥ 3	≥ 1	0–22
FIR1a-b	98 × 51	30–200	0.5–2.2 -0.3–0.0 -0.5–-0.3	0.03–0.3 0.02–0.2 ...	0.4–5	0.1–1	87–100
MMS9-a	173 × 55	80–200	0.3–3.0 0.3–0.8 0.2–0.5	0.2–1.0 0.2–0.7 0.1–0.4	3–19	2–7	0–23
MMS9-b	20 × 20	50–200	-0.3–2.7 -0.1–0.3 -0.1–0.2	0.1–1.5 0.1–1.3 0.2–1.3	3–31	0.05–0.5	0–22
MMS9-c	39 × 39	30–200	0.3–2.3 0.1–0.5 0.0–0.4	0.03–0.5 0.03–0.3 ...	0.6–7	0.03–0.5	47–100
MMS9-d	51 × 51	10–20	-0.5–2.6	0.3–2.4 0.3–1.4 ...	5–37	0.5–4	...
MMS5	59 × 51	140–200	0.4–2.7 0.1–0.5 0.0–0.3	0.4–1.0 0.3–0.7 ...	6–16	1–2	56–100
MMS2-a	51 × 51	120–200	0.3–3.0 0.5–1.0 0.4–0.8	0.4–1.2 0.3–0.9 0.1–0.3	7–20	1–2	0–23
MMS2-b	51 × 47	80–200	-0.2–2.2 0.2–0.6 0.2–0.5	0.3–1.7 0.2–1.3 0.1–0.6	6–29	1–5	0–22
CSO3-b	...	10–200 ≥ -1.4	... ≥ 0.01 ...	≥ 0.2	≥ 0.01	...
SIMBA-a	51 × 43	160–200	-0.1–3.3 0.3–0.8 0.2–0.6	0.7–2.2 0.6–1.6 0.4–0.7	16–36	1–3	0–23

Table C.2. Bolometric and radiative temperatures, T_{bol} and T_{rad} , for the four sources of our sample that are single systems, their corresponding dust parameters (β , $M_{\text{env+disk}}$), and the free-free emission percentage.

Source	T_{bol} [K]	β_{Tbol}	M_{Tbol} [$\times 10^{-2} M_{\odot}$]	FF _{Tbol} [%]	T_{rad} [K]	β_{rad}	M_{Trad} [$\times 10^{-2} M_{\odot}$]	FF _{Trad} [%]
FIR6c-a	28.4	89–134	0.1–0.3	1.5–4	0–21
FIR2	100.6	0.4–1.6	1.1–1.9	56–100	108	0.4–1.6	1.0–1.8	55–100
MMS5	42.4	149–159	0.5–1.8	1.0–1.9	60–100
CSO3-b	123	≥ -0.7	≥ 0.02	≥ 0	265–324
SIMBA-a	35.6	126–136

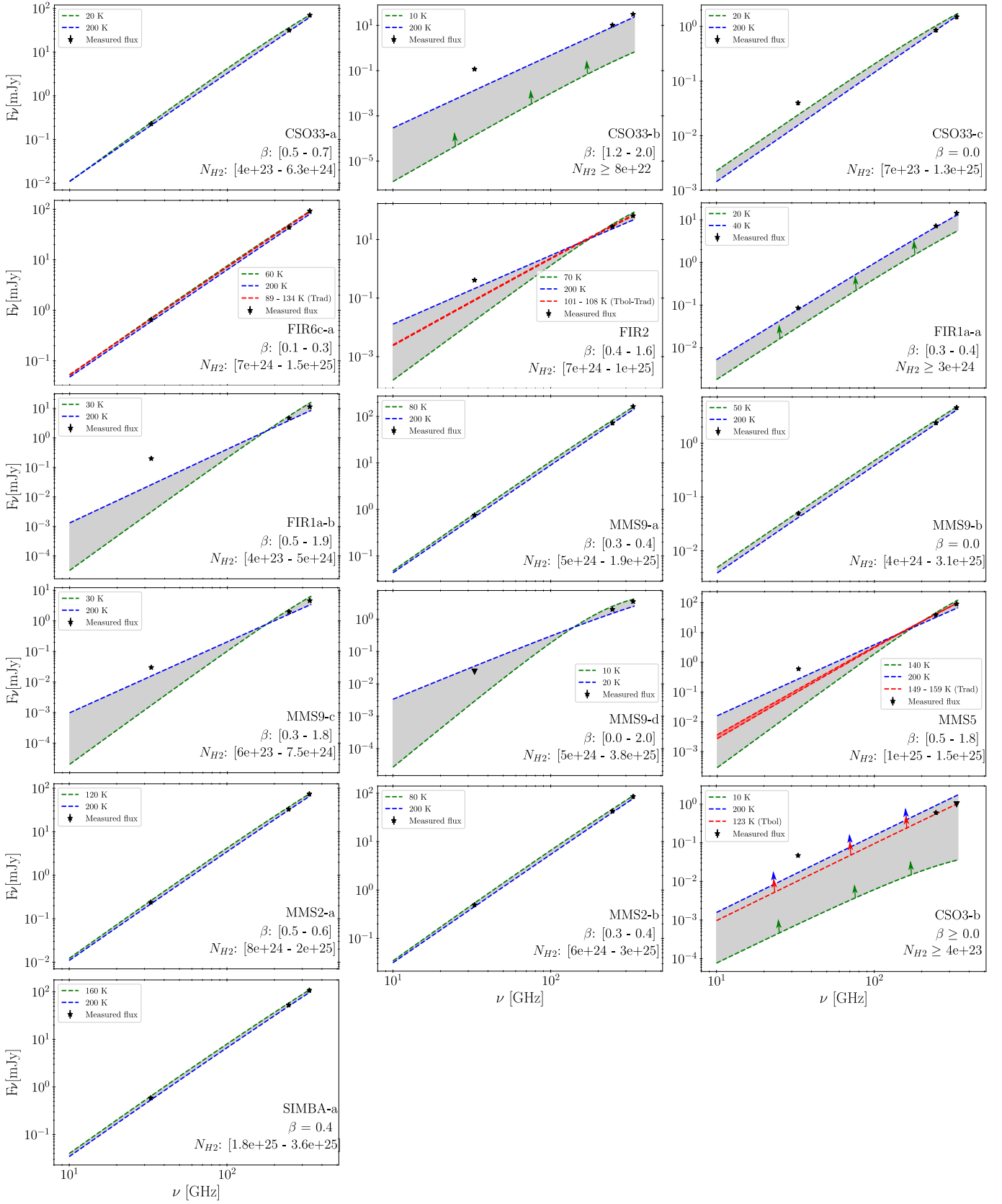


Fig. C.5. Dust SED obtained for each source from the derived dust temperatures; dust emissivity spectral indexes, β , and H_2 column density, N_{H_2} . For each source the dust SED of the two extreme values for the corresponding dust temperature range are indicated by blue and green dashed lines. The possible dust SEDs corresponding to the intermediate values of dust temperatures are represented by the grey shaded area. For FIR6c-a, FIR2, MMS5, and CSO3-b the dust SEDs corresponding to the derived range of T_{rad} and/or T_{bol} are also represented by red dashed lines and a red shaded area. Measured flux densities are represented by black stars. Lower limits are represented by coloured arrows.

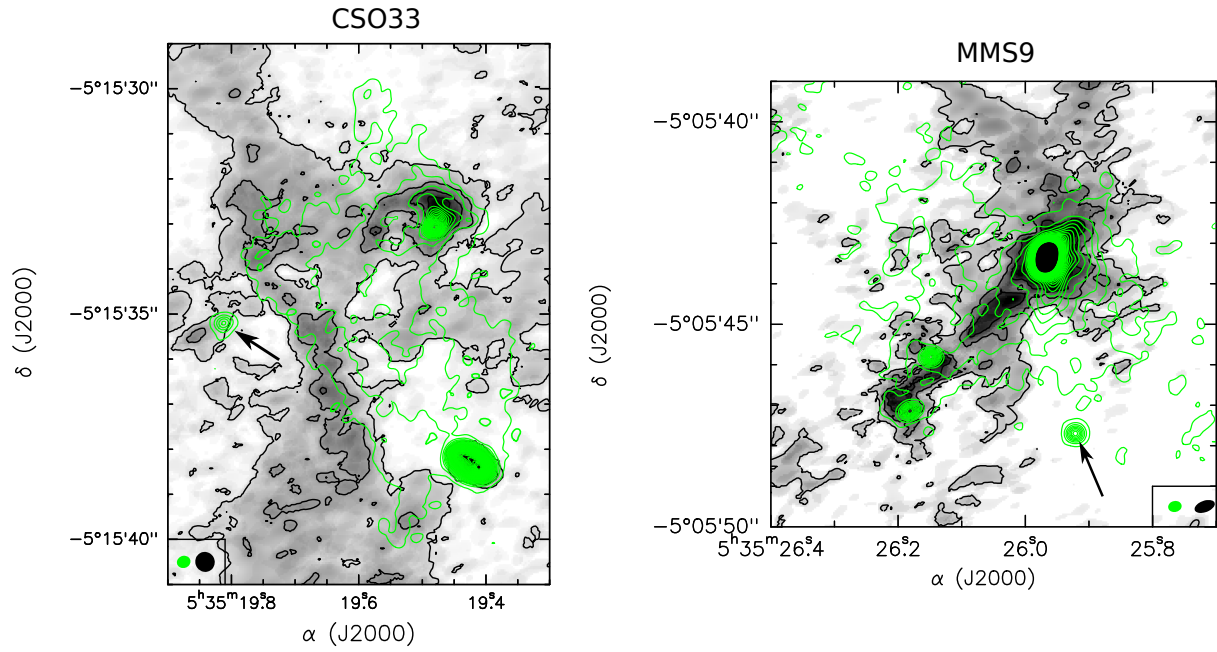


Fig. D.1. CSO33 and MMS9 maps of C^{18}O ($J=2-1$) (in grey shades and black contours) with the 246.2 GHz continuum contours superposed (in green). The C^{18}O contours starts at 3σ ($1\sigma = 4.8\text{mJy/beam}$ for CSO33 and $1\sigma = 3\text{mJy/beam}$ for MMS9) with steps of 5σ . Continuum contours starts at 5σ with steps of 10σ (see Table 1 for the 1σ values). The complete description for the molecular observations setup will be presented in a forthcoming paper (Bouvier et al. in prep.). Arrows are pointing towards CSO33-c and MMS9-d.

3.2 The chemical nature of Orion protostars: Are ORANGES different from PEACHES? ORANGE II.

Investigating the chemical nature of solar-mass protostars to understand the chemical past of our Sun is not easy because solar-mass protostars do not share the same chemical history. In particular, hot corinos and WCCC objects, two chemically distinct types of solar-mass protostars, show how wide the range of composition of protostellar envelopes can be. Nonetheless, recent studies showed similarities between the abundance of iCOMs in hot corinos and comets (e.g. [Bianchi et al. 2019](#); [Drozdovskaya et al. 2019](#); [Rivilla et al. 2020](#)). Our Sun is therefore thought to be an ancient hot corino.

Until recently, only about a dozen of hot corinos had been identified. Thanks to the arrival of powerful (sub)-mm interferometers such as ALMA, many new hot corinos have been discovered. The recent PEACHES project found that hot corinos are likely prevailing in the low-mass star-forming region of Perseus ($\sim 56\%$ of the source sample; [Yang et al. 2021](#)). However, PEACHES and most of the studies aiming to investigate the chemical nature of solar-mass protostars (e.g. [Bergner et al. 2017](#); [Belloche et al. 2020](#); [van Gelder et al. 2020](#); [Yang et al. 2021](#)) focus on low-mass star-forming regions whilst our Sun is likely born in a large cluster, with massive stars in its vicinity ([Adams 2010](#); [Pfalzner et al. 2015](#)). Are hot corinos also abundant in such regions? We need to target solar-mass protostars in regions similar to the one in which our Sun is more likely born, i.e. close to massive stars. The OMC-2/3 filament is the best and closest analogue to the Sun's birth environment as several nearby HII regions bound the filament. Very recently, the intermediate-mass protostars MMS6 and HOPS-370 (OMC-2 FIR3) and the solar-mass protostar HOPS-108 were the first hot corinos to be identified in OMC-2/3 ([Tobin et al. 2019](#); [Hsu et al. 2020](#); [Chahine et al. 2021](#)). Hot corinos are, therefore, present in massive star-forming regions, but the statistic is too poor to conclude on the ancient chemical nature of our Sun. The goals of this second ORANGES study are to identify how many hot corinos are present in the OMC-2/3 filament and to understand whether the environment plays a role in the chemical composition of protostellar envelopes. To this end, we performed a molecular line analysis focussing on methanol, the most common and abundant iCOM found in hot corinos.

We detected methanol lines towards the centre of 5 out of the 19 investigated sources. In these sources, using non-LTE radiative transfer methods, we found that the gas from which methanol is emitted is hot (≥ 85 K), dense ($n \geq 3 \times 10^6$ cm⁻³), and compact ($\theta \sim 39$ – 136 au in diameter). Following the definition of hot corinos ([Ceccarelli 2004](#); [Ceccarelli et al. 2007](#)), these five sources are bona fide hot corinos. Recently, [De Simone et al. \(2020a\)](#) showed that molecular lines from a hot corino could be hidden by dust if the latter is optically thick enough. Therefore, to check that dust optical depth is not hiding hot corinos also in the OMC-2/3 filament, we compared the integrated intensity of one of the methanol line emissions with the dust optical depths derived in [Bouvier et al. \(2021\)](#). We found no correlation which strongly suggests that the dust optical depth is not the main parameter affecting the detection of hot corinos in this region.

Finally, adding to the five new hot corinos, MMS6, HOPS-370 and HOPS-108, we have a detection rate of hot corinos in OMC-2/3 of $(31 \pm 20)\%$. Compared to the $(56 \pm 14)\%$ found in the Perseus region, hot corinos might be scarcer in a high-UV illuminated region. The environment, therefore, perhaps plays a role in solar-mass chemical content, but the statistics are too poor to draw a definite conclusion.

The hereafter paper has been accepted to the *Astrophysical Journal* on February, 26th, 2022.

The chemical nature of Orion protostars: Are ORANGES different from PEACHES? ORANGES II.

MATHILDE BOUVIER ¹, CECILIA CECCARELLI ¹, ANA LÓPEZ-SEPULCRE ^{1,2}, NAMI SAKAI ³, SATOSHI YAMAMOTO ^{4,5}
AND YAO-LUN YANG ^{3,6}

¹Univ. Grenoble Alpes, CNRS, IPAG, F-38000 Grenoble, France

²Institut de Radioastronomie Millimétrique (IRAM), 300 rue de la Piscine, F-38400 Saint-Martin d'Hères, France

³The Institute of Physical and Chemical Research (RIKEN), 2-1, Hirosawa, Wako-shi, Saitama 351-0198, Japan

⁴Department of Physics, The University of Tokyo, Bunkyo-ku, Tokyo 113-0033, Japan

⁵Research Center for the Early Universe, The University of Tokyo, 7-3-1, Hongo, Bunkyo-ku, Tokyo 113-0033, Japan

⁶Department of Astronomy, University of Virginia, Charlottesville, VA 22904-4235, USA

Submitted to ApJ

ABSTRACT

Understanding the chemical past of our Sun and how life appeared on Earth is no mean feat. The best strategy we can adopt is to study newborn stars located in an environment similar to the one in which our Sun was born and assess their chemical content. In particular, hot corinos are prime targets since recent studies showed correlations between interstellar Complex Organic Molecules (iCOMs) abundances from hot corinos and comets. The ORion ALMA New GEneration Survey (ORANGES) aims to assess the number of hot corinos in the closest and best analogue to our Sun's birth environment, the OMC-2/3 filament. In this context, we investigated the chemical nature of 19 solar-mass protostars and found that 26% of our sample sources shows warm methanol emission indicative of hot corinos. Compared to the Perseus low-mass star-forming region, where the PERseus ALMA CHEMistry Survey (PEACHES) detected $\sim 60\%$ of hot corinos, the latter seem to be relatively scarce in the OMC-2/3 filament. While this suggests that the chemical nature of protostars in Orion and Perseus is different, improved statistics is needed in order to consolidate this result. If the two regions are truly different, this would indicate that the environment is likely playing a role in shaping the chemical composition of protostars.

Keywords: Astrochemistry (75) — Protostars (1302) — Star formation (1569) — Chemical abundances (224)

1. INTRODUCTION

Understanding how life appeared on Earth is one of the Holy Grail in Science. From the astrophysical point of view, the Sun's birth environment being long dissipated, we cannot see what happened in its youth. We can, however, study solar-mass protostars that are currently forming in other regions of our Galaxy to understand the full story of our planetary system formation.

The discovery of two chemically distinct types of solar-mass protostars, hot corinos and Warm Carbon Chain Chemistry (WCCC) sources, shows that the story might

not be the same for every solar-mass protostar. While hot corinos are compact (≤ 100 au), hot (≥ 100 K), and dense ($\geq 10^7 \text{cm}^{-3}$) regions (Ceccarelli 2004; Ceccarelli et al. 2007), enriched in interstellar Complex Organic Molecules (iCOMs; Herbst & Van Dishoeck 2009; Ceccarelli et al. 2017), WCCC objects are deficient in iCOMs but show a larger zone (~ 2000 au) enriched in unsaturated carbon chain molecules (Sakai et al. 2008; Sakai & Yamamoto 2013). In between these two extreme cases, there exist objects called hybrids that present both hot corino and WCCC features (e.g. L483, B335; Imai et al. 2016; Oya et al. 2017; Jacobsen et al. 2019).

Until recently, only a dozen hot corinos were discovered, but thanks to the arrival of powerful (sub)-mm interferometers such as ALMA, more hot corinos are iden-

tified. In particular, the recent Perseus ALMA Chemistry Survey (PEACHES; Yang et al. 2021) targeted 50 solar-mass protostars in the Perseus Molecular Cloud, a region forming only low-mass stars. They found that $\sim 56\%$ of their source sample show warm methanol emission, indicating that hot corinos are likely prevailing in this region. The Perseus Molecular Cloud is, however, different from the Solar birth environment. The latter was most likely a dense protocluster with high-mass stars in its vicinity (e.g. Adams 2010; Pfalzner et al. 2015). Are hot corinos also abundant in an environment analogue to that where our Sun was born? Recent studies showed similarities between the abundances of iCOMs found in hot corinos compared to those found in comets (Bianchi et al. 2019; Drozdovskaya et al. 2019; Rivilla et al. 2020). Did our Sun experience a hot corino phase? We need to target low-mass protostars belonging to massive star-forming regions (SFRs).

The closest and best analogue of our Sun’s birth environment is the OMC-2/3 filament, located in the Orion A molecular cloud. Very recently, three hot corinos were detected in this region, the intermediate-mass protostars HOPS-87 (also known as MMS6) and HOPS-370 (also known as OMC2-FIR3) (Hsu et al. 2020; Tobin et al. 2019) and the solar-type protostar HOPS-108 located in the OMC-2 FIR4 protocluster (Tobin et al. 2019; Chahine et al. 2022). Although hot corinos are present in massive SFRs (Codella et al. 2016; Hsu et al. 2020; Chahine et al. 2022), the statistics is too poor to draw any conclusion on the chemical past of our Sun. We, therefore, need more systematic studies of hot corinos in massive SFRs.

The ORion ALMA New GEneration Survey (ORANGES) is a project aiming to study the chemical nature of the Solar-type protostars located in the OMC-2/3 filament, (393 ± 25) pc from the Sun (Großschedl et al. 2018), with an angular resolution of $0.25''$ (~ 100 au). ORANGES is analogous to PEACHES because the two studies have been designed to have the same sensitivity (corrected for the distance), spatial resolution and spectral setup. It allows a direct comparison of the two environments, i.e. the OMC-2/3 filament and the Perseus Molecular Cloud. One of the goals of ORANGES is to assess the number of hot corinos in the OMC-2/3 region, and provide a first answer concerning the chemical past of our Sun. In ORANGES, we targeted the same protostars targeted by Bouvier et al. (2021). They were initially 9 chosen protostellar sources based on single-dish studies (e.g. Chini et al. 1997; Lis et al. 1998; Nielbock et al. 2003) satisfying the following three criteria: (1) detection in the (sub-)mm continuum emission; (2) estimated envelope mass $\leq 12 M_{\odot}$; (3)

bona fide Class 0 and I protostars (see Bouvier et al. 2020). The recent interferometric studies showed that most of these systems are in fact multiple systems (Tobin et al. 2020; Bouvier et al. 2021) which led to a total number of 19 studied targets.

The results of a previous single-dish study (Bouvier et al. 2020) towards the same targets showed that the large scale ($\leq 10^4$ au) line emission is dominated by the Photo-Dissociation Region (PDR) or by the molecular cloud, rather than the protostellar envelopes. Interferometric observations are thus essential to detect hot corinos in this highly illuminated region. In this study, we investigated the most common tracer of hot corinos, CH_3OH , in a sample of 19 embedded solar-type protostars. Table A.1 lists the targeted protostars and their coordinates.

2. OBSERVATIONS

The observations were performed between 2016 October 25th and 2017 May 5th during Cycle 4, under the ALMA project 2016.1.00376.S. The observations were performed in Band 6 using two different spectral setups. The ranges of frequencies covering the methanol transitions relevant for this work are 243.88 – 243.97 GHz and 261.77 – 261.88 GHz for setup 1, and 218.38 – 218.50 GHz, 230.33 – 234.08 GHz, and 234.64 – 234.76 GHz for setup 2. For setup 1, a total of 41 antennas of the 12-m array were used with a baseline length range of 18.6m – 1100m. The integration time is ~ 20 min per source. For setup 2, a total of 45 antennas of the 12-m array were used with a baseline range of 18.6m – 1400m. The integration time is ~ 8 min per source. The ALMA correlator was configured to have both narrow and wide spectral windows (spws), with 480 and 1920 channels respectively. Narrow spws have a bandwidth of 58.59 MHz with a channel spacing of 122 kHz (~ 0.15 - 0.17 km/s) while the wide spws have a bandwidth of 1875 MHz with a channel spacing of 0.977 MHz (~ 1.2 - 1.3 km/s). The bandpass and flux calibrators were J0510+1800 and J0522-3627, and the phase calibrators were J0607-0834 and J0501-0159. The flux calibration error is estimated to be better than 10%. The precipitable water vapour (PWV) was typically less than 1mm and the phase root-mean-square (rms) noise less than 60° . In the context of the ORANGES project, several molecular species were targeted but we focus here in particular on methanol (CH_3OH), the typical tracer of hot corinos. The methanol lines were found in six (both narrow and wide) spws. The rest frequencies of the methanol transition lines and the associated primary beam sizes are shown in Table A.2.

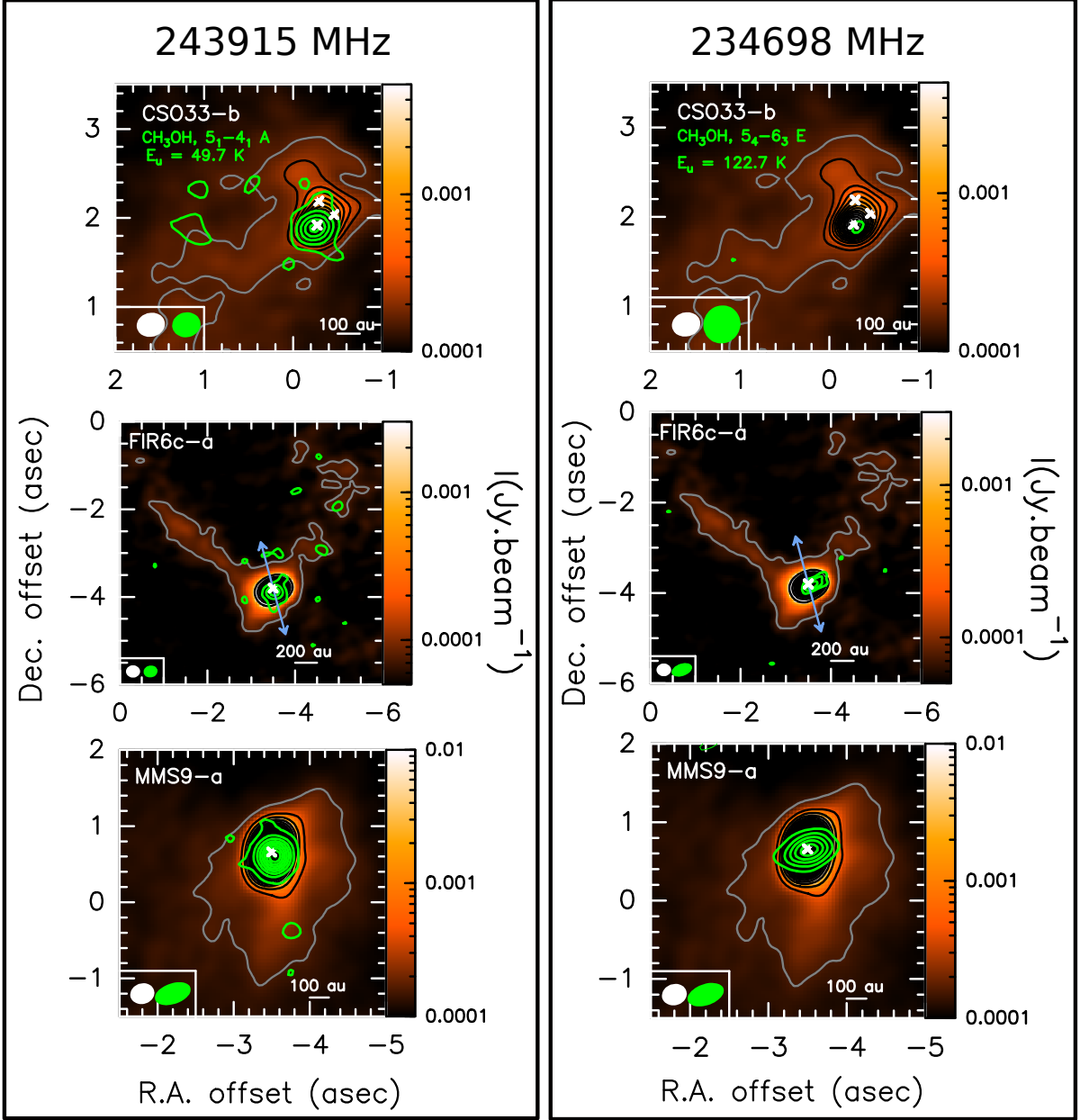


Figure 1. 1.3mm continuum maps of CSO33-b-a, FIR6c-a, and MMS9-a (coloured area, grey and black contours). The first contour levels are in grey. Levels start at 15σ for CSO33-b-a ($1\sigma = 44\mu\text{Jy}/\text{beam}$) and 10σ for MMS9-a ($1\sigma = 50\mu\text{Jy}/\text{beam}$), and 20σ for FIR6c-a ($1\sigma = 60\mu\text{Jy}/\text{beam}$). Level steps are 50σ except for CSO33-b-a where the step is 10σ . The moment 0 emission of the CH_3OH transitions at 243915 MHz ($E_u = 49.7$ K) and at 234698 MHz ($E_u = 122.7$ K) are shown with green contours in the left and right columns, respectively. For the 243915 MHz transition line, contours start at 3σ ($1\sigma = 6, 9, 8$ mJy.beam $^{-1}$.km.s $^{-1}$ for CSO33-b-a, FIR6c-a, and MMS9-a, respectively) with steps of 3σ for CSO33-b-a and FIR6c-a, and steps of 5σ for MMS9-a. For the 234698 MHz transition line, contours start at 3σ ($1\sigma = 9, 9, 12$ mJy.beam $^{-1}$.km.s $^{-1}$ for CSO33-b-a, FIR6c-a, and MMS9-a, respectively) with steps of 1σ for CSO33-b-a, FIR6c-a and 3σ for MMS9-a. The continuum and methanol associated synthesised beams are in white and green respectively and are depicted in the lower left corner of the boxes. Light blue arrows represent the orientation of the outflow of the source when known (e.g. Williams et al. 2003; Takahashi et al. 2008; Shimajiri et al. 2009; Tanabe et al. 2019; Gómez-Ruiz et al. 2019; Feddersen et al. 2020). White crosses represent the position of the sources.

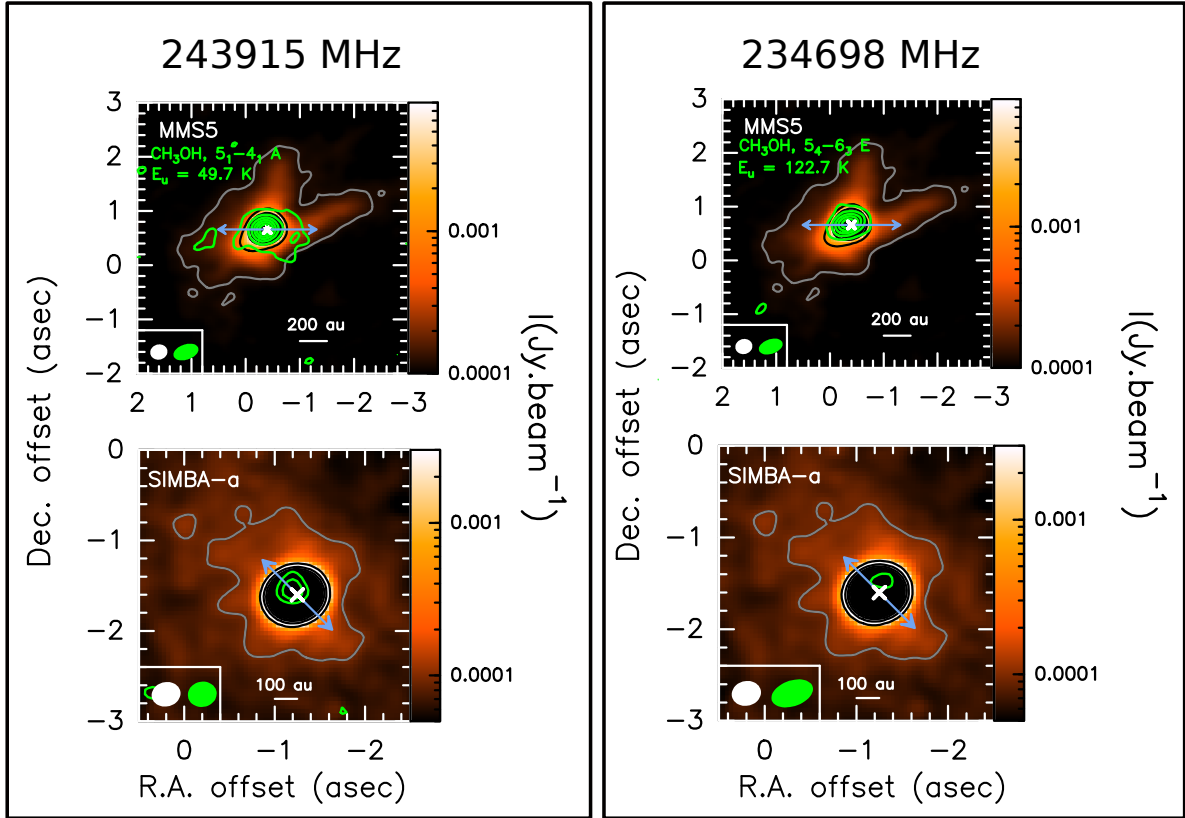


Figure 2. 1.3mm continuum maps for MMS5 and SIMBA-a (coloured area, grey and black contours). The first contour levels are in grey. Levels start at 15σ for MMS5 ($1\sigma = 80\mu\text{Jy}/\text{beam}$) and 10σ for SIMBA-a ($1\sigma = 50\mu\text{Jy}/\text{beam}$). Level steps are 50σ . The moment 0 emission of the CH_3OH transitions at 243915 MHz ($E_u = 49.7$ K) and at 234698 MHz ($E_u = 122.7$ K) are shown with green contours in the left and right columns, respectively. For the 243915 MHz transition line, contours start at 3σ ($1\sigma = 7$ and 5 $\text{mJy}\cdot\text{beam}^{-1}\cdot\text{km}\cdot\text{s}^{-1}$ for MMS5 and SIMBA-a, respectively) with steps of 10σ for MMS5 and 1σ for SIMBA-a. For the 234698 MHz transition line, contours start at 3σ ($1\sigma = 10$ and 7 $\text{mJy}\cdot\text{beam}^{-1}\cdot\text{km}\cdot\text{s}^{-1}$ for MMS5 and SIMBA-a, respectively) with steps of 5σ for MMS5 and 1σ for SIMBA-a. The continuum and methanol associated synthesized beams are in white and green respectively and are depicted in the lower left corner of the boxes. Light blue arrows represent the orientation of the outflow of the source when known (e.g. Williams et al. 2003; Takahashi et al. 2008; Tanabe et al. 2019; Gómez-Ruiz et al. 2019; Matsushita et al. 2019; Feddersen et al. 2020). White crosses represent the position of the sources.

We used the Common Astronomy Software Application (CASA; McMullin et al. 2007) for the data calibration. We then exported the calibrated visibility tables to GILDAS¹ format and performed the imaging in MAPPING. We first produced a continuum image by averaging line-free channels in the visibility plane using an automatic procedure. We then subtracted the continuum from the line emission directly in the visibility plane. We cleaned the cubes using natural weighting (with the CLEAN procedure) down to $\sim 24\text{mJy}/\text{beam}$ on average. The phase self-calibration performed on the continuum of the sources (see Bouvier et al. 2021) has been applied to the cubes. The narrow spws were re-

sampled to a channel spacing of 0.5 $\text{km}\cdot\text{s}^{-1}$. The maps shown in this paper are not corrected for the primary beam attenuation but we took into account the correction to measure the line intensities. The resulting synthesized beam and rms for each source and each spectral window are presented in Table B.1.

3. RESULTS

3.1. Methanol Lines

Methanol is detected towards the centre of 5 out of the 19 protostars: CSO33-b-a, FIR6c-a, MMS9-a, MMS5 and SIMBA-a. In these sources, the line spectra were extracted from the pixel corresponding to the position of the methanol peak, which often corresponds to the continuum emission peak. The coordinates of the position where the spectra have been extracted are indicated in

¹ <http://www.iram.fr/IRAMFR/GILDAS>

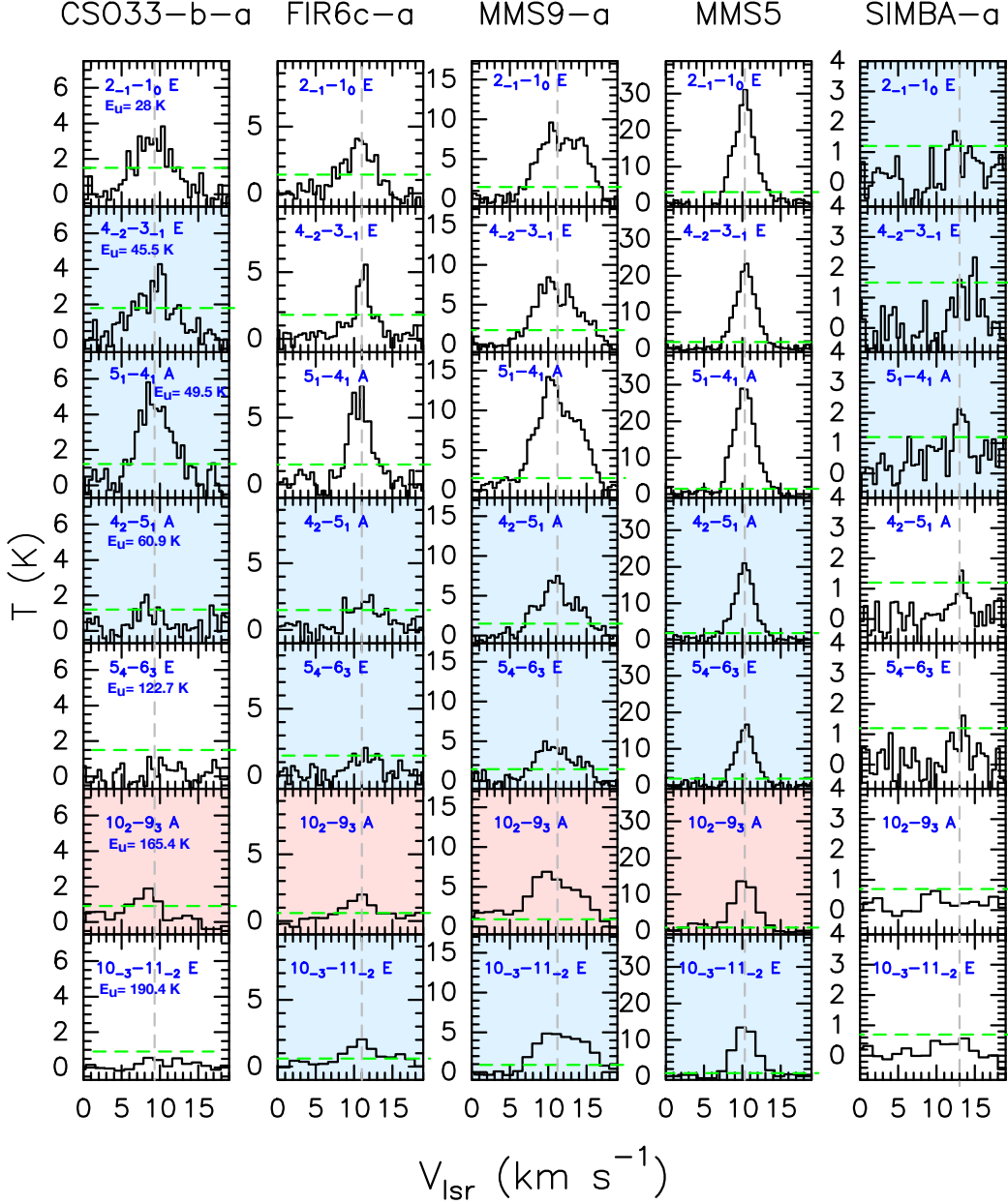


Figure 3. Methanol spectral lines detected in each source. The lines taken into account in the LVG analysis are with the blue background. The lines with the red background are likely contaminated by a line of $^{33}\text{SO}_2$ and are thus left out from the LVG analysis. The transition of each line is marked in the top left corner of the boxes. Dashed green lines show the 3σ level and dashed grey lines the averaged fitted peak velocity of all transitions of the associated source, V_{peak} , determined from the Gaussian line fitting.

Table A.1. The line detection threshold is set to 3σ at the line emission peak. Figures 1 and 2 show the moment 0 map of the two CH_3OH lines at 243915 MHz and 234698 MHz, which have different upper-level energies E_u , overlaid on the 1.3mm dust continuum emission of each source. We note that for CSO33-b-a and SIMBA-a, the methanol transition at 234698 MHz ($E_u = 122.7$ K) is considered as undetected as the emission is shown

only by a 3σ contour which is not centred on the source’s continuum peak. We found that whilst the emission of methanol lines with low upper-level energy, such as the 243915 MHz transition, is resolved and extended in most sources, the emission of methanol lines with high upper-level energy, such as the 234698 MHz transition, is compact. Methanol emission is seen near other sources of the sample but not at the position of the protostars. As

we are interested in detecting hot corinos, we will focus in this letter only on the 5 sources cited above.

We detected up to eleven CH₃OH lines with upper level energies E_{up} from 28 to 537 K and Einstein coefficients A_{ij} between 6.3×10^{-6} and $1 \times 10^{-4} \text{ s}^{-1}$. The extracted spectra of methanol lines for each source are shown in Fig. 3. We performed a Gaussian line fitting to each source in order to extract the line width (FWHM) and the peak velocity (V_{peak}). To extract the integrated intensity, we did a Gaussian fit ($\int T_B dV \text{ G.}$) and we also measured it by direct integration of the channel intensities ($\int T_B dV \text{ D.}$). Only MMS5 has lines with Gaussian profiles so we used the Gaussian fit results for this source and the results of the direct integration for the other sources. The line fitting results are reported in Table B.1, as well as the rms computed for each spectral window. Line widths range between ~ 2 and 7 km.s^{-1} .

Methanol lines can be very optically thick towards hot corinos (Bianchi et al. 2020). We therefore looked for the isotopologue CH₃¹⁸OH which is usually optically thin, in order to derive the methanol column density more accurately. Among the seven CH₃¹⁸OH lines expected to be the most intense, we detected and used only one line. The other lines are either undetected ($\leq 3\sigma$), or contaminated by lines from other molecules such as C₂H₅OH, C₂H₅CN, or CH₂DOH. The spectral parameters and Gaussian fit results of the transition used in this work, which is the $5_{0,5} - 4_{0,4}$ A transition at 231758 MHz, are reported in Table B.1. The frequencies of the seven CH₃¹⁸OH spectral lines expected to be the most intense are indicated in Fig. B.1.

3.2. Non-LTE LVG Analysis

To derive the physical properties of the gas where methanol is emitted, we performed a non-LTE analysis using the Large Velocity Gradient(LVG) code *greivg*, originally developed by Ceccarelli et al. (2003). We used the CH₃OH-H₂ collisional rates from Flower et al. (2010) between 10 and 200 K for the first 256 levels, provided by the BASECOL database² (Dubernet et al. 2013). We assumed a spherical geometry to compute the line escape probability (de Jong et al. 1980), a ratio CH₃OH-E/CH₃OH-A equal to 1, and an H₂ ortho-to-para ratio of 3. The assumed line widths are those measured from the spectral lines towards each source (see Table B.1) and we included the calibration error of 10% in the observed intensities.

The detected methanol transitions span a large range of E_{up} . First, methanol lines with E_{up} higher than 400

K have been excluded from the analysis as the collisional coefficients are not computed at these energies. Second, low energy transitions can eventually trace a different region than the higher energy level transitions. Indeed, the low upper energy level transitions ($E_u \leq 50$ K) show extended emission towards most of the sources, while the high upper level ones are compact. We, therefore, did not consider the low upper energy lines when performing the LVG analysis, except for CSO33-b-a and SIMBA-a where we detected only three low level energy transitions. Additionally, the line at 232418 MHz ($E_u = 165$ K) is likely contaminated by a ³³SO₂ line falling at the same frequency. We do not have enough information (i.e. other lines) to evaluate the possible contribution of this line. We, thus, excluded this line from the LVG analysis as well.

In the case of MMS5, we also included the detected line of CH₃¹⁸OH-A with the ¹⁸O/¹⁶O ratio equal to 560 (Wilson & Rood 1994) to better constrain the derived total CH₃OH column density for this source. For each source, the lines that are *not* used for the LVG analysis are shown in *italic* in Table B.1. In most cases, we ran the LVG radiative transfer code with only three lines so that the accuracy of the fit is not very elevated.

For each source we ran a large grid of models varying the total (CH₃OH-E + CH₃OH-A) column density from $2 \times 10^{14} \text{ cm}^{-2}$ to $3 \times 10^{19} \text{ cm}^{-2}$, the gas temperature from 20 to 200 K, and the H₂ density from $3 \times 10^5 \text{ cm}^{-3}$ to $1 \times 10^{10} \text{ cm}^{-3}$. These ranges for the parameters are those expected in hot corinos and in outflows shocks, as we expect the emission coming from either of these two types of environments. We fitted the measured CH₃OH-E and CH₃OH-A lines intensities simultaneously via comparison with the LVG model predictions, leaving $N_{\text{CH}_3\text{OH}}$, n_{H_2} , T_{kin} and the source size (θ) as free parameters. Then, since the lines are optically thin in the cases of CSO33-b-a and SIMBA-a, there is a degeneracy between the source size and the column density and the best fit of the LVG analysis actually provides the product $\theta \times N_x$. For these sources, we reran the best-fitting procedure, this time by fixing the source size and leaving $N_{\text{CH}_3\text{OH}}$, n_{H_2} , and T_{kin} as free parameters. We then varied the source size around its best-fit value to find when the $\theta \times N_x$ product does not give the same chi square, namely, where the degeneracy disappears.

The best fit for the total CH₃OH column densities range between 8×10^{15} and $4 \times 10^{18} \text{ cm}^{-2}$ with reduced χ_{red}^2 between 0.1 and 1.6. All the lines for CSO33-b-a, SIMBA-a, and the CH₃¹⁸OH line for MMS5 are optically thin ($\tau_L \leq 1$; τ_L being the line optical depth). For the other sources, methanol lines are mostly optically thick

² <https://basecol.vamdc.eu/>

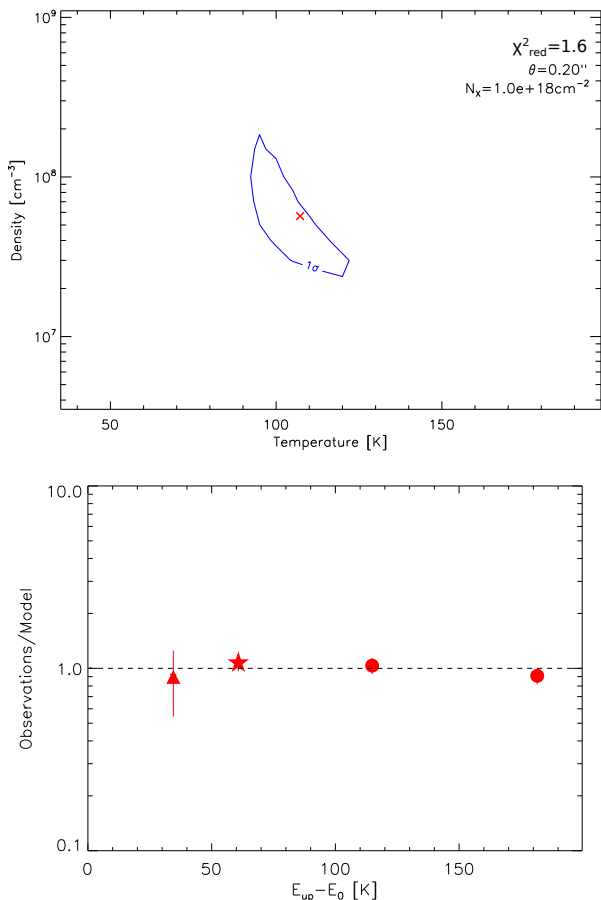


Figure 4. Result of the LVG for MMS5. *Top:* Density-temperature χ^2 contour plot. The best-fit solution is marked by a red star and the blue contours represent the 1σ confidence level, assuming the best-fit values for $N_{\text{CH}_3\text{OH-E}}$ and θ (Table 1). *Bottom:* Ratio between the observed line intensities with those predicted by the best fit model as a function of the line upper level energy E_u . Circles and stars refers to $\text{CH}_3\text{OH-E}$ and $\text{CH}_3\text{OH-A}$ respectively, whilst the triangle refers to the $\text{CH}_3^{18}\text{OH-A}$ detected line. E_0 is the ground rotational level energy which is 0 K for $\text{CH}_3\text{OH-A}$ and 7.7 K for $\text{CH}_3\text{OH-E}$ (Flower et al. 2010).

(FIR6c-a: $\tau_L = [1.1 - 5.2]$, MMS9-a: $\tau_L = [1.2 - 5.7]$, MMS5: $\tau_L = [0.9 - 4.2]$. The derived gas temperature and density are ≥ 85 K and $\geq 3 \times 10^6 \text{ cm}^{-3}$ for all sources, with the highest gas density for CSO33-b-a and the lowest gas density for FIR6c-a. The highest gas temperature is derived towards MMS9-a (≥ 130 K). The observed lines are predicted to be emitted by sources between 0.07 and $0.6''$ ($\sim 28 - 236$ au) in diameter. Figure 4 shows as an example the result of the LVG fit for MMS5. The best-fit solutions and ranges obtained for each source are reported in Table 1.

3.3. LTE versus non-LTE analysis

We provide the results we obtained with the rotational diagram method (LTE) using the same lines as in the LVG analysis in Table 1, in Figure C.1. Depending on the sources, the LTE and non-LTE analyses can give similar or different results. In the cases of FIR6c-a and MMS9, the column densities can differ by up to two orders of magnitude. However, this is because, for these sources, we did not know a priori the size of the emitting region and we thus used the sizes from Bouvier et al. (2021) which happened to be larger (up to $\sim 40\%$) than those we derived with the LVG analysis. Additionally, we see that the lines in these sources are optically thick. In general, the optical depth and the source size can be corrected using the population diagram method (Goldsmith & Langer 1999). However, a population diagram cannot correct for non-LTE effects if they are present.

For each transition line, the excitation temperature corresponding to the best fit of the LVG analysis is indicated in Table B.1. Comparing with the kinetic temperatures derived in the LVG analysis, we can see that some lines are sub-thermally populated and that there are maser lines at 218440 and 261805 MHz. We note that for CSO33-a, where the lines are optically thin and under LTE conditions, we find consistent results between the LTE and LVG analyses. For the source FIR6c-a, for which the excitation temperatures are very different from the derived kinetic temperature, we checked that non-LTE effects remain present even after correcting the rotational diagram for the size and the optical depth (there is still a scatter of points). In other words and as expected, the population diagram method can give a good approximation of the results if the lines are close to being thermally populated, which is only known when a non-LTE analysis is carried-out.

3.4. Derivation of Methanol Abundances

In the previous ORANGES study, we focused on the continuum analysis of the sources (Bouvier et al. 2021). We used the spectral energy distribution (SED) method to constrain several dust parameters such as the optical depth, the temperature, the H_2 column density and the (envelope+disk) mass. These parameters were estimated for a source size derived from a fit in the visibility plane and are reported in Table 1 with the associated source size.

We therefore used these H_2 column densities to derive the methanol abundance with respect to H_2 , $X(\text{CH}_3\text{OH})$, towards each of the 5 sources. The results are reported in Table 1. However, since the source size derived from Bouvier et al. (2021) can be larger (up to $\sim 40\%$) than the size of the methanol emission derived

Table 1. Source properties, LTE results, best fit results and 1σ confidence level (range) from the Non-LTE LVG analysis, and derived methanol abundances with respect to H_2 .

	CSO33-b-a	FIR6c-a	MMS9-a	MMS5	SIMBA-a
Source properties ^a					
source size [$'' \times ''$]	0.6×0.6	0.31×0.13	0.44×0.14 ^b	0.15×0.13	0.13×0.11
(envelope + disk) mass [$\times 10^{-2} M_\odot$]	≥ 0.2	1.5 – 4	2 – 7	1 – 2	1 – 3
T_d [K]	10 – 200	89 – 134	80 – 200	149 – 159	160 – 200
H_2 [$\times 10^{24} \text{cm}^{-2}$]	≥ 0.08	7 – 15	5 – 19	10 – 15	18 – 36
LTE results					
size used [$''$] ^c	0.6	0.2	0.25	0.14	0.12
T_{rot} [K]	124 ± 262	169 ± 54	142 ± 22	117 ± 14	151 ± 598
N_{tot} [$\times 10^{15} \text{cm}^{-2}$]	13 ± 11	21 ± 6	48 ± 7	150 ± 20	20 ± 30
LVG results					
n_{H_2} [$\times 10^7 \text{cm}^{-3}$] best fit	300	0.4	0.7	5	1.5
n_{H_2} [$\times 10^7 \text{cm}^{-3}$] range	≥ 20	0.3 – 0.5	0.6 – 1	2 – 20	≥ 0.7
T_{kin} [K] best fit	105	180	170	105	190
T_{kin} [K] range	95 – 120	≥ 85	≥ 130	90 – 125	≥ 100
$N_{\text{CH}_3\text{OH}}$ [$\times 10^{16} \text{cm}^{-2}$] best fit	1.4	120	400	200	0.8
$N_{\text{CH}_3\text{OH}}$ [$\times 10^{16} \text{cm}^{-2}$] range	0.7 – 16	80 – 200	200 – 600	140 – 800	0.1 – 3
size [$''$] best fit	0.39	0.1	0.12	0.2	0.17
size [$''$] range	0.1 – 0.6	0.07 – 0.13	0.1 – 0.13	0.13 – 0.24	0.08 – 0.38
$X(\text{CH}_3\text{OH}) \times 10^{-8}$ ^d	≤ 200	5.3 – 29 [*]	10 – 120 [*]	9.3 – 80	0.003 – 0.2

^aDerived from a continuum analysis in Bouvier et al. (2021).

^bDerived from a continuum analysis in Tobin et al. (2020).

^cThe size is calculated using the formula $\sqrt{a \times b}$, where a and b are the major and minor axes of the source size derived in Bouvier et al. (2021).

^dThe H_2 column densities can be underestimated when the source size is larger than the region of emission of methanol. The abundances derived in this work should then be taken as upper limits in these cases.

^{*}The methanol abundances are likely upper limits, as the source sizes used to derive the H_2 column densities are larger than the methanol emission sizes derived in the LVG analysis.

from the LVG analysis, the H_2 column densities can be thus underestimated in some cases, and the derived abundances would then need to be taken as upper limits. The abundances range between 3×10^{-11} and 2×10^{-6} . For CSO33-b-a, only a lower limit could be derived for the H_2 column density, so the methanol abundance derived here is an upper limit. SIMBA-a seems to have a lower methanol abundance than the other sources but since the LVG analysis has been performed with only a few data points for most of the sources, the accuracy of the fit is not very elevated.

4. DISCUSSION

4.1. New Hot Corinos Discovered in the OMC-2/3 Filament

So far, only three hot corinos have been identified in the OMC-2/3 filament, the intermediate mass protostars HOPS-87 and HOPS-370 (Hsu et al. 2020; Tobin et al.

2019), and HOPS-108 (Tobin et al. 2019; Chahine et al. 2022). One of the questions we aim to answer is: how many hot corinos are present in the OMC-2/3 filament?

Our results show that methanol is detected towards 5 protostars from our source sample and that the emission comes from a hot (≥ 85 K), dense ($\geq 3 \times 10^6 \text{cm}^{-3}$) and compact ($0.1 - 0.6''$ or $\sim 39 - 236$ au) region. According to the hot corino definition, i.e. a compact (≤ 100 au), hot (≥ 100 K), and dense ($\geq 10^7 \text{cm}^{-3}$) region enriched in iCOMs (Ceccarelli 2004; Ceccarelli et al. 2007), CSO33-b-a, FIR6c-a, MMS9-a, MMS5 and SIMBA-a are, therefore, bona fide hot corinos.³ The methanol

³ In this work, we targeted only CH_3OH which is the most abundant iCOMs found in hot corinos. Other iCOMs could be also present but their identification will be the subject of a future work.

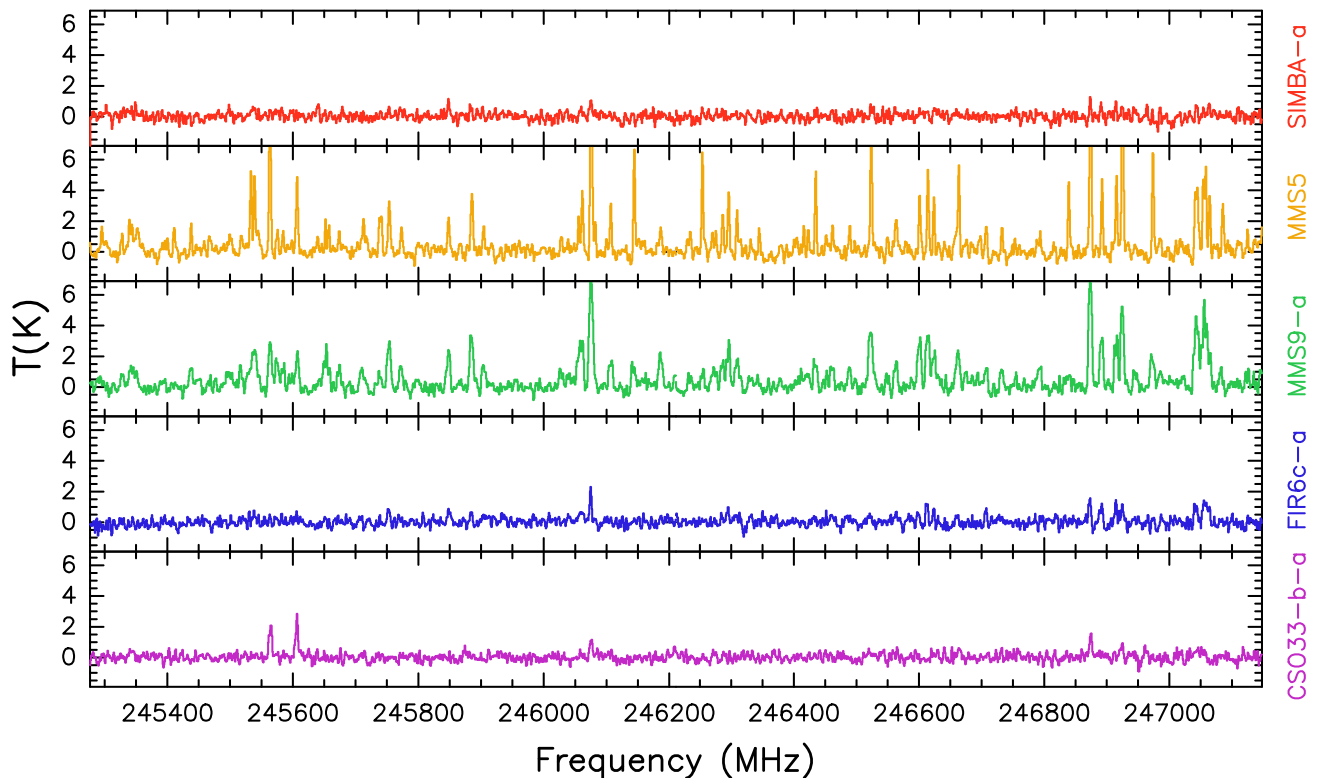


Figure 5. Spectra of each source from the large spectral window, setup 1. The spectra is extracted from a pixel at the peak of the emission.

abundances derived towards the OMC-2/3 hot corinos are comparable to what is derived in other hot corinos in Orion (HOPS-87, HOPS-168, HOPS-288, G192.12-11.10, HH212; Lee et al. 2019; Hsu et al. 2020) and in other star-forming regions (e.g. B335, IRAS16293-2422; Imai et al. 2016; Jørgensen et al. 2016, 2018), except for SIMBA-a for which the methanol abundance is about 2 orders of magnitude lower. However, for FIR6c-a and MMS9-a, the abundances could be overestimated (see Sec. 3.4), and most of the LVG analyses were performed with only three lines. Our results should thus be taken with caution.

The five hot corinos show very different spectra as shown in Fig. 5. MMS5 and MMS9-a present line-rich spectra with strong iCOM emission whilst CSO33-b-a, FIR6c-a and SIMBA-a present line-poor spectra, likely because the iCOM emission is faint. We will address the analysis of the other iCOMs detected towards the sources in a forthcoming paper.

4.2. Is the Dust Hiding Other Hot Corinos?

A recent study by De Simone et al. (2020) showed that hot corinos detected at centimetre wavelengths could be obscured by optically thick dust at millimetre wavelengths. Could it be the case for some of our sources?

Figure 6 shows the line intensity of the CH_3OH transition line at 243915 MHz as a function of the dust opacity. The latter has been derived for each source of the sample in Bouvier et al. (2021). For sources where no methanol is detected, we calculated the 3σ upper limit for the line intensity. If the optical depth was a dominant factor, we would expect to see an anti-correlation between the methanol intensity and τ , with the sources presenting methanol lines having the lowest range of dust optical depths. We do not see any anti-correlation which suggests that the dust opacity is not the main parameter affecting the detection of methanol, and hence the detection of hot corinos, in the OMC-2/3 filament. However, we note that the dust optical depth ranges derived in Bouvier et al. (2021) do not always correspond to the sizes derived from the LVG analysis performed in this work. In some cases (FIR6c-a and MMS9-a), we derived methanol emission sizes that are smaller than the size of the continuum emission. This would indicate that we are underestimating the dust optical depth at the scale probed by the methanol emission. Therefore, our conclusion needs to be taken with caution. Additionally, we can see that for four of our sample sources (MMS2-a, MMS2-b, MMS9-b, and MMS9-d), the upper limits for the derived dust optical depths are larger than 1. In

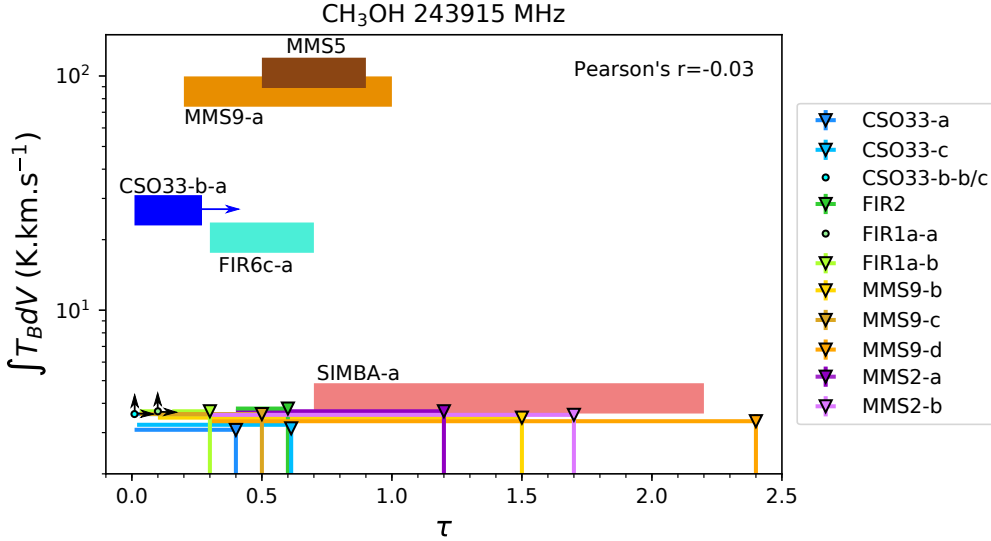


Figure 6. Line intensity of the CH_3OH line at 243915 MHz as a function of the dust optical depth, τ . For clarity, we slightly shifted vertically the upper limits for the line intensity of several sources. The initial upper limit for the CH_3OH line is 3.6 K.km.s^{-1} for the components of the systems CSO33 and MMS9, 3.7 K.km.s^{-1} for the FIR1a and MMS2 components and for CSO33-b, and 3.8 K.km.s^{-1} for FIR2. Upper limits are represented by coloured filled triangles or arrows.

these sources, we, thus, cannot exclude the possibility that the dust absorbs methanol emission at 1.3mm .

4.3. Are ORANGES Different From PEACHES?

Several studies targeting methanol and other iCOMs towards low-mass protostars have been conducted. Yang et al. (2021) surveyed 50 sources in the Perseus Molecular cloud in the context of PEACHES. They detected CH_3OH towards 56% of their source sample and other O-bearing iCOMs towards 32% of the source sample. Belloche et al. (2020) surveyed 16 class 0 protostars located in various low-mass star-forming regions as part of the Continuum And Lines in Young ProtoStellar Objects (CALYPSO) IRAM Large Program survey, with the Plateau de Bure Interferometer (PdBI, the predecessor of the current NOEMA interferometer). They detected methanol emission towards 50% of their source sample, but no more than 30% of them with at least three iCOMs detected. van Gelder et al. (2020) (ALMA) surveyed 7 Class 0 sources in the Perseus and Serpens molecular clouds and detected methanol towards three of them ($\sim 43\%$). Finally, Bergner et al. (2017) IRAM-30m targeted iCOMs towards 16 Class 0/I protostars and detected the iCOMs CH_3CHO , CH_3OCH_3 , and CH_3OCHO towards 37%, 13%, and 13% of the sources, respectively. However, contrarily to the other surveys cited above, the temperatures derived by Bergner et al. (2017) being too low ($\leq 30 \text{ K}$) for the iCOMs to originate from a hot corino region, the emission of iCOMs could trace a more external component. These surveys

show that selecting a mix of usual targets, methanol is largely detected in solar-mass protostars located in low-mass star-forming regions. Here, we compare our results with those of PEACHES only, as this is the only unbiased survey targeting iCOMs towards all the protostars of a single low-mass star-forming region. Additionally, the PEACHES and ORANGES were designed to compare directly the low-mass protostellar chemical content of two different environments, the Perseus Molecular Cloud and the OMC-2/3 filament. In both regions, the selected targets are mostly Class 0, I, or 0/I protostars with a low fraction of other (Class II or unknown) sources (7% and 11% of the sources in PEACHES and ORANGES, respectively). The relative fraction of Class 0 and I sources in each region cannot be determined accurately as the current classification of the protostars is either based on Herschel observations, for which the angular resolution is not sufficient to disentangle close multiple systems, or not certain. However, as hot corinos are detected both towards Class 0 and I sources, this parameter is not particularly relevant when comparing the two regions. Finally, the distances of the two clouds have been taken into account to achieve the same sensitivity ($\sim 22 \text{ mJy/beam}$ for PEACHES and $\sim 24 \text{ mJy/beam}$ for ORANGES) and spatial resolution for the two projects.

The results from PEACHES showed that $(56 \pm 14)\%$ of their source sample present warm methanol emission (Yang et al. 2021), which means that bona fide hot corinos are common in the Perseus Molecular Cloud. On the other hand, we targeted 19 solar-mass protostars located

in the OMC-2/3 filament and detected only five bona fide hot corinos. Even though three other hot corinos are located in the OMC-2/3 filament (HOPS-87, HOPS-370, HOPS-108; Tobin et al. 2019; Hsu et al. 2020; Chahine et al. 2022) we do not take them into account. Indeed, unlike the above-cited studies, we performed a blind search for hot corinos using an observational setup completely analogous to that done in Perseus by Yang et al. (2021). We, thus, do not want to bias our results by adding only positive hot corino detections from other studies. Finally, using only our results, we have a hot corino detection rate of $(26 \pm 23)\%$ in the OMC-2/3 filament. Therefore, hot corinos seem to be scarcer in the OMC-2/3 filament, compared to the Perseus Molecular Cloud.

The two star-forming regions seem to have different chemical protostellar content but the high uncertainty for the ORANGES survey prevents us from firmly concluding. We need to increase the statistics and to do so, a possibility would be to include the Class 0 and I population of the OMC-4 cloud, located south of OMC-1. Additionally, as mentioned in Sec. 4.2, we cannot exclude that dust could hide hot corinos towards some of our source sample and, therefore, that the detection rate of 26% is underestimated. If there is truly a difference between ORANGES and PEACHES, then the environment most likely plays a role in shaping the chemical content of protostellar cores. Bounded by 3 HII regions, the OMC-2/3 filament is highly illuminated by ultraviolet photons, and if hot corinos are less abundant in this kind of region, it would be in line with recent modelling and observational studies (Aikawa et al. 2020; Lattanzi et al. 2020; Kalvans 2021): a cloud exposed to interstellar irradiation is very likely to be less rich in O-bearing species and in iCOMs than a more shielded one.

Although we cannot totally dismiss the possibilities that (1) some of our protostars may have small hot corino regions, preventing us from detecting iCOMs at our current resolution, (2) high dust optical depths could still play a role in the non-detection of hot corinos in some of our sample sources, this study provides tentative evidence of a differentiation of the chemical nature of solar-mass protostars that are located in two different environments or, in other words, that ORANGES may be different from PEACHES.

5. CONCLUSION

The ORion ALMA New GENeration Survey aims to study the small-scale (≤ 100 au) chemical content of

solar-mass protostars located in the highly illuminated OMC-2/3 filament. We detected methanol emission centred towards 5 out of the 19 targeted sources. After performing a non-LTE LVG analysis, we showed that the methanol-emitting regions are hot ($T \geq 85$ K), dense ($n_{\text{H}_2} \geq 3.10^6 \text{ cm}^{-2}$) and compact ($\sim 0.1 - 0.6''$ or $\sim 39 - 236$ au in diameter), and correspond to hot corino regions. We thus detected five new bona fide hot corinos in the OMC-2/3 filament, which corresponds to $(26 \pm 23)\%$ of the sample sources.

On the other hand, a similar study performed in the less illuminated low-mass star-forming region of Perseus found a high detection rate, $(56 \pm 14)\%$, of hot corinos (Yang et al. 2021). Hot corinos seem thus scarcer in a highly illuminated environment such as the OMC-2/3 filament. This result indicates that the environment may very likely play a role in solar-mass protostars chemical content and that ORANGES are different from PEACHES.

Are hot corinos always abundant in low-mass star-forming regions analogue to Perseus and more scarce in analogues to the OMC-2/3 filament? We would need to perform more studies analogous to PEACHES and ORANGES in other star-forming regions to confirm this result. Finally, although hot corinos are present in a region similar to the one in which our Sun is born, they are not prevailing. The question of whether our Sun experienced a hot corino phase in its youth needs further investigations before being answered.

Acknowledgments. We deeply thank the anonymous referee for their helpful comments that contributed to significantly improving the paper. While the paper was under review, three additional hot corinos were detected in the OMC-2/3 filament (HOPS-84-A, HOPS-84-B, and MMS1) by Hsu et al. (2022). Moreover, they targeted 56 Class 0/I protostars throughout the Orion Molecular cloud and detected warm methanol towards 20% of their sample sources, which is comparable to what we found in this work. This project has received funding from the European Research Council (ERC) under the European Union’s Horizon 2020 research and innovation programme, for the Project *The Dawn of Organic Chemistry* (DOC), grant agreement No 741002. This paper makes use of the following ALMA data: ADS/JAO.ALMA#2016.1.00376.S. ALMA is a partnership of ESO (representing its member states), NSF (USA) and NINS (Japan), together with NRC (Canada) and NSC and ASIAA (Taiwan), in cooperation with the Republic of Chile. The Joint ALMA Observatory is operated by ESO, AUI/NRAO and NAOJ.

REFERENCES

- Adams, F. C. 2010, *ARA&A*, 48, 47
- Aikawa, Y., Furuya, K., Yamamoto, S., & Sakai, N. 2020, *ApJ*, 897, 110
- Belloche, A., Maury, A. J., Maret, S., et al. 2020, *A&A*, 635, A198
- Bergner, J. B., Öberg, K. I., Garrod, R. T., & Graninger, D. M. 2017, *ApJ*, 841, 120
- Bianchi, E., Chandler, C. J., Ceccarelli, C., et al. 2020, *MNRAS*, 498, L87
- Bianchi, E., Codella, C., Ceccarelli, C., et al. 2019, *MNRAS*, 483, 1850
- Bouvier, M., López-Sepulcre, A., Ceccarelli, C., et al. 2020, *A&A*, 636, A19
- . 2021, *A&A*, 653, A117
- Ceccarelli, C. 2004, *Astronomical Society of the Pacific Conference Series*, 323, 195
- Ceccarelli, C., Caselli, P., Herbst, E., Tielens, A. G. G. M., & Caux, E. 2007, *Protostars and Planets V*, eds. B. Reipurth, B. Jewitt and K. Keil, p.47
- Ceccarelli, C., Maret, S., Tielens, A. G. G. M., Castets, A., & Caux, E. 2003, *A&A*, 410, 587
- Ceccarelli, C., Caselli, P., Fontani, F., et al. 2017, *ApJ*, 850, 176
- Chahine, L., López-Sepulcre, A., Neri, R., et al. 2022, *A&A*, 657, A78
- Chini, R., Reipurth, B., Ward-Thompson, D., et al. 1997, *ApJ*, 474, L135
- Codella, C., Ceccarelli, C., Cabrit, S., et al. 2016, *A&A*, 586, L3
- de Jong, T., Boland, W., & Dalgarno, A. 1980, *A&A*, 91, 68
- De Simone, M., Codella, C., Ceccarelli, C., et al. 2020, *ApJL*, 896, L3
- Drozdovskaya, M. N., van Dishoeck, E. F., Rubin, M., Jørgensen, J. K., & Altwegg, K. 2019, *MNRAS*, 490, 50
- Dubernet, M.-L., Alexander, M. H., Ba, Y. A., et al. 2013, *A&A*, 553, A50
- Feddersen, J. R., Arce, H. G., Kong, S., et al. 2020, *ApJ*, 896, 11
- Fischer, W. J., Megeath, S. T., Stutz, A. M., et al. 2013, *AN*, 334, 53
- Fisher, J., Paciga, G., Xu, L.-H., et al. 2007, *J. Mol. Spectrosc.* 245, 7
- Flower, D. R., Pineau des Forêts, G., & Rabli, D. 2010, *MNRAS*, 409, 29
- Furlan, E., Fischer, W. J., Ali, B., et al. 2016, *ApJS*, 224, 5
- Goldsmith, P. F., & Langer, W. D. 1999, *ApJ*, 517, 209
- Gómez-Ruiz, A. I., Gusdorf, A., Leurini, S., et al. 2019, *A&A*, 629, 77
- Großschedl, J. E., Alves, J., Meingast, S., et al. 2018, *A&A*, 619, A106
- Herbst, E., & Van Dishoeck, E. F. 2009, *ARA&A*, 47, 427
- Hsu, S.-Y., Liu, S.-Y., Liu, T., et al. 2020, *ApJ*, 898, 107
- . 2022, *ApJ*, in press
- Imai, M., Sakai, N., Oya, Y., et al. 2016, *ApJ*, 830, L37
- Jacobsen, S. K., Jørgensen, J. K., Di Francesco, J., et al. 2019, *A&A*, 629, A29
- Jørgensen, J. K., Müller, H. S. P., Calcutt, H., et al. 2018, *A&A*, 620, A170
- Jørgensen, J. K., van der Wiel, M. H. D., Coutens, A., et al. 2016, *A&A*, 595, A117
- Kalvans, J. 2021, *ApJ*, 910, 54
- Lattanzi, V., Bizzocchi, L., Vasyunin, A. I., et al. 2020, *A&A*, 633, A118
- Lee, C.-F., Codella, C., Li, Z.-Y., & Liu, S.-Y. 2019, *ApJ*, 876, 63
- Lis, D. C., Serabyn, E., Keene, J., et al. 1998, *ApJ*, 509, 299
- Matsushita, Y., Takahashi, S., Machida, M. N., & Tomisaka, K. 2019, *ApJ*, 871, 221
- McMullin, J. P., Waters, B., Schiebel, D., Young, W., & Golap, K. 2007, *ASPC*, 376, 127
- Müller, H. S. P., Schlöder, F., Stutzki, J., et al. 2005, *IAUS*, 235P, 62
- Nielbock, M., Chini, R., & Müller, S. A. H. 2003, *A&A*, 408, 245
- Oya, Y., Sakai, N., Watanabe, Y., et al. 2017, *ApJ*, 837, 174
- Pfalzner, S., Davies, M. B., Gounelle, M., et al. 2015, *PhysS*, 90f8001P
- Rivilla, V. M., Drozdovskaya, M. N., Altwegg, K., et al. 2020, *MNRAS*, 492, 1180
- Sakai, N., Sakai, T., Hirota, T., & Yamamoto, S. 2008, *ApJ*, 672, 371
- Sakai, N., & Yamamoto, S. 2013, *ChRv*, 113, 8981
- Shimajiri, Y., Takahashi, S., Takakuwa, S., Saito, M., & Kawabe, R. 2009, *PASJ*, 61, 1055
- Takahashi, S., Saito, M., Ohashi, N., et al. 2008, *ApJ*, 688, 244
- Tanabe, Y., Nakamura, F., Tsukagoshi, T., et al. 2019, *PASJ*, 71, 8
- Tobin, J. J., Megeath, S. T., van't Hoff, M., et al. 2019, *ApJ*, 886, 6
- Tobin, J. J., Sheehan, P. D., Megeath, S. T., et al. 2020, *ApJ*, 890, 130
- van Gelder, M. L., Tabone, B., Tychoniec, L., et al. 2020, *A&A*, 639, A87
- Williams, J. P., Plambeck, R. L., & Heyer, M. H. 2003, *ApJ*, 591, 1025
- Wilson, T. L., & Rood, R. 1994, *ARA&A*, 32, 191

Xu, L.-H., Fischer, J., Lees, R. M., et al. 2008, *J. Mol. Spectrosc.* 251, 305

Yang, Y.-L., Sakai, N., Zhang, Y., et al. 2021, *ApJ*, 910, 20

APPENDIX

A. OBSERVATIONAL DETAILS

We present here the details of the observations. Table A.1 lists the targeted sources and their coordinates and Table A.2 shows the list of methanol transitions detected and used in this work, and their spectral parameters. Channel spacing and primary beam size for the spectral windows containing the methanol lines are also indicated.

Table A.1. Sample sources, coordinates of the dust peak continuum (D), coordinates of the positions selected to extract the spectra (P), source classification, and associated HOPS names.

Source	R.A. (D) [J2000]	Dec. (D) [J2000]	R.A. (P) [J2000]	Dec. (P) [J2000]	HOPS name ^{a,b}	Classification ^c	Notes
CSO33-a	05:35:19.41	-05:15:38.41	HOPS-56-B	0 or I	
CSO33-b	05:35:19.48	-05:15:33.08	05:35:19.48	-05:15:33.10	HOPS-56-A-A/B/C	0	triple system ^d
CSO33-c	05:35:19.81	-05:15:35.22	V2358 Ori	II	
FIR6c-a	05:35:21.36	-05:13:17.85	05:35:21.36	-05:13:17.85	HOPS-409	0	
FIR2	05:35:24.30	-05:08:30.74	HOPS-68	I	
FIR1a-a	05:35:24.87	-05:07:54.63	HOPS-394-B	0 or I	
FIR1a-b	05:35:24.05	-05:07:52.07	HOPS-394-A	0	
MMS9-a	05:35:25.97	-05:05:43.34	05:35:25.96	-05:05:43.39	HOPS-78-A	0	
MMS9-b	05:35:26.15	-05:05:45.80	HOPS-78-B	0 or I	
MMS9-c	05:35:26.18	-05:05:47.14	HOPS-78-C	0 or I	
MMS9-d	05:35:25.92	-05:05:47.70	HOPS-78-D	II?	
MMS5	05:35:22.47	-05:01:14.34	05:35:22.48	-05:01:14.35	HOPS-88	0	
MMS2-a	05:35:18.34	-05:00:32.96	HOPS-92-A-A/B	I	binary ^d
MMS2-b	05:35:18.27	-05:00:33.95	HOPS-92-B	I	
CSO3-b	05:35:16.17	-05:00:02.50	HOPS-94	I	
SIMBA-a	05:35:29.72	-04:58:48.60	05:35:29.72	-04:58:48.56	HOPS-96	0	

^aFischer et al. 2013 ^bFurlan et al. 2016 ^cBouvier et al. 2021 ^dTobin et al. 2020

Table A.2. Methanol transition lines detected in this work, their parameters, and channel spacing and primary beam size of the associated spectral windows.

Molecule	Frequency [MHz]	Transition	E_{up} [K]	g_{up}	A_{ij} [$\times 10^{-5} \text{s}^{-1}$]	channel spacing [km.s ⁻¹]	primary beam size [$''$]
CH ₃ OH	218440	4 _{-2,3} - 3 _{-1,2} E	45.5	36	4.69	0.5	28.8
	232418	10 _{2,8} - 9 _{3,7} A	165.4	84	1.87	1.3	27.1
	232945	10 _{-3,7} - 11 _{-2,9} E	190.4	84	2.13	1.3	27.1
	234683	4 _{2,3} - 5 _{1,4} A	60.9	36	1.87	0.5	26.8
	234698	5 _{4,2} - 6 _{3,3} E	122.7	44	0.63	0.5	26.8
	243915	5 _{1,4} - 4 _{1,3} A	49.7	44	5.97	0.5	25.8
	261805	2 _{1,1} - 1 _{0,1} E	28.0	20	5.57	0.5	24.1
CH ₃ ¹⁸ OH	231758	5 _{0,5} - 4 _{0,4} A	33.4	44	5.33	1.3	27.1

NOTE—Frequencies and spectroscopic parameters have been extracted from the CDMS catalogue (Müller et al. 2005). For CH₃OH (TAG 032504, version 3*) and CH₃¹⁸OH (TAG 034504, version 1*), the available data are from Xu et al. (2008) and Fisher et al. (2007), respectively.

B. GAUSSIAN FIT RESULTS AND CH₃¹⁸OH SPECTRUM

The Gaussian fit results of the CH₃OH and CH₃¹⁸OH lines are reported in Table B.1. Contaminated lines are not reported in the table as they are not included into the LVG fit. Figure B.1 shows the detected transition of CH₃¹⁸OH towards MMS5.

Table B.1. List of frequencies of the detected methanol lines, synthesized beams, and line fitting and LVG results.

Molecule	Frequency [MHz]	Synthesized Beam MAJ["] × MIN["] (PA[°])	$\int T_B dV$ G. [K.km.s ⁻¹]	$\int T_B dV$ D. [K.km.s ⁻¹]	V_{peak} [km.s ⁻¹]	FWHM [km.s ⁻¹]	rms [K]	T_{kin} [K]	T_{ex} [K]	τ_L	
CSO33-b-a											
CH ₃ OH	218440	0.52×0.29 (106)	18.5 ± 2.6	17.2 ± 2.2	9.4 ± 0.5	5.7 ± 0.7	0.6	105	126	6.10^{-2}	
	234683	0.43×0.41 (-27)	6.0 ± 1.2	5.2 ± 1.2	8.2 ± 0.5	3.4 ± 1.0	0.4		101	$2.4.10^{-3}$	
	243915	0.32×0.28 (101)	26.8 ± 3.1	25.6 ± 2.6	9.2 ± 0.5	5.1 ± 0.5	0.4		105	9.10^{-2}	
	<i>261805</i>	<i>0.29×0.25 (-78)</i>	<i>19.4 ± 2.6</i>	<i>17.3 ± 2.0</i>	<i>9.2 ± 0.5</i>	<i>6.7 ± 0.7</i>	<i>0.5</i>		<i>112</i>	<i>4.10^{-2}</i>	
FIR6c-a											
CH ₃ OH	<i>218440</i>	<i>0.52×0.29 (107)</i>	<i>10.4 ± 1.4</i>	<i>11.2 ± 1.3</i>	<i>11.2 ± 0.1</i>	<i>2.5 ± 0.4</i>	<i>0.6</i>	180	<i>13200</i>	<i>5.10^{-2}</i>	
	232945	0.48×0.27 (-71)	9.3 ± 1.4	8.9 ± 1.6	10.8 ± 0.2	4.4 ± 0.6	0.2		44.8	5.2	
	234683	0.47×0.27 (109)	10.2 ± 2.2	8.6 ± 1.7	11.4 ± 0.3	3.6 ± 0.8	0.5		50.3	3.9	
	234698	0.47×0.27 (109)	6.7 ± 1.5	5.2 ± 0.9	10.9 ± 0.6	3.3 ± 1.1	0.5		39.6	1.1	
	<i>243915</i>	<i>0.32×0.27 (-78)</i>	<i>22.4 ± 2.6</i>	<i>20.4 ± 2.2</i>	<i>10.7 ± 0.1</i>	<i>3.2 ± 0.3</i>	<i>0.5</i>		<i>169</i>	<i>4.8</i>	
	<i>261805</i>	<i>0.30×0.25 (-77)</i>	<i>16.6 ± 2.6</i>	<i>12.1 ± 1.4</i>	<i>10.8 ± 0.4</i>	<i>4.0 ± 1.0</i>	<i>0.5</i>		<i>99.5</i>	<i>3.4</i>	
MMS9-a											
CH ₃ OH	<i>218440</i>	<i>0.53×0.29 (107)</i>	<i>51.9 ± 5.4</i>	<i>51.0 ± 5.3</i>	<i>11.0 ± 0.5</i>	<i>6.7 ± 0.5</i>	<i>0.6</i>	170	<i>1130</i>	<i>0.9</i>	
	232945	0.49×0.27 (-71)	40.8 ± 4.4	39.2 ± 4.1	11.8 ± 1.2	7.5 ± 1.2	0.3		70.1	5.7	
	234683	0.48×0.27 (109)	40.8 ± 4.6	40.0 ± 4.2	11.1 ± 0.5	6.2 ± 0.5	0.5		75	4.4	
	234698	0.48×0.27 (109)	28.1 ± 3.7	27.3 ± 3.0	10.9 ± 0.5	6.1 ± 0.6	0.5		73.6	1.2	
	<i>243915</i>	<i>0.32×0.27 (-256)</i>	<i>89.6 ± 9.1</i>	<i>85.8 ± 8.7</i>	<i>11.1 ± 0.5</i>	<i>6.7 ± 0.5</i>	<i>0.5</i>		<i>165</i>	<i>7.8</i>	
	<i>261805</i>	<i>0.30×0.25 (-75)</i>	<i>62.9 ± 6.7</i>	<i>60.3 ± 6.1</i>	<i>11.8 ± 0.5</i>	<i>7.0 ± 0.5</i>	<i>0.5</i>		<i>122</i>	<i>4.4</i>	
MMS5											
CH ₃ OH	<i>218440</i>	<i>0.52×0.3 (107)</i>	<i>73.2 ± 7.4</i>	<i>73.9 ± 7.5</i>	<i>10.4 ± 0.5</i>	<i>3.2 ± 0.5</i>	<i>0.6</i>	105	<i>139</i>	<i>11.2</i>	
	232945	0.48×0.28 (-71)	52.5 ± 5.4	52.2 ± 5.2	10.3 ± 1.2	3.5 ± 1.2	0.3		93.5	4.2	
	234683	0.46×0.27 (-71)	65.3 ± 6.7	65.6 ± 6.7	10.3 ± 0.5	3.2 ± 0.5	0.6		93.5	5.0	
	234698	0.46×0.27 (-71)	49.2 ± 5.1	49.2 ± 5.0	10.3 ± 0.5	3.0 ± 0.5	0.6		120	0.9	
	<i>243915</i>	<i>0.32×0.28 (-78)</i>	<i>102.8 ± 10.3</i>	<i>103.2 ± 10.4</i>	<i>10.3 ± 0.5</i>	<i>3.4 ± 0.5</i>	<i>0.5</i>		<i>105</i>	<i>105</i>	<i>17.7</i>
	<i>261805</i>	<i>0.30×0.25 (-77)</i>	<i>96.1 ± 9.8</i>	<i>96.5 ± 9.9</i>	<i>10.3 ± 0.5</i>	<i>3.1 ± 0.5</i>	<i>1.0</i>		<i>110</i>	<i>7.6</i>	
CH ₃ ¹⁸ OH	231758	0.48×0.28 (-71)	3.5 ± 1.3	3.3 ± 1.3	10.3 ± 1.2	2.6 ± 1.1	0.3		108	6.10^{-2}	
SIMBA-a											
CH ₃ OH	218440	0.52×0.3 (106)	2.6 ± 0.8	3.0 ± 0.7	13.0 ± 0.3	2.0 ± 0.7	0.5	190	195	-7.10^{-2}	
	243915	0.32×0.28 (-259)	4.7 ± 1.0	5.0 ± 1.0	13.2 ± 0.4	2.2 ± 0.6	0.4		172	9.10^{-2}	
	261805	0.30×0.26 (-78)	1.9 ± 1.0	1.7 ± 0.6	13.1 ± 0.3	1.8 ± 0.6	0.4		3150	$-2.5.10^{-3}$	

NOTE—Results of the Gaussian fit (G.) and of the direct integration of channel intensities (D.) for the integrated intensities are reported in Cols. 4 and 5, respectively. The calibration uncertainty of 10% has been included in the line intensity errors. T_{kin} is the best fit for the kinetic temperature obtained from the LVG analysis, and T_{ex} and τ_L are the associated excitation temperature and line optical depth. The *italic* lines are those that were *not* taken into account in the LTE and LVG analyses.

C. LTE ANALYSIS: ROTATIONAL DIAGRAMS

We show here the rotational diagram (RD) obtained for each source. We can clearly see that the line at 45.4 K is masing and that points are scattered due to optically thick and/or non-LTE effects.

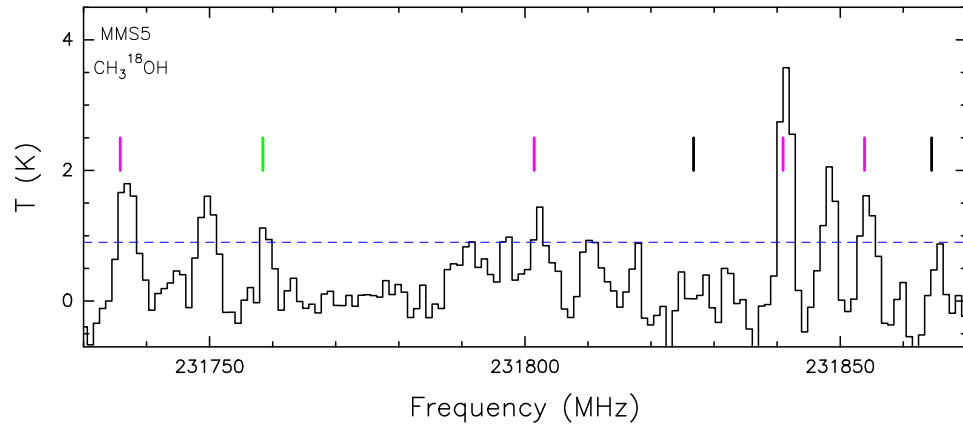


Figure B.1. Spectra towards MMS5 where the frequencies of the seven $\text{CH}_3^{18}\text{OH}$ lines expected to be the most intense ($E_u < 75K$) are indicated. Detected lines are marked in green, contaminated lines are marked in magenta, and undetected lines are marked in black. The 3σ -level is indicated by the dashed blue line.

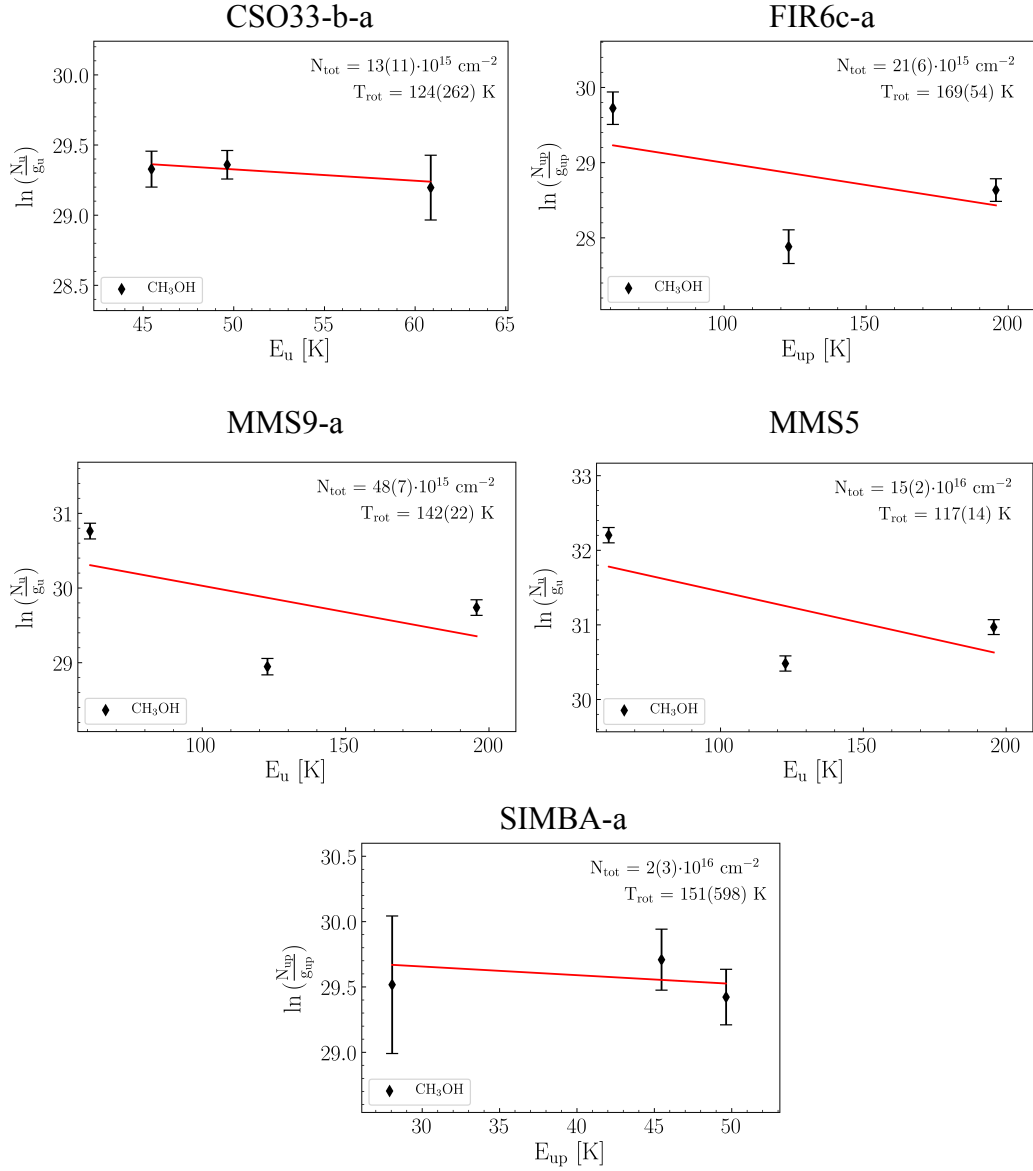


Figure C.1. Rotational diagrams. Non-LTE and optically thick effects are clearly visible in FIR6c-a, MMS9-a and MMS5, as the points are scattered through the plots.

3.3 The challenging identification of WCCC objects in the OMC-2/3 filament

3.3.1 The spatial distribution of carbon chains in WCCC objects

With ORANGES, we aim to investigate the WCCC nature of the OMC-2/3 protostars. To identify WCCC objects, one needs to investigate hydrocarbons. The most targeted species in surveys are CCH, C_4H and $c-C_3H_2$ because they are main hydrocarbons-related molecules that are abundant in WCCC sources (Sakai et al. 2008a, 2009a). The carbon chains produced by the WCCC mechanism are distributed between ~ 1000 up to ~ 3000 au around the protostar (e.g. Sakai et al. 2010, 2014a,b, 2016; Sakai & Yamamoto 2013; Oya et al. 2017; Taniguchi et al. 2021b). Additionally, carbon chains emission show a slight dip ranging between 100 up to 600 au (in radius) around the continuum peak position of the sources. Therefore, we expect to see similar features in the carbon chain emission towards the OMC-2/3 source sample, should they have a WCCC zone. The ORANGES setups include several transitions of CCH and $c-C_3H_2$. Following my study with the single-dish observations (Chapter 2), I first investigated the CCH emission. I also present preliminary results for $c-C_3H_2$.

3.3.2 ORANGES looking at hydrocarbons: CCH and $c-C_3H_2$ moment 0 maps

The CCH transition included in the ORANGES spectral setups is the $N=3-2$ transition with upper energy level $E_{up} = 25.2$ K. I chose to map the most intense line among the various hyperfine structure components, which has its frequency at 262064 MHz, and an Einstein coefficient of $A_{ij} = 4.89 \times 10^{-5} s^{-1}$. For $c-C_3H_2$, I selected the $3_{2,1} - 2_{1,2}$ transition line at a frequency of 244222 MHz, and with the spectral parameters $E_{up} = 18.2$ K and $A_{ij} = 5.9 \times 10^{-5} s^{-1}$.

CCH is detected towards each of the nine targeted fields while $c-C_3H_2$ is detected only towards FIR2. The moment 0 maps of the CCH and $c-C_3H_2$ (for FIR2) lines are shown in Fig. 3.1 to 3.3. In FIR6c-a, the CCH emission seems to trace the outflow cavity walls. This result is consistent with what is found in other sources as CCH is known to be a good tracer of outflow cavities (e.g. Oya et al. 2014; Zhang et al. 2018; Tychoniec et al. 2021; Okoda et al. 2020; Chuang et al. 2021). For several other systems (FIR2, MMS5, SIMBA-a, FIR1a-b) this could be also the case but the emission is too amorphous to conclude. In the literature, outflows have been detected towards all ORANGES systems except towards COS3 (e.g. Williams et al. 2003; Takahashi et al. 2008; Tobin et al. 2016b; Tanabe et al. 2019; Gómez-Ruiz et al. 2019; Matsushita et al. 2019; Feddersen et al. 2020; Nagy et al. 2020). The direction of the large scale outflow of the systems CSO33, MMS2 and MMS9 is known but since there exist no high-angular resolution observations of these systems outflow, it is not known which of the components drives the outflow. In the other sources, the origin of emission of CCH is not clear (e.g. MMS9-a, CSO33-b) and seems to trace several components (e.g. outflow cavity, circumstellar envelopes). Overall, additional information on the sources outflows is mandatory to interpret the CCH emission accurately. For FIR2, the emission of $c-C_3H_2$ is similar to that of CCH, although slightly less extended.

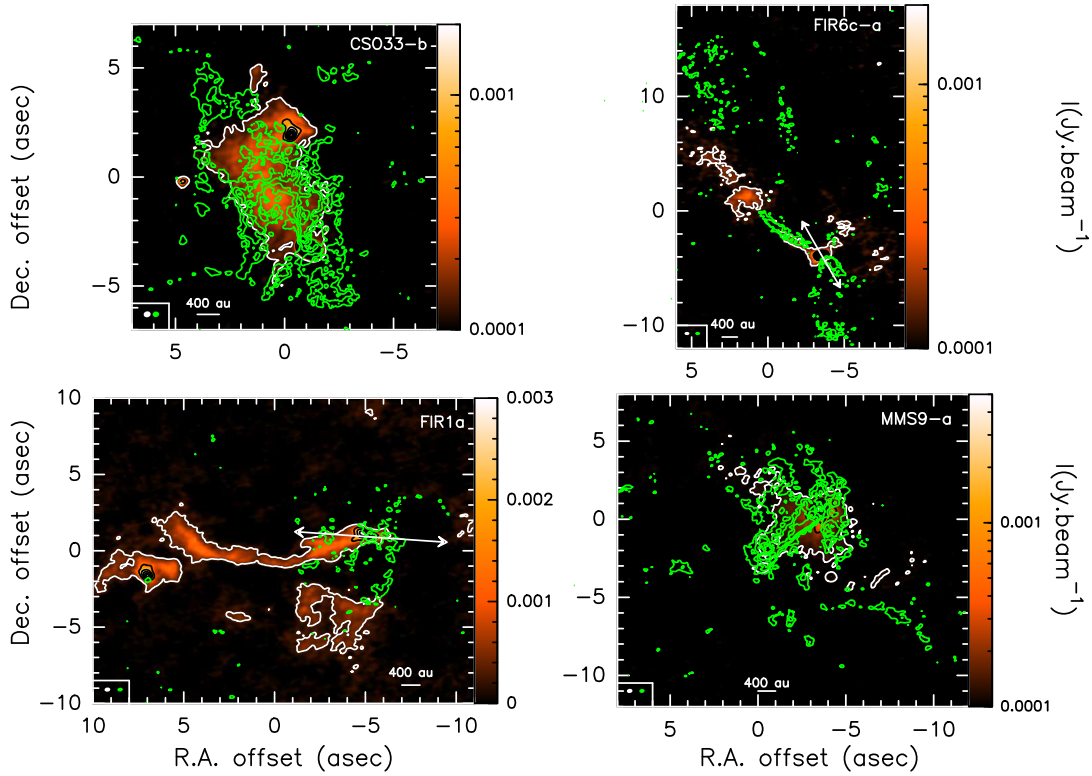


Figure 3.1: 1.3mm continuum maps (coloured area). Levels start at 5σ (white contours) with steps of 20σ (black contours; $1\sigma = 44, 60, 58,$ and $50 \mu\text{Jy}/\text{beam}$ for CS033-b, FIR6c, FIR1a, and MMS9, respectively). The moment 0 map of the CCH transition at 262064 MHz is shown with green contours. Contours start at 5σ with steps of 5σ . The 1σ values for CCH are 2.2 mJy/beam for FIR1a and 2.3 mJy/beam for the other sources. The continuum and CCH associated synthesised beam are in white and green, respectively, and are depicted in the lower-left corner of the boxes. White arrows represent the orientation of the outflow of the source when known.

3.3.3 Conclusions

The results of the hydrocarbon emission investigation towards the OMC-2/3 sources show that the CCH emission is relatively shapeless in every system, except for FIR6c-a in which it clearly traces the outflow cavity walls. Additionally, $c\text{-C}_3\text{H}_2$ is seen only in one object (FIR2) while this species is rather widespread in WCCCs. I mentioned in Sec. 3.3.1 that if a WCCC zone is present around the protostar, the emission is seen at scales from 100 up to 3000 au. The largest angular scale recoverable with the ORANGES observations is about 800 au. This suggests that either there are no WCCC objects, or the WCCC zone, if present, might be resolved out. The protostar FIR2 could be a possible WCCC candidate but as the emission is filtered out, I cannot evaluate properly the presence of WCCC sources at the scales probed by the ALMA observations.

These results suggest that targeting CCH and $c\text{-C}_3\text{H}_2$ are not sufficient to detect WCCC sources. To draw strong conclusions, targeting other (long) carbon chains (e.g. CH_3CCH , HC_5N , C_4H_2) might be necessary. Moreover, we need to probe larger scales than those with ORANGES to avoid resolving out a possible WCCC zone. This conclusion was

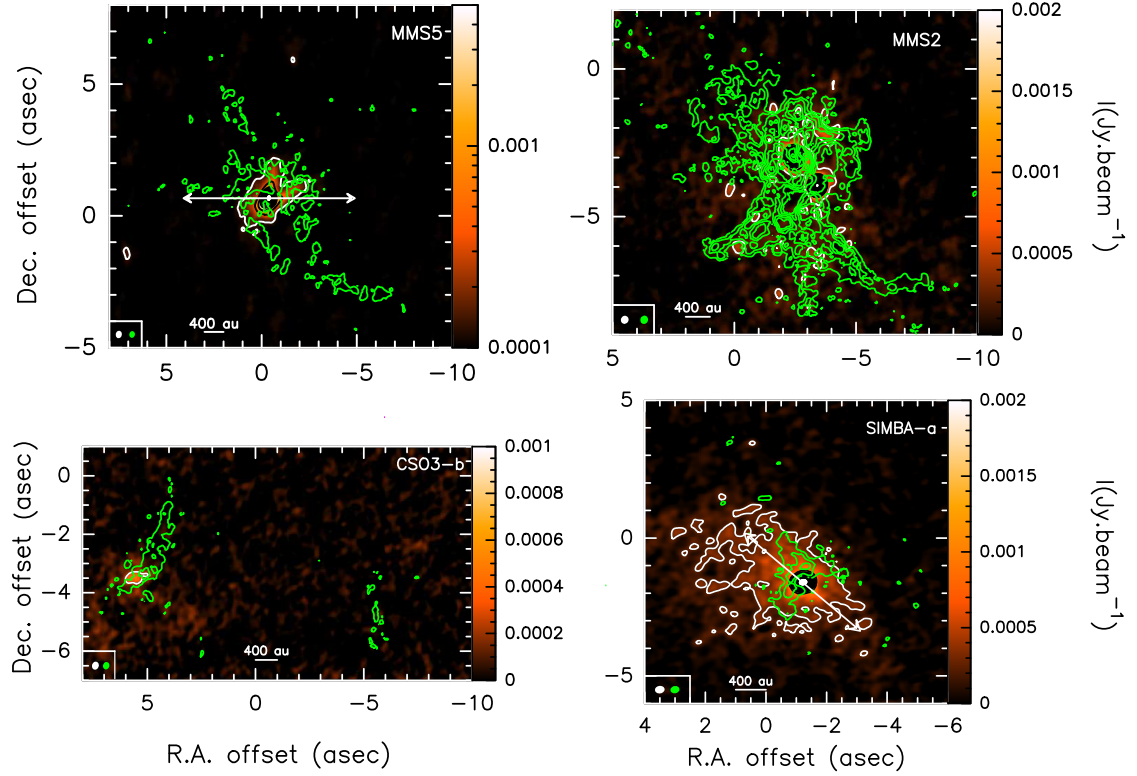


Figure 3.2: 1.3mm continuum maps (coloured area). Levels start at 5σ (white contours) with steps of 20σ (black contours; $1\sigma = 80, 60, 49,$ and $50 \mu\text{Jy/beam}$ for MMS5, MMS2, CSO3-b, and SIMBA-a, respectively). The moment 0 maps of the CCH line at 262064 MHz are shown in green contours. Contours start at 5σ with steps of 5σ . The 1σ values for CCH are 2.4, 2.1, 2.3, and 2.2 mJy/beam for MMS5, MMS2, CSO3-b, and SIMBA-a, respectively. The continuum and CCH associated synthesised beam are in white and green, respectively, and are depicted in the lower-left corner of the boxes. White arrows represent the orientation of the outflow of the source.

also reached by [Yang et al. \(2021\)](#) with the PEACHES survey. They found that the CCH emission is associated with the sources outflow. On the other hand, $c\text{-C}_3\text{H}_2$ is not detected (see their Fig. 7) towards any of the Perseus sources, whereas this species is seen at a larger scale (~ 3000 au; [Higuchi et al. 2018](#)). They also conclude that observations probing intermediate scales are necessary.

In conclusion, using the ORANGES observations, I was not able to detect WCCC objects in the OMC-2/3 filament. This is mostly due to a sub-optimal observational strategy in terms of probed angular scales, variety of molecular tracers, and possibly also of sensitivity. Additional observations are needed to address the question of whether these objects are present in the OMC-2/3 filament, and hence in an environment similar to the one in which our Sun is born (see Sec. 5.2.1).

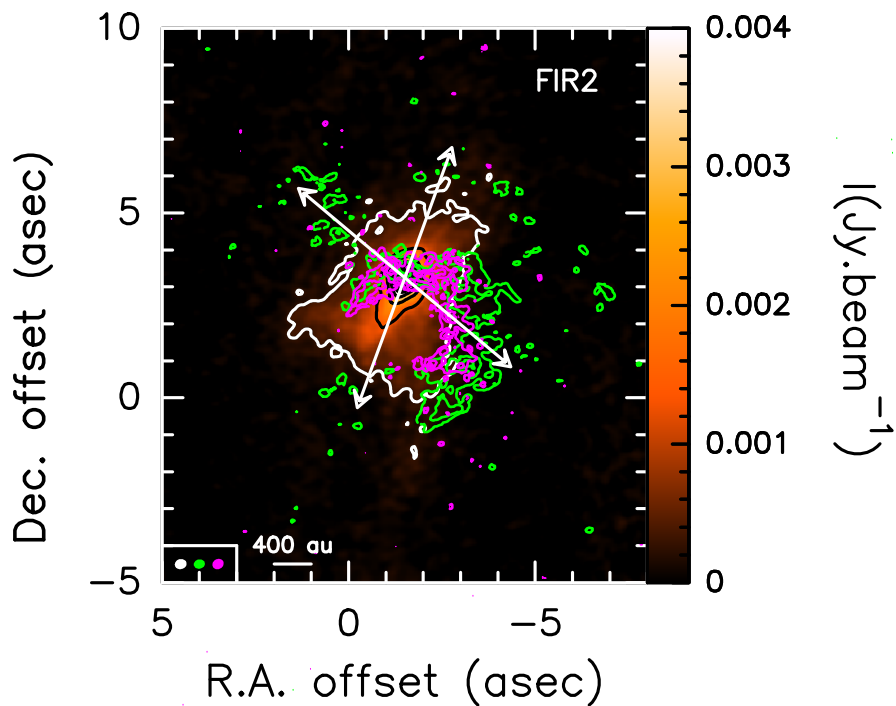


Figure 3.3: 1.3mm continuum maps (coloured area). Levels start at 5σ (white contours) with steps of 20σ (black contours; $1\sigma = 54 \mu\text{Jy}/\text{beam}$). The moment 0 maps of the CCH line at 262064 MHz (green contours) and the *c*-C₃H₂ line at 244222 MHz (magenta contours) are superposed on the continuum. Contours start at 5σ with steps of 5σ . The 1σ values are 2.3 mJy/beam for CCH and 2.1 mJy/beam for *c*-C₃H₂. The continuum, CCH and *c*-C₃H₂ associated synthesised beam are in white, green, and magenta, respectively, and are depicted in the lower-left corner of the boxes. White arrows represent the orientation of the outflow of the source.

Ongoing project: The OMC-2 FIR6c-a outflow, a new astrochemical laboratory

So far, I investigated only the molecular complexity in the protostellar envelopes. However, outflows that are driven by Class 0 and I protostars can also show a molecular complexity (see Sec. 1.2). In a general way, I am interested in the protostellar chemical complexity as a whole. I find it essential to investigate both the envelope and the outflow of the sources to understand (1) what level of chemical complexity can be found in these two components, and (2) whether, and how, the outflow chemistry is impacted by the surroundings of the protostars. Luckily, one of the ORANGES sources presents a molecular complexity in its outflow. This is relatively precious as objects showing this feature are only a few. I took the opportunity in the framework of my thesis to investigate the outflow of this object. I present this project in the following.

4.1 OMC-2 FIR6c-a: The discovery of a chemically active outflow

Among the ORANGES source sample, the source OMC-2 FIR6c-a (hereafter FIR6c-a) happened to show particularly interesting features. FIR6c-a is a Class 0 protostar that drives an extended ($\sim 45''$) bipolar outflow in the north-south direction that is seen in several CO transitions (Takahashi et al. 2008; Shimajiri et al. 2009; Gómez-Ruiz et al. 2019; Tanabe et al. 2019). Two well collimated SiO ($v=0, J=2-1$) components have been detected too, in alignment with the axis of the blueshifted (northern) lobe of the outflow, so probably tracing the well-collimated jet component ejected by the protostar (Shimajiri et al. 2009). Until now, only large-scale ($\sim 2000 - 10000$ au) studies have been performed on the outflow (Takahashi et al. 2008; Shimajiri et al. 2009; Tobin et al. 2016b; Tanabe et al. 2019; Gómez-Ruiz et al. 2019). With ORANGES, I can study the source outflow at small scales (≤ 1000 au) for the first time.

A first line analysis of methanol (see Chapter 3) showed the first result: the methanol emission traces the outflow cavity, the terminal bow shock along with several possible shock spots as shown in Figure 4.1. The width of the outflow cavity traced by methanol is $\sim 3''$. Other molecules are detected towards the outflow among which a SiO component, whose emission exclusively traces the jet (see also Shimajiri et al. (2009)), and a CCH component that unambiguously traces the well separated and extended outflow cavities

(see Sec.3.3), as shown in Fig. 4.1.

It is, however, the first time that an iCOM is detected towards the outflow of FIR6c. The detection of CH₃OH in the outflow and at the shock positions indicates the possibility of rich and complex chemistry occurring as this molecule is known to be a precursor of other iCOMs. Among the ORANGES sources, FIR6c-a is the only source showing such extended features in its outflow. The chemical richness, the particular geometry, and the environment of the FIR6c-a outflow make it a perfect (and) new astrochemical laboratory where to test iCOMs formation paradigms. Following this discovery, I submitted a NOEMA proposal as PI and obtained the full requested observing time in winter 2020-2021. In the following, I present the arguments that motivates the new observations in Sec. 4.2, the observations in Sec. 4.3, and the preliminary results in Sec. 4.4.

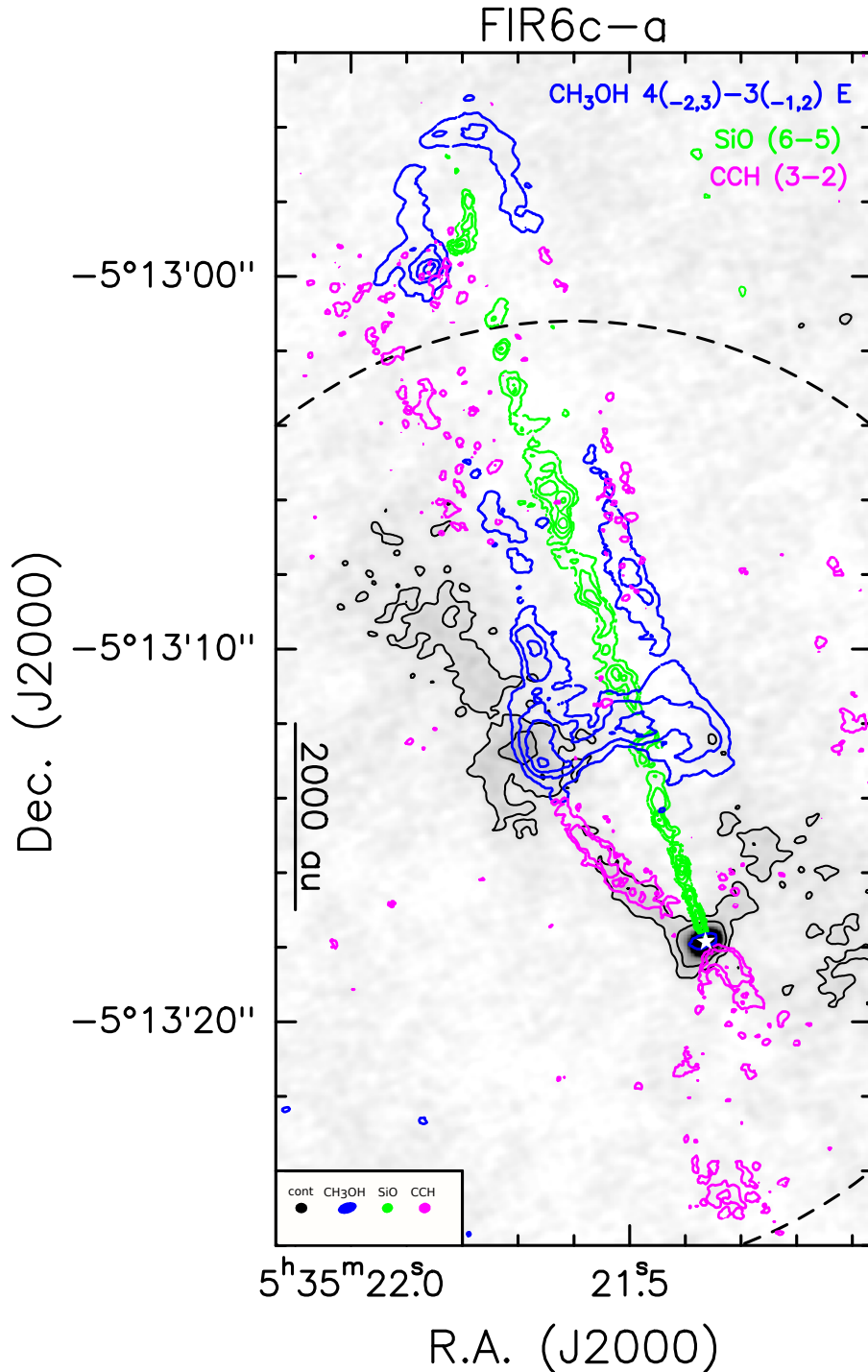


Figure 4.1: Superposition of 1.3mm continuum emission (grey shaded area with black contours) with the CH_3OH ($4_{-2,3}-3_{-1,2}$) transition integrated between 5.1 and 16.3 km.s^{-1} (blue), the SiO ($6-5$) transition integrated between 3.4 and 20.7 km.s^{-1} (green), and the CCH ($3-2$) transition integrated between 9.6 and 21.3 km/s (magenta). The blueshifted lobe of the outflow is almost perpendicular to the 1.3mm continuum emission. Contour levels are 4σ , 10σ , 100σ and 500σ for the 1.3mm continuum emission ($1\sigma=0.06$ mJy/beam). Contour levels start at 7σ with steps of 15σ for CH_3OH and SiO ($1\sigma=3.2$ mJy/beam for CH_3OH and $1\sigma=4.6$ mJy/beam for SiO). For CCH , levels start at 5σ with steps of 5σ ($1\sigma = 2.3\text{mJy/beam}$). The associated beams are depicted in the lower left side of the Figure. The protostar is marked by a filled white star.

4.2 Motivation for new observations

I mentioned in Sec. 1 that iCOMs could be the building blocks of more complex prebiotic species (Caselli & Ceccarelli 2012), hence their importance in the Astrobiological context. Yet, their routes of formation are still a matter of debate (see Section 3.2.3). As a quick reminder, two main theories in the literature invoke iCOM formation: (A) on the interstellar dust grain surfaces (e.g. Garrod & Herbst 2006; Garrod et al. 2008) and (B) in the gas phase (e.g. Millar et al. 1991; Vasyunin & Herbst 2013; Balucani et al. 2015; Skouteris et al. 2018). However, distinguishing which theory is more efficient, where, and when, is quite challenging. The general goal of the NOEMA project is to add a piece to this puzzle by exploring a new chemically active region discovered towards FIR6c-a.

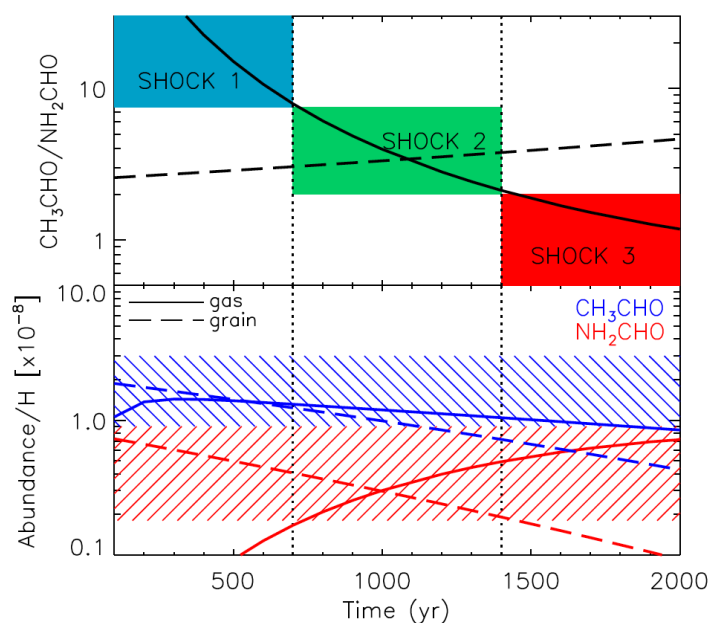


Figure 4.2: Model predictions from Codella et al. (2017). *Upper panel:* Relative calculated abundance of CH_3CHO and NH_2CHO as a function of time after the shock. Solid lines refer to a model in which both species are injected into the gas phase directly from the grain surfaces where they are formed. The coloured boxes represent the measured ranges of $\text{CH}_3\text{CHO}/\text{NH}_2\text{CHO}$ at different shock positions, including uncertainties. *Lower panel:* Abundances of CH_3CHO (blue) and NH_2CHO (red) with respect to H-nuclei, as a function of time after the shock. The dashed blue and red regions represent the ranges of measured abundances.

Usually, iCOMs formation routes are constrained by comparing their measured abundances in hot cores/corinos with model predictions (e.g. Occhiogrosso et al. 2011; Antñolo et al. 2016; Agúndez et al. 2019; Balucani et al. 2015; Coutens et al. 2018; Skouteris et al. 2018; Awad et al. 2021). A more compelling method is to make the comparison in molecular shocked gas thanks to the additional constraint of time-dependence (Codella et al. 2017). Indeed, once the shock has passed, the chemistry of the shocked gas evolves with time. Thus, depending on where iCOMs form, their observed abundance in the gas phase differs (see Figure 4.2). There are two possible scenarios: (A) If iCOMs form on the grain surfaces, they are injected into the gas phase right after the shock passage: the

iCOMs abundances in the gas phase will jump-step increase, and then monotonically decrease. (B) On the contrary, if iCOMs are a gas phase product, they form from precursor molecules ejected from dust grain ice coatings: their synthesis takes some time, which means that their abundances will increase within a few tens/thousands yr (depending on the species) after the shock passage. Since each position in the outflow corresponds to a different ejection/shock passage that matches a precise age, spatially resolved observations of iCOMs can provide the time constraint (Podio et al. 2016; Codella et al. 2020). The crucial point to use this method is the ability to spatially disentangle the iCOM emissions. To do so, interferometric high-angular resolution observations are mandatory.

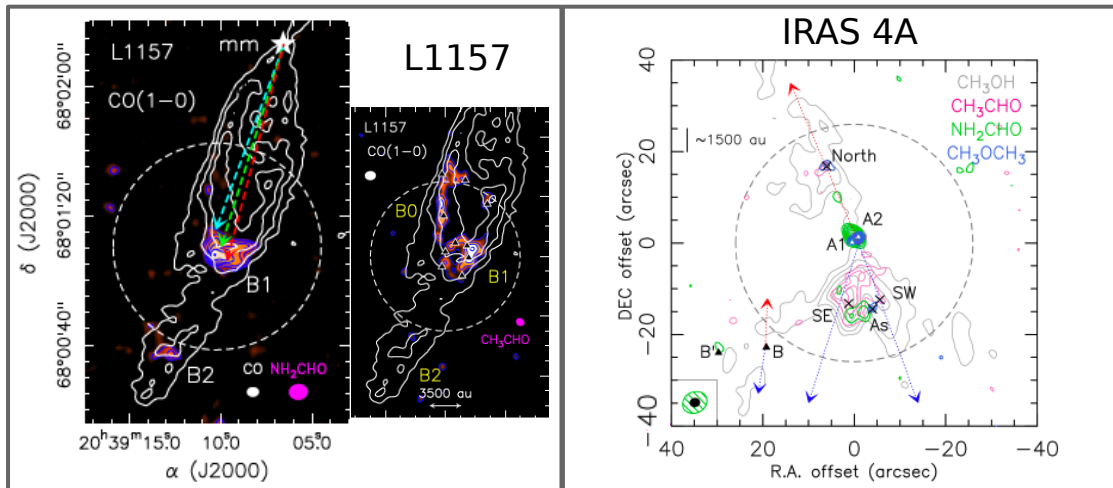


Figure 4.3: Protostellar outflows and shocks in which iCOMs have been detected and studied using the method from Codella et al. (2017). *Left:* L1157 southern blue-shifted outflow lobe seen in CO (transition 1-0; white contours by Gueth et al. 1996). Emission map of NH₂CHO (4_{1,4}-3_{1,3}) and CH₃CHO (5_{0,4}-4_{0,4} E) are shown in colour scales. The associated primary beam is indicated by a dashed white circle. The synthesised beams of NH₂CHO, CH₃CHO, and CO are indicated by magenta/white filled ellipses. The images are taken from Codella et al. (2017, 2020). *Right:* Contour map of the detected iCOMs at 3mm towards the IRAS4A system outflow. Grey contours are for CH₃OH transitions (2_{0,2}-1_{0,1} A, 2_{0,2}-1_{0,1} E, and 2_{-1,2}-1_{-1,1}), magenta contours are for CH₃CHO (5_{0,5}-4_{0,4} A), green contours are for NH₂CHO (4_{1,4}-3_{1,3}), and blue contours are for CH₃OCH₃ (4_{1,4}-3_{0,3}). The primary beam is indicated by the dashed grey circle and the synthesized beams for NH₂CHO and the other species are shown in dashed green and filled black ellipses, respectively. The image is taken from De Simone et al. (2020b).

Using this approach, only two protostellar shocks were studied so far (towards L1157 and IRAS4A), and for only two iCOMs (formamide and acetaldehyde; see Figure 4.3; Codella et al. 2017, 2020; De Simone et al. 2020b). These studies favour a gas-phase formation path for formamide (Codella et al. 2017) and acetaldehyde (De Simone et al. 2020b). However, do these results only apply to L1157 and IRAS 4A? What about other iCOMs? What happens in different environments like the one where supposedly the Solar System was born? It is important to apply this method to other iCOMs and other protostellar shocks to answer these questions and, consequently, to understand when and where gas phase or grain surface chemistry dominates. FIR6c-a drives a chemically active outflow for which we could resolve the structure as well as the methanol emission. Finally,

Table 4.1: Targeted species with associated targeted lines. The relative expected abundances between the species and the expected signal for each species are also indicated.

Species	Targeted Lines Eup range [K]	Relative expected abundances	Expected signal [K]
CH ₃ OH	4.8 – 91.2	100	9.8
CH ₃ CHO	0.6 – 63.0	10	3.1
C ₂ H ₅ OH	19.8 – 86.8	13	1.0
DME-MF	7.1 – 95.4 / 6.0 – 47.9	10	0.8 – 0.5
HCOCH ₂ OH	6.1 – 66.1	3	0.5
NH ₂ CHO	13.1 – 42.3	1	1.5

this source external conditions differ from that of L1157 and IRAS 4A, as it is highly illuminated by nearby HII regions (e.g. M42; ≤ 1.2 pc) like the Sun’s birth environment (e.g. Adams 2010; Pfalzner et al. 2015). Therefore, it also provides information on whether external conditions play a role in the chemistry of protostellar shocks (e.g. Lesaffre et al. 2013; Nguyen-Luong et al. 2013). With the new NOEMA observations, I aim to search for iCOMs in the FIR6c-a outflow and constrain their formation routes.

Numerous observational and theoretical chemistry works from our team on iCOMs showed that some of them are chemically linked. On the observational side, a correlation was found between ethanol (C₂H₅OH) and glycolaldehyde (HCOCH₂OH) (Lefloch et al. 2017), methanol (CH₃OH) and acetaldehyde (CH₃CHO) (Taquet et al. 2015; De Simone et al. 2020b; Codella et al. 2020), and methyl formate (CH₃OCHO) and dimethyl ether (CH₃OCH₃) (Jaber Al-Edhari et al. 2014). On the theoretical chemistry side, we predicted that ethanol is the precursor of glycolaldehyde and acetaldehyde (Skouteris et al. 2018; Vazart et al. 2020), and methyl formate of dimethyl ether (Balucani et al. 2015), via gas-phase reactions. Alternatively, these iCOMs could be grain-surface chemistry products (Garrod & Herbst 2006; Garrod et al. 2008). However, our ab initio quantum chemistry computations predict that such reactions are unlikely to occur in the case of acetaldehyde and formamide and that these species are likely gas-phase products (Barone et al. 2015; Enrique-Romero et al. 2016, 2020, 2021; Skouteris et al. 2017). In the case of formamide, observations seem to back up this formation route (Codella et al. 2017; López-Sepulcre et al. 2019; De Simone et al. 2020b).

With the new NOEMA observations, I aim to test the theoretical predictions with observations of iCOMs in the OMC-2 FIR6c-a shocked regions. The list of targeted species and expected relative abundances and signals are shown in Table 4.1. The synergy between observations and theoretical/experimental works on iCOMs is fundamental to understanding their formation routes.

4.3 Observations

The FIR6c-a outflow has been observed with the IRAM/NOEMA interferometer on December, 30th 2020, and between January 2nd and 3rd, 2021. The array used is the C configuration with a baseline ranging from 24 to 328m. The frequency setup covers the ranges between 92.5 – 100.2 GHz and 107.8 – 115.6 GHz. The spectral resolution of the

wideband is 2 MHz (~ 6 km/s) and the spatial resolution is $2''$ (or ~ 800 au).

The phase center is on the protostar at coordinates ($\alpha = 05:35:21.363$; $\delta = -05:13:17.83$). The main flux calibrators used were 0420-014, and MWC349 and the bandpass calibrators used were 3C454.3, and 0420-014. The phase and amplitude calibrations were done using J0542-0913 and 0458-020. The precipitable water vapor (pwv) is less than 5mm, and calibration uncertainties are estimated to be better than 10%. The data were reduced during Summer 2021 using the CLIC software from the GILDAS package. I produced a continuum image by averaging line-free channels in the visibility plane and I cleaned the cube using natural weighting (via the CLEAN procedure). In the following, very basic cleanings of the cubes have been performed so the cleaning is not optimized. The results I present are preliminary, purely qualitative, and need further work before being suitable for publication. The resulting synthesised beam is $3.2'' \times 1.6''$ (P.A. = -11°). The maps shown in the following are not corrected for the primary beam. The half-power primary beam is $45.9''$ ($\sim 1.8 \times 10^4$ au).

4.4 Preliminary results

4.4.1 A new iCOMs-rich outflow

The main goal of the project focuses on the detection of other iCOMs than methanol in the FIR6c-a outflow and on the use of time-dependent models to constrain their formation route. I performed a preliminary line identification on the outflow. I only did the line identification in the PolyFix wideband (only in the upper inner (ui), upper outer (uo), and lower inner (li) part), whose resolution is 2 MHz. I detected six transitions for methanol, eight transitions for acetaldehyde, and one transition for formamide. For now, I do not detect any of the other targeted iCOMs but the line identification is not yet complete. Table 4.2 summarises the preliminary detected molecules in the outflow, their transitions, and their associated parameters.

Figure 4.1 presents a first map with the 3mm continuum of FIR6c-a on which are superposed the velocity-integrated emission of methanol, acetaldehyde and formamide. Compared to the ALMA data (Fig. 4.1), we retrieve the shape of the outflow with a widespread methanol emission. The NOEMA beam does not, however, allow to disentangle the two sides of the outflow cavity as with the ALMA observations. The spatial distribution of acetaldehyde and formamide are discussed in the next section.

The detection of several iCOMs in the FIR6c-a outflow confirms that it is the first chemically active outflow discovered in the OMC-2/3 filament. The OMC-2 FIR6c-a outflow also joins the list of outflows in which iCOMs have been detected (IRAS2A, IRAS 4A, L1157, L1448, SMM4, B1b, SN68 ; e.g. Arce et al. 2008; Öberg et al. 2011; Mendoza et al. 2014; Gerin et al. 2015; Codella et al. 2015, 2017, 2020; Lefloch et al. 2017, 2018; Holdship et al. 2019b; De Simone et al. 2020b; Tychoniec et al. 2021). Several lines of methanol and acetaldehyde are detected which will allow me to perform LTE and non-LTE analysis. From these analyses, I will be able to derive physical conditions (kinetic temperatures, volume densities) and compute the iCOMs relative abundance in the outflow that can then give constraints on their formation route as well as to give constraints to the methanol abundance.

Table 4.2: List of detected iCOMs towards the FIR6c-a outflow, and their spectral parameters. The frequencies and spectroscopic parameters are retrieved from the CDMS (Cologne Database for Molecular Spectroscopy: Müller et al. 2005) and the JPL molecular spectroscopy database (Jet Propulsion Laboratory: Pickett et al. 1998) databases. The available data are from Xu et al. (2008), Kirchhoff et al. (1973), and Kleiner et al. (1996) for CH₃OH, NH₂CHO, and CH₃CHO, respectively.

Molecule	Frequency [GHz]	Transition	E_{up} [K]	A_{ij} $\times 10^{-5} \text{s}^{-1}$
CH ₃ OH	96.739	2 _{1,2} – 1 _{1,1} E	12.5	0.3
	96.741	2 _{0,2} – 1 _{0,1} A	7.0	0.3
	96.744	2 _{0,2} – 1 _{0,1} E	20.1	0.3
	97.755	2 _{-1,1} – 1 _{-1,0} E	28.0	0.3
	97.582	2 _{1,1} – 1 _{1,0} A	21.6	0.3
	108.894	0 _{0,0} – 1 _{1,1} E	13.1	1.5
	CH ₃ CHO	96.475	5 _{2,3} – 4 _{2,2} E	23.0
96.632		5 _{2,3} – 4 _{2,2} A	23.0	2.5
98.863		5 _{1,4} – 4 _{1,3} E	16.6	3.1
98.900		5 _{1,4} – 4 _{1,3} A	16.5	3.1
112.248		6 _{1,6} – 5 _{1,5} A	21.1	4.7
112.254		6 _{1,6} – 5 _{1,5} E	21.2	4.7
114.940		6 _{0,6} – 5 _{0,5} E	19.4	5.1
114.959		6 _{0,6} – 5 _{0,5} A	19.4	5.1
NH ₂ CHO	109.753	5 _{1,4} – 4 _{1,3}	18.8	8.8

4.4.2 Spatial distribution of acetaldehyde and formamide

From Fig. 4.4, we can see segregation in the spatial distribution of formamide and acetaldehyde emission. On the one hand, the acetaldehyde emission is present at two different positions: in the terminal bow shock with the peak in intensity at relatively the same position as the methanol one, and close to the source. At this position, there are two peaks of intensity. The first one is aligned with the outflow and the terminal bow shock while the second one is located on the eastern side of the outflow, near a candidate pre-stellar core (Kainulainen et al. 2017). On the other hand, formamide is detected at a single position on the eastern side of the outflow, with an intensity peak relatively close to that of acetaldehyde.

Remarkably, the spatial distribution of acetaldehyde and formamide is the same as observed in L1157-B1 (Codella et al. 2017), with the acetaldehyde peaking closer to the source than formamide. The comparison of the two outflows is shown in Fig. 4.5. This strongly suggests that the mechanisms causing the emission of formamide and acetaldehyde are the same as in L1157-B1, and, therefore, that the formamide production via gas-phase mechanisms dominates here too. Comparing the NOEMA observations with models will allow me to confirm and constrain accurately the formation routes of acetaldehyde and formamide as well as to constrain the methanol and the formamide precursors abundances.

4.4.3 A shock-induced star formation?

Particularly interesting is the fact that the FIR6c-a outflow is almost parallel to the dust ridge seen on the northeast side of the protostar. [Kainulainen et al. \(2017\)](#) detected a candidate pre-stellar core on the north side of the FIR6c-a source, in the dust ridge. The pre-stellar core location coincides with a shock position of the outflow seen in methanol, formamide, and acetaldehyde. Several questions then arise: Can we confirm the presence a pre-stellar core there? If so, is the interaction between the FIR6c-a outflow and the pre-stellar core causing the shock seen on the east side of the outflow? Or, on the contrary, did the pre-stellar core form as a result of the interaction between the outflow and the dust ridge? In other words, this is a chicken and egg situation: which of these features (shock or pre-stellar core) appeared first? I performed velocity-integrated maps of the NH_2D ($1_{1,1} - 1_{0,1}$) and of the C^{18}O (1-0) transitions at a frequencies of 110.154 GHz and 109.782 GHz, respectively. I chose these two molecules because high deuteration levels are usually seen in pre-stellar cores (see Sect. 1.1), and NH_2D is the only deuterated molecule present in the observed band, and C^{18}O because it is a good tracer of high gas column densities and is the most optically thin isotopologue of CO. Fig. 4.6 shows the emission of these two species, superposed on the 3mm continuum and to the formamide emission.

From the NH_2D emission, it appears that there are two components. The first component coincides with the formamide emission. This suggests that this NH_2D component is associated with the outflow shock: the ammonia contained in the ice mantle of grains is sputtered out. The second component seems to be connected to the dust ridge. This ammonia emission can be explained by either gas-phase formation, and in that case, we see ammonia that is not yet frozen out onto the dust grains, or by UV photo-desorption of ammonia from the dust grains. The second hypothesis would be in line with the fact that three B stars (M43 HII regions) are located on the eastern side of the source, thus illuminating the dust ridge from the south. I will investigate the two hypotheses by looking at the linewidths: if the NH_2D linewidths are narrower at the edge of the dust ridge than those located close to the formamide emission peak, this would strengthen the hypothesis on the different origin of the NH_2D emission in the regions.

We can see that the second component of NH_2D is also seen in C^{18}O , but the emission of the latter is confined at the external part of the ridge. Another component is seen near the location of the formamide peak. This can be explained by an increase in the column density due to the shock compression. At the location of the pre-stellar core, the lack of C^{18}O emission in the central part seems to be clear evidence of the existence of the pre-stellar core: the CO is depleted onto the dust grains. This result strongly suggests that the pre-stellar core is pre-existing and its formation is not triggered by the outflow interaction with the dust ridge. The peak emission seen in formamide indicates that the outflow crashed against the already existing core and its enhanced emission is due to the shock of a pre-existing larger density gas.

In conclusion, I have presented in this Chapter the preliminary results of the NOEMA observations of which I am the PI. Besides methanol, I detected acetaldehyde and formamide. The OMC-2/3 FIR6c-a outflow thus enters the limited list of iCOMs-rich outflows. This project is an ongoing project and the next step will be to optimize the maps cleaning and to carry out the full analysis of the results which will lead to the preparation of a fourth paper.

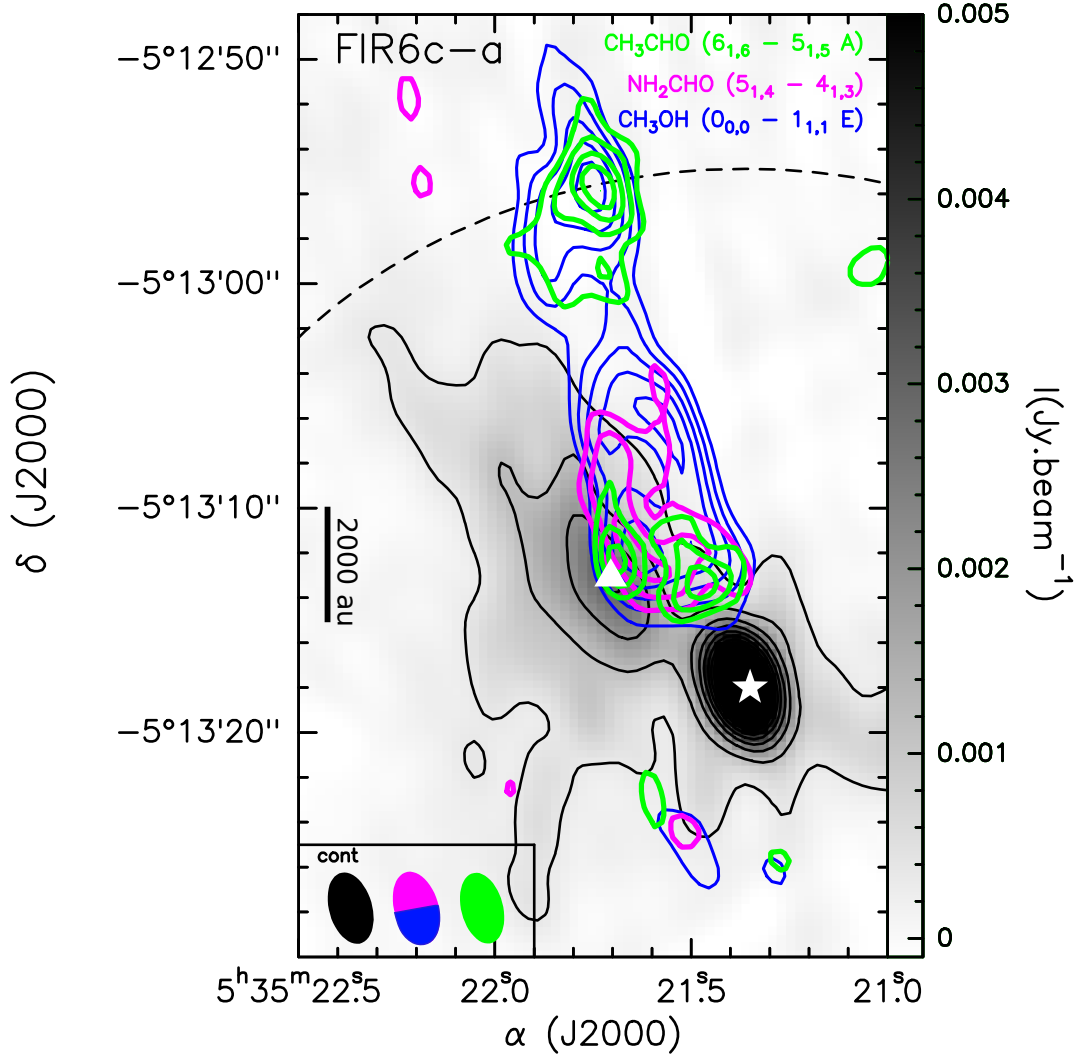


Figure 4.4: 3mm continuum map (grey shaded area and black contours). Levels starts at 20σ with steps of 50σ ($1\sigma = 17\mu\text{Jy}$). Coloured contours represents the velocity-integrated emissions of CH_3OH (blue), CH_3CHO (green) and NH_2CHO (magenta). Levels start at 5σ with steps of 3σ for CH_3OH and they start at 3σ with steps of 1σ for CH_3CHO and NH_2CHO . The 1σ values are 7, 7.9 and 6 mJy/beam for CH_3OH , CH_3CHO , and NH_2CHO , respectively. The dashed black circle represents the primary beam size of $45.9''$. The continuum (cont), methanol (ui), formamide (ui) and acetaldehyde (uo) associated synthesized beam size are depicted in the lower left side of the figure. The protostar FIR6c-a is represented by the white filled star. The white filled triangle represents the position of a pre-stellar core (coordinates from [Kainulainen et al. \(2017\)](#)).

CH₃CHO vs NH₂CHO

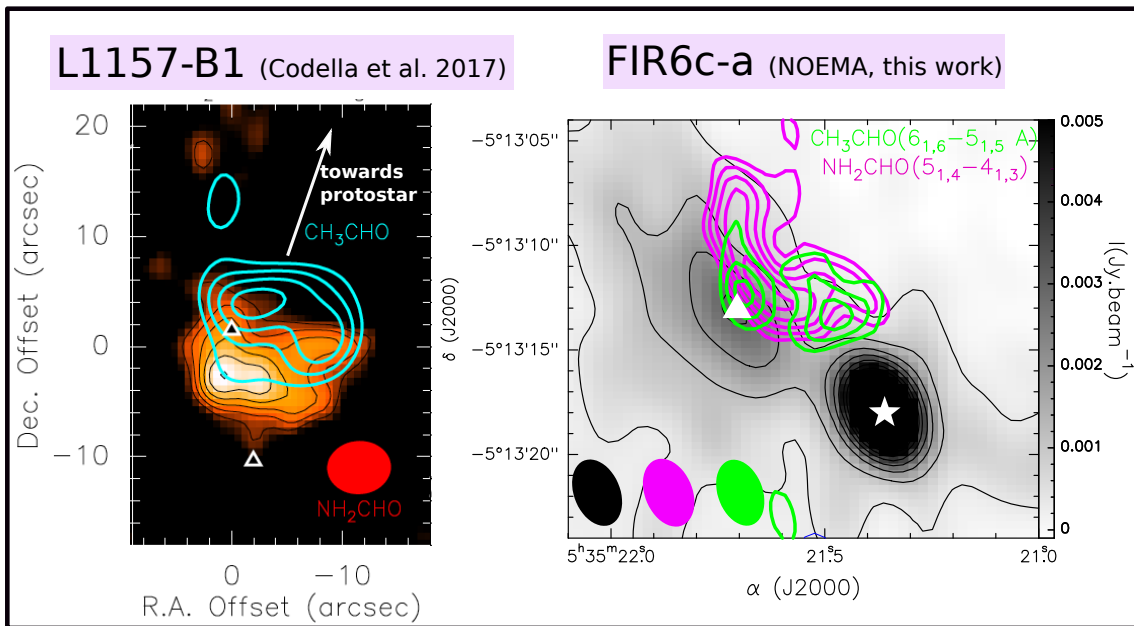


Figure 4.5: Spatial distribution of acetaldehyde (CH₃CHO) and formamide (NH₂CHO) in L1157-B1 and FIR6c-a. *Left:* CH₃CHO ($7_{0,7} - 6_{0,6}$ E+A) velocity-integrated emission in Cyan contours (Codella et al. 2015, 2017) superposed on the NH₂CHO velocity-integrated emission map (coloured scale and black contours). The northern and southern triangles represent the youngest and oldest shocks, respectively. The white arrow indicates the direction of the L1157 protostar. *Right:* Close up view of Fig. 4.4 with the velocity-integrated emissions of acetaldehyde and formamide only. The FIR6c-a protostar is marked by a white filled star, and the white filled triangle represents the pre-stellar core position identified by Kainulainen et al. (2017).

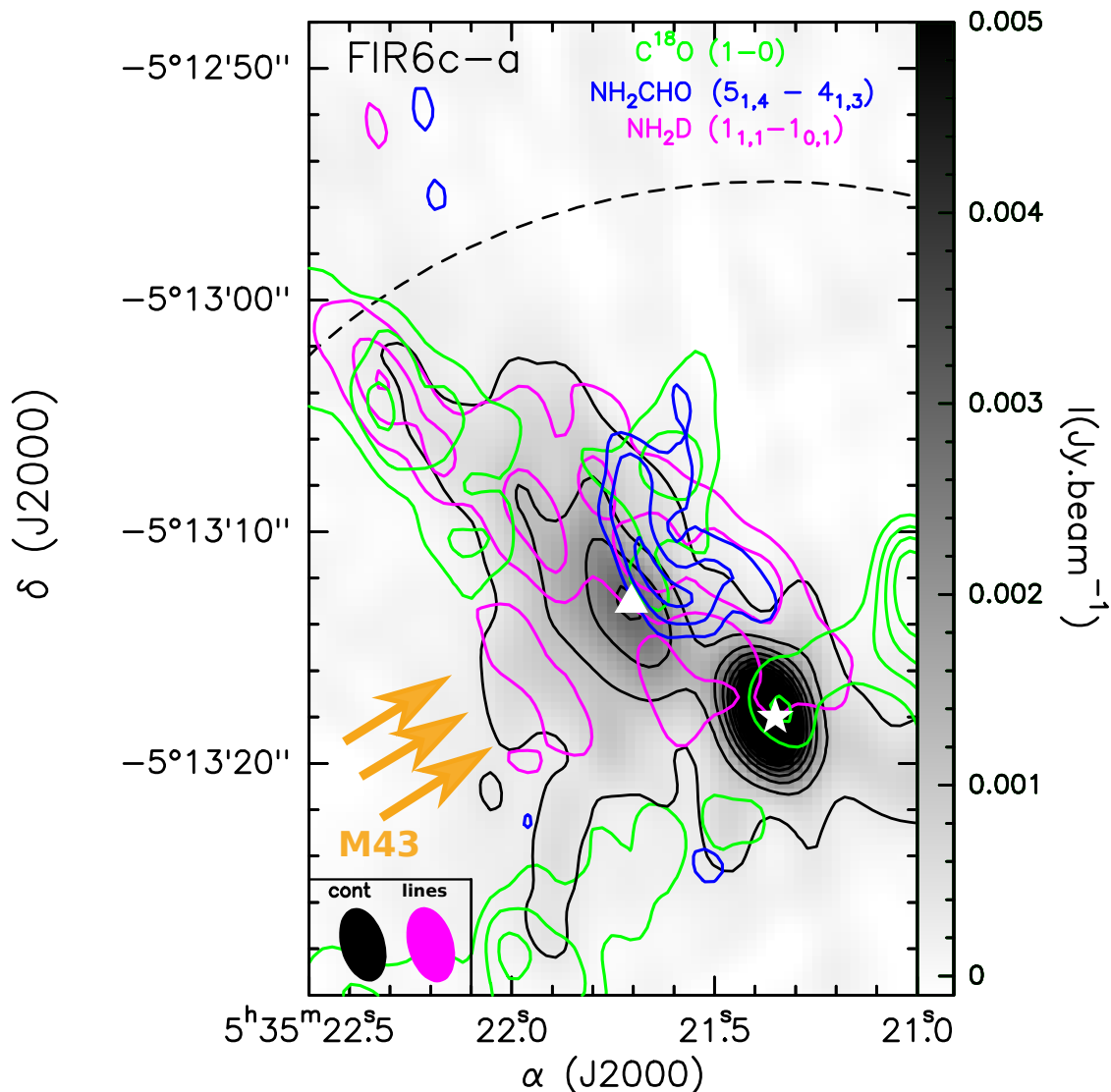


Figure 4.6: 3mm continuum map (grey shaded area and black contours). Levels starts at 20σ with steps of 50σ ($1\sigma = 17\mu\text{Jy}$). Coloured contours represents the velocity-integrated emissions of C^{18}O (green), NH_2CHO (blue), and NH_2D (magenta). Levels start at 3σ with steps of 1σ for NH_2CHO and they start a 5σ with steps of 3σ for NH_2D and C^{18}O (1σ are 5.8, 8.5, and 5.1 mJy/beam for NH_2CHO , NH_2D , and C^{18}O , respectively). The dashed black circle represents the primary beam size of $45.9''$. The continuum and lines associated synthesized beam size are depicted in the lower left side of the figure. The protostar FIR6c-a is represented by the white filled star. The white filled triangle represents the position of a pre-stellar core (coordinates from [Kainulainen et al. \(2017\)](#)). The UV illumination from the nearby M43 HII region is symbolised by orange arrows.

Conclusions & Prospects

5.1 Conclusions

The ultimate goal of this thesis was to shed light on the chemical nature of solar-mass protostars in an environment similar to the one in which our Sun is likely born. In practice, I aimed to answer the following main questions:

1. What is the chemical nature of solar-mass protostars located in a region analogue to the Sun's birth environment? Are there predominantly hot corinos, WCCC objects, hybrid sources? Is our Sun an ancient hot corino?
2. Does the environment play a role in shaping the chemical nature of solar-mass protostars and if yes, how? Is it causing the chemical diversity seen among solar-type protostars?

To address the above questions, I investigated the chemical nature of a sample of solar-mass protostars located in the OMC-2/3 filament, the closest best analogue to the Sun's birth environment, at large (≤ 10000 au) and small (~ 100 au) scales. I used several observational datasets, from both single-dish and interferometric observations, and I performed dust and molecular line analysis. The main results of the thesis are summarized below.

5.1.1 The large-scale study or how to face a PDR wall

The large-scale (≤ 10000 au) study happened to be littered with traps. The first goal of this study was to determine whether hot corinos and WCCC candidates are present along the OMC-2/3 filament. To do so, I used IRAM-30m and Nobeyama-45m observations towards nine solar-mass (Class 0 and I) protostars from the OMC-2/3 filament. I targeted two species, CCH and CH₃OH, known to be standard tracers of WCCC sources and hot corinos, respectively. More specifically, following previous works ([Graninger et al. 2016](#); [Lindberg et al. 2016](#); [Higuchi et al. 2018](#)), I used the abundance ratio $[\text{CCH}]/[\text{CH}_3\text{OH}]$ to assess whether the protostar is a hot corino ($[\text{CCH}]/[\text{CH}_3\text{OH}] \leq 0.5$) or a WCCC candidate ($[\text{CCH}]/[\text{CH}_3\text{OH}] \geq 2$). The second goal of the study was to assess the reliability of this method.

Unexpectedly, I found that the line profile of CCH and CH₃OH were similar and narrow (≤ 2 km/s), suggesting that both species originate from the outer part of the protostars

envelope and/or the parental cloud, rather than the inner part. The molecular line analysis, using LTE and non-LTE radiative transfer methods, showed that these species are emitted from a cold (≤ 30 K) gas filling the telescope beams. The gas density and temperature do not change across nor within the OMC-2/3 filament, which indicates that the emission region is common to the protostars. Additionally, I found relatively constant abundance ratios $[\text{CCH}]/[\text{CH}_3\text{OH}]$ of about 5-7 for all the sources, suggesting homogeneous chemistry at work. All these results together strongly suggest that the line emission of both CCH and CH_3OH is not associated with the protostars envelope but with a more external common component. Comparing the CCH and CH_3OH column density of the OMC-2/3 protostars with that found in protostars of the Perseus Molecular cloud, photo-dissociation regions, and in pre-stellar cores/molecular clouds, I found that the line emission is very likely contaminated by the surrounding photo-dissociation region (PDR), powered by the nearby OB stars, or by the placental cloud in which the sources are embedded. I concluded that the abundance ratio $[\text{CCH}]/[\text{CH}_3\text{OH}]$ obtained with single-dish observations is unreliable to infer the chemical nature of the solar-mass protostars. Consequently, from these observations, I could not detect any hot corinos or WCCC candidates in the OMC-2/3 filament.

5.1.2 The small-scale study or how to see protostars in ORANGES

As the large-scale (≤ 10000 au) chemistry is governed by the nearby OB stars, which create the PDR described in Sec. 5.1.1 and, thus, prevents us from detecting hot corinos and WCCC sources, small-scale (~ 100 au) interferometric observations are mandatory. The project ORion ALMA NEw GEneration Survey (ORANGES) consists of 1.3mm ALMA observations with a spatial angular resolution of $0.25''$, equivalent to ~ 100 au at the distance of the OMC-2/3 filament. The goal of ORANGES is to characterise the chemical content of solar-mass protostars in the OMC-2/3 filament at small scales.

The first ORANGES study consisted of a dust continuum and free-free emission analysis of the OMC-2/3 filament protostars. The goals were to (1) characterise the protostars dust properties (dust temperature, column density, optical depth, free-free emission, and emissivity spectral index) and (2) understand whether they are affected by the nearby OB stars, as in the case of the line emission at a larger scale (Sec. 5.1.1). To reach these goals, I have extracted and used various dust parameters and constructed each source's SED from the millimetre to the centimetre domain. To achieve this, I used the 1.3mm ORANGES data, supplemented with archival ALMA (0.87mm) and VLA (9mm) data from the VANDAM survey (Tobin et al. 2020). The main result shows that there is no clear trend in the dust temperature and the derived (envelope + disk) masses of the sources along the filament. I concluded that the small-scale dust properties are likely not affected by the high UV-illumination of the region.

The second ORANGES study investigated the number of hot corinos in the OMC-2/3 filament. The goals were to determine whether hot corinos are abundant in the OMC-2/3 filament and to understand whether, and how, the highly UV-illuminated environment of the region affects the chemical nature of the sources. To achieve this goal, I first examined the methanol emission, methanol being the most common and abundant iCOM found in hot corinos, to detect the presence of hot corinos. Then, I compared the results of the OMC-2/3 filament with those of the Perseus ALMA Chemistry Survey (PEACHES; Yang et al. 2021) performed in the Perseus Molecular Cloud, a low-mass star-forming

region that is less UV-illuminated with respect to OMC-2/3. The results of the Perseus survey showed that hot corinos are rather abundant in Perseus, with $(56 \pm 14)\%$ of the targeted sources showing strong evidence of a hot corino region. In OMC-2/3, I detected five new hot corinos out of a source sample of 19 solar-mass protostars. Adding the already known hot corinos and the statistics from previous studies (Tobin et al. 2019; Hsu et al. 2020; Chahine et al. 2021), this result leads to a detection rate of hot corinos in the OMC-2/3 filament of $(31 \pm 20)\%$. Hot corinos seem, therefore, to be scarcer in a more UV-illuminated environment. Although the statistics are too small to draw firm conclusions, this result suggests that the environment may play a role in the chemical diversity of solar-mass protostars. From a statistical point of view, however, the two regions show only a marginal difference in their hot corinos content. We need to investigate more solar-type protostars from the OMC-2/3 filament to increase the statistics and to draw a solid conclusion. Finally, although hot corinos are present in an environment similar to the one in which our Sun is likely born, they do not seem to prevail. Elucidating whether our Sun experienced a hot corino phase requires further investigations.

Finally, one of the initial goals of the thesis, and ORANGES, was to understand whether WCCC sources can form in a region analogue to the Sun's birth environment and if so, if they are abundant. To address this point, I targeted two carbon chains, CCH and $c\text{-C}_3\text{H}_2$, common and abundant carbon chain molecules found in WCCC sources. CCH is detected throughout the filament but its emission is relatively shapeless and is thus not clear which component of the protostar it traces. On the other hand, $c\text{-C}_3\text{H}_2$ species is seen only towards FIR2. The latter could be a possible WCCC candidate but I could not draw strong conclusions due to filtered out emission. Therefore, I was not able to detect WCCC sources in the OMC-2/3 filament because of sub-optimal observing strategies. Follow-up observations probing the protostars envelope at scales between 1000 and 3000 au, are mandatory to understand whether WCCC sources are present in the OMC-2/3 filament. Follow-up observations are thus planned with either the ACA configuration of ALMA or with NOEMA as I will discuss in Sec. 5.2.1.

5.1.3 The OMC-2 FIR6c outflow or how to be an unexpected guest joining the party

During the methanol investigation towards the OMC-2/3 sources, I found that one of the sources, FIR6c-a, harbours an intriguing extended methanol emission. It appeared that the methanol emission traces the outflow cavity of the northern lobe, the terminal bow shock and several other shocked positions. The presence of methanol, a known precursor for other iCOMs, indicates a possible rich and complex chemistry in the outflow. Due to the particular geometry of the outflow and its location in the OMC-2/3 filament, the FIR6c-a outflow turned out to be a perfect new astrochemical laboratory where to test iCOMs formation paradigms. Therefore, I submitted a NOEMA proposal as P.I. and obtained new observations at 3mm. The ultimate project goal is to use iCOMs observations and test theoretical predictions to understand and constrain their formation routes. From a preliminary line identification and line emission mapping, I could extract three results.

First, besides methanol, I detected two other iCOMs: acetaldehyde and formamide. The detection of these two species confirms that the FIR6c-a outflow is chemically active. This is also the first time that such an outflow is discovered in the OMC-2/3 filament. Second, the formamide and acetaldehyde show spatial segregation in their emission. Ac-

etaldehyde is present at two distinct positions in the outflow. The first position is close to the protostar and the second position coincides with the outflow terminal bow shock. On the other hand, formamide is detected towards only one location, close to the protostar and coinciding with the acetaldehyde emission. At this position, the formamide and acetaldehyde distributions are similar to what is observed in the L1157-B1 shock: the acetaldehyde peaks closer to the source compared to formamide. This striking result strongly suggests that the formamide production is dominated by the gas phase also in FIR6c-a. Third, and at last, A particular feature of the FIR6c-a outflow is that the shock position where both acetaldehyde and formamide are seen is close to a candidate pre-stellar core identified by [Kainulainen et al. \(2017\)](#). To confirm the presence of a pre-stellar core and to understand whether it is a pre-existing core or the product of the interaction between the dust ridge near the source and the outflow, I investigated the distributions of the NH_2D and C^{18}O emissions. The result strongly suggests that the existence of the pre-stellar core is authentic and that it is a pre-existing core. Consequently, the shock that is seen in both acetaldehyde and formamide is the result of the FIR6c-a outflow crashing on the pre-stellar core.

This project is still ongoing, and future steps remain to be achieved. First, as I detected several lines of acetaldehyde and methanol, I will derive the physical conditions of the gas emitting these two species, compute their relative abundance and compare with the other outflows. Second, I will compare the observations with models following the strategy from [Codella et al. \(2017\)](#) to constrain accurately the formation routes of both acetaldehyde and formamide and constrain the methanol and formamide precursors abundances.

5.1.4 Conclusive remarks

In this thesis, I aimed to determine the chemical nature of solar-mass protostars located in a region analogue to the Sun's birth environment and understand whether our Sun experienced a hot corino phase in its youth. I also addressed the question of whether the environment plays a role in shaping the protostars chemical content.

I first showed that one needs to be careful when aiming to determine the chemical nature of solar-mass protostars with single-dish observations. This warning is especially relevant with some species (small carbon chains, methanol) that can be detected in other environments than protostellar envelopes (e.g. in PDRs and molecular clouds). Class 0 and I protostars are still deeply embedded in the molecular cloud where they form and the scales probed by single-dish telescopes are enough to encompass both the protostar envelope and its surroundings, preventing us to disentangle the emission of the different components.

Then using interferometric observations, I found that the detection rate of hot corinos in the OMC-2/3 region is less than $\sim 50\%$. Therefore, hot corinos do not seem to prevail in an environment such as the OMC-2/3 filament, i.e. a strongly UV-illuminated region. Consequently, I showed that the chemical content of solar-mass protostars in two physically different star-forming regions likely differ.

To conclude, our Sun could have been a hot corino and the environment may play a role in shaping the chemical nature of solar-mass protostars, but we need to increase the statistical studies of solar-mass protostars in other analogues to the Sun's birth environment to draw strong conclusions.

5.2 Prospects

My thesis gave some key elements to understand whether our Sun was a former hot corino and whether the environment is what causes the chemical diversity seen among the solar-mass protostars. However, the road is still long to reach decisive conclusions on these issues. I present in the following some ideas to continue on the road I started to follow more than three years ago.

5.2.1 Short-term prospects

WCCC does not make a good salad with PEACHES and ORANGES A first incoming project is obviously to address the question of whether WCCC sources are present in the OMC-2/3 filament. I could not reach this goal with the ORANGES project because of the too high-angular resolution, as explained in Sec. 5.1.2. This issue has also been reported in the PEACHES survey (Yang et al. 2021) where they detected only CCH that seem also to trace mostly the outflow cavity walls of the protostars outflow. The chemical content of the OMC-2/3 and Perseus protostars is thus characterized at large (≤ 10000 au) and small (~ 100 au) scales but the intermediate scale (between 100 and 3000 au) where the WCCC zone can be present, is not covered. To thoroughly compare the chemical content of the protostars and perform a complete census of hot corinos, WCCC and hybrid objects in the two regions, it is thus mandatory to fill this gap. Additionally, understanding whether WCCC and hybrid sources are present in the OMC-2/3 filament can provide further information on the former chemical nature of our Sun. If it turns out that WCCC or hybrid sources are more abundant than hot corinos, then the fact that our Sun might have experienced one of these two phases needs to be considered.

A follow-up of the ORANGES project would be to observe the protostars envelope at scales between 800 to ~ 3000 au, where the WCCC zone is (e.g. Caselli & Ceccarelli 2012; Sakai & Yamamoto 2013). To classify a source as WCCC, we need to detect long carbon chains which have most of their transitions occurring at low frequencies. A good strategy would then be to observe at 3mm. In this context, I plan to write and submit a NOEMA or an ALMA (ACA configuration) proposal in 2022, the Orion region being observable with the two interferometers.

Hot corino falafels wrapped in methanol bread: a VLA project Another upcoming project is to use the VLA interferometer to do the complete inventory of hot corinos in the OMC-2/3 filament. With the ORANGES project, I detected five new hot corinos in this region. There is, however, an important parameter that we should take into account: dust. De Simone et al. (2020a) (which I co-authored) showed that a large dust optical depth could hide the presence of iCOMs molecular lines and, thus, the presence of a hot corino at millimetre wavelengths. With this in mind, in paper III (Sec. 3.2), I compared the integrated intensity of a methanol line with the dust optical depth, previously derived with the dust continuum study (Sec. 3.1). I found no correlation between the two parameters which strongly suggests that the dust optical depth is not the main parameter affecting the detection of hot corinos in the OMC-2/3 filament. However, I cannot completely exclude that for sources with high dust optical depth, a hot corino could be hidden. Furthermore, a second result from the study by De Simone et al. (2020a) is that even the iCOMs emission line seen at millimetre wavelengths can be affected by the dust. In practice, we showed

that for the hot corino seen at millimetre wavelengths, the derived iCOMs abundances are underestimated. Therefore, if we aim to accurately detect hot corinos and derive correct molecular abundances, we need to determine whether, and to what extent, the dust optical depth affects the iCOMs line emission.

In this context, the best strategy is to perform follow-up observations of the OMC-2/3 protostars at centimetre wavelengths, where the dust is very likely, if not surely, optically thin. Following the same strategy as in [De Simone et al. \(2020a\)](#), I aim to write a VLA proposal to perform observations of the methanol at 25 GHz. If the dust turns out, in the end, to be a determinant factor in the search for hot corinos, it can have several consequences. First, if several new hot corinos are discovered in the OMC-2/3 filament, the result could strengthen the hypothesis that our Sun experienced a hot corino phase in its youth. Additionally, it could increase the detection rate of hot corinos in the OMC-2/3 filament which would become closer to that found in the Perseus region. The suspected effect of the environment on the chemical differentiation of solar-mass protostars could then be questioned.

As the source sample that I used in this thesis includes 19 protostars, I will do a first pilot project with two sources selected. The two sources selected have one of the highest derived range of dust optical depths, and show no hint of multiplicity at scales as low as 40 au (the VLA observations used for the continuum study have an angular resolution of $\sim 0.1''$ or ~ 40 au at the distance of OMC-2/3). As I plan to submit the VLA proposal for the C-configuration (resolution of $1.2''$ or ~ 470 au) in February 2022, this will avoid entangling multiple sources from the same system. Finally, to make sure that the hot corino inventory of the OMC-2/3 filament is complete, one needs to target every solar-mass protostar located in the region. Initially, nine solar-mass protostars have been targeted based on single-dish studies. With the fast-growing capabilities of interferometers such as ALMA and NOEMA, several single protostars seen at single-dish scales revealed themselves to be multiples systems, as shown in particular by the VANDAM project ([Tobin et al. 2016a, 2020](#)). Therefore, we need to complete the source sample that I used in this thesis to perform an unbiased survey of the chemical nature of the OMC-2/3 filament protostars.

Fifty AU Study (FAUST) of the chemistry in the disk/envelope system of Solar-like protostars The chemical differentiation seen in solar-mass protostars is present at scales between 100 au and ~ 3000 au. Is such diversity also seen in the inner envelope/disk system (~ 50 au) where planets are suspected to form? What molecules are passed from the large scale envelope to the disk? Understanding to what extent the chemical material seen in protostellar envelopes and protoplanetary disks is transmitted to the forming planets is important for the chemical content available for future planetary systems. I am involved



in the ALMA large program FAUST (Fifty AU STudy of the inner envelope/disk system of Solar-type protostars; P.Is.: S. Yamamoto, C. Ceccarelli, C. Chandler, C. Codella, and N. Sakai) which aims to address the above questions by investigating the 50 au scale chemical content of a sample of 13 Class 0 and I protostars.

Due to the variety of the targeted sources (different chemical nature and/or environment), the FAUST Large Program will be useful to reveal and quantify the variety of chemical compositions of the envelope/disk system of Class 0 and I solar-like protostars. FAUST also consists of VLA observations. A first pilot VLA proposal (P.I.: Claire Chandler) has been set up to investigate the ice mantle compositions of two chemically distinct types of protostars: the hot corino NGC1333-IRAS 4A and the WCCC source L1527. The goal will be to derive a reliable relative abundance ratio of NH_3 and CH_3OH in both sources, to understand how the ice mantles composition depends on the physical conditions set during the pre-stellar core phase. By being involved in FAUST, I aim to further investigate whether the environment plays a role in the source chemistry, on the ice mantle composition and, hence, on the chemical diversity of solar-mass protostars. To this end, I am implicated in the study of three of the source sample and I will tackle different types of studies such as gas ionization, deuteration, molecular complexity.

5.2.2 Long-term prospects

5.2.2.1 Unraveling the Sun's chemical past

During my thesis, I investigated the chemical content of the OMC-2/3 filament. The results I have found raise new questions. Is the OMC-2/3 filament representative of high-mass star-forming regions, and more particularly of other analogues to the Sun's birth environment, or is it peculiar? What happens at different galactic distances? Addressing these questions requires increasing the statistics. Ultimately, the goal is to perform unbiased chemical surveys of solar mass protostars located in high-mass star-forming regions to assess their chemical content and, therefore, bring new key elements to determine the chemical past of our Sun.

Where are high-mass star-forming regions located? [Motte et al. \(2018\)](#) listed the closest high-mass star-forming regions, i.e. which are located within 3 kpc. All of them (except for Orion) have a typical distance ≥ 1 kpc as shown in [Figure 5.1](#). Observations are, therefore, particularly challenging if we aim to distinguish the solar-mass protostars from their surroundings. With the planned upgrades of the ALMA and NOEMA interferometers, and the upcoming facilities (e.g. ngVLA, Square Kilometer Array), it will be possible to perform similar and more complete chemical surveys as I did for OMC-2/3.

The next point we need to address is the targeted region itself. In my thesis, I examined the OMC-2/3 filament because it is part of the closest high-mass star-forming region, the Orion Molecular Cloud Complex and is, thus, easily observed with the currently available facilities. Additionally, due to the nearby OB stars bounding the region, I considered the OMC-2/3 filament to be the closest best analogue to the Sun's birth environment but could we find better analogues? Certainly, yes. We need to further investigate which regions are the most suitable to represent the Sun's birth environment. There are several studies examining today's properties of the Solar System to understand what kind of stellar group hosted the forming system (e.g. [Ida et al. 2000](#); [Kenyon & Bromley 2004](#); [Adams et al. 2006](#); [Mitchell & Stewart 2011](#); [Li & Adams 2015](#); [Dai et al. 2018](#)).

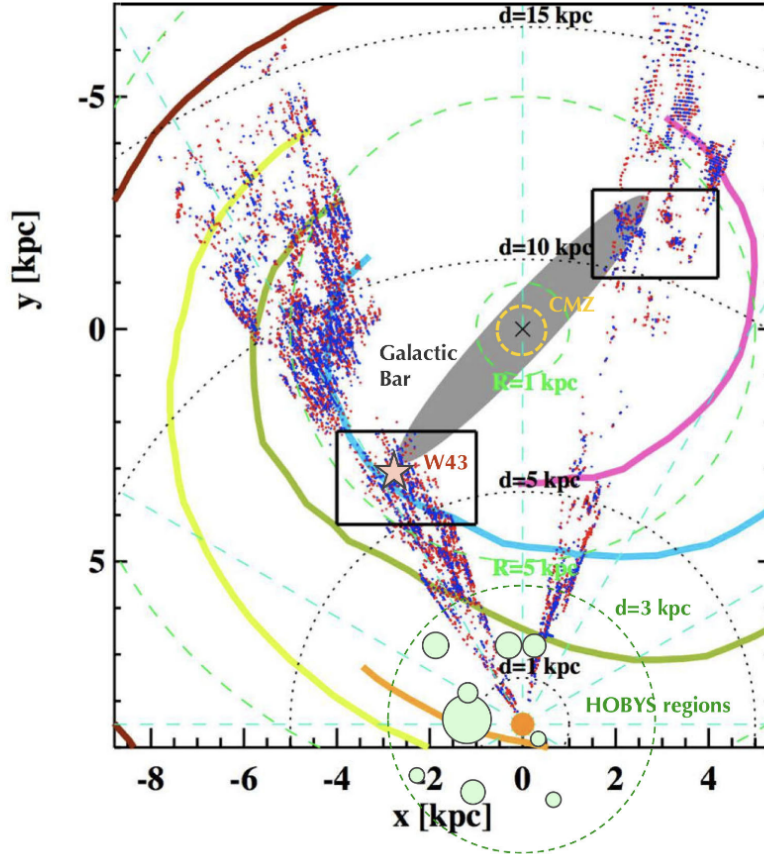


Figure 5.1: Galactic distribution of massive clumps covering the tip of the long bar and one of the cloud complex, W43. Light green circles represent the location of the nearby massive cloud complexes (within 3 kpc). The coloured thick curves trace the different Galactic spiral arms and the orange circle represents the Sun. Figure from [Motte et al. \(2018\)](#).

Very recently, [Pfalzner & Vincke \(2020\)](#) showed that two regions, NGC6611 and M44, could be considered as the present-day equivalent to the Sun’s birth environment. The study relies on the hypothesis that the sharp outer edge of the Solar System is due to flybys, considered to be a more probable explanation than external photo-evaporation due to nearby massive stars (e.g. [Adams et al. 2004](#); [Winter et al. 2020a](#)). This assumption can exclude other suitable regions. [Pfalzner & Vincke \(2020\)](#) indicate that cosmo-chemical considerations need to be taken into account to determine more accurately what was the Sun’s birth environment. Indeed, the Sun probably moved to its current position from a birthplace closer to the galactic centre ([Wielen et al. 1996](#)). It is thus crucial to take into account cosmic chemical evolution because the present chemical composition of the Solar System may not exactly reflect that of the local ISM 4.5 Gyr ago.

In conclusion, targeting several high-mass star-forming regions at larger distances is important to (1) increase the statistics of studied solar-mass protostars in high-mass star-forming regions, and (2) probe different environments (with different metallicities) that could reflect the chemical conditions in which our Solar System formed. These surveys are mandatory if we aim to unravel the Sun’s chemical past and I wish to continue in this direction in the future.

5.2.2.2 To galaxies and beyond!

Part of my future research plan concerns extra-galactic astrochemical studies as I wish to broaden my field of expertise.

During my thesis, I investigated the chemical nature of solar-mass protostars located in the OMC-2/3 filament and compared the chemical content of this region with that of the Perseus Molecular Cloud, a relatively different region. I aim to do the same with galaxies: I would like to compare the chemical content of local galaxies and compare them with galaxies located further away. Do all the galaxies have the same chemical footprints? If not, what causes this difference? Is there a relation between the large scale chemistry of a galaxy and its evolutionary status? Are there chemical differences between low- and high-metallicity galaxies? And more generally, how do galaxies form and evolve? What role do molecular outflows have on the evolution of a galaxy and its stellar content? These are questions I am truly interested in, and I aim to tackle them in the future.

Moving from a region such as the OMC-2/3 filament to galaxies is also quite natural. There are several similarities between the work I have performed in my thesis and that in galaxies. For instance, the OMC-2/3 filament is highly illuminated by nearby OB stars, generating a photo-dissociation region (PDR) surrounding the filament. In galaxies, most of the line emission arises from PDRs, quiescent gas, and star-forming regions (Viti 2017). Besides PDRs, we can also take the example of outflows. Outflows are ubiquitous in young stars and are very often accompanied by jets and shocked regions. Those features impact the immediate surroundings of the protostars and can lead to rich chemistry and/or clusters formation and, hence, produce star formation. This is also seen in the case of outflows driven by galaxies (AGN and/or starburst): they can trigger star formation through direct feedback mechanisms.

We can, therefore, expect that the main molecular tracers found in the different components of galaxies are the same as in Galactic molecular clouds. The Orion region is actually used as a template for extra-galactic studies and links are made between what is seen in Orion, and more generally in galactic molecular clouds and galaxies (e.g. Goicoechea et al. 2015; Rybak et al. 2020; Pabst et al. 2021). In general, I believe that the Galactic and extra-galactic fields are going to meet with the upcoming observational capabilities. Today it is possible to separate the different main components of the nearest galaxies to perform molecular line surveys (e.g. Nakajima et al. 2018; Watanabe et al. 2019; Scourfield et al. 2020; Martín et al. 2021) but with tomorrow's observational capabilities, we will be able to study nearby galaxies like we are now studying distant high-mass star-forming regions. I wish to contribute to this new endeavour.

To conclude, we are in an exceptional observational area, which allows us to go further and further in search of answers. For sure, astrochemistry has a bright future and I aim to be part of it.

Bibliography

- Aannestad, P. A. 1975, *ApJ*, 200, 30
- Adams, F. C. 2010, *ARA&A*, 48, 47
- Adams, F. C., Hollenbach, D., Laughlin, G., & Gorti, U. 2004, *ApJ*, 611, 360
- Adams, F. C., Lada, C. J., & Shu, F. H. 1987, *ApJ*, 312, 788
- Adams, F. C., Proszkow, E. M., Fatuzzo, M., & Myers, P. C. 2006, *ApJ*, 641, 504
- Agladze, N. I., Sievers, A. J., Jones, S. A., Burlitch, J. M., & Beckwith, S. V. W. 1996, *ApJ*, 462, 1026
- Agúndez, M., Cernicharo, J., & Guélin, M. 2015, *A&A*, 577, L5
- Agúndez, M., Cernicharo, J., Guélin, M., et al. 2008, *A&A*, 478, L19
- Agúndez, M., Marcelino, N., Cernicharo, J., Roueff, E., & Tafalla, M. 2019, *A&A*, 625, A147
- Agúndez, M., Roueff, E., Cabezas, C., Cernicharo, J., & Marcelino, N. 2021, *A&A*, 649, A171
- Aikawa, Y., Furuya, K., Yamamoto, S., & Sakai, N. 2020, *ApJ*, 897, 110
- Aikawa, Y., Wakelam, V., Garrod, R. T., & Herbst, E. 2008, *ApJ*, 674, 984
- Aikawa, Y., Wakelam, V., Hersant, F., Garrod, R. T., & Herbst, E. 2012, *ApJ*, 760, 40
- Aladro, R., Martín, S., Riquelme, D., et al. 2015, *A&A*, 579, A101
- Ali, B. & Depoy, D. L. 1995, *AJ*, 109, 709
- Allamandola, L. J., Bernstein, M. P., Sabdford, S. A., & Walker, R. L. 1999, *Space Science Reviews*, 90, 219
- Allen, L., Megeath, S. T., Gutermurth, R., et al. 2007, *Protostars and Planets V*, eds: B. Reipurth, D. Jewitt, and K. Keil, University of Arizona Press, Tucson, 951, 361
- Alwegg, K., Balsiger, H., & Fuselier, S. A. 2019, *ARA&A*, 57, 113
- Amelin, Y., Krot, A. N., Hutcheon, I. D., & Ulyanov, A. A. 2002, *Science*, 297, 1678

- André, P. 1996, ASPC, 93, 273
- André, P. 2011, Encyclopedia of Astrobiology, Eds: Gargaud M. et al., Springer, Berlin, Heidelberg
- André, P. & Montmerle, T. 1994, ApJ, 420, 837
- André, P., Montmerle, T., Feigelson, E. D., Stine, P. C., & Klein, K. L. 1988, ApJ, 335, 940
- André, P., Ward-Thompson, D., & Barsony, M. 1993, ApJ, 406, 122
- André, P., Ward-Thompson, D., & Motte, F. 1996, A&A, 314, 625
- Andrews, S. M. & Williams, J. P. 2007, ApJ, 659, 705
- Andrews, S. M., Wilner, D. J., Hugues, A. M., Qi, C., & Dullemond, C. P. 2009, ApJ, 700, 1502
- Andrews, S. M., Wilner, D. J., Hugues, A. M., Qi, C., & Dullemond, C. P. 2010, ApJ, 723, 1241
- Anglada, G. 1995, RMxAC, 1, 67
- Anglada, G. 1996, ASPC, 93, 3
- Anglada, G., Rodríguez, L. F., & Carrasco-González, C. 2018, A&ARv, 26, 3
- Anglada, G., Rodríguez, L. F., Torrelles, J. M., et al. 1989, ApJ, 341, 208
- Anglada, G., Villuendas, E., Estalella, R., et al. 1998, AJ, 116, 2953
- Ansdell, M., Haworth, T. J., Williams, J. P., et al. 2020, AJ, 160, 248
- Antiñolo, M., Agundez, M., Jiménez, E., et al. 2016, ApJ, 823, 25
- Araki, M., Takano, S., Sakai, N., et al. 2017, ApJ, 847, 51
- Arce, H. G., Santiago-García, J., Jørgensen, J. K., Tafalla, M., & Bachiller, R. 2008, ApJ, 681, 21
- Arce, H. G. & Sargent, A. I. 2006, ApJ, 646, 107
- Aso, Y., Tatematsu, K., Sekimoto, Y., et al. 2000, ApJS, 131, 465
- Awad, Z., Coutens, A., Viti, S., & Holdship, J. 2021, MNRAS, 506, 1019
- Awad, Z., Viti, S., Collings, M. P., & Williams, D. A. 2010, MNRAS, 407, 2511
- Bachiller, R. 1996, ARA&A, 34, 111
- Bacmann, A., Caux, E., Hily-Blant, P., et al. 2010, A&A, 521, L42
- Bacmann, A., Lefloch, B., Ceccarelli, C., et al. 2002, A&A, 389, L6
- Bacmann, A., Lefloch, B., Ceccarelli, C., et al. 2003, ApJ, 585, 55

- Bacmann, A., Taquet, V., Faure, A., Kahane, C., & Ceccarelli, C. 2012, *A&A*, 541, L12
- Baker, J., Bizzarro, M., Wittig, N., Connelly, J., & Haack, H. 2005, *Nature*, 436, 1127
- Bally, J., Langer, W. D., & Liu, W. 1991, *ApJ*, 383, 645
- Bally, J., Langer, W. D., Stark, A. A., & Wilson, R. W. 1987, *ApJ*, 312, 45
- Balucani, N., Ceccarelli, C., & Taquet, V. 2015, *MNRAS*, 449, 16
- Barnard, E. E. 1919, *ApJ*, 49, 1
- Barone, V., Latouche, C., Skouteris, D., et al. 2015, *MNRAS*, 453, 31
- Bate, M. R., Tricco, T. S., & Price, D. J. 2014, *MNRAS*, 437, 77
- Batria, W., Wilson, T. L., Bastien, P., & Ruf, K. 1983, *A&A*, 128, 279
- Beckwith, S. V. W. & Sargent, A. I. 1991, *ApJ*, 381, 250
- Beichman, C. A., Myers, P. C., Emerson, J. P., et al. 1986, *ApJ*, 307, 337
- Belloche, A., Garrod, R. T., Müller, H. S. P., et al. 2009, *A&A*, 499, 215
- Belloche, A., Maury, A. J., Maret, S., et al. 2020, *A&A*, 635, A198
- Belloche, A., Menten, K. M., Comito, C., et al. 2008a, *A&A*, 482, 179
- Belloche, A., Menten, K. M., Comito, C., et al. 2008b, *A&A*, 492, 769
- Belloche, A., Müller, H. S. P., Menten, K. M., Schilke, P., & Comito, C. 2013, *A&A*, 559, A47
- Benson, P. J., Caselli, P., & Myers, P. C. 1998, *ApJ*, 506, 743
- Benson, P. J. & Myers, P. C. 1989, *ApJS*, 71, 89
- Bergin, E. A., Aikawa, Y., Blake, G. A., & van Dishoeck, E. F. 2007, in Reipurth, B., Jewitt, D. and Keil, K. eds, *Protostars and Planets V*, p. 751
- Bergin, E. A., Alves, J., Huard, T., & Lada, C. J. 2002, *ApJ*, 570, 101
- Bergner, J. B., Guzmán, V. G., Öberg, K. I., Loomis, R. A., & Pegues, J. 2018, *ApJ*, 857, 69
- Bergner, J. B., Martín-Doménech, R., Öberg, K. I., et al. 2019, *ACS Earth and Space Chemistry*, 3, 8, 1564
- Bergner, J. B., Öberg, K. I., Garrod, R. T., & Graninger, D. M. 2017, *ApJ*, 841, 120
- Bernstein, M. P., Sandford, S. A., Allamandola, L. J., et al. 1999, *Science*, 283, 1135
- Bianchi, E., Chandler, C. J., Ceccarelli, C., et al. 2020, *MNRAS*, 498, L87
- Bianchi, E., Codella, C., Ceccarelli, C., et al. 2019, *MNRAS*, 483, 1850

- Bisschop, S. E., Jørgensen, J. K., Bourke, T. L., Bottinelli, S., & van Dishoeck, E. F. 2008, *A&A*, 488, 959
- Blake, G. A., van Dishoeck, E. F., Jansen, D. J., Groesbeck, T. D., & Mundy, L. G. 1994, *ApJ*, 428, 680
- Bonanno, A., Schlattl, H., & Paternò, L. 2002, *A&A*, 390, 1115
- Bontemps, S., André, P., Terebey, S., & Cabrit, S. 1996, *A&A*, 311, 858
- Bontemps, S., André, P., & Ward-Thompson, D. 1995, *A&A*, 297, 98
- Boogert, A. C. A., Gerakines, P. A., & Douglas, C. B. W. 2015, *ARA&A*, 53, 541
- Booth, A. S., Walsh, C., Terwisscha van Scheltinga, J., et al. 2021, *NatAs*, 5, 684
- Bottinelli, S., Ceccarelli, C., Lefloch, B., et al. 2004, *ApJ*, 615, 354
- Bottinelli, S., Ceccarelli, C., Williams, J. P., & Lefloch, B. 2007, *A&A*, 463, 601
- Boudet, N., Mutschke, H., Nayral, C., et al. 2005, *ApJ*, 633, 272
- Bouvier, M., López-Sepulcre, A., Ceccarelli, C., et al. 2021, *A&A*, 653, A117
- Brasser, R., Duncan, M. J., Levison, H. F., Schwamb, M. E., & Brown, M. E. 2012, *Icarus*, 217, 1
- Brown, P. D., Charnley, S. B., & Millar, T. J. 1988, *MNRAS*, 231, 409
- Brown, R. D., Crofts, J. G., Gardner, F. F., et al. 1975, *ApJ*, 197, 29
- Busquet, G., Palau, A., Estalella, R., et al. 2010, *A&A*, 517, L6
- Calcutt, H., Fiechter, M. R., Willis, E. R., et al. 2018b, *A&A*, 617, A95
- Calcutt, H., Jørgensen, J. K., Müller, H. S. P., et al. 2018a, *A&A*, 616, A90
- Calcutt, H., Viti, S., Codella, C., et al. 2014, *MNRAS*, 443, 3157
- Carpenter, J. M. 2000, *AJ*, 120, 3139
- Caselli, P. & Ceccarelli, C. 2012, *A&ARv*, 20, 56
- Caselli, P., Hartquist, T. W., & Havnes, O. 1997, *A&A*, 322, 296
- Caselli, P., Hasegawa, T. I., & Herbst, E. 1993, *ApJ*, 408, 548
- Caselli, P., Keto, E., Bergin, E. A., et al. 2012, *ApJ*, 759, L37
- Caselli, P., Stantcheva, T., Shalabeia, O., Shematovich, V. I., & Herbst, E. 2002, *P&SS*, 50, 1257
- Caselli, P., van der Tak, F. F. S., Ceccarelli, C., & Bacmann, A. 2003, *A&A*, 403, L37
- Caselli, P., Vastel, C., Ceccarelli, C., et al. 2008, *A&A*, 492, 703

- Caselli, P., Walmsley, C. M., Tafalla, M., Dore, L., & Myers, P. C. 1999, *ApJ*, 523, 165
- Caselli, P., Walmsley, C. M., Terzieva, R., & Herbst, E. 1998, *ApJ*, 499, 234
- Castets, A. & Langer, W. D. 1995, *A&A*, 294, 835
- Caux, E., Kahane, C., Castets, A., et al. 2011, *A&A*, 532, A23
- Cazaux, S., Caux, E., Parise, B., & Teyssier, D. 2003, *ApJ*, 593, 51
- Ceccarelli, C. 2004, ASPC, *Star Formation in the Interstellar Medium: In Honor of David Hollenbach*, 323, 195
- Ceccarelli, C., Bacmann, A., Boogert, A., et al. 2010, *A&A*, 521, L22
- Ceccarelli, C., Caselli, P., Bockelée-Morvan, D., et al. 2014a, *Protostars and Planets VI*, eds: H. Beuther, R. S. Klessen, C. P. Dullemond and T. Henni g, University of Arizona Press, Tucson, 914pp., p. 859-882
- Ceccarelli, C., Caselli, P., Fontani, F., et al. 2017, *ApJ*, 850, 176
- Ceccarelli, C., Caselli, P., Herbst, E., Tielens, A. G. G. M., & Caux, E. 2007, in Reipurth, B., Jewitt, B. and Keil, K. eds, *Protostars and Planets V*, p.47
- Ceccarelli, C., Castets, A., Caux, E., et al. 2000a, *A&A*, 355, 1129
- Ceccarelli, C., Castets, A., Loinard, L., Caux, E., & Tielens, A. G. G. M. 1998, *A&A*, 338, 143
- Ceccarelli, C., Dominik, C., López-Sepulcre, A., et al. 2014b, *ApJL*, 790, L1
- Ceccarelli, C., Loinard, L., & Castets, A. 2000b, *A&A*, 357, L9
- Ceccarelli, C., Loinard, L., Castets, A., et al. 2001, *A&A*, 372, 998
- Ceccarelli, C., Maret, S., Tielens, A. G. G. M., Castets, A., & Caux, E. 2003, *A&A*, 410, 587
- Ceccarelli, C., Vastel, C., Tielens, A. G. G. M., et al. 2002, *A&A*, 381, L17
- Cernicharo, J., Agúndez, M., Cabezas, C., et al. 2021, *A&A*, 647, L2
- Cernicharo, J., Marcelino, N., Roueff, E., Gerin, M., & Jiménez-Escobar, A. 2012, *ApJ*, 759, L43
- Chahine, L., López-Sepulcre, A., Neri, R., et al. 2021, In peer review
- Chandler, C. J., Brogan, C. L., Shirley, Y. L., & Loinard, L. 2005, *ApJ*, 632,371
- Charnley, S. B., Tielens, A. G. G. M., & Millar, T. J. 1992, *ApJ*, 399, L71
- Charnley, S. B., Tielens, A. G. G. M., & Rodgers, S. D. 1997, *ApJ*, 482, L203
- Chen, H., Grenfell, T. G., Myers, P. C., & Hughes, J. D. 1997, *ApJ*, 478, 295

Chen, H., Myers, P. C., Ladd, E. F., & Woods, D. O. S. 1995, *ApJ*, 445, 377

Chevalier, R. A. 2000, *ApJ*, 538, 151

Chevance, M., Kruijssen, J. M. D., Vazquez-Semideni, E., et al. 2020, *Space Science Reviews*, 216, 50

Chini, R., Reipurth, B., Ward-Thompson, D., et al. 1997, *ApJ*, 474, L135

Choudhury, R., Schilke, P., Stéphan, G., et al. 2015, *A&A*, 575, A68

Chuang, C.-Y., Aso, Y., Hirano, N., Hirano, S., & Machida, M. N. 2021, *ApJ*, 916, 82

Chuang, K.-J., Fedoseev, G., Ioppolo, S., van Dishoeck, E. F., & Linnartz, H. 2016, *MNRAS*, 455, 1702

Cleeves, L. I., Bergin, E. A., & Alexander, C. M. O. 2014, *Science*, 345, 1590

Cleeves, L. I., Bergin, E. A., Alexander, C. M. O., et al. 2016, *ApJ*, 819, 13

Clerke, A. M. 1903, London, A. & C. Black 567

Close, J. L. & Pittard, J. M. 2017, *MNRAS*, 469, 1117

Codella, C., Bianchi, E., Tabone, B., et al. 2018, *A&A*, 617, A10

Codella, C., Cabrit, S., Gueth, F., et al. 2014, *A&A*, 568, L5

Codella, C., Ceccarelli, C., Bianchi, E., et al. 2020, *A&A*, 635, A17

Codella, C., Ceccarelli, C., Cabrit, S., et al. 2016, *A&A*, 586, L3

Codella, C., Ceccarelli, C., Caselli, P., et al. 2017, *A&A*, 605, L3

Codella, C., Fontani, F., Ceccarelli, C., et al. 2015, *MNRAS*, 449, L11

Codella, C., Lefloch, B., Ceccarelli, C., et al. 2010, *A&A*, 518, L112

Coleman, G. A. L. 2021, *MNRAS*, 506, 3596

Collings, M. P., Anderson, M. A., Chen, R., et al. 2004, *MNRAS*, 354, 1133

Comito, C., Schilke, P., Philips, T. G., et al. 2005, *ApJS*, 156, 127

Commerçon, B., Launhardt, R., Dullemond, C., & Henning, T. 2012, *A&A*, 545, A98

Compiègne, M., Verstraete, L., Jones, A., et al. 2011, *A&A*, 525, A103

Corbelli, E., Braine, J., Bandiera, R., et al. 2017, *A&A*, 601, A146

Cordiner, M. A., Charnley, S. B., Buckle, J. V., Walsh, C., & Millar, T. J. 2011, *ApJ*, 730, L18

Cordiner, M. A., Charnley, S. B., Wirström, E. S., & Smith, R. G. 2012, *ApJ*, 744, 131

Coudert, L. H., Margulès, L., Vastel, C., et al. 2019, *A&A*, 624, A70

Coupeaud, A., Demyk, K., Meny, C., et al. 2011, *A&A*, 535, A124

Coutens, A., Jørgensen, J. K., van der Wiel, M. H. D., et al. 2016, *A&A*, 590, L6

Coutens, A., Persson, M. V., Jørgensen, J. K., Wampfler, S. F., & Lykke, J. M. 2015, *A&A*, 576, A5

Coutens, A., Vastel, C., Caux, E., et al. 2012, *A&A*, 539, A132

Coutens, A., Willis, E. R., Garrod, R. T., et al. 2018, *A&A*, 612, A107

Cuadrado, S., Goicoechea, J. R., Cernicharo, J., et al. 2017, *A&A*, 603, A124

Cuadrado, S., Goicoechea, J. R., Pilleri, P., et al. 2015, *A&A*, 575, A82

Curiel, S., Rodriguez, L. F., Moran, J. M., & Canto, J. 1993, *ApJ*, 415, 191

Dai, Y.-Z., Liu, H.-G., Wu, W.-B., et al. 2018, *MNRAS*, 480, 4080

Dalgarno, A. & Lepp, S. 1984, *ApJ*, 287, L47

Dauphas, N. & Chaussidon, M. 2011, *Annu. Rev. Earth Planet. Sci.*, 39, 351

de Jong, T., Chu, S., & Dalgarno, A. 1975, *ApJ*, 199, 69

De Simone, M., Codella, C., Ceccarelli, C., et al. 2020a, *ApJL*, 896, L3

De Simone, M., Codella, C., Ceccarelli, C., et al. 2020b, *A&A*, 640, A75

De Simone, M., Codella, C., Testi, L., et al. 2017, *A&A*, 599, A121

De Simone, M., Fontanni, F., Codella, C., et al. 2018, *MNRAS*, 476, 1982

Dellar, A. T., Forbrich, J., & Loinard, L. 2013, *A&A*, 552, A51

Diehl, R., Lugaro, M., Heger, A., et al. 2021, *PASA*, in press, arXiv: 2019.08558

Draine, B. T. 2003, *ARA&A*, 41, 241

Draine, B. T. 2006, *ApJ*, 636, 1114

Draine, B. T. & Lee, H. M. 1984, *ApJ*, 285, 89

Drozdovskaya, M. N., van Dishoeck, E. F., Jørgensen, J. K., Calmonte, U., & van der Wiel, M. H. D. 2018, *MNRAS*, 476, 4949

Drozdovskaya, M. N., van Dishoeck, E. F., Rubin, M., Jørgensen, J. K., & Altwegg, K. 2019, *MNRAS*, 490, 50

Dunham, M. M., Allen, L. E., Evans, N. J. I., et al. 2015, *ApJS*, 220, 11

Dunham, M. M., Stutz, A. M., Allen, L. E., et al. 2014, *Protostars and Planets VI*, eds. H. Beuther, R. S. Klessen, C. P. Dullemond and T. Henning, 914, 195

Dutrey, A., Guilloteau, S., & Guelin, M. 1997, *A&A*, 317, L55

Dwarkadas, V. V., Dauphas, N., Meyer, B., Boyajian, P., & Bojazi, M. 2017, *ApJ*, 851, 147

Dwek, E. 1997, *ApJ*, 484, 779

Dzib, S., Loinard, L., Mioduszewski, A. J., et al. 2010, *ApJ*, 718, 610

Dzib, S. A., Loinard, L., Mioduszewski, A. J., et al. 2013, *ApJ*, 775, 63

Dzib, S. A., Ortiz-León, G. N., & Hernández-Gómez, A. 2018, *A&A*, 614, A20

Eisner, J. A., Arce, H. G., Ballering, N. P., et al. 2018, *ApJ*, 860, 77

Eisner, J. A., Plambeck, R. L., Carpenter, J. M., et al. 2008, *ApJ*, 683, 304

Elsila, J. E., Glavin, D. P., & Dworkin, J. P. 2009, *M&PS*, 44, 1323

Engargiola, G., Plambeck, R. L., Rosolowsky, E., & Blitz, L. 2003, *ApJS*, 149, 343

Enoch, M. L., Corder, S., Duchêne, G., et al. 2011, *ApJS*, 195, 21

Enrique-Romero, J., Ceccarelli, C., Rimola, A., et al. 2021, *A&A*, 655, A9

Enrique-Romero, J., Rimola, A., Ceccarelli, C., & Balucani, N. 2016, *MNRAS*, 459, L6

Enrique-Romero, J., Rimola, A., Ceccarelli, C., et al. 2019, *ECS*, 3, 2158

Enrique-Romero, J., S., A.-B., Kolb, F. J., et al. 2020, *MNRAS*, 493, 2523

Evans, N. J., I., Dunham, M. M., Jørgensen, J. K., et al. 2009, *ApJS*, 181, 321

Favre, C., Ceccarelli, C., López-Sepulcre, A., et al. 2018, *ApJ*, 859, 136

Favre, C., Cleeves, L. I., Bergin, E. A., Qi, C., & Blake, G. A. 2013, *ApJ*, 776, L38

Feddersen, J. R., Arce, H. G., Kong, S., et al. 2020, *ApJ*, 896, 11

Fedoseev, G., Chuang, K.-J., Ioppolo, S., et al. 2017, *ApJ*, 842, 52

Fedoseev, G., Cuppen, H. M., Ioppolo, S. and Lamberts, T., & Linnartz, H. 2015, *MNRAS*, 448, 1288

Feigelson, E. D., Carkner, L., & Wilking, B. A. 1998, *ApJ*, 494, L215

Feigelson, E. D. & Montmerle, T. 1985, *ApJ*, 289, L19

Ferrero, S., Zamirri, L., Ceccarelli, C., et al. 2020, *ApJ*, 904, 11

Fischer, W. J., Megeath, S. T., Stutz, A. M., et al. 2013, *AN*, 334, 53

Fontani, F., Quaia, G., Ceccarelli, C., et al. 2020, *MNRAS*, 493, 3412

Fossé, D., Cerniccharo, J., Gerin, M., & Cox, P. 2001, *ApJ*, 552, 168

Fourikis, N., Sinclair, M. W., Robinson, B. J., Godfrey, P. D., & Brown, R. D. 1974, *AuJPh*, 27, 425

- Frank, A., Ray, T. P., Cabrit, S., et al. 2014, *Protostars and Planets VI*, Eds. H. Beuther, R. S. Klessen, C. P. Dullemond, T. Henning, University of Arizona Press, Tucson, 914, 451
- Froebrich, D. 2005, *ApJS*, 156, 169
- Fuente, A., Rodríguez-Franco, A., García-Burillo, S., Martín-Pintado, J., & Black, J. H. 2003, *A&A*, 406, 899
- Furlan, E., Fischer, W. J., Ali, B., et al. 2016, *ApJS*, 224, 5
- Garrod, R. T. & Herbst, E. 2006, *A&A*, 457, 927
- Garrod, R. T. & Widicus Weaver, S. L. 2013, *Chemical Reviews*, 113, 8939
- Garrod, R. T., Widicus Weaver, S. L., & Herbst, E. 2008, *ApJ*, 682, 283
- Gatley, I., Becklin, E. E., Matthews, K., et al. 1974, *ApJ*, 191, L121
- Gerin, M., Combes, F., Wlodarczak, G., Encrenaz, P., & Laurent, C. 1992a, *A&A*, 253, L29
- Gerin, M., Goicoechea, J. R., Pety, J., & Hily-Blant, P. 2009, *A&A*, 494, 977
- Gerin, M., Pety, J., Commerçon, B., et al. 2017, *A&A*, 606, A35
- Gerin, M., Pety, J., Fuente, A., et al. 2015, *A&A*, 577, L2
- Gerin, M., Wootten, H. A., Combes, F., et al. 1987, *A&A*, 173, L1
- Goicoechea, J. R., Teyssier, D., Etxaluze, M., et al. 2015, *ApJ*, 812, 75
- Goldsmith, P. F. & Langer, W. D. 1999, *ApJ*, 517, 209
- Gómez-Ruiz, A. I., Gusdorf, A., Leurini, S., et al. 2019, *A&A*, 629, A77
- Gould, R. J. & Salpeter, E. E. 1963, *ApJ*, 138, 393
- Gounelle, M. 2015, *A&A*, 582, A26
- Gounelle, M., Meibom, A., Hennebelle, P., & Inutsuka, S.-I. 2009, *ApJ*, 694, L1
- Gounelle, M. & Meynet, G. 2012, *A&A*, 545, A4
- Gounelle, M. & Russel, S. S. 2005, *GeCoA*, 69, 3129
- Gounelle, M., Shu, F. H., Shang, H., et al. 2006, *ApJ*, 640, 1163
- Graninger, D. M., Wilkins, O. H., & Öberg, K. I. 2016, *ApJ*, 819, 140
- Gratier, P., Majumdar, L., Ohishi, M., et al. 2016, *ApJS*, 225, 25
- Green, J. D., Evans, N. J. I., Jørgensen, J. K., et al. 2013, *ApJ*, 770, 123
- Großschedl, J. E., Alves, J., Meingast, S., et al. 2018, *A&A*, 619, A106

Gueth, F., Guilloteau, S., & Bachiller, R. 1996, *A&A*, 307, 891

Guilloteau, S., Dutrey, A., Piétu, V., & Boehler, Y. 2011, *A&A*, 529, A105

Guzmán, V. V., Goicoechea, J. R., Pety, J., et al. 2013, *A&A*, 560, A73

Gúzman, V. V., Pety, J., Goicoechea, J. R., et al. 2015, 800, L33

Harju, J., Pineda, J. E., Vasyunin, A. I., et al. 2020, *ApJ*, 895, 101

Harsono, D., Jørgensen, J. K., van Dishoeck, E. F., et al. 2014, *A&A*, 562, A77

Hartmann, L., Ballesteros-Paredes, J., & Bergin, E. A. 2001, *ApJ*, 562, 852

Hasegawa, T. I., Herbst, E., & Leung, C. M. 1992, *ApJS*, 82, 167

Hassel, G. E., Harada, N., & Herbst, E. 2011, *ApJ*, 743, 182

Hassel, G. E., Herbst, E., & Garrod, R. T. 2008, *ApJ*, 681, 1385

Haworth, T. J., Facchini, S., Clarke, C. J., & Cleeves, L. I. 2017, *MNRAS*, 468, L108

Henkel, C., Jacq, T., Mauersberger, R., Menten, K. M., & Steppe, H. 1987, *A&A*, 188, L1

Hennebelle, . & Fromang, S. 2008, *A&A*, 477, 9

Herbst, E. & van Dishoeck, E. F. 2009, *ARA& A*, 47, 427

Hernández-Gómez, A., Loinard, L., Chandler, C. J., et al. 2019, *ApJ*, 875, 94

Herschel, W. 1785, *Phil. Trans.* 75, 213

Higuchi, A. E., Sakai, N., Watanabe, Y., et al. 2018, *ApJS*, 236, 52

Hildebrand, R. H. 1983, *QJRAS*, 24, 267

Hily-Blant, P., Bonal, L., Faure, A., & Quirico, E. 2013, *Icarus*, 223, 582

Hily-Blant, P., Maret, S., Bacmann, A., et al. 2010, *A&A*, 521, L52

Hirota, T., Maezawa, H., & Yamamoto, S. 2004, *ApJ*, 617, 399

Hirota, T., Ohishi, M., & Yamamoto, S. 2009, *ApJ*, 699, 585

Holdship, J., Rawlings, J., Viti, S., et al. 2019a, *ApJ*, 878, 65

Holdship, J., Viti, S., Codella, C., et al. 2019b, *ApJ*, 880, 138

Hollenbach, D. & Salpeter, E. 1970, *J. Chem. Phys.*, 53, 79

Hollenbach, D. & Salpeter, E. 1971, *ApJ*, 163, 155

Hsieh, T.-H., Hirano, N., Belloche, A., et al. 2019, *ApJ*, 871, 100

Hsu, S.-Y., Liu, S.-Y., Liu, T., et al. 2020, *ApJ*, 898, 107

- Huang, H.-C., Kuan, Y.-J., Charnley, S. B., et al. 2005, *Advances in Space Research*, 36, 146
- Huss, G. R., Meyer, B. S., Srinivasan, G., Goswami, J. N., & Sahijpal, S. 2009, *GeCoA*, 73, 4922
- Ida, S., Larwood, J., & Burkert, A. 2000, *ApJ*, 528, 351
- Imai, M., Sakai, N., Oya, Y., et al. 2016, *ApJ*, 830, L37
- Ivlev, A. V., Röcker, T. B., Vasyunin, A., & Caselli, P. 2015, *ApJ*, 805, 59
- Jaber Al-Edhari, A., Ceccarelli, C., Kahane, C., & Caux, E. 2014, *ApJ*, 791, 29
- Jaber Al-Edhari, A., Ceccarelli, C., Kahane, C., et al. 2017, *A&A*, 597, A40
- Jacobsen, S. K., Jørgensen, J. K., Di Francesco, J., et al. 2019, *A&A*, 629, A29
- Jensen, S. S., Jørgensen, J. K., Furuya, K., Haugbølle, T., & Aikawa, Y. 2021, *A&A*, 649, A66
- Jílková, L., Portegies Zwart, S., Pijloo, T., & Hammer, M. 2015, *MNRAS*, 453, 3157
- Jiménez-Serra, I., Vasyunin, A. I., Caselli, P., et al. 2016, *ApJ*, 830, L6
- Jin, . & Garrod, R. T. 2020, *ApJS*, 249, 26
- Johansen, A., blum, J., tanaka, H., et al. 2014, *Protostars and Planets VI*, Eds. H. beuther, R. S. Klessen, C. P. Dullemond, and T. Henning, University of Arizona Press, Tucson, 914 pp., p. 547
- Johansen, A. & Lambrechts, M. 2017, *AREPS*, 45, 359
- Johnston, K. G., Hoare, M. G., Beuther, H., et al. 2020, *ApJ*, 896, 35
- Johnstone, D. & Bally, J. 1999, *ApJ*, 510, L49
- Jones, A. P., Fanciullo, L., Köhler, M., et al. 2013, *A&A*, 558, A62
- Jones, A. P., Köhler, M., Ysard, N., Bocchio, M., & Verstraete, L. 2017, *A&A*, 602, A46
- Jones, T. J., Mergen, J., Odewahn, S., et al. 1994, *AJ*, 107, 2120
- Jørgensen, J. K., Bourke, T. L., Myers, P. C., et al. 2005, *ApJ*, 632, 973
- Jørgensen, J. K., Bourke, T. L., Nguyen, L. Q., & Takakuwa, S. 2011, *A&A*, 534, A100
- Jørgensen, J. K., Favre, C., Bisschop, S. E., et al. 2012, *ApJ*, 757, L4
- Jørgensen, J. K., van der Wiel, M. H. D., Coutens, A., et al. 2016, *A&A*, 595, A117
- Jørgensen, J. K., van Dishoeck, E. F., Visser, R., et al. 2009, *A&A*, 507, 861
- Kahane, C., Ceccarelli, C., Faure, A., & Caux, E. 2013, *ApJ*, 763, L38
- Kahane, C., Jaber Al-Edhari, A., Ceccarelli, C., et al. 2018, *ApJ*, 852, 130

Kaifu, N., Ohishi, M., Kawaguchi, K., et al. 2004, PASJ, 56, 69

Kainulainen, J., Stutz, A. M., Stanke, T., et al. 2017, A&A, 600, A141

Kalvans, J. 2021, ApJ, 910, 54

Kaur, T. & Sahijpal, S. 2019, MNRAS, 490, 1620

Kawamura, A., Mizuno, Y., Minamidani, T., et al. 2009, ApJS, 184, 1

Kenyon, S. J. & Bromley, B. C. 2004, Nature, 432, 598

Kim, J. S., Clarke, C. J., Fang, M., & Facchini, S. 2016, ApJ, 826, L15

Kirchhoff, W. H., Johnson, D. R., & Lovas, F. J. 1973, Journal of Physical and Chemical Reference Data, 2, 1

Kita, N. T., Huss, G. R., Tachibana, S., et al. 2005, ASPC, 341, 558

Kleiner, I., ovas, F. J., & Godefroid, M. 1996, Journal of Physical and Chemical Reference Data, 25, 1113

Kristensen, L. E. & Dunham, M. M. 2018, A&A, 618, A158

Kuan, Y.-J., Huang, H.-C., Charnley, S. B., et al. 2004, ApJ, 616, L27

Kurtz, S., Cesaroni, R., Churchwell, E., et al. 2000, Protostars and Planets IV, Eds V. Mannings, A. P. Boss, S. S. Russell, Tucson: University of Arizona Press, 299

Kutner, M. L., Evans, N. J. I., & Tucker, K. D. 1976, ApJ, 209, 452

Lada, C. J. 1987, IAUS, 115, 1

Lada, C. J. & Lada, E. A. 2003, ARA&A, 41, 57

Lada, C. J. & Wilking, B. A. 1984, ApJ, 287, 610

Lambrechts, M. & Johansen, A. 2012, A&A, 544, A32

Larson, R. B. 1969, MNRAS, 145, 271

Lattanzi, V., Bizzocchi, L., Vasyunin, A. I., et al. 2020, A&A, 633, A118

Le Roy, L., Altwegg, K., Balsiger, H., et al. 2015, A&A, 583, A1

Lee, C.-F., Lee, Z.-Y., Ho, P. T. P., et al. 2017, ApJ, 843, 27

Lee, C.-F., Codella, C., Li, Z.-Y., & Liu, S.-Y. 2019, ApJ, 876, 63

Lee, J.-E., Lee, S., Baek, G., et al. 2019, NatAs, 3, 314

Lefloch, B., Bachiller, R., Ceccarelli, C., et al. 2018, MNRAS, 477, 4792

Lefloch, B., Ceccarelli, C., Codella, C., et al. 2017, MNRAS, 469, L73

Leger, A., Jura, M., & Ormont, A. 1985, A&A, 144, 147

Lesaffre, P., Pineau des Forêts, G., Godard, B., et al. 2013, *A&A*, 550, A106

Leurini, S., Parise, B., Schilke, P., Pety, J., & Rolffs, R. 2010, *A&A*, 511, A82

Li, G. & Adams, F. C. 2015, *MNRAS*, 448, 344

Ligterink, N. F. W., Calcutt, H., Coutens, A., et al. 2018, *A&A*, 619, A28

Lindberg, J. E., Charnley, S. B., & Cordiner, M. A. 2016, *ApJL*, 833, L14

Linsky, J. L., Diplas, A., Wood, B. E., et al. 1995, *ApJ*, 451, 335

Lis, D. C., Serabyn, E., Keene, J., et al. 1998, *ApJ*, 509, 299

Lissauer, J. J. 1993, *ARA&A*, 31, 129

Loinard, L., Castets, A., Ceccarelli, C., et al. 2000, *A&A*, 359, 1169

Loinard, L., Chandler, C. J., Rodríguez, L. F., et al. 2007, *ApJ*, 670, 1353

Loinard, L., Rodríguez, L. F., D'Alessio, P., Wilner, D. J., & Ho, P. T. P. 2002, *ApJ*, 581, 109

Loomis, r. A., Burkhardt, A. M., Shingledecker, C. N., et al. 2021, *Nature Astronomy*, 5, 188

Loomis, R. A., Cleeves, L. I., Öberg, K. I., et al. 2018, *ApJ*, 859, 131

Looney, L. W., Mundy, L. G., & Welch, W. J. 2000, *ApJ*, 529, 477

Looney, L. W., Tobin, J. J., & Fields, B. D. 2006, *ApJ*, 652, 1755

López-Sepulcre, A., Balucani, N., Ceccarelli, C., et al. 2019, *ECS*, 3, 2122

López-Sepulcre, A., Jaber Al-Edhari, A., Mendoza, E., et al. 2015, *MNRAS*, 449, 2438

López-Sepulcre, A., Sakai, N., Neri, R., et al. 2017, *A&A*, 606, A121

Lugaro, M., Ott, U., & Kereszturi, A. 2018, *Progress in Particle and Nuclear Physics*, 102, 1

Múnoz Caro, G. M., Meierhenrich, U. J., Schutte, W. A., et al. 2002, *Nature*, 416, 403

Macías, E., Anglada, G., Osorio, M., et al. 2016, *ApJ*, 829, 1

Manigand, S., Calcutt, H., Jørgensen, J. K., et al. 2019, *A&A*, 632, A69

Manigand, S., Coutens, A., Loison, J.-C., et al. 2021, *A&A*, 645, A53

Manigand, S., Jørgensen, J. K., Calcutt, H., et al. 2020, *A&A*, 635, A48

Mann, R. K., Di Francesco, J., Johnstone, D., et al. 2014, *ApJ*, 784, 82

Marcelino, N., Brüken, S., Cernicharo, J., et al. 2010, *A&A*, 516, A105

Marcelino, N., Gerin, M., Cernicharo, J., et al. 2018, *A&A*, 620, A80

Maret, S., Ceccarelli, C., Caux, E., et al. 2004, *A&A*, 416, 577

Markwick, A. J., Millar, T. J., & Charnley, S. B. 2000, *ApJ*, 535, 256

Martín, S., Mangum, J. G., Harada, N., et al. 2021, *A&A*, in press, arXiv: 2019.08638

Martín, S., Martín-Pintado, J., & Mauersberger, R. 2006, *A&A*, 450, L13

Martín-Doménech, R., Bergner, J. B., Öberg, K. I., & Jørgensen, J. K. 2019, *ApJ*, 880, 130

Martín-Doménech, R., Bergner, J. B., Öberg, K. I., et al. 2021, *ApJ*, in press, arXiv: 2109.11512

Masunaga, H., Miyama, S. M., & Inutsuka, S.-i. 1998, *ApJ*, 495, 346

Mathis, J. S., Rumpl, W., & Nordsieck, K. H. 1977, *ApJ*, 217, 425

Matsumoto, T. & Hanawa, T. 2011, *ApJ*, 728, 47

Matsushita, Y., Takahashi, S., Machida, M. N., & Tomisaka, K. 2019, *ApJ*, 871, 221

Maureira, M. J., Pineda, J. E., Segura-Cox, D. M., et al. 2020, *ApJ*, 897, 59

Maury, A. J., André, P., Hennebelle, P., et al. 2010, *A&A*, 512, A40

May, P. W., Pineau des Forêts, G., Flower, D. R., et al. 2000, *MNRAS*, 318, 809

McCaughrean, M. J. & O'dell, C. R. 1996, *AJ*, 111, 1977

McGuire, B. A. 2018, *ApJS*, 239, 17

McGuire, B. A. 2021, *ApJS*, in press, arXiv: 2109.13848

Megeath, S. T., Gutermuth, R., Muzerolle, J., et al. 2012, *AJ*, 144, 192

Meidt, S. E., Hugues, A., Dobbs, C. L., et al. 2015, *ApJ*, 806, 72

Melosso, M., Bizzocchi, L., Sipilä, O., et al. 2020, *A&A*, 641, A153

Mendoza, E., Lefloch, B., López-Sepulcre, A., et al. 2014, *MNRAS*, 445, 151

Mennella, V., Brucato, J. R., Colangeli, L., et al. 1998, *ApJ*, 496, 1058

Meyer, B. S. & Clayton, D. D. 2000, *Space Science Reviews*, 92, 133

Mezger, P. G., Wink, J. E., & Zylka, R. 1990, *A&A*, 228, 95

Millar, T. J., Herbst, E., & Charnley, S. B. 1991, *ApJ*, 369, 147

Mininni, C., Beltrán, M. T., Rivilla, V. M., et al. 2020, *A&A*, 644, A84

Minissale, M., Dulieu, F., Cazaux, S., & Hocuk, S. 2016, *A&A*, 585, A24

Mitchell, T. R. & Stewart, G. R. 2011, *AJ*, 142, 168

- Miyake, K. & Nakagawa, Y. 1993, *Icarus*, 106, 20
- Montmerle, T., Augereau, J.-C., Chaudisson, M., et al. 2006, *AM&P*, 98, 39
- Mookerjea, B., Hassel, G. E., Gerin, M., et al. 2012, *A&A*, 546, A75
- Morbidelli, A. & Levison, H. F. 2004, *AJ*, 128, 2564
- Motte, F., Bontemps, S., & Louvet, F. 2018, *ARA&A*, 56, 41
- Müller, H. S. P., Schlöder, F., Stutzki, J., et al. 2005, *IAUS*, 235P, 62
- Muller, S., Beelen, A., Black, J. H., et al. 2013, *A&A*, 551, A109
- Muller, S., Beelen, A., Guélin, M., & othets. 2011, *A&A*, 535, A103
- Mundy, L. G., Wootten, A., Wilking, B. A., Blake, G. A., & Sargent, A. I. 1992, *ApJ*, 385, 306
- Murillo, N. M., Lai, S.-P., Bruderer, S., Harsono, D., & van Dishoeck, E. F. 2013, *A&A*, 560, A103
- Myers, P. C. & Benson, P. J. 1983, *ApJ*, 266, 309
- Myers, P. C., Fuller, G. A., Mathieu, R. D., et al. 1987, *ApJ*, 319, 340
- Myers, P. C. & Ladd, E. F. 1993, *ApJ*, 413, L47
- Nagy, Z., Menechella, A., Megeath, S. T., et al. 2020, *A&A*, 642, A137
- Nakajima, T., Takano, S., Kohno, K., Harada, N., & Herbst, E. 2018, *PASJ*, 70, 21
- Nguyen-Luong, Q., Motte, F., Carlhoff, P., et al. 2013, *ApJ*, 775, 88
- Nicholson, R. B. & Parker, R. J. 2017, *MNRAS*, 464, 4318
- Nielbock, M., Chini, R., & Müller, S. A. H. 2003, *A&A*, 408, 245
- Nyquist, H. 1928, *Transactions of the American Institute of Electrical Enginneers*, 47, 617
- Öberg, K. I., Bottinelli, S., Jørgensen, J. K., & van Dishoeck, E. F. 2010, *ApJ*, 716, 825
- Öberg, K. I., Garrod, R. T., van Dishoeck, E. F., & Linnartz, H. 2009c, *A&A*, 504, 891
- Öberg, K. I., Guzmán, V. V., Furuya, K., et al. 2015, *Nature*, 520, 198
- Öberg, K. I., Guzmán, V. V., Merchantz, C. J., et al. 2017, *ApJ*, 839, 43
- Öberg, K. I., Lauck, T., & Graninger, D. 2014, *ApJ*, 788, 68
- Öberg, K. I., Linnartz, H., Visser, R., & van Dishoeck, E. F. 2009b, *ApJ*, 693, 1209
- Öberg, K. I., van der Marel, N., Kristensen, L. E., & van Dishoeck, E. F. 2011, *ApJ*, 740, 14

Öberg, K. I., van Dishoeck, E. f., & Linnartz, H. 2009a, A&A, 496, 281

Occhiogrosso, A., Viti, S., Modica, P., & Palumbo, M. E. 2011, MNRAS, 418, 1923

Ohashi, N., Saigo, K., Aso, Y., et al. 2014, ApJ, 796, 131

Okoda, Y., Oya, Y., Sakai, N., Watanabe, Y., & Yamamoto, S. 2020, ApJ, 900, 40

Olofsson, S. & Olofsson, G. 2009, A&A, 498, 455

Ormel, C. W. & Klahr, H. H. 2010, A&A, 520, A43

Ortiz-León, G. N., Loinard, L., Dzib, S. A., et al. 2018, ApJ, 869, L33

Osinski, G. R. nad Cockell, C. S., Pontefract, A., & Sapers, H. M. 2020, AsBio, 20, 1121

Ospina-Zamudio, J., Lefloch, B., Ceccarelli, C., et al. 2018, A&A, 618, A145

Ossenkopf, V. & Henning, T. 1994, A&A, 291, 943

Osterbrock, D. E. 1974, A Series of Books in Astronomy and Astrophysics, San Francisco: Freeman,

Owen, J. E., Scaife, A. M. M., & Ercolano, B. 2013, MNRAS, 434, 3378

Oya, Y., Sakai, N., López-Sepulcre, A., et al. 2016, ApJ, 824, 88

Oya, Y., Sakai, N., Sakai, T., et al. 2014, ApJ, 795, 152

Oya, Y., Sakai, N., Watanabe, Y., et al. 2017, ApJ, 837, 174

Pabst, C. H. M., Hacar, A., Goicoechea, J. R., et al. 2021, A&A, 651, A111

Panagia, N. & Felli, M. 1975, A&A, 39, 1

Pantaleone, S., Enrique-romero, J., Ceccarelli, C., et al. 2021, ApJ, 917, 49

Parise, B., Castets, A., Herbst, E., et al. 2004, A&A, 416, 159

Parise, B., Caux, E., Castets, A., et al. 2005, A&A, 431, 547

Parise, B., Ceccarelli, C., Tielens, A. G. G. M., et al. 2002, A&A, 393, L49

Parise, B., Ceccarelli, C., Tielens, A. G. G. M., et al. 2006, A&A, 453, 949

Parker, R. J., Church, R. P., Davies, M. B., & Meyer, M. R. 2014, MNRAS, 437, 946

Pascucci, I. & Gorti, U. andHollenbach, D. 2012, ApJ, 751, L42

Pech, G., Loinard, L., Chandler, C. J., et al. 2010, ApJ, 712, 1403

Pech, G., Loinard, L., Dzib, S. A., et al. 2016, ApJ, 818, 116

Pelupessy, F. I. & Portegies Zwart, S. 2012, MNRAS, 420, 1503

Persson, M. V., Jørgensen, J. K., Müller, H. S. P., et al. 2018, A&A, 610, A54

Peterson, D. E., Megeath, S. T., Luhman, K. L., et al. 2008, *ApJ*, 685, 313

Pety, J., Teyssier, D., Fosse, D., et al. 2005, *A&A*, 435, 885

Pfalzner, S. 2009, *A&A*, 498, L37

Pfalzner, S. 2013, *A&A*, 549, A82

Pfalzner, S., Bhandare, A., Vincke, K., & Lacerda, P. 2018, *ApJ*, 863, 45

Pfalzner, S., Davies, M. B., Gounelle, M., et al. 2015, *PhyS*, 90f8001P

Pfalzner, S. & Vincke, K. 2020, *ApJ*, 897, 60

Pfalzner, S., Vogel, P., Scharwächter, J., & Olczak, C. 2005, *A&A*, 437, 967

Pickett, H. M., Poynter, R. L., Cohen, E. A., et al. 1998, *JQSRT*, 60, 883

Pineau des Forêts, G., Roueff, E., Schilke, P., & Flower, D. R. 1993, *MNRAS*, 262, 915

Pizzarello, S., Krishnamurthy, R. V., Epstein, S., & Cronin, J. R. 1991, *GeCoA*, 55, 905

Podio, L., Codella, C., Gueth, F., et al. 2016, *A&A*, 593, L4

Podio, L., Tabone, B., Codella, C., et al. 2021, *A&A*, 648, A45

Porras, A., Christopher, M., Allen, L., et al. 2003, *AJ*, 126, 1916

Portegies Zwart, S. 2019, *A&A*, 622, A69

Portegies Zwart, S. F. 2009, *ApJ*, 696, L13

Portegies Zwart, S. F. 2016, *MNRAS*, 457, 313

Potapov, A., Sánchez-Monge, A., Schilke, P., et al. 2016, *A&A*, 594, 117

Pratap, P., Dickens, J. E., Snell, R. L., et al. 1997, *ApJ*, 486, 862

Punanova, A., Caselli, P., Feng, S., et al. 2018, *ApJ*, 855, 112

Qiu, J., Wang, J., Shi, Y., et al. 2018, *A&A*, 613, A3

Quénard, D., Jiménez-Serra, I., Viti, S., Hildship, J., & Coutens, A. 2018, *MNRAS*, 474, 2796

Rawlings, J. M. C., Williams, D. A., Viti, S., & Cecchi-Pestellini, C. 2013, *MNRAS*, 436, L59

Rayner, J., McLean, I., McCaughrean, M., & Aspin, C. 1989, *MNRAS*, 241, 469

Reipurth, B., Rodríguez, L. F., & Chini, R. 1999, *ApJ*, 118, 983

Remijan, A. J. & Hollis, J. M. 2006, *ApJ*, 640, 842

Requena-Torres, M. A., Martín-Pintado, J., Rodríguez-Franco, A., et al. 2006, *A&A*, 455, 971

- Rimola, A., Skouteris, D., & Balucani, N. a. o. 2018, ECS, 2, 720
- Rivilla, V. M., Drodovskaya, M. N., Altwegg, K., et al. 2020, MNRAS, 492, 1180
- Roberts, H. & Millar, T. J. 2007, A&A, 471, 849
- Rodriguez, L. F. 1994, Revista Mexicana de Astronomia y Astrofisica, 29, 69
- Rodriguez, L. F. 1997, Herbig-Haro Flows and the Birth of Stars, IAUS, 182, 83
- Rodriguez, L. F., Curiel, S., Moran, J. M., et al. 1989, ApJL, 386, 85
- Rodriguez, L. F., Marti, J., Canto, J., Moran, J. M., & Curiel, S. 1993, Revista Mexicana de Astronomia y Astrofisica, 25, 23
- Rosotti, G. P., Dale, J. E., de Juan Ovelar, M., et al. 2014, MNRAS, 441, 2094
- Roueff, E., Lis, d. C., van der Tak, F. F. F., Gerin, M., & Goldsmith, P. F. 2005, A&A, 438, 585
- Ruud, M., Loison, J. C., Hickson, K. M., et al. 2015, MNRAS, 447, 4004
- Rubin, R. H., Swenson Jr., G. W., Benson, R. C., Tigelaar, H. L., & Flygare, W. H. 1971, ApJ, 169, L39
- Rybak, M., Hodge, J. A., Vegetti, S., et al. 2020, MNRAS, 494, 5542
- Saigo, K. & Tomisaka, K. 2006, ApJ, 645, 381
- Sakai, N., Oya, Y., Higuchi, A. E., et al. 2017, MNRAS, 467, L76
- Sakai, N., Oya, Y., López-Sepulcre, A., et al. 2016, ApJ, 820, L34
- Sakai, N., Oya, Y., Sakai, T., et al. 2014b, ApJ, 791, L38
- Sakai, N., Sakai, T., Aikawa, Y., & Yamamoto, S. 2008c, ApJ, 675, L89
- Sakai, N., Sakai, T., Hirota, T., Burton, M., & Yamamoto, S. 2009a, ApJ, 697, 769
- Sakai, N., Sakai, T., Hirota, T., & Yamamoto, S. 2008a, ApJ, 672, 371
- Sakai, N., Sakai, T., Hirota, T., & Yamamoto, S. 2009b, ApJ, 702, 1025
- Sakai, N., Sakai, T., Hirota, T., & Yamamoto, S. 2010, ApJ, 722, 1633
- Sakai, N., Sakai, T., Hirota, T., et al. 2014a, Nature, 507, 78
- Sakai, N., Sakai, T., Osamura, Y., & Yamamoto, S. 2007, ApJ, 667, L65
- Sakai, N., Sakai, T., & Yamamoto, S. 2008b, ApJ, 673, L71
- Sakai, N. & Yamamoto, S. 2013, ChRv, 113, 8981
- Saladino, R., Botta, G., Pino, S., CCostanzo, G., & Di Mauro, E. 2012, ChemSocRev, 41, 5526

Saladino, R., CCarota, E., & Botta, G. 2016, OLEB

Saraceno, P., André, P., Ceccarelli, C., Griffin, M., & Molinari, S. 1996, A&A, 309, 827

Saul, M., Tothill, N. F. H., & Purcell, C. R. 2015, ApJ, 798, 36

Schilke, P., Benford, D. J., Hunter, T. R., Lis, D. C., & Phillips, T. G. 2001, ApJS, 132, 281

Schilke, P., Comito, C., Thorwirth, S., et al. 2006, A&A, 454, L41

Schilke, P., Groesbeck, T. D., Blake, G. A., & Phillips, T. G. 1997a, ApJS, 108, 301

Schilke, P., Walmsley, C. M., Pineau des Forêts, G., & Flower, D. R. 1997b, A&A, 321, 293

Schöier, F. L., Jørgensen, J. K., van Dishoeck, E. F., & Blake, G. A. 2004, A&A, 418, 185

Schwarz, K. R., Bergin, E. A., Cleeves, L. I., et al. 2016, ApJ, 823, 91

Scibelli, S. & Shirley, Y. 2020, ApJ, 891, 73

Scibelli, S., Shirley, Y., Vasyunin, A., & Launhardt, R. 2021, MNRAS, 504, 5754

Scourfield, M., Viti, S., García-Burillo, S., et al. 2020, MNRAS, 496, 5308

Scoville, N. Z. & Solomon, P. M. 1974, ApJ, 187, L67

Segura-Cox, D. M. aand Looney, L. W., Tobin, J. J., et al. 2018, ApJ, 866, 161

Sewilo, M., Indebetouw, R., Charnley, S. B., et al. 2018, ApJ, 853, L19

Shannon, R. J., Cossou, C., Loison, J.-C., et al. 2014, RSC Adv., 4, 26342

Shen, C. J., Greenberg, J. M., Scchutte, W. A., & van dishoeck, E. F. 2004, A&A, 415, 203

Shimajiri, Y., Takahashi, S., Takakuwa, S., Saito, M., & Kawabe, R. 2009, PASJ, 61, 1055

Shingledecker, C. N., Tennis, J., Le Gal, R., & Herbst, E. 2018, ApJ, 861, 20

Shirley, Y. L., Claussen, M. J., Bourke, T. L., Young, C. H., & Blake, G. A. 2007, ApJ, 667, 329

Shu, F. H. 1977, ApJ, 214, 488

Shu, F. H., Adams, F. C., & Lizano, S. 1987, ARA&A, 25, 23

Skouteris, D., Balucani, N., Ceccarelli, C., Faginas Lago, N., et al. 2019, MNRAS, 482, 3567

Skouteris, D., Balucani, N., Ceccarelli, C., et al. 2018, ApJ, 854, 135

Skouteris, D., Vazart, F., Ceccarelli, C., et al. 2017, MNRAS, 468, L1

Smith, N., Bally, J., & Morse, J. A. 2003, ApJ, 587, L105

Snyder, L. E., Buhl, D., Schwartz, P. R., et al. 1974, *ApJ*, 191, L79

Sobolev, V. V. 1960, *Moving envelopes of stars*. Cambridge: Harvard University Press

Soma, T., Sakai, N., Watanabe, Y., & Yamamoto, S. 2018, *ApJ*, 854, 116

Spezzano, S., Bizzocchi, L., Caselli, P., Harju, J., & Brünken, S. 2016, *A&A*, 592, L11

Spezzano, S., Caselli, P., Pineda, J. E., et al. 2020, *A&A*, 643, A60

Stark, R., Sandell, G., Beck, S. C., et al. 2004, *ApJ*, 608, 341

Strazzulla, G. & Palumbo, M. E. 2001, *Advances in Space Research*, 27, 237

Stutz, A. M., Tobin, J. J., Stanke, T., et al. 2013, *ApJ*, 767, 36

Suzuki, H., Yamamoto, S., Ohishi, M., et al. 1992, *ApJ*, 392, 551

Tafalla, M., Myers, P. C., Caselli, P., Walmsley, C. M., & Comito, C. 2002, *ApJ*, 569, 815

Tafalla, M., Myers, P. C., Mardones, D., & Bachiller, R. 2000, *A&A*, 359, 967

Tafalla, M., Santiago-García, J., Myers, P. C., et al. 2006, *A&A*, 455, 577

Takahashi, S., Saito, M., Ohashi, N., et al. 2008, *ApJ*, 688, 244

Tanabe, Y., Nakamura, F., Tsukagoshi, T., et al. 2019, *PASJ*, 71, 8

Taniguchi, K., Herbst, E., Majumdar, L., et al. 2021a, *ApJ*, 908, 100

Taniguchi, K., Majumdar, L., Takakuwa, S., et al. 2021b, *ApJ*, 910, 141

Taniguchi, K., Miyamoto, Y., Saito, M., et al. 2018a, *ApJ*, 866, 32

Taniguchi, K., Saito, M., Majumdar, L., et al. 2018b, *ApJ*, 866, 150

Taquet, V., Bianchi, E., Codella, C., et al. 2019, *A&A*, 632, A19

Taquet, V., Ceccarelli, C., & Kahane, C. 2012, *A&A*, 538, A42

Taquet, V., López-Sepulcre, A., Ceccarelli, C., et al. 2015, *ApJ*, 804, 81

Terebey, S., Chandler, C. J., & André, P. 1993, *ApJ*, 414, 759

Testi, L., Birnstiel, T., Ricci, L., et al. 2014, *Protostars and Planets VI*, H. Beuther, R. S. Klessen, C. P. Dullemond, and Th. Henning (eds.), 914, 339

Teyssier, D., Fossé, D., Gerin, M., et al. 2004, *A&A*, 417, 135

Tielens, A. G. G. M. 1983, *A&A*, 119, 177

Tielens, A. G. G. M. & Hagen, W. 1982, *A&A*, 114, 245

Tobin, J. J., Chandler, C. J., Wilner, D. J., et al. 2013, *ApJ*, 779, 93

Tobin, J. J., Hartmann, L., Chiang, H.-F., et al. 2012, *Nature*, 492, 83

Tobin, J. J., Looney, L. W., Li, Z. Y., et al. 2016a, *ApJ*, 818, 73

Tobin, J. J., Megeath, S. T., van't Hoff, M., et al. 2019, *ApJ*, 886, 6

Tobin, J. J., Sheehan, P. D., Megeath, S. T., et al. 2020, *ApJ*, 890, 130

Tobin, J. J., Stutz, A. M., Manoj, P., et al. 2016b, *ApJ*, 831, 36

Torres, R. M., Loinard, L., Mioduszewski, A. J., & Rodríguez, L. F. 2007, *ApJ*, 671, 1813

Trumpler, R. J. 1930, *PASP*, 42, 214

Tsuboi, Y., Koyama, K., Hamaguchi, K., et al. 2001, *ApJ*, 554, 734

Tychoniec, L., Tobin, J. J., Karska, A., et al. 2018, *ApJ*, 852, 18

Tychoniec, L., van Dishoeck, E. F., van 't Hoff, M. R. L., et al. 2021, Accepted for publication in *A&A*, in press, arXiv: 2107.03696

van der Tak, F. F. S., Schilke, P., Müller, H. S. P., et al. 2002, *A&A*, 388, L53

van Dishoeck, E. F. & Blake, G. A. 1998, *ARA&A*, 36, 317

van Dishoeck, E. F., Blake, G. A., Jansen, D. J., & Groesbeck, T. D. 1995, *ApJ*, 447, 760

van Gelder, M. L., Tabone, B., Tychoniec, L., et al. 2020, *A&A*, 639, A87

Vastel, C., Caselli, P., Ceccarelli, C., et al. 2006, *ApJ*, 645, 1198

Vastel, C., Ceccarelli, C., Caux, E., et al. 2010, *A&A*, 521, L31

Vastel, C., Ceccarelli, C., Lefloch, B., & Bachiller, R. 2014, *ApJL*, 795, L2

Vastel, C., Phillips, T. G., Ceccarelli, C., & Pearson, J. 2003, *ApJ*, 593, L97

Vastel, C., Phillips, T. G., & Yoshida, H. 2004, *ApJ*, 606, L127

Vastel, C., Quénard, D., Le Gal, R., et al. 2018, *MNRAS*, 478, 5514

Vasyunin, A. I., Caselli, P., Dulieu, F., & Jiménez-Serra, I. 2017, *ApJ*, 842, 33

Vasyunin, A. I. & Herbst, E. 2013, *ApJ*, 769, 34

Vazart, F., Ceccarelli, C., Balucani, N., Bianchi, E., & Skouteris, D. 2020, *MNRAS*, 499, 5547

Vicente, S. M. & Alves, J. 2005, *A&A*, 441, 195

Vidali, G. 2013, *Chem. Rev.*, 113, 8762

Vincke, K., Breslau, A., & Pfalzner, S. 2015, *A&A*, 577, A115

Visser, R., van Dishoeck, E. F., Doty, S. D., & Dullemond, C. P. 2009, *A&A*, 495, 881

Viti, S. 2017, *A&A*, 607, A118

- Viti, S., Collings, M. P., Dever, J. W., McCoustra, M. R. S., & Williams, D. A. 2004, *MNRAS*, 354, 1141
- Viti, S. & Williams, D. A. 1999, *MNRAS*, 305, 755
- Wadhwa, M., Amelin, Y., Davis, A. M., et al. 2007, *Protostars and Planets V*, Editions B. Reipurth, D. Jewitt, and K. Keil, University of Arizona Press, Tucson, 951, 835
- Wadhwa, M. & Russel, S. S. 2000, *Protostars and Planets IV*, eds. V. Mannings, A. P. Boss, S. S. Russel, University of Arizona Press, Tucson, p. 995
- Wakelam, V., Castets, A., Ceccarelli, C., et al. 2004, *A&A*, 413, 609
- Wakelam, V., Dartois, E., Chabot, M., et al. 2021, *A&A*, 652, A63
- Wakelam, V., E. B., Cazaux, S., et al. 2017, *MolAs*, 9, 1
- Walsh, C., Loomis, R. A., Öberg, K. I., et al. 2016, *ApJ*, 823, L10
- Walsh, C., Millar, T. J., Nomura, H., et al. 2014, *A&A*, 563, A33
- Wang, Y., Chang, Q., & Wang, H. 2019, *A&A*, 622, A185
- Ward-Thompson, D., Motte, F., & André, P. 1999, *MNRAS*, 305, 143
- Watanabe, Y., Nishimura, Y., Sorai, K., et al. 2019, *ApJS*, 242, 26
- Watson, W. D. 1976, *Reviews of Modern Physics*, 48, 513
- Wielen, R., Fuchs, B., & Dettbarn, C. 1996, *A&A*, 314, 438
- Wilking, B. A., Lada, C. J., & Young, E. T. 1989, *ApJ*, 340, 823
- Williams, J. P. & Cieza, L. A. 2011, *ARA&A*, 49, 67
- Williams, J. P. & Gaidos, E. 2007, *ApJ*, 663, L33
- Williams, J. P., Plambeck, R. L., & Heyer, M. H. 2003, *ApJ*, 591, 1025
- Winter, A. J., Clarke, C. J., Rosotti, G., et al. 2018, *MNRAS*, 478, 2700
- Winter, A. J., Kruijssen, J. M. D., Chevance, M., Keller, B. W., & Longmore, S. N. 2020a, *MNRAS*, 491, 903
- Winter, A. J., Kruijssen, J. M. D., Longmore, S. N., & Chevance, M. 2020b, *Nature*, 586, 528
- Wong, Y. H. V., Hirashita, H., & Li, Z. Y. 2016, *PASJ*, 68, 67
- Wootten, A. 1989, *ApJ*, 337, 858
- Wright, N. J., Drake, J. J., Drew, J. E., et al. 2012, *ApJ*, 746, L21
- Wu, Y., Liu, X., Chen, X., et al. 2019, *MNRAS*, 488, 495
- Wyatt, M. C., Panić, O., Kennedy, G. M., & Matrá, L. 2015, *Ap&SS*, 357, 103

- Xu, L.-H., Fischer, J., Lees, R. M., et al. 2008, *J. Mol. Spectrosc.* 251, 305
- Yagoubov, P., Mroczowski, T., Belitsky, V., et al. 2020, *A&A*, 634, A46
- Yamamoto, S. 2017, *Introduction to Astrochemistry: Chemical Evolution from Interstellar Clouds to Star and Planet Formation*, *Astronomy and Astrophysics Library* (Springer)
- Yang, Y.-L., Evans, N. J. I., Smith, A., et al. 2020, *ApJ*, 891, 61
- Yang, Y.-L., Green, J. D., Evans, N. J. I., et al. 2018, *ApJ*, 860, 174
- Yang, Y.-L., Sakai, N., Zhang, Y., et al. 2021, *ApJ*, 910, 20
- Yen, H.-W., Koch, P. M., Takakuwa, S., et al. 2017, *ApJ*, 834, 178
- Yoshida, K., Sakai, N., Nishimura, Y., et al. 2019, *PASJ*, 71, 18
- Young, E. D. 2014, *E&PSL*, 392, 16
- Ysard, N., Koehler, M., Jimenez-Serra, I., Jones, A. P., & Verstraete, L. 2019, *A&A*, 631, A88
- Yu, K. C., Bally, J., & Devine, D. 1997, *ApJ*, 485, L45
- Yu, K. C., Billawala, Y., Smith, M. D., Bally, J., & Butner, H. M. 2000, *AJ*, 120, 1974
- Zhang, C., Wu, Y., Liu, X. C., et al. 2021, *A&A*, 648, A83
- Zhang, Y., Higuchi, A. E., Sakai, N., et al. 2018, *ApJ*, 864, 76
- Zhou, Y., Quan, D.-H., Zhang, X., & Qin, S.-L. 2020, *RAA*, 20, 125

List of Figures

1	Formation Steps of a Solar-like planetary system	2
2	Scheme of the three main steps for molecular deuteration	4
3	iCOMs abundances with respect to methanol in a hot corino compared to that of comets	7
4	All-sky view of the Milky Way by the Gaia satellite	9
5	Dust interstellar reddening process	9
6	Average Spectral Energy Distribution of the ISM in the Milky Way	10
7	Spectral Classification of embedded young stellar objects	11
8	Spectral Energy Distribution of VLA 1623 and SM1	13
9	Typical Class 0/I envelope structure	14
10	Scheme of a hot corino structure.	15
11	IRAS 16293-2422 continuum image	18
12	The two paradigms of the iCOMS formations	19
13	Scheme of a WCCC object structure.	22
14	CCH and C ₄ H intensity maps	23
15	Carbon chain formation in a WCCC zone	24
16	Hot corino versus WCCC spectra	25
17	Intensity maps of CCCH, NH ₂ CHO, and HCOOCH ₃ in B335 and L483	26
18	Formation of WCCC source versus hot corino depending on the pre-stellar core phase timescale	28
19	Effect of UV illumination on pre-stellar cores	30
20	Scheme of the Sun's birth environment	33
21	The location of the OMC-2/3 filament	34
22	Overview of the OMC-2/3 stellar content	36
23	ERC DOC proposal extract	38
1.1	Schematic view of the electromagnetic radiation absorption by the Earth's atmosphere	42
1.2	Scheme of a single-dish telescope	44
1.3	Scheme of the conversion of the sky frequency into an intermediate frequency by a mixer	44
1.4	Scheme of the beam power pattern	46
1.5	The IRAM-30m telescope	48
1.6	The IRAM-30m atmospheric transmissions	49
1.7	The Nobeyama-45m single-dish telescope	50

1.8	Schematic diagram of the Nobeyama-45m single-dish telescope	51
1.9	Scheme of a 2-element interferometer	52
1.10	Scheme of the coordinate system used to project the baseline plane onto the sky plane	53
1.11	Examples of Fourier transforms on different functions	54
1.12	ALMA, NOEMA and JVLA radio interferometers. Image credits: NRAO for ALMA and JVLA and IRAM for NOEMA.	56
1.13	Scheme explaining the radiative transfer problem	59
1.14	Example of a rotational diagram	66
1.15	Scheme illustrating the LVG method	67
3.1	CSO33-b, FIR6c-a, FIR1a, and MMS9-a CCH maps	150
3.2	MMS5, MMS2, CSO3-b , and SIMBA-a maps	151
3.3	FIR2 CCH and c-C ₃ H ₂ maps	152
4.1	ALMA view of the FIR6c-a outflow	155
4.2	Model predictions from Codella et al. (2017)	156
4.3	Protostellar outflows and shocks in which iCOMs have been detected and studied using the method from Codella et al. (2017)	157
4.4	NOEMA view of the FIR6c-a outflow	162
4.5	Spatial distribution of acetaldehyde and formamide in L1157-B1 and FIR6c-a	163
4.6	C ¹⁸ O and NH ₂ D emission maps	164
5.1	Galactic distribution of massive clumps	172

List of Tables

1	List of detected or potentially detected hot corinos, their classification and location. Hybrid sources (see Sec. 3.4.1) are shown in <i>italic</i>	16
2	List of detected WCCC objects, their classification and location. Hybrids (see Sec. 3.4.1) are shown in <i>italic</i>	20
3	Characteristics of hot corinos and WCCC sources	24
1.1	EMIR and HERA available backends	49
1.2	Some characteristics of NOEMA, ALMA and JVLA.	58
4.1	Targeted species with associated targeted lines	158
4.2	List of detected iCOMs towards the FIR6c-a outflow, and their spectral parameters	160

Résumé Français

Introduction

Depuis la nuit des temps, une question demeure : D'où vient la vie ? Aussi philosophique que puisse être cette question, de nombreuses théories scientifiques existent. En effet, cette question concerne de nombreux domaines : exobiologie, biochimie, astronomie, paléontologie, parmi tant d'autres. De plus, on n'est pas toujours d'accord sur le lieu et le moment où l'histoire a pu commencer : est-ce sur Terre il y a 3,5 milliards d'années avec les cyanobactéries ? Ou bien est-ce bien avant dans l'espace ? Le débat reste ouvert. Je présente ici un morceau de l'histoire du point de vue d'une astrochimiste.

L'histoire de notre système solaire a commencé il y a 4,5 milliards d'années dans un amas de nuages moléculaires, dans le bras spiral d'Orion de la Voie lactée. Comme toute autre étoile de masse solaire, notre Soleil a connu plusieurs phases différentes avant d'atteindre le stade de système planétaire final que nous connaissons aujourd'hui. Les questions centrales en astronomie sont 1) qu'est-ce qui est arrivé aux premières phases de la formation du système solaire et 2) comment ont-elles pu influencer le développement précoce de la chimie organique, et peut-être l'apparition de la vie sur Terre. Un saut dans le passé est nécessaire pour répondre à ces questions. Pour ce faire, nous pouvons rechercher d'autres systèmes planétaires naissants de type solaire et chercher à comprendre ce qui s'y passe. La chimie est un outil puissant et fondamental utilisé dans cette thèse pour fournir une partie des réponses.

Les étoiles de type solaire peuvent se former dans différents types de régions de formation d'étoiles, bien que le processus global de leur formation soit à peu près le même et indépendant de leur environnement de naissance. Leur lieu de naissance est situé dans les nuages interstellaires, composés de gaz et de grains de poussière, et donc où la chimie peut se produire à la fois dans la phase gazeuse et sur les surfaces glacées des grains de poussière. Au cours de la formation des étoiles de type solaire, les molécules qui se forment deviennent de plus en plus complexes (Caselli & Ceccarelli 2012; Yamamoto 2017). Les molécules contenant du C avec au moins six atomes sont appelées molécules organiques complexes interstellaires (iCOMs ; Herbst & van Dishoeck (2009); Ceccarelli et al. (2017)) et pourraient être essentielles pour former des molécules pré-biotiques, elles-mêmes importantes pour façonner les briques de la vie. La littérature évoque la possibilité que les iCOMs aient joué un rôle important dans l'apparition de la vie sur Terre en étant préservés et retravaillés durant les différentes étapes de la formation de notre système solaire avant d'être finalement libérés sur Terre par des impacts de comètes et d'astéroïdes.

I.1 La phase du noyau pré-stellaire : Une ère glacée

La phase de noyau pré-stellaire correspond au début de la formation des étoiles et commence au sein des nuages moléculaires (Benson & Myers 1989; Bergin et al. 2007). Durant cette phase, des fragments de nuages denses ($n > 10^4 \text{ cm}^{-3}$; André et al. (1996); Ward-Thompson et al. (1999)) et froids ($T \approx 10 \text{ K}$) avec des tailles typiques de 0.1 pc ($\approx 2000 \text{ au}$; Myers & Benson (1983); Benson & Myers (1989)) se contractent lentement en raison de l'interaction entre la force gravitationnelle, le champ magnétique, la pression thermique et la turbulence (Shu 1977; Shu et al. 1987; Hennebelle & Fromang 2008). Ces fragments sont appelés noyaux pré-stellaires (PSC). La durée de cette phase est de $\approx 10^6$ ans (Beichman et al. 1986).

Les températures étant basses, les atomes (par exemple C, O, N) et les molécules (par exemple CO, CS, N_2 , H_2O , HCN, HCO) se figent à la surface des grains de poussière, formant des manteaux de grains glacés (par ex. Tielens & Hagen 1982; Hasegawa et al. 1992; Caselli et al. 1999; Bacmann et al. 2002; Bergin et al. 2002; Tafalla et al. 2002, 2006). Ces molécules subissent des processus d'hydrogénation qui conduisent à la production de glaces H_2O principalement, ainsi que de petites quantités de glaces de méthanol (CH_3OH), de formaldéhyde (H_2CO), d'ammoniac (NH_3), de méthane (CH_4) et de dioxyde de carbone (CO_2) (Tielens & Hagen 1982, Boogert et al. 2015 et leurs références). Sous l'effet de processus de désorption non thermiques et d'une irradiation UV (photodésorption), les petites molécules peuvent se désorber dans la phase gazeuse des nuages moléculaires (par ex. Leger et al. 1985; Shen et al. 2004; Öberg et al. 2009a,b; Ivlev et al. 2015; Wakelam et al. 2021) où elles sont détectées (par exemple, CO, CS, C_2H , H_2O , HNC, HNCO; (par ex. Pratap et al. 1997; Marcelino et al. 2010; Caselli et al. 2012)). De manière inattendue, ce ne sont pas seulement de petites molécules qui sont détectées dans la phase gazeuse de tels environnements, mais aussi des molécules plus complexes comme les iCOMs (par exemple CH_3OH , HCOOCH_3 , CH_3OCH_3 ; (par ex. Öberg et al. 2010; Bacmann et al. 2012; Cernicharo et al. 2012; Vastel et al. 2014; Jiménez-Serra et al. 2016; Punanova et al. 2018; Scibelli & Shirley 2020; Harju et al. 2020), qui sont censées se former à une température plus élevée ($>20 \text{ K}$) où d'autres réactions de surface des grains que l'hydrogénation peuvent se produire. La présence de telles molécules, leur formation et leurs voies de destruction sont encore une source de débat : (par ex. Vasyunin & Herbst 2013; Balucani et al. 2015; Jin & Garrod 2020).

Enfin, le fractionnement du deutérium est un processus important qui a lieu dans l'environnement froid des noyaux pré-stellaires. Des niveaux élevés de fractionnement du deutérium ont été mesurés vers les noyaux denses : (par ex. Gerin et al. 1987; Bacmann et al. 2002, 2003; Caselli et al. 2003; Roueff et al. 2005; Caselli et al. 2008). En phase gazeuse, les ions H_3^+ réagissent avec les espèces HD conduisant à la production de H_2D^+ et de H_2 (Watson 1976). Le rapport d'abondance $\text{H}_2\text{D}^+/\text{H}_3^+$ est alors supérieur à l'abondance de l'élément D par rapport à H de $1,5 \times 10^{-5}$ (Linsky et al. 1995). Lorsque la congélation des espèces est suffisamment importante, et en particulier celle du CO et de l'oxygène, les deux principales espèces destructrices de H_2D^+ , le fractionnement du deutérium est renforcé (Dalgarno & Lepp 1984; Caselli et al. 1998). Un rapport D/H important dans la phase gazeuse conduit à une deutération efficace des espèces de surface (par ex. Tielens 1983; Charnley et al. 1997; Caselli et al. 2002; Taquet et al. 2012). Plusieurs molécules singulièrement, doublement et triplement deutérées ont en effet été observées dans les noyaux pré-stellaires (par ex. Ceccarelli et al. 2002; Bacmann et al. 2003; Vastel et al. 2004, 2006, 2018; Roueff et al. 2005).

I.2 La phase du noyau proto-stellaire: la complexité moléculaire dans toute sa splendeur

Lorsque la force gravitationnelle prend le dessus, l'effondrement gravitationnel commence et la phase proto-stellaire débute (Shu et al. 1987). L'énergie gravitationnelle sous forme de rayonnement chauffe la partie centrale jusqu'à 3000 K. Pendant cette phase, la plupart de l'enveloppe est accrétée, et dure $\sim 0.5\text{Myr}$ (Evans et al. 2009). Deux classes différentes de proto-étoiles sont définies : Les proto-étoiles de classe 0 et les proto-étoiles de classe I basées sur le rapport $L_{\text{smm}}/L_{\text{bol}}$ (André et al. 1993).

Les proto-étoiles de classe 0 Les proto-étoiles de classe 0 sont les proto-étoiles les plus jeunes et représentent la phase d'accrétion principale (précoce). Les proto-étoiles de classe 0 sont encore très encastrées dans le nuage moléculaire, et leur émission continue est dominée par les grains de poussière de l'enveloppe qui réémettent un rayonnement dans le domaine millimétrique et (sub)-millimétrique (André et al. 1993; André & Montmerle 1994). Pendant cette phase d'accrétion, des jets et des écoulements bipolaires puissants et fortement collimatés sont présents et propulsent de la matière dans le milieu interstellaire (e.g. Bontemps et al. 1996; Bachiller 1996). La présence d'un disque circumstellaire a déjà été établie dans plusieurs sources de classe 0 (e.g. Jørgensen et al. 2009; Tobin et al. 2012; Murillo et al. 2013; Ohashi et al. 2014; Codella et al. 2014; Tobin et al. 2016a; Yen et al. 2017; Oya et al. 2016, 2017; Gerin et al. 2017; Sakai et al. 2017; Segura-Cox et al. 2018; Hsieh et al. 2019; Tobin et al. 2020).

Les proto-étoiles de classe I Les proto-étoiles de classe I sont des proto-étoiles de classe 0 évoluées. La masse de l'objet protostellaire devient plus grande que la masse de l'enveloppe lorsque cette dernière s'accrète sur l'objet central (Dunham et al. 2014) : c'est la phase d'accrétion tardive. Les proto-étoiles de classe I sont encore associées à du gaz moléculaire dense (Myers et al. 1987). Elles présentent un disque et une enveloppe circumstellaire. Les proto-étoiles de classe I présentent des écoulements de CO moins puissants et moins collimatés que les proto-étoiles de classe 0 (Bontemps et al. 1996; Saraceno et al. 1996).

Pendant le réchauffement de la phase protostellaire, après avoir atteint une température de 10 à 20-30 K dans l'enveloppe, les manteaux de glace mixte se subliment avec un peu de monoxyde de carbone (CO), de CH_4 et d'azote (N_2). Les radicaux plus lourds comme le radical formyle (HCO) et le radical méthyle (CH_3), entre autres, acquièrent une mobilité à la surface des grains, ce qui conduit à la formation de molécules plus complexes (par exemple, l'acétaldéhyde : CH_3CHO) même si des études récentes remettent en cause cette théorie : (par ex. Enrique-Romero et al. 2019, 2020). Ensuite, lorsque la température est suffisamment élevée pour que le manteau se sublime ($T \geq 100\text{K}$), les molécules complexes précédemment piégées dans les glaces sont libérées dans la phase gazeuse où se produit la formation de molécules encore plus complexes par des réactions avec le gaz de l'enveloppe des protoétoiles (par ex. Skouteris et al. (2018); López-Sepulcre et al. (2019); Vazart et al. (2020)). De plus, les écoulements et les jets qui accompagnent l'effondrement éjectent de la matière dans l'ISM. Les chocs entre les écoulements/jets et le nuage moléculaire quiescent environnant produisent la pulvérisation de grains, et les molécules piégées dans les glaces sont libérées, permettant aux réactions en phase gazeuse de se produire et pouvant conduire à la formation d'iCOMs. Une poignée de molécules complexes est

trouvée dans les écoulements (par ex. [Codella et al. 2010](#); [Lefloch et al. 2017](#); [Codella et al. 2017](#); ?). L'étape protostellaire est donc connu pour être particulièrement enrichi chimiquement.

I.3 La phase du disque protoplanétaire : Jouer à cache-cache

Une fois que l'enveloppe autour de la proto-étoile est presque entièrement accrétée ou dissipée en raison des écoulements qui sont présents pendant la phase protostellaire, il ne reste qu'un disque circumstellaire (ou disque protoplanétaire) autour des proto-étoiles. La durée de vie de la phase protoplanétaire est d'environ $(2-3) \cdot 10^6$ ans (par ex. [Evans et al. 2009](#); [Williams & Cieza 2011](#)). La phase du disque protoplanétaire commence et les proto-étoiles sont des protoétoiles de classe II et de classe III, également appelées étoiles de la séquence pré-principale (PMS) (respectivement des étoiles T Tauri classiques et Tauri faibles). De la phase de la classe II à la phase de la classe III, le disque circumstellaire riche en gaz et accrétant des matériaux devient un disque évolué pauvre en gaz. Les disques de classe III sont appelés disques de débris (par ex. [Williams & Cieza 2011](#); [Dunham et al. 2014](#); [Wyatt et al. 2015](#)). On pense que la formation des planètes a lieu à l'intérieur des disques protoplanétaires, par des processus d'accrétion de grains de poussière (e.g. [Lissauer 1993](#); [Montmerle et al. 2006](#); [Ormel & Klahr 2010](#); [Lambrechts & Johansen 2012](#); [Johansen et al. 2014](#); [Johansen & Lambrechts 2017](#); [Coleman 2021](#)), formant des structures plus grandes appelées planétésimaux.

Pendant cette étape, de nouvelles molécules complexes peuvent être formées dans les régions chaudes du disque, près de l'objet central, tandis que dans les régions froides du disque, les molécules formées pendant la phase précédente se figent à nouveau sur les manteaux de grains. Environ 25 espèces ont été détectées dans les disques ([McGuire 2018, 2021](#)), parmi lesquelles seules quelques molécules porteuses de l'atome d'O, définies comme point de départ vers la complexité moléculaire, ont été détectées dans la phase gazeuse des disques protoplanétaires (CH_3OH , H_2CO et HCOOH ; par ex.: [Dutrey et al. \(1997\)](#); [Walsh et al. \(2016\)](#); [Öberg et al. \(2017\)](#); [Bergner et al. \(2018\)](#); [Favre et al. \(2018\)](#); [Loomis et al. \(2018\)](#); [Lee et al. \(2019\)](#); [Booth et al. \(2021\)](#)). Cette absence de détection des iCOMs est due au fait qu'ils sont beaucoup plus difficiles à observer car ils sont censés être gelés sur des grains de poussière dans le disque. En effet, les molécules doivent être dans la phase gazeuse afin d'être observables et identifiées par des télescopes (sub)-millimétriques par exemple. De plus, compte tenu des petites tailles angulaires des disques (\leq quelques arcsecs) et de l'émission relativement faible des iCOMs, une haute résolution angulaire et une haute sensibilité sont nécessaires pour les détecter (e.g. [Walsh et al. \(2014\)](#)). On pense qu'une quantité substantielle du réservoir de carbone est stockée dans les espèces organiques et en particulier dans les espèces complexes ([Favre et al. 2013](#); [Schwarz et al. 2016](#)). Au cours du processus de formation des planétésimaux, les manteaux de grains représentant une partie de notre héritage chimique sont "vraisemblablement préservés" jusqu'à la phase suivante ([Caselli & Ceccarelli 2012](#)).

I.4 Le système planétaire: Le terrain de jeu de la vie ?

Une fois que les planétésimaux ont nettoyé leur orbite, les planètes se forment et la formation du système planétaire est terminée. Le processus de formation des planètes a laissé quelques résidus, de petits corps appelés comètes et astéroïdes. Ces résidus sont

généralement recouverts de glaces dans lesquelles des molécules complexes, héritées des phases précédentes, sont probablement piégées. Ces molécules complexes ont-elles été livrées à la Terre ? Si oui, comment ? Des événements d'impact de météorites "tombant en pluie" sur la Terre, auraient pu éventuellement livrer l'héritage chimique préservé des phases précédentes, et ainsi contribuer à l'apparition de la vie sur Terre quelques centaines de millions d'années plus tard : (par ex. [Alwegg et al. 2019](#); [Osinski et al. 2020](#), et les références qui y figurent). Aucun consensus clair n'existe aujourd'hui.

I.5 L'héritage chimique : Un possible fil d'Ariane ?

La question de notre héritage chimique est toujours ouverte et sans réponse. Nous devons prouver qu'il existe un lien chimique entre les phases les plus anciennes et les plus récentes de la formation de notre système solaire. Une façon de le faire est de comparer les abondances chimiques, les niveaux de deutération de l'eau et d'autres espèces par exemple entre les phases pré- et proto- stellaires avec ce que l'on trouve dans les comètes (par ex. [Busquet et al. 2010](#); [Ceccarelli et al. 2014b](#); [Cleeves et al. 2016](#)). Le fractionnement isotopique et la deutération montrent que le système solaire a hérité du matériel moléculaire de la phase du noyau pré-stellaire (par exemple, l'eau ; [Visser et al. 2009](#); [Cleeves et al. 2014](#); [Jensen et al. 2021](#)). En particulier, les molécules organiques complexes sont ciblées puisque des espèces telles que le formamide se sont avérées être la base de la synthèse de molécules pré-biotiques (par exemple, les acides aminés) dans des versions des expériences d'Urey-Miller ([Saladino et al. 2012, 2016](#)).

Plusieurs études ont visé à comparer le contenu chimique des différentes phases de la formation d'un système planétaire ([Öberg et al. 2015](#); [Drozdovskaya et al. 2018](#); ?; [Rivilla et al. 2020](#)). En particulier, [Drozdovskaya et al. \(2019\)](#) comparent les abondances relatives observées de plusieurs espèces (par exemple les molécules porteuses de CHO-, N-, S-) entre le disque protostellaire de la proto-étoile IRAS16293-2422 B, supposée être le système naissant de type solaire le plus proche, et la comète 67P/Churyumov-Gerasimenko (ci-après 67P), considérée comme représentative de la majeure partie des glaces cométaires. Ils ont observé une corrélation entre les abondances des molécules contenant du CHO, du N et du S, avec une certaine dispersion, ce qui implique une préservation partielle de la chimie pré-stellaire et proto-stellaire dans les glaces cométaires. Dans une autre étude, ? ont comparé les abondances relatives des iCOMs entre les proto-étoiles de classe I SVS13-A et quatre comètes (Hale-Bopp, Lemmon, Lovejoy et 67P) et ont trouvé des résultats différents selon les iCOMs. En effet, alors que le formiate de méthyle (HCOOCH_3) et l'éthanol ($\text{CH}_3\text{CH}_2\text{OH}$) sont cohérents avec ce qui est trouvé dans les comètes à un facteur 10 près, l'acétaldéhyde (CH_3CHO) et le formamide (NH_2CHO) montrent jusqu'à un facteur 30 de différence, à titre d'exemple. Outre ces études spécifiques, un grand nombre de molécules observées dans les comètes sont également détectées dans les régions de formation d'étoiles et avec des abondances similaires (par ex. [Le Roy et al. 2015](#); [Drozdovskaya et al. 2018](#); ?). En particulier, le formamide (NH_2CHO), une des molécules avec une liaison amide, a été détecté dans les comètes et les météorites ([Pizzarello et al. 1991](#); [Elsila et al. 2009](#)) mais aussi dans les proto-étoiles de type solaire ([Kahane et al. 2013](#); [López-Sepulcre et al. 2015](#)). Cela implique un lien possible entre la chimie organique dans l'ISM et dans le système solaire ([Ceccarelli et al. 2007, 2014b](#)).

Les molécules peuvent-elles survivre au voyage et jouer un rôle dans l'apparition de

la vie sur Terre ? Nous avons besoin de beaucoup plus d'études avant d'obtenir une réponse quelque peu définitive. Les statistiques sont assez pauvres et il faut multiplier les études systématiques des abondances moléculaires mesurées entre les phases de disques protostellaires/planétaires et les comètes avant de tirer des conclusions définitives. De plus, il faut trouver des analogues précis du progéniteur de notre Soleil pour effectuer la comparaison. En effet, dans la suite nous verrons que toutes les protoétoiles ne partagent pas le même contenu chimique et qu'aujourd'hui, nous ne savons pas quel est le passé chimique de notre Soleil. Nous verrons ensuite que toutes les étoiles de type solaire ne naissent pas dans le même type d'environnement et que notre Soleil se serait formé dans un type d'environnement spécifique.

II La poussière interstellaire: joueuse de lumière d'étoile

La nuit est déjà bien entamée. Les lumières publiques du village le plus proche sont faibles, il fait plutôt sombre. Une couverture, une torche rouge, et le silence le plus complet. Les étoiles sont brillantes et une bande de couloirs clairs et sombres s'étend au-dessus de ma tête : notre galaxie natale, la Voie lactée. Les régions sombres traversant le plan galactique indiquent la présence de nuages de poussière et de gaz interstellaires en avant-plan, qui absorbent la lumière des étoiles situées derrière. Ces nuages sont ceux mentionnés dans la section précédente, ils sont le berceau des étoiles.

Historiquement, il n'a pas été facile de déduire la présence de poussière interstellaire. En 1785, Herschel ([Herschel 1785](#)) a catalogué plusieurs nébuleuses "sombres" et les a décrites comme des "trous dans le ciel". Au début du 20^{ème} siècle, il a été reconnu que les "trous sans étoiles" étaient des structures devant les étoiles capables d'absorber la lumière des étoiles ([Clerke 1903](#); [Barnard 1919](#)). Enfin, en 1930, l'existence d'une poussière interstellaire diffuse a été déduite par R. J. Trumpler ([Trumpler 1930](#)) de l'obscurcissement ou "extinction" de la lumière des étoiles. Nous savons maintenant que l'ISM est composé de poussière et de gaz et que la poussière représente 1/100^e du gaz en masse. Malgré sa petite fraction de l'ISM, la poussière interstellaire est importante et joue des rôles substantiels : elle est la source dominante d'opacité dans l'ISM, elle domine la distribution spectrale d'énergie (SED) de l'ISM à toutes les longueurs d'onde à partir de 912 Å et c'est là que se forme la molécule la plus abondante de l'univers, H₂.

II.1 Grains interstellaires et propriétés

La poussière interstellaire est composée de petits grains de matière solide, à savoir des silicates et des grains carbonés. Une fraction substantielle d'éléments lourds est verrouillée sur ces grains. Ceci est important pour la formation des planètes et peut-être de la vie, car ce qui est bloqué sur les grains de poussière régit les éléments disponibles pour la chimie biotique. De plus, comme je le décrirai dans les prochaines sections, plusieurs réactions chimiques peuvent se produire à la surface des grains de poussière, et en particulier celle de H₂ (e.g. [Gould & Salpeter 1963](#); [Hollenbach & Salpeter 1970, 1971](#); [Vidali 2013](#); [Wakelam et al. 2017](#); [Pantaleone et al. 2021](#)), le principal composant de l'ISM.

Les propriétés des grains interstellaires sont dérivées des observations, sur la façon dont ils absorbent, émettent et diffusent les photons. D'après ces observations, nous savons que les grains de poussière ont des formes irrégulières et sont plutôt petits, avec des tailles allant de 0,005 μ m à 0,25 μ m ([Mathis et al. 1977](#)). Dans la Voie lactée, leur

taille moyenne en diamètre est de $0,1 \mu\text{m}$. Dans les environnements froids tels que les nuages moléculaires, les grains de poussière interstellaire peuvent être entourés de manteaux glacés. Absorber, émettre et diffuser les photons sont les propriétés de la poussière interstellaire. La combinaison de l'absorption et de la diffusion entraîne l'extinction de la lumière des étoiles par la poussière interstellaire. Ce processus est également appelé *rougissement* car la lumière bleue étant plus facilement diffusée que la lumière rouge, les étoiles semblent rougir. Pour une revue plus complète des propriétés observées des grains de poussière interstellaire, voir [Draine \(2003\)](#).

II.2 Emission de la poussière

La température moyenne de la poussière varie entre 10 et 1500 K. Au-dessus de 1500 K, les grains sont vaporisés. La poussière absorbe les photons interstellaires du visible à l'UV, est chauffée et réémet dans le proche IR jusqu'aux longueurs d'onde millimétriques où nous pouvons les observer. La SED peut être caractérisée par deux composantes, une composante froide (15-20 K) émettant vers le long terme dans le FIR et une composante chaude (500 K) émettant dans le proche et moyen IR. La composante froide est due à de gros grains ($\sim 0.1\mu\text{m}$) tandis que la composante chaude est due à de petits et très petits grains (VSG), et à de grosses molécules à chaîne de carbone appelées Hydrocarbures Poly-Aromatiques (PAHs) contenant plus de 50 atomes de carbone.

Historiquement, les jeunes objets stellaires (YSOs) ont été classés dans une séquence évolutive, des proto-étoiles (Classe I) aux étoiles de la pré-séquence principale en utilisant la SED infrarouge (IR) (Classe III) ([Lada & Wilking 1984](#); [Lada 1987](#)). Les sources infrarouges ont d'abord été divisées en 3 catégories, en fonction de la forme de la distribution d'énergie observée et de l'indice spectral IR. L'indice spectral infrarouge est défini pour la plage de longueur d'onde $\lambda = 2 - 25\mu\text{m}$:

$$\alpha = \frac{d(\log \lambda F_\lambda)}{d(\log \lambda)} \quad (1)$$

où F_λ est la densité de flux spectral par intervalle de longueur d'onde.

Dans un premier temps, les sources de classe I ont été classées comme les proto-étoiles les plus jeunes, leur luminosité provenant principalement de l'accrétion. Leur indice spectral IR est $\alpha \geq 0$ et leur SED culmine dans l'infrarouge. Les classes II et III sont des sources moins encastrées. Les sources de classe II ont un indice spectral $-2\alpha \leq 0$, leur SED atteint son maximum dans l'infrarouge proche mais elles présentent un excès dans l'infrarouge moyen. La classe III a $\alpha \leq -2$ et leur SED ressemble à des corps noirs rougis. Cette séquence évolutive a été soutenue par la modélisation théorique de la SED ([Adams et al. 1987](#)).

Plus tard, des sources de classe 0 ont été ajoutées à la séquence évolutive. Ces sources ont été définies comme étant encore plus incrustées dans le nuage moléculaire et plus jeunes que les sources de classe I ([André et al. 1993](#)). Leur SED culmine à plus de $100 \mu\text{m}$ et leur émission dans le proche infrarouge est faible. La frontière entre les objets de classe 0 et I a été définie à l'aide du rapport entre la luminosité submillimétrique ($\lambda > 350\mu\text{m}$) et la luminosité bolométrique, $L_{s\text{mm}}/L_{\text{bol}}$: une protoétoile de classe 0 a $L_{s\text{mm}}/L_{\text{bol}} \geq 0.05$. Une approche alternative pour classer les YSOs est basée sur la température bolométrique ([Myers & Ladd 1993](#); [Chen et al. 1995, 1997](#)) et sur la masse (enveloppe + disque) ([Terebey et al. 1993](#); [André et al. 1993](#); [André & Montmerle 1994](#)).

À partir de la gamme de longueur d'onde millimétrique et au-delà (à des fréquences plus élevées), l'émission thermique de la poussière domine le spectre global des YSOs et plus généralement, des régions de formation d'étoiles. Cependant, en dessous de ~ 100 GHz, c'est-à-dire dans le domaine radio, d'autres mécanismes d'émission peuvent également contribuer au SED, tels que l'émission thermique Bremsstrahlung (également appelée *free-free*), l'émission gyrosynchrotron non thermique et l'émission micro-onde anormale (AME). Entre ~ 1 et 100 GHz, l'émission AME ne domine pas et je n'en parlerai donc pas dans ce qui suit. Cependant, je présenterai les autres types d'émission qui peuvent contribuer à l'émission radio des YSOs car ils sont pertinents dans le contexte de cette thèse.

La plupart des YSOs montrent une émission radio compacte (Bontemps et al. 1995; Anglada 1995; Rodriguez 1997; Tychoniec et al. 2018). Comme je viens de l'expliquer ci-dessus, cette émission n'est pas nécessairement une contribution de l'émission de la poussière. Selon le stade évolutif du YSO, l'émission radio peut être attribuée à différents mécanismes. Habituellement, l'émission radio des objets de classe III est due au rayonnement gyrosynchrotron (Feigelson & Montmerle 1985; André 1996; Anglada et al. 1998; Dzib et al. 2013; Pech et al. 2016) à cause des électrons relativistes légers qui tournent dans la magnétosphère de la source. Ce type d'émission peut également être détecté dans certaines sources de classe I et II (Dzib et al. 2010; Dellar et al. 2013). D'autre part, l'émission radio des YSOs plus jeunes (principalement les classes 0 et I et quelques classes II) est généralement attribuée à l'émission "free-free" associée à l'activité de l'écoulement de la source (e.g. Anglada 1996; Anglada et al. 1998; Rodriguez 1997; Tychoniec et al. 2018) ou associée à la photoévaporation du disque de classe II (e.g. Pascucci & Gorti 2012; Owen et al. 2013; Macías et al. 2016). Il peut y avoir quelques exceptions où l'émission non thermique peut être détectée vers des jets associés à de jeunes proto-étoiles (classes 0 et I) ou parce que les sources ont leur émission dominée par l'émission gyrosynchrotron : rodriguez1989,curiel1993, feigelson1998, dzib2013, deller2013,tychoniec2018a, anglada2018.

L'indice spectral α aux longueurs d'onde centimétriques, défini comme $F_\nu \propto \nu^\alpha$, peut être utilisé pour déterminer si l'émission est thermique ou non thermique. Pour l'émission thermique, l'indice spectral est plat ou positif, c'est-à-dire $-0, 1 \leq \alpha \leq 2$ alors que pour l'émission non thermique, l'indice spectral est négatif, c'est-à-dire $\alpha \leq -0, 1$ (e.g. Panagia & Felli 1975; Rodriguez et al. 1993; Anglada et al. 1998). L'émission thermique de la poussière a également un indice spectral positif ($\alpha = 2 + \beta$; β est l'indice spectral d'émissivité de la poussière) mais sa contribution domine aux longueurs d'onde IR et (sub)-mm alors qu'elle est faible aux longueurs d'onde centimétriques.

La plupart des très jeunes proto-étoiles, c'est-à-dire les proto-étoiles de classe 0 et I, génèrent de puissants écoulements et jets : (Bontemps et al. 1996; Bachiller 1996; Arce & Sargent 2006; Frank et al. 2014; Podio et al. 2021). Il a été démontré que l'émission radio thermique associée à ces sources, est due au rayonnement de particules chargées qui sont désaccentuées dans des jets thermiques, c'est-à-dire des écoulements collimatés (partiellement) ionisés par des chocs (e.g. Rodriguez 1994; Anglada 1995; Rodriguez 1997; Anglada et al. 2018). Sur la SED, l'émission "free-free" se traduit par un excès centimétrique. L'émission "free-free" n'est présente que vers VLA1623, car nous voyons que les mesures de densité de flux s'écartent de la courbe ajustée d'un corps noir.

III Le stade protostellaire : Une chimie riche

Notre Soleil est passé par le stade protostellaire au cours de son enfance. Si l'apparition de la vie sur Terre a été soutenue par un quelconque héritage chimique provenant du milieu interstellaire (ISM), l'étude du stade protostellaire connu pour être chimiquement riche semble être un bon point de départ. Cependant, la détermination du contenu moléculaire du proto-Soleil s'avère être une tâche plus compliquée que prévu.

Au cours du stade protostellaire, une pléthore de molécules se forment à mesure que la température augmente de 10 K à plus de 100 K. La température augmentant progressivement, différentes zones chimiques se forment dans les enveloppes des proto-étoiles. Selon [Caselli & Ceccarelli \(2012\)](#), la structure des proto-étoiles de classe O/I peut être représentée par quatre zones principales: la zone externe, l'enveloppe froide, la zone "Warm Carbon Chain Chemistry" ou chimie des chaînes carbonées chaude (WCCC) et la zone "hot corino". La zone externe est chimiquement similaire au nuage moléculaire présent autour des jeunes classe O/I proto-étoiles. La température est autour de 10 K. L'enveloppe froide, aussi appelée zone de déplétion du CO, est présente dans plusieurs proto-étoiles de class O/I ([Jørgensen et al. 2005](#)). La température est assez froide ($T \leq 22$ K) pour que les espèces chimiques gèlent à la surface des grains. La zone WCCC est la zone de sublimation du méthane. La température doit être de minimum 25 K pour que le méthane soit relâché dans la phase gazeuse où la formation de chaînes carbonées va commencer. Cependant, afin de déclencher une chimie WCCC significative, l'abondance de CH_4 doit être supérieure à 10^{-7} . Cette zone peut s'étendre à environ quelques milliers d'au autour de la proto-étoile. Enfin, la zone "hot corino" est la plus interne, où les manteaux de glace riches en eau se subliment et où une chimie des gaz chauds se produit. La température est de ≥ 100 K, ce qui entraîne la sublimation de la glace d'eau. Toutes les molécules qui étaient piégées dans les manteaux de glace sont ainsi libérées dans la phase gazeuse. Une chimie riche est alors déclenchée entre les espèces libérées et le gaz environnant, conduisant à la formation des iCOMs. Cette zone a un rayon d'environ une centaine d'au ou moins.

En suivant ce schéma, nous nous attendrions alors naïvement à ce que toutes les proto-étoiles de classe O/I partagent la même structure d'enveloppe et la même composition. Or, ce n'est pas le cas, et c'est pourquoi la compréhension du passé chimique de notre Soleil est un défi et est importante. Certains objets du même âge présentent des différences chimiques extrêmes. Ces deux types d'objets sont respectivement appelés "hot corinos" et objets WCCC, et sont considérés comme des éléments clés de la preuve qu'une diversité chimique particulièrement riche peut se produire au stade protostellaire.

III.1 Les "hot corinos"

Les "hot corinos" sont les premiers objets découverts parmi la population de proto-étoiles de type solaire présentant un type de chimie spécifique ([Ceccarelli et al. 2000b](#); [Cazaux et al. 2003](#)). Bien qu'ils présentent des caractéristiques particulières, leur identification n'est pas toujours simple en raison d'un manque de résolution spatiale et de sensibilité, ou d'une opacité élevée de la poussière. Par conséquent, seule une douzaine de "hot corinos" ont été confirmés jusqu'à présent.

Les "hot corinos" sont des régions compactes (≤ 100 au), chaudes ($T \geq 100$ K) et denses ($n \geq 10^7$ cm^{-3}) autour de l'objet central ([Ceccarelli 2004](#); [Ceccarelli et al. 2007](#)). Le nom vient du fait qu'il y a beaucoup de similitudes avec les coeurs chauds, des proto-

étoiles de haute masse montrant une riche chimie organique : (e.g. Snyder et al. 1974; Fourikis et al. 1974; Brown et al. 1975; van Dishoeck & Blake 1998; Kurtz et al. 2000; Schilke et al. 1997a, 2001; Comito et al. 2005; Schilke et al. 2006; Belloche et al. 2008a,b, 2009, 2013; Calcutt et al. 2014; Mininni et al. 2020). De nombreux iCOMs trouvés vers les coeurs chauds ont été détectés dans le prototype "hot corino" IRAS16296-2422 avec des abondances au moins dix fois plus élevées que ce qui a été trouvé dans les coeurs chauds (Ceccarelli et al. 2000b; Cazaux et al. 2003), ce qui suggère que les "hot corinos" ne sont pas seulement plus petits en taille mais qu'ils sont aussi chimiquement différents de leur homologue massif. Une étude récente de Higuchi et al. (2018) dans le nuage moléculaire Perseus a montré que les "hot corinos" auraient tendance à être situés profondément à l'intérieur des nuages moléculaires.

La principale spécificité des "hot corinos" par rapport aux autres proto-étoiles de faible masse est leur enrichissement particulier en iCOMs (par exemple CH_3OH , CH_3OCH_3 , HCOOCH_3) dans la région interne de l'enveloppe protostellaire (<150 au), c'est-à-dire dans la zone des "hot corinos" (Ceccarelli et al. 2007). Une poignée d'études ont été consacrées à la détection des iCOMs dans ces objets (par exemple Bottinelli et al. 2004; Jørgensen et al. 2005, 2016; Kahane et al. 2013; Öberg et al. 2014; De Simone et al. 2017; López-Sepulcre et al. 2017; ?; Belloche et al. 2020; Yang et al. 2021). Cependant, ceux-ci ne montrant qu'une augmentation dans les iCOMs ne sont pas toujours catégorisés comme "hot corino". Une deuxième condition sine qua non est une déficience en chaînes carbonées dans la région de 2000 au autour de l'objet central, c'est-à-dire dans la zone WCCC, par rapport aux objets WCCC purs. Cependant, quelques petites chaînes carbonées sont encore détectées vers les "hot corinos", mais avec de faibles abondances par rapport aux autres objets : (Sakai et al. 2009a).

Une autre caractéristique des "hot corinos" est un niveau de deutération élevé. Des molécules deutérées ont été détectées vers les "hot corinos" (e.g. Ceccarelli et al. 1998; van der Tak et al. 2002; Parise et al. 2002; Vastel et al. 2003, 2010; Parise et al. 2004; Coudert et al. 2019; Agúndez et al. 2021), et des grands niveaux de fractionnement du deutérium ont été calculés, en particulier pour CH_3OH et H_2CO (e. g. Ceccarelli et al. 1998; Loinard et al. 2000; Ceccarelli et al. 2001, 2007; Parise et al. 2006; Martín-Doménech et al. 2021). Le grand fractionnement du deutérium est une caractéristique partagée avec les coeurs pré-stellaires les plus froids.

III.2 Les proto-étoiles WCCC

Après la découverte des "hot corinos", on a d'abord pensé que chaque proto-étoile de faible masse cachait alors un "hot corino" en son cœur, y compris le proto-soleil (Bottinelli et al. 2007). Plusieurs études visant à détecter les iCOMs dans les proto-étoiles de type solaire et donc à détecter de nouveaux "hot corinos" ont ensuite fleuri. De manière surprenante, c'est en recherchant des iCOMs dans IRAS 04368+2557 (ci-après L1527) que Sakai et al. (2008a) a découvert un objet chimiquement différent, la première proto-étoile WCCC. Contrairement aux "hot corinos", peu d'autres sources protostellaires WCCC ont été confirmées depuis. Au total, quatre objets ont été classés comme proto-étoiles WCCC mais il y a actuellement 17 candidats WCCC.

Les objets WCCC sont enrichis en molécules de chaînes carbonées, c'est-à-dire en molécules de la forme HC_{2n+1}N , C_nH , C_nH_2 , entre autres. Contrairement aux "hot corinos" où les iCOMs sont principalement situés au centre de la région interne des en-

veloppes protostellaires, les molécules de chaîne carbonées sont situées jusqu'à ~ 2000 au autour de l'objet central, où la température de l'enveloppe dépasse 25 K. Les résultats de grands relevés observationnels ont montré que les sources WCCC auraient tendance à être situées au bord des nuages moléculaires ou de manière isolée (Lefloch et al. 2018; Higuchi et al. 2018). Il existe deux conditions principales à remplir pour classer un objet comme un objet WCCC (Sakai & Yamamoto 2013) : (1) Abondance de diverses molécules à chaîne carbonée présentes dans le noyau protostellaire et (2) émission de chaînes carbonées concentrée autour de la proto-étoile, dans la partie dense et chaude.

Cependant, la présence de petites chaînes carbonées uniquement ne suffit pas pour classer un objet comme source WCCC. La présence de longues chaînes carbonées est également requise. Plusieurs d'entre elles ont été détectées vers des sources WCCC (par exemple C_6H , C_7H , C_6H_2 , HC_7N , HC_9N ; Sakai et al. 2008a; Cordiner et al. 2012; Araki et al. 2017; Yoshida et al. 2019). Enfin, les molécules à chaîne carbonée détectées vers les sources WCCC proviennent d'une partie chaude (≈ 30 K) et dense de l'enveloppe de la proto-étoile, car des raies avec des conditions d'excitation élevées sont détectées.

Une autre caractéristique des sources WCCC est qu'en plus d'être enrichies en chaînes carbonées, elles présentent une déficience en iCOMs dans la zone interne de l'enveloppe protostellaire. Cela ne signifie pas qu'aucun iCOM n'est détecté, mais qu'ils sont présents en plus petite quantité par rapport aux autres proto-étoiles. Par rapport aux coeurs pré-stellaires, les molécules contenant du S et du N sont plutôt déficientes dans les sources WCCC (Sakai et al. 2008b; Yoshida et al. 2019) tandis que les molécules à chaînes carbonées et les molécules complexes CH_3OH et CH_3CHO ont des densités de colonne similaires dans les deux types d'objets (Yoshida et al. 2019). Par rapport aux "hot corinos", les molécules contenant du S semblent également déficientes dans les sources WCCC (Yoshida et al. 2019). Une autre caractéristique des sources WCCC est la détection d'anions moléculaires (C_6H^- , C_4H^- ; par exemple Sakai et al. (2007, 2008b); Agúndez et al. (2008); Cordiner et al. (2011)). Enfin, les sources WCCC présentent un fractionnement modéré du deutérium, compris entre 2 et 7 % (Sakai et al. 2009b; Yoshida et al. 2019), ce qui est inférieur à celui des "hot corinos", et similaire ou inférieur à celui des coeurs pré-stellaires "évolués" (par exemple L1544, L63, L1689B ; Sakai et al. 2009b).

III.3 A la recherche de l'origine de la différenciation chimique

La chimie du "hot corino" et du WCCC est déclenchée par la sublimation de molécules piégées dans les manteaux de glace des grains de poussière. Il semble y avoir une quantité significative de glace CH_4 dans les manteaux entourant les grains de poussière des objets WCCC, alors qu'il semble y avoir une grande quantité de CH_3OH dans les manteaux des grains des sources "hot corino". La différence de composition chimique des proto-étoiles est donc due à la différence de composition des manteaux de grains. Qu'est-ce qui pourrait causer cette différence de composition chimique ? La réponse se cache dans la façon dont les grains se sont formés, ont évolué et dans quelles circonstances. Aujourd'hui, l'origine des différentes compositions chimiques des manteaux de grains dans les "hot corino" et les objets WCCC est toujours une question ouverte. Je présente ici deux hypothèses majeures.

Une première explication implique la différence des échelles de temps pendant la phase du coeur pré-stellaire (Sakai et al. 2008a, 2009a). L'échelle de temps typique pendant laquelle le carbone atomique du gaz est verrouillé sur la molécule de CO est

d'environ 3×10^5 an (Sakai & Yamamoto 2013). Dans le cas de la formation d'un "hot corino", la durée de la phase prestellaire dépasserait cette échelle de temps. Les molécules de CO gèlent sur les manteaux des grains de poussière, où elles subissent des processus d'hydrogénation aboutissant à la formation de CH_3OH et H_2CO , molécules clés pour la formation d'autres iCOMs. D'autre part, si la durée de la phase du coeur prestellaire est plus rapide ou similaire à l'échelle de temps chimique donnée ci-dessus, les atomes de carbone n'ont pas le temps de se verrouiller sur les molécules de CO et sont dirigés vers les grains sous forme atomique. Le résultat de l'hydrogénation des atomes de carbone conduit à la formation de méthane. Une fois que CH_4 est libéré dans la phase gazeuse, il produira principalement des molécules de chaînes carbonées, conduisant à la formation d'un objet WCCC. Cette théorie ne fonctionne que si l'on considère une structure en couches du manteau des grains (Taquet et al. 2012). Dans le cas d'une longue phase de noyau sans étoile, le CH_4 solide formé précédemment est piégé dans une couche plus interne que le CH_3OH et le H_2CO . Ainsi, à des températures atteignant la température de sublimation de CH_4 , CH_4 ne peut pas se désorber et reste piégé. Lorsque l'ensemble du manteau se sublime à $T \geq 100$ K, CH_4 peut alors se désorber, mais il ne peut pas réagir avec C^+ pour former des chaînes carbonées, car l'ion est très peu abondant. Inversement, dans le cas d'une courte phase de noyau pré-stellaire, la couche externe contient des quantités substantielles de CH_4 car CH_3OH et H_2CO ne pourraient pas se former en grande quantité. Ainsi, CH_4 sera capable de se désorber plus tôt que dans le cas précédent ($T=25\text{K}$) et de déclencher la chimie WCCC. Enfin, cette théorie a récemment été réfutée par des calculs de modèles chimiques. Aikawa et al. (2020) ont testé la dépendance de la chimie du "hot corino" et du WCCC à la durée de la phase du noyau prestellaire. Ils ont fait varier plusieurs paramètres physiques de la phase statique tels que les températures, l'extinction visuelle et la durée de la phase statique. Ils ont trouvé que la variation des paramètres pouvait reproduire les "hot corinos" et les sources hybrides, où les iCOMs et les chaînes carbonées sont présents simultanément, mais ils ne pouvaient pas reproduire les sources WCCC typiques, où les iCOMs sont déficients.

Une deuxième hypothèse pour la variation chimique des manteaux de glace des grains de poussière est le rayonnement UV du champ de rayonnement interstellaire (ISRF) pendant la phase du coeur pré-stellaire (Spezzano et al. 2016, 2020; Lattanzi et al. 2020). Spezzano et al. (2016) ont cartographié l'émission de méthanol et de la chaîne carbonée $c\text{-C}_3\text{H}_2$ à travers le coeur pré-stellaire L1544. Ils ont trouvé une différenciation chimique à travers le nuage en raison de son exposition à l'ISRF. La partie du nuage la plus exposée à ce dernier présente un maximum d'émission de $c\text{-C}_3\text{H}_2$ alors que la partie du nuage la plus protégée de l'ISRF présente un maximum de méthanol. Plus récemment, Spezzano et al. (2020) ont cartographié les mêmes espèces vers un échantillon de 6 coeurs denses, situés dans des environnements différents et avec des âges évolutifs différents (coeurs sans étoile et pré-stellaires). Les coeurs situés dans un ISRF non homogène montrent la même tendance que pour L1544 : une chimie active du carbone est observée là où le nuage est plus exposé à l'ISRF, tandis que l'émission de méthanol atteint son maximum là où le nuage est plus protégé. De même, Lattanzi et al. (2020) a comparé la composition chimique de L1544 avec celle de L183. Les deux coeurs pré-stellaires sont situés dans des environnements différents. D'une part, L1544 se trouve au bord du nuage moléculaire du Taureau et est plus exposée à l'ISRF que L183, qui est, d'autre part, plus enfoui dans le nuage environnant. Leurs résultats ont montré que L1544 est plus riche en espèces carbonées alors que L183 est plus riche en espèces oxygénées. Toutes les études susmentionnées conclu-

ent que les différences chimiques au sein des coeurs denses et entre eux sont dues à leur exposition non homogène à l'ISRF. Les photons de l'ultraviolet lointain (FUV) brisent les petites molécules dans un processus appelé photochimie. La photochimie empêche le carbone atomique de se fixer sur les molécules de CO. Les atomes de carbone gèlent donc sur les grains et forment des glaces CH₄ conduisant à la formation d'objets WCCC au stade protostellaire. Les régions exposées au champ UV de l'ISRF sont appelées régions de photodissociation. D'autre part, dans les régions protégées de l'ISRF, l'absence de photochimie permet aux atomes de carbone d'être verrouillés dans les molécules de CO, enrichissant les glaces en CH₃OH et H₂CO et conduisant ainsi à la formation d'un "hot corino" par la production d'iCOMs. Ce scénario ne fonctionne que pour les cas d'illumination uniforme. Si l'illumination n'est pas homogène, les glaces formées peuvent présenter un mélange de molécules de CH₃OH et de CH₄ (Spezzano et al. 2016). Cette hypothèse est cohérente avec les résultats de Higuchi et al. (2018) et Lefloch et al. (2018), qui ont montré que les "hot corinos" auraient tendance à être situés au centre des nuages moléculaires, tandis que les objets WCCC sont plus exposés à l'ISRF, car ils sont situés en bordure des nuages moléculaires ou de manière isolée. Récemment, Kalvans (2021) ont réalisé des simulations chimiques d'une parcelle de gaz dans une proto-étoile avec différents niveaux d'irradiation pour étudier la chimie de la chaîne carbinée dans les sources WCCC. Ils ont constaté que la chimie des WCCC peut être reproduite sous irradiation interstellaire ou par les rayons cosmiques. En conclusion, l'environnement pourrait être le principal paramètre de la diversité chimique des proto-étoiles de masse solaire. Nous devons augmenter les statistiques des "hot corinos" et des sources WCCC, et étudier leur environnement pour confirmer cette hypothèse.

Des "hot corinos" aux sources WCCC, nous sommes confrontés à un large éventail de passés chimiques possibles pour notre Soleil. Il est donc légitime de se poser les questions suivantes : Quel est l'environnement de naissance de notre Soleil ? Peut-on y trouver des "hot corinos" et/ou des objets WCCC ? Si oui, lequel des deux prévaut ?

IV L'environnement de naissance du Soleil : Une pouponnière animée

Nous avons vu précédemment que les étoiles naissent dans la partie la plus dense des nuages moléculaires géants. Les observations de ces nuages moléculaires ont montré que nous pouvons distinguer deux types différents de régions de formation d'étoiles : des noyaux denses isolés qui ne forment que des protoétoiles de faible masse ($\leq 8 M_{\odot}$) (par exemple, le nuage moléculaire du Taureau) et des concentrations massives de gaz (par exemple, le complexe OMC, également appelé amas), dans lesquelles se forment des protoétoiles de masse élevée et faible. Dans lequel de ces environnements notre Soleil est-il né ? S'agit-il de la même région où l'on trouve des "hot corinos" et des objets WCCC ? Si nous voulons comprendre si notre Soleil a subi une phase "hot corino", une phase de WCCC ou aucune des deux, nous devons chercher des analogues à l'environnement de naissance du Soleil. Dans ce qui suit, je présente d'abord l'environnement de naissance de notre Soleil, sur la base de ce qui est actuellement connu. Ensuite, je présente le meilleur et le plus proche analogue à l'environnement de naissance du Soleil, qui est visé dans cette thèse.

IV.1 Sur la piste du passé du Soleil

La plupart des étoiles se forment au sein de groupes ou d'amas d'étoiles (e.g. [Carpenter 2000](#); [Lada & Lada 2003](#); [Porras et al. 2003](#); [Evans et al. 2009](#)). Ces amas se dissolvent généralement en quelques dizaines de millions d'années, voire moins (par ex. [Hartmann et al. 2001](#); [Engargiola et al. 2003](#); [Kawamura et al. 2009](#); [Meidt et al. 2015](#); [Corbelli et al. 2017](#); [Chevance et al. 2020](#), et leurs références). Ainsi, notre Soleil étant âgé de 4,6 Gyr ([Bonanno et al. 2002](#); [Amelin et al. 2002](#); [Baker et al. 2005](#)), son environnement de naissance a été dissipé depuis longtemps. Comment pouvons-nous alors savoir à quoi il ressemblait ? Heureusement, tous les morceaux de ce lieu de naissance passé n'ont pas disparu : certaines caractéristiques du système solaire actuel nous donnent des indices sur les premières phases de sa formation. Trois caractéristiques principales constituent de puissantes contraintes sur le processus de formation du Système solaire :

- Présence d'espèces radioactives à courte durée de vie précurseurs du ^{26}Al et du ^{60}Fe dans les météorites;
- Limite extérieure du système planétaire située à ~ 30 au et limite intérieure de la ceinture de Kuiper à 45 au;
- les objets de la ceinture de Kuiper ont des excentricités et angles d'inclinaison plus élevés que pour les planètes.

Toutes ces caractéristiques indiquent que notre Soleil est probablement né dans un environnement en amas (par ex. [Adams 2010](#); [Pfalzner & Vincke 2020](#)):

Tout d'abord, les espèces radioactives à courte durée de vie (SLRs) sont des espèces pour lesquelles le temps de demi-vie est inférieur à environ 10 Myr. Par conséquent, elles ont dû être incorporées dans le système solaire primitif peu de temps (~ 1 Myr) après leur production, ce qui fournit des contraintes sur les conditions dans lesquelles elles ont été produites (e.g. [Gounelle et al. 2006](#); [Adams 2010](#); [Diehl et al. 2021](#)). Par conséquent, les SLRs sont d'excellents outils pour retracer le lien entre le Soleil et d'autres étoiles nées dans le même nuage moléculaire, et sont utilisés pour estimer le nombre d'étoiles/masse de l'amas de naissance solaire (par ex. [Dauphas & Chaussidon 2011](#); [Gounelle & Meynet 2012](#); [Parker et al. 2014](#); [Nicholson & Parker 2017](#); [Portegies Zwart 2019](#)), et/ou pour estimer les types d'étoiles présentes dans le voisinage du Système solaire primitif, donc l'environnement astrophysique dans lequel le Soleil a évolué (e.g. [Meyer & Clayton 2000](#); [Looney et al. 2006](#); [Gounelle et al. 2006](#); [Gounelle & Meynet 2012](#); [Huss et al. 2009](#); [Lugaro et al. 2018](#); [Kaur & Sahijpal 2019](#); [Portegies Zwart 2019](#)).

La présence antérieure de SLRs dans le Système solaire primitif peut être déduite en mesurant leurs isotopes descendant dans les matériaux météoritiques tels que ^{26}Mg pour ^{26}Al et ^{60}Ni pour ^{60}Fe . La relation SLR-isotope descendant, appelée chronomètre à courte durée de vie, peut aider à déterminer l'époque à laquelle les SLRs se sont formés avec une résolution de 1 Myr ou moins ; [e.g.] [[WR00](#), [kita2005](#), [GR05](#), [wad-hwa2007](#). Certains SLRs montrent des abondances particulières : ^{26}Al est surabondant alors que ^{60}Fe est sous-abondant. Ces abondances anormales peuvent être expliquées par la présence de vents d'une étoile de type Wolf-Rayet ou par des explosions de supernovae (SN) à proximité : [e.g.] [[looney2006](#), [WG07](#), [gounelle2009](#), [gounelle2015](#), [young2014](#), [dwarkadas2017](#), [portegies-zwart2019](#). Avoir une étoile Wolf-Rayet et une succession

d'explosions de SN dans le même environnement de naissance semble être une association assez rare, à moins que l'on considère que notre Soleil est né dans un grand amas. L'origine des SLRs est encore débattue aujourd'hui (voir [Diehl et al. 2021](#) pour une revue). Cependant, l'amas dans lequel notre Soleil est né doit être relativement massif afin d'expliquer la présence de SLRs à un stade précoce de la formation du Soleil.

Ensuite, pour les proto-étoiles de type solaire, les tailles (rayons) observées pour les disques protoplanétaires vont de ~ 10 au à quelques 100 au, avec la majorité des disques entre 100 et 200 au (par ex. [McCaughrean & O'dell 1996](#); [Vicente & Alves 2005](#); [Eisner et al. 2008](#); [Andrews & Williams 2007](#); [Andrews et al. 2009, 2010](#); [Williams & Cieza 2011](#)). Les limites actuelles du système solaire situées à 30 au pour les planètes, et à 45 au pour la ceinture de Kuiper, impliquent probablement que le disque protoplanétaire du système solaire primitif a été tronqué à un moment donné par un (ou plusieurs) processus. Différents processus pourraient conduire à la troncature du disque, tels que des rencontres rapprochées (e.g. [Pfalzner et al. 2005](#); [Rosotti et al. 2014](#); [Vincke et al. 2015](#); [Portegies Zwart 2016](#); [Pfalzner et al. 2018](#)), la photoévaporation par des étoiles massives proches (e.g. [Smith et al. 2003](#); [Mitchell & Stewart 2011](#); [Wright et al. 2012](#); [Mann et al. 2014](#); [Kim et al. 2016](#); [Winter et al. 2018](#); [Haworth et al. 2017](#); [Eisner et al. 2018](#)) ou par l'explosion d'une supernova ([Chevalier 2000](#); [Pelupessy & Portegies Zwart 2012](#); [Close & Pittard 2017](#)), bien que la dernière hypothèse soit controversée ([Ansdell et al. 2020](#)). Cependant, le processus le plus probable à l'origine de la troncature supposée du disque et expliquant également les excentricités et inclinaisons élevées des objets de la ceinture de Kuiper, est la rencontre rapprochée (e.g. [Ida et al. 2000](#); [Morbidelli & Levison 2004](#); [Kenyon & Bromley 2004](#); [Jílková et al. 2015](#); [Pfalzner et al. 2018](#)). Par conséquent, les propriétés physiques et dynamiques du système solaire pourraient être une conséquence naturelle d'un amas de naissance dense.

Enfin, pour expliquer l'enrichissement météoritique en espèces filles des SLRs, la troncature du disque ou les propriétés dynamiques des objets de la ceinture de Kuiper, nous avons besoin d'un grand amas de naissance. Or, il existe deux types différents d'amas massifs : les amas de combustion d'étoiles et les amas "fuyants" (également appelés associations OB). Les amas de combustion d'étoiles sont des amas compacts (0,1 pc) avec des densités initiales élevées ($10^5 - 10^6 M_{\odot} \text{pc}^{-3}$) qui s'étendent sur quelques parsecs (1-3 pc) en 10 ans ou plus sans perdre leur masse. D'autre part, les amas "fuyants" sont des amas plus diffus (~ 5 pc) qui s'étendent jusqu'à des tailles de quelques dizaines de pc tout en perdant de la masse au cours du processus ([Pfalzner 2009](#)). Le système solaire s'est probablement formé dans l'un de ces deux environnements, mais lequel ? [Pfalzner \(2013\)](#) ont montré que les amas d'étoiles en combustion comme l'amas de naissance conduiraient à un disque trop petit par rapport à la géométrie actuelle du système solaire et que la forte concentration d'étoiles massives entraînerait une destruction supplémentaire du disque. Par conséquent, il est plus probable que le Soleil soit né dans un grand amas avec des étoiles de forte masse dans son voisinage : ([Adams 2010](#); [Portegies Zwart 2009](#); [Brasser et al. 2012](#); [Pfalzner 2013](#); [Pfalzner et al. 2015](#); [Pfalzner & Vincke 2020](#); [Winter et al. 2020b](#)).

IV.2 Le filament OMC-2/3 : L'analogie le plus proche de l'environnement de naissance de notre Soleil

Existe-t-il des "hot corinos" et/ou des objets WCCC dans des environnements de naissance de type solaire ? Avant le début de cette thèse, presque tous les "hot corinos" et objets WCCC connus étaient situés dans des régions de formation d'étoiles de faible masse telles que les régions de Persée, du Serpens, du Taureau, entre autres. Le "hot corino" situé dans le Nuage Moléculaire d'Orion (OMC), HH212-MM1, est assez isolé des étoiles massives. Son environnement ne remplit pas tous les critères pour être considéré comme analogue à celui du Soleil. Du côté de l'OMC, aucun objet de masse solaire situé dans une région de formation d'étoiles de forte masse n'a été détecté. Par conséquent, nous ne savions pas si les "hot corinos" et/ou les objets WCCC étaient présents dans un environnement analogue à celui dans lequel notre Soleil est né. Afin de déterminer si le Soleil a connu une phase de "hot corino", une phase de WCCC, ou ni l'un ni l'autre, nous devons rechercher ces objets dans un environnement de naissance similaire à celui du Soleil.

Jusqu'à présent, l'analogie le mieux connue est le filament OMC-2/3. Ce filament est situé dans le nuage moléculaire d'Orion A à une distance de (393 ± 25) pc ([Großschedl et al. 2018](#)) et fait partie du filament de forme intégrale (ISF ; [Bally et al. 1987](#)) de 1° de long. OMC-2/3 est situé dans la partie nord de l'ISF, au nord de OMC-1, le "cœur chaud" connu ([Batria et al. 1983](#)) qui est associé à la nébuleuse d'Orion. Le filament OMC-2/3 est composé de deux nuages moléculaires, OMC-2 et OMC-3. OMC-2 est le nuage sud et a été identifié pour la première fois par [Gatley et al. \(1974\)](#) tandis que OMC-3 est le nuage nord et a été clairement identifié en 1997 par [Chini et al.](#) (bien que la toute première référence à OMC-3 apparaisse dans [Kutner et al. 1976](#)). Les deux nuages sont limités par deux régions HII majeures, NGC1977 au nord (alimentée par des étoiles B), et l'amas du Trapèze au sud (alimenté par des étoiles O et B). De plus, trois étoiles B sont situées à l'Est du filament OMC-2/3, il s'agit de la région HII M43. Les deux nuages OMC semblent avoir des stades d'évolution différents, OMC-3 étant plus jeune que OMC-2 : (par ex. [Castets & Langer 1995](#); [Chini et al. 1997](#); [Lis et al. 1998](#)).

OMC-2/3 est l'un des sites actifs les plus connus des régions de formation d'étoiles (e.g [Rayner et al. 1989](#); [Bally et al. 1991](#); [Jones et al. 1994](#); [Ali & Depoy 1995](#)) et a été largement étudié depuis sa découverte. Une multitude d'objets pré-stellaires, de classe 0, de classe I et d'étoiles PMS ont été détectés dans la région grâce à des observations submillimétriques et infrarouges : ([Rayner et al. 1989](#); [Mezger et al. 1990](#); [Jones et al. 1994](#); [Chini et al. 1997](#); [Lis et al. 1998](#); [Johnstone & Bally 1999](#); [Nielbock et al. 2003](#); [Megeath et al. 2012](#); [Stutz et al. 2013](#); [Furlan et al. 2016](#); [Kainulainen et al. 2017](#); [Tobin et al. 2020](#)). Grâce à la haute résolution angulaire atteinte par les interféromètres tels que VLA et ALMA, le nombre de sources détectées dans le filament OMC-2/3 est loin des six sources originales détectées dans OMC-2 par [Mezger et al. \(1990\)](#) (étiquetées FIR1 à FIR6). La population relativement jeune du filament OMC-2/3 est confortée par la présence de plusieurs écoulements moléculaires, de nœuds H_2 et d'objets Herbig-Haro (e.g. [Castets & Langer 1995](#); [Yu et al. 1997, 2000](#); [Aso et al. 2000](#); [Williams et al. 2003](#); [Takahashi et al. 2008](#); [Gómez-Ruiz et al. 2019](#); [Feddersen et al. 2020](#)) ainsi que des émissions radio et de rayons X vers certaines des sources (par ex. [Reipurth et al. 1999](#); [Tsuboi et al. 2001](#); [Tobin et al. 2020](#)). D'autres types d'objets, tels que de jeunes naines brunes, ont également été détectés dans OMC-2/3 ([Peterson et al. 2008](#)).

Le filament d'OMC-2/3 est particulièrement intéressant car c'est la région la plus

proche contenant des étoiles en formation de faible à forte masse, et elle est entourée d'étoiles OB brillantes. Par conséquent, cette région remplit toutes les conditions pour être étiquetée comme un environnement semblable à la naissance du Soleil. De plus, OMC-2/3 est une cible unique pour sonder l'effet d'un environnement fortement illuminé sur une possible diversité chimique parmi les proto-étoiles de type solaire d'OMC-2/3.

V Faire la lumière sur le passé chimique du Soleil : Objectifs de la thèse

Il est maintenant clair que toutes les proto-étoiles de masse solaire ne partagent pas le même contenu chimique. Cela ne facilite pas la compréhension du passé chimique de notre Soleil. En raison de la corrélation trouvée entre l'abondance des iCOMs dans les "hot corinos" et ceux trouvés dans les comètes, on soupçonne que notre Soleil a connu une phase de corino chaud [e.g.] [CC2014, drozdovskaya2019, bianchi2019]. Mais est-ce vraiment le cas ? Notre Soleil pourrait-il, au contraire, avoir subi une phase WCCC, ou même une phase hybride ? Jusqu'à récemment, la plupart des proto-étoiles de masse solaire qui ont été ciblées pour des études astronomiques sont situées dans des régions de formation d'étoiles de faible masse. Ces régions sont relativement proches (≤ 300 pc) et sont donc faciles à observer. Néanmoins, notre Soleil est plus probablement né dans un grand amas stellaire, avec des étoiles de forte masse dans son voisinage. Des efforts pour caractériser la nature chimique des proto-étoiles de masse solaire situées dans ce type de régions sont nécessaires pour faire un pas en avant dans la compréhension de l'histoire chimique de notre Soleil.

Avant de commencer cette thèse, il n'existait aucune étude systématique de la nature chimique des proto-étoiles de masse solaire situées dans une région similaire à celle dans laquelle notre Soleil est né. De plus, il n'y avait aucune détection de "hot corino" ou de sources WCCC dans de telles régions. Le but ultime de ma thèse était (et est toujours) de faire la lumière sur la nature chimique des proto-étoiles de masse solaire dans une région analogue à l'environnement de naissance du Soleil. Je souhaite également apporter de nouveaux éléments de preuve pour compléter le puzzle du passé chimique du Soleil. De plus, cette thèse vise aussi à comprendre ce qui pourrait causer la diversité chimique observée au stade protostellaire.

Le premier objectif immédiat de la thèse est de comprendre l'influence d'un champ de rayonnement UV accru dans une région de formation d'étoiles et l'augmentation de la température du nuage natal, qui sont deux paramètres susceptibles de jouer un rôle dans le résultat chimique de l'environnement protosolaire. Je cherche donc à comprendre quels types d'objets sont présents dans une région similaire à celle dans laquelle notre Soleil est probablement né. Y a-t-il principalement des "hot corinos", des objets WCCC ou des objets hybrides dans ce type de région ? Pour répondre à cette question, j'ai étudié la nature chimique de plusieurs proto-étoiles de masse solaire situées dans le filament OMC-2/3, le meilleur analogue le plus proche de l'environnement de naissance du Soleil. Si un type d'objet est plus abondant que les autres, cela peut constituer une première piste sur l'ancienne nature chimique du Soleil : si les "hot corinos" sont prédominants, cela indiquerait l'ancienne nature "hot corino" de notre Soleil. Si, au contraire, les objets WCCC sont prédominants dans cette région, alors l'ancienne nature chimique de notre Soleil pourrait être davantage liée à une chimie de type WCCC.

Le second objectif de cette thèse concerne la diversité chimique des proto-étoiles de masse solaire. Les deux principales hypothèses sur ce qui pourrait causer la diversité chimique parmi les proto-étoiles de faible masse sont l'échelle de temps de la phase du noyau pré-stellaire et l'illumination UV externe. Dans cette thèse, j'ai étudié l'illumination UV externe, c'est-à-dire le facteur environnemental. La région ciblée, le filament OMC-2/3, est délimitée par plusieurs régions HII, ce qui la rend particulièrement lumineuse. J'ai comparé le contenu chimique des proto-étoiles de masse solaire situées dans le filament OMC-2/3 et dans le nuage moléculaire de Persée. Le premier est une région de formation d'étoiles de faible à forte masse qui est fortement illuminée par les UV, tandis que le second est une région de formation d'étoiles qui n'abrite que des proto-étoiles de faible masse et qui est nettement moins illuminée par les UV qu'OMC-2/3. La comparaison de ces deux régions est utile pour comprendre si, et comment, l'environnement joue un rôle dans la diversité chimique observée au stade protostellaire. Si les "hot corinos" prédominent dans l'une des deux régions et que les sources WCCC prédominent dans l'autre, cela suggérerait que l'illumination UV peut jouer un rôle dans le façonnement de la nature chimique des proto-étoiles. Au contraire, si les deux régions présentent un contenu similaire en termes de "hot corinos", d'objets WCCC ou de sources hybrides, alors l'environnement n'est peut-être pas à l'origine de la diversité chimique observée parmi les proto-étoiles de masse solaire.

VI Résultats

VI.1 Papier I: La chasse aux "hot corinos" et aux objets WCCC dans le filament OMC-2/3

Le premier projet que j'ai réalisé était de chercher des "hot corinos" et des candidats WCCC dans le filament OMC-2/3, en utilisant des observations venant de télescopes à antenne unique ("single-dish telescopes"). Au moment de cette première étude, il n'y avait aucune preuve de la présence de tels objets dans cette région. Le seul "hot corino" détecté dans le nuage moléculaire d'Orion est la proto-étoile HH212 (Codella et al. 2016). Cependant, la proto-étoile HH212 est isolée et n'est pas considérée comme étant située dans un environnement similaire à celui dans lequel notre Soleil est né.

Une poignée d'études ont été réalisées pour évaluer la nature chimique des proto-étoiles de faible masse et pour comprendre les "hot corino" et les objets WCCC. Ces travaux ont étudié plusieurs régions de formation d'étoiles de faible masse en utilisant des observations venant de télescopes à antenne unique (échelle ~ 10000 au) de petites chaînes carbonées (CC) et de iCOMs, molécules caractéristiques des sources WCCC et des "hot corinos", respectivement. Ils ont dérivé le rapport d'abondance $[CC]/[iCOMs]$ (par exemple $[CCH]/[CH_3OH]$, $[C_4H]/[CH_3OH]$; Lindberg et al. 2016; Graninger et al. 2016; Higuchi et al. 2018) et deux résultats principaux sont ressortis de ces études : (1) la majorité des sources étudiées présentent un contenu chimique qui est en transition entre les "hot corinos" et les sources WCCC, c'est-à-dire $[CC]/[iCOMs] \sim 1$ (Lindberg et al. 2016; Graninger et al. 2016; Higuchi et al. 2018), et (2) les "hot corinos" ont tendance à être situés au centre du nuage tandis que les sources WCCC sont situées près des bords des nuages ou de manière isolée (Lefloch et al. 2017; Higuchi et al. 2018). Il existe des mises en garde concernant le choix de molécules effectué par ces études. Tout d'abord, les chaînes carbonées sont généralement abondantes dans les régions de photodissociation

(PDR), ce qui signifie que leur distribution spatiale peut être assez étendue (par ex. [Pety et al. 2005](#); [Cuadrado et al. 2015](#)). Deuxièmement, le méthanol, l'iCOM le plus utilisé dans ces études, est détecté dans les PDRs et les nuages moléculaires (par ex. [Leurini et al. 2010](#); [Guzmán et al. 2013](#); [Cuadrado et al. 2017](#); [Punanova et al. 2018](#)). Les observations effectuées avec des télescopes à antenne unique sont limitées en résolution spatiale, et il n'est pas toujours possible de séparer les proto-étoiles de leur environnement. Des contributions importantes peuvent donc être attribuées au PDR environnant ou au nuage moléculaire dans lequel se trouvent les sources.

Les objectifs de cette étude étaient doubles : (1) rechercher des candidats "hot corino" et des sources WCCC dans le filament OMC-2/3 et (2) vérifier la fiabilité de l'utilisation de télescopes à antenne unique pour observer des chaînes carbonées et du méthanol, et pour déterminer la nature chimique des proto-étoiles de masse solaire. Pour atteindre ces objectifs, j'ai dérivé le rapport d'abondance $[CCH]/[CH_3OH]$ pour neuf proto-étoiles de masse solaire (classes 0 et I) en utilisant trois ensembles d'observations. Deux d'entre eux sont des observations à pointage unique (IRAM-30m à 1,3 mm et Nobeyama 45m à 3 mm ; P.I. Ana López-Sepulcre), et le troisième est constitué d'observations cartographiques à 3 mm (IRAM-30m ; P.I. Mathilde Bouvier), centrées sur l'une des sources.

Les résultats des observations à pointage unique ont montré que les raies de CCH et CH_3OH étaient plus étroites que prévu, avec des largeurs de raie comprises entre 0,8 et 1,6 $km.s^{-1}$. Les paramètres physiques dérivés, obtenus à la fois avec des analyses assumant l'équilibre thermodynamique local (ETL) et des analyses hors ETL, ont montré que toutes les sources ont une densité de gaz et une température similaires, cette dernière étant faible (≤ 30 K) pour CCH et CH_3OH . Ces deux résultats sont incompatibles avec l'hypothèse que les raies émises proviennent de la partie interne de l'enveloppe des proto-étoiles. Dans toute la région cartographiée, nous avons trouvé que le gaz émettant du méthanol avait une température et une densité constantes. Nous avons également constaté une diminution du rapport d'abondance $[CCH]/[CH_3OH]$ du nord au sud du nuage, le nord étant plus éclairé et le sud étant plus protégé des radiations UV. Nous avons donc conclu que l'émission de raies n'est pas associée aux proto-étoiles mais plutôt au gaz du nuage parent. Enfin, nous avons comparé les densités de colonne de CCH et CH_3OH dérivées dans cette étude avec celles d'autres objets WCCC, "hot corinos", PDRs et nuages moléculaires. Nous avons constaté que l'émission de raies des deux espèces, CCH et CH_3OH , est probablement dominée par le PDR entourant le nuage moléculaire dans lequel se trouvent les proto-étoiles.

En conclusion, il faut être prudent lorsqu'on détermine la nature chimique des proto-étoiles de masse solaire en utilisant des télescopes à antenne unique pour observer CH_3OH , CCH, et autres petites chaînes carbonées par extension. Ces espèces peuvent être émises par des composants externes qui ne sont pas directement liés aux proto-étoiles. L'utilisation du rapport d'abondance $[CC]/[iCOMs]$ n'est pas fiable, notamment dans les régions fortement illuminées par l'UV. Nous n'avons pas pu trouver de "hot corinos" ou de candidats WCCC dans le filament OMC-2/3. La prochaine étape consiste à utiliser l'interférométrie qui nous permettra de nous débarrasser de la contamination externe et de sonder la région interne de l'enveloppe des proto-étoiles.

VI.2 Papier II & III: ORion Alma New GEneration Survey (ORANGES)

L'étude précédente a montré que pour le filament OMC-2/3 fortement illuminé par les radiations UV, les observations du radical éthyne (CCH) et du méthanol (CH_3OH) en utilisant des télescopes à antenne unique ne sont pas fiables pour détecter les candidats "hot corinos" et WCCC. Nous devons sonder des échelles plus petites pour limiter la contamination de la région par le PDR omniprésent l'entourant. L'interférométrie est le meilleur moyen pour cela, et les deux études suivantes sont basées sur des observations interférométriques.

L'étude ORANGES ("ORion Alma New GEneration Survey") vise à étudier le contenu moléculaire des proto-étoiles de masse solaire situées dans le filament OMC-2/3. Il s'agit du suivi de l'étude précédente. Pour déterminer la nature chimique des proto-étoiles de masse solaire d'Orion, nous avons besoin d'une résolution angulaire suffisamment élevée pour sonder la partie interne de leur enveloppe. Le projet ORANGES consiste en des observations ALMA à 1,3mm avec une résolution angulaire de $0,25''$ (~ 100 au) (P.I. Ana López-Sepulcre). Un fait notable concernant ORANGES est que ce projet a été conçu pour être directement comparable au "PERseus Alma CHEmistry Survey" ("PEACHES", PECHES en français ; P.I. N. Sakai). PECHES est un projet de suivi de l'étude des proto-étoiles de masse solaire situées dans le nuage moléculaire de Persée (Higuchi et al. 2018) qui sonde la complexité chimique de ces proto-étoiles. Les projets ORANGES et PECHES sont complémentaires car ils ciblent deux environnements très différents. D'une part, le nuage moléculaire de Persée est un proto-amas dépourvu d'étoiles massives, où seulement des étoiles de faible masse se forment. D'autre part, le filament OMC-2/3 est un amas plus dense avec des étoiles de masse élevée ($\geq 8 M_\odot$) dans son voisinage. La comparaison de la nature chimique des proto-étoiles de masse solaire situées dans ces deux environnements peut donner des contraintes sur le rôle de l'environnement sur la chimie des régions protostellaires internes. La distance entre les deux nuages a été prise en compte pour éviter tout biais observationnel. Le projet ORANGES sonde donc les mêmes échelles angulaires et atteint la même sensibilité que le projet PECHES.

Ce chapitre est divisé en trois sous-sections correspondant à trois études. La première est l'étude du continuum de la poussière de 16 proto-étoiles de masse solaire du filament OMC-2/3. Plusieurs paramètres de la poussière et de l'émission "free-free" sont extraits des proto-étoiles et l'objectif principal de l'étude est de comprendre si la forte illumination UV du filament a un impact sur les propriétés de la poussière des proto-étoiles. Ensuite, la deuxième étude se concentre sur l'analyse du méthanol. L'objectif est de déterminer combien de "hot corinos" sont situés dans le filament OMC-2/3 et si la nature chimique des proto-étoiles de masse solaire est affectée par l'environnement dans lequel elles sont situées. Avant de commencer la thèse de doctorat, aucun "hot corino" ni d'objet WCCC n'avait été identifié dans le filament OMC-2/3. Au moment où j'ai travaillé sur le projet ORANGES, deux "hot corinos" (Hsu et al. 2020; Chahine et al. 2021) ont été identifiés dans le filament. Enfin, la dernière étude concerne la chasse au CCH dans le filament OMC-2/3. J'ai cartographié l'émission CCH sur mon échantillon de sources. Comme expliqué ci-dessous, les données ALMA actuellement disponibles sont insuffisantes pour permettre la recherche des objets WCCC.

VI.2.1 Papier II: ORANGES I. Continuum de poussière et émission "free-free" des proto-étoiles du filament OMC-2/3

Plusieurs propriétés physiques peuvent être extraites de l'analyse du continuum de la poussière des sources protostellaires. Les distributions d'énergie spectrale (SED) sont un outil puissant pour classer les jeunes objets stellaires (YSO) et dériver leurs paramètres physiques, ainsi que plusieurs paramètres de la poussière. La présence d'émission Bremsstrahlung thermique peut également être extraite des SEDs. Pour ce faire, nous avons besoin de points de données dans le centimètre, où l'émission Bremsstrahlung peut dominer. La détermination de la présence (ou de l'absence) de l'émission Bremsstrahlung peut fournir des indications sur la jeunesse de la source : (par ex. [André et al. 1988](#); [Anglada 1995](#); [Anglada et al. 2018](#); [Shirley et al. 2007](#)). Si nous ne tenons pas compte de cette contribution Bremsstrahlung, cela peut conduire à une sous-estimation des indices spectraux. Il est donc essentiel de dissocier la poussière de l'émission Bremsstrahlung.

Les études de continuum de la poussière sur les proto-étoiles de masse solaire dans les régions de formation d'étoiles de faible à forte masse, comme le filament OMC-2/3, sont rares. Ces régions sont plus éloignées que les régions de formation d'étoiles de faible masse, ce qui signifie qu'elles sont plus difficiles à observer. Les seules études disponibles sont celles de l'*Herschel* Orion Protostar Survey (HOPS; [Megeath et al. 2012](#); [Fischer et al. 2013](#); [Furlan et al. 2016](#)) et de l'étude VANDAM (par ex. [Tobin et al. 2019, 2020](#)). La première vise à classer et à caractériser la population de proto-étoiles d'Orion, tandis que la seconde vise à étudier les disques protostellaires des proto-étoiles de classe 0 et I.

Cette première étude ORANGES vise à caractériser les propriétés de la poussière des sources OMC-2/3, et à comprendre si les propriétés de la poussière sont affectées à petite échelle (≤ 100 au) par les régions HII proches, comme c'est le cas pour l'émission de raies à plus grande échelle (≤ 10000 au). Pour atteindre ces objectifs, j'ai construit des SEDs du millimétrique au centimétrique en utilisant des données d'archives ALMA (0.87mm) et VLA (9mm) du projet VANDAM ([Tobin et al. 2020](#)). J'ai pu dériver des propriétés essentielles pour chaque source : multiplicité, contraintes sur la température et la masse de la poussière dans la région immédiate autour de la proto-étoile (échelle de 100-1000 au), indice spectral d'émissivité de la poussière et émission Bremsstrahlung.

Les observations sont centrées sur les neuf proto-étoiles de masse solaire détectées avec des observations faites avec des télescopes à antenne unique. Grâce à la haute résolution angulaire de nos observations ALMA, plusieurs sources ont montré une multiplicité. Au total, j'ai détecté 28 sources, dont 18 à l'intérieur du rayon primaire. Il n'y avait pas assez de données pour 2 de ces 18 sources, donc seulement 16 sources ont été analysées. Les cartes du continuum des sources montrent que la plupart d'entre elles sont bien concentrées et que l'émission de la poussière s'étend de manière asymétrique. Nous avons trouvé que 67% de nos sources sont des systèmes multiples, ce qui est cohérent avec ce qui a été trouvé dans d'autres études : [par ex.] [looney2000](#), [maury2010](#), [enoch2011](#), [tobin2013](#). Nous avons également trouvé une anticorrélation marginale (coefficient de Pearson de -0.58) entre le nombre de proto-étoiles dans chaque système et la distance du système dans le filament OMC-2/3. La multiplicité des sources semble être plus élevée au sud du filament, mais les statistiques sont trop faibles pour confirmer ce résultat.

A partir des SEDs, nous avons pu contraindre plusieurs paramètres de la poussière. Pour les sources ne présentant pas de multiplicité à la résolution angulaire de nos observations, nous avons utilisé leur luminosité bolométrique (provenant de HOPS) pour calculer la température radiative de la poussière. Cette température peut être utilisée comme une

approximation de la température de la poussière et fournit des contraintes supplémentaires sur ce paramètre. Nous avons pu contraindre la température de la poussière pour 11 des 16 sources. Nous avons classé six sources comme très chaudes ($T \geq 90$ K), trois sources comme chaudes ($T \geq 50$ K) et deux sources comme froides ($T \leq 50$ K).

Une fois la température de la poussière contrainte, nous avons pu contraindre tous les autres paramètres. Pour les indices spectraux d'émissivité de la poussière, la majorité des sources (9/16) ont des indices < 1 . Différentes interprétations peuvent expliquer le faible indice, comme la croissance des grains (contribution du disque), une grande profondeur optique et/ou l'auto-diffusion de la poussière, et la composition des grains de poussière [par ex.] [aanestadt1975, MN1993, OH94, agladze1996, mennella1998, draine2006, coupeaud2011, jones2013, jones2017, wong2016, ysard2019]. Nous avons pris en compte la profondeur optique de la poussière lors de la construction des SEDs, ce paramètre ne devrait donc pas être la principale explication des faibles indices spectraux d'émissivité de la poussière. Les masses dérivées (enveloppe+disque) sont comprises entre 2×10^{-4} et $0,1 M_{\odot}$. Elles sont pour la plupart en bon accord avec celles dérivées dans [Tobin et al. \(2020\)](#). Ensuite, $\sim 31\%$ de l'échantillon de sources montrent des preuves d'émission Bremsstrahlung. En comparant avec l'étude précédente de [Reipurth et al. \(1999\)](#), nous avons trouvé quelques divergences. Ils ont détecté une émission Bremsstrahlung vers MMS2 alors que nous l'avons pas fait et ils n'ont pas détecté d'émission Bremsstrahlung vers FIR2 et MMS5 alors que nous l'avons fait. Cela peut être dû soit à une différence de sensibilité entre les observations de l'étude VANDAM et celles de [Reipurth et al. \(1999\)](#), soit à la différence de fréquence à laquelle les observations ont été effectuées. Enfin, nous avons pu confirmer ou corriger la classification des proto-étoiles du filament OMC-2/3 à partir des indices spectraux d'émissivité de la poussière extraits, de la température de la poussière, de la température bolométrique et de la présence d'accrétion provenant d'études précédentes : (par ex. [Williams et al. 2003](#); [Takahashi et al. 2008](#); [Tobin et al. 2016b](#); [Tanabe et al. 2019](#); [Feddersen et al. 2020](#)). Nous avons confirmé et corrigé la classification de 10 et 6 sources, respectivement.

Un des objectifs de cette étude est également de comprendre si les régions HII proches affectent les propriétés de la poussière des proto-étoiles OMC-2/3 de masse solaire. Tout d'abord, nos résultats montrent que les sources les plus froides semblent être situées au centre du filament OMC-2/3 alors que les sources les plus chaudes semblent être situées sur les bords. Cependant, en raison des pauvres statistiques et parce que nous n'avons pas pu contraindre suffisamment la température pour 5 sources, nous ne pouvons pas conclure si la température de la poussière des sources est affectée par les régions HII proches. Ensuite, nous n'avons pas trouvé de corrélation entre la masse (enveloppe+disque) et la position des sources dans le filament, ni entre l'indice spectral d'émissivité de la poussière et la position des sources dans le filament. Nos résultats montrent donc que les propriétés de la poussière des proto-étoiles OMC-2/3 de masse solaire ne sont probablement pas affectées à petite échelle par les régions HII proches, et que la formation des proto-étoiles a lieu simultanément dans tout le filament. De toute évidence, des études statistiques plus importantes sont nécessaires pour tirer des conclusions définitives sur l'impact de la présence de sources UV externes et proches sur la formation des proto-étoiles.

VI.2.2 La nature chimique des proto-étoiles d'Orion : Les ORANGES sont-elles différentes des PECHES ? ORANGE II.

L'étude de la nature chimique des proto-étoiles de masse solaire pour comprendre le passé chimique de notre Soleil n'est pas facile car les proto-étoiles de masse solaire ne partagent pas toutes la même histoire chimique. En particulier, les "hot corinos" et les objets WCCC, deux types de proto-étoiles chimiquement distincts, montrent à quel point la gamme de composition des enveloppes protostellaires peut être large. Néanmoins, des études récentes ont montré des similitudes entre l'abondance des iCOMs dans les corinos chauds et les comètes (par ex. ?Drozdovskaya et al. 2019; Rivilla et al. 2020). On pense donc que notre Soleil est un ancien "hot corino".

Jusqu'à récemment, seule une douzaine de "hot corinos" avaient été identifiés. Grâce à l'arrivée de puissants interféromètres (sub)-millimétriques tels que ALMA, de nombreux nouveaux "hot corinos" ont été découverts. Le récent projet PECHES a révélé que les "hot corinos" sont probablement prédominants dans la région de formation d'étoiles de faible masse de Persée (Yang et al. 2021). PECHES et la plupart des études visant à étudier la nature chimique des proto-étoiles de masse solaire (par exemple Bergner et al. 2017; Belloche et al. 2020; van Gelder et al. 2020; Yang et al. 2021) se concentrent sur les régions de formation d'étoiles de faible masse alors que notre Soleil est probablement né dans un grand amas, avec des étoiles massives dans son voisinage (Adams 2010; Pfalzner et al. 2015). Les "hot corinos" sont-ils également abondants dans de telles régions ? Nous devons cibler les proto-étoiles de masse solaire dans des régions similaires à celle dans laquelle notre Soleil est plus probablement né, c'est-à-dire à proximité d'étoiles massives. Le filament OMC-2/3 est le meilleur et le plus proche analogue de l'environnement de naissance du Soleil, car plusieurs régions HII proches entourent le filament. Très récemment, les protoétoiles de masse intermédiaire MMS6 et HOPS-370 (OMC-2 FIR3), et la protoétoile de masse solaire HOPS-108 ont été les premiers "hot corinos" à être identifiés dans le filament OMC-2/3 Hsu et al. 2020; Chahine et al. 2021. Les "hot corinos" sont donc présents dans les régions de formation d'étoiles massives, mais la statistique est trop faible pour conclure sur l'ancienne nature chimique de notre Soleil. Les objectifs de cette deuxième étude ORANGES sont d'identifier combien de "hot corinos" sont présents dans le filament OMC-2/3 et de comprendre si l'environnement joue un rôle dans la composition chimique des enveloppes protostellaires, ou non. Pour cela, nous avons effectué une analyse des raies moléculaires en nous concentrant sur le méthanol, l'iCOM le plus communément trouvé dans les "hot corinos".

Nous avons détecté du méthanol vers le centre de 5 des 19 sources étudiées. En utilisant des méthodes de transfert radiatif, nous avons constaté que le gaz à partir duquel le méthanol est émis est chaud (≥ 85 K), dense ($n \geq 3 \times 10^6$ cm⁻³), et compact ($\theta \sim 39-136$ au de diamètre). Suivant la définition large des "hot corinos" (Ceccarelli 2004; Ceccarelli et al. 2007) ces cinq sources sont des authentiques "hot corinos". En comparant l'intensité intégrée de l'une des raies d'émission du méthanol avec les profondeurs optiques de la poussière dérivées dans Bouvier et al. (2021), nous n'avons trouvé aucune corrélation. La profondeur optique de la poussière n'est donc pas le principal paramètre affectant la détection des "hot corinos". Enfin, en ajoutant aux 5 nouveaux corinos chauds, MMS6, HOPS-370 et HOPS-108, nous avons un taux de détection des corinos chauds dans OMC-2/3 qui est inférieur à 51% dans les barres d'erreur. Comparé au (56 pm14)% trouvé dans la région de Persée, les corinos chauds semblent être plus rares dans une région illuminée par un fort rayonnement UV. L'environnement joue donc probablement un rôle dans le

contenu chimique de la masse solaire.

VI.2.3 L'identification difficile des objets WCCC dans le filament OMC-2/3

Avec ORANGES, nous cherchons à étudier la nature WCCC des proto-étoiles de l'OMC-2/3. Pour identifier les objets WCCC, il faut étudier les hydrocarbures. Les espèces les plus ciblées dans les études sont CCH, C₄H et c-C₃H₂ car ce sont les principales molécules liées aux hydrocarbures qui sont abondantes dans les sources WCCC (Sakai et al. 2008a, 2009a). Les chaînes de carbone produites par le mécanisme WCCC sont distribuées entre ~1000 et ~3000 au autour de la proto-étoile (e.g. Sakai et al. 2010, 2014a,b, 2016; Sakai & Yamamoto 2013; Oya et al. 2017; Taniguchi et al. 2021b). De plus, l'émission des chaînes carbonées montre un léger manque d'émission allant de 100 à 600 au de rayon autour de la position du pic du continuum des sources. Par conséquent, nous nous attendons à voir des caractéristiques similaires dans l'émission des chaînes carbonées vers l'échantillon de sources OMC-2/3, si elles ont une zone WCCC. Les configurations observationnelles d'ORANGES comprennent plusieurs transitions de CCH et de c-C₃H₂. Suite à mon étude avec les observations "single-dish" (Chapitre 2), j'ai d'abord étudié l'émission CCH. Je présente également des résultats préliminaires pour c-C₃H₂.

La transition CCH incluse dans les configurations spectrales ORANGES est la transition N=3-2 avec un niveau d'énergie supérieur $E_{\text{up}} = 25.2$ K. J'ai choisi de cartographier la raie la plus intense parmi les diverses composantes de la structure hyperfine, qui a sa fréquence à 262064 MHz, et un coefficient d'Einstein de $A_{ij} = 4.89 \times 10^{-5} \text{s}^{-1}$. Pour c-C₃H₂, j'ai sélectionné la raie de transition $3_{2,1} - 2_{1,2}$ à une fréquence de 244222 MHz, et avec les paramètres spectraux $E_{\text{up}} = 18,2$ K et $A_{ij} = 5,9 \times 10^{-5} \text{s}^{-1}$.

CCH est détecté vers chacun des neuf champs ciblés tandis que c-C₃H₂ est détecté uniquement vers FIR2. Dans FIR6c-a, l'émission CCH semble tracer les parois de la cavité de l'écoulement moléculaire. Ce résultat est cohérent avec ce qui est trouvé dans d'autres sources, car CCH est connu pour être un bon traceur des cavités de sortie (e.g. Zhang et al. 2018; Tychoniec et al. 2021; Okoda et al. 2020; Chuang et al. 2021). Pour plusieurs autres systèmes (FIR2, MMS5, SIMBA-a, FIR1a-b) cela pourrait être aussi le cas mais l'émission est trop amorphe pour conclure. Dans la littérature, des outflows ont été détectés vers tous les systèmes ORANGES sauf vers COS3 (e.g. Williams et al. 2003; Takahashi et al. 2008; Tobin et al. 2016b; Tanabe et al. 2019; Gómez-Ruiz et al. 2019; Matsushita et al. 2019; Feddersen et al. 2020; Nagy et al. 2020). La direction de l'écoulement à grande échelle des systèmes CSO33, MMS2 et MMS9 est connue, mais comme il n'existe pas d'observations à haute résolution angulaire de l'écoulement de ces systèmes, on ne sait pas lequel des composants conduit l'écoulement. Dans les autres sources, l'origine de l'émission de CCH n'est pas totalement claire (e.g. MMS9-a, CSO33-b) et semble tracer plusieurs composants (e.g. cavité d'écoulement, enveloppes circumstellaires). Dans l'ensemble, des informations supplémentaires sur les écoulements des sources sont obligatoires pour interpréter l'émission CCH avec précision. Pour FIR2, l'émission de c-C₃H₂ est similaire à celle de CCH, bien que légèrement moins étendue.

Les résultats de l'étude de l'émission des chaînes carbonées vers les sources d'OMC-2/3 montrent que l'émission CCH est relativement informe dans tous les systèmes, à l'exception de FIR6c-a dans lequel elle trace clairement les parois de la cavité de l'écoulement moléculaire. De plus, l'émission de c-C₃H₂ n'est observée que dans un seul objet (FIR2) alors que cette espèce est plutôt répandue dans les WCCCs. J'ai mentionné précédemment que si une zone WCCC est présente autour de la proto-étoile, l'émission est observée à des

échelles allant de 100 à 3000 au (de rayon). La plus grande échelle angulaire récupérable avec les observations d'ORANGES est d'environ 800 au. Ceci suggère qu'il n'y a pas d'objets WCCC, ou que la zone WCCC, si elle est présente, pourrait être résolue. La proto-étoile FIR2 pourrait être un candidat WCCC possible, mais comme l'émission est filtrée, je ne peux pas évaluer correctement la présence de sources WCCC aux échelles sondées par les observations ALMA.

Ces résultats suggèrent que le ciblage seul de CCH et $c\text{-C}_3\text{H}_2$ n'est pas suffisant pour détecter des sources WCCC. Pour tirer des conclusions solides, il pourrait être nécessaire de cibler d'autres (longues) chaînes carbonées (par exemple CH_3CCH , HC_5N , C_4H_2). De plus, nous devons sonder des échelles plus grandes que celles d'ORANGES pour éviter de résoudre une éventuelle zone WCCC. Cette conclusion a également été faite par [Yang et al. \(2021\)](#) avec le projet PEACHES. Ils ont trouvé que l'émission CCH est associée à l'outflow des sources. D'autre part, le $c\text{-C}_3\text{H}_2$ n'est détecté (voir leur Fig. 7) vers aucune des sources de Persée, alors que cette espèce est observée à plus grande échelle (à ~ 3000 au ; [Higuchi et al. 2018](#)). Ils concluent également que des observations sondant des échelles intermédiaires sont nécessaires.

En conclusion, en utilisant les observations ORANGES, je n'ai pas été capable de détecter des objets WCCC dans le filament OMC-2/3. Ceci est principalement dû à une stratégie d'observation sous-optimale en termes d'échelles angulaires sondées, de variété de traceurs moléculaires, et peut-être aussi de sensibilité. Des observations supplémentaires sont nécessaires pour répondre à la question de savoir si ces objets sont présents dans le filament OMC-2/3, et donc dans un environnement similaire à celui dans lequel notre Soleil est né.

VII Conclusions et perspectives

VII.1 Conclusions

Le but ultime de cette thèse était de faire la lumière sur la nature chimique des proto-étoiles de masse solaire dans un environnement similaire à celui dans lequel notre Soleil est probablement né. En pratique, j'ai cherché à répondre aux questions suivantes :

1. Quelle est la nature chimique des proto-étoiles de masse solaire situées dans une région analogue à l'environnement de naissance du Soleil ? Y a-t-il des majoritairement des "hot corinos", des objets WCCC, des sources hybrides ? Notre Soleil est-il un ancien "hot corino" ?
2. L'environnement joue-t-il un rôle dans le façonnement de la nature chimique des proto-étoiles de masse solaire et si oui, comment ? Est-il à l'origine de la diversité chimique observée parmi les proto-étoiles de type solaire ?

Pour répondre à ces questions, j'ai étudié la nature chimique d'un échantillon de proto-étoiles de masse solaire situées dans le filament OMC-2/3, le meilleur analogue de l'environnement de naissance du Soleil, à grande (≤ 10000 au) et petite (~ 100 au) échelles. J'ai utilisé plusieurs jeux de données observationnelles, provenant d'observations "single-dish" et interférométriques, et j'ai effectué des analyses de la poussière et des raies moléculaires. Les principaux résultats de la thèse sont résumés ci-dessous.

L'étude à grande échelle ou comment faire face à un mur de PDR L'étude à grande échelle (≤ 10000 au) s'est avérée être parsemée de pièges. Le premier objectif de cette étude était de déterminer si des "hot corinos" et des candidats WCCC étaient présents le long du filament OMC-2/3. Pour cela, j'ai utilisé les observations IRAM-30m et Nobeyama-45m vers neuf proto-étoiles de masse solaire (Classes 0 et I) du filament OMC-2/3. J'ai ciblé deux espèces, CCH et CH₃OH, connues pour être des traceurs standards des sources WCCC et des "hot corinos", respectivement. Plus précisément, en suivant les travaux précédents (Graninger et al. 2016; Lindberg et al. 2016; Higuchi et al. 2018), j'ai utilisé le rapport d'abondance [CCH]/[CH₃OH] pour évaluer si la proto-étoile est un candidat "hot corino" ([CCH]/[CH₃OH] ≤ 0.5) ou un candidat WCCC ([CCH]/[CH₃OH] ≥ 2). Le second objectif de l'étude était d'évaluer la fiabilité de cette méthode.

De manière inattendue, j'ai constaté que le profil des raies de CCH et de CH₃OH était similaire et étroit (≤ 2 km/s), ce qui suggère que les deux espèces proviennent de la partie externe de l'enveloppe de la proto-étoile et/ou du nuage parental, plutôt que de la partie interne. L'analyse des raies moléculaires, en utilisant des méthodes de transfert radiatif LTE et non-LTE, a montré que ces espèces sont émises par un gaz froid (≤ 30 K) remplissant le faisceau du télescope. La densité et la température du gaz ne changent pas dans le filament OMC-2/3, ce qui indique que la région d'émission est commune aux proto-étoiles. De plus, j'ai trouvé des rapports d'abondance [CCH]/[CH₃OH] relativement constants d'environ 5-7 pour toutes les sources, ce qui suggère une chimie homogène. Tous ces résultats suggèrent fortement que l'émission des raies de CCH et de CH₃OH n'est pas associée à l'enveloppe des proto-étoiles mais à une composante commune plus externe. En comparant la densité de colonne de CCH et CH₃OH des proto-étoiles OMC-2/3 avec celle trouvée dans les proto-étoiles du nuage moléculaire de Persée, dans les régions de photo-dissociation, et dans les noyaux pré-stellaires/nuages moléculaires, j'ai trouvé que l'émission de raies est très probablement contaminée par la région de photo-dissociation (PDR) environnante, alimentée par les étoiles OB proches, ou par le nuage parental dans lequel les sources sont intégrées. J'ai conclu que le rapport d'abondance [CCH]/[CH₃OH] obtenu avec les observations "single-dish" n'est pas fiable pour déduire la nature chimique des proto-étoiles de masse solaire. Par conséquent, à partir de ces observations, je n'ai pas pu détecter de candidats "hot corinos" ou WCCC dans le filament OMC-2/3.

L'étude à petite échelle ou comment voir les proto-étoiles en ORANGES Comme la chimie à grande échelle (≤ 10000 au) est régie par les étoiles OB proches, qui créent le PDR et nous empêche ainsi de détecter les "hot corinos" et les sources WCCC, les observations interférométriques à petite échelle (~ 100 au) sont obligatoires. Le projet "ORion ALMA NEw GEneration Survey" (ORANGES) consiste en des observations ALMA de 1,3 mm avec une résolution angulaire spatiale de 0,25'', équivalente à ~ 100 au à la distance du filament OMC-2/3. L'objectif d'ORANGES est de caractériser le contenu chimique des proto-étoiles de masse solaire dans le filament OMC-2/3 à petite échelle.

La première étude ORANGES a consisté en une analyse du continuum de la poussière et de l'émission dite "free-free" des proto-étoiles du filament OMC-2/3. Les objectifs étaient (1) de caractériser les propriétés de la poussière des proto-étoiles (température de la poussière, densité de colonne de la poussière, profondeur optique, émission "free-free" et indice spectral d'émissivité) et (2) de comprendre si elles sont affectées par les étoiles OB proches, comme dans le cas de l'émission de raies à plus grande échelle. Pour atteindre ces objectifs, j'ai extraits et utilisé divers paramètres de poussière et construit la

SED de chaque source du domaine millimétrique au domaine centimétrique. Pour ce faire, j'ai utilisé les données ORANGES de 1,3 mm, complétées par des données d'archives ALMA (0,87 mm) et VLA (9 mm) provenant du projet VANDAM (Tobin et al. 2020). Le résultat principal montre qu'il n'y a pas de tendance claire dans la température de la poussière et les masses dérivées (enveloppe + disque) des sources le long du filament. J'en ai conclu que les propriétés de la poussière à petite échelle ne sont probablement pas affectées par la forte illumination UV de la région.

La deuxième étude ORANGES a porté sur le nombre de "hot corinos" dans le filament OMC-2/3. Les objectifs étaient de déterminer si les "hot corinos" sont abondants dans le filament OMC-2/3 et de comprendre si, et comment, l'environnement fortement éclairé par les UV de la région affecte la nature chimique des sources. Pour atteindre cet objectif, j'ai d'abord examiné l'émission de méthanol, le méthanol étant l'iCOM le plus commun et le plus abondant trouvé dans les "hot corinos", pour détecter la présence de ces objets. Ensuite, j'ai comparé les résultats du filament OMC-2/3 avec ceux du Perseus ALMA Chemistry Survey (PEACHES ; Yang et al. 2021) réalisé dans le nuage moléculaire de Persée, une région de formation d'étoiles de faible masse qui est moins illuminée par l'UV que OMC-2/3. Les résultats de l'étude de Persée ont montré que les "hot corinos" sont plutôt abondants dans Persée, avec (56pm14)% des sources ciblées montrant une forte évidence d'une région "hot corino". Dans OMC-2/3, j'ai détecté cinq nouveaux "hot corinos" sur un échantillon de 19 proto-étoiles de masse solaire. En ajoutant ceux qui étaient déjà connus et les statistiques des études précédentes (Tobin et al. 2019; Hsu et al. 2020; Chahine et al. 2021), ce résultat conduit à un taux de détection de "hot corinos" dans le filament OMC-2/3 de $(31 \pm 20)\%$. Les "hot corinos" semblent donc être plus rares dans un environnement plus illuminé par les UV. Bien que les statistiques soient trop faibles pour tirer des conclusions définitives, ce résultat suggère que l'environnement peut jouer un rôle dans la diversité chimique des proto-étoiles de masse solaire. D'un point de vue statistique, cependant, les deux régions ne montrent qu'une différence marginale dans leur contenu en "hot corinos". Nous devons étudier plus de proto-étoiles de type solaire du filament OMC-2/3 pour augmenter les statistiques et tirer une conclusion solide. Enfin, bien que les "hot corinos" soient présents dans un environnement similaire à celui dans lequel notre Soleil est probablement né, ils ne semblent pas prédominer. Elucider si notre Soleil a connu une phase "hot corino" nécessite des investigations supplémentaires.

Enfin, l'un des objectifs initiaux de la thèse, et d'ORANGES, était de comprendre si les sources WCCC peuvent se former dans une région analogue à l'environnement de naissance du Soleil et si oui, si elles sont abondantes. Pour aborder ce point, j'ai ciblé deux chaînes carbonées, CCH et $c\text{-C}_3\text{H}_2$, des molécules communes et abondantes trouvées dans les sources WCCC. CCH est détecté dans tout le filament mais son émission est relativement informe et il n'est donc pas clair quel composant de la proto-étoile il trace. D'autre part, l'espèce $c\text{-C}_3\text{H}_2$ n'est observée que vers FIR2. Cette dernière pourrait être une candidate WCCC possible mais je n'ai pas pu tirer de conclusions fortes en raison de l'émission filtrée. Par conséquent, je n'ai pas été en mesure de détecter des sources WCCC dans le filament OMC-2/3 en raison de stratégies d'observation non optimales. Des observations de suivi sondant l'enveloppe des proto-étoiles à des échelles entre 1000 et 3000 au, sont obligatoires pour comprendre si des sources WCCC sont présentes dans le filament d'OMC-2/3. Des observations de suivi sont donc prévues soit avec la configuration ACA d'ALMA, soit avec NOEMA, comme je le discuterai dans la Sec. 5.2.1.

L'écoulement de OMC-2 FIR6c-a ou comment se joindre à la partie de manière inattendue

Remarques finales Dans cette thèse, j'ai cherché à déterminer la nature chimique des proto-étoiles de masse solaire situées dans une région analogue à l'environnement de naissance du Soleil et à comprendre si notre Soleil a connu une phase "hot corino" dans sa jeunesse. J'ai également cherché à savoir si l'environnement joue un rôle dans la formation du contenu chimique des proto-étoiles.

J'ai d'abord montré qu'il faut faire attention lorsqu'on cherche à déterminer la nature chimique des proto-étoiles de masse solaire à l'aide d'observations "single-dish". Cet avertissement est particulièrement pertinent avec certaines molécules (petites chaînes carbonées, méthanol) qui peuvent être détectées dans d'autres environnements que les enveloppes protostellaires (par exemple dans les PDRs et les nuages moléculaires). Les proto-étoiles de classe 0 et I sont encore profondément enfouies dans le nuage moléculaire où elles se forment et les échelles sondées par les télescopes "single-dish" sont suffisantes pour englober à la fois l'enveloppe de la proto-étoile et son environnement, ce qui nous empêche de démêler l'émission des différentes composantes.

Ensuite, à l'aide d'observations interférométriques, j'ai trouvé que le taux de détection des "hot corinos" dans la région OMC-2/3 est inférieur à $\sim 50\%$. Par conséquent, ces objets ne semblent pas prédominer dans un environnement tel que le filament OMC-2/3, c'est-à-dire une région fortement illuminée par l'UV. En conséquence, j'ai montré que le contenu chimique des proto-étoiles de masse solaire dans deux régions de formation d'étoiles physiquement différentes est probablement différent.

En conclusion, notre Soleil pourrait avoir été un ancien "hot corino" et l'environnement pourrait jouer un rôle dans le façonnement de la nature chimique des proto-étoiles de masse solaire, mais nous devons augmenter les études statistiques des proto-étoiles de masse solaire dans d'autres analogues à l'environnement de naissance du Soleil pour tirer des conclusions solides.

VII.2 Perspectives

Ma thèse a fourni des éléments clés pour comprendre si notre Soleil était un ancien "hot corino" et si l'environnement est à l'origine de la diversité chimique observée parmi les proto-étoiles de masse solaire. Cependant, la route est encore longue pour arriver à des conclusions décisives sur ces questions. Je présente ci-dessous quelques idées pour continuer sur la voie que j'ai commencé à suivre il y a plus de trois ans.

VII.2.1 Perspectives à court terme

Le WCCC ne fait pas bon ménage avec les PEACHES et les ORANGES Un premier projet est évidemment d'aborder la question de savoir si des sources WCCC sont présentes dans le filament OMC-2/3. Je n'ai pas pu atteindre cet objectif avec le projet ORANGES à cause de la trop haute résolution angulaire. Ce problème a également été signalé dans le relevé de PEACHES (Yang et al. 2021) où ils n'ont détecté que des CCH qui semblent également tracer principalement les parois de la cavité des écoulements moléculaires des proto-étoiles. Le contenu chimique des proto-étoiles OMC-2/3 et Persée est donc caractérisé aux grandes (≤ 10000 au) et petites échelles (~ 100 au) mais

l'échelle intermédiaire (entre 100 et 3000 au) où la zone WCCC peut être présente, n'est pas couverte. Pour comparer de manière approfondie le contenu chimique des proto-étoiles et effectuer un recensement complet des "hot corinos", des WCCC et des objets hybrides dans les deux régions, il est donc obligatoire de combler cette lacune. De plus, comprendre si les sources WCCC et hybrides sont présentes dans le filament OMC-2/3 peut fournir des informations supplémentaires sur l'ancienne nature chimique de notre Soleil. S'il s'avère que les sources WCCC ou hybrides sont plus abondantes que les "hot corinos", alors le fait que notre Soleil ait pu connaître l'une de ces deux phases doit être considéré.

Un suivi du projet ORANGES serait d'observer l'enveloppe des proto-étoiles à des échelles comprises entre 800 et ~ 3000 au, où la zone WCCC est (e.g. [Caselli & Ceccarelli 2012](#); [Sakai & Yamamoto 2013](#)). Pour classer une source comme WCCC, nous devons détecter les longues chaînes carbonées dont la plupart des transitions se produisent à basse fréquence. Une bonne stratégie serait alors d'observer à 3mm. Dans ce contexte, je prévois d'écrire et de soumettre une demande de temps d'observation NOEMA ou ALMA (configuration ACA) en février 2022, la région d'Orion étant observable avec les deux interféromètres.

Falafels corino chauds entouré de pain saveur méthanol : un projet VLA Un autre projet à venir consiste à utiliser l'interféromètre VLA pour faire l'inventaire complet des "hot corino" dans le filament OMC-2/3. Avec le projet ORANGES, j'ai détecté cinq nouveaux "hot corinos" dans cette région. Il y a cependant un paramètre important que nous devons prendre en compte : la poussière. [De Simone et al. \(2020a\)](#) (papier dont je suis co-auteur) ont montré qu'une grande profondeur optique de la poussière pouvait cacher la présence de raies moléculaires associées aux iCOMs et donc la présence d'un "hot corino", dans les longueurs d'onde millimétriques. Avec cela en tête, dans le papier III (Sec. 3.2), j'ai comparé l'intensité intégrée d'une raie de méthanol avec la profondeur optique de la poussière, précédemment dérivée avec l'étude du continuum de la poussière (Sec. 3.1). Je n'ai trouvé aucune corrélation entre les deux paramètres, ce qui suggère fortement que la profondeur optique de la poussière n'est pas le principal paramètre affectant la détection des "hot corinos" dans le filament OMC-2/3. Cependant, je ne peux pas complètement exclure que pour les sources avec une profondeur optique de poussière élevée, un "hot corino" puisse être caché. En outre, un deuxième résultat de l'étude de [De Simone et al. \(2020a\)](#) est que même les raies d'émissions associées aux iCOMs vues dans les longueurs d'onde millimétriques peut être affectée par la poussière. En pratique, nous avons montré que pour le "hot corino" vu dans le millimétriques, les abondances des iCOMs dérivées sont sous-estimées. Par conséquent, si nous voulons détecter avec précision les "hot corinos" et dériver des abondances moléculaires correctes, nous devons déterminer si, et dans quelle mesure, la profondeur optique de la poussière affecte l'émission des raies des iCOMs.

Dans ce contexte, la meilleure stratégie à adopter consiste à effectuer des observations de suivi des proto-étoiles d'OMC-2/3 dans le domaine centimétrique, où la poussière est très probablement, voire sûrement, optiquement mince. En suivant la même stratégie que dans [De Simone et al. \(2020a\)](#), je vise à rédiger une demande de temps VLA pour effectuer des observations du méthanol à 25 GHz. Si la poussière s'avère, au final, être un facteur déterminant dans la recherche de "hot corinos", cela peut avoir plusieurs conséquences. Tout d'abord, si plusieurs nouveaux "hot corinos" sont découverts dans le filament OMC-

2/3, le résultat pourrait renforcer l'hypothèse que notre Soleil a connu une phase de "hot corino" dans sa jeunesse. De plus, cela pourrait augmenter le taux de détection des "hot corinos" dans le filament OMC-2/3 qui se rapprocherait de celui trouvé dans la région de Persée. L'effet suspecté de l'environnement sur la différenciation chimique des proto-étoiles de masse solaire pourrait alors être remis en question.

Comme l'échantillon de sources que j'ai utilisé dans cette thèse comprend 19 proto-étoiles, je vais faire un premier projet pilote avec deux sources sélectionnées. Ces deux sources ont les plus grande profondeurs optiques de poussière dérivées, et ne montrent aucun signe de multiplicité à des échelles aussi basses que 40 au (les observations VLA utilisées pour l'étude du continuum ont une résolution angulaire de $\sim 0.1''$ ou ~ 40 au à la distance de OMC-2/3). Comme je prévois de soumettre la demande de temps VLA pour la configuration C (résolution de $1.2''$ ou ~ 470 au) en février 2022, cela évitera d'enchevêtrer plusieurs sources du même système. Enfin, pour s'assurer que l'inventaire des "hot corinos" du filament OMC-2/3 est complet, il faut cibler chaque proto-étoile de masse solaire située dans la région. Initialement, neuf proto-étoiles de masse solaire ont été ciblées sur la base d'études "single-dish". Avec les capacités croissantes des interféromètres tels que ALMA et NOEMA, plusieurs proto-étoiles vues à l'échelle "single-dish" se sont révélées être des systèmes multiples, comme le montre notamment le projet VANDAM : (Tobin et al. 2016a, 2020). Par conséquent, nous devons compléter l'échantillon de sources que j'ai utilisé dans cette thèse pour réaliser une étude non biaisée de la nature chimique des proto-étoiles à filament d'OMC-2/3.

FAUST: Etude à 50 au de la chimie du système disque/enveloppe des proto-étoiles de type solaire. La différenciation chimique observée dans les proto-étoiles de masse solaire est présente à des échelles comprises entre 100 au et ~ 3000 au. Une telle diversité est-elle également observée dans le système enveloppe/disque interne (~ 50 au) où l'on soupçonne la formation de planets ? Quelles sont les molécules qui passent de l'enveloppe à grande échelle au disque ? Comprendre dans quelle mesure le matériel chimique observé dans l'enveloppe protostellaire et les disques protoplanétaires est transmis aux planètes en formation est important pour le contenu chimique disponible pour les futurs systèmes planétaires. Je suis impliqué dans le grand programme ALMA FAUST (Fifty AU STudy of the inner envelope/disk system of Solar-type protostars ; PIs : S. Yamamoto, C. Ceccarelli, C. Chandler, C. Codella, et N. Sakai) qui vise à répondre aux questions ci-dessus en étudiant le contenu chimique à l'échelle de 50 au d'un échantillon de 13 proto-étoiles de classe 0 et I.

En raison de la variété des sources ciblées (nature chimique et/ou environnement différents), le grand programme FAUST sera utile pour révéler et quantifier la variété des compositions chimiques du système enveloppe/disque des proto-étoiles de classe 0 et I de type solaire. FAUST comprend également des observations VLA. Une première proposition pilote VLA (PI : Claire Chandler) a été mise en place pour étudier les compositions du manteau de glace de deux types chimiquement distincts de proto-étoiles : le "hot corino" NGC1333-IRAS 4A et la source WCCC L1527. Le but sera de dériver un rapport d'abondance relatif fiable de NH_3 et CH_3OH dans les deux sources, afin de comprendre comment la composition des manteaux de glace dépend des conditions physiques établies pendant la phase de noyau pré-stellaire.

En étant impliqué dans FAUST, je cherche à savoir si l'environnement joue un rôle dans la chimie de la source, dans la composition du manteau de glace et, par conséquent,

dans la diversité chimique des proto-étoiles de masse solaire. A cette fin, je suis impliqué dans l'étude de trois des échantillons sources et je m'attaquerai à différents types d'études comme l'ionisation des gaz, la deutération, la complexité moléculaire.

VII.2.2 Perspectives à long terme

Dévoiler le passé chimique de notre Soleil Au cours de ma thèse, j'ai étudié le contenu chimique du filament OMC-2/3. Les résultats que j'ai trouvés soulèvent de nouvelles questions. Le filament OMC-2/3 est-il représentatif des régions de formation d'étoiles massives, et plus particulièrement de régions analogues à l'environnement de naissance du Soleil, ou est-il particulier ? Que se passe-t-il à différentes distances galactiques ? Pour répondre à ces questions, il faut augmenter les statistiques. En définitive, l'objectif est de réaliser des études chimiques non biaisées des proto-étoiles de masse solaire situées dans les régions de formation d'étoiles de forte masse afin d'évaluer leur contenu chimique et, par conséquent, d'apporter de nouveaux éléments clés pour déterminer le passé chimique de notre Soleil.

Où sont situées les régions de formation d'étoiles massive ? [Motte et al. \(2018\)](#) ont répertorié les régions de formation d'étoiles massive les plus proches, c'est-à-dire qui sont situées à moins de 3 kpc. Toutes (à l'exception d'Orion) ont une distance typique ≥ 1 kpc. Les observations sont donc particulièrement difficiles si l'on veut distinguer les proto-étoiles de masse solaire de leur environnement. Avec les améliorations prévues des interféromètres ALMA et NOEMA, et les installations à venir (par exemple, ngVLA, Square Kilometer Array), il sera possible de réaliser des études chimiques similaires et plus complètes comme je l'ai fait pour OMC-2/3.

Le point suivant que nous devons aborder est la région ciblée elle-même. Dans ma thèse, j'ai examiné le filament OMC-2/3 parce qu'il fait partie de la région de formation d'étoiles massive la plus proche, le complexe du nuage moléculaire d'Orion, et qu'il est donc facilement observable avec les installations actuellement disponibles. De plus, en raison des étoiles OB proches qui délimitent la région, j'ai considéré le filament OMC-2/3 comme le meilleur analogue le plus proche de l'environnement de naissance du Soleil, mais pourrait-on trouver un meilleur analogue ? Certainement, oui. Nous devons poursuivre nos recherches afin de déterminer quelles régions sont les plus appropriées pour représenter l'environnement de naissance du Soleil. Il existe plusieurs études qui examinent les propriétés actuelles du système solaire afin de comprendre quel type de groupe stellaire a accueilli notre système solaire au moment de sa formation ([Ida et al. 2000](#); [Kenyon & Bromley 2004](#); [Adams et al. 2006](#); [Mitchell & Stewart 2011](#); [Li & Adams 2015](#); [Dai et al. 2018](#)). Très récemment, [Pfalzner & Vincke \(2020\)](#) ont montré que deux régions, NGC6611 et M44, pouvaient être considérées comme l'équivalent actuel de l'environnement de naissance du Soleil. L'étude repose sur l'hypothèse selon laquelle la limite externe du système solaire a été façonnée par des survols d'étoiles, une explication considérée comme plus probable que la photo-évaporation externe due aux étoiles massives proches (e.g. [Adams et al. 2004](#); [Winter et al. 2020a](#)). Cette hypothèse peut exclure d'autres régions appropriées. [Pfalzner & Vincke \(2020\)](#) indiquent que des considérations cosmo-chimiques doivent être prises en compte pour déterminer plus précisément quel était l'environnement de naissance du Soleil. En effet, le Soleil s'est probablement déplacé vers sa position actuelle depuis un lieu de naissance plus proche du centre galactique ([Wielen et al. 1996](#)). Il est donc crucial de prendre en compte l'évolution chimique cosmique car la composition chimique actuelle du système solaire ne reflète peut-être pas

exactement celle de l'ISM local il y a 4,5 milliards d'année.

En conclusion, il est important de cibler plusieurs régions de formation d'étoiles massives, et à de plus grandes distances pour (1) augmenter la statistique des proto-étoiles étudiées de masse solaire dans les régions de formation d'étoiles massives, et (2) sonder différents environnements (avec différentes métallicités) qui pourraient refléter les conditions chimiques dans lesquelles notre Système solaire s'est formé. Ces études sont obligatoires si nous voulons élucider le passé chimique du Soleil et je souhaite continuer dans cette direction à l'avenir.

Vers les galaxies et au-delà ! Une partie de mon futur plan de recherche concerne les études astrochimiques extra-galactiques car je souhaite élargir mon champ d'expertise.

Au cours de ma thèse, j'ai étudié la nature chimique des proto-étoiles de masse solaire situées dans le filament OMC-2/3 et j'ai comparé le contenu chimique de cette région avec celui du nuage moléculaire de Persée, une région relativement différente. Je souhaite faire de même avec les galaxies : j'aimerais comparer le contenu chimique des galaxies locales et les comparer avec des galaxies plus lointaines. Toutes les galaxies ont-elles les mêmes empreintes chimiques ? Si non, quelle est la cause de cette différence ? Existe-t-il une relation entre la chimie à grande échelle d'une galaxie et son statut évolutif ? Existe-t-il des différences chimiques entre les galaxies à faible et à forte métallicité ? Et plus généralement, comment les galaxies se forment-elles et évoluent-elles ? Quel rôle jouent les flux moléculaires dans l'évolution d'une galaxie et de son contenu stellaire ? Ce sont des questions qui m'intéressent vraiment, et j'ai l'intention de les aborder à l'avenir.

Passer d'une région telle que le filament OMC-2/3 aux galaxies est également assez naturel. Il y a plusieurs similitudes entre le travail que j'ai effectué dans ma thèse et celui dans les galaxies. Par exemple, le filament OMC-2/3 est fortement illuminé par des étoiles OB proches, générant une région de photo-dissociation (PDR) autour du filament. Dans les galaxies, la plupart de l'émission de raies provient des PDR, du gaz quiescent et des régions de formation d'étoiles (Viti 2017). Outre les PDR, nous pouvons également prendre l'exemple des écoulements moléculaires. Celles-ci sont omniprésentes dans les jeunes étoiles et sont très souvent accompagnés de jets et de régions impactées. Ces caractéristiques ont un impact sur l'environnement immédiat des proto-étoiles et peuvent conduire à une chimie riche et/ou à la formation d'amas et, par conséquent, à la formation d'étoiles. C'est également ce que l'on observe dans le cas des écoulements générés par les galaxies (AGN et/ou starburst) : ils peuvent déclencher la formation d'étoiles par des mécanismes de rétroaction directe.

Nous pouvons donc nous attendre à ce que les principaux traceurs moléculaires trouvés dans les différentes composantes des galaxies soient les mêmes que dans les nuages moléculaires galactiques. La région d'Orion est d'ailleurs utilisée comme modèle pour les études extra-galactiques et des liens sont établis entre ce que l'on observe dans Orion, et plus généralement dans les nuages moléculaires galactiques et les galaxies : (Goicoechea et al. 2015; Rybak et al. 2020; Pabst et al. 2021). De manière générale, je pense que les domaines de recherche galactiques et extra-galactiques vont se rejoindre avec les télescopes à venir. Aujourd'hui, il est possible de séparer les différentes composantes principales des galaxies les plus proches pour effectuer des relevés de lignes moléculaires (Nakajima et al. 2018; Watanabe et al. 2019; Scourfield et al. 2020; Martín et al. 2021) mais avec les capacités observationnelles de demain, nous serons en mesure d'étudier les galaxies proches comme nous étudions actuellement les régions lointaines de formation d'étoiles

de forte masse. Je souhaite contribuer à ce nouvel effort.

Pour conclure, nous sommes dans une aire d'observation exceptionnelle, qui nous permet d'aller toujours plus loin dans la recherche de réponses. Il est certain que l'astrochimie a un bel avenir et je souhaite en faire partie.

